School of Earth and Planetary Sciences

Commissioning and First Science Results of the Desert Fireball Network: a Global-Scale Automated Survey for Large Meteoroid Impacts

Hadrien Arnaud Romain Devillepoix

**This thesis is presented for the Degree of
Doctor of Philosophy
of
Curtin University**

September 2018

DECLARATION OF AUTHORSHIP

I, Hadrien Arnaud Romain Devillepoix, declare that to the best of my knowledge and belief that this thesis entitled, *"Commissioning and first science results of the Desert Fireball Network: a global-scale automated survey for large meteoroid impacts "* contains no material previously published by any other person except where due acknowledgement has been made. This thesis contains no material which has been accepted for the award of any other degree or diploma in any university.

The author acknowledges that copyright of published works contained within this thesis resides with the copyright holder(s) of those works. I warrant that I have obtained, where necessary, permission from the copyright owners to use any third-party copyright material reproduced in the thesis, or to use any of my own published work (e.g. journal articles) in which the copyright is held by another party (e.g. publisher, co-author).

Hadrien A. R. Devillepoix

Date: **September 19, 2018**

iv

ABSTRACT

Meteorites that have fallen onto the Earth offer an easy access to a diversity of samples from other bodies in the Solar System. The study of this material is essential to understanding what the building blocks of our Solar System were made of, and what dynamics led to the configuration of planets and small bodies we observe today.

With the aim to systematise the meteorite recovery process and determine the origins of fallen meteorites, networks of wide angle cameras have been set up to monitor the Earth's atmosphere for meteoroid impacts. These observations cover only a very short arc of the meteoroids' orbit but, using the principle of triangulation, relatively precise trajectories can be determined. Such trajectories are capable of pointing to likely source regions, and sometimes predicting meteorite fall positions.

The Desert Fireball Network (DFN) is the first to do so on a very large scale, operating 52 camera stations in Australia, but through international partnerships totalling over 100 systems. This effort currently (2018) covers 4 million km^2 (0.8% of the Earth's surface), and aims to monitor 2% of the Earth by 2020 (7% of the landmass).

The DFN is operated with a limited number of people, and in order to extract the most of the science out of the observations, the data reduction must be automated. This notably includes precisely determining the trajectory of a meteoroid through the atmosphere, as well as characterising its physical parameters. This is essential to making accurate precision of where the meteorites might land, but also to calculate its pre-encounter orbit — where it came from in the

Solar System.

This thesis details some of the innovative methods used in the reduction process. From this, the reduced data are then used to answer key science questions that the DFN can tackle, by looking at the meteoroid population at various mass ranges. Firstly metre-scale impactors are studied. These create bolides visible from orbit, with meteoroid bodies that typically get almost entirely destroyed by our atmosphere. Studying these objects is important because they are at the small mass range of asteroids that can cause severe damage on the ground. Thanks to its very large collecting area, the DFN is uniquely placed to do this, as only very few (< 50) impact the Earth every year. Toward a smaller mass range, a study is then performed on the meteoroid that led to the recovered Dingle Dell meteorite. This decimetre-scale meteoroid is in the typical size-range of most meteorite droppers and is a worked example of the whole reduction process and results, from orbital evolution to the fall positions on the ground. Finally, smaller still, the analysis of a class of objects that is usually to small to be efficiently sampled by fireball networks: cometary debris. Cometary debris in the Taurids Complex is found to contain unusually large objects, which is difficult to reconcile with traditional cometary ejection models.

Astronomy is just like geology, except that East is on the left.

-Joshua E. G. Peek, whilst speaking at ADASS XXV

CONTENTS

LIST OF PUBLICATIONS INCLUDED AS PART OF THIS THESIS

This thesis comprises a collection of research papers that were either published or in preparation at the time of writing this document. The objectives and relationship amongst the different papers are described in the introductory chapter. The final chapter summarises the papers and places them into a wider context. All papers have statement of co-authorships in Appendix A, along with reprints of published papers.

The research papers contained within this thesis that are published in peer-reviewed journals are listed below.

> PAPER 1 − H. A. R. Devillepoix, P. A. Bland, E. K. Sansom, M. C. Towner, M. Cupák, R. M. Howie, B. A. D. Hartig, T. Jansen-Sturgeon, M. A. Cox. Observation of metre-scale impactors by the Desert Fireball Network . *Monthly Notices of the Royal Astronomical Society*, 2019, Volume 483, Issue 4, p. 5166-5178.

> PAPER 2 − H. A. R. Devillepoix, E. K. Sansom, P. A. Bland, M. C. Towner, M. Cupák, R. M. Howie, T. Jansen-Sturgeon, M. A. Cox, B. A. D. Hartig, G. K. Benedix, and J. P. Paxman. The Dingle Dell meteorite: a Halloween treat from the Main Belt. *Meteoritics and Planetary Science*, 2018, Volume 53, Issue 10, p. 2212-2227.

The formatting of each chapter within this thesis may appear to vary, and may differ to the published form based on the requirements and formatting guidelines of each individual journal and this thesis. Due to the nature of this thesis as a composite of peer-reviewed manuscripts, there is a degree of repetition in the introductory sections of each chapter.

LIST OF ADDITIONAL PUBLICATIONS RELEVANT TO THIS THESIS

Several papers were published as co-author during the research period and so do not form part of the main thesis. They are listed below, along with a justification for their inclusion. The contribution of the author to these publications are for the most part the application of various expertise developed throughout the research period (detailed in chapter 2). Reprints may be found in Appendix B.

PAPER A − B. Sicardy, J. Talbot, E. Meza, J. I. B. Camargo, J. Desmars, D. Gault, D. Herald, S. Kerr, H. Pavlov, F. Braga-Ribas, M. Assafin, G. Benedetti-Rossi, A. Dias-Oliveira, A. R. Gomes-Júnior, R. Vieira-Martins, D. Bérard, P. Kervella, J. Lecacheux, E. Lellouch, W. Beisker, D. Dunham, M. Jelınek, R. Duffard, J. L. Ortiz, A. J. Castro-Tirado, R. Cunniffe, R. Querel, P. C. Yock, A. A. Cole, A. B. Giles, K. M. Hill, J. P. Beaulieu, M. Harnisch, R. Jansen, A. Pennell, S. Todd, W. H. Allen, P. B. Graham, B. Loader, G. McKay, J. Milner, S. Parker, M. A. Barry, J. Bradshaw, J. Broughton, L. Davis, **H. Devillepoix**, J. Drummond, L. Field, M. Forbes, D. Giles, R. Glassey, R. Groom, D. Hooper, R. Horvat, G. Hudson, R. Idaczyk, D. Jenke, B. Lade, J. Newman, P. Nosworthy, P. Purcell, P. F. Skilton, M. Streamer, M. Unwin, H. Watanabe, G. L. White, and D. Watson. **Pluto's Atmosphere from the 2015 June 29 Ground-based Stellar Occultation at the Time of the New Horizons Flyby**. *ApJ*, 819:L38, Mar. 2016. doi: 10.3847/2041-8205/819/2/L38.

Reason for inclusion − I participated in the observation campaign to observe the occultation of a star by Pluto, although unsuccessful because of clouds. This work yielded important results on Pluto's atmosphere, putting in context observation of spacecraft New Horizons, that flew by Pluto 2 weeks later (July 2015).

PAPER B − R. M. Howie, J. Paxman, P. A. Bland, M. C. Towner, E. K. Sansom, and **H. A. R. Devillepoix**. **Submillisecond fireball timing using de Bruijn timecodes**. *Meteoritics and Planetary Science*, 52:1669–1682, Aug. 2017. doi: 10.1111/maps.12878.

Reason for inclusion − I performed orbit calculation for manuscript example fireball and assisted with manuscript editing.

PAPER C − R. M. Howie, J. Paxman, P. A. Bland, M. C. Towner, M. Cupák, E. K. Sansom, and **H. A. R. Devillepoix**. **How to build a continental scale fireball camera network**. *Experimental Astronomy*, May 2017. doi: 10.1007/s10686-017-9532-7.

Reason for inclusion − I assisted with data reduction for the Murrili meteorite recovery and assisted with manuscript editing.

PAPER D − LIGO Scientific Collaboration, Virgo Collaboration, Fermi GBM, INTEGRAL, IceCube Collaboration, AstroSat Cadmium Zinc Telluride Imager Team, IPN Collaboration, The Insight-HXMT Collaboration, ANTARES Collaboration, The Swift Collaboration, AGILE Team, The 1M2H Team, The Dark Energy Camera GW-EM Collaboration, the DES Collaboration, The DLT40 Collab-

oration, GRAWITA: GRAvitational Wave Inaf TeAm, The Fermi Large Area Telescope Collaboration, ATCA: Australia Telescope Compact Array, ASKAP: Australian SKA Pathfinder, Las Cumbres Observatory Group, OzGrav, DWF(Deeper, Wider, Faster Program), AST3, and CAASTRO Collaborations, The VINROUGE Collaboration, MASTER Collaboration, J-GEM GROWTH, JAGWAR, Caltech-NRAO, TTU-NRAO, and NuSTAR Collaborations, Pan-STARRS, TheMAXITeam, TZACConsortium, KU Collaboration, NordicOptical Telescope, ePESSTO, GROND, Texas Tech University, SALT Group, TOROS: Transient Robotic Observatory of the SouthCollaboration, The BOOTES Collaboration, MWA: Murchison Widefield Array, The CALET Collaboration, IKI-GW Follow-up Collaboration, H.E.S.S. Collaboration, LOFAR Collaboration, LWA: Long Wavelength Array, HAWC Collaboration, The Pierre Auger Collaboration, ALMA Collaboration, Euro VLBI Team, Pi of the Sky Collaboration, The Chandra Team at McGill University, **DFN: Desert Fireball Network**, ATLAS, High Time Resolution Universe Survey, RIMAS, RATIR, and SKA South Africa/MeerKAT. **3677 authors**, including **H. A. R. Devillepoix**). **Multi-messenger Observations of a Binary Neutron Star Merger**. *ApJ*, 848:L12, Oct. 2017. doi: 10.3847/2041-8213/aa91c9.

Reason for inclusion − The Desert Fireball Network was the only optical instrument on sky a the time gravitational wave event GW170817 happened, putting an upper limit on the brightness of the optical counterpart to the neutron star merger observed by other instruments. I helped collect and reduce the DFN optical images.

PAPER E − I. Andreoni, K. Ackley, J. Cooke, A. Acharyya, J. R. Allison, G. E. Anderson, M. C. B. Ashley, D. Baade, M. Bailes, K. Bannister, A. Beardsley, M. S. Bessell, F. Bian, P. A. Bland, M. Boer, T. Booler, A. Brandeker, I. S. Brown, D. A. H. Buckley, S. W. Chang, D. M. Coward, S. Crawford, H. Crisp, B. Crosse, A. Cucchiara, M. Cupák, J. S. de Gois, A. Deller, **H. A. R. Devillepoix**, D. Dobie, E. Elmer, D. Emrich, W. Farah, T. J. Farrell, T. Franzen, B. M. Gaensler, D. K. Galloway, B. Gendre, T. Giblin, A. Goobar, J. Green, P. J. Hancock, B. A. D. Hartig, E. J. Howell, L. Horsley, A. Hotan, R. M. Howie, L. Hu, Y. Hu, C. W. James, S. Johnston, M. Johnston-Hollitt, D. L. Kaplan, M. Kasliwal, E. F. Keane, D. Kenney, A. Klotz, R. Lau, R. Laugier, E. Lenc, X. Li, E. Liang, C. Lidman, L. C. Luvaul, C. Lynch, B. Ma, D. Macpherson, J. Mao, D. E. McClelland, C. McCully, A. Möller, M. F. Morales, D. Morris, T. Murphy, K. Noysena, C. A. Onken, N. B. Orange, S. Osłowski, D. Pallot, J. Paxman, S. B. Potter, T. Pritchard, W. Raja, R. Ridden- Harper, E. Romero-Colmenero, E. M. Sadler, E. K. Sansom, R. A. Scalzo, B. P. Schmidt, S. M. Scott, N. Seghouani, Z. Shang, R. M. Shannon, L. Shao, M. M. Shara, R. Sharp, M. Sokolowski, J. Sollerman, J. Staff, K. Steele, T. Sun, N. B. Suntzeff, C. Tao, S. Tingay, M. C. Towner, P. Thierry, C. Trott, B. E. Tucker, P. Väisänen, V. V. Krishnan, M. Walker, L. Wang, X. Wang, R. Wayth, M. Whiting, A. Williams, T. Williams, C. Wolf, C. Wu, X. Wu, J. Yang, X. Yuan, H. Zhang, J. Zhou, and H. Zovaro. **Follow Up of GW170817 and Its Electromagnetic Counterpart by Australian-Led Observing Programmes**. *Publications of the Astronomical Society of Australia*, 34:e069, Dec. 2017. doi: 10.1017/pasa.2017.65.

Reason for inclusion − This paper is more detailed account of the observations by Australian teams than in the main paper (D).

PAPER F − X. Zhang, P. Hancock, **H. A. R. Devillepoix**, R. B. Wayth, A. Beardsley, B. Crosse, D. Emrich, T. M. O. Franzen, B. M. Gaensler, L. Horsley, M. Johnston-Hollitt, D. L. Kaplan, D. Kenney, M. F. Morales, D. Pallot, K. Steele, S. J. Tingay, C. M. Trott, M. Walker, A. Williams, C. Wu, J. Ji, and Y. Ma. **Limits on radio emission from meteors using the MWA**. *MNRAS*, 477:5167–5176, July 2018. doi: 10.1093/mnras/sty930.

Reason for inclusion − I coordinated and participated in the multi-instrument, distributed, multi-wavelength, Geminid observation campaign. I brought in expertise for reducing the optical data.

PAPER G − E. K. Sansom, T. Jansen-Sturgeon, M. G. Rutten, **H. A. R. Devillepoix**, P. A. Bland, R. M. Howie, M. A. Cox, M. C. Towner, M. Cupák, , B. A. D. Hartig. **3D meteoroid trajectories**. *Icarus*, Volume 321, p. 388-406, March 2019. doi:10.1016/j.icarus.2018.09.026.

Reason for inclusion − I assisted with data reduction for the fireballs and assisted with manuscript editing.

PAPER H − P. Jenniskens, J. Utas, Q-Z. Yin, R. D. Matson, M. Fries, J. A. Howell, D. Free, J. Albers, Jim and **H. A. R. Devillepoix**, P. A. Bland, A. Miller, R. Verish, L. A. J Garvie, M. E. Zolensky, K. Ziegler, M. E. Sanborn, K. L. Verosub, D. J. Rowland, D. R. Ostrowski, K. Bryson, M. Laubenstein, Q. Zhou, Q-L. Li, X-H. Li, Y.

Liu, G-Q Tang, K. Welten, M. W. Caffee, M. M. M. Meier, A. A. Plant, C. Maden, H. Busemann, M. Granvik, and The Creston Meteorite Consortium. **The Creston, California, meteorite fall and the origin of L chondrites**. *Meteoritics and Planetary Science*, in press, 2019. doi:10.1111/maps.13235.

Reason for inclusion − I did the astrometric calibration, as well as the trajectory and orbit determination.

LIST OF CONFERENCE ABSTRACTS RELEVANT TO THIS THESIS

Several conference contributions were made during the research period though were not peer-reviewed and so do not form part of the main thesis. The titles are listed below, including justification for their inclusion.

CONFERENCE ABSTRACT A − *Transient astronomy with the Desert Fireball Network*. May 2015 at the Hot-Wiring the Transient Universe (Hotwired) conference, Santa Barbara, CA, USA.

> **Reason for inclusion** − This work was presented as a oral presentation at an international conference and outlined the potential to use the expertise of the DFN to build ultra-wide angle observatories distributed all around the world for astronomy purposes. This laid out the basic principles that led to the contribution to the work of LIGO Scientific Collaboration et al., 2017 and Andreoni et al., 2017.

CONFERENCE ABSTRACT B − *A satellite survey with the Desert Fireball Network*. September 2015 at the Australian Space Research Conference (ASRC), Canberra, ACT, Australia.

> **Reason for inclusion** − This work was presented as a oral presentation during the special Space Situational Awareness session, outlying to defence industry actors the potential to use observation techniques and reduction algorithms invented by the Desert Fireball Network to track satellites, laying ground work for

project FireOPAL.

CONFERENCE ABSTRACT C — *Handling Ultra-Wide Field Astronomical Data: the Story of a Continent-Scale Observatory*. November 2015 at the Astronomical Data Analysis Software and Systems (ADASS) conference, Sydney, NSW, Australia.

Reason for inclusion — This work was presented as a oral presentation at an international conference and outlined the work that led to Chapter 2.

CONFERENCE ABSTRACT D — *Status of the Desert Fireball Network*. June 2016 at the International Meteor Conference (IMC), Egmond, the Netherlands.

Reason for inclusion — This work was presented as a oral presentation at an international conference, and outline the work that led to Chapter 2, detailing the methods that led to the successfully recovery of the Murrili meteorite (Devillepoix et al., 2016; Howie et al., 2017a,b) , and subsequently the Dingle Dell meteorite (Devillepoix et al., 2018b).

CONFERENCE ABSTRACT E — *Commissioning the Desert Fireball Network data pipeline*. June 2016 at the Meteoroids conference, ESTEC, Noordwijk, the Netherlands.

Reason for inclusion — This work was presented as an oral presentation at an international conference and outlined the methods detailed in Chapter 2, that led to the work of (Devillepoix et al., 2018a) and Chapter 5.

CONFERENCE ABSTRACT F − *New insights on the Taurid Complex from Desert Fireball Network Observations*. April 2017 at the Asteroids, Comets, Meteors (ACM) conference, Montevideo, Uruguay.

Reason for inclusion − This work was presented as an oral presentation at an international conference and outlined the results in Chapter 5.

CONFERENCE ABSTRACT G − *Fall and Recovery of the Dingle Dell Meteorite*. July 2017 at the Annual Meeting of The Meteoritical Society, Santa Fe, New Mexico, USA.

Reason for inclusion − This work was presented as a poster presentation at an international conference. It explains the methods that led to the successfully recovery of the Dingle Dell meteorite (Devillepoix et al., 2018b).

CONFERENCE ABSTRACT H − *Science outcomes from the Desert Fireball Network*. November 2017 at the Planetary Frontiers workshop, Sydney, NSW, Australia.

Reason for inclusion − This work was presented as an oral presentation at a major planetary science meeting in Australia. It presented the results of Devillepoix et al., 2016,2018b, as well as on-going work on delivery methods of meteorites to Earth.

CONFERENCE ABSTRACT I − *Monitoring the Transient Sky With the Desert Fireball Network*. December 2017, at the Franco-Australian Astrobiology and Exoplanet (FAAbExo) Workshop, Canberra, ACT, Australia.

Reason for inclusion − This work was presented as a oral presentation at an international conference and outlined the potential to use the expertise of the DFN to build ultra-wide angle observatories distributed all around the world for astronomy purposes. This showed the DFN contribution to transient astronomy, published by LIGO Scientific Collaboration et al., 2017 and Andreoni et al., 2017.

Conference Abstract J − *Towards a Global Fireball Observatory: new fireball observation hardware*. September 2018 at the International Meteor Conference (IMC), Pezinok, Slovakia.

Reason for inclusion − This presentation layed out the plan for the future Global Fireball Observatory, and also discussed the results of LIGO Scientific Collaboration et al,. 2017, Andreoni et al., 2017, and Howie et al., 2017a).

LIST OF FIGURES

LIST OF TABLES

LIST OF ABBREVIATIONS USED IN THIS THESIS

AU	**A**stronomical **U**nit
CAMS	**C**ameras for **A**llsky **M**eteor **S**urveillance
CCD	**C**harge-**c**oupled **D**evice
CMOS	**C**omplementary **M**etal-**O**xide-**S**emiconductor
Dec	**Dec**lination
DFN	**D**esert **F**ireball **N**etwork
DSLR	**D**igital **S**ingle-**L**ens **R**eflex camera
ECEF	**E**arth **C**entred, **E**arth **F**ixed reference system
ECI	**E**arth **C**entred **I**nertial reference system
ENU	local **E**ast, **N**orth, **U**p reference system
ESA	**E**uropean **S**pace **A**gency
FITS	**F**lexible **I**mage **T**ransport **S**ystem
FoV	**F**ield **o**f **V**iew
GFO	**G**lobal **F**ireball **O**bservatory
GNSS	**G**lobal **N**avigation **S**atellite **S**ystem
GPS	**G**lobal **P**ositioning **S**ystem, a special type of GNSS
IAU	**I**nternational **A**stronomical **U**nion
LC	**L**iquid **C**rystal
LOS	**L**ine **o**f **S**ight
mag	Astronomical **mag**nitude
MORP	**M**eteorite **O**bservation and **R**ecovery **P**roject
NASA	**N**ational **A**eronautics and **S**pace **A**dministration
PSF	**P**oint-**S**pread **F**unction

RA	**R**ight **A**scension
SNR	**S**ignal-to-**N**oise **R**atio
SSA	**S**pace **S**ituational **A**wareness
TDB	**B**arycentric **D**ynamical **T**ime
TNT	**T**ri**nit**rotoluene energy equivalent, $1\,\mathrm{kT\,TNT} = 4.184 \times 10^{12}$ Joules
UCAC	**U**nited **S**tates **N**aval **O**bservatory **CCD** **A**strograph **C**atalogs
USG	**U**nited **S**tates **G**overnment
UT	**U**niversal **T**ime
UTC	**C**oordinated **U**niversal **T**ime
WCS	**W**orld **C**oordinate **S**ystem

CHAPTER 1

INTRODUCTION

1.1. FORMATION OF THE SOLAR SYSTEM

One of the main objectives of planetary science is to understand what was happening in the protoplanetary disk, and how the objects orbiting our Sun formed and evolved. These objects include planets and large asteroids; however the study of planetary rocks yields limited information about what the building blocks of our Solar System were like, because most of the cosmo-chemical history has been lost through secondary processes including differentiation of these larger bodies. Smaller bodies on the other hand have been much less recycled, making them good test candidates for study of the primitive disk composition.

Small, non-differentiated, Solar System bodies preserve these records. Most of our solar system has been has been stable for the better part of its lifetime, and it is unlikely to evolve significantly before the Sun turns into a red giant (Laskar and Gastineau, 2009). The stability of the orbits are in principle a powerful way to study where things formed and what was the gas/dust composition like in different parts of the disk. However there is some evidence that shows that the

planetesimals were reshuffled early-on (small Mars, late heavy bombardment, asteroid radial mixing, high inclinations and eccentricities in the main belt etc.), and some of the mass was lost (ejected). Mapping the composition of small bodies left today is nevertheless the key to solving this difficult inverse problem.

Direct samples obtained from various classes of such objects are key to putting strong constraints on where and how primordial planetesimals formed. One of the ways to study these samples directly is to commission a sample return mission to visit a Solar System object and return material from these bodies. Sample return mission like Apollo to the Moon, Stardust to comet Wild 2 (Brownlee et al., 2006), and Hayabusa to S-type asteroid Itokawa (Nakamura et al., 2011), have brought back a variety of samples. These have not only yielded important results shortly after they came back to Earth, but continue to be studied decades later as methods of analyses and instruments improve.

When sample return to Earth is particularly difficult and/or costly, remote laboratories like Rosetta on comet 67P (Glassmeier et al., 2007), and the Mars rovers have been built to study the rocks in situ. These endeavours are costly, and have not gone far beyond Near-Earth space because of delta-v issues. Analyses are limited to the technology available at the time of the mission design and are non-repeatable.

Another, much cheaper, way to study such primitive samples is to look at material readily available on Earth — *meteorites*. Over 60,000 meteorites have been recovered and identified as such. These are incredibly valuable samples from a very wide range of parent bodies, from primitive main belt material to even samples of the Moon and Mars. Unfortunately $< 1\%$ have known origins (Bland et al., 2012) and without this spatial context, the story is not complete.

1.2. RECOVERING METEORITES WITH ORBITS

To determine where meteorites come from and better understand the physical phenomena associated with the entry of a meteoroid in the atmosphere, a network of cameras was built in the 1950's in Czechoslovakia (Ceplecha, 1961). Although this was not the first systematic effort to observe meteors to derive trajectories and orbits, it was the first to do so with the aim of surveying a large enough collecting area to have a reasonable chance of catching a rare meteorite dropping fireballs on two or more stations, to allow triangulation. These efforts paid off in 1959, with the recovery of the Příbram meteorite (ordinary chondrite) (Ceplecha, 1961), with its pre-encounter orbit pointing to a main belt origin. Following this, the Czechoslovakian network was expanded to cover a larger area in central Europe. Similar efforts were initiated elsewhere: the Prairie network in the USA starting in the 1960's, and the Meteorite Observation and Recovery Project (MORP) in Canada starting in the 70's (Halliday, 1973), both yielding one meteorite each in their 10-15 years of operation. The next Czech network success only came more than 40 years later with the Neuschwanstein meteorite (Spurný et al., 2003).

This relatively low yield is not caused by the rareness of meteorite falls — MORP observed 46 fireballs with $> 100\,\mathrm{g}$ terminal masses (Halliday et al., 1996) — but likely linked with the difficulty of finding meteorites in temperate climates, where the meteorites' typical black fusion crust competes with relatively dark landscapes, and quickly become undistinguishable from normal rocks because of weathering.

These considerations led Bland (2004) to set up similar observation hardware in the Australian Desert starting in 2005, rapidly returning results in 2007 and 2010 (Bland et al., 2009; Spurný et al., 2012a). In 2012, thanks to advances in digital camera technology, the Desert Fireball Network started designing a new

camera system that would be cheap and reliable enough to be deployed on a continental scale (0.6% Earth covered in 2016). It started science operations in November 2014, and quickly gave results in the years that followed: Murrili in 2015 (Devillepoix et al., 2016), and Dingle Dell in 2016 (Devillepoix et al., 2018).

Following these successes, the Global Fireball Observatory collaboration was formed in 2017, partnering up 14 research institutions in 6 different countries (Australia, Saudi Arabia, Morocco, United Kingdom, Canada, and USA) with the goal to cover 2% of the Earth by 2020. This collaboration aims to sample as many types of meteorites as possible, with the ultimate aim of mapping the source region for each meteorite type. It is expected that a lot of ordinary chondrites will be recovered; but each new specimen of an already sampled type adds statistical robustness to source region linking, primarily because the models that can map a near-earth object's osculating orbital elements to a likely source regions, are statistical in nature.

This can inform us about NEO populations and asteroid families and possibly to the identification of debris streams. However, to get a good statistical assessment of incoming material, the biases associated meteorite delivery must be understood.

1.2.1. BIASES ASSOCIATED WITH METEORITES SAMPLING

A class of small solar system bodies that is easily accessible for study are the Near-Earth Objects (NEOs); these include comets, asteroids, meteoroids, and, by extension, meteorites.

ARE NEOS REPRESENTATIVE OF THE SOLAR SYSTEM SMALL BODY POPULATION?

 NEOs are broadly defined as small bodies that have a perihelion distance < 1.3 AU. Being constantly swept by interactions with planets, this region

of orbital space is not stable. The objects that live there have a high chance of falling into the Sun, being ejected, or more rarely hitting a planet, all on relatively small timescales (a few million years). Therefore this population must be continuously replenished. Bottke et al. (2002) has shown that the largest source of NEO replenishment is from the asteroid main belt (94%), while the rest likely comes from Jupiter Family Comets (JFC). This means that NEOs are representative of some regions of the main belt and the comet population, but not of dynamically stable regions like the Jovian Trojans or trans-Neptunian objects, for example.

DO NEOS SAMPLE THE MAIN ASTEROID BELT EQUITABLY?

Wisdom (1985) and Morbidelli et al. (1994) have shown that orbital resonances are efficient delivery routes for main belt asteroid to near-Earth space, by increasing eccentricities. Asteroids occasionally collide, and the fragments find their way into these resonant parts of orbital space through non-gravitational forces, namely the Yarkovsky effect. This causes a slow drift in semi-major axis (a), depending on the physical characteristics of the body (Vokrouhlicky and Farinella, 1998). The closer the parent body is to a resonance in orbital space (in (a) for mean-motion resonances, or (a, i) for secular ones), the faster the collisional family starts injecting the smallest members into this resonance.

A relatively well-determined example of this is the L-chondrite forming event 466 million years ago, known to have delivered a large number of meteorites to Earth, starting less than a million years after it happened (Heck et al., 2004, 2008), through the 5:2 mean-motion resonance with Jupiter (2.82 AU) (Nesvorný et al., 2009). Heck et al. (2017) provide additional evidence of changes in the meteorite flux over geological time scales. This shows how efficient the meteorite delivery process can be, how collisions in the main asteroid belt can then rapidly affect the near-Earth environment, but this also inherently means that asteroids living far from resonance are poorly represented in the NEO population.

DOES THE KILOMETRE-SIZE NEO POPULATION SCALE TO OBJECTS REGULARLY HITTING THE TOP OF EARTH'S ATMOSPHERE?

Kilometre-size NEOs are big enough to be spectrally surveyed by telescopes, however the composition of this population is not exactly the same for smaller asteroids, as the Yarkovsky effect on semi-major axis drifts is size dependant. This is illustrated by the V-shape identification technique of Bolin et al. (2017). Because of this drift, the effects of a main belt collision will result in smaller objects being pushed more rapidly into resonances than larger material. This is outlined by de-biased observational evidence in the steady-state NEO model of Granvik et al. (2016, 2018), where each source region contributes in different proportions to the NEO population depending on size. This effect was also hinted by Vernazza et al. (2008), when they noticed that $\sim 1/3^{rd}$ of the NEO population bright enough to be spectrally studied are LL-chondrite compatible asteroids, while LL chondrites only represent 8% of meteorite falls.

ARE METEORITES REPRESENTATIVE OF THE DECIMETRE TO METRE-SCALE NEO POPULATION?

Even if the compositional distribution of material at the top of the atmosphere was uniform across all sizes, the Earth's atmosphere operates a severe selection bias of what material makes it to the ground. The orbital speed accelerated by a powerful gravity well, combined with a relatively dense atmosphere, impose ram pressures of several megapascals to any meteoroid trying to survive entry and be found as a macroscopic meteorite.

There is an environmental bias due to terrestrial weathering and erosional processes. This is governed by parameters such as macroscopic structure, composition, and porosity. Understanding such parameters in the decimetre/metre scale can yield practical insights of how slightly larger — potentially hazardous— objects might behave when entering the Earth's atmosphere.

In the context of a coordinated effort to observe meteorite falls to recover

meteorites, being able to derive these physical parameters from fireball observations has a practical application: can we recognise and recover meteoroids that survive entry, even when the fireball observation look unfavourable (evidence of destruction by large amounts of fragmentation, low penetrating depth in the atmosphere)? By looking at characteristics of historical events, Brown et al. (2013) attempt to derive entry parameters criteria for which meteorite survivability is possible.

Understanding these issues is essential to limit the introduction of human biases in the meteorite recovery process. A practical example is the impact of F-type asteroid 2008 TC3 and the recovery of the resulting Almahata Sitta meteorites (Jenniskens et al., 2009). With the asteroid getting destroyed at $\sim 37\,$km altitude, no material was expected to have survived entry. More than 99% of the body was indeed destroyed, but the meteorites that survived proved to be invaluable samples from a rare class of meteorites (mainly anomalous ureilites). The extra attention this event got, because of the size of the asteroid and the fact that it was detected in space before impact, arguably played in favour for a successful meteorite search campaign. To some extent, similar events played in the favour of other non ordinary chondrite falls recoveries. Three of these events were strongly followed up because of the size of the incoming body, the media attention the fireball created, but not because a detailed analysis of bright flight data determined that meteorites had survived: Tagish Lake (Brown et al., 2000), Sutter's Mill (Jenniskens et al., 2012), and Maribo (Spurný et al., 2013). Bunburra Rockhole (Bland et al., 2009; Spurný et al., 2012b) was observed with dedicated instruments, and it was prioritised for searching because of its unusual Aten orbit, not solely on its entry parameters (final height, speed, and mass).

Apart from Bunburra Rockhole, the compiled data by Borovička et al. (2015) shows that the "dedicated search from detailed computation of trajectory from fireball observations" category of has only yielded ordinary chondrites. Con-

sidering the small number of cases, this is not statistically significant, especially considering that 90% of falls are ordinary chondrites anyway. As fireball networks aiming to find meteorites increase the number of recoveries, this should be thought about nonetheless.

1.2.2. BEYOND METEORITES

Not every observed fireball results in a meteorite and these samples are only part of the picture. As seen above, the meteorites that make it to the ground are strongly selected by the atmosphere, but all the other recorded meteoroid impacts (Fig. 2.18) have a story to tell.

The meteoroid orbit population observed can be used to yield insights on the NEO population models at the centimetre to metre scale. At this size range, the reference results remain those from MORP (Halliday et al., 1996). The DFN is in a unique position to put strong constraints on the flux density of material hitting the Earth, and where this material comes from.

The atmosphere can also be used as a measurement tool for probing the macroscopic structure of meteoroids. Far from being uniform, these bodies experience fragmentation under several orders of magnitude of dynamic pressure less than the tensile strengths of meteorites on the ground.

1.3. THESIS STRUCTURE

This work aims to cover the methodologies used to reduce fireball data and tackle some of the science results that this type of instrument can help answer. The work is decomposed into four main chapters covering the main aims of this thesis.

Chapter 2— An automated data processing pipeline for the Desert Fireball Network is a technical chapter devoted to the automated data reduction pipeline of the Desert Fireball Network. Although many parts of this pipeline have been assigned to other team members, I have played a fundamental role in integrating these to produce useable results. This chapter explains in depth the algorithms and codes that I have developed for this purpose as well as for the astrometric and photometric calibration of fireball data.

The following chapters present the first science results from DFN data, they relate to the observation of different sizes of meteoroids, from very bright bolides caused by small asteroids, to small fragile cometary dust.

Chapter 3— Observation of metre-scale impactors by the Desert Fireball Network (Devillepoix et al., 2019) details the two biggest asteroid impacts the DFN has observed, with a typical mass of $10^3 - 10^4$ kg. These asteroids are the only metre-scale objects observed by the DFN from the beginning of science operations in 2014 to mid-2018.

Chapter 4— The Dingle Dell meteorite: a Halloween treat from the Main Belt (Devillepoix et al., 2018) is inherently linked with the main science goal of the DFN: recovering meteorites with orbits. The typical meteorite droppers are $10^1 - 10^2$ kg at the top of the atmosphere. Chapter 4 is the complete analysis of the fall of the Dingle Dell meteorite, from pre-encounter orbit to the calculation of where the meteorite landed on the ground — a worked application of the data processing pipeline.

Chapter 5— Taurid meteoroid stream 628: a reservoir of large impactors is an example of how the DFN can be used for meteor shower science. Although the DFN observes meteor showers, the sensors are not optimised for this purpose. In this case we study the return of a branch of

the Southern Taurids shower, one of the only cases an instrument dedicated to observing much brighter fireballs gets a significant number of detections (typical mass observed $10^{-3} - 10^0$ kg). Interestingly, the most spectacular return of a meteor shower identifiable in the historical MORP dataset (Halliday et al., 1996) was also from these Southern Taurids, in 1981.

The development of a streamlined data reduction pipeline has lead to over 1000 orbits of fireballs for the DFN to analyse in less than 4 years of science operations. I have investigated the suitability of the DFN to fulfil its main meteorite recovery goal, as well as its versatility to answer different science questions about other types of meteoroids.

1.4. REFERENCES

P. A. Bland. Fireball cameras: The Desert Fireball Network. *Astronomy and Geophysics*, 45:5.20–5.23, Oct. 2004. doi: 10.1046/j.1468-4004.2003.45520.x.

P. A. Bland, P. Spurný, M. C. Towner, A. W. R. Bevan, A. T. Singleton, W. F. Bottke, R. C. Greenwood, S. R. Chesley, L. Shrbený, J. Borovička, Z. Ceplecha, T. P. McClafferty, D. Vaughan, G. K. Benedix, G. Deacon, K. T. Howard, I. A. Franchi, and R. M. Hough. An Anomalous Basaltic Meteorite from the Innermost Main Belt. *Science*, 325:1525, Sept. 2009. doi: 10.1126/science. 1174787.

P. A. Bland, P. Spurný, A. W. R. Bevan, K. T. Howard, M. C. Towner, G. K. Benedix, R. C. Greenwood, L. Shrbený, I. A. Franchi, G. Deacon, J. Borovička, Z. Ceplecha, D. Vaughan, and R. M. Hough. The Australian Desert Fireball Network: a new era for planetary science. *Australian Journal of Earth Sciences*, 59:177–187, Mar. 2012. doi: 10.1080/08120099.2011.595428.

B. T. Bolin, M. Delbo, A. Morbidelli, and K. J. Walsh. Yarkovsky V-shape

identification of asteroid families. Icarus, 282:290–312, Jan. 2017. doi: 10.1016/ j.icarus.2016.09.029.

J. Borovička, P. Spurný, and P. Brown. *Small Near-Earth Asteroids as a Source of Meteorites*, pages 257–280. University of Arizona Press, 2015. doi: 10.2458/ azu_uapress_9780816532131-ch014.

W. F. Bottke, A. Morbidelli, R. Jedicke, J.-M. Petit, H. F. Levison, P. Michel, and T. S. Metcalfe. Debiased Orbital and Absolute Magnitude Distribution of the Near-Earth Objects. Icarus, 156:399–433, Apr. 2002. doi: 10.1006/icar.2001. 6788.

P. Brown, V. Marchenko, D. E. Moser, R. Weryk, and W. Cooke. Meteorites from meteor showers: A case study of the Taurids. *Meteoritics and Planetary Science*, 48:270–288, Feb. 2013. doi: 10.1111/maps.12055.

P. G. Brown, A. R. Hildebrand, M. E. Zolensky, M. Grady, R. N. Clayton, T. K. Mayeda, E. Tagliaferri, R. Spalding, N. D. MacRae, E. L. Hoffman, D. W. Mittlefehldt, J. F. Wacker, J. A. Bird, M. D. Campbell, R. Carpenter, H. Gingerich, M. Glatiotis, E. Greiner, M. J. Mazur, P. J. McCausland, H. Plotkin, and T. Rubak Mazur. The Fall, Recovery, Orbit, and Composition of the Tagish Lake Meteorite: A New Type of Carbonaceous Chondrite. *Science*, 290: 320–325, Oct. 2000. doi: 10.1126/science.290.5490.320.

D. Brownlee, P. Tsou, J. Aléon, C. M. O. D. Alexander, T. Araki, S. Bajt, G. A. Baratta, R. Bastien, P. Bland, P. Bleuet, J. Borg, J. P. Bradley, A. Brearley, F. Brenker, S. Brennan, J. C. Bridges, N. D. Browning, J. R. Brucato, E. Bullock, M. J. Burchell, H. Busemann, A. Butterworth, M. Chaussidon, A. Cheuvront, M. Chi, M. J. Cintala, B. C. Clark, S. J. Clemett, G. Cody, L. Colangeli, G. Cooper, P. Cordier, C. Daghlian, Z. Dai, L. D'Hendecourt, Z. Djouadi, G. Dominguez, T. Duxbury, J. P. Dworkin, D. S. Ebel, T. E. Economou, S. Fakra, S. A. J. Fairey, S. Fallon, G. Ferrini, T. Ferroir, H. Fleckenstein, C. Floss, G. Flynn, I. A. Franchi, M. Fries, Z. Gainsforth, J. P. Gallien, M. Genge, M. K.

Gilles, P. Gillet, J. Gilmour, D. P. Glavin, M. Gounelle, M. M. Grady, G. A. Graham, P. G. Grant, S. F. Green, F. Grossemy, L. Grossman, J. N. Grossman, Y. Guan, K. Hagiya, R. Harvey, P. Heck, G. F. Herzog, P. Hoppe, F. Hörz, J. Huth, I. D. Hutcheon, K. Ignatyev, H. Ishii, M. Ito, D. Jacob, C. Jacobsen, S. Jacobsen, S. Jones, D. Joswiak, A. Jurewicz, A. T. Kearsley, L. P. Keller, H. Khodja, A. L. D. Kilcoyne, J. Kissel, A. Krot, F. Langenhorst, A. Lanzirotti, L. Le, L. A. Leshin, J. Leitner, L. Lemelle, H. Leroux, M.-C. Liu, K. Luening, I. Lyon, G. MacPherson, M. A. Marcus, K. Marhas, B. Marty, G. Matrajt, K. Mc-Keegan, A. Meibom, V. Mennella, K. Messenger, S. Messenger, T. Mikouchi, S. Mostefaoui, T. Nakamura, T. Nakano, M. Newville, L. R. Nittler, I. Ohnishi, K. Ohsumi, K. Okudaira, D. A. Papanastassiou, R. Palma, M. E. Palumbo, R. O. Pepin, D. Perkins, M. Perronnet, P. Pianetta, W. Rao, F. J. M. Rietmeijer, F. Robert, D. Rost, A. Rotundi, R. Ryan, S. A. Sandford, C. S. Schwandt, T. H. See, D. Schlutter, J. Sheffield-Parker, A. Simionovici, S. Simon, I. Sitnitsky, C. J. Snead, M. K. Spencer, F. J. Stadermann, A. Steele, T. Stephan, R. Stroud, J. Susini, S. R. Sutton, Y. Suzuki, M. Taheri, S. Taylor, N. Teslich, K. Tomeoka, N. Tomioka, A. Toppani, J. M. Trigo-Rodríguez, D. Troadec, A. Tsuchiyama, A. J. Tuzzolino, T. Tyliszczak, K. Uesugi, M. Velbel, J. Vellenga, E. Vicenzi, L. Vincze, J. Warren, I. Weber, M. Weisberg, A. J. Westphal, S. Wirick, D. Wooden, B. Wopenka, P. Wozniakiewicz, I. Wright, H. Yabuta, H. Yano, E. D. Young, R. N. Zare, T. Zega, K. Ziegler, L. Zimmerman, E. Zinner, and M. Zolensky. Comet 81P/Wild 2 Under a Microscope. *Science*, 314: 1711, Dec. 2006. doi: 10.1126/science.1135840.

Z. Ceplecha. Multiple fall of Příbram meteorites photographed. 1. Double-station photographs of the fireball and their relations to the found meteorites. *Bulletin of the Astronomical Institutes of Czechoslovakia*, 12:21, 1961.

H. A. R. Devillepoix, P. A. Bland, M. C. Towner, M. Cupák, E. K. Sansom, T. Jansen-Sturgeon, R. M. Howie, J. Paxman, and B. A. D. Hartig. Status of the Desert Fireball Network. In A. Roggemans and P. Roggemans, editors,

International Meteor Conference Egmond, the Netherlands, 2-5 June 2016, pages 60–62, Jan. 2016.

H. A. R. Devillepoix, E. K. Sansom, P. A. Bland, M. C. Towner, M. CupáK, R. M. Howie, T. Jansen-Sturgeon, M. A. Cox, B. A. D. Hartig, G. K. Benedix, and J. P. Paxman. The Dingle Dell meteorite: A Halloween treat from the Main Belt. *Meteoritics and Planetary Science*, 53:2212–2227, Oct. 2018. doi: 10.1111/maps.13142.

H. A. R. Devillepoix, P. A. Bland, E. K. Sansom, M. C. Towner, M. Cupák, R. M. Howie, B. A. D. Hartig, T. Jansen-Sturgeon, and M. A. Cox. Observation of metre-scale impactors by the Desert Fireball Network. MNRAS, 483:5166–5178, Mar 2019. doi: 10.1093/mnras/sty3442.

K.-H. Glassmeier, H. Boehnhardt, D. Koschny, E. Kührt, and I. Richter. The Rosetta Mission: Flying Towards the Origin of the Solar System. Space Sci. Rev., 128:1–21, Feb. 2007. doi: 10.1007/s11214-006-9140-8.

M. Granvik, A. Morbidelli, R. Jedicke, B. Bolin, W. F. Bottke, E. Beshore, D. Vokrouhlický, M. Delbò, and P. Michel. Super-catastrophic disruption of asteroids at small perihelion distances. Nature, 530:303–306, Feb. 2016. doi: 10.1038/nature16934.

M. Granvik, A. Morbidelli, R. Jedicke, B. Bolin, W. F. Bottke, E. Beshore, D. Vokrouhlický, D. Nesvorný, and P. Michel. Debiased orbit and absolute-magnitude distributions for near-Earth objects. Icarus, 312:181–207, Sept. 2018. doi: 10.1016/j.icarus.2018.04.018.

I. Halliday. Photographic Fireball Networks. *NASA Special Publication*, 319:1, 1973.

I. Halliday, A. A. Griffin, and A. T. Blackwell. Detailed data for 259 fireballs from the Canadian camera network and inferences concerning the influx of

large meteoroids. *Meteoritics and Planetary Science*, 31:185–217, Mar. 1996. doi: 10.1111/j.1945-5100.1996.tb02014.x.

P. R. Heck, B. Schmitz, H. Baur, A. N. Halliday, and R. Wieler. Fast delivery of meteorites to Earth after a major asteroid collision. Nature, 430:323–325, July 2004. doi: 10.1038/nature02736.

P. R. Heck, B. Schmitz, H. Baur, and R. Wieler. Noble gases in fossil micrometeorites and meteorites from 470 Myr old sediments from southern Sweden, and new evidence for the L-chondrite parent body breakup event. *Meteoritics and Planetary Science*, 43:517–528, Mar. 2008. doi: 10.1111/j.1945-5100.2008. tb00669.x.

P. R. Heck, B. Schmitz, W. F. Bottke, S. S. Rout, N. T. Kita, A. Cronholm, C. Defouilloy, A. Dronov, and F. Terfelt. Rare meteorites common in the Ordovician period. *Nature Astronomy*, 1:0035, Jan. 2017. doi: 10.1038/s41550-016-0035.

P. Jenniskens, M. H. Shaddad, D. Numan, S. Elsir, A. M. Kudoda, M. E. Zolensky, L. Le, G. A. Robinson, J. M. Friedrich, D. Rumble, A. Steele, S. R. Chesley, A. Fitzsimmons, S. Duddy, H. H. Hsieh, G. Ramsay, P. G. Brown, W. N. Edwards, E. Tagliaferri, M. B. Boslough, R. E. Spalding, R. Dantowitz, M. Kozubal, P. Pravec, J. Borovička, Z. Charvat, J. Vaubaillon, J. Kuiper, J. Albers, J. L. Bishop, R. L. Mancinelli, S. A. Sandford, S. N. Milam, M. Nuevo, and S. P. Worden. The impact and recovery of asteroid 2008 TC$_3$. Nature, 458: 485–488, Mar. 2009. doi: 10.1038/nature07920.

P. Jenniskens, M. D. Fries, Q.-Z. Yin, M. Zolensky, A. N. Krot, S. A. Sandford, D. Sears, R. Beauford, D. S. Ebel, J. M. Friedrich, K. Nagashima, J. Wimpenny, A. Yamakawa, K. Nishiizumi, Y. Hamajima, M. W. Caffee, K. C. Welten, M. Laubenstein, A. M. Davis, S. B. Simon, P. R. Heck, E. D. Young, I. E. Kohl, M. H. Thiemens, M. H. Nunn, T. Mikouchi, K. Hagiya, K. Ohsumi, T. A. Cahill, J. A. Lawton, D. Barnes, A. Steele, P. Rochette, K. L. Verosub, J. Gattacceca, G. Cooper, D. P. Glavin, A. S. Burton, J. P. Dworkin, J. E. Elsila,

S. Pizzarello, R. Ogliore, P. Schmitt-Kopplin, M. Harir, N. Hertkorn, A. Verchovsky, M. Grady, K. Nagao, R. Okazaki, H. Takechi, T. Hiroi, K. Smith, E. A. Silber, P. G. Brown, J. Albers, D. Klotz, M. Hankey, R. Matson, J. A. Fries, R. J. Walker, I. Puchtel, C.-T. A. Lee, M. E. Erdman, G. R. Eppich, S. Roeske, Z. Gabelica, M. Lerche, M. Nuevo, B. Girten, and S. P. Worden. Radar-Enabled Recovery of the Sutter's Mill Meteorite, a Carbonaceous Chondrite Regolith Breccia. *Science*, 338:1583, Dec. 2012. doi: 10.1126/science.1227163.

J. Laskar and M. Gastineau. Existence of collisional trajectories of Mercury, Mars and Venus with the Earth. Nature, 459:817–819, June 2009. doi: 10.1038/nature08096.

A. Morbidelli, R. Gonczi, C. Froeschle, and P. Farinella. Delivery of meteorites through the nu$_6$ secular resonance. A&A, 282:955–979, Feb. 1994.

T. Nakamura, T. Noguchi, M. Tanaka, M. E. Zolensky, M. Kimura, A. Tsuchiyama, A. Nakato, T. Ogami, H. Ishida, M. Uesugi, T. Yada, K. Shirai, A. Fujimura, R. Okazaki, S. A. Sandford, Y. Ishibashi, M. Abe, T. Okada, M. Ueno, T. Mukai, M. Yoshikawa, and J. Kawaguchi. Itokawa Dust Particles: A Direct Link Between S-Type Asteroids and Ordinary Chondrites. *Science*, 333:1113, Aug. 2011. doi: 10.1126/science.1207758.

D. Nesvorný, D. Vokrouhlický, A. Morbidelli, and W. F. Bottke. Asteroidal source of L chondrite meteorites. Icarus, 200:698–701, Apr. 2009. doi: 10.1016/j.icarus.2008.12.016.

P. Spurný, J. Oberst, and D. Heinlein. Photographic observations of Neuschwanstein, a second meteorite from the orbit of the Příbram chondrite. Nature, 423:151–153, May 2003. doi: 10.1038/nature01592.

P. Spurný, P. A. Bland, J. Borovička, M. C. Towner, L. Shrbený, A. W. R. Bevan, and D. Vaughan. The Mason Gully Meteorite Fall in SW Australia: Fireball Trajectory, Luminosity, Dynamics, Orbit and Impact Position from

Photographic Records. In *Asteroids, Comets, Meteors 2012*, volume 1667 of *LPI Contributions*, page 6369, May 2012a.

P. Spurný, P. A. Bland, L. Shrbený, J. Borovička, Z. Ceplecha, A. Singelton, A. W. R. Bevan, D. Vaughan, M. C. Towner, T. P. McClafferty, R. Toumi, and G. Deacon. The Bunburra Rockhole meteorite fall in SW Australia: fireball trajectory, luminosity, dynamics, orbit, and impact position from photographic and photoelectric records. *Meteoritics and Planetary Science*, 47: 163–185, Feb. 2012b. doi: 10.1111/j.1945-5100.2011.01321.x.

P. Spurný, J. Borovička, H. Haack, W. Singer, K. Jobse, and D. Keuer. Trajectory and orbit of the Maribo CM2 meteorite from optical, photoelectric and radar records. In *Meteoroids 2013*, 2013.

P. Vernazza, R. P. Binzel, C. A. Thomas, F. E. DeMeo, S. J. Bus, A. S. Rivkin, and A. T. Tokunaga. Compositional differences between meteorites and near-Earth asteroids. Nature, 454:858–860, Aug. 2008. doi: 10.1038/nature07154.

D. Vokrouhlicky and P. Farinella. Orbital evolution of asteroidal fragments into the nu_6 resonance via Yarkovsky effects. A&A, 335:351–362, July 1998.

J. Wisdom. Meteorites may follow a chaotic route to Earth. Nature, 315:731–733, June 1985. doi: 10.1038/315731a0.

CHAPTER 2

AN AUTOMATED DATA PROCESSING PIPELINE FOR THE DESERT FIREBALL NETWORK

Hadrien A. R. Devillepoix[a]

[a]School of Earth and Planetary Sciences, Curtin University, GPO Box U1987, Bentley, Perth, WA 6845, Australia

2.1. INTRODUCTION

2.1.1. SCIENCE REQUIREMENTS

The primary science goals of the DFN and its data reduction pipeline are:

- Getting fall positions of meteorites

- Calculating pre-encounter orbits of parent meteoroids

- Orbit evolution modelling from a large event dataset

These goals were the objective of Ceplecha (1961) when establishing the first fireball network in the Czech Republic in the 1950's, in the hope of understanding where meteorites come from. With the calculation of the pre-entry orbit of the Příbram meteorite, Ceplecha (1961) proved that meteorites are linked with the main asteroid belt, and the delivery mechanism (the Yarkovsky effect combined with orbital resonances) was fully explained later, with the work of Morbidelli et al. (1994); Farinella et al. (1998). Since then, theses goals have not fundamentally changed because we have yet to instrumentally observe the fall of rarer classes of meteorites, like irons, stony-irons, and even some classes of ordinary chondrites (Borovička et al., 2015). Furthermore the dynamical origin identification of a meteorite through its pre-encounter orbit remains statistical (Granvik and Brown, 2018), so a significant number of the samples of the same class are required to fully validate a meteorite - main belt region connection.

The direct requirement that falls from these goals is the **reliability** of the data. An undetected systematic error not only has consequences on the science conclusions about the structure of the solar system, but it can also result in people searching for meteorites in dangerous environment in the wrong location.

An other requirement, that is perhaps not captured in historical meteorite recovery endeavours, is **scalability**. So far most fireball networks endeavours have operated sub-million km^2 networks (Halliday, 1973; Oberst et al., 1998). Since 2016 the DFN covers 3 million km^2, and plans to expand to 10 million km^2 by 2020 (2% Earth) through the Global Fireball Observatory (GFO) collaboration. More generally, getting a large number of orbits (hundreds per year) requires a certain degree of **automation** for the processing routines.

The last primary requirement relates to **decision making**, as the network is operated by a small team. The pipeline must not only produce reduced data for researchers to analyse, but also the necessary high level reporting information to make decisions to get the maximum science returns, a concept that is not far from Operational Research (OR) theory.

The DFN observation facility is also suited to tackle a number of secondary science objectives:

- Collect bright flight data on a large number of meteoroids to test entry models (not only meteorite droppers).

- Determine pre-impact physical parameters (mass, structure...) of the meteoroid.

- Investigate fireball showers.

- Derive impact flux of meteoroids on Earth.

- Use the collected imagery for other non meteor related purposes (transient astronomy, Space Situational Awareness (SSA)...).

2.1.2. TECHNICAL REQUIREMENTS

The DFN observatories have been designed to be low-power, light-weight, low-cost, autonomous, and able to support long gaps between servicing visits

(Howie et al., 2017a). Furthermore, most of the DFN is set in outback Australia, where network connectivity is very limited if at all possible.

The daily bandwidth objective is 1 MB per day, this include both engineering data as well as information about fireball events. It is acceptable to spend a few hundred megabytes to retrieve raw data for selected events of interest. Each camera takes ~1000, 45 MB raw images per night, so it is not possible to send back full-resolution compressed version of the images. The event detection has to be done on-board the low-power single-board computer (currently Commell LE-37G using 15W), and the results have to fit in the 1 MB daily bandwidth limit. If bandwidth was not such a big issue, the cameras would send all the raw detected events data (including false positives) to the central server immediately after detection. However some camera stations in the remote outback are located very far away from cell towers, and only average a couple of kilobytes per second of bandwidth, or are even unable to communicate in some weather conditions. Therefore only the confirmed events of interest must have their raw data transmitted.

These problems resemble the ones faced by some space probes exploring the solar system. Maintenance and software/firmware updates have to be smartly scheduled and very well tested, and data transfers limited to the bare minimum.

Contrary to space probes, the observatories can be serviced, but this must be limited as much as possible as some sites require thousands of dollars of logistics and several person days to be visited.

These considerations constitute the technical requirements for the steps that happen before the data can be analysed in depth (Fig. 2.1).

Once the data is on the server, these low-power use and low-CPU usage constraints disappear; however the server still needs to have a very high degree of automation, as the network is operated by a small team of researchers.

The central part of the reduction pipeline must be:

- **Scalable**: not dependent on a single central server doing everything; able to share the workload between machines.

- **Fault proof**: ability to redeploy everything in a timely manner on a brand new machine if the central server crashes.

- **Automated**: minimum human intervention,

- **Sensitive** to **new data** and **software** updates.

- **Error reporting**: problems must be disseminated to humans in a readable way, and in a manageable volume.

- **Relatively fast**: in case of a meteorite alert, the team needs to have the necessary information to make a decision in a timely manner after the alert.

2.1.3. HOW TO READ THIS CHAPTER

In the following sections I am going to present the DFN data reduction pipeline, and how it meets the requirements mentioned above.

The first section (Sec. 2.2) is an overview of the various steps in the pipeline. It includes some of my work, as well as my colleagues'.

The following sections (Sec. 2.3, 2.4, 2.5, 2.6) then detail the tasks that I have single-handedly worked on and developed (notably the astrometric and photometric calibrations).

2.2. OVERVIEW OF THE PROCESSING STEPS
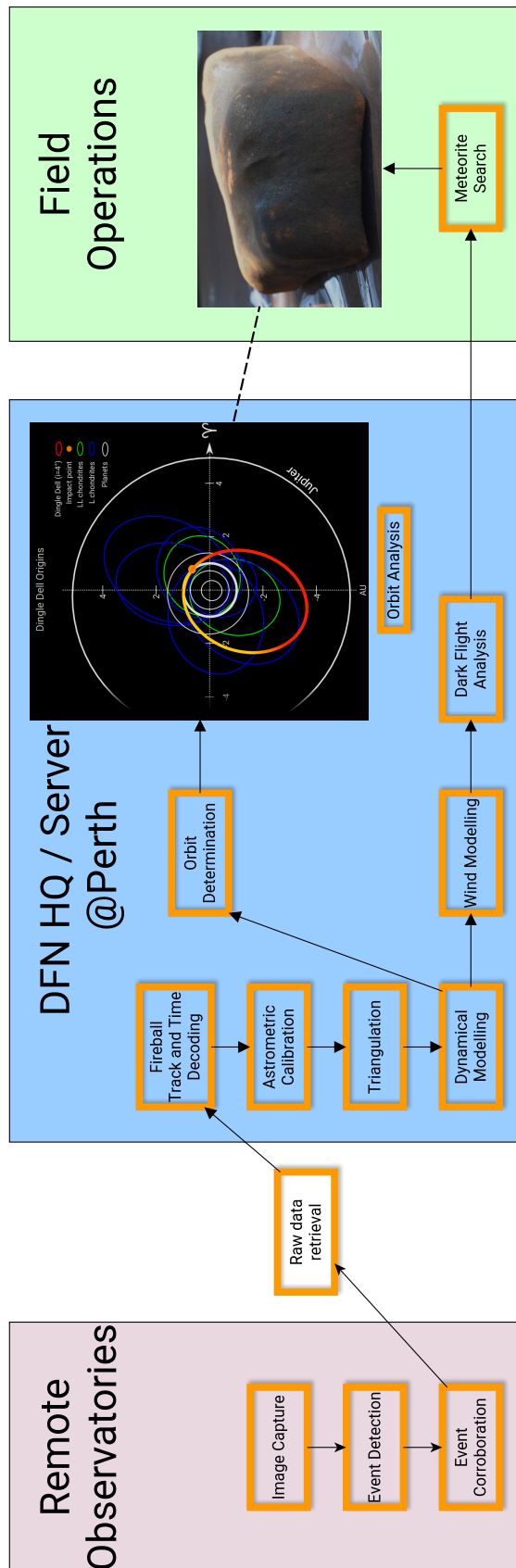
FIGURE 2.1: Overview of the DFN data processing pipeline, from image capture to meteorite recovery.

2.2.1. CAPTURE AND DETECTION

This section deals with the main software tasks running on-board the observatory. See Howie et al. (2017a) for a description of the hardware parts.

Still images are captured using a custom-made capture control software. Its main functions are:

- Turning things on and off by sending commands to the micro-controller. Example: the power to the DSLR and video camera is physically cut using a relay when not in use to save power.

- Checking GPS module status to ensure that absolute time is encoded with acceptable precision (Howie et al., 2017b) (typically 0.4 milliseconds).

- Logging all the metadata necessary for science reduction (observatory coordinates, version of micro-controller firmware used...).

- Logging engineering data to remotely diagnose malfunctions.

- Calculating sunrise and sunset times, and adjusting exposure settings during twilight.

- Handling communication with the DSLR, through the gPhoto library (`http://www.gphoto.org/`).

- Triggering calibration images with the liquid crystal shutter open (currently set to one every 30 minutes).

- Temporarily interrupting captures when the sky is too cloudy, to reduce wear on the mechanical shutter and save disk space.

Captured images are fed through the event detection software after they have been retrieved from the DSLR memory card.

However when available power during the night is limited (in winter for example), this operation can be delayed till morning, when the sun shines on the solar panels. More generally the observatories record the input power voltage, allowing them to run at reduced functionality if it is determined that normal operation would cause a power failure before the end of the night.

The fireball detection process is explained by Towner and et al. (submitted). The algorithm is based on blurring and image differencing, then a Hough transform to detect transient meteor streaks.

The line pixel coordinates of the events detected are subsequently converted to sky coordinates using a simple optical formula: the Samyang $f = 8\,\mathrm{mm}$ $f/3.5$ lens produces a stereographic projection, the distance from the centre R can then be related to the zenith angle θ with this relation: $R = 2 \cdot f \cdot \tan(\theta/2)$. The variable parameters (pointing and rotation) of this transformation are automatically calculated using a locally installed version of the *astrometry.net* blind solver (Lang et al., 2010). *Astrometry.net* does not deal well with fisheye images, but is able to robustly solve a crop of the centre of the image (1000 pixels $\simeq 30°$). This removes the need for precise pointing of the observatories, or manual editing of these parameters every time a camera system changes location.

This formula is not good enough for precise astrometry (see Sec. 2.4 for the full science grade astrometric solver), but it is enough for roughly pinpointing the meteor tracks to a couple of degrees precision, in a completely unsupervised and reliable manner.

2.2.2. SERVER EVENT CORROBORATION

The server synchronises a small number of files from each observatory, usually $\simeq 1\,\mathrm{MB}$ — 5 orders of magnitude smaller than the collected data volume. These

files include engineering logs, as well as fireball detections files (postage stamp cutouts of detections, and astrometric files).

The detections usually include a large number of false positives. The common suspects are satellites, planes, lightning, or cloud edges.

In order to only ingest valid double station fireballs, the server attempts to calculate which simultaneous streaks correspond to a meteor. To do this, the method of planes of Ceplecha (1987) is used on detection pairs. This basic but robust method always gives a result (planes almost always intersect somewhere), and the location of the intersection is used to determine if the double detection likely corresponds to a meteor: meteors are only detectable by the camera system between 10-150 km. Anything higher will most likely be a satellite, whilst anything else likely corresponds to uncorrelated events.

Likely meteor detections are then sent as an email to a team member, who has a final say after reviewing the postage stamps detection images.

After this process, valid events are ingested in the main science database, and software automatically retrieves all the relevant data for the precise reduction steps (science images, calibration images, metadata, etc.).

2.2.3. RAW DATA RETRIEVAL

The raw data is retrieved only once an event is confirmed, in order to limit bandwidth usage. By the time the event is confirmed, the corresponding raw data can be in different places:

   i On the internal Solid State Drive (SSD) of the observatory (accessible when observatory is online). Typical availability period after the image was taken: seconds to days.

ii On one of the external hard drives of the observatory (accessible when observatory is online and hard drives are turned on). Typical availability period: days to years.

iii On external hard drive in transit or waiting to be ingested in the datastore (temporarily inaccessible). Typical unavailability period: weeks.

iv On the data centre (Pawsey HPC Data Store). Typical availability period: month to years.

v Missing (permanently inaccessible).

The server will try the data centre (iv) first, because it is the fastest to get to and query from. If this query is unsuccessful the server will send lists of wanted files to the remote observatories. Then the observatories will copy the requested files to an outgoing folder from (i) (very recent events), or from (ii) when the drives are turned on. Finally the server synchronises these folders (the opposite is not possible, cameras cannot push to the server for security reasons), and moves the files to their appropriate locations in the event folders. Because the data can be temporarily inaccessible (iii), this process has to be attempted at regular intervals.

The same process is applied to calibration images, with the added twist that the pulled calibration image requested might be cloudy, adding another loop that runs until a satisfactory calibration image is found and retrieved (see Sec. 2.4.2 for more information on calibration image requirements).

In the unlikely event that some data go permanently missing (v), the full resolution image of a particularly important event can be virtually re-built using the low-resolution detection tiles, and calibration can be achieved using an astrometric solution from another event nearby in time.

Dealing with incomplete data

After an event has been processed, there is always a chance that it is going to require re-processing. The obvious reason for that is the release of a new version of the processing software, but it can also be because some new data is available. For instance the Murrili meteorite fall (Sansom and et al., 2018) was initially reported by 7 online stations. The first trajectory solution showed that the data reduction would greatly benefit from having the data from another 2 off-the-grid stations (William Creek and Etadunna; no 3G connectivity at these stations), therefore a decision was made to drive there to recover the data. It turns out that the fireball had been caught on an other off-line station (Kalamurina), but the data was recovered on a regular servicing trip nearly a year later, long after detailed analysis was done and the meteorite was recovered. Software must be able to cope with this, and not put too much strain on the server as the dataset grows. This is implemented using a wrapper script that checks for new data and software. It checks which version of the software was last run for each event, and with what input data, and accordingly re-runs were necessary. As re-calculating trajectory solutions, bright flight analysis, and orbits can take the better part of a day to run on all events, this wrapper is only run once a week on the whole dataset. However a fast track version is run only on the most recent events (more recent than a month) every couple of hours, in order to get relevant information about potential meteorite dropping events in a timely manner.

2.2.4. Pre-processing and calibration

The digital cameras record raw images in a proprietary format, it must be decoded and linked to relevant metadata. This process is detailed in Sec. 2.3.

The main output of the image analysis is astrometric measurements of the

meteoroid positions as it enters the atmosphere. Thanks to the large number of stars recorded in the image, the sensor (x, y) pixel coordinates can be precisely matched to sky coordinates (typically equatorial (Right Ascension, Declination) or horizontal (azimuth, elevation)). The automation of this process is detailed in Sec. 2.4. Fireball positions in the images are extracted using the semi-automated software tool described by Howie et al. (2017a).

Photometric measurements are automatically measured and calibrated, this is detailed in Sec. 2.5.

2.2.5. TRAJECTORY DETERMINATION

STRAIGHT LINE ASSUMPTION The meteoroid's motion through the atmosphere can usually be approximated to a straight line locally, as its initial velocity ($> 11 \text{km s}^{-1}$) dominates the influence of lateral forces like gravity, wind, or lift, as long as the trajectory remains short (seconds). The approximation of this radiant can be calculated from 2 camera viewpoints using the methods of two intersecting planes of Ceplecha (1987). This method has the benefit of being purely geometrical (no observation timing needed), almost always convergent, however it does not directly allow the use of more than two viewpoints. To solve this issue, Borovička (1990) proposed a straight line least square method that minimises astrometric residuals from all observations. To accelerate convergence of the Borovička (1990) method in the DFN pipeline, the initial guess solution is calculated using the Ceplecha (1987) first on the two viewpoints that have the highest convergence angle. Although Borovička (1990) say that their method can be applied in an inertial frame (by changing the observer coordinates on Earth), not many works citing the method have actually clarified which reference frame they work in. For short lived meteors this method can be applied in either an Earth-Centered/Earth-Fixed (ECEF) reference frame, requiring no timing information on the astrometric datapoints; or in an Earth-

Centered Inertial (ECI) frame if absolute timing is known. ECEF can be used as long as Earth rotation effects are dominated by astrometric uncertainty. The Earth rotates at a rate of $\sim 15''s^{-1}$, so its effect on arcminute precision observations only becomes apparent if the fireball lasts longer than a couple of seconds. For longer events, the use of ECI frame is necessary.

Working closer to the observation data   The straight line assumption has the advantage of always yielding a solution unless the observation geometry is very poor, as it smooths out noise in the observation data. However it does not say anything about uncertainties, and this smoothing effect might hide subtleties in the data.

The most obvious modelled force that is not taken into account by the straight line model is gravity. The total displacement due to gravity is equal to $\hat{g}t^2/2$, from the equations of motion, with $\hat{g}$ is the local acceleration vector due to gravity, and t the duration of observation. The effect is negligible for second-long meteor ($\sim 5m$) compared to observation precision, however it rapidly adds up for longer fireballs: over 2.1 km for the 21.7 s long fireball reported by Sansom et al. (2019).

Sansom et al. (2019) introduce a new trajectory determination method, individually triangulating astrometric line of sights, which gets rid of the straight line assumption, and allows entry models to work more closely to "raw" astrometric observations. They notably find that gravity alone does not account for the observed non-straightness of the meteoroid trajectories, and that it is even dominated by other unmodelled forces, possibly of aerodynamic origin. More about this method is discussed in Sec. 2.2.6.

2.2.6. Determination of physical and dynamical parameters

Ideally one would want to know the dynamical (position and velocity) and physical (shape, density) parameters throughout the bright flight. However, from a practical point of view, knowing these at the start and the end of the bright flight is sufficient to attain the main goals set in Sec. 2.1.1.

The pre-entry dynamical parameters are required to determine the pre-encounter orbit of the meteoroid (Sec. 2.2.7), while the pre-entry physical parameters give useful information for size-frequency population studies.

Estimating these parameters at the end of the brightflight is important to successfully propagate meteorites through the dark flight integration to potential fall locations on the ground (Sec. 2.2.8).

The state of the art brightflight analysis model used by the European Network is the "multiple fragmentation model". It uses a "trial and error" approach (Borovička et al., 2013) to minimise residuals on both meteoroid positions and light curve. Its main advantage resides in the fact that it models all fragments, even the smallest ones, by relying on the fact that all pieces ablating have to add up to the total measured light curve. Its main drawback is that it does not do a thorough search of the parameter space, therefore it does not guarantee that the solution found is even close to the truth, and it does not yield formal uncertainties.

The DFN observatories do not currently have the capability to record high frequency ($> 500\,\text{Hz}$) light curve data. In order to reliably model the trajectory without the use of photometric data and tackle the uncertainty issue, several methods have been developed by Sansom et al. (2015, 2017, 2019). These apply modern mathematical statistical techniques to the single body ablation problem, using just the positional data.

- Sansom et al. (2015) use a minimisation algorithm to determine optimum dynamic parameters with which to perform an extended Kalman filter and smoother (EKF and EKS) on observational data. The smoothing algorithm uses pre-triangulated positions, and a single body ablation model in one dimension, to estimate the state of the meteoroid (position, mass and speed). As both observation and model uncertainties are quantified, the EKS is able to provide comprehensive formal uncertainty estimates for these states throughout the trajectory.

- Sansom et al. (2017) use an evolutionary algorithm iterated over the successive measured positions of the meteoroid. It effectively performs a wide-scale search of the parameter space (position, velocity, mass, density, shape), with the aim to have a cloud of particles that is statistically representative of the meteoroid main mass at the last time step (ie. the end of bright flight). At each step, a cloud of possible particle is propagated forward through the ablation equations, and the fitness of each particle is evaluated against the next observation. Particles are re-sampled at each step from the previous population, preferably selecting the best fitting parent particles, and also adding process noise to account for model errors. This technique gave very encouraging results for the Dingle Dell meteorite, only needing the last second of observation to get an accurate result (Devillepoix et al., 2018).

- Sansom et al. (2019) revisit the particle filter method of Sansom et al. (2017), but add degrees of freedom in the parameter space by letting the meteoroid evolve in 3 dimensions instead of being constrained by a pre-triangulated solution like the one described in Sec. 2.2.5. This method works closer to the data as it uses the raw astrometric observations with corresponding uncertainties (Sec. 2.2.4), instead of a pre-triangulated positions that do not have associated formal uncertainties since they are the result of a mathematical fit. The method of Sansom et al. (2019) is also

a good general trajectory solver to use on long shallow meteoroid entries, for which the straight line assumption does not necessarily hold (due to gravity, and possible unmodelled forces).

These methods require a good knowledge of measurement uncertainties, but also model errors. The model uncertainties are in theory well constrained under the single body ablation equations, however unpredictable fragmentation events perturbs this.

Sansom et al. (2016) have tried a multiple model approach: using small model errors in general, but jumping to a higher model error when it is more likely to best represent the observations. This accounts to some extent for fragmentation events, where a steady ablation model is temporarily not a good representation of what the meteoroid is experiencing.

Not only do these methods yield valuable physical information, they also give estimates of positions and velocities with associated uncertainties. Getting formal uncertainties on the meteoroid velocity is key to determining formal uncertainties on its pre-encounter orbit. To my knowledge, along with the work of Egal et al. (2017); Vida et al. (2018), these approaches are the only ones described in the literature that give formal uncertainties on the velocities of a meteoroid.

The work of Sansom et al. (2017) and Sansom et al. (2019) have been made available online, freely usable by the community [1].

2.2.7. ORBIT CALCULATION

Orbits are calculated using the backwards integration routine described by Jansen-Sturgeon et al. (2018). The method is more robust and precise than the

---

[1]`https://github.com/desertfireballnetwork/brightflight`

historical method of Ceplecha (1987), as it takes into account the following effects:

- pre-observation deceleration due to the atmosphere.
- Earth oblateness (J2).
- secondary perturbators (Moon and planets).

Using the formal uncertainties calculated by the methods described in Sec. 2.2.6, the uncertainties on the orbital elements are calculated using Monte Carlo sampling. The number of orbital clones used ranges from 24 for daily processing (limiting the CPU load), to 500-1000 for publication, or even more for long-term simulations if required (Devillepoix et al., 2018).

2.2.8. WIND MODEL & DARKFLIGHT INTEGRATION

A traditional approach to darkflight calculations is to propagate a best guess of the state vector of the meteoroid at the end of the observed bright flight to the ground, using a best guess of what the weather conditions are. As the uncertainty on mass and shape is usually relatively large, a search corridor (usually called "fall line") is derived, as a change in shape or mass will mostly result in a shift along the search corridor. The meteorite is then deemed to be close to this so-called fall line, plus or minus some uncertainty on either side of the line. The strategy for searching is then to start at the best guess for mass and shape, and gradually move along the search corridor until a meteorite is found.

One of the requirements set in Sec. 2.1.1 is that the reduction pipeline should yield results useful for making decisions. This approach does not make the most of the statistical distributions given by the methods detailed in Sec.2.2.6.

To maximise searching efficiency, the uncertainty in the observation data needs to be propagated all the way to ground to produce searching heat maps,

using all the information inferred during the analysis of the bright flight as Bayesian priors. A full example of this process is detailed by Devillepoix et al. (2018).

Pushing the Bayesian paradigm even further, we could assign recovery likelihood based on characteristics of the terrain, and convolve this with meteorite location probability heat maps. However in practice this step is examined manually by humans, as other factors not easily modelled with a computer come into play, like accessibility of the search site and logistics in general.

2.3. DATA INTEGRITY & PRE-PROCESSING

The first step of the data reduction process is making sure the images are in a usable format, and have all the necessary metadata attached to them. On a typical astronomy instrument, the images are recorded straight into an open raw format (usually FITS), and the useful observatory environmental parameters (location, pointing, temperature, exposure, time, filter used...) are saved as metadata (file header for FITS). The off-the-shelf digital cameras that the DFN uses record to a proprietary format and do not embed all the needed metadata in the files, therefore a conversion is required before they can be used. Here I describe all the "house keeping" tasks that I have implemented and are required to happen before the images can be analysed.

2.3.1. DE BAYERING

The main issue with off-the-self DSLRs for astronomy applications is their colour sensors. Most of these colours sensors use a Bayer matrix of micro-filters to capture colour information (Fig. 2.2). Although such devices look tempting for capturing multi-colour photometry of astronomical targets in a single frame,

they are rarely used for that purpose because of the large amount of light lost in each channel, and because of issues accurately focusing all 3 bands. Furthermore, the spectral response in each channel is not an ideal well-defined pass-band function but rather a broad curve that overlaps with other bands. Processing the colour channels independently becomes necessary for scientific applications that rely on high spatial resolution. Physically de-Bayering the sensors is a rather complicated process and therefore does not achieve the commercial off-the-self (COTS) hardware requirements of Howie et al. (2017a). Therefore a solution must be found to keep the advantage of the large number of pixels for spatial resolution. We must then use the 3 colour bands separately. The blue and red pixels each only make up $1/4^{th}$ of the sensor area, therefore a loss of spatial resolution is inevitable when using these. On the other hand, the green pixels cover half the matrix in a regular checkboard pattern. I chose to use the green pixels and virtually re-create the full resolution image by doing a simple bilinear interpolation to fill in the gaps (Fig. 2.2). One of the issues with doing this is that a green hot pixel will look like a point spread function (PSF) source.

2.3.2. TIME KEEPING

On Nikon digital SLRs, time stamps recorded in the digital files are only rounded to the nearest second, and setting the time on the camera is only accurate to 1-2 s anyway.

The observatories time is maintained by a Network Time Protocol service (*ntpd*) on the computer, enhanced with Pulse-Per-Second (PPS) information given by the GNSS module. This prevents the observatories' clocks from drifting, even after being disconnected for years from the network. System clock sub-second precision is not vital, as time critical parts of the observatories are handled at micro-controller level, which gets its time from the GNSS module,
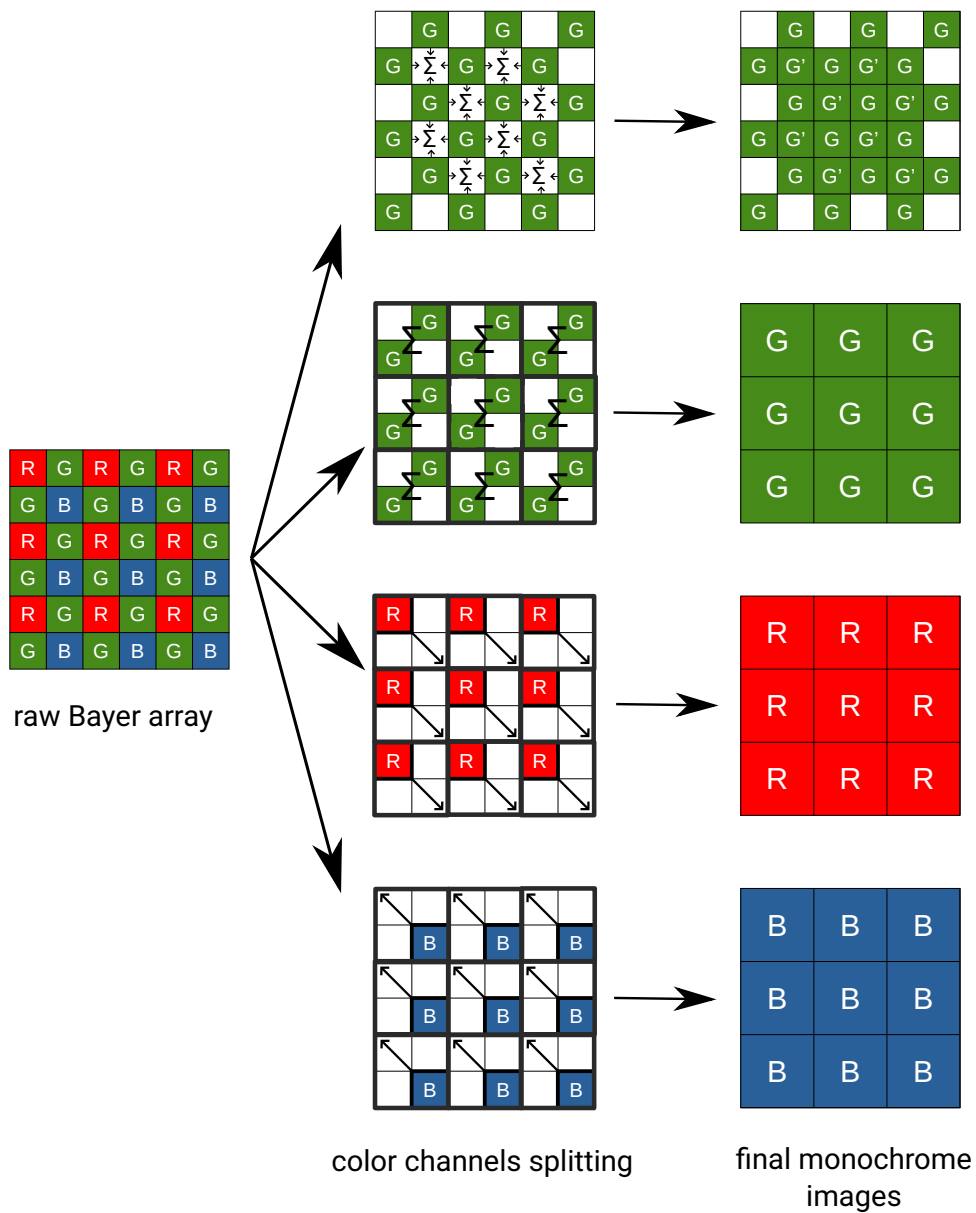
FIGURE 2.2: De-Bayering processes. A: green bi-linear interpolation to reconstruct a monochrome image that is the same resolution as the original frame. B, C, and D: 2x2 binning of only the green, red, and blue pixels, respectively.

Camera system	suggested timing offset (s)
DFNSMALL60	-0.002
DFNSMALL12	+0.000
DFNSMALL62	+0.000
DFNSMALL43	-0.006
DFNEXT007	+0.010
DFNSMALL33	-0.006
DFNSMALL38	+0.009
DFNSMALL14	+0.003

TABLE 2.1: Possible absolute timing offset from each camera system, as calculated from trajectory data, from for event DN170607_01.

and is a real-time processing unit. Howie et al. (2017b) show that the Liquid Crystal (LC) shutter absolute time encoding is better than $1\,\mathrm{ms}$, the time response of the shutter being the limiting factor. This precision is then guaranteed as long as the GNSS module is working properly, and has a GPS fix. This is why the system regularly logs the fix quality by reading the GPSGGA sentence (0 = invalid, 1 = GPS fix (SPS), 2 = DGPS fix, 3 = PPS fix, 4 = Real Time Kinematic, 5 = Float RTK, 6 = estimated (dead reckoning), 7 = Manual input mode, 8 = Simulation mode). This information is recorded in log files, copied over as FITS keyword in the images, and then as metadata in the tables, so that the data reduction pipeline is aware of possible timing issues.

The timing coordination between various observatories' LC shutters can be incidentally verified using the fireball data, using this simple test:

- assume each camera suffers from an absolute timing offset ϵ_i.
- build an interpolation function f to match the relative time of one arbitrary camera (t_0) to the distance from the first triangulated point D_0.
- for each camera i, find potential absolute timing offset ϵ_i by minimising $\Sigma(f(t_i + \epsilon_i) - D_i)^2$.
- to remove the assumption that camera 0 has zero offset, calculate new offsets $\epsilon_i' = \epsilon_i + \delta$ such that the median of the (ϵ') sequence is zero.

I have applied this to a 3.2 seconds long fireball observed by 8 cameras in

South Australia. The absolute timings offsets (ϵ') suggested by the algorithm are presented in Tab. 2.1, they show better than 10 millisecond match between the different viewpoints. This is remarkable, considering this encompasses a wide range of possible systematic, including shutter encoding, astrometric calibration, and point picking.

This millisecond absolute time accuracy on the fireball measurements is not crucial for orbit determination (~ 1 second precision is sufficient), however this extreme precision gives the DFN a unique capability of doing point-wise triangulation of fireballs (Sansom et al., 2019).

2.3.3. Observatory location

Accurately keeping track of the positions of the fixed observatories seems like an easy task, however this has not always been the case before wide-scale use of GNSS systems (Spurný et al., 2014).

The DFN capture control software systematically records the camera system's location using the GNSS module, ensuring the science record is always correct (Fig. 2.3). The removes the potential human factor, which is particularly important when the observatory system is moved. In the same way as in Sec. 2.3.2, the software also records whether the the GNSS module was functioning properly.

Warnings are raised in the downstream steps of the pipeline when the location may not be accurate, such as in the case where the default observatory coordinates (set manually) are used, the downstream steps of the pipeline are aware that the location may not be accurate, and raise warnings where appropriate.
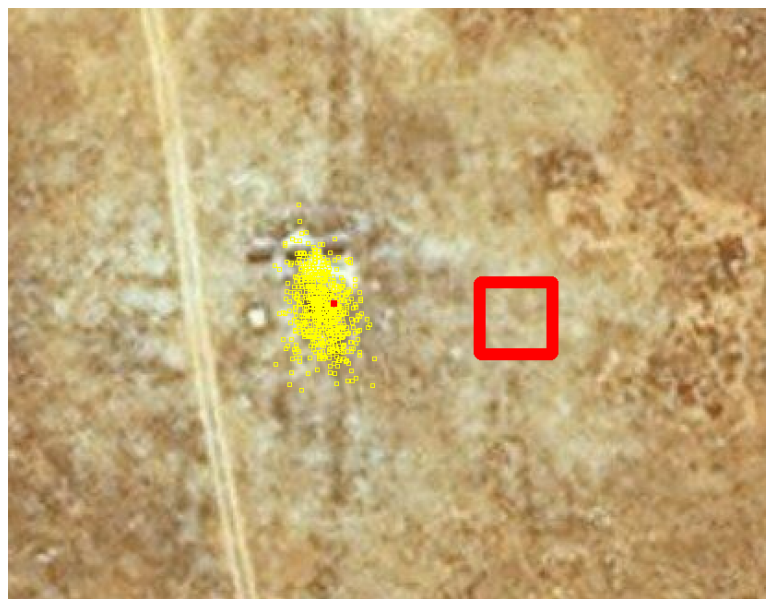
FIGURE 2.3: GPS logged positions of the Forrest observatory (30.85806° South 128.11505° East WGS84, 154 m altitude A.S.L.), recorded for over 2 years of uninterrupted operation between December 2014 and December 2016. Red dot is the camera position as spotted on the satellite imagery (imagery may not be perfectly aligned with coordinates). Red square is 10 m on the side, to visualise extent of the spread of the points. σ =2.5 m, maximum deviation from mean = 14.5 m. Satellite imagery attribution: Microsoft Corporation, DigitalGlobe, Earthstar Geographics, CNES/Airbus DS.

2.3.4. Conclusion

The code I have developed is capable of processing a 36 MPixel NEF image, adding all the necessary environment metadata (accurate exposure start time, observatory coordinates, reliability of the GNSS unit...), de-Bayering the array, and saving the result to disk as a usable FITS in less than 1 second (on a typical 2016 laptop).

It has been made available online at `https://github.com/desertfireballnetwork/RAW2FITS`, released under an MIT license.

2.4. Astrometry

2.4.1. Introduction

In the early 2000's, Greisen and Calabretta (2002); Calabretta and Greisen (2002) have standardised the way focal plane coordinates are related to sky coordinates, creating the World Coordinate System (WCS). This standardisation allows simple and automated workflow for the astrometric calibration of most astronomical images, using two simple steps:

- instrument control software records a rough mount pointing in the metadata of the images (FITS header typically), as well as other parameters like pixel size.
- a WCS solution is generated or refined using the stars in the field of view, with the help of a tool like *SCAMP* (Bertin, 2006).

This workflow works well, as long as the input metadata is recorded. However in some cases, the metadata are not available (amateur picture, photographic plate with lost record, etc.). This is the type of issues that Lang et al. (2010)

tackles, by introducing a completely blind astrometric solver (hereafter referred to as *astrometry.net*). This tool has simplified the process, not requiring a rough known pointing or even a plate scale, and has helped bring astrometry to the masses, allowing anybody to submit their work, whether it is an image taken with a multi-million dollar telescope or using a hand-held point-and-shoot camera, and determine what part of the sky the image corresponds to. However one of the issues with *astrometry.net* is that it struggles to solve very wide fields of view.

While doing astrometry on images captured by all-sky systems is evidently not limited by the available catalogue precision or depth, there is no standard automated solution to do so. This mostly comes from the strong distortions induced by the wide angle optics. Previous efforts to do precise astrometry on these were very labour intensive and required some knowledge of the optical design. The work of Borovička (1992) and subsequently refined by (Borovička et al., 1995) is aimed at characterising the optical system as well as possible, empirically developing functions to described the mapping between plate and sky coordinates. These efforts were made even more complicated by the fact that film imagers were taking night-long exposures, with possible weather interruptions, making automated star detection not impossible, but rather tricky.

I aimed here to develop a blind solver that could lead to sub-pixel astrometric calibration, in order to have a solid reference frame for meteors appearing all the way down to $5°$ above the horizon. This has been successfully implemented in the DFN pipeline and is detailed below.

2.4.2. METHODS & RESULTS

QUALITY REQUIREMENTS FOR CALIBRATION IMAGES

The cameras are fixed (not tracking the sky), which implies that the mapping from chip to horizontal coordinates $(x, y) \leftrightarrow (Alt, Az)$ changes very little over time. The only factors that can affect this on a night scale is a change in atmospheric conditions, which is only relevant close to the horizon. Over several weeks, a slight move of the camera can be expected as well (ground move, stress on the stand anchoring due to weather, temperature, etc.). The stability of the camera pointing needs to be checked, but in principle a fireball event can be astrometrically calibrated using an exposure taken at a different time.

The DFN observatories save all the captured images even when no fireball is detected. This is possible thanks to the availability of large capacity hard drives at reasonable costs. This was particularly useful to investigate the robustness of the detection algorithms in early testing phase. But it is still useful in some cases to get additional viewpoints on a fireball, even if the signal to noise ratio is too small to have been detected on some of the cameras. This large dataset also offers a large number of good quality images of the sky, useful for performing astrometric calibration of the instruments. From 2014 to 2017, most of the DFN observatories were breaking fireball trails in the long exposure images using the dash method detailed by Howie et al. (2017b). With this mode of imaging, the limiting magnitude on a dark night is around $m_V = 7$. This yields over 1000 stars $m_V < 6.0$ that are reliably detected by star detection algorithms.

In June 2017, the DFN initiated a firmware upgrade across the network to change the time encoding technique on the observatories' micro-controller. This upgrade is an attempt to tackle a dynamic range issue which affects typical meteorite droppers. The liquid crystal (LC) shutter encodes short pulses instead of dashes. The de Bruijn encoding is retained: a long dash (0.06 s open followed by 0.04 s closed) becomes two 0.01 s pulses, and a short dash (0.02 s open followed by 0.08 s closed) becomes a single 0.01 s pulse. This had very positives effects

on fireballs, helping resolve brighter fireballs, while making the centroiding easier to model. However the LC shutter remains closed for longer periods of time, further cutting star light. During testing of this new encoding it became apparent that the starlight loss would be an issue for calibration, especially low on the horizon, so it was decided to perform calibration frames at regular intervals, with the LC fully open for these exposures. With the shutter fully open, the limiting magnitudes increases to around $m_V = 8$, delivering comparable astrometric results as with the old encoding method. These calibration frames come at the cost of a small dead time for fireball observation (+3.3% dead time at the chosen cadence of 1 every half hour). A choice has been made to have the calibration images synchronised network wide, meaning that if a fireball appears during the calibration exposure, all timing information is lost for this event, in a quality over quantity approach.

As the fisheye lens used has 185°hemispherical field of view, it is common for foreground ground objects to appear in the images. These objects include trees, buildings, antennas, mountains. In the desert systems, when the moon is not up, these generally reflect/emit very little light, so the worse they do is occulting some of the stars and sometimes fireballs. However when these foreground objects shine directly at the camera (such as vehicle headlights) this can become an be an issue. They interfere with the star detection software, adding large numbers of fake sources close to the horizon, as well as creating halos. Furthermore, observatories that suffer from this issue are often located in very light polluted areas, where only a handful of stars dominate the background in the frames. One approach to solve this is masking out the foreground objects. However this is a tedious manual process, that needs to be repeated every time something moves in the frame. The sky movement can work in our advantage. In light polluted areas, the star density is very low, therefore any random sky pixel has very high chances of being pure background, whereas land-based pixels are unlikely to change much (in the case of fixed lights shin-
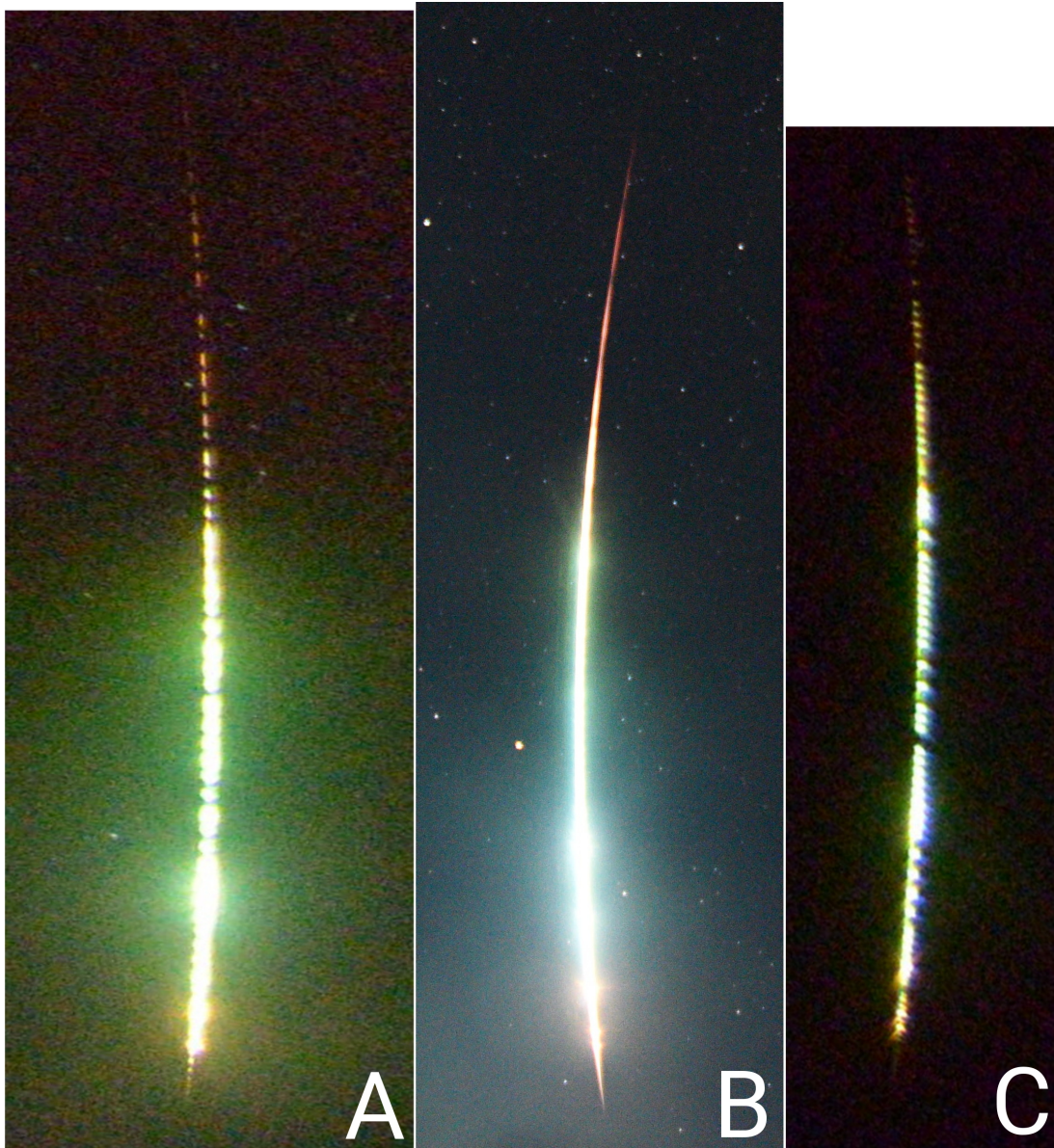
FIGURE 2.4: Long exposure pictures of a particularly bright fireball, observed from different observatories. A: de-Bruijn dash encoding (Howie et al., 2017b) from 200 km. B: LC shutter not in operation (bad quality lens used for testing) from 100 km. C: pulse encoding (see Sec. 2.4.2) from 250 km. All 3 images are saturated to some degree, however astrometric data points can be precisely extracted all along the track in C, while this is not possible in A. B displays spectacular colour changes, but is of limited use for astrometric purposes because of the lack of timing information.

ning at the camera). For constructing a background frame for an astrometric image taken at time T, we can combine surrounding exposures, in a stacked image where each pixel is the median of a number of frames, taken at $T \pm n * I$ with $n \in [1, 2, ...]$. The sky moves at maximum at a $15''\text{s}^{-1}$ rate, therefore an interval I of a couple of minutes is sufficient to avoid having a bright star overlap with itself in another frame. Having n even adds a bit more robustness to the process, as no pixel in the master background frame will have exact same value as one of the actual frames. This technique was developed to calibrate the DFN camera that recorded the Creston meteorite fall (Jenniskens et al., 2019), when the camera was in the middle of the Silicon Valley in California, one of the most light polluted places on Earth, with fireball datapoints as low as $8°$ above the horizon. Since then this process has been systematically and successfully used for heavily light polluted observatories. Note that this method also acts as a master dark frame in a sense that it removes hot pixels. For Creston, the calibration frame time was chosen so that a bright star was located in the same sensor area as the fireball.

We note that the requirements on the quality of the calibration images presented here are mostly relevant in the context of precise automated calibration; an image that has the moon is not impossible to calibrate, the solver will be less reliable, and potentially yields a solution that is not as precise as it could be.

STAR CATALOGUE

We use the ACT-Hipparcos reference catalogue as star catalogue (Urban et al., 1998). This catalogue outperforms our all-sky cameras by orders of magnitude, both in limiting magnitude and astrometric precision. Its main advantage compared to more recent catalogues is that it is perfectly complete from the brightest star Sirius to about magnitude 11. The only pre-processing needed is to eliminate the smaller components of multiple stars systems that are not

resolvable by our system. To be absolutely rigorous, one would need to apply proper motions to the star catalogue and enhance the catalogue with bright planets and asteroids ephemerides, however these two populations make up only a very small fraction of detected objects.

Interestingly, the star catalogue compiled by de La Caille at the Cape of Good Hope in 1751-1752 (de Lacaille et al., 1847) would be sufficient in both precision and depth to be used as a reference catalogue for doing astrometry with the DFN cameras.

BLIND POINTING SOLUTION

The first step towards getting a global solution is to determine a pointing solution for some part of the field of view that can be used as a starting point. Although we know some of the parameters of the system (rough pointing, pixel scale), it is very convenient to use *Astrometry.net* (Lang et al., 2010), as this tool does not need any hint about rough pointing direction or the plate scale. *Astrometry.net* is not able to solve the entire field of view, nor even a random crop due to the radial lens distortion, but the cropped region of the centre of the image can be solved with a standard WCS TAN (gnomic projection). With trial and error, we have found that on the DFN imaging system a 1000×1000 pixels ($\sim 30 \times 30°$) area is ideal: it is a good balance between having a sufficient number of stars and maintaining low distortion. In practice, a hint on the size of the field of view is passed to *Astrometry.net* in order to speed up the search, but this is not technically necessary.

DEFINITION OF PIXEL TO SKY TRANSFORMATION

We define a custom transformation function to go from pixel coordinates to equatorial coordinates, re-using the polynomial transformation T defined by

Sokolowski (2008). T (order n) transforms sensors pixel coordinates (x, y) to sky coordinates (λ, δ):

$$\begin{cases} \lambda = \sum_{i=0}^{n} \sum_{j=0}^{n} p_{ij} \cdot x^i \cdot y^j \\ \delta = \sum_{i=0}^{n} \sum_{j=0}^{n} q_{ij} \cdot x^i \cdot y^j \end{cases} \tag{2.1}$$

The polynomial coefficients (p) and (q) are the parameters, with the following condition to maintain the order: $p_{ij} = q_{ij} = 0$ if $i + j > n$.

GLOBAL BLIND ASTROMETRIC SOLUTION

Using the pointing information calculated in Sec. 2.4.2, we express the plate astrometric solution using the new transformation defined in Sec. 2.4.2. From that point, the solution has to be iteratively extended to the entire image area, using T as an extrapolant. This choice of the interpolant is particularly important: it needs to have enough orders of freedom to compensate for instrument distortion and avoid having too many mis-matches between detections and catalogue, but it also needs to avoid overfitting at all costs because overfits are generally bad extrapolators (Hawkins, 2004). Once a solution is determined in the central $30°$ area, $5°$ increments are used to extend the FoV (Fig. 2.6), adding more stars and making the fit more robust (Fig. 2.5). Stars "entering" the FoV are cross-matched using the positions computed by transforming detections with T, and the catalogue. This process is repeated until the whole FoV is matched ($90°$ from the centre on an all-sky fisheye lens).
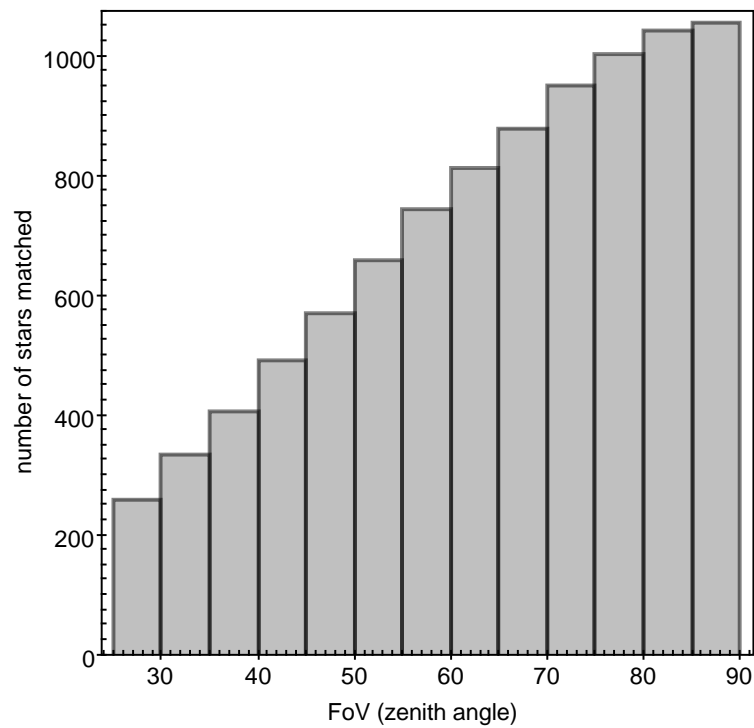
FIGURE 2.5: Number of stars matched at each iteration. As the field of view approaches the horizon, the number of "new" stars decreases, because of extinction, obstacles, and possibly vignetting.
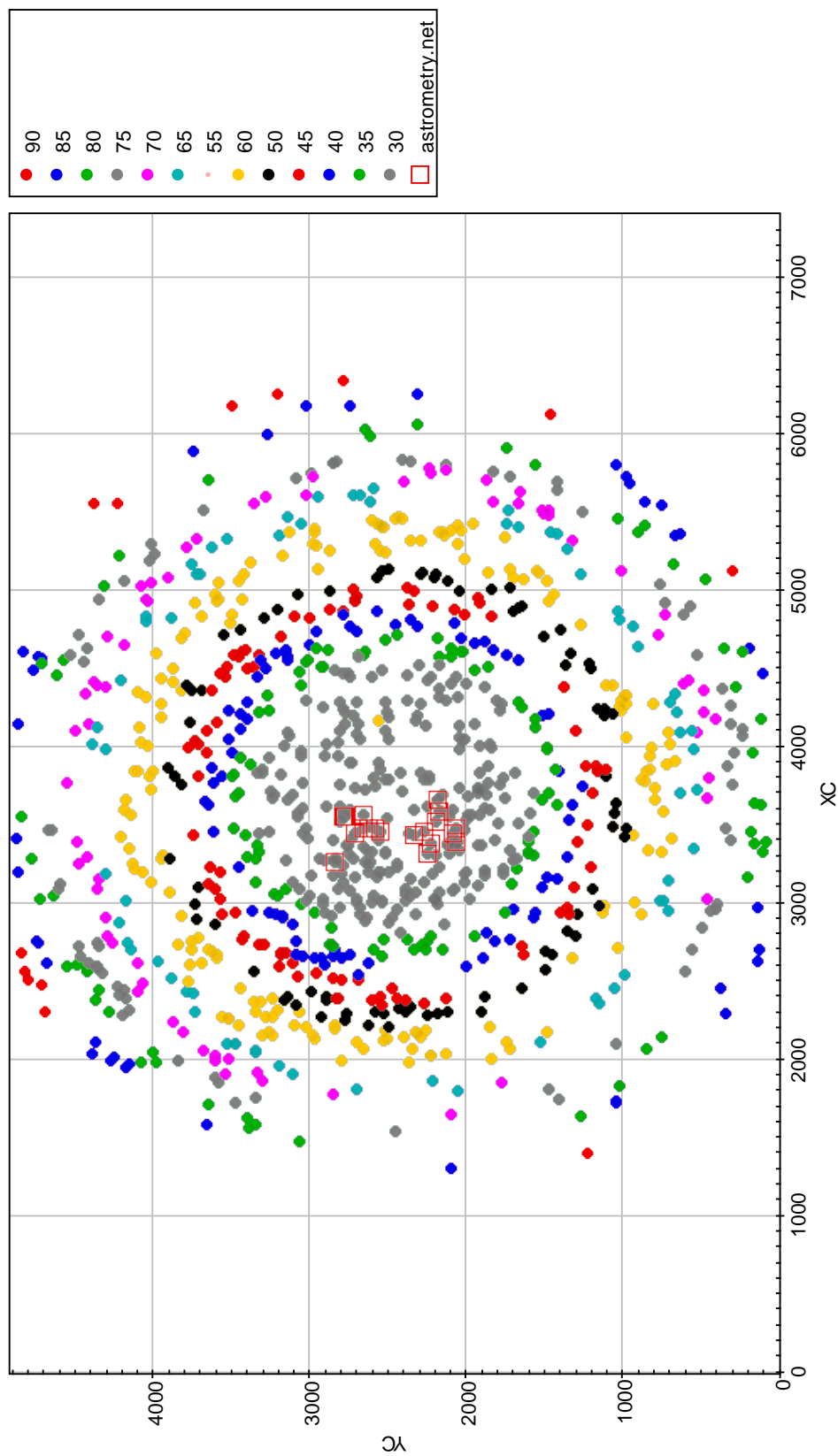
FIGURE 2.6: Extension of the astrometric solution to the entire all-sky field-of-view by iterative extrapolation. The initial solution is determined on a 30x30° crop with *Astrometry.net*, requiring very few stars. The solution is converted to a custom polynomial fit using as many stars as possible, this under-fit transformation is used as a robust extrapolant and is re-adjusted at every field-of-view increment (5° of sky starting from the optical center).
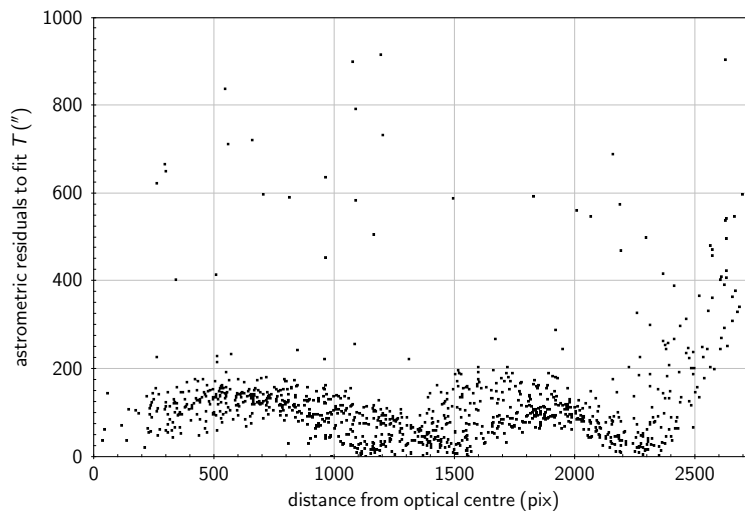
FIGURE 2.7: Astrometric residuals to he T fit, as a function of the distance from the optical centre, clearly showing the need for a radial correction in the final astrometric solution.

RADIAL CORRECTION

The transformation T used in Sec. 2.4.2 to iteratively match the entire FoV is robust enough to avoid star confusion, however it is not of high enough order if we wanted the best possible fit. Fig. 2.7 shows that the dominating residuals are heavily correlated with the distance of the star from the optical centre, i.e. the radial distortion is not perfectly accounted for in the fit. As the camera is pointing directly up, the distance from the optical centre forms a near one-to-one relation with the altitude axis in horizontal coordinates, we further outline the residuals correlation in Fig. 2.8 in horizontal coordinates, using signed residuals.

To correct for this in the final "science grade" astrometric solution, we use a third order polynomial to fit the radial component of angular residuals of reference stars to the distance from the optical centre. We note that we operate an outlier removal of dubious stars that have astrometric residuals $> 600''$. After this correction, we get astrometric residuals mostly contained within half a minute of arc (Fig. 2.9). We have searched for other correlations in the
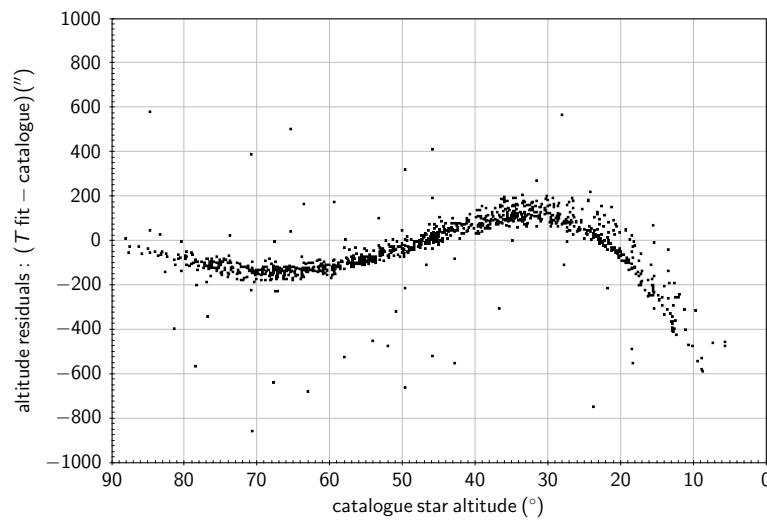
FIGURE 2.8: Altitude residuals as a function of the star altitude, further outlining the radial correlation of the residuals shown by Fig. 2.7.

residuals, without finding anything that could make the solution significantly better. We have also tried local re-fitting around the area of interest (the fireball), but we did not see any significant improvements over the T transform combined with the radial correction.
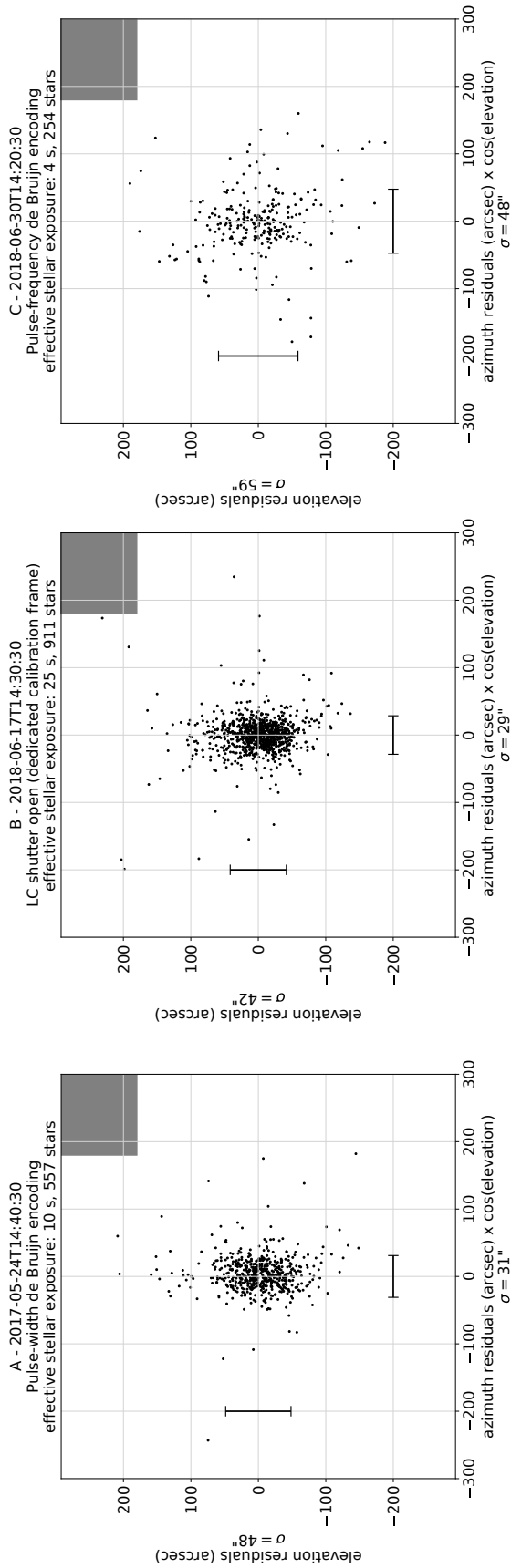
FIGURE 2.9: Effect of various LC shutter operation modes on the quality of the astrometric fit residuals on the same camera system, on the same location (Billa Kalina in South Australia), near the same sidereal time. A is the original de Bruijn pulse-width mode described by Howie et al. (2017b), calibration image can be taken as any image that satisfies the requirements of 2.4.2. With the introduction of the pulse-frequency encoding described by Devillepoix et al. (2019) (C), the standard fireball exposures show better contrast on fireballs (Fig. 2.4), however too much star light is obscured by the shutter to get a satisfactory astrometric solution. Hence special calibration exposures (1 every 30 minutes) with the LC shutter fully open were introduced, which results in comparable and even slightly better astrometric results (B). A-B-C correspond to A-B-C in Fig. 2.4. Error bars correspond to the standard deviation (1σ) of the residuals. They grey dots represent the on-sky pixel size at the centre of the field of view for the camera systems.

UNCERTAINTIES

Since the precision of the star catalogue used outperforms the camera system by orders of magnitude, the main sources of errors are:

- **under-fitting**: we expect to see local systematic effects on the residuals if the limitations of the fit dominate the noise introduced by centroiding. We did not find further obvious correlations in the residuals other than the radial one (Sec. 2.4.2), and the final residuals distribution look mostly Gaussian (Fig. 2.9).

- **over-fitting**: this happens when the interpolating function is of too high order compared to the number of datapoints. Here it is excluded by design with the use of a low-order polynomial (3), compared to the > 1000 reference stars available.

- **centroiding**: we expect this source of error to be assimilated to Gaussian noise with a standard deviation (σ) that mostly depends on the optical quality, and is well represented by the astrometric residuals.

Since centroiding likely dominates the errors in a Gaussian way, we can approximate the uncertainty on the converted astrometric positions for a fireball (ϵ) using:

$$\epsilon^{\theta} = \sigma^{\theta}_{<30°} + \epsilon^{pix} \cdot C$$

with:

- $\sigma_{<30°}$ the residuals to the global astrometric fit on local stars (°). Local stars are defined as being separated by $< 30°$.
- ϵ^{pix} the fireball centroiding uncertainty (pixel).
- C the plate scale (° pix^{-1}).
- θ the considered axis (altitude or azimuth).

The uncertainty is calculated separately for altitude and azimuth, as the residuals are usually larger in altitude than in azimuth (Fig. 2.9).

In case a fireball datapoint is outside the convex hull of reference stars on the chip and/or the number of local reference stars is too low (< 5), its astrometric uncertainties are marked as unconstrained, and in practice set to a default of $0.1°$.

For important events like meteorite droppers, the event diagnosis routine warns the user that the event's trajectory has been computed with partly unconstrained astrometry. Devillepoix et al. (2019) show an example where the astrometry goes unconstrained at extreme observation angles ($< 5°$ elevation).

At high elevations, the density of stars is roughly 0.3 stars per square degree of sky. When we get down to $5°$ elevation, stars are observed through over 10 airmasses. This effectively reduces the star density by a factor of 10, making it difficult to get good astrometric information below this elevation limit. Note that for an especially important event that is only visible very low on the horizon one could calculate when bright stars are transiting the $< 5°$ elevation area in the direction of the fireball, and use the corresponding images to augment the detection catalogue with stars from different epochs. But even this technique would be limited by refraction issues. As seen earlier, ideally one wants the calibration image to be as close as possible in time to the science image, in order to have the fireball and the star be affected by refraction in the same way.
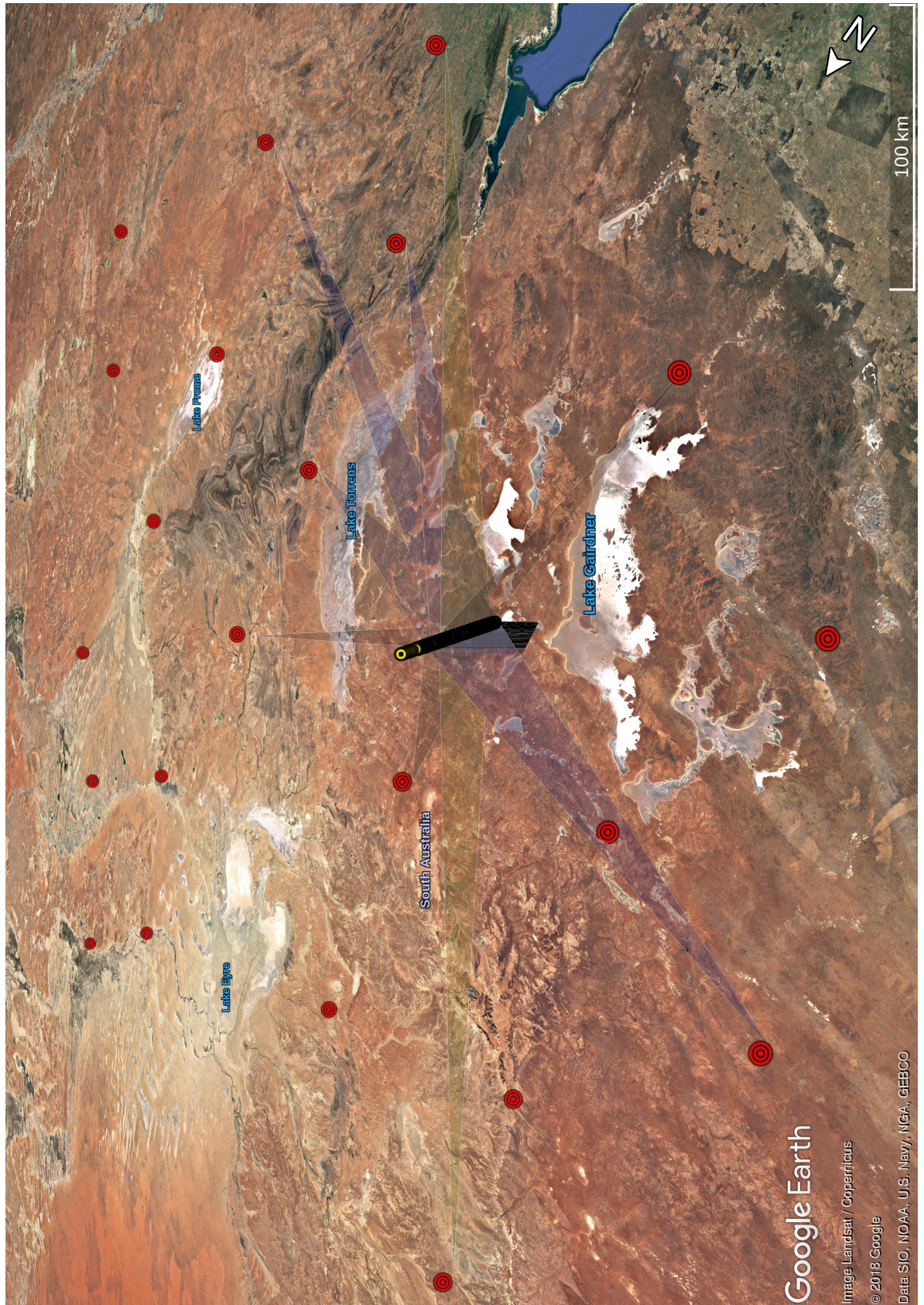
Figure 2.10: Overview of the straight line trajectory solution for event DN170607_01.
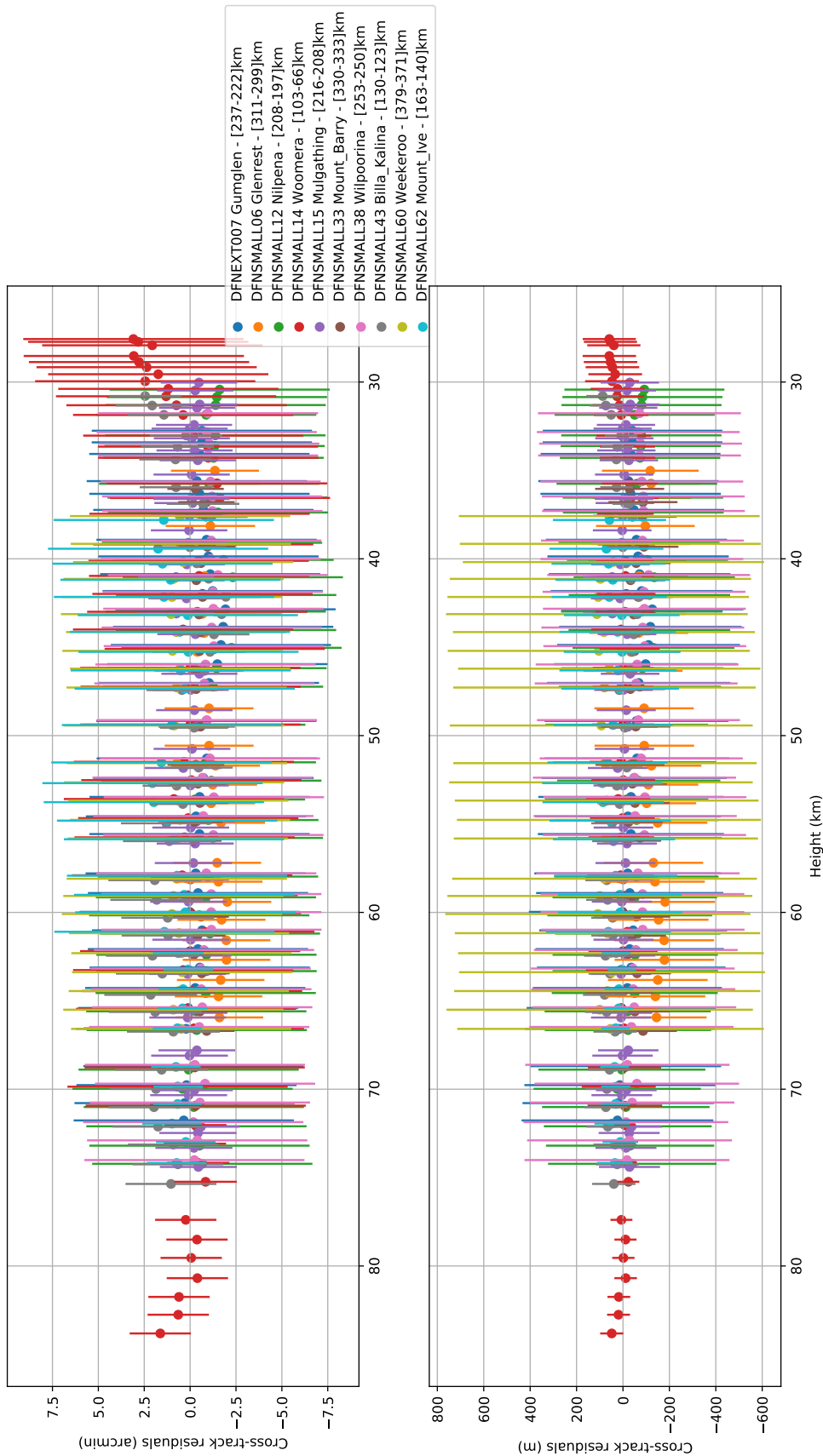
FIGURE 2.11: Astrometric residuals to the straight line trajectory fit of event DN170607_01 (Fig. 2.10). The dots correspond to astrometric residuals (a), and the astrometric residuals projected on a perpendicular plane to the line of sight (b), positive when the line of sight falls above the trajectory solution. The error bars have nothing to do with the straight fit, but represent the formal astrometric uncertainties. The fact that the straight line fit residuals fall within observation uncertainties suggest that the straight line fit is a valid approximation of the trajectory. However this is not a proof that astrometric measurements are free from systematic errors, but can be used as an indication that this is unlikely to be the case. The distances in the legend correspond to the observation range [highest point - lowest point].

TESTING FOR SYSTEMATIC ERRORS

Searching for systematic errors is not easy without any ground truth fireball positions, though this is possible in theory by observing in parallel with an instrument that is inherently more precise (like a higher angular resolution imager). We have checked the internal consistency of the astrometric solution (Sec. 2.4.2), but this does not say anything about the consistency between star centroiding and fireball track picking, for example. A way to test the entire astrometric process is to look at a triangulated fireball event. Using a large number of viewpoints, with a wide variety of observing geometries, and from different distances to the event, it is unlikely that systematic errors in the astrometry would get randomly hidden in the residuals to the fit. We can see in Fig. 2.11, most of the astrometric residuals seem to be contained within 2′, all within calculated astrometric uncertainties. We note that a straight line fit to a meteoroid trajectory may not always be a valid assumption, especially as trajectories get longer (Sansom et al., 2019).

Another way to test for systematic errors could be to look at calculating astrometry for a bright Low Earth Orbit (LEO) satellite, and comparing the results with the ephemerides from a satellite database. The angular velocity for these objects is just high enough for the DFN cameras to be able to resolve the shutter breaks.

STABILITY OF THE ASTROMETRIC SOLUTION IN TIME

Fig. 2.12 shows that although the camera anchoring is remarkably stable, it is not enough to be able to re-use calibration information over long periods of time (weeks to months), and ideally one would always want to use a calibration image taken within a few minutes of the science images (for similar atmospheric effects). A typical example of when getting a close-by calibration frame is
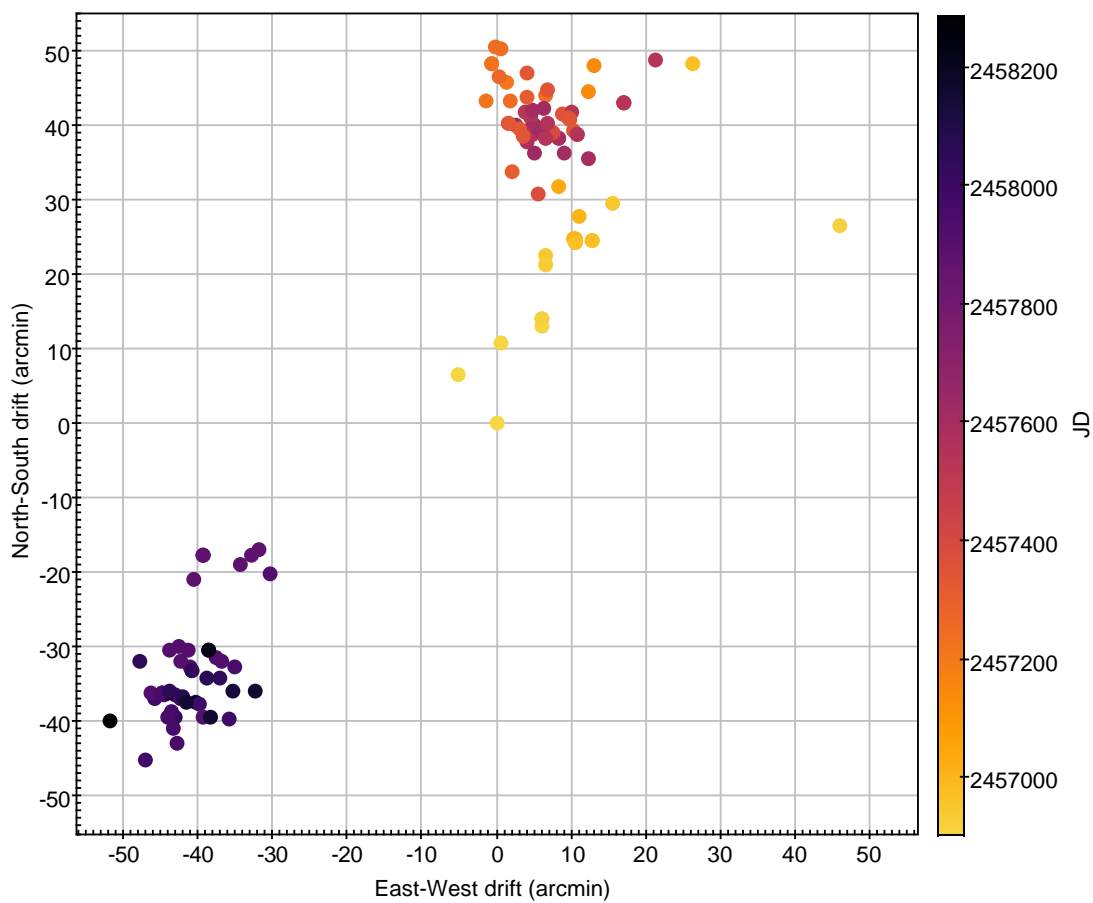
FIGURE 2.12: Drift of the zenith coordinates on the sensor of the Wilpoorina camera station over almost 4 years, based on calibration images used for reducing recorded fireballs (detected between 2014-08-31 and 2018-06-18). The camera box slowly moves in the weeks after the station was installed, as the metal stand of Howie et al. (2017a) settles (yellow dots). The pointing then remains relatively stable to $\pm 10'$ for 2 years. Then the camera box is swapped during servicing, significantly changing the orientation (purple/blue dots).

difficult is when a fireball is recorded close in time to a full moon in the summer, as moonless nautical night conditions are a few days away. In this case we can check that the astrometric solutions calculated a couple of days before and after the event are consistent. Another check that can be made, perhaps a more robust one, is to check the stars detected in the science frame match the catalogue coordinates when converting from pixel values to sky coordinates using the astrometric solution. In both cases, the detected deviations can be used as error estimates induced by science/calibration frame pointing change.

LIMITATIONS

It is expected that most fisheye lenses yield degraded angular resolution towards the edge of the field of view. However the lens used in DFN observatories has a stereographic projection which increases the number of pixels per degree of sky when going towards the edges. The plate scale goes from $\sim 120''\text{pix}^{-1}$ at then centre of the FoV, to about $\sim 70''\text{pix}^{-1}$ at a zenith angle of $85°$. In practice this means that the effective resolution of the system is uniform across the FoV, for elevation between $5°$ and the zenith, as the loss of light on the horizon due to the increase in airmass is compensated by the better pixel scale. We note that this $5°$ limit only holds when the horizon is clear of obstacles and light pollution is minimal. Devillepoix et al. (2018) quote an astrometric elevation limit of $10°$ when dealing with a partially obstructed horizon.

Below the astrometric elevation limit, astrometric uncertainties are essentially unconstrained. Devillepoix et al. (2019) show an example where the trajectory fit residuals rapidly diverges to $10'$ (mostly on the altitude axis) for an observation at $3°$ above the horizon. This particular astrometric point corresponds to the meteoroid at an altitude of $32\,\text{km}$ seen at a $500\,\text{km}$ distance. With the typical spacing between DFN cameras being 100-150 km, no such datapoint should need to be astrometrically calibrated during normal operations, i.e. when the

fireball of interest falls within the nominal triangulation area of the network.

PORTABILITY TO OTHER INSTRUMENTS

The all-sky astrometric method detailed here benefits greatly from the complete blind capabilities of *astrometry.net*, which does not require any hint on location in the sky, pixel scale, nor the parity of the image.

This method works perfectly on the DFN imager (36 Mpixel Nikon D810 + Samyang 8 mm f/3.5 UMC Fish-eye CS II (stereographic projection)), however we have also tested the blind solver on the following all-sky systems:

- Canon 5DSR (50 Mpixel) + Canon 8-15 mm f/4 (equisolid projection, operated at 8 mm focal).

- 1 Mpixel CCD sensor fitted with an unknown fisheye lens, with a 2 nm filter centred on 572.4 nm (Unewisse and Cool, 2017).

In both cases the solver worked flawlessly, yielding an astrometric fit better than sub-pixel. The only adjustment that was made is the size of the centre crop before running the *astrometry.net* solver. This could easily be automated, using a brute force trial and error search for a crop size until *astrometry.net* finds a solution.

2.4.3. CONCLUSION

The all-sky astrometric method developed here is the first solution astrometric all-sky solver that is robust, portable, and blind. The solver takes about 20 minutes on the single core of a standard 2012 workstation, and the memory footprint is small. The speed of the solver could certainly be improved, at least using parallelisation for numerical methods, however speed was not the

objective as the code is run on a scalable server rather than on remote resources limited computers.

The method shows sub-pixel astrometric calibration down to $5°$ above the horizon. This is particularly important for the Desert Fireball Network, as the spacing between observatories is typically greater than in other fireball networks, and these low-elevation datapoints are often crucial to getting reliable trajectory solution for the meteoroids. This $5°$ astrometric elevation limit corresponds to an object at $\sim 20\,$km altitude seen from a $200\,$km slant range, so the astrometric solution developed here outperforms the 100-150 km observatory spacing of the network.

However more work needs to be done to standardise the expression of the astrometric solution, for example using one the standard World Coordinate System (WCS) projections (Greisen and Calabretta, 2002; Calabretta and Greisen, 2002). This standardisation step is important is it will allow easier re-use of the DFN imaging data by other research groups.

2.5. PHOTOMETRY

2.5.1. INTRODUCTION

Previous works that describe meteor photographic photometry techniques have exclusively been on film based systems (Spurný et al., 2007). The European network uses radiometers as main sources of brightness data, however these instruments cannot be calibrated automatically. Lightcurve results therefore need to compared to photographic records. This calibration is performed when the brightness of the fireball is at a favourable SNR for the photographic system (Spurný et al., 2012), using film density measurements and a software called *Fishscan*. Not only does the radiometer offer a very hight sampling rate (500 Hz,

and later up to 5000 Hz) on a very large dynamic range, this instrument is absolutely necessary for European Network photographic stations to derive absolute timing for the fireball.

On the digital DFN observatories, the absolute time information is encoded in the astrometric data, removing the tedious need to manually combine the data from two instruments to get absolute timing (Howie et al., 2017b,a).

The use of photometric data in the DFN reduction process is very limited (Sec. 2.2), as the work of Sansom et al. (2015, 2016, 2017, 2019) has shown good results using the astrometric data only. Nevertheless we describe here how photometric data can be obtained from the digital images taken by the DFN.

When designing the observatories, the driver for choosing a camera has mainly been focussed on astrometric performance (see Sec. 2.4), reliability, availability of a control Linux API, and unit cost (to allow high scalability). When choosing a camera in 2012, these constraints pointed to the Nikon D800E (later replaced by the D810), for its 36 MPixel sensor, its acceptable low-noise performance, its ability to be fully controlled on Linux through the open source gPhoto API, and a tag price around AUD3500 (2012). Since then, this camera has met all expectations, and has even proven more reliable than anticipated: Nikon indicates a mean time between shutter failures of 200,000 exposures, but experience has shown that most units survive much longer, with a significant fraction reaching over a million exposures. However this camera model associated with its mode of operation suffers from several issues for photometric use:

1. The commercial digital camera (here a Nikon D810) is essentially a black box. Although lossless compressed "raw" frames are saved, there is no guarantee that the data are completely unprocessed before they are saved.

2. The dynamic range is much more limited than the film-based system of Spurný et al. (2007). Film has a logarithmic response, giving it a useful

dynamic range *[detection limit, saturation]* of about 15 stellar magnitudes, whereas the CMOS sensor used here is mostly linear and only has a usable dynamic range of about 8 magnitudes.

3. Twilight flat field frames are not possible with all-sky lenses because of large variations in sky brightness during twilight.

4. Dark frames cannot be captured because the camera does not allow an exposure without the shutter being open. Building a mechanism to achieve this would create a weak point in the reliability of the system (the observatory has no moving parts apart from fans and hard drive disks).

5. To avoid smudging of the shutter breaks in the picture when the fireball is bright, the duty cycle of the Liquid Crystal shutter is relatively short: 40% on the de Bruijn encoding of Howie et al. (2017b), 15% on the current version of the encoding (Devillepoix et al., 2019). This effectively severely reduces the amount of time the sensor is exposed to fireball light.

6. The Bayer array on the sensor further limits the amount of collecting area in each individual band (see Sec. 2.3.1).

From these considerations, it is reasonable to assume that this system would not reach milli-magnitude precision, as would a dedicated fully calibrated, cooled CCD.

2.5.2. METHODS & RESULTS

Until mid-2017, DFN cameras captured two 25 second-long exposures every minute. Of the 25 second exposure, the sensor is actually exposed for 11 seconds because of the action of the Liquid Crystal (LC) shutter. The LC shutter changes between two states, open and closed, and the time the shutter is opened is modulated to encode absolute timing information. In order to fully understand

what follows, it is useful to read the work of Howie et al. (2017a) for a precise description of the shutter and its operation, and (Howie et al., 2017b) for a full mathematical explanation of the de Bruijn time code. On top of that, the LC shutter leaks some light even when closed. Therefore we must make careful corrections when calibrating meteor brightness using stars as reference.

In the following sections quantities relating to the meteor (or fireball) are subscripted with $_f$, while those relating to a given reference star are subscripted with $_0$.

CALIBRATION OF THE INSTRUMENT: INSTRUMENTAL MAGNITUDE

Stars in the images can be used as references for determining instrumental magnitude. Here we define the necessary equations to relate star photometric measurements with meteor photometric measurements, given the different exposure times caused by the action of the LC shutter and the movement of meteors. I then apply this correction model to actual star measurements. By looking at the resulting distribution, I aim to derive a mean instrumental magnitude for the camera, get a feel for what the precision of this measurement may be, and highlight possible localised effects such as vignetting or partial cloudiness.

To compute the star exposure time, the LC shutter characteristics and operation must be accounted for. I aim to compute the instrumental magnitude at 1 airmass, with the zero-point vignetting in the centre of the lens, for the equivalent of 1 second exposure time with the LC shutter open. For a given star observed S_0, we have $T_0 = T_0^o + T_0^c$, with T_0 the duration of the exposure, ^{c} is with LC shutter closed, ^{o} is with LC shutter open.

Let D_c^o be the shutter average duty cycle, the average fraction of time the LC shutter is in the open state during the 25 second exposure: $D_c^o = T_0^o/T_0$.

The LC shutter lets some light through, even when it is closed. Let ϵ be that transmittance ratio between closed and open states: $\epsilon = f_0^c/f_0^o$ where f_0^o is the flux for when the shutter is open, and f_0^c when it is closed. Let's now determine f_0^o from the measured electron count I_0.

After simplification using the above definitions, we get:

$$f_0^o = \frac{I_0}{T_0(D_c^o + \epsilon(1 - D_c^o))} \tag{2.2}$$

We define the instrumental magnitude m_0^{inst}, as:

$$m_0^{inst} = m_0 + 2.5\log(f_0^o) + kX_0 \tag{2.3}$$

The first term, m_0, is the catalogue apparent magnitude of the star, the second term is the measurement (as defined in Eq. 2.2), and the last one is the atmospheric extinction contribution (with X_0 the airmass the star is observed through, and k the first order extinction coefficient in the considered spectral band).

Using aperture photometry, we determine the instrumental magnitude for a large number of reference stars in one image. Starting from the astrometric catalogue defined in Sec. 2.4.2, we only keep stars that have an acceptable signal to noise ratio (SNR): we exclude the stars fainter than $m_V = 5.5$ because of low SNR, as well as saturated stars (saturation usually happens for stars brighter than $m_V = 2$ observed through 1 airmass). The resulting instrumental magnitude measurements are plotted against the stars' elevations in Fig. 2.13, with no significant correlation between the two. We conclude that vignetting (if any) is dominated by other factors (poor optics, noise...). m_0^{inst} has therefore been sufficiently corrected: the mean value m^{inst} can reliably be used as photometric zero-point, and residuals (with $\sigma = 0.23$ mag in this case) are representative of the error on those measurements. Note that when the image is partially cloudy,
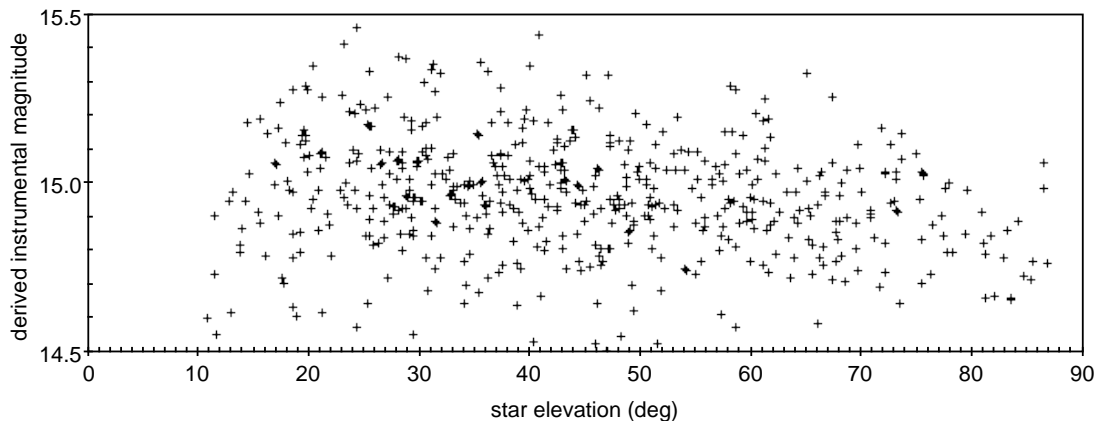
FIGURE 2.13: Instrumental magnitude calculated with 567 stars across the field of view ($\sigma = 0.23$ mag). 8 outliers, making up 1.4% of the final star set, are not shown on this plot. The original reference star set contained 792 stars, 28% of them were discarded because of poor SNR, dubious astrometric catalogue match, or too close neighbours.

we may do the same analysis in a localised approach around the meteor instead of using the whole field of view.

BRIGHTNESS MEASUREMENTS ON THE METEOR

The basic time step for meteor photometry measurements is driven by the action of the LC shutter. The LC shutter runs at 10 Hz, which gives 10 measurements per second. To get the light curve of the fireball, the luminosity from each dash is integrated. We perform rectangular aperture photometry on each dash (see Fig. 2.14) using the Astropy Photutils package (Bradley et al., 2016). In Fig. 2.14 we can see a fireball modulated by the LC shutter, the boxes drawn represent the apertures used. The integration time T_f corresponding to each box depends on the modulation: with the encoding used here a short dash represents $0.02\,\text{s}$ of open state, and a long dash $0.06\,\text{s}$ of open state. Howie et al. (2017b) showed that the change in transmittance between open and closed states is close enough to a rectangular function to neglect edge effects introduced by the electronics on the photometry. The sky background is subtracted, and the result I_f is normalised by the exposure time of the dash, and we obtain the mean flux for a
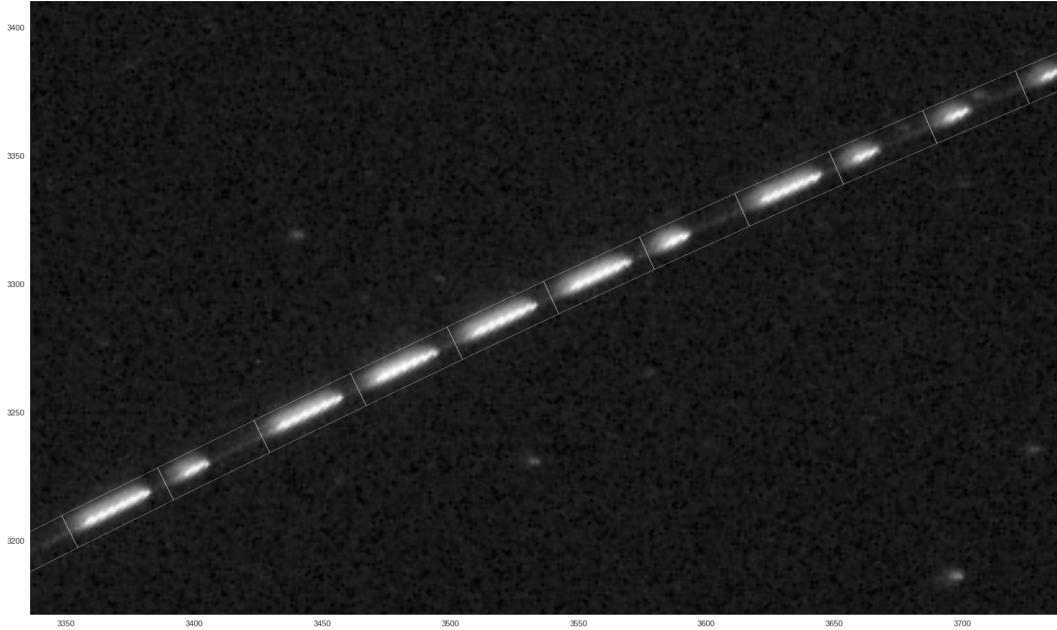
FIGURE 2.14: Rectangular aperture photometry automatically performed on a Taurid fireball.

given dash: $f_f = I_f/T_f$

The biggest limitation of this method is the saturation of the sensor, which translates into large negative uncertainties in the magnitudes. In practice, this saturation happens at around $m_V = -8$. Because the LC shutter is not open all the time and the large possible variations of the brightness on a short time scale (mainly caused by fragmentation), some features of the light curve can be missed. This technique is therefore expected to slightly underestimate the overall brightness by missing some short-lived peaks.

MAGNITUDE OF THE METEOR

We are now able to relate flux for the reference (stars) and the object of interest (meteor), which lets us calculate the apparent magnitude of the meteor m_f:

$$m_f = m^{inst} - 2.5\log(f_f) - kX_f \tag{2.4}$$

Note that we neglect atmospheric extinction happening in the upper layers of the atmosphere, so we can then assume that the extinction affecting the meteor would be the same as a star located at the same elevation on the sky.

Once the meteor is triangulated, we can calculate the distance of each point to the observer, and the absolute magnitude, M_f, can be derived by correcting for distance:

$$M_f = m_f - 2.5 \log\left(\left(\frac{range}{100 \text{km}}\right)^2\right)$$

An example of a calibrated light curve is shown in Fig. 2.15. Most brightness values are in agreement when measured from different cameras (to within ± 0.5 mag in most cases). This result is reasonably satisfying considering the measured variability in instrumental magnitude on one camera has $\sigma = 0.23$ mag. The larger inconsistencies can be caused by a variety of other effects, such as saturation, bad optics quality, and clouds.

2.5.3. CONCLUSION

The extraction of the photometry in DFN images is highly limited by the dynamic range of the cameras (Devillepoix et al., 2019), it is notably far inferior in quality compared to dedicated instruments like radiometers. These measurements can be use nonetheless as additional observation data to constrain the meteoroid's physical parameters as it ablates through the atmosphere (Sansom et al., 2019).

The method presented here is automatically routinely applied to the *green* band on the cameras, but it can also be applied to the *blue* and *red* bands with very little code modification, to derive colour indices. Although the spectral coverage of the sensor is limited ($400 - 700$ nm), the colour indices could be used for fireball taxonomy.
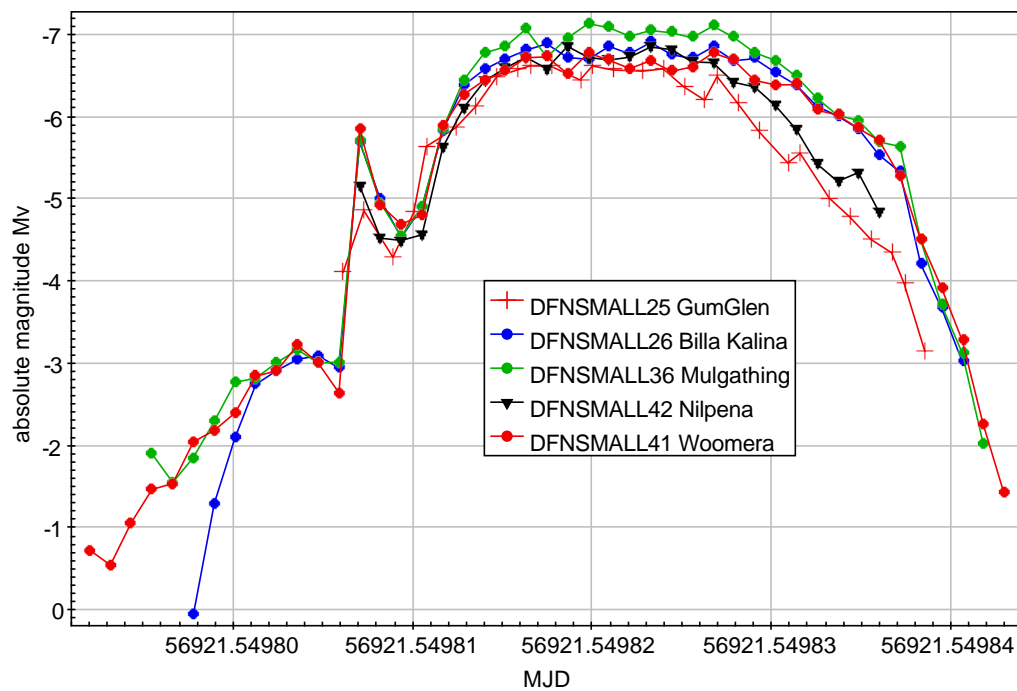
FIGURE 2.15: Light curve of fireball DN140921_01, as derived from multiple observatories, automatically calibrated spectrally and temporally by the software. The good match between the different stations (mostly to within ±0.5 mag) shows the quality of the measurements and calibration, accounting for the varying observing conditions, optics quality, and elevation angles, as the distance from the observatories varies from 116 to 287 km.

2.6. DE-BIASING THE FIREBALL DATASET: PROOF OF CONCEPT

2.6.1. INTRODUCTION

Meteor detection rate measurements started with visual counting, notably to quantify the activity of meteor showers (Jenniskens, 2006). Although visual counting of meteors is still used, mostly by amateur astronomer, this technique has been made mostly obsolete by the wide-scale use of video cameras to continuously capture meteors. Not only are cameras less prone to biases when counting meteors, they can also derive radiants, orbits, and some physical characteristics (Jenniskens et al., 2011). The current state of the art in meteor flux de-biasing methods is described by Blaauw et al. (2016). The authors continuously calculate a surveying time-area product, and also calculate a detection limit in order to take sky conditions into account.

For fireball networks, the reference for de-biasing work remains the clear-sky survey work by Halliday et al. (1996) on the Meteorite Observation and Recovery Project (MORP) data. The reduction of the MORP data included visually classifying photographic plates as "clear" or "cloudy", based on the number of stars visible on the all-night exposures.

These efforts resulted into unprecedented insights on the meteoroid flux around the $10^0 - 10^2$ kg mass range, a body size that is hard to study with other methods: too infrequent for meteor surveys like CAMS (Jenniskens et al., 2011), but below the reporting limit of satellite borne sensors (Brown et al., 2002).

The MORP data plotted on a size frequency distribution plot shows a bend near the 10^1 kg mark (Bland and Artemieva, 2006). Higher masses seem to fit on the same slope as the power law that fits flux densities in the $10^3 - 10^{10}$ kg
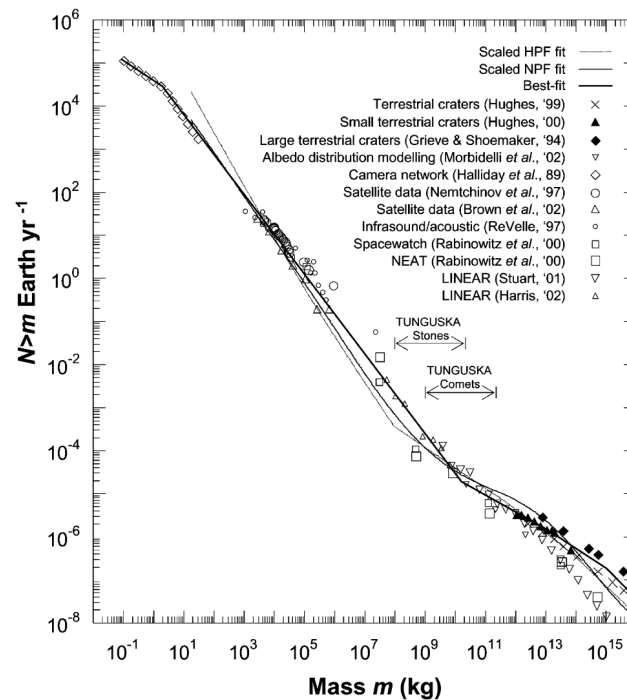
FIGURE 2.16: Fig. 15 from Bland and Artemieva (2006).

range (Fig. 2.16), whereas lower masses are on a shallower slope. The origin of this kink in the curve is still debated today (Rubincam, 2018). Therefore more studies are needed, at least to reproduce and verify the Halliday et al. (1996) results, but hopefully to yield new insights on what mechanism can cause this change.

Here I lay out a proof of concept for on-going work by the DFN team on de-biasing the fireball dataset.

2.6.2. METHODS

The digital nature of the DFN imaging systems makes it in principle easy to determine clear-sky conditions in an automated manner. Furthermore the DFN keeps all the still imagery ever recorded, and archives it in the Pawsey datastore, making it possible to reprocess it.
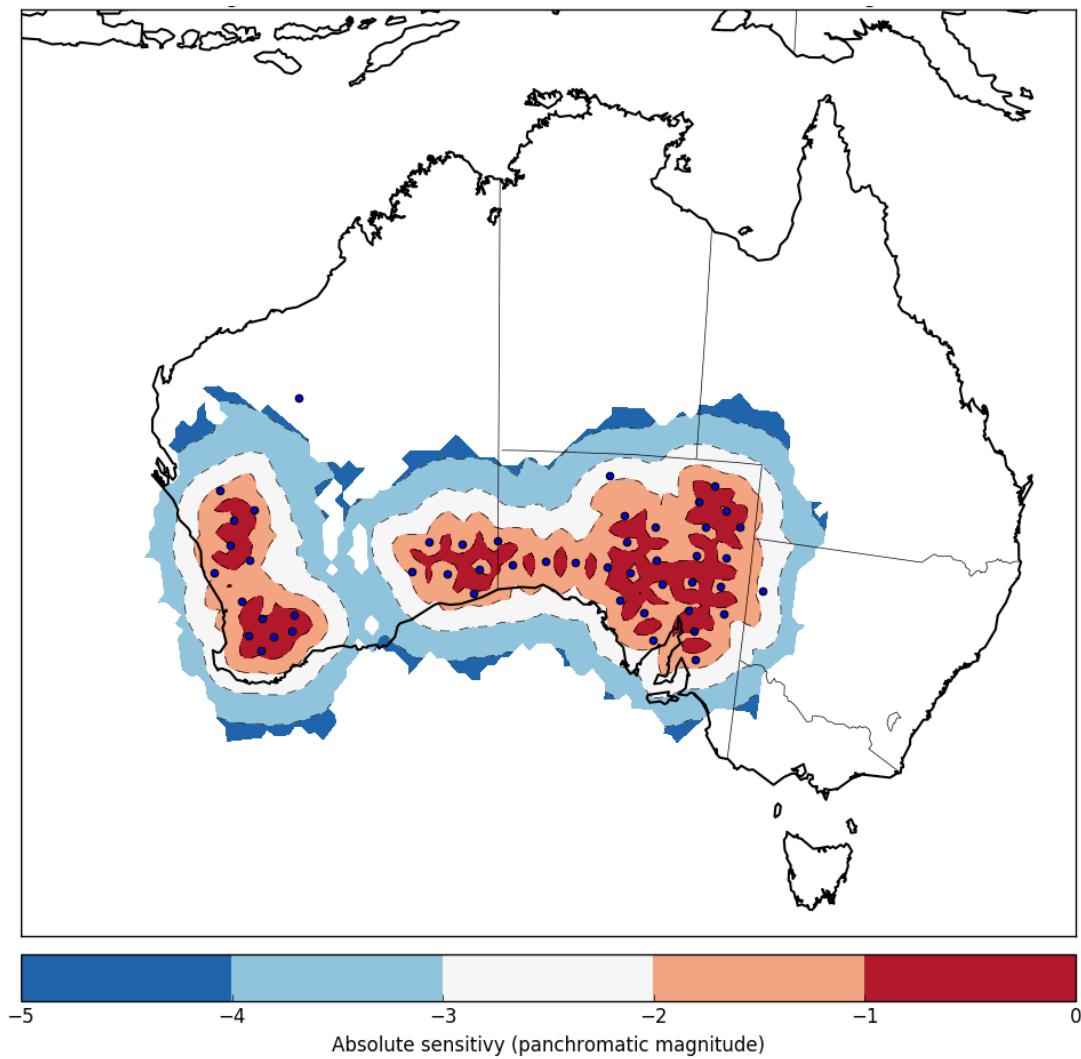
FIGURE 2.17: Simulation of the double station coverage area covered by the
DFN. This takes into account local sky conditions, potential hardware failures,
obstructions in the field of view, camera sensitivity. The colour scale shows the
absolute magnitude sensitivity, it can be read as: "how bright does a meteor
need to be to be triangulated by at least 2 stations?". Operational observatories
are marked as blue dots.

We want to make this as precise as possible, by having a small time resolution, a high spatial precision, and also consider detection limits. As cameras take an image every 30 seconds, we want to aim to have the time step as small as 30 seconds. Different parts of the field of view will have varying sensitivity because of clouds, vignetting, obstructions, sky transparency, etc. It is therefore desirable to generate a sensitivity map for each exposure using stars as references. Assuming a nominal altitude of 70 km as a height that most fireballs get to, it is possible to project the apparent sensitivity to absolute sensitivity, taking the observation distance into account. We can then intersect these maps: fireballs have to be observed by at least two stations to be triangulable, so we build maps of double station viewing area, indexed by the absolute magnitude the fireball has to be to be detected by at least two stations. This type of map can be visualised in Fig. 2.17. To form the clear sky survey, the detection areas are tallied over time.

The DFN team is currently implementing the necessary backend tools to support this heavy task. This effort notably includes a housekeeping relational database, in order to keep track of all the observatories, engineering and clear sky status.

2.7. CONCLUSION

Along with operations and science studies, the development of the data reduction pipeline software and method is one of the main tasks of the DFN team members. On top of developing some of the methods presented here, my work involves coordinating the team of five that works on various parts of the pipeline. This includes work on standardising input/output formats, writing documentation, testing, handling operations, and monitoring quality. As of 2018, the data reduction code repository contains over 150,000 lines of python
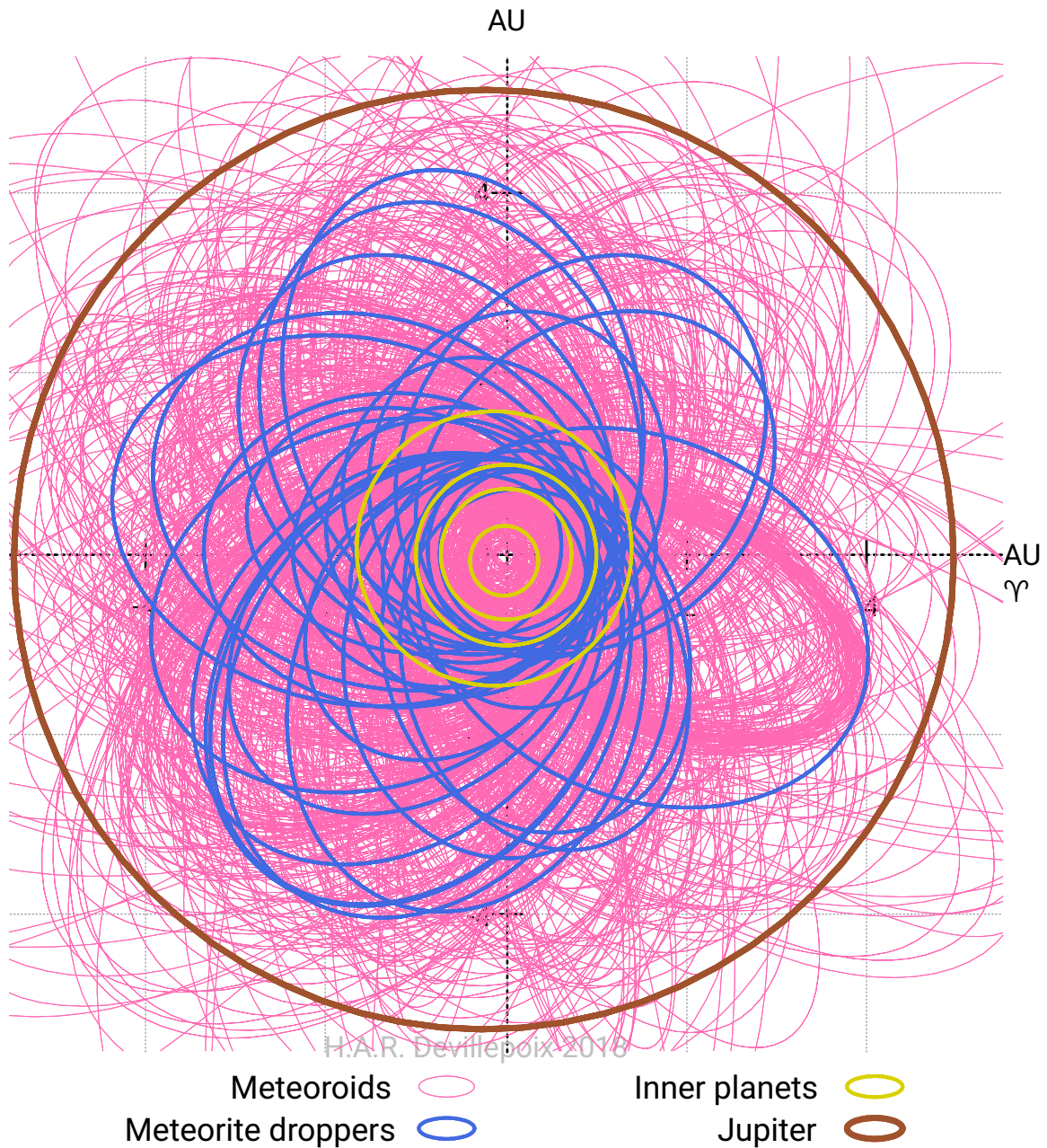
FIGURE 2.18: Ecliptic inner Solar System plot of the DFN orbital dataset as of mid-2018 (pink). Potential meteorite droppers are highlighted in blue.

code contributed by DFN team members.

In its next generation of observatories — tailored for the Global Fireball Observatory — the DFN is adding digital video cameras in parallel to the long-exposure high resolution imagers. Among other things, this will allow daytime imaging of bright fireballs to be possible. In principle, finding the centroids of the fireball and decoding the timing is inherently simpler, as the fireball will look like a point source instead of a time encoded streak. With the use of long calibration exposures on the digital video cameras yielding a large number of stars, the astrometric solver developed (Sec. 2.4) should be ported to these instruments with little modification.

The accuracy of the reduction routines has been proven by the swift recovery of the Murrili meteorite in December 2015 (Devillepoix et al., 2016), and Dingle Dell meteorite in November 2016 (Devillepoix et al., 2018). The automated nature of the reduction package has also permitted the study of a large number of meteoroid orbits (Fig. 2.18), as detailed in Chap. 5.

As of the meteorite recovery process, the last important step that needs to be automated is the searching procedure. This concept of automated meteorite searching has been tested using Unmanned Aerial Vehicles (UAV) and machine learning algorithms to identify meteorites. Some encouraging results have shown that it is possible (Citron et al., 2017), however it remains to be tested and deployed on a large scale.

ACKNOWLEDGMENTS

(Kluyver et al., 2016), *Pandas* (McKinney, 2010), and *scikit-image* (van der Walt et al., 2014); it also benefits from the *Topcat* and *Stilts* packages (Taylor, 2005).

This tasks also benefits from the facilities of the Pawsey supercomputing centre: the supercomputer Magnus is used for some heavy processing tasks, and the Petascale Datastore stores all of the imagery data.

2.8. REFERENCES

Astropy Collaboration, T. P. Robitaille, E. J. Tollerud, P. Greenfield, M. Droettboom, E. Bray, T. Aldcroft, M. Davis, A. Ginsburg, A. M. Price-Whelan, W. E. Kerzendorf, A. Conley, N. Crighton, K. Barbary, D. Muna, H. Ferguson, F. Grollier, M. M. Parikh, P. H. Nair, H. M. Unther, C. Deil, J. Woillez, S. Conseil, R. Kramer, J. E. H. Turner, L. Singer, R. Fox, B. A. Weaver, V. Zabalza, Z. I. Edwards, K. Azalee Bostroem, D. J. Burke, A. R. Casey, S. M. Crawford, N. Dencheva, J. Ely, T. Jenness, K. Labrie, P. L. Lim, F. Pierfederici, A. Pontzen, A. Ptak, B. Refsdal, M. Servillat, and O. Streicher. Astropy: A community Python package for astronomy. A&A, 558:A33, Oct. 2013. doi: 10.1051/0004-6361/201322068.

E. Bertin. Automatic Astrometric and Photometric Calibration with SCAMP. In C. Gabriel, C. Arviset, D. Ponz, and S. Enrique, editors, *Astronomical Data Analysis Software and Systems XV*, volume 351 of *Astronomical Society of the Pacific Conference Series*, page 112, July 2006.

R. C. Blaauw, M. Campbell-Brown, and A. Kingery. Optical meteor fluxes and application to the 2015 Perseids. MNRAS, 463:441–448, Nov. 2016. doi: 10.1093/mnras/stw1979.

P. A. Bland and N. A. Artemieva. The rate of small impacts on Earth. *Meteoritics*

and Planetary Science, 41:607–631, Apr. 2006. doi: 10.1111/j.1945-5100.2006. tb00485.x.

J. Borovička. The comparison of two methods of determining meteor trajectories from photographs. *Bulletin of the Astronomical Institutes of Czechoslovakia*, 41: 391–396, Dec. 1990.

J. Borovička, P. Spurný, and J. Keclikova. A new positional astrometric method for all-sky cameras. *Astronomy and Astrophysics Supplement*, 112:173, July 1995.

J. Borovička, J. Tóth, A. Igaz, P. Spurný, P. Kalenda, J. Haloda, J. Svoreǎ, L. Kornoš, E. Silber, P. Brown, and M. HusáRik. The Košice meteorite fall: Atmospheric trajectory, fragmentation, and orbit. *Meteoritics and Planetary Science*, 48:1757–1779, Oct. 2013. doi: 10.1111/maps.12078.

J. Borovička, P. Spurný, and P. Brown. *Small Near-Earth Asteroids as a Source of Meteorites*, pages 257–280. University of Arizona Press, 2015. doi: 10.2458/ azu_uapress_9780816532131-ch014.

J. Borovička. Astrometry with all-sky cameras. *Publications of the Astronomical Institute of the Czechoslovak Academy of Sciences*, 79, Jan. 1992.

L. Bradley, B. Sipocz, T. Robitaille, E. Tollerud, Z. Vinícius, C. Deil, K. Barbary, H. M. Günther, M. Cara, M. Droettboom, A. Bostroem, E. Bray, L. A. Bratholm, T. E. Pickering, M. Craig, G. Barentsen, S. Pascual, adonath, J. Greco, W. Kerzendorf, StuartLittlefair, L. Ferreira, F. D'Eugenio, and B. A. Weaver. astropy/photutils: v0.3, Nov. 2016.

P. Brown, R. E. Spalding, D. O. ReVelle, E. Tagliaferri, and S. P. Worden. The flux of small near-Earth objects colliding with the Earth. Nature, 420:294–296, Nov. 2002. doi: 10.1038/nature01238.

M. R. Calabretta and E. W. Greisen. Representations of celestial coordinates in FITS. A&A, 395:1077–1122, Dec. 2002. doi: 10.1051/0004-6361:20021327.

Z. Ceplecha. Multiple fall of Příbram meteorites photographed. 1. Double-station photographs of the fireball and their relations to the found meteorites. *Bulletin of the Astronomical Institutes of Czechoslovakia*, 12:21, 1961.

Z. Ceplecha. Geometric, dynamic, orbital and photometric data on meteoroids from photographic fireball networks. *Bulletin of the Astronomical Institutes of Czechoslovakia*, 38:222–234, July 1987.

R. I. Citron, A. Shah, S. Sinha, C. Watkins, and P. Jenniskens. Meteorite Recovery Using an Autonomous Drone and Machine Learning. In *Lunar and Planetary Science Conference*, page 2528, Mar. 2017.

N. L. de Lacaille, T. Henderson, F. Baily, and S. Herschel, John Frederick William. *A Catalogue of 9766 Stars in the Southern Hemisphere, for the beginning of the year 1750, from the observations of the Abbé de Lacaille, made at the Cape of Good Hope in the years 1751 and 1752.* 1847.

H. A. R. Devillepoix, P. A. Bland, M. C. Towner, M. Cupák, E. K. Sansom, T. Jansen-Sturgeon, R. M. Howie, J. Paxman, and B. A. D. Hartig. Status of the Desert Fireball Network. In A. Roggemans and P. Roggemans, editors, *International Meteor Conference Egmond, the Netherlands, 2-5 June 2016*, pages 60–62, Jan. 2016.

H. A. R. Devillepoix, E. K. Sansom, P. A. Bland, M. C. Towner, M. CupáK, R. M. Howie, T. Jansen-Sturgeon, M. A. Cox, B. A. D. Hartig, G. K. Benedix, and J. P. Paxman. The Dingle Dell meteorite: A Halloween treat from the Main Belt. *Meteoritics and Planetary Science*, 53:2212–2227, Oct. 2018. doi: 10.1111/maps.13142.

H. A. R. Devillepoix, P. A. Bland, E. K. Sansom, M. C. Towner, M. Cupák, R. M. Howie, B. A. D. Hartig, T. Jansen-Sturgeon, and M. A. Cox. Observation of metre-scale impactors by the Desert Fireball Network. MNRAS, 483:5166–5178, Mar 2019. doi: 10.1093/mnras/sty3442.

A. Egal, P. S. Gural, J. Vaubaillon, F. Colas, and W. Thuillot. The challenge associated with the robust computation of meteor velocities from video and photographic records. Icarus, 294:43–57, Sept. 2017. doi: 10.1016/j.icarus.2017.04.024.

P. Farinella, D. Vokrouhlický, and W. K. Hartmann. Meteorite Delivery via Yarkovsky Orbital Drift. Icarus, 132:378–387, Apr. 1998. doi: 10.1006/icar.1997.5872.

M. Granvik and P. Brown. Identification of meteorite source regions in the Solar System. Icarus, 311:271–287, Sept. 2018. doi: 10.1016/j.icarus.2018.04.012.

E. W. Greisen and M. R. Calabretta. Representations of world coordinates in FITS. A&A, 395:1061–1075, Dec. 2002. doi: 10.1051/0004-6361:20021326.

I. Halliday. Photographic Fireball Networks. *NASA Special Publication*, 319:1, 1973.

I. Halliday, A. A. Griffin, and A. T. Blackwell. Detailed data for 259 fireballs from the Canadian camera network and inferences concerning the influx of large meteoroids. *Meteoritics and Planetary Science*, 31:185–217, Mar. 1996. doi: 10.1111/j.1945-5100.1996.tb02014.x.

D. M. Hawkins. The problem of overfitting. *Journal of Chemical Information and Computer Sciences*, 44(1):1–12, 2004. doi: 10.1021/ci0342472. PMID: 14741005.

R. M. Howie, J. Paxman, P. A. Bland, M. C. Towner, M. Cupák, E. K. Sansom, and H. A. R. Devillepoix. How to build a continental scale fireball camera network. *Experimental Astronomy*, May 2017a. doi: 10.1007/s10686-017-9532-7.

R. M. Howie, J. Paxman, P. A. Bland, M. C. Towner, E. K. Sansom, and H. A. R. Devillepoix. Submillisecond fireball timing using de Bruijn time-codes. *Meteoritics and Planetary Science*, 52:1669–1682, Aug. 2017b. doi: 10.1111/maps.12878.

T. Jansen-Sturgeon, E. K. Sansom, and P. A. Bland. Comparing Analytical and Numerical Approaches to Meteoroid Orbit Determination using Hayabusa Telemetry. *ArXiv e-prints*, art. arXiv:1808.05768, Aug. 2018.

P. Jenniskens. *Meteor Showers and Their Parent Comets*. Cambridge University Press, 2006. ISBN 9780521853491.

P. Jenniskens, P. S. Gural, L. Dynneson, B. J. Grigsby, K. E. Newman, M. Borden, M. Koop, and D. Holman. CAMS: Cameras for Allsky Meteor Surveillance to establish minor meteor showers. Icarus, 216:40–61, Nov. 2011. doi: 10.1016/j. icarus.2011.08.012.

P. Jenniskens, J. Utas, Q.-Z. Yin, R. D. Matson, M. Fries, J. A. Howell, D. Free, J. Albers, H. Devillepoix, P. Bland, A. Miller, R. Verish, L. A. J. Garvie, M. E. Zolensky, K. Ziegler, M. E. Sanborn, K. L. Verosub, D. J. Rowland, D. R. Ostrowski, K. Bryson, M. Laubenstein, Q. Zhou, Q.-L. Li, X.-H. Li, Y. Liu, G.-Q. Tang, K. Welten, M. W. Caffee, M. M. M. Meier, A. A. Plant, C. Maden, H. Busemann, M. Granvik, and T. C. M. Consortium). The creston, california, meteorite fall and the origin of l chondrites. *Meteoritics & Planetary Science*, in press, 2019. doi: 10.1111/maps.13235. URL `https://onlinelibrary. wiley.com/doi/abs/10.1111/maps.13235`.

E. Jones, T. Oliphant, P. Peterson, et al. SciPy: Open source scientific tools for Python, 2001–. URL `http://www.scipy.org/`. [Online; accessed ¡today¿].

T. Kluyver, B. Ragan-Kelley, F. Pérez, B. Granger, M. Bussonnier, J. Frederic, K. Kelley, J. Hamrick, J. Grout, S. Corlay, P. Ivanov, D. Avila, S. Abdalla, and C. Willing. Jupyter notebooks – a publishing format for reproducible computational workflows. In F. Loizides and B. Schmidt, editors, *Positioning and Power in Academic Publishing: Players, Agents and Agendas*, pages 87 – 90. IOS Press, 2016.

D. Lang, D. W. Hogg, K. Mierle, M. Blanton, and S. Roweis. Astrometry.net:

Blind Astrometric Calibration of Arbitrary Astronomical Images. *The astronomical journal*, 139:1782–1800, May 2010. doi: 10.1088/0004-6256/139/5/1782.

W. McKinney. Data structures for statistical computing in python. In S. van der Walt and J. Millman, editors, *Proceedings of the 9th Python in Science Conference*, pages 51 – 56, 2010.

A. Morbidelli, R. Gonczi, C. Froeschle, and P. Farinella. Delivery of meteorites through the nu_6 secular resonance. A&A, 282:955–979, Feb. 1994.

J. Oberst, S. Molau, D. Heinlein, C. Gritzner, M. Schindler, P. Spurny, Z. Ceplecha, J. Rendtel, and H. Betlem. The "European Fireball Network": Current status and future prospects. *Meteoritics and Planetary Science*, 33, Jan. 1998. doi: 10.1111/j.1945-5100.1998.tb01606.x.

T. E. Oliphant. *Guide to NumPy*. CreateSpace Independent Publishing Platform, USA, 2nd edition, 2015. ISBN 151730007X, 9781517300074.

F. Pérez and B. E. Granger. IPython: a system for interactive scientific computing. *Computing in Science and Engineering*, 9(3):21–29, May 2007. ISSN 1521-9615. doi: 10.1109/MCSE.2007.53. URL `https://ipython.org`.

D. P. Rubincam. Possible lack of low-mass meteoroids in the Earth's meteoroid flux due to space erosion? Icarus, 299:161–165, Jan. 2018. doi: 10.1016/j.icarus.2017.07.020.

E. Sansom and et al. Fall and recovery of the Murrili meteorite. *submitted to MAPS*, 2018.

E. K. Sansom, P. Bland, J. Paxman, and M. Towner. A novel approach to fireball modeling: The observable and the calculated. *Meteoritics and Planetary Science*, 50:1423–1435, Aug. 2015. doi: 10.1111/maps.12478.

E. K. Sansom, P. A. Bland, M. G. Rutten, J. Paxman, and M. C. Towner. Filtering Meteoroid Flights Using Multiple Unscented Kalman Filters. AJ, 152:148, Nov. 2016. doi: 10.3847/0004-6256/152/5/148.

E. K. Sansom, M. G. Rutten, and P. A. Bland. Analyzing Meteoroid Flights Using Particle Filters. AJ, 153:87, Feb. 2017. doi: 10.3847/1538-3881/153/2/87.

E. K. Sansom, T. Jansen-Sturgeon, M. G. Rutten, H. A. R. Devillepoix, P. A. Bland, R. M. Howie, M. A. Cox, M. C. Towner, M. Cupák, and B. A. D. Hartig. 3D meteoroid trajectories. Icarus, 321:388–406, Mar 2019. doi: 10.1016/j. icarus.2018.09.026.

M. Sokolowski. *Investigation of astrophysical phenomena in short time scales with "Pi of the Sky" apparatus.* PhD thesis, -, Oct. 2008.

P. Spurný, J. Borovička, and L. Shrbený. Automation of the Czech part of the European fireball network: equipment, methods and first results. In *Near Earth Objects, our Celestial Neighbors: Opportunity and Risk*, volume 236, pages 121–130, May 2007. doi: 10.1017/S1743921307003146.

P. Spurný, P. A. Bland, L. Shrbený, J. Borovička, Z. Ceplecha, A. Singelton, A. W. R. Bevan, D. Vaughan, M. C. Towner, T. P. McClafferty, R. Toumi, and G. Deacon. The Bunburra Rockhole meteorite fall in SW Australia: fireball trajectory, luminosity, dynamics, orbit, and impact position from photographic and photoelectric records. *Meteoritics and Planetary Science*, 47: 163–185, Feb. 2012. doi: 10.1111/j.1945-5100.2011.01321.x.

P. Spurný, J. Haloda, J. Borovička, L. Shrbený, and P. Halodová. Reanalysis of the Benešov bolide and recovery of polymict breccia meteorites - old mystery solved after 20 years. A&A, 570:A39, Oct. 2014. doi: 10.1051/0004-6361/ 201424308.

M. B. Taylor. TOPCAT & STIL: Starlink Table/VOTable Processing Software. In P. Shopbell, M. Britton, and R. Ebert, editors, *Astronomical Data Analysis*

Software and Systems XIV, volume 347 of *Astronomical Society of the Pacific Conference Series*, page 29, Dec. 2005.

M. Towner and et al. Fireball streak detection with minimal CPU processing requirements for the Desert Fireball Network data processing pipeline. *PASA*, submitted.

A. Unewisse and A. Cool. A Guide to the DST Airglow Database. Technical Report DST-Group-GD-0978, Defence Science and Technology (DST) Group, Oct. 2017.

S. E. Urban, T. E. Corbin, and G. L. Wycoff. The ACT Reference Catalog. AJ, 115:2161–2166, May 1998. doi: 10.1086/300344.

S. van der Walt, J. L. Schönberger, J. Nunez-Iglesias, F. Boulogne, J. D. Warner, N. Yager, E. Gouillart, and T. a. Yu. scikit-image: image processing in python. *PeerJ*, 2:e453, June 2014. ISSN 2167-8359. doi: 10.7717/peerj.453.

D. Vida, P. G. Brown, and M. Campbell-Brown. Modelling the measurement accuracy of pre-atmosphere velocities of meteoroids. MNRAS, 479:4307–4319, Oct. 2018. doi: 10.1093/mnras/sty1841.

CHAPTER 3

OBSERVATION OF METRE-SCALE IMPACTORS BY THE DESERT FIREBALL NETWORK

Hadrien A. R. Devillepoix[a], Philip Bland[a], Eleanor K. Sansom[a], Martin C. Towner[a],

Martin Cupák[a], Robert M. Howie[a], Benjamin A. D. Hartig[a], Trent Jansen-Sturgeon[a], Morgan A. Cox[a]

[a]School of Earth and Planetary Sciences, Curtin University, GPO Box U1987, Bentley, Perth, WA 6845, Australia

Abstract

The Earth is impacted by 35-40 metre-scale objects every year. These meteoroids are the low mass end of impactors that can do damage on the ground. Despite this they are very poorly surveyed and characterised, too infrequent for ground based fireball observation efforts, and too small to be efficiently detected by NEO telescopic surveys whilst still in interplanetary space. We want to evaluate the suitability of different instruments for characterising metre-scale impactors and where they come from. We use data collected over the first 3 years of operation of the continent-scale Desert Fireball Network, and compare results with other published results as well as orbital sensors. We find that although the orbital sensors have the advantage of using the entire planet as collecting area, there are several serious problems with the accuracy of the data, notably the reported velocity vector, which is key to getting an accurate pre-impact orbit and calculating meteorite fall positions. We also outline dynamic range issues that fireball networks face when observing large meteoroid entries.

3.1. Introduction

The Earth is impacted by 35-40 metre-scale objects every year (Brown et al., 2002; Bland and Artemieva, 2006). These large meteoroids are at the low mass end of potentially damage-causing impacting asteroids like Chelyabinsk (Brown et al., 2013). The study of the atmospheric behaviour, physical nature, numbers, and dynamical origin of these objects is therefore important in order to assess the hazard they pose, and prepare an appropriate response should an asteroid be detected and determined to be on a collision course with Earth.

3.1.1. HOW FREQUENTLY DO THESE IMPACTS HAPPEN?

One of the ways the size frequency distribution (SFD) of metre-scale has been surveyed is by using the so-called US Government (USG) sensors[1], which are able to detect flashes all around the world, day and night, measure flash energy, and sometimes derive velocities and airburst heights. As outlined by Brown et al. (2013), there might be subtleties in the SFD, namely a larger number of 10-50 m objects. Indeed the 1-100 m size range is largely unobserved, with objects too small for telescopes and too infrequent for impact monitoring systems to get representative surveys. So far, there have been 3 cases of asteroids detected before atmospheric impact. These are asteroids 2008 TC3 (Jenniskens et al., 2009; Farnocchia et al., 2017), 2014 AA (Farnocchia et al., 2016), and 2018 LA, all discovered by the Catalina Sky Survey only hours before impact. As large deep surveyors like LSST (Ivezic et al., 2008) come online these types of detections are going to become more common, and predicting the consequences of these impacts is going to be desirable. While the impact location of 2008 TC3 was well constrained to sub kilometre precision thanks to a very large number (≃900) of astrometric measurements, the prediction for 2014 AA was much more uncertain and covered a large area of the Atlantic ocean, as only a total of 7 astrometric positions were available. The impact location of 2018 LA was very uncertain, until 2 extra observation by the Asteroid Terrestrial-impact Last Alert System (ATLAS) increased the observation arc length from 1.3 hours to 3.7 hours, which narrowed down the impact location to South Africa. The number of astrometric observations and the length of the observation arc are therefore a critical factors to precisely determining the impact point. Well coordinated, large follow-up networks of telescopes can provide large numbers of such observations and will aid in future impact predictions (Lister et al., 2016).

---

[1] https://cneos.jpl.nasa.gov/fireballs/ accessed November 22, 2017

3.1.2. HOW DANGEROUS ARE THESE IMPACTS?

The damage from an impact depends not only on dynamical parameters, but also on: size, rock type, structure, strength (s) and density (ρ). To illustrate this, we can use the equations of Collins et al. (2005) to simulate the outcome of the impact of a 2 m object, with an entry angle of $18°$, a velocity of $19\,\text{km s}^{-1}$ at the top of the atmosphere (same entry angle and velocity as Chelyabinsk), and various bulk strengths and densities corresponding to different classes of objects (from Chyba et al. (1993)):

- a weak cometary body ($s = 10^5\,\text{Pa}$, $\rho = 1000\,\text{kg m}^{-3}$) will break up at a high altitude (60 km), causing no significant direct damage because the predicted 0.18 kT TNT of energy released cannot be transferred efficiently to the ground due to the thin atmosphere (1 kT TNT = 4.184×10^{12} J).

- a chondritic body ($s = 10^7\,\text{Pa}$, $\rho = 3500\,\text{kg m}^{-3}$) is likely going to airburst at relatively low altitudes (the model predicts an airburst at 27 km), releasing around 0.44 kT TNT of energy that can be propagated more efficiently by the denser atmosphere.

- an iron ($s = 10^8\,\text{Pa}$, $\rho = 7900\,\text{kg m}^{-3}$) monolith will reach the surface at hypersonic velocity ($3.8\,\text{km s}^{-1}$), causing important but very localised damage, as it only yields 10^{-1} kT TNT.

This is a simplistic example, but it shows how much the response to an imminent asteroid impact depends on both physical and dynamical characteristics of the impactor.

Several observation techniques can be levied while the asteroid is still in interplanetary space:

- Multi-band photometry in Vis-NIR: size and rotation period, and lower constraint on cohesive strength as a consequence.

- Spectroscopy: likely composition.

- Astrometric observations: pre-encounter orbit, and predictions about the impact geometry, velocity, and location.

- Radar observations: size, shape, rotation period, presence of satellites.

While the size and impacting velocity are well constrained factors using astrometric observations, determining the rock type and structure from remote sensing instruments is more challenging.

To some extent spectroscopy can provide insights on the mineralogy of the impactor, but this technique requires a good knowledge of how asteroid spectral types match meteorite types.

Another approach is the work of Mommert et al. (2014b,a) on small (metre-scale) asteroids for which spectroscopic work is generally impractical. They used a thermophysical model combined with an orbital model that takes non-gravitational forces into accounts. This model derives physical parameters (likely surface composition, size) by combining both astrometric observations and Near-Infrared photometry.

In order to be reliable on large scales, these techniques have to be qualified with direct sample analysis. This active area of research can be tackled in two ways: either direct sample return missions (like Stardust, Hayabusa, Hayabusa 2, OSIRIS-REx), or from a large number of meteorite recoveries with associated orbits that can link to asteroid families: the aim of ground-based efforts like the Desert Fireball Network.

The Desert Fireball Network (DFN) is a fireball camera network currently operating in the the Australian outback, designed for the detection and recovery of meteorite falls with associated orbits. Currently 52 observatories are deployed. On January 2, 2015, a particularly bright fireball was observed

over South Australia, large enough to be simultaneously detected by the US government (USG) sensors, and by the DFN, which had just started science operation 2 months before. Another similarly bright event, also observed by both the DFN and the USG sensors, happened on June 30, 2017 over South Australia.

Over the 3 million km^2 that the DFN covers in Australia, the observation of a metre-scale impactor is only expected to happen once every 4-5 years (Brown et al., 2002), and once every 8-10 years during night time when most dedicated fireball networks operate (without considering clear sky conditions). The observation of two such events during the first 3 years of operation of the DFN, although outside the nominal collecting area, is somewhat lucky with respect to the size frequency distribution numbers of Brown et al. (2002). These two superbolides are described here and add to the small list of metre-scale impactors that have precisely determined trajectories:

- 13 events compiled and discussed by Brown et al. (2016).

- the "Romanian" bolide (Borovička et al., 2017).

- the Dishchii'bikoh meteorite, for which initial trajectory details have been reported by Palotai et al. (2018).

- the meteorite fall near Crawford Bay in British Columbia (Canada), for which initial trajectory details have been reported by Hildebrand et al. (2018).

3.1.3. WHERE DO THEY COME FROM?

The current state of the art for source region model for Near-Earth Objects (NEO) is detailed by Granvik et al. (2018). They report a significant size dependence of NEO origins, which had not been investigated by earlier similar works

(Bottke et al., 2002; Binzel et al., 2004; Greenstreet et al., 2012). Their work covers the absolute magnitude range $17 < H < 25$ (corresponds to diameter $1200 > D > 30\,\mathrm{m}$ with an S-type albedo of 0.2), providing little insight on the the metre-size region ($H = 32$).

Several outstanding issues show that it is not possible to simply interpolate the characteristics of the population of typical macroscopic meteorite dropper meteoroids (decimetre-scale) and the kilometre-scale well surveyed by telescopes. For instance, LL chondrites make up 8% of meteorite falls, but it is generally thought that $1/3^{rd}$ of observable near-Earth small body space is made up of LL compatible asteroids (Vernazza et al., 2008). Granvik et al. (2016) shows that an unmodelled destructive effect prevents small bodies from stably populating the low perihelion region, further outlying the need to consider body size in the dynamical models.

Brown et al. (2016) are the first to perform a source region analysis on metre-class NEO bodies, using the Bottke et al. (2002) model on USG events. Considering the small number statistics they get intermediate source regions proportion that are comparable to previous works on kilometre-size NEO population (Bottke et al., 2002; Binzel et al., 2004; Greenstreet et al., 2012). However they also argue for a Halley-type comet (HTC) source region, comparable in importance to the Jupiter-family comets (JFC) source. This source has not been identified previously in NEO works, because of a near-complete lack of such objects in asteroid databases. Their argument is based on three fireball events in the USG dataset that have a Tisserand parameter with Jupiter, $T_J < 2$: identified as *20150102-133919*, *20150107-010559*, and *20150311-061859*, not associated to a meteor shower. Because the first two of these events have independently estimated trajectories, an issue that we are interested in is determining if this surprising outcome could be the results of limitations of USG data.

This work aims to compile independent information not just for these cases,

but for several other metre-scale bodies, to determine the reliability of USG data in general, for population study, orbit determination, as well as undertaking meteorite searches based on these data. We also evaluate the suitability of hardware currently deployed by fireball networks to observe these particularly bright events.

3.2. DATA AND METHODS

3.2.1. DESERT FIREBALL NETWORK

The Desert Fireball Network (DFN) is the world's biggest fireball observation facility (3 million km^2 coverage), set up in a desert environment where meteorites are more likely to be successfully recovered. The DFN is built to overcome the challenges of operating a distributed network of high technology devices in a harsh remote environment. The observatories operate completely autonomously for up to two years before maintenance is required: swapping the hard drives and replacing the mechanical shutter in the off-the-shelf camera. The systems can operate with network connectivity for event notifications, or completely offline. Due to their low power usage, simple solar photo-voltaic systems ($\approx$160-240 W of solar panels) with 12 V deep-cycle lead acid battery storage are used to power most of the observatories across the network.

The main imaging system consists of a high-resolution digital camera and a fisheye all-sky lens, taking long exposures with shutter breaks embedded by the GNSS synchronised operation of a liquid crystal shutter. This mode of imaging has historically been the most successful method for determining positions of fallen meteorites from fireball observation, as shown in the compilation of Borovička et al. (2015). The DFN has recovered 3 meteorites in the first 3 years of operation (Devillepoix et al., 2018). The automated observatories are more

completely described by Howie et al. (2017a), and the encoding method used to record absolute and relative timing (to derive velocity information) is detailed by Howie et al. (2017b).

In June 2017, the DFN initiated a firmware upgrade across the network to change the time encoding technique on the observatories' microcontroller. These were deployed to all online cameras remotely. The main new feature of this update was a new mode of operation for the liquid crystal shutter, different from the one described by Howie et al. (2017b). This new mode retained the absolute timing encoding through the use of a de Bruijn sequence, but made the pulses much shorter and equal in duration, replacing the 60 ms long dash with two 10 ms pulses and the short 20 ms dash into a single 10 ms pulse, in order to reduce saturation issues on bright fireballs, and make automated centroid determination easier. In Tab. 3.2 and 3.5 we refer to this new method as pulse-frequency (PF), as opposed to the pulse-width (PW) method of Howie et al. (2017b).

Standard data reductions methods are detailed by Devillepoix et al. (2018). The DFN is optimised to observe macroscopic meteorite dropping events at the low mass end. The observatories are sensitive to apparent magnitude 0, in order observe a small (~ 5 cm) meteoroid high-enough before significant atmospheric deceleration happens, to derive a precise orbit. But they can also astrometrically observe the brightest phases of ablation of a half-metre size rock (magnitude 15), albeit with saturating the sensor.

Thanks to the large number of stars imaged by the long exposure, the cameras typically achieve their nominal arcminute astrometric precision down to 5°elevations above the horizon (Devillepoix et al., 2018). Typical kilogram scale meteorites usually ablate down to ~ 20 km height, therefore the network is spaced in order to have 3 camera observation down to this height, which roughly corresponds to a 200 km slant range. Outside of these ideal observation

conditions, fireballs are accurately imaged in the high altitude phase of the flight (useful for orbital calculations), but getting precise meteorite fall positions becomes more difficult due to decreased astrometric precision.

Fireball trajectories are calculated using a modified version of the least-square method of Borovička (1990), and fireball dynamics are analysed using the methods of Sansom et al. (2015) and Gritsevich et al. (2017). Pre-encounter orbits are determined using numerical integration, as described by Jansen-Sturgeon et al. (2018).

The DFN observatories were designed with a low-resolution video system in parallel of the high-resolution still imager, initially as absolute timing device, but later kept on some systems for future daytime observations. These data are too low-resolution to provide useful astrometric data, although they can be helpful in getting high temporal resolution photometric data. However the sensor gets saturated when the fireball gets brighter than $m_V = -5$, and the auto-gain on the cameras can only attenuate the signal by a factor of about 4 stellar magnitudes. Large fireballs still saturate the sensor, however Devillepoix et al. (2018) have successfully used the sum of all pixels in each field as a proxy for all sky brightness. This method is particularly successful at detecting large fragmentation events. The effect of auto-gain are corrected by performing traditional photometry on a non saturated bright star, planet, or fixed light in the field of view. Unfortunately because of the lossy compression of the record and the sensor saturation, it is not possible to get a satisfying absolutely calibrated photometry from the video, and therefore the resulting light curve is only used qualitatively.
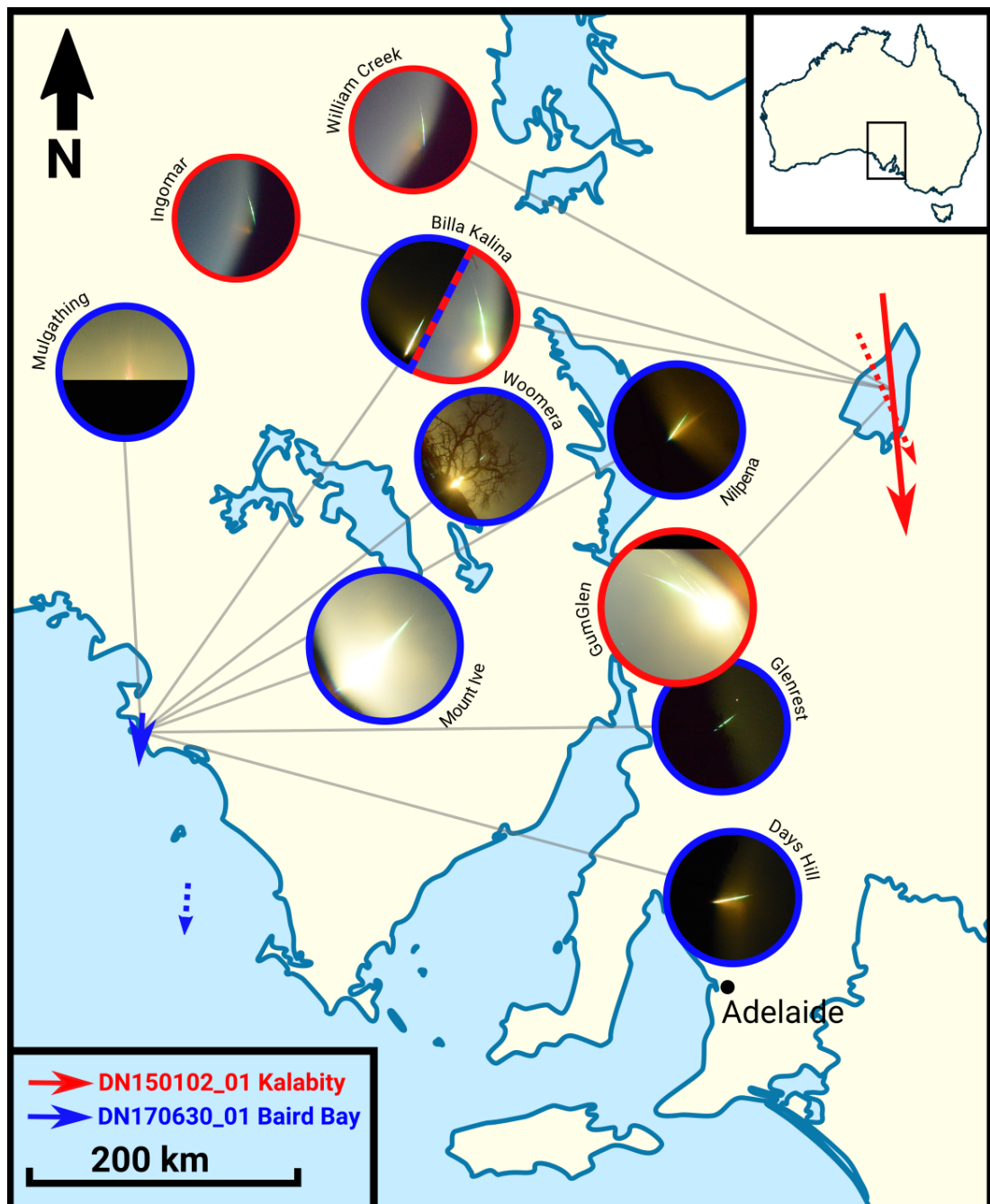
FIGURE 3.1: Cropped all-sky images of the fireballs from the DFN observatories. Images are of the same pixel scale with the centre of each image positioned at the observatory location on the map. For the Kalabity fireball (red arrow, East), light from the main explosion is particlaurly scattered in the Gum Glen image because of clouds. For the Baird Bay event (blue arrow, West), the Mulgathing image is cropped because the sensor is not large enough to accommodate the full image circle on its short side. The fireball on the Woomera picture was partially masked by a tree. The O'Malley station only recorded video and is missing in this map, details are given in Tab. 3.5. The dashed arrows show the USG sensors trajectory solutions for both events (vectors are generated by backtracking the state vector at the time of peak brightness to $t - 5$ seconds).

3.2.2. US GOVERNMENT SENSORS

Large fireballs detected by the so-called "US Government (USG) sensors" are reported on the JPL website[2]. These sensors are apparently able to detect flashes all around the world, day and night, measure flash energy, and sometimes derive velocities and airburst heights. These data were used for size-frequency studies of metre-scale objects by Brown et al. (2002), and later to derive orbital and physical properties of this population (Brown et al., 2016).

In Tab. 3.1 we give the data for a the subset of events for which all the parameters are reported (time, energy, location, velocity), and for which independent observations have been published (references in Tab 3.7). The USG sensors data do not come with uncertainties, therefore we assume the last significant figure represents the precision of the measurement.

We calculate the radiant and pre-entry orbits for these meteoroids, based on USG data, using the numerical method of Jansen-Sturgeon et al. (2018). The various numbers reported in USG data relate to the instant of peak brightness, typically quite deep into the atmosphere. Since we are dealing with metre-scale bodies, we ignore deceleration due to the atmosphere and use a purely gravitational model from that point for calculating the orbit.

The online table converts the total radiated energy measured into an equivalent impact energy using an empirical relation determined by Brown et al. (2002). This total energy estimate, combined with the impacting speed, can be used to derive a photometric mass using the classical kinetic energy relation ($E = \frac{1}{2}mv^2$), and a rough size assuming a density. Only $>= 0.1$ kT TNT impacts are reported by the USG[3], which roughly corresponds to a 1 m diameter object

---

[2]https://cneos.jpl.nasa.gov/fireballs/ accessed November 22, 2017

[3]Johnson L. (2017) - SBAG meeting: https://www.lpi.usra.edu/sbag/meetings/jan2017/presentations/Johnson.pdf and remarks at 32 m and answer to questions at 56 m in online talk: https://ac.arc.nasa.gov/p98hreesxa9/, accessed August 24, 2018.

at typical impact speeds on Earth.

peak brightness date/time UT	H km	V km s⁻¹	V_x	V_y km s⁻¹	V_z ECEF	radiated E. J	impact E. kT TNT	lat °N+	long °E+	α_{inf} °	δ_{inf} °	a AU	e	i °	ω °	Ω °
2018-06-02 16:44:12	28.7	16.9	0.9	-16.4	3.9	3.8e+11	0.98	-21.2	23.3	235.0	-13.3	1.33	0.42	4.4	258.3	71.88
2017-09-05 05:11:27	36.0	14.7	12.7	-6.1	-4.2	3.8e+10	0.13	49.3	243.1	216.5	16.7	2.06	0.54	3.4	147.2	162.69
2017-06-30 14:26:45	20.0	15.2	10.9	-9.7	4.2	9.4e+10	0.29	-34.3	134.5	273.6	-16.1	1.24	0.35	3.6	259.7	98.80
2015-01-07 01:05:59	45.5	35.7	-35.4	1.8	-4.4	1.4e+11	0.4	45.7	26.9	119.7	7.1	4.78	0.93	20.7	111.9	106.19
2015-01-02 13:39:19	38.1	18.1	4.5	-14.4	-10.0	2.0e+10	0.073	-31.1	140.0	53.8	33.5	9.33	0.90	8.0	207.4	281.61
2013-02-15 03:20:33	23.3	18.6	12.8	-13.3	-2.4	3.8e+14	440.0	54.8	61.1	329.2	7.3	1.71	0.56	4.1	109.7	326.46
2010-02-28 22:24:50	37.0	15.1	-11.7	2.7	-9.1	1.5e+11	0.44	48.7	21.0	121.7	37.2	2.70	0.65	3.2	204.0	340.14
2008-11-21 00:26:44	28.2	12.9	3.9	-4.1	-11.6	1.4e+11	0.41	53.1	250.1	200.6	64.0	0.79	0.26	10.4	3.1	239.04
2008-10-07 02:45:45	38.9	13.3	-9.0	9.0	3.8	4.0e+11	1.0	20.9	31.4	12.4	-16.7	1.65	0.43	3.9	36.2	14.16

TABLE 3.1: USG sensors fireball events that have reported velocities, and have been observed independently. Left of the table is from https://cneos.jpl.nasa.gov/fireballs/ (accessed November 22, 2017). Apparent radiants and orbits have been calculated (angles are equinox J2000). The number of decimals is not representative of uncertainty. A similar work has been done by Brown et al. (2016) on the 6 older events in the list, in agreement. Corresponding ground based observation details of the two highlighted events are presented in this work, references for the other events are in Tab. 3.7.

3.3. Results

In this section we analyse in detail the atmospheric entry of 2 large meteoroids as observed by the DFN, these were also observed by the USG sensors (highlighted rows in Tab. 3.1).

3.3.1. DN150102_01 - Kalabity

On January 2, 2015 a bright bolide lit up the skies over lake Frome in South Australia (Fig. 3.1), starting at 2015-01-02T13:39:11.086 UTC (9 minutes after midnight ACDT) for 10.54 seconds. In early 2015 the DFN had just finished its initial expansion phase in South Australia with 16 cameras, unfortunately the bolide happened outside the standard network covering area at that time. Therefore a combination of cameras mostly over 300 km from the event had to be used to determine the trajectory (Tab. 3.2). The best convergence angle is 22°(between Gum Glen and William Creek). The convergence angle between the Billa Kalina and Ingomar stations is less then 1°, therefore the latter distant viewpoint does not help much in constraining the trajectory. The trajectory follows a relatively shallow slope of 20°to the horizon, visible on the images from 83.3 km altitude. Astrometric uncertainties vary between 1.5-3′(equates to 130-260 m once projected at 300 km). These are obtained by compounding astrometric calibration uncertainties (typically 1′) and fireball picking uncertainties (usually 0.5-1 pixel, depending on optics quality and fireball brightness). Most of the residuals to the straight line fit (Fig. 3.2) are then in agreement with astrometric uncertainties. As expected from an unconstrained astrometric solution under 5°elevation, the observation residuals to the straight line fit start diverging for observations below this elevation, this is visible on around the 52 km altitude mark on the Ingomar and William Creek viewpoints.

The all-sky light curves display early fragmentation events under 0.05 and

TABLE 3.2: Locations and nature of instrumental records DN150102_01. P: Photographic record (long-exposure high resolution image), V: compressed PAL video (25 frames per second). *PW* designates the de Bruijn encoding method, as described in Sec. 3.2.1. Ranges are from the fireball at 70 km altitude. Photographic imaging system was out of order for Nilpena.

Observatory	Instruments	Latitude	Longitude	Altitude (m)	Range (km)
Gum Glen - DFNSMALL25	P_{PW}, V	32.20554 S	138.24121 E	242	246
Billa Kalina - DFNSMALL26	P_{PW}	30.23769 S	136.51565 E	114	328
William Creek - DFNSMALL30	P_{PW}	28.91566 S	136.33495 E	79	392
Ingomar - DFNSMALL27	P_{PW}	29.58556 S	135.03865 E	197	480
Nilpena - DFNSMALL42	V	31.02331 S	138.23256 E	112	175

FIGURE 3.2: Cross-track residuals of the straight line least squares fit to the trajectory from each view point. These distances correspond to astrometric residuals projected on a perpendicular plane to the line of sight, positive when the line of sight falls above the trajectory solution. The distances in the legend correspond to the observation range [highest point - lowest point]. The Ingomar and William Creek observation residuals start diverging after 52 km altitude, this corresponds to observation elevation angles of about 4°and 5°, respectively.
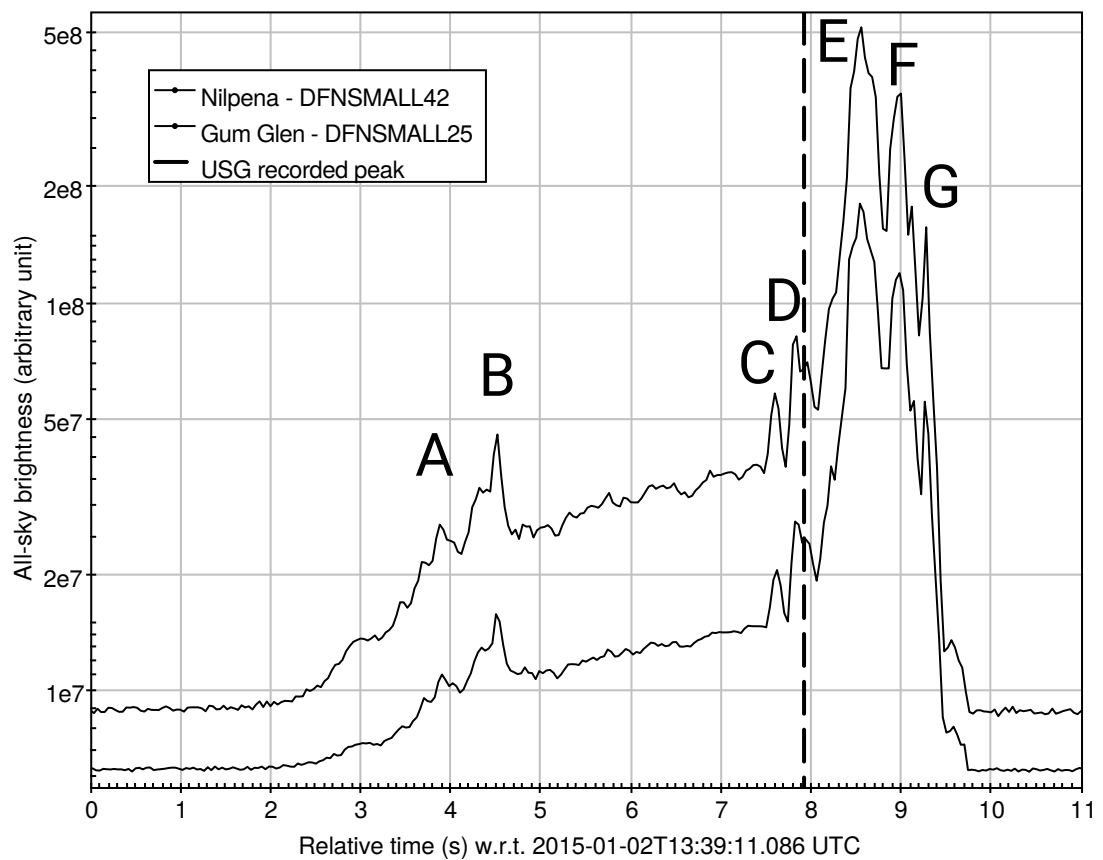
FIGURE 3.3: All-sky brightness (sum of all the pixels) from the Kalabity fireball, as recorded with the video cameras at the Gum Glen and Nilpena observatories. Using traditional PSF photometry on star Sirius the light curve is corrected to take into account the effect of auto-gain. The Nilpena curve has been shifted up for clarity. The peak brightness time recorded by the USG sensors (rounded to the nearest second) is marked by a vertical line.

Event	Time s	Speed m s⁻¹	Height m	Longitude °E	Latitude °N	Dynamic pressure MPa
Beginning	0.0	15406±79	83317	139.73897	-30.25421	
A	3.90	15351	62586	139.85081	-30.74874	0.05
B	4.50	15320	59453	139.86679	-30.82416	0.08
C	7.61	14487	43432	139.95010	-31.21547	0.52
D	7.83	14272	42571	139.95466	-31.23679	0.57
E - max	8.55	13463	40286	139.96683	-31.29360	0.69
F	8.95	13014	39017	139.97359	-31.32517	0.77
G	9.26	12665	38033	139.97883	-31.34963	0.83
End	10.54	8433	33420	140.00311	-31.46438	

TABLE 3.3: Summary table of bright flight events for DN150102_01 Kalabity. Fragmentation event letters are defined on the light curve (Fig. 3.3). Times are relative to 2015-01-02T13:39:11.086 UTC. Positions and speeds at the peaks are interpolated from astrometric data.

0.08 MPa and (peaks A and B in Fig. 3.3). The following part of the light curve is uneventful until the body encounters an order of magnitude higher dynamic pressures that eventually almost entirely destroys it (peaks C to G in Fig. 3.3). This adds to the list of large meteoroids (Popova et al., 2011) that undergo fragmentation under pressures several orders of magnitude smaller than the surviving material tensile strength on the ground, or pressures required to destroy the body in our case.

We note that the time reported by the USG sensor (2015-01-02T13:39:19 UTC) is in good agreement with the brightest peak (E) in our light curve determined to be 0.6 s later (Fig. 3.3 and Tab. 3.3). However the reported altitude is 38 km. This does not correspond to our brightest peak E at 40.2 km, but rather to the end of the very bright phase (peak G).

Only 6 shutter breaks are resolvable on the image after the explosion on the Billa Kalina image, all $< 4°$ on the horizon. Using the particle filter method of Sansom et al. (2017) on these data, we find that the main mass at this stage was only a couple of kilograms at the most. We are only able to track down to 33.4 km at 8.4 km s⁻¹. We suspect that this main mass is not visible down to ablation speed limit ($\simeq 3$ km s⁻¹), because of a sensitivity issue: at this

stage the meteoroid is at a large distance from the observatory ($>360\,\mathrm{km}$), observed on an extreme elevation angle ($\simeq 3.5°$), and the sky background is unusually bright because of the light from the main explosions (peaks E-G) raising the background. We suspect the reason this feature is not visible on the closer Gum Glen image is because of the presence of clouds in the direction of the fireball, which efficiently scattered the light from the explosion and subsequently saturated the sensor on a much larger area than for Billa Kalina.

The particle filter method of Sansom et al. (2017) can also be used to put a lower bound on the initial mass of the meteoroid. The near lack of deceleration before the main explosion implies that the mass to cross-section area ratio was large. Using reasonable assumptions on shape (spherical), and density ($\rho = 3500\,\mathrm{kg\,m^{-3}}$, chondiric), we find that the meteoroid was $>2600\,\mathrm{kg}$ ($>1.1\,\mathrm{m}$) before impact. We note that this assumes that the meteoroid is a single ablating body before the airbursts (peaks E-G). We know this assumption not to be well-founded because some fragmentation happened early on (peaks A and B in Fig. 3.3), explaining why this number is given as a lower limit.

Using the velocity calculated at the brightest instant on DFN data (peak E in Tab. 3.3), and the impact energy measured by the USG sensors (Tab. 3.1), we derive a $3400\,\mathrm{kg}$ mass for this meteoroid, roughly equivalent to a $1.2\,\mathrm{m}$ diameter body, larger than the Brown et al. (2016) estimate because of a different impact speed used.

The DFN dynamic initial size ($>1.1\,\mathrm{m}$) is in good agreement with the USG photometric mass ($1.2\,\mathrm{m}$).

The orbit of Kalabity is a typical main belt one with a semi-major axis of $1.80\,\mathrm{AU}$ (Tab. 4.4 and Fig. 3.4), very different from the HTC type orbit derived from USG data (Tab. 3.1).
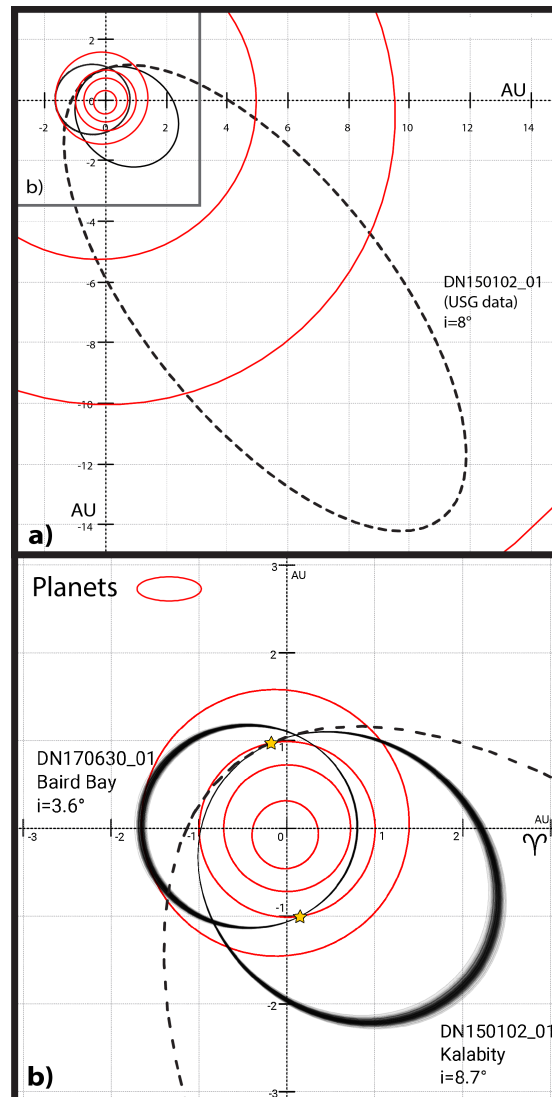
FIGURE 3.4: Ecliptic plot of the pre-atmospheric orbit of the Kalabity and Baird Bay meteoroids. **b** is limited to the inner solar system, while **a** goes out all the way to the orbit of Uranus. The solid lines are orbits using DFN data (the shades of grey in **b** represent the confidence region as calculated by Monte Carlo simulations), whereas the dashed lines are using USG data. The orbit of Baird Bay calculated from USG data is indistinguishable from the DFN one. On the other hand the orbit of Kalabity is very different, mostly because of a speed issue with USG data.

parameter	unit	DN150102_01 Kalabity	DN170630_01 Baird Bay
Epoch	TDB	2015-01-02T13:39:11	2017-06-30T14:26:41
a	AU	1.80 ± 0.02	1.23 ± 0.01
e		0.498 ± 0.006	0.35 ± 0.01
i	°	8.73 ± 0.02	3.57 ± 0.05
ω	°	219.8 ± 0.09	259.06 ± 0.07
Ω	°	281.619 ± 0.001	98.801 ± 0.002
q	AU	0.908 ± 0.001	0.805 ± 0.004
Q	AU	2.70 ± 0.04	1.66 ± 0.03
α_g	°	64.3 ± 0.1	272.14 ± 0.02
δ_g	°	51.7 ± 0.2	-12.5 ± 0.1
V_g	$\mathrm{m\,s^{-1}}$	10776 ± 115	10007 ± 260
T_J		3.89	5.14
α_{inf}	°	70.14 ± 0.02	271.74 ± 0.02
δ_{inf}	°	38.05 ± 0.02	-15.89 ± 0.02

TABLE 3.4: Estimated orbital elements of DN150102_01 Kalabity and DN170630_01 Baird Bay, with 1σ formal uncertainties. (equinox *J2000*).

3.3.2. DN170630_01 - Baird bay

The Baird Bay meteoroid entered the atmosphere on a very steep trajectory (72° to the horizon), on a trajectory that starts over land in Sceale Bay, and ended in the Southern Ocean ~10 km West of the Carca Peninsula (Fig. 3.1). The bolide was visible from 2017-06-30T14:26:41.50 UTC (3 minutes before midnight ACST) for 5.46 s on the DFN camera systems (Tab. 3.5). Several eye witnesses reported the bolide, notably from Adelaide, the closest densely populated area, 450 km away.

The closest DFN camera is Mount Ive station (190 km away). The Mulgathing camera (250 km directly North from the event) only caught the top of the fireball, as the image circle is cropped on the short side of the sensor (usually North and South).

Like Kalabity, Baird Bay experienced early fragmentation under pressure < 1 MPa (peak A at 0.08 MPa), however a much larger pressure was required to destroy it (peak D, most likely between 1 and 2 MPa).

TABLE 3.5: Locations and nature of instrumental records DN170630_01. P: Photographic record (long-exposure high resolution image), V: compressed PAL video (25 frames per second). PW and PF designate the de Bruijn encoding method, as described in Sec. 3.2.1. Ranges are from the fireball at 70 km altitude. Photographic imaging system was out of order for O'Malley. Note that the Mulgathing camera did not receive the PF firmware update immediately because of a temporary internet connectivity issue.

Observatory	Instruments	Latitude	Longitude	Altitude (m)	Range (km)
Mount Ive - DFNSMALL62	P_{PF}	32.45919 S	136.10332 E	293	201
Days Hill - DFNEXT005	P_{PF}	34.20749 S	138.66151 E	363	439
Nilpena - DFNSMALL12	P_{PF}	31.02328 S	138.23260 E	122	447
Glenrest - DFNSMALL06	P_{PF}	33.01963 S	138.57554 E	722	414
Billa Kalina - DFNSMALL43	P_{PF}	30.23759 S	136.51566 E	113	387
Mulgating - DFNSMALL15	P_{PW}	30.66078 S	134.18608 E	149	274
Woomera - DFNSMALL14	P_{PF}	31.19609 S	136.82682 E	163	329
O'Malley - DFNSMALL40	V	30.50663 S	131.19534 E	117	410

FIGURE 3.5: DN170630_01 Baird bay. Cross-track residuals of the straight line least squares fit to the trajectory from each view point. These distances correspond to astrometric residuals projected on a perpendicular plane to the line of sight, positive when the line of sight falls above the trajectory solution. The distances in the legend correspond to the observation range [highest point - lowest point].

Event	Time	Speed	Height	Longitude	Latitude	Dynamic pressure
	s	m s^{-1}	m	°E	°N	MPa
Beginning	0.0	15095±61	86782	134.23858	-32.99306	
A	2.51	14906	52111	134.21168	-33.08981	0.08
B	3.51	13786	38817	134.20123	-33.12718	0.42
C	3.71	13140	36240	134.19919	-33.13445	0.58
last astrometric datapoint	3.80	12783	35181	134.19836	-33.13743	0.65
D - max	4.61	9568*	25648*	134.19083*	-33.16432*	2.31*
End	5.46					

TABLE 3.6: Summary table of bright flight events for DN170630_01 Baird Bay. Fragmentation event letters are defined on the light curve (Fig. 3.6). Times are relative to 2017-06-30T14:26:41.50 UTC. * marks figures that have been extrapolated. The end parameters have not been extrapolated as it is not possible to know what mass is left after the large explosion (peak D), and how this mass decelerated.
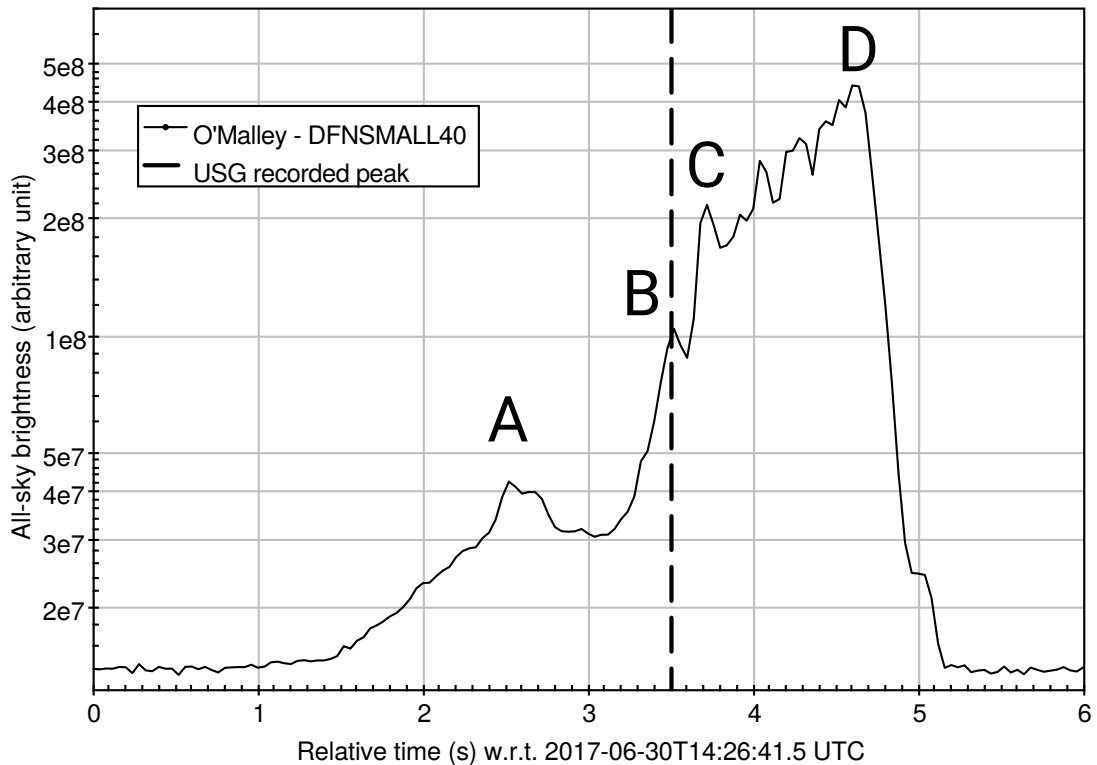
FIGURE 3.6: All-sky brightness (sum of all the pixels) from the Baird Bay fireball, as recorded with the video camera at the O'Malley observatory. Using traditional PSF photometry on star α Centauri the light curve is corrected to take into account the effect of auto-gain. The peak brightness time recorded by the USG sensors (rounded to the nearest second) is marked by a vertical line.

Using the same particle technique as in Sec. 3.3.1, with a reasonable assumptions on shape (spherical), and density ($\rho = 3500\,\mathrm{kg\,m^{-3}}$, chondiric), we find that the meteoroid was $> 9400\,\mathrm{kg}$ ($> 1.7\,\mathrm{m}$) before impact. Using the particle filter we also find that the main mass was $\simeq 7000\,\mathrm{kg}$ when it airburst at 26 km altitude. Unfortunately no astrometric data is available after the airburst, as the only camera close enough to image the bolide at the end, Mount Ive, has a large area of the sensor saturated because of the airburst (peak D in Fig. 3.6). The video record from the very distant O'Malley camera (410 km) shows that some material was still ablating for at least 0.85 s after the instant of peak brightness. This means that there is a distinct possibility that a main mass survived, and fell in the Southern Ocean, less than 10 km from the coast off Point Labatt.

The USG sensors locate the airburst $\lambda = 134.5°$ $\phi = -34.3°$ (WGS84) at h=20 km altitude (Tab. 3.1). This position is $\sim$100 km off to the South from our calculated entry parameters (Fig. 3.1).

On the other hand the USG geocentric velocity vector is consistent with our calculation. The radiant solutions are separated by only $0.4°$, and the speeds are different only by $0.1\,\mathrm{km\,s^{-1}}$, in agreement within uncertainties. This implies that even with the wrong position, the orbit calculated from USG data (Tab. 3.1) is in agreement with the DFN orbit (Tab. 4.4 and Fig. 3.4).

3.4. Discussion

3.4.1. Reliability of USG fireball data

We have compiled in Table 3.7 how well USG events match independent observations of those events, using data both from the literature and the two fireballs described here.

It is possible to discuss the reliability of the USG data in terms of different desired outcomes.

Event	Date (UTC)	Instruments	location	airburst height	speed	radiant	energy	ref
2018 LA	2018-06-02T16:44:12	CSS	NR-L	NR-L	✓	✓	NR-L	+
Crawford Bay	2017-09-05T05:11:27	CV,I	≈	✓	✗	✗	✓	1
DN170630 - Baird Bay	2017-06-30T14:26:45	P,V	✗	✗	✓	✓	✓	0
Dishchii'bikoh	2016-06-02T10:56:32	V,CV	✗	NR-U	NR-U	NR-U	≈	10
Romanian	2015-01-07T01:05:59	CV,PE,P	✓	≈	✗	≈	✓	2,3
DN150102 - Kalabity	2015-01-02T13:39:10	P,V	✓	✓	✗	✗	✓	0,2
Chelyabinsk	2013-02-15T03:20:21	CV	≈	✗	✗	✗	✓	2,4
Košice	2010-02-28T22:24:47	V,P,PE	✓	≈	✓	≈	✓*	2,5
Buzzard Coulee	2008-11-21T00:26:40	CV	✓	≈	✗	✗	NR-L	2,7
Almahata Sita (2008 TC3)	2008-10-07T02:45:40	CSS	≈	✓	✗	✗	✓	2, 6, 8, 9

TABLE 3.7: USG events that have their trajectory independently estimated. Note that the date/times of the events all match the independent measurements. The location is considered valid if the (latitude, longitude, height) is somewhere on the trajectory. CSS: Catalina Sky Survey, V: video, P: photographic, PE: photometer, CV: casual video, I: infrasound. ✓: correct within errors. ≈: incorrect, but not far off. ✗: incorrect. NR-U: not reported or yet published in literature. *: NR-L: not reported by USG. [5] conclude that the impact kinetic energy for Košice is > 0.1 kT, without an upper limit. From light curve and infrasound data, [5] conclude that the impact kinetic energy for Košice is > 0.1 kT, without an upper limit. References: (0) this work; (1) Hildebrand et al. (2018); (2) Brown et al. (2016); (3) Borovička et al. (2017); (4) Borovička et al. (2013a); (5) Borovička et al. (2013b); (6) Farnocchia et al. (2017); (7) Milley (2010); (8) Jenniskens et al. (2009); (9) Borovička and Charvát (2009); (10) Palotai et al. (2018); (+) JPL Horizons ephemeris service, using CSS and ATLAS astrometry.

For orbital studies

The factors that come into play to calculate a meteoroid orbit are the accuracy of the *location*, the absolute *time*, and the geocentric *velocity vector*.

All USG events in Table 3.7 agree in absolute time with independent records to within a few seconds.

Locations are correct in most cases, except for the Baird Bay event described in this work. However this $\sim$100 km location issue is this case is not important for orbit calculation.

Hence the questions lie with the 3 geocentric cartesian velocity components. Granvik and Brown (2018) show that in most cases a precision of $0.1\,\mathrm{km\,s^{-1}}$ on the velocity is good enough for source region analysis, so we do not expect the lack of precision on the USG numbers to be an issue here. An accurate height can be useful to take into account the deceleration in the atmosphere, but it is not essential as we are looking at massive bodies that hardly decelerate before the airburst. Because radiant and speed are less likely to be correlated than the cartesian velocity components, we have re-projected these velocity components as radiant and speed. The speeds are inconsistent in most cases (Tab. 3.7). The worst USG estimates are for the Buzzard Coulee meteorite ($18.1\,\mathrm{km\,s^{-1}}$ calculated by Milley (2010) compared to $12.9\,\mathrm{km\,s^{-1}}$ USG), and the Romanian bolide ($27.8\,\mathrm{km\,s^{-1}}$ calculated by Borovička et al. (2017) compared to $35.7\,\mathrm{km\,s^{-1}}$ USG). These were underestimated by 28%, and overestimated by 28%, respectively. The USG radiant vector is off for most events, sometimes by only a couple of degrees (which does not drastically affect the orbit), but sometimes by as much as 90°(Buzzard Coulee and Crawford Bay events). From these considerations, only 4 out of 10 events in Table 3.7 would have a reasonably accurate orbit if calculated from USG data: 2018 LA, Baird Bay, Chelyabinsk, and Košice. The USG orbits of some meteoroids are even misleadingly peculiar: Kalabity and Romanian would be on unusual HTC orbits (as already noted by Brown et al.

(2016)).

Therefore USG data can generally not be relied on for orbit determination, and there is no way to know for which events the data are reliable.

For material properties studies

The atmospheric behaviour of a meteoroid can yield some insights on what the meteoroid is made of and how it is held together. If no meteorite is recovered, the small set of USG sensors parameters contains very limited information regarding the rock itself, but it is nevertheless possible to derive the bulk strength of the body. An basic way of achieving this is to look at the dynamic pressure required to destroy the body (using $s = \rho_{atm} v^2$ from Bronshten (1981)). This is not a perfect indicator as it does not show subtleties in the rock structure, but it should be able to distinguish iron, chondritic, and cometary material, as these differ in bulk strengths by orders of magnitude. The key parameters are then the *height* of peak brightness (to determine atmospheric density ρ_{atm}), and the *speed v*.

As shown by Brown et al. (2016) (Tab. 4), the USG sensors tend to report reasonably accurate heights of peak brightness. We note that most of height inconsistencies are usually due to another peak in the light curve being recorded.

As seen in the previous paragraph, speeds can be wrong by as much as 28%, which induce a factor of 2 error in strength. We conclude that the inaccuracy of USG numbers do not affect strengths by more than an order of magnitude, this is good enough with respect to our original aim.

For size-frequency studies

The USG data have the advantage of using the entire planet as a collector, yielding large sample sizes that ground-based networks will never be able to reach for this class of objects. Hence they can be a good tool for size-frequency studies, provided the *size* of the impacting bodies can be accurately determined, and the *detection efficiency* is well constrained.

As detailed in Sec. 3.2.2, using the empirical relation of Brown et al. (2002) and assuming a density, the radiated energy reported by the USG sensors can be converted into mass and size, with the caveat of speed accuracy. The energy estimates seem to match independent observation for the events presented here (Tab. 3.7).

As of the detection efficiency, Brown et al. (2002) mentions a 60-80% Earth observation coverage by the USG sensors for their study on 1994-2002 data. If we subset the USG events in two different groups, before and after the study of Brown et al. (2002), we get on average 19 events per year before, and 26-27 events per year after September 2002. This 40% increase would suggest a 100% Earth coverage after 2002. However it is interesting to note that the 0.4 kT impact of *2014 AA* (Farnocchia et al., 2016) was not reported by the sensors.

USG data is therefore useful for size frequency studies (like the work done by Brown et al. (2002), Brown et al. (2013), as long as the sub-population grouping is done by other means than by the orbit calculated using the USG velocity data.

For meteorite searching

Although metre-scale impactors are usually too big to be able to decelerate enough before reaching dynamic pressures that destroy them, these objects

still have a large chance of surviving as meteorites. We try to assess here the viability of initiating dark flight calculations using a weather model combined the USG entry vector. All the parameters in Tab. 3.7 (apart from time) need to be accurate.

Although the height of peak brightness is wrong for Chelyabinsk, the reported *(latitude, longitude, height)* triplet is located near the ground truth track, hence the fall analysis would not significantly change for large masses. Therefore of the events compiled in Table 3.7, only 2 out of 9 events (Košice and Chelyabinsk) would have reasonably accurate fall positions if computed from USG records.

But even worse, the $0.1°$ error on latitude/longitude translates into a $\pm 5\,\mathrm{km}$ error on position on the ground, this is particularly large for undertaking meteorite searching activities.

From these considerations, it would be ill-advised to undertake meteorite searching solely based on USG data.

3.4.2. On the ground-based imaging capabilities of metre-scale impactors

With the help from collaborators outside Australia, the DFN is expanding into the Global Fireball Observatory, and will eventually cover 2% of the Earth surface in the next few years. Metre-scale object will fall on the covered area every 1-2 years on average, but is the currently deployed technology fit to observe such events?

NIGHT TIME OBSERVATIONS

Fireball observatories are typically optimised to observe the behaviour of macroscopic meteorite droppers throughout their trajectory during the night. The challenge is mostly a dynamic range one: being sensitive enough to observe the smaller meteoroid at a high altitudes to get precise entry speed for orbit calculation, whilst not saturating the records of larger rocks shining 100 million times brighter when they reach the dense layers of the atmosphere.

So far no iron meteorite fall has been instrumentally observed, but it is expected that this class of objects contains the smallest meteoroids (ie. the faintest fireball) that can drop a meteorite, as their large strength allows them to enter with limited mass loss due to fragmentation. For instance, if we assume little to no gross fragmentation (Revelle and Ceplecha, 1994), to produce a 100 g meteorite the parent meteoroid ($\rho = 7900\,\mathrm{kg\,m^{-3}}$) can be as small as $0.5\,\mathrm{kg} \equiv$ 5 cm diameter, assuming the most favourable entry conditions (vertical entry at $12\,\mathrm{km\,s^{-1}}$). It is desirable to observe the meteor before the rock starts being affected by the atmosphere too much, 80 km, altitude at which it would glow at magnitude M_V=-1.5 (assuming a luminous efficiency of 0.05).

On the bright end, we look at the compilation of Borovička et al. (2015) and see that metre-scale events usually approach $M_V^{max} = -18$, although this is highly dependent on their atmospheric behaviour, where and how important the fragmentation events are.

The set goal is then to have instruments that can cover 20 stellar magnitudes of effective dynamic range.

Long exposure high resolution fireball camera systems have a long track record for yielding meteorite ground locations and orbits (listed as "dedicated search from detailed computation of trajectory" by Borovička et al. (2015)), compared to video systems. Thanks to their logarithmic response, film based

imagers cover a very wide dynamic range (∼15 stellar magnitudes), but those systems are costly and impractical for large distributed autonomous fireball networks (Howie et al., 2017a), and do not achieve the 0 magnitude sensitivity objective. The DFN (Howie et al., 2017a) and the European Network (Spurný et al., 2016) have recently switched from film to digital camera technology. This shift has simplified some operational aspects (eg. enhanced autonomy, better reliability, eased data reduction), but it has come at the cost of a much limited dynamic range: ∼8 magnitudes without saturation. For astrometric purposes this range can be extended to 15 magnitudes (Devillepoix et al., 2018), but this is still quite far from the 20 magnitudes objective.

Video cameras are generally more sensitive than the still imagers, but suffer from the same limited dynamic range. Although a lot of events have been recorded, fixed frame rate TV systems have not been proficient in yielding meteorite fall positions. This is likely to be due to the low resolution offered by those systems (a PAL video system with a matching circular fisheye lens has an average pixel size over $10\times$ larger than the DFN cameras'), and the difficulty of getting enough stars for astrometric calibration across the field of view (most of these cameras cannot shoot long exposures). However recent advances in digital video camera technology allow higher resolutions, long exposures for calibration, and higher bit depth, so we expect networks based on these systems to be more successful at meteorite recovery in the near future (eg. the Fireball Recovery and InterPlanetary Observation Network (*FRIPON*) network of Colas et al. (2015)).

Day time observations

The easy exposure control on industrial digital cameras allows low-noise long exposure calibration shot to be taken at night, but also permits very short exposures to operate during the day. The *FRIPON* network endeavours to oper-

ate their cameras during both nighttime and daytime (Audureau et al., 2014), however fireball detection on daytime frames appears somewhat challenging (Egal et al., 2016). Even if calculating fall positions turns out to be difficult from daytime data, the prospects of being able to calculate orbits for meteorites that have been independently recovered are very interesting (9 out of 14 US meteorite falls in the last 10 years do not have a trajectory solution published), as the astrometric calibration of casual footage can be very time consuming.

3.5. CONCLUSIONS

This work investigates the Near-Earth Objects (NEO) impacting population around the metre-scale size range. Such events are relatively rare (35-40 per year), therefore a large collecting area is crucial in order to study them. The Desert Fireball Network (DFN) is leading the effort as a ground based instrument, covering over 3 million km^2.

Meteoroids that have been observed by both the USG sensors and independent means comprises a small set of 9 events. In this study we use a precise comparison of these events to assess the reliability of the USG sensors for NEO studies, yielding the following unequivocal conclusions:

1. USG sensors data are generally unreliable for orbit calculations. The new metre-scale impactors source region of Brown et al. (2016) (Halley-type comet orbits) is based on 3 particular USG meteoroid orbits. We have shown that 2 of these are erroneous, seriously questioning the existence of this source region.

2. Size frequency distribution work relies on determining rough sizes and having a good knowledge of the probing time-area. The USG seem to

achieve both with reasonably good precision. This confirms the sound basis of the work done by Brown et al. (2002) and Brown et al. (2013).

3. Basic impactor physical properties (size and strength) can be well constrained with USG data. This validates the conclusions of Brown et al. (2016) that relate to physical properties of objects.

4. Based on how often the derived trajectories are wrong, it would be naive to invest large amounts of resources to undertake meteorite searching using USG data.

We also note that ground based fireball networks must find solutions to increase the dynamic range of their observations, in order to get sound observation data when metre-scale objects impact the atmosphere.

ACKNOWLEDGEMENTS

3.6. REFERENCES

Astropy Collaboration, T. P. Robitaille, E. J. Tollerud, P. Greenfield, M. Droettboom, E. Bray, T. Aldcroft, M. Davis, A. Ginsburg, A. M. Price-Whelan,

W. E. Kerzendorf, A. Conley, N. Crighton, K. Barbary, D. Muna, H. Ferguson, F. Grollier, M. M. Parikh, P. H. Nair, H. M. Unther, C. Deil, J. Woillez, S. Conseil, R. Kramer, J. E. H. Turner, L. Singer, R. Fox, B. A. Weaver, V. Zabalza, Z. I. Edwards, K. Azalee Bostroem, D. J. Burke, A. R. Casey, S. M. Crawford, N. Dencheva, J. Ely, T. Jenness, K. Labrie, P. L. Lim, F. Pierfederici, A. Pontzen, A. Ptak, B. Refsdal, M. Servillat, and O. Streicher. Astropy: A community Python package for astronomy. A&A, 558:A33, Oct. 2013. doi: 10.1051/0004-6361/201322068.

Y. Audureau, C. Marmo, S. Bouley, M.-K. Kwon, F. Colas, J. Vaubaillon, M. Birlan, B. Zanda, P. Vernazza, S. Caminade, and J. Gattecceca. FreeTure: A Free software to capTure meteors for FRIPON. In J.-L. Rault and P. Roggemans, editors, *Proceedings of the International Meteor Conference, Giron, France, 18-21 September 2014*, pages 39–41, Feb. 2014.

R. P. Binzel, A. S. Rivkin, J. S. Stuart, A. W. Harris, S. J. Bus, and T. H. Burbine. Observed spectral properties of near-Earth objects: results for population distribution, source regions, and space weathering processes. Icarus, 170: 259–294, Aug. 2004. doi: 10.1016/j.icarus.2004.04.004.

P. A. Bland and N. A. Artemieva. The rate of small impacts on Earth. *Meteoritics and Planetary Science*, 41:607–631, Apr. 2006. doi: 10.1111/j.1945-5100.2006.tb00485.x.

J. Borovička. The comparison of two methods of determining meteor trajectories from photographs. *Bulletin of the Astronomical Institutes of Czechoslovakia*, 41: 391–396, Dec. 1990.

J. Borovička and Z. Charvát. Meteosat observation of the atmospheric entry of 2008 TC$_3$ over Sudan and the associated dust cloud. A&A, 507:1015–1022, Nov. 2009. doi: 10.1051/0004-6361/200912639.

J. Borovička, P. Spurný, P. Brown, P. Wiegert, P. Kalenda, D. Clark, and

L. Shrbený. The trajectory, structure and origin of the Chelyabinsk asteroidal impactor. Nature, 503:235–237, Nov. 2013a. doi: 10.1038/nature12671.

J. Borovička, J. Tóth, A. Igaz, P. Spurný, P. Kalenda, J. Haloda, J. Svoreå, L. Kornoš, E. Silber, P. Brown, and M. HusáRik. The Košice meteorite fall: Atmospheric trajectory, fragmentation, and orbit. *Meteoritics and Planetary Science*, 48:1757–1779, Oct. 2013b. doi: 10.1111/maps.12078.

J. Borovička, P. Spurný, and P. Brown. *Small Near-Earth Asteroids as a Source of Meteorites*, pages 257–280. University of Arizona Press, 2015. doi: 10.2458/azu_uapress_9780816532131-ch014.

J. Borovička, P. Spurný, V. I. Grigore, and J. Svoreň. The January 7, 2015, superbolide over Romania and structural diversity of meter-sized asteroids. Planet. Space Sci., 143:147–158, Sept. 2017. doi: 10.1016/j.pss.2017.02.006.

W. F. Bottke, A. Morbidelli, R. Jedicke, J.-M. Petit, H. F. Levison, P. Michel, and T. S. Metcalfe. Debiased Orbital and Absolute Magnitude Distribution of the Near-Earth Objects. Icarus, 156:399–433, Apr. 2002. doi: 10.1006/icar.2001.6788.

V. A. Bronshten. The physics of meteoritic phenomena. *Moscow Izdatel Nauka*, 1981.

P. Brown, R. E. Spalding, D. O. ReVelle, E. Tagliaferri, and S. P. Worden. The flux of small near-Earth objects colliding with the Earth. Nature, 420:294–296, Nov. 2002. doi: 10.1038/nature01238.

P. Brown, P. Wiegert, D. Clark, and E. Tagliaferri. Orbital and physical characteristics of meter-scale impactors from airburst observations. Icarus, 266:96–111, Mar. 2016. doi: 10.1016/j.icarus.2015.11.022.

P. G. Brown, J. D. Assink, L. Astiz, R. Blaauw, M. B. Boslough, J. Borovička, N. Brachet, D. Brown, M. Campbell-Brown, L. Ceranna, W. Cooke, C. de

Groot-Hedlin, D. P. Drob, W. Edwards, L. G. Evers, M. Garces, J. Gill, M. Hedlin, A. Kingery, G. Laske, A. Le Pichon, P. Mialle, D. E. Moser, A. Saffer, E. Silber, P. Smets, R. E. Spalding, P. Spurný, E. Tagliaferri, D. Uren, R. J. Weryk, R. Whitaker, and Z. Krzeminski. A 500-kiloton airburst over Chelyabinsk and an enhanced hazard from small impactors. Nature, 503: 238–241, Nov. 2013. doi: 10.1038/nature12741.

C. F. Chyba, P. J. Thomas, and K. J. Zahnle. The 1908 Tunguska explosion - Atmospheric disruption of a stony asteroid. Nature, 361:40–44, Jan. 1993. doi: 10.1038/361040a0.

F. Colas, B. Zanda, J. Vaubaillon, S. Bouley, C. Marmo, Y. Audureau, M. K. Kwon, J.-L. Rault, S. Caminade, P. Vernazza, J. Gattacceca, M. Birlan, L. Maquet, A. Egal, M. Rotaru, C. Birnbaum, F. Cochard, and O. Thizy. French fireball network FRIPON. In J.-L. Rault and P. Roggemans, editors, *International Meteor Conference Mistelbach, Austria*, pages 37–40, Jan. 2015.

G. S. Collins, H. J. Melosh, and R. A. Marcus. Earth Impact Effects Program: A Web-based computer program for calculating the regional environmental consequences of a meteoroid impact on Earth. *Meteoritics and Planetary Science*, 40:817, June 2005. doi: 10.1111/j.1945-5100.2005.tb00157.x.

H. A. R. Devillepoix, E. K. Sansom, P. A. Bland, M. C. Towner, M. CupáK, R. M. Howie, T. Jansen-Sturgeon, M. A. Cox, B. A. D. Hartig, G. K. Benedix, and J. P. Paxman. The Dingle Dell meteorite: A Halloween treat from the Main Belt. *Meteoritics and Planetary Science*, 53:2212–2227, Oct. 2018. doi: 10.1111/maps.13142.

A. Egal, M.-K. Kwon, F. Colas, J. Vaubaillon, and C. Marmo. The challenge of meteor daylight observations. In A. Roggemans and P. Roggemans, editors, *International Meteor Conference Egmond, the Netherlands, 2-5 June 2016*, pages 73–75, Jan. 2016.

D. Farnocchia, S. R. Chesley, P. G. Brown, and P. W. Chodas. The trajectory and
    atmospheric impact of asteroid 2014 AA. Icarus, 274:327–333, Aug. 2016. doi:
    10.1016/j.icarus.2016.02.056.

D. Farnocchia, P. Jenniskens, D. K. Robertson, S. R. Chesley, L. Dimare, and
    P. W. Chodas. The impact trajectory of asteroid 2008 TC$_3$. Icarus, 294:218–226,
    Sept. 2017. doi: 10.1016/j.icarus.2017.03.007.

M. Granvik and P. Brown. Identification of meteorite source regions in the Solar
    System. Icarus, 311:271–287, Sept. 2018. doi: 10.1016/j.icarus.2018.04.012.

M. Granvik, A. Morbidelli, R. Jedicke, B. Bolin, W. F. Bottke, E. Beshore,
    D. Vokrouhlický, M. Delbò, and P. Michel. Super-catastrophic disruption of
    asteroids at small perihelion distances. Nature, 530:303–306, Feb. 2016. doi:
    10.1038/nature16934.

M. Granvik, A. Morbidelli, R. Jedicke, B. Bolin, W. F. Bottke, E. Beshore,
    D. Vokrouhlický, D. Nesvorný, and P. Michel. Debiased orbit and absolute-
    magnitude distributions for near-Earth objects. Icarus, 312:181–207, Sept.
    2018. doi: 10.1016/j.icarus.2018.04.018.

S. Greenstreet, H. Ngo, and B. Gladman. The orbital distribution of Near-Earth
    Objects inside Earth's orbit. Icarus, 217:355–366, Jan. 2012. doi: 10.1016/j.
    icarus.2011.11.010.

M. Gritsevich, V. Dmitriev, V. Vinnikov, D. Kuznetsova, V. Lupovka, J. Pel-
    toniemi, S. Mönkölä, J. Brower, and Y. Pupyrev. Constraining the Pre-
    atmospheric Parameters of Large Meteoroids: Košice, a Case Study.
    In *Assessment and Mitigation of Asteroid Impact Hazards, Astrophysics and Space
    Science Proceedings, Volume 46. ISBN 978-3-319-46178-6. Springer International
    Publishing Switzerland, 2017, p. 153*, volume 46, page 153, Jan. 2017. doi:
    10.1007/978-3-319-46179-3_8.

A. H. Hildebrand, L. T. J. Hanton, F. Ciceri, R. Nowell, E. Lyytinen, E. A. Silber, P. G. Brown, N. Gi, P. Jenniskens, J. Albers, and D. Hladiuk. Characteristics of a Well Recorded, Bright, Meteorite-Dropping Fireball, British Columbia. In *Lunar and Planetary Science Conference*, volume 49 of *Lunar and Planetary Inst. Technical Report*, page 3006, Mar. 2018.

R. M. Howie, J. Paxman, P. A. Bland, M. C. Towner, M. Cupák, E. K. Sansom, and H. A. R. Devillepoix. How to build a continental scale fireball camera network. *Experimental Astronomy*, May 2017a. doi: 10.1007/s10686-017-9532-7.

R. M. Howie, J. Paxman, P. A. Bland, M. C. Towner, E. K. Sansom, and H. A. R. Devillepoix. Submillisecond fireball timing using de Bruijn time-codes. *Meteoritics and Planetary Science*, 52:1669–1682, Aug. 2017b. doi: 10.1111/maps.12878.

Z. Ivezic, T. Axelrod, W. N. Brandt, D. L. Burke, C. F. Claver, A. Connolly, K. H. Cook, P. Gee, D. K. Gilmore, S. H. Jacoby, R. L. Jones, S. M. Kahn, J. P. Kantor, V. V. Krabbendam, R. H. Lupton, D. G. Monet, P. A. Pinto, A. Saha, T. L. Schalk, D. P. Schneider, M. A. Strauss, C. W. Stubbs, D. Sweeney, A. Szalay, J. J. Thaler, J. A. Tyson, and LSST Collaboration. Large Synoptic Survey Telescope: From Science Drivers To Reference Design. *Serbian Astronomical Journal*, 176:1–13, June 2008. doi: 10.2298/SAJ0876001I.

T. Jansen-Sturgeon, E. K. Sansom, and P. A. Bland. Comparing Analytical and Numerical Approaches to Meteoroid Orbit Determination using Hayabusa Telemetry. *ArXiv e-prints*, art. arXiv:1808.05768, Aug. 2018.

P. Jenniskens, M. H. Shaddad, D. Numan, S. Elsir, A. M. Kudoda, M. E. Zolensky, L. Le, G. A. Robinson, J. M. Friedrich, D. Rumble, A. Steele, S. R. Chesley, A. Fitzsimmons, S. Duddy, H. H. Hsieh, G. Ramsay, P. G. Brown, W. N. Edwards, E. Tagliaferri, M. B. Boslough, R. E. Spalding, R. Dantowitz, M. Kozubal, P. Pravec, J. Borovička, Z. Charvat, J. Vaubaillon, J. Kuiper, J. Albers, J. L. Bishop, R. L. Mancinelli, S. A. Sandford, S. N. Milam, M. Nuevo,

and S. P. Worden. The impact and recovery of asteroid 2008 TC_3. Nature, 458: 485–488, Mar. 2009. doi: 10.1038/nature07920.

T. Lister, S. Greenstreet, E. Gomez, E. J. Christensen, and S. M. Larson. The LCOGT NEO Follow-up Network. In *AAS/Division for Planetary Sciences Meeting Abstracts*, volume 48 of *AAS/Division for Planetary Sciences Meeting Abstracts*, page 405.06, Oct. 2016.

E. P. Milley. Physical properties of fireball-producing earth-impacting meteoroids and orbit determination through shadow calibration of the buzzard coulee meteorite fall. Master's thesis, University of Calgary, 7 2010.

M. Mommert, D. Farnocchia, J. L. Hora, S. R. Chesley, D. E. Trilling, P. W. Chodas, M. Mueller, A. W. Harris, H. A. Smith, and G. G. Fazio. Physical Properties of Near-Earth Asteroid 2011 MD. ApJ, 789:L22, July 2014a. doi: 10.1088/2041-8205/789/1/L22.

M. Mommert, J. L. Hora, D. Farnocchia, S. R. Chesley, D. Vokrouhlický, D. E. Trilling, M. Mueller, A. W. Harris, H. A. Smith, and G. G. Fazio. Constraining the Physical Properties of Near-Earth Object 2009 BD. ApJ, 786:148, May 2014b. doi: 10.1088/0004-637X/786/2/148.

C. Palotai, R. Sankar, D. L. Free, J. A. Howell, E. Botella, and D. Batcheldor. Analysis of June 2, 2016 bolide event. *ArXiv e-prints*, Jan. 2018.

O. Popova, J. Borovička, W. K. Hartmann, P. Spurný, E. Gnos, I. Nemtchinov, and J. M. Trigo-Rodríguez. Very low strengths of interplanetary meteoroids and small asteroids. *Meteoritics and Planetary Science*, 46:1525–1550, Oct. 2011. doi: 10.1111/j.1945-5100.2011.01247.x.

D. O. Revelle and Z. Ceplecha. Analysis of identified iron meteoroids: Possible relation with M-type Earth-crossing asteroids? A&A, 292:330–336, Dec. 1994.

E. K. Sansom, P. Bland, J. Paxman, and M. Towner. A novel approach to fireball

modeling: The observable and the calculated. *Meteoritics and Planetary Science*, 50:1423–1435, Aug. 2015. doi: 10.1111/maps.12478.

E. K. Sansom, M. G. Rutten, and P. A. Bland. Analyzing Meteoroid Flights Using Particle Filters. AJ, 153:87, Feb. 2017. doi: 10.3847/1538-3881/153/2/87.

P. Spurný, J. Borovička, J. Haloda, L. Shrbený, and D. Heinlein. Two Very Precisely Instrumentally Documented Meteorite Falls: Žďár nad Sázavou and Stubenberg - Prediction and Reality. In *79th Annual Meeting of the Meteoritical Society*, volume 1921 of *LPI Contributions*, page 6221, Aug. 2016.

P. Vernazza, R. P. Binzel, C. A. Thomas, F. E. DeMeo, S. J. Bus, A. S. Rivkin, and A. T. Tokunaga. Compositional differences between meteorites and near-Earth asteroids. Nature, 454:858–860, Aug. 2008. doi: 10.1038/nature07154.

CHAPTER 4

The Dingle Dell meteorite: a Halloween treat from the Main Belt

Hadrien A. R. Devillepoix[a], Eleanor K. Sansom[a], Philip A. Bland[a], Martin C. Towner[a],

Martin Cupák[a], Robert M. Howie[a], Trent Jansen-Sturgeon[a], Morgan A. Cox[a],

Benjamin A. D. Hartig[a], Gretchen K. Benedix[a], Jonathan Paxman [b]

[a]School of Earth and Planetary Sciences, Curtin University, GPO Box U1987, Bentley, Perth, WA 6845, Australia

[b]School of Civil and Mechanical Engineering, Curtin University, GPO Box U1987, Bentley, Perth, WA 6845, Australia

Abstract

We describe the fall of the Dingle Dell (L/LL 5) meteorite near Morawa in Western Australia on October 31, 2016. The fireball was observed by six observatories of the Desert Fireball Network (DFN), a continental scale facility optimised to recover meteorites and calculate their pre-entry orbits. The $30\,\mathrm{cm}$ meteoroid entered at $15.44\,\mathrm{km\,s^{-1}}$, followed a moderately steep trajectory of $51°$ to the horizon from 81 km down to 19 km altitude, where the luminous flight ended at a speed of $3.2\,\mathrm{km\,s^{-1}}$. Deceleration data indicated one large fragment had made it to the ground. The four person search team recovered a 1.15 kg meteorite within 130 m of the predicted fall line, after 8 hours of searching, 6 days after the fall. Dingle Dell is the fourth meteorite recovered by the DFN in Australia, but the first before any rain had contaminated the sample. By numerical integration over 1 Ma, we show that Dingle Dell was most likely ejected from the main belt by the 3:1 mean-motion resonance with Jupiter, with only a marginal chance that it came from the nu_6 resonance. This makes the connection of Dingle Dell to the Flora family (currently thought to be the origin of LL chondrites) unlikely.

4.1. Introduction

As of mid-2017 there are nearly 60k meteorite samples classified in the Meteoritical Bulletin Database[1]. However, apart from a handful of Lunar ($\simeq 300$) and Martian ($\simeq 200$) meteorites that have a well known origin, the link with other solar system bodies is limited. From the instrumentally documented fall of the Příbram meteorite in 1959 (Ceplecha, 1961), we learned that chondritic material comes from the asteroid main belt. The way this material evolves onto an Earth

---

[1] https://www.lpi.usra.edu/meteor/metbull.php

crossing orbit starts with a disruption in the main belt. The small members of the debris field can be strongly affected by the Yarkovsky effect (Farinella et al., 1998) and as a consequence their semi-major axis is continually altered. If the debris field is close to a powerful resonance (in semi-major axis, inclination, eccentricity space), the break up event feeds material into that resonance, which will in turn push the debris' perihelia into the inner solar system. This can occur on a timescale of less than a million years in some cases (Morbidelli et al., 1994).

Calculating the orbit of a meteoroid using only the luminous trajectory as the observation arc is in most cases not precise enough to allow unequivocal backtracking into a specific region of the main belt, hence the statistical results reported by Bland et al. (2009); Brown et al. (2011); Jenniskens et al. (2014); Trigo-Rodríguez et al. (2015). In order to understand the origin of the different groups of meteorites from the main asteroid belt, it is therefore essential to collect several dozen samples with orbits and look at source regions in a broader, statistical way.

4.1.1. DEDICATED NETWORKS TO RECOVER METEORITES WITH KNOWN PROVENANCE

In the decade following 2000, the recovery rate of meteorites with determined orbits has dramatically increased (Borovička et al., 2015), without a significant increase in collecting area of the major dedicated fireball networks. While the initial phase of the Desert Fireball Network (DFN) started science operations in December 2005, covering $0.2 \times 10^6 \, \mathrm{km}^2$ (Bland et al., 2012), other major networks ceased operations. The Prairie network in the USA ($0.75 \times 10^6 \, \mathrm{km}^2$ (McCrosky and Boeschenstein, 1965)) shut down in 1975, the Canadian Meteorite Observation and Recovery Project (MORP) - $1.3 \times 10^6 \, \mathrm{km}^2$- stopped observing in 1985 (Halliday et al., 1996), and the European Network's covering area of $\sim 1 \times 10^6 \, \mathrm{km}^2$ has not significantly changed (Oberst et al., 1998). If not

due to a larger collecting area, this increase can be explained by other factors:

- Existing networks improving their data reduction techniques (Spurný et al., 2014).

- Democratisation and cheap operating cost of recording devices (surveillance cameras, consumer digital cameras...) (Borovička et al., 2003).

- Use of doppler radar designed for weather observations to constrain the location of falling meteorites (Jenniskens et al., 2012; Fries et al., 2014; Fries and Fries, 2010).

- Deployment of the Desert Fireball Network expressly on favourable terrain to search for meteorites. In its early stage, within its first 5 years of science operation, the DFN yielded 2 meteorites (Bland et al., 2009; Spurný et al., 2011), whilst MORP only yielded one (Halliday et al., 1981) in 15 years of operations over a larger network.

- To a lesser extent, development of NEO telescopic surveillance programmes. One single case so far (the Catalina Sky Survey detecting the Almahata Sita meteoroid several hours before impact Jenniskens et al. (2009)), however this technique is likely to yield more frequent successes with new deeper and faster optical surveyors, like LSST, which comes online in 2021 (Ivezic et al., 2008).

The DFN started developing digital observatories to replace the film based network in 2012 with the goal of covering $10^6 \, \text{km}^2$, the more cost effective than expected digital observatories allowed the construction of a continent-scale network covering over $2.5 \times 10^6 \, \text{km}^2$ (Howie et al., 2017a). This programme rapidly yielded results, less than a year after starting science operation (in November 2014). One of the observatories lent to the SETI institute in California was a crucial viewpoint to calculating an orbit for the Creston fall in California

in October 2015 (Jenniskens et al., 2019), and the first domestic success came 2 months later with the Murrili meteorite recovery on Kati Thanda–Lake Eyre (Devillepoix et al., 2016). We report here the analysis of observations of a bright fireball that led to the fourth find by the Desert Fireball Network in Australia: the Dingle Dell meteorite. Dingle Dell was originally classified as an LL ordinary chondrite, petrographic type 6 (Met, 2017). However, further analysis revealed that it in fact sits on the L/LL boundary (Benedix et al., 2017). The sample has experienced a low level of shock, but has been heated enough to show recrystallisation of minerals and matrix. There is no evidence of terrestrial weathering visible on the metal or sulphide grains, which is consistent with its extremely fast retrieval from the elements.

4.1.2. CURRENT UNDERSTANDING OF THE ORIGIN OF THE MAIN GROUPS OF L AND LL CHONDRITES

L CHONDRITES L chondrites represent 32% of total falls. Schmitz et al. (2001) first identified a large amount of fossil L chondrites meteorites in $\simeq 467\,\mathrm{Ma}$ sedimentary rock, which suggests that a break up happened not too long before, near an efficient meteorite transport route. From spectroscopic and dynamical arguments, Nesvorný et al. (2009) proposed that the Gefion family break up event, close to the 5:2 MMR with Jupiter, might be the source of this bombardment, given the rapid delivery time, and a likely origin of L chondrite asteroids outside of the 2.5 AU. Most shocked L5 and L6 instrumentally observed falls also seem to come from this break up, with an $^{39}Ar - ^{40}Ar$ age around $\simeq 470\,\mathrm{Ma}$ ago: Park Forest (Brown et al., 2004), Novato (Jenniskens et al., 2014), Jesenice (Spurný et al., 2010), and Innisfree (Halliday et al., 1981). Only the Villalbeto de la Peña L6 (Trigo-Rodríguez et al., 2006) does not fit in this story because of its large cosmic ray exposure age (48 Ma), inconsistent with a 8.9 Ma collisional lifetime (Jenniskens, 2014).

LL CHONDRITES Thanks to Vernazza et al. (2008), we know that S- and Q-type asteroids observed in NEO space are the most likely asteroidal analogue to LL type ordinary chondrites. The Hayabusa probe returned samples from S-type (25143) Itokawa, finally unequivocally matching the largest group of meteorites recovered on Earth (ordinary chondrites) with the most common spectral class of asteroids in the main belt (Nakamura et al., 2011). The sample brought back from Itokawa is compatible with LL chondrites. Indeed, LL compatible asteroids make up two thirds of near-Earth space. The spectrally compatible Flora family from the inner main belt can regenerate this population through the ν_6 secular resonance. But one large problem remains: only 8% of falls are LL chondrites (Vernazza et al., 2008). The orbits determined for some LL samples have so far not helped solve this issue. If we exclude Benešov (Spurný et al., 2014), which was a mixed fall, scientists had to wait until 2013 to get an LL sample with a precisely calculated orbit: Chelyabinsk (Brown et al., 2013; Borovička et al., 2013). The pre-atmospheric orbit and composition of the Chelyabinsk meteorite seems to support the Flora family origin for LL chondrites, although a more recent impact could have reset the cosmic ray exposure age to $1.2 \pm 0.2\,\mathrm{Ma}$, and the presence of impact melts (very rare in ordinary chondrites due to the large impact velocities required (Keil et al., 1997)). Reddy et al. (2014) argued that an impact melt such as the one observed in the Chelyabinsk meteorites, or shock darkening, can alter the spectra of an S/Q-type asteroid to make it look like a C/X-type spectrally. The implication of this is that the Baptistina family members (C/X-type), which overlaps dynamically with the Flora (S-type), could be the remains of a large impact on a Florian asteroid, and meteorites from both families can be confused both in their spectral signature and dynamical origin. It must be noted however that Reddy et al. (2014) do not make any conclusions on the origin of Chelyabinsk from the Baptistina family. The Chelyabinsk meteorite is also not a typical LL sample found on Earth, because of its size ($\simeq 17\,m$), and the presence of impact melts.

Based on it's classification, we put the orbit of the Dingle Dell meteorite in context with other calculated orbits from L and LL chondrites and discuss the resonances from which it may have originated.

4.2. FIREBALL OBSERVATION AND TRAJECTORY DATA

On Halloween night shortly after 8 PM local time, several reports of a large bolide were made via the *Fireballs In The Sky* smart-phone app (Sansom et al., 2016) from the Western Australian Wheatbelt area. These were received a few hours prior to the daily DFN observatory reports, apprising the team of the event expeditiously. The DFN observatory sightings are routinely emailed after event detection has been completed on the nights' data-set. It revealed that six nearby DFN observatories simultaneously imaged a long fireball starting at 12:03:47.726 UTC on October 31, 2016 (Figure 4.1).

4.2.1. INSTRUMENTAL RECORDS

The main imaging system of the DFN fireball observatories is a 36 MPixel sensor: Nikon D810 (or D800E on older models), combined with a Samyang lens 8mm F/3.5. Long exposure images are taken every 30 seconds. The absolute and relative timing (from which the fireball velocity is derived) is embedded into the luminous trail by use of a liquid crystal (LC) shutter between the lens and the sensor, modulated according to a de-Brujin sequence (Howie et al., 2017b). The LC shutter operation is tightly regulated by a micro-controller synced with a Global Navigation Satellite System (GNSS) module to ensure absolute timing accurate to ± 0.4 ms. For further details on DFN observatory specifications, see Howie et al. (2017a).

Some DFN observatories also include video systems operating in parallel
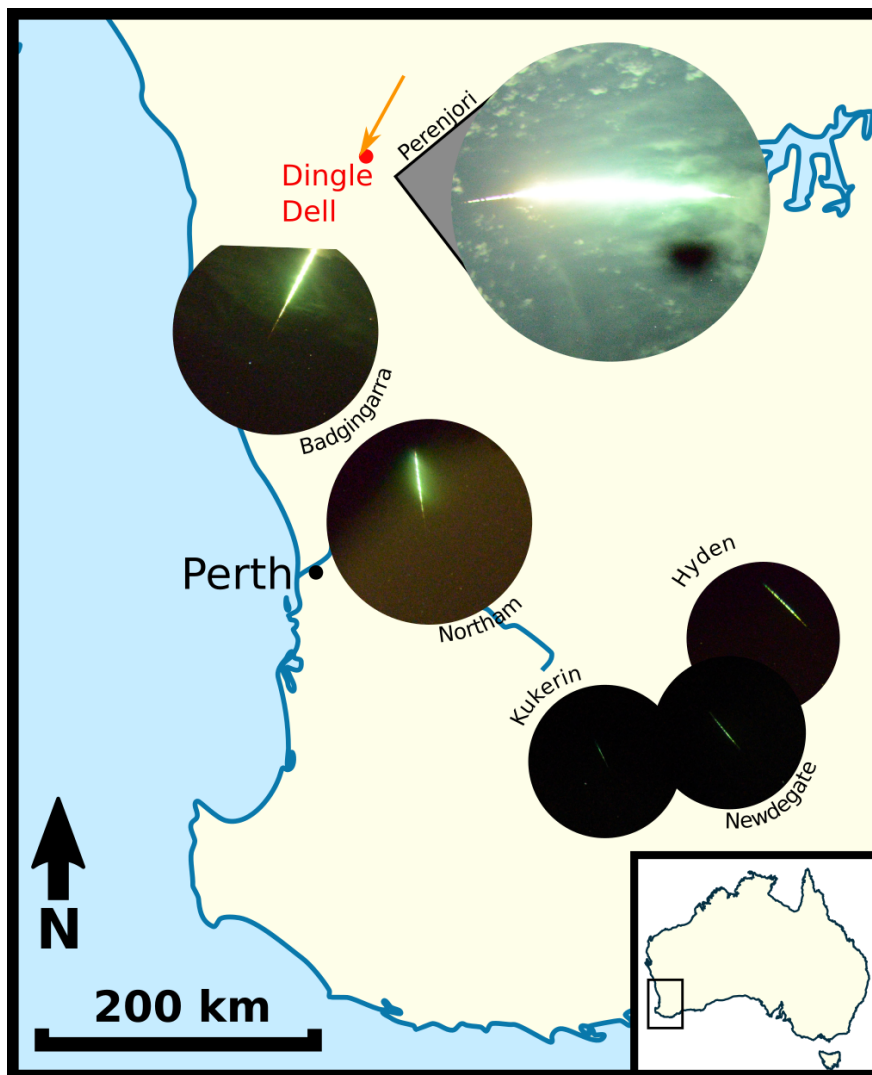
FIGURE 4.1: Cropped all-sky images of the fireball from the six DFN observatories. Images are of the same pixel scale with the centre of each image positioned at the observatory location on the map (with the exception of Perenjori, whose location is indicated). The Badgingarra image is cropped because the sensor is not large enough to accommodate the full image circle on its short side. The saturation issue is exacerbated by light scattered in the clouds on cameras close to the event, this is particularly visible on the Perenjori image. The black blotch in the Perenjori image is an artefact that thankfully did not extend far enough to affect the quality of the data. Approximate trajectory path shown by orange arrow. Location of the recovered meteorite is shown by the red dot.

with the long exposure photographic imaging system (Table 4.1). The video cameras are Watec 902H2 Ultimate CCIR (8 bit 25 interlaced frames per second), with a Fujinon fisheye lens. Originally intended as a backup device for absolute timing, these video systems have been retained for future daytime observation

capabilities. Here we make use of the video data to acquire a light curve, as the event saturated the still camera sensors. The closest camera system to this event was in Perenjori (Table 4.1), located almost directly under the fireball, and was the only station to image the end of the luminous trajectory (Fig. 4.1). Other nearby camera sites were overcast and did not record the event. In order to triangulate the trajectory of the fireball, distant stations had to be used, all over 200 km away. The Hyden, Kukerin and Newdegate systems were all around 500 km from the event and, although still managing to capture the fireball, were too low on the horizon for accurate calibration.

TABLE 4.1: Locations and nature of instrumental records. We use cameras < $400\,km$ away for trajectory determination. P: Photographic record (exposures: 25 seconds, 6400 ISO, F/4.), V: video record. *: distance from the meteoroid at 70 km altitude

Observatory	Instruments	Latitude	Longitude	altitude (m)	distance* (km)
Perenjori	P, V	29.36908 S	116.40654 E	242	91
Badgingarra	P	30.40259 S	115.55077 E	230	204
Northam	P	31.66738 S	116.66571 E	190	323
Hyden	P	32.40655 S	119.15325 E	390	484
Kukerin	P	33.25337 S	118.00628 E	340	520
Newdegate	P	33.05436 S	118.93534 E	302	534

4.2.2. ASTROMETRY

All images captured by the DFN observatories are saved even when no fireball is detected. This is possible thanks to the availability of large capacity hard drives at reasonable costs. Not only does this mitigate event loss during initial testing of detection algorithms, but it gives a snapshot of the whole visible sky down to 7.5 point source limiting magnitude, every 30 seconds. The astrometric calibration allows the points picked along the fireball image to be converted to astrometric sky coordinates. The associated astrometric uncertainties are dominated by the uncertainty on identifying the centroids along the segmented fireball track.
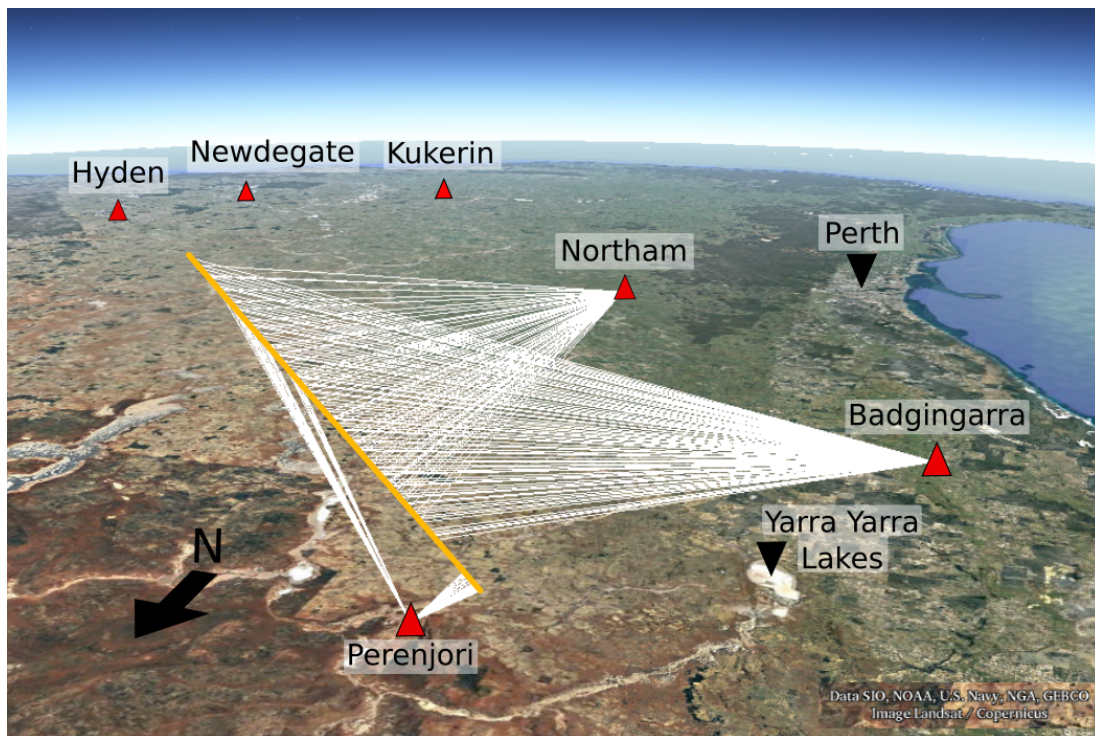
FIGURE 4.2: Configuration of DFN station observations for the Dingle Dell fireball. White rays show observations used in triangulation of the trajectory (approximated to the yellow line, starting NE and terminating to the SW of Perenjori). Hyden, Newdegate and Kukerin stations were all around 500 km away from the event and were not used in triangulation.

We have carried out studies on the long-term camera stability by checking the camera pointing using astrometry. On the outback system tested, the pointing changed less than 1′ over the 3 month period assessed. The pointing is therefore remarkably stable, and the relevant fireball image can thus be astrometrically calibrated using a picture taken at a different epoch. This is particularly useful when a bright fireball overprints nearby stars, and especially in this case where clouds are present. In general however, we aim to use a calibration frame taken as close as possible from the science frame, particularly when studying an important event, such as a meteorite fall. In the following paragraph we present the methods used for astrometrically calibrating the still images, using as an example the Perenjori data. This technique is implemented in an automated way in the reduction pipeline for all detected events.

The astrometric solution for the Perenjori camera is obtained using an image taken a few hours after the event, once the clouds had cleared (2016-10-31T16:00:30 UTC), containing 1174 stars of apparent magnitude $m_V \in [1.5, 5.5]$. A 3rd order polynomial fit is performed to match detected stars to the Tycho-2 star catalogue. The transformation is further corrected using a 2nd order polynomial on the radial component of the optics. The stability of the solution can be checked at regular intervals. The slight degradation in altitude precision for altitudes below $20°$ in Fig. 4.3, is due to a partly obstructed horizon from this camera (eg. trees, roofs). This degradation usually starts around $10°$ on cameras with a clear horizon, as is the case for most outback systems.

The beginning of the fireball on the Perenjori image is partially masked by clouds, yielding only a handful of points. The middle section is not usable as the sensor was saturated in large blobs, rendering impossible timing decoding or even reliable identification of the centre of the track. However the Perenjori image provides a good viewpoint for the end of the fireball.

Well calibrated data were also obtained from the Badgingarra camera, before it went outside the sensor area at 30.6 km altitude. Although the Northam camera was very cloudy, we were able to pick the track of the main meteoroid body without timing information, and use it as a purely geometric constraint. Hyden, Kukerin, and Newdegate also picked up the fireball, however the astrometry so low on the horizon ($< 5°$) was too imprecise (between 2 and 4 arcminutes) to refine the trajectory solution.

4.2.3. PHOTOMETRY

The automated DFN data reduction pipeline routinely calculates brightness for non-saturated fireball segments. For this bright event however, the brightness issue was exacerbated by large amounts of light scattered in the clouds (Fig. 4.1), so it was impossible to produce a useful light curve from the photograph. On
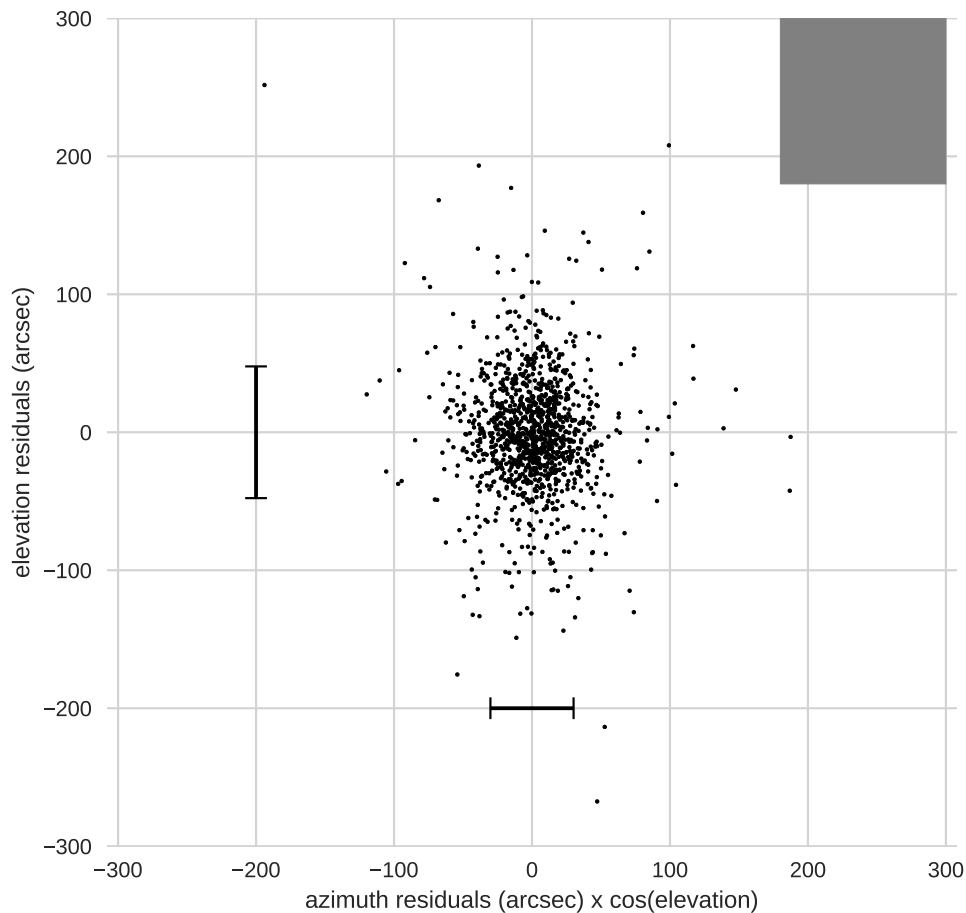
FIGURE 4.3: Residuals on the global astrometric solution for the Perenjori camera. The pixel size at the centre of the FoV is shown by the grey square in order to gauge the quality of the solution, as well as the 1σ residual bars on the stars. The azimuth residuals are artificially large around the pole of the spherical coordinate system, so we have multiplied them by $cos(elevation)$ to cancel out this artefact.

the other hand, the Perenjori observatory recorded a low-resolution compressed video through the clouds. Although it is not possible to calibrate this signal, we can get a remarkably deep dynamic range reading of the all-sky brightness, thanks to the large amount of light scattered in the numerous clouds. By de-interlacing the analogue video frames, we were able to effectively double the time resolution (25 interlaced frames per second to 50 fields per second, which

are equally as precise for all-sky brightness measurements). To correct how the auto-gain affects the signal, we perform aperture photometry on Venus throughout the event. The analogue video feed is converted to digital by the Commell MPX-885 capture card, and then processed by the compression algorithm (H264 VBR, FFmpeg *ultrafast* preset) (Howie et al., 2017a) before being written to disk, divided into 1 minute long segments. The PC clock is maintained by the Network Time Protocol (NTP) service, fed with both GNSS and network time sources. However the timestamp on the file created by the PC suffers from a delay. We measured the average delay using a GPS video time inserter (IOTA-VTI) on a test observatory. This allowed us to match the light curve obtained from the video to astrometric data to within $20\,\mathrm{ms}$. Peak *A*
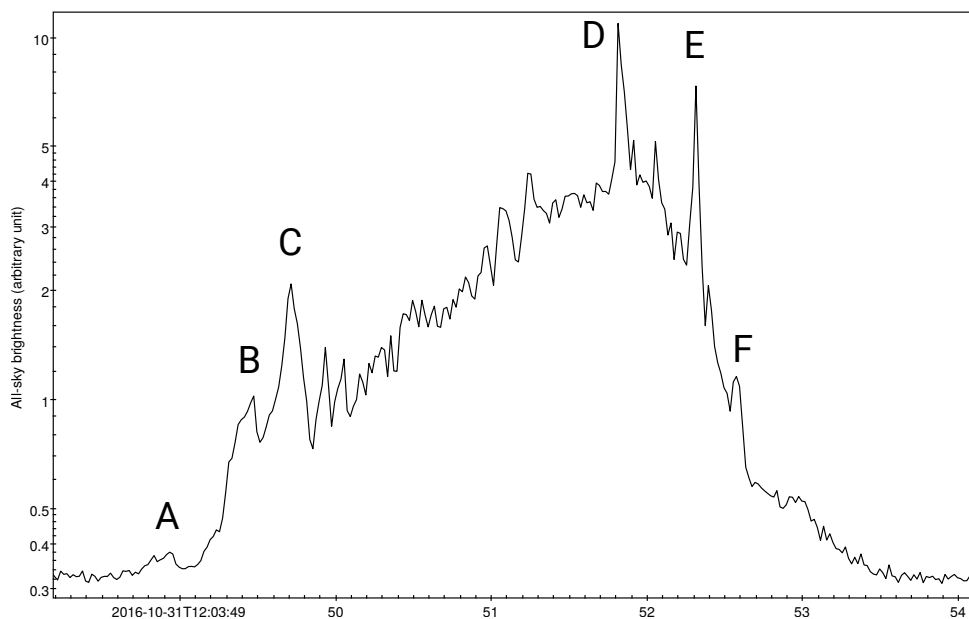
FIGURE 4.4: All-sky brightness (sum of all the pixels) from the video camera at the Perenjori observatory. The light curve is corrected to take into account the effect of auto-gain.

in Figure 4.4 is visible on the photographs from both Badgingarra and Hyden. These are used to validate the absolute timing alignment of the video data.

Reporting Means	Report Time (UTC)	Location	Approx. Distance From Event (km)	Reported Duration (s)	Reported Brightness (stellar Mag)	Reported Colour
FITS	12:04	Perth region	300	2.6	-8	Orange
FITS	12:59	Ballidu	150	6.4	-7	Green
FITS	13:35	Dowerin	230	8.6	-9	Pink
eye witness	N/A	Koolanooka Hills	7.4	> 5	> -12.6 (full moon)	

TABLE 4.2: Observer reports from eyewitness accounts and *Fireballs in the Sky* app (FITS).

4.2.4. Eye witnesses

Three anecdotal reports of the fireball were received via the *Fireballs in the Sky* smartphone app (Paxman and Bland, 2014; Sansom et al., 2016) within two hours of the event (Table 4.2). The free app is designed to enable members of the public to easily report fireball sightings. Phone GPS, compass, and accelerometers are utilised to report the direction of observations, while a fireball animation aids users in estimating the colour, duration and brightness of the event. This app is an interactive alternative to the popular web-based reporting tool of the International Meteor Organisation (Hankey and Perlerin, 2015).

The app reports were the first notification of the fireball received by the DFN team, even before the receipt of daily emails from the fireball observatories. The azimuth angles reported by the observers were not sufficiently consistent to enable a triangulation based on app reports alone.

The fireball was also reported by several nearby witnesses, and was described in detail by an eye witness only 7.4 km from the fall position (Table 4.2) who also reported hearing sounds, which due to the time of arrival may have been electrophonic in nature (Keay, 1992).

4.3. Fireball Trajectory Analysis

4.3.1. Geometry

To determine the trajectory of the fireball through the atmosphere, we use a modified version of the Borovička (1990) straight-line least squares (SLLS) method. This involves creating a radiant in 3D space that best fits all the observed lines of sight, minimising the angular residuals between the radiant line and the observed lines of sight. While angular uncertainties will be similar across different camera systems, the effect of distance results in larger cross-track errors for more distant observatories (Fig. 4.5), and therefore have less influence on the resulting radiant fit. The end of the fireball from the Perenjori image was used, along with Badgingarra and Northam camera data to triangulate the geometry of the fireball trajectory. The inclusion of astrometric data from Hyden, Kukerin, and Newdegate (see section 4.2.2) degraded the solution: the cross-track residuals from all viewpoints increased significantly, suggesting a systematic issue with the above mentioned camera data. Therefore we only used the trajectory solution yielded by the 3 closest view points (Fig. 4.5). The best combination of viewpoints (Perenjori and Badgingarra) yields an excellent convergence angle of $86°$. The trajectory solution points to a moderately steep entry with a slope of $51°$ from the horizon, with ablation starting at an altitude of 80.6 km and ending at 19.1 km (see Table 4.3).

4.3.2. Dynamic modelling of the trajectory, including velocity and mass determination

Filter Modelling The method described in Chapter 4 of Sansom (2016) is an iterative Monte Carlo technique that aims to determine the path and physical characteristics such as shape (A: the cross section area to volume
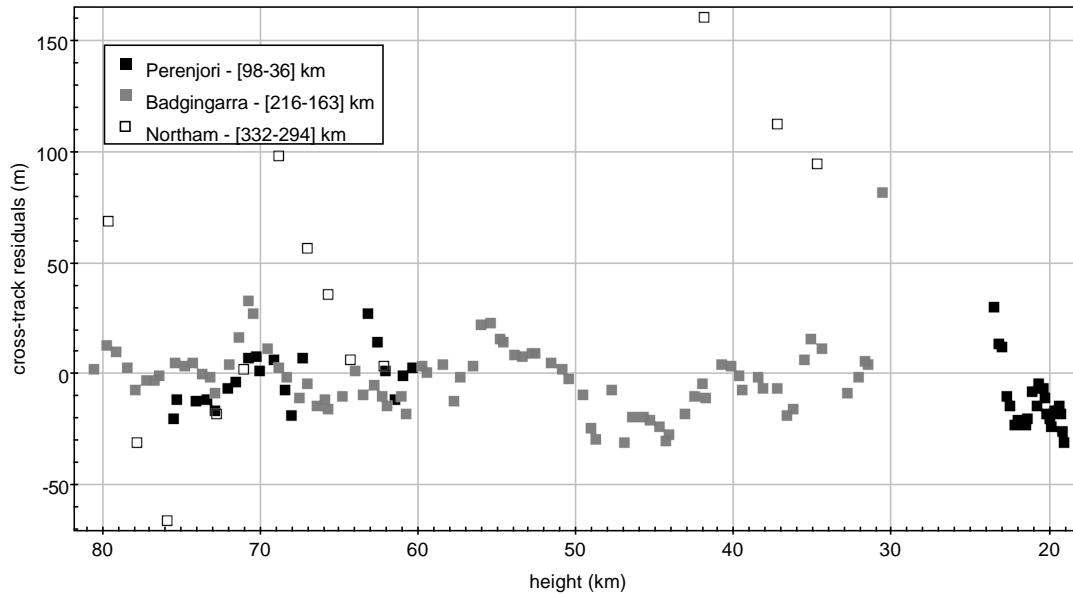
FIGURE 4.5: Cross-track residuals of the straight line least squares fit to the trajectory from each view point. These distances correspond to astrometric residuals projected on a perpendicular plane to the line of sight, positive when the line of sight falls above the trajectory solution. Note that the larger residuals on the Northam camera do not equate to larger astrometric uncertainties, but rather reflect a rather large distance from the observatory. The distances in the legend correspond to the observation range [highest point - lowest point].

Event	Time* s	Speed m s^{-1}	Height m	Longitude °E	Latitude °N	Dynamic pressure MPa
Beginning	0.0	15443±60	80594	116.41678	-28.77573	
A	1.20	15428	65819	116.36429	-28.86973	0.03
B	1.72	15401	59444	116.34151	-28.91045	0.08
C	1.96	15378	56531	116.33108	-28.92909	0.11
D	4.08	13240	32036	116.24270	-29.08672	2.28
E	4.58	10508	27302	116.22547	-29.11738	3.09
F	4.84	8988	25019	116.21716	-29.13217	3.27
Terminal	6.10	3243 ± 465	19122	116.19564	-29.17045	

TABLE 4.3: Summary table of bright flight events. Fragmentation event letters are defined on the light curve (Fig. 4.4). *: past 2016-10-31T12:03:47.726 UTC.

ratio), density (ρ_m), and ablation coefficient (σ) of a meteoroid from camera network data. In this approach, one is able to model meteoroid trajectories based on raw astrometric data. This avoids any preconceived constraints

imposed on the trajectory, such as the straight line assumption used in Section 4.3.1. Unfortunately this requires multiple view points with accurate absolute timing information to record the meteoroid position. For this event, timings encoded in the trajectory were distinguishable for only the initial 4.2 seconds by the Badgingarra system (before any significant deceleration) and for the final 1.1 seconds by the Perenjori system. In this case we must rely on the straight-line least squares (SLLS) triangulation to determine meteoroid positions (see Section 4.3.1). We therefore applied the three dimensional particle filter model outlined in Chapter 4 of Sansom (2016) using instead triangulated geocentric coordinates as observation measurements. Uncertainties associated with using pre-triangulated positions based on an assumed straight line trajectory are incorporated. The distribution of particle positions using such observations will be overall greater than if we had been able to use the raw measurements.

As a straight line may be an oversimplification of the trajectory, to most reliably triangulate the end of the luminous flight using the SLLS method, the final 1.1 seconds were isolated (this being after all major fragmentation events described in Section 4.3.3). The filter was run using these positions and initiated at $t_0 = 5.0$ seconds (2016-10-31T12:03:52.726 UTC). Particle mass values at this time would be more suitably initiated using a logarithmic distribution between the range of $0\,\text{kg}$ to $1000\,\text{kg}$. The initiation of other filter parameters, including the multimodal density distribution, are described in Sansom et al. (2017) with ranges given in Table 1 of the work. As a calibrated light curve was not attainable, brightness values were not included in this analysis, making it a purely dynamic solution.

The adaptive particle filter technique applied here uses the same state vector and three dimensional state equations as in Chapter 4 of Sansom (2016), to evaluate the meteoroid travelling through the atmosphere. As we are using pre-triangulated geocentric positions as observations, the measurement function here is linear. The particles are still allowed to move in 3D space, and an
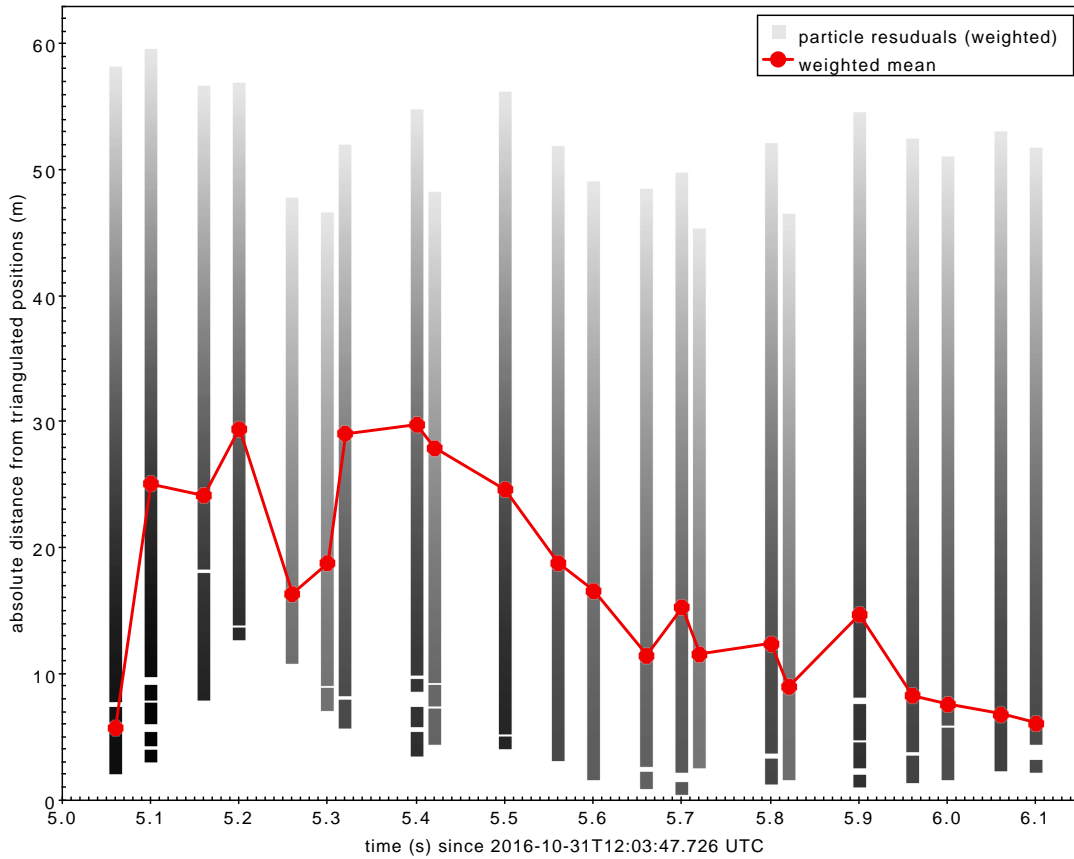
FIGURE 4.6: Position residuals of the 3D particle filter fit to the SLLS triangulated observations for the final $1.1\,s$ of the luminous trajectory. Individual particle weightings are shown in greyscales, with weighted mean values shown in red.

evaluation of the model fit is performed as the absolute distance between the pre-triangulated SLLS point and the evaluated particle position. This is shown in Figure 4.6 for all particles, with the distance to the mean value also shown. Mean particle positions show a good fit to the SLLS triangulated observations, with a maximum of $30\,m$ differences early on, decreasing to $6\,m$ at the end.

The filter estimates not only the position and velocity of the meteoroid at each observation time, but also the mass, ablation coefficient, σ, and shape density coefficient, κ. At the final observation time $t_f = 6.1\,s$ (2016-10-31T12:03:53.826 UTC), the state estimate results in weighted median values of $mass_f = 1.49 \pm 0.23\,\text{kg}$, $speed_f = 3359 \pm 72\,\text{m s}^{-1}$, $\sigma_f = 0.0154 \pm 0.0054\,s^2\,\text{km}^{-2}$ and $\kappa_f = 0.0027 \pm 0.0001$ (SI). Although κ may be used to calculate densities for a given shape

and drag coefficient, to avoid introducing assumptions at this stage we may gauge its value by reviewing the density with which surviving particles were initiated. The distribution of final mass estimates is plotted against this initial density attributed to each given particle in Figure 4.7, along with the recovered Dingle Dell meteorite mass of $1.150\,\mathrm{kg}$ and bulk density of $3450\,\mathrm{kg\,m^{-3}}$. In this figure, the distribution of the main cluster of particles is consistent with the recovered mass, however the initial densities are lower. The weighted median value of initial bulk densities (at $t_0 = 5.0\,\mathrm{s}$) for all particles re-sampled at t_f is $3306\,\mathrm{kg\,m^{-3}}$. It is expected that the bulk density of a meteoroid body may slightly increase throughout the trajectory as lower density, more friable material is preferentially lost. This could justify the slightly lower bulk densities attributed at t_0.

In order to obtain the entry speed of the meteoroid with appropriate errors, we apply an extended Kalman smoother (Sansom et al., 2015) to the straight line solution for the geometry, considering the timing of the points independently for each observatory. Of the two cameras that have timing data for the beginning of the trajectory, only Badgingarra caught the start, giving an entry speed of $15402 \pm 60\,\mathrm{m\,s^{-1}}$ (1σ) at $80596\,\mathrm{m}$ altitude. To determine whether speeds calculated are consistent between observatories, the first speed calculated for Perenjori – $15384 \pm 64\,\mathrm{m\,s^{-1}}$ at $75548\,\mathrm{m}$ altiude – is compared to the Badgingarra solution at this same altitude $-15386 \pm 43\,\mathrm{m\,s^{-1}}$. The results are remarkably consistent, validating the use of a Kalman smoother for determining initial velocities.

DIMENSIONLESS COEFFICIENT METHOD As a comparison to the particle filter method, the dimensionless parameter technique described by Gritsevich (2009) was also applied. The ballistic parameter (α) and the mass loss parameter (β) were calculated for the event, resulting in $\alpha = 9.283$ and $\beta = 1.416$ (Figure 4.8). As the particle filter technique in this case was not able to be performed on the first 5.0 seconds of the luminous trajectory, these parameters may be used
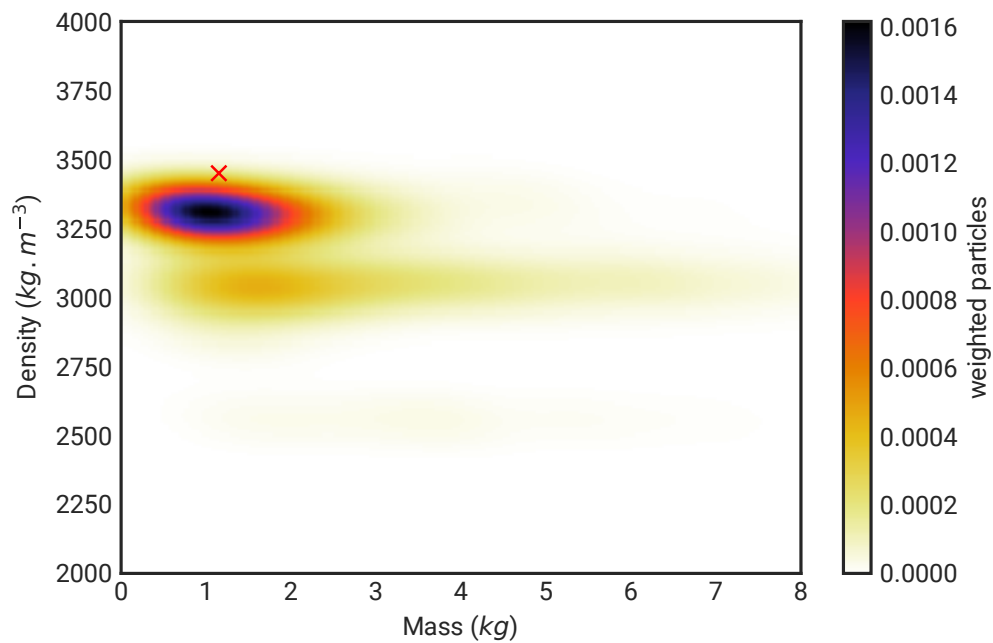
FIGURE 4.7: Results of the 3D particle filter modelling, showing the distribution of final mass estimates along with the densities with which particles were initiated at $t_0 = 5\,\text{s}$. Mass estimates are consistent with the recovered meteorite mass found (red cross), with initial densities slightly below the bulk rock value.

to determine both initial[1], and final[2] main masses, given assumed values of the shape and density of the body. Using the same parameters as Gritsevich (2009) ($c_d = 1$, $A = 1.55$) along with the density of the recovered meteorite, $\rho = 3450 \, \text{kg m}^{-3}$, gives an entry mass, $m_e = 81.6 \, \text{kg}$, and a $m_f = 1.4 \, \text{kg}$. Varying the shape of the body to spherical values, $A = 1.21$ (Bronshten, 1983) gives an initial mass of $m_e = 38.8 \, \text{kg}$. Instead of assuming values for c_d and A, we can also insert the κ value calculated by the particle filter to give $m_e = 41.1 \, \text{kg}$. These results can be approximated to a 30 cm diameter initial body. Note that this method is the most reliable for calculating a minimum entry mass of the Dingle Dell meteoroid. The photometric method would require a calibrated light curve, and the particle filter method requires good astrometric data coverage where significant deceleration occurs (the missing data between 4.2 and 5.0 seconds).

4.3.3. ATMOSPHERIC BEHAVIOUR

In Table 4.3 we report the ram pressure ($P = \rho_a v^2$) required to initiate the major fragmentation events labelled on the light curve in Fig. 4.4. The density of the atmosphere, ρ_a, is calculated using the *NRLMSISE-00* model of Picone et al. (2002), and v is the calculated speed. The meteoroid started fragmenting quite early (events *A*, *B*, and *C*), starting at 0.03 MPa. These early fragmentation events suggest that the meteoroid had a much weaker lithology than the meteorite that was recovered on the ground. Then no major fragmentation happened until two very bright peaks in the light curve: *D* (2.28 MPa) and *E* (3.09 MPa). These large short-lived peaks suggest a release of a large number of small pieces that quickly burnt up. A small final flare (*F*–3.27 MPa) 1.26 second before the end is also noted.

---

[1] see equation 14 in Gritsevich (2009)
[2] see equation 6 in Gritsevich (2009)
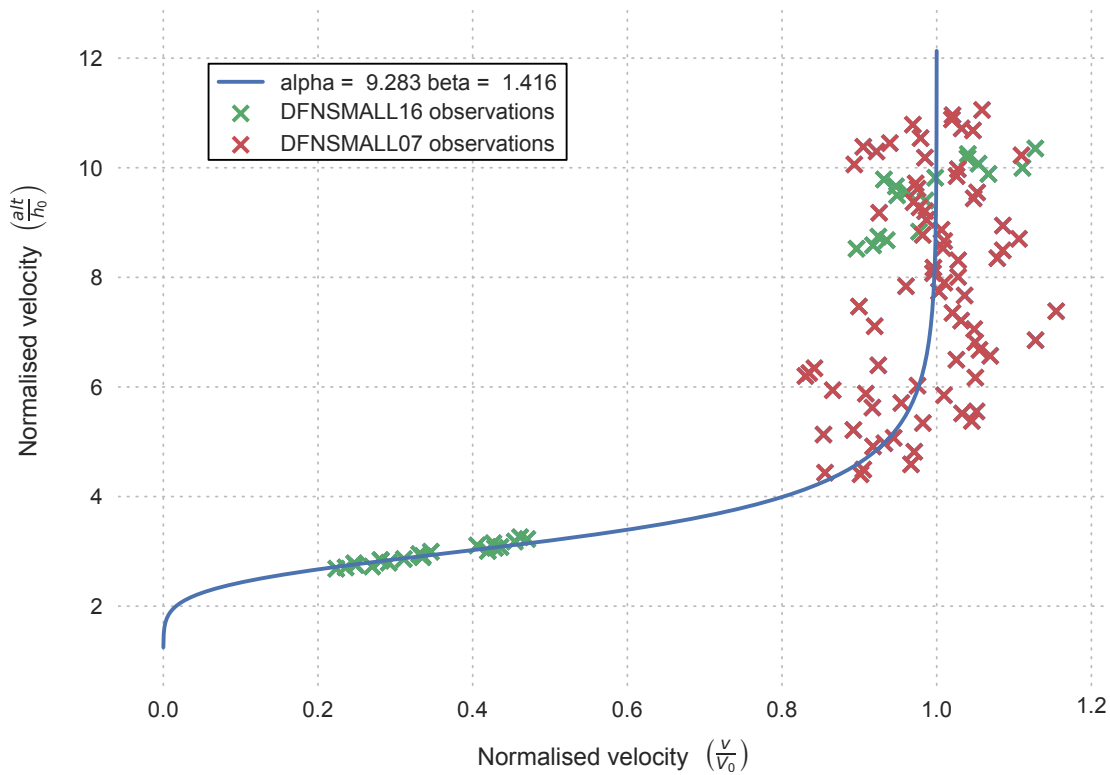
FIGURE 4.8: Trajectory data from both Perenjori and Badgingarra observatories, with speeds normalised to the speed at the top of the atmosphere (15.443 km s^{-1}; Tab. 4.3), V_0, and altitudes normalised to the atmospheric scale height, $h_0 = 7.16$ km. The best fit to Equation 10 of Gritsevich (2009) results in $\alpha = 9.283$ and $\beta = 1.416$ and is shown by the blue line. These dimensionless parameters can be used to determine the entry and terminal mass of the Dingle Dell meteoroid.

4.4. DARK FLIGHT AND METEORITE RECOVERY

The results of the dynamic modelling (Fig. 4.7) are fed directly into the dark flight routine. By using the state vectors (both dynamical and physical parameters) from the cloud of possible particles, we ensure that there is no discontinuity between the bright flight and the dark flight, and we get a simulation of possible impact points on the ground that is representative of the modelling work done on bright flight data.

4.4.1. WIND MODELLING

The atmospheric winds were numerically modelled using the Weather Research and Forecasting (WRF) software package version 3.8.1 with the Advanced Research WRF (ARW) dynamic solver (Skamarock et al., 2008). The weather modelling was initialised using global $1°$ resolution National Centers for Environmental Prediction (NCEP) Final analysis (FNL) Operational Model Global Tropospheric Analysis data. As a result, a 3 km resolution WRF product with 30 minutes history interval was created and weather profile at the end of the luminous flight for 2016-10-31T12:00 UTC extracted (Fig. 4.9). The weather profile includes wind speed, wind direction, pressure, temperature and relative humidity at heights ranging up to 30 km (Fig. 4.9), providing complete atmospheric data for the main mass from the end of the luminous phase to the ground, as well as for fragmentation events *E* and *F* (Table 4.3). Different wind profiles have been generated, by starting the WRF integration at different times: 2016 October 30d12h, 30d18h, 31d00h, 31d06h, and 31d12h UTC. Three of the resulting wind models converge to a similar solution in both speed and direction (30d12h, 31d00h, 31d12h) and will be hereafter referred to as solution *W1* (Fig. 4.9). The other two models from 30d18h (*W2*) and 31d00h (*W3*) differ significantly. For example, the maximum jet stream strength is $\simeq 47\,\mathrm{m\,s^{-1}}$ for

W1, $\simeq 34 \, \mathrm{m \, s^{-1}}$ for *W3*, and $\simeq 29 \, \mathrm{m \, s^{-1}}$ for *W2*. To discriminate which wind profile is closer to the truth, we ran the model next to the Geraldton balloon launches of 2016 October 31d00h and 31d06h UTC, but no discrepancy was noticeable between all 5 scenarios. Considering that 3 model runs clump around *W1*, whereas *W3* and *W2* are isolated, we choose *W1* as a preferred solution. The investigation of why *W3* and *W2* are different is beyond the scope of this paper, nonetheless we discuss how these differences affect the dark flight of the meteorites in the next section (4.4.2).
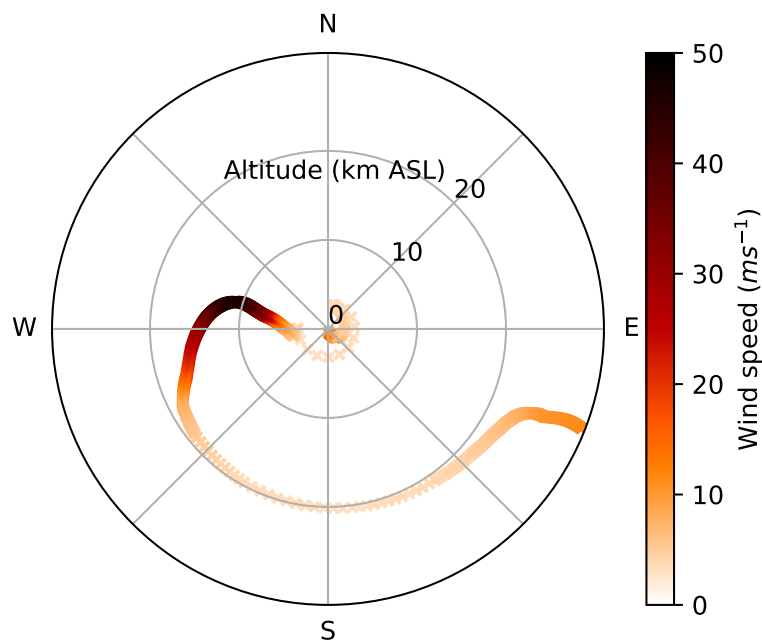
FIGURE 4.9: Wind model profile *W1*, extracted as a vertical profile at the coordinates of the lowest visible bright flight measurement.

4.4.2. DARK FLIGHT INTEGRATION

The calculations of the unobserved terminal part of the ablation phase and the dark flight are performed using an 8th order explicit Runge-Kutta integrator with adaptive step-size control for error handling. The physical model uses the single body equations for meteoroid deceleration and ablation (Hoppe, 1937;

Whipple, 1939). In this model, rotation is accounted for such that the cross sectional area to volume ratio (A) remains constant throughout the trajectory. The variation in flow regimes and Mach ranges passed through by the body alter the values used for the drag coefficient, which can be approximated using Table 1 in (Sansom et al., 2015).

The integration of all the particles from Section 4.3.2 allows the generation of probability heat maps to maximise field searching efficiency. The ground impact speed for the mass corresponding to the recovered meteorite is evaluated at $67\,\mathrm{m\,s^{-1}}$.

In calculating a fall line for an arbitrary range of masses, the assumed shape of the body and the wind model used both affect the final fall position. However for a given wind model a change in shape only shifts the masses along the fall line.

We also calculate dark flight fall lines from fragmentation events that happened within the wind model domain: *E* and *F*. Unsurprisingly, the main masses from those events are a close match to the corresponding main mass started from the end of the visible bright flight. However small fragments are unlikely to be found as they fell into the Koolanooka Hills bush land (Fig. 4.10).

4.4.3. SEARCH AND RECOVERY

Within two days, two of the authors (PB and MT) visited the predicted fall area, about 4 hours' drive from Perth, Western Australia to canvas local farmers for access and information. Having gained landowner permission to search, a team was sent to the area 3 days later. Searching was carried out by a team of 4 (MT, BH, TJS, and HD), mostly on foot and with some use of mountain biking in open fields. The open fields' searching conditions were excellent, although the field boundaries were vegetated. The team managed to cover about 12 ha per
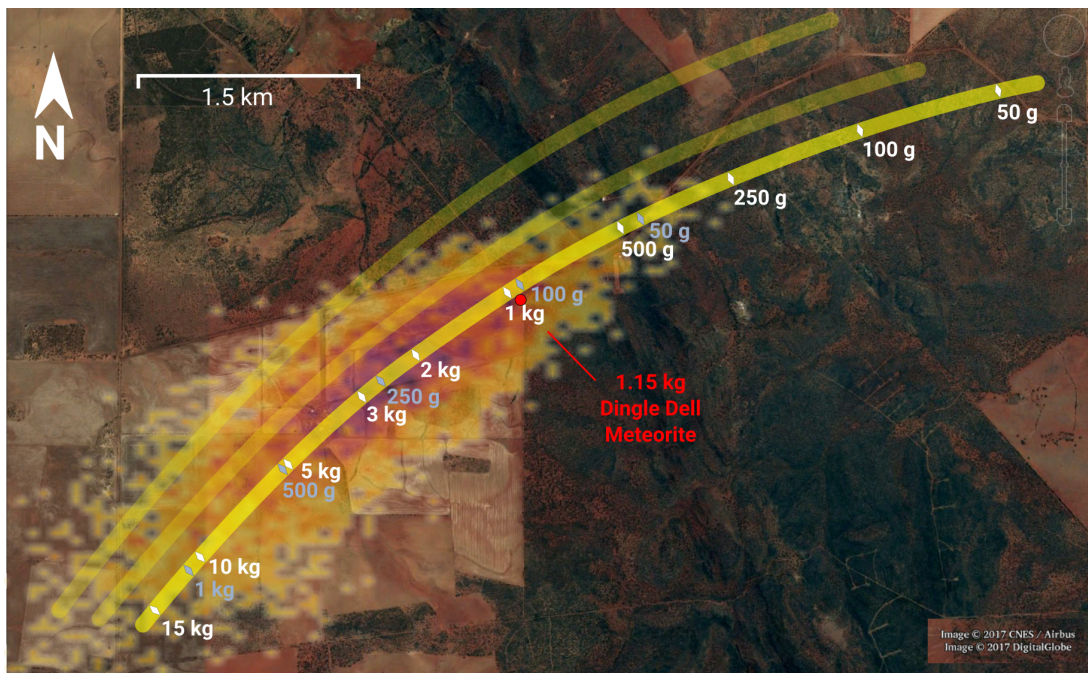
FIGURE 4.10: Fall area around Dingle Dell farm and Koolanooka Hills. Fall lines in yellow represent different wind model solutions: *W1* (bottom), *W2* (middle) and *W3* (top). Mass predictions for the preferred wind model are shown for spherical (light blue markings; $A = 1.21$) and cylindrical (white markings; $A = 1.5$) assumptions. The particle filter results are propagated through dark flight using wind model *W1*, and are shown as a heat map. The location of the recovered meteorite (red dot) is $\simeq 100\,\mathrm{m}$ from the *W1* fall line.

hour when looking for a $> 1\,\mathrm{kg}$ mass on foot. On the second day, a meteorite was found (Fig. 4.11) close to the Dingle Dell farm boundary, at coordinates $\lambda = 116.215439°\ \phi = -29.206106°$ (WGS84), about $130\,\mathrm{m}$ from the originally calculated fall line, after a total of 8 hours of searching. The recovered meteorite weighs $1.15\,\mathrm{kg}$, with a rounded brick shape of approximately $16\,\mathrm{x}\,9\,\mathrm{x}\,4\,\mathrm{cm}$, and a calculated bulk density of $3450\,\mathrm{kg\,m}^{-3}$ (Fig. 4.11). The condition of the meteorite is excellent, having only been on ground for 6 days, 16 hours. Discussion with the local landowner, and checking the weather on the nearest Bureau Of Meteorology observation station (Morawa Airport, $20\,\mathrm{km}$ away) showed that no precipitation had fallen between times of landing and recovery. The meteorite was collected and stored using a Teflon bag, and local soil samples were also collected in the same manner for comparison. No trace of impact on

the ground was noticed. The meteorite was found intact (entirely covered by fusion crust) on hard ground, resting up-right (Fig. 4.11), and covered with dust. So it is possible that the meteorite fell a few metres away in softer ground and bounced or rolled to the recovered position.

FIGURE 4.11: Dingle Dell meteorite as it was found. Image available at `https://commons.wikimedia.org/wiki/File:Dingle_Dell_meteorite_as_it_was_found.jpg` under a Creative Commons Attribution-ShareAlike 4.0 International.

4.5. PRE-ENCOUNTER ORBIT

The backward propagation of the observed trajectory into an orbit requires the calculation of the direction of the fireball (known as the radiant), and the position and speed at the top of the atmosphere. The associated uncertainties on these two components are mostly un-correlated. In order to minimise issues associated with the oversimplified straight line trajectory for orbit purposes, we re-triangulate the observations using only points that fall $> 60\,\text{km}$ altitude on the initial triangulation. In this case, as the trajectory is fairly steep, the difference in apparent radiant between the two solutions is less than 5 arcmin. To calculate the errors on the radiant, we use the co-variance matrix from the least squares trajectory fit (see section 4.3.1), this gives us the apparent radiant: slope to the horizontal = $51.562 \pm 0.002°$, azimuth of the radiant (East of North) = $26.17 \pm 0.03°$, which corresponds to ($\alpha = 353.38 \pm 0.02°$, $\delta = 6.34 \pm 0.01°$) in equatorial J2000 coordinates.

To calculate the formal uncertainty on the initial velocity, we apply the Kalman filter methods of Sansom et al. (2015) as outlined in Section 4.3.2. Using the time, position, radiant, speed, and their associated uncertainties, we determine the pre-atmospheric orbit by propagating the meteoroid trajectory back through time, considering the atmospheric deceleration, Earth's oblate shape effects (J2), and other major perturbing bodies (such as the Moon and planets), until the meteoroid has gone beyond $10\times$ the Earth's sphere of influence. From here, the meteoroid is propagated forward in time to the impact epoch, ignoring the effects of the Earth-Moon system. Uncertainties (Table 4.4) are calculated using a Monte Carlo approach on 1000 test particles randomly drawn using uncertainties on the radiant and the speed.

We scanned the *Astorb*[3] asteroid orbital database (Bowell et al., 2002) for close

---

[3]`ftp://ftp.lowell.edu/pub/elgb/astorb.html`, downloaded June 24, 2017
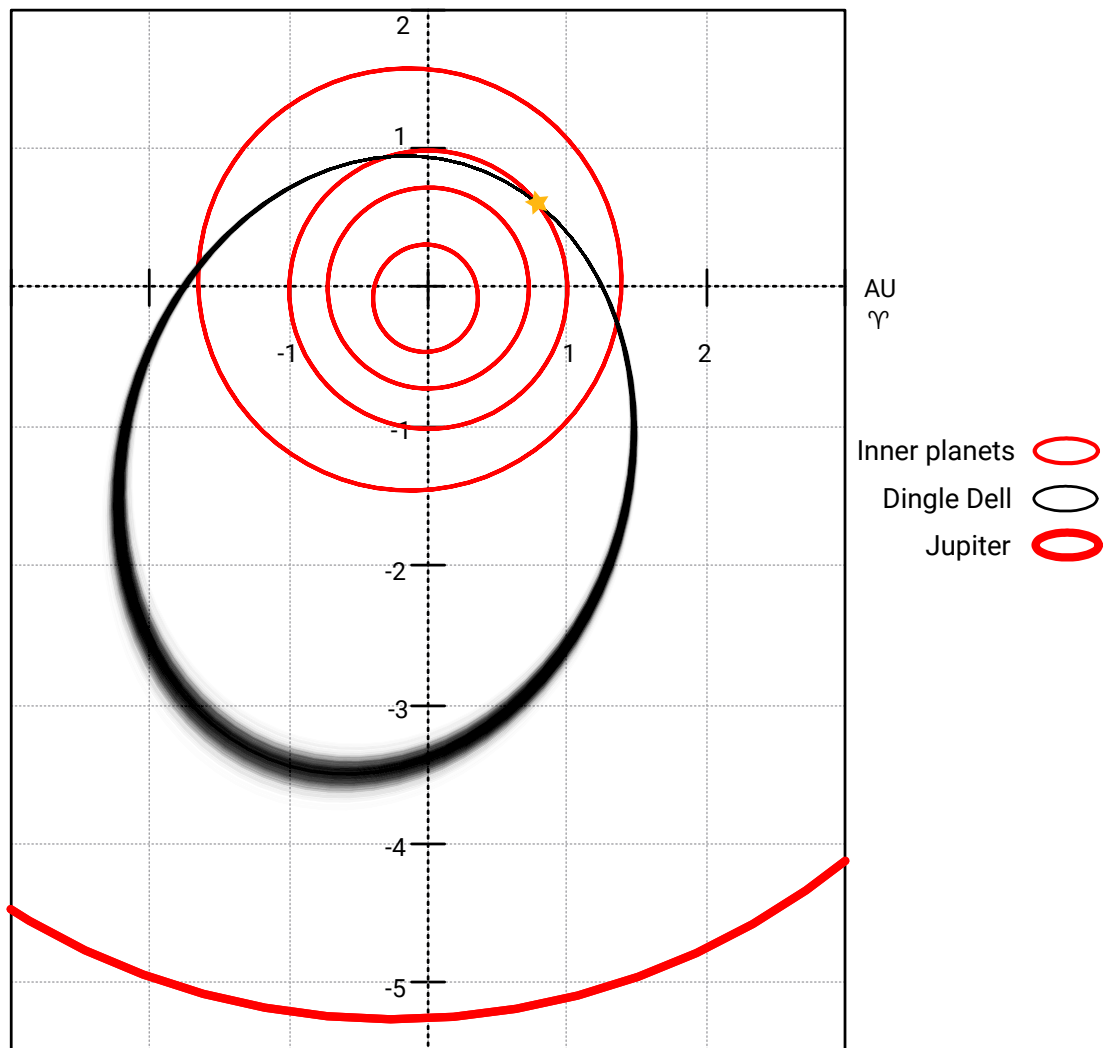
FIGURE 4.12: Ecliptic projection of the pre-encounter orbit of Dingle Dell. The shades of grey represent the likelihood as calculated from 1000 Monte Carlo simulations based on formal uncertainties on the radiant and the speed.

matches in a, e, i, ω, Ω orbital space using the similarity criterion of Southworth and Hawkins (1963). The closest match is the small ($H = 24.6$) *2015 TD179* asteroid, that came into light in November 2015 when it flew by Earth at $\simeq 10$ lunar distances. But the large difference between these orbits, $D = 0.04$, makes the dynamical connection between the two highly unlikely.

To calculate the likely source region and dynamical pathway that put the meteoroid on an Earth crossing orbit, we use the *Rebound* integrator (Rein and Tamayo, 2015) to backward propagate the orbit of the meteoroid. We use 10,000

Epoch	TDB	2016-10-31
a	AU	2.254 ± 0.034
e		0.5904 ± 0.0063
i	°	4.051 ± 0.012
ω	°	215.773 ± 0.049
Ω	°	218.252 ± 0.00032
q	AU	0.92328 ± 0.00032
Q	AU	3.586 ± 0.067
α_g	°	354.581 ± 0.037
δ_g	°	13.093 ± 0.081
V_g	m s^{-1}	10508 ± 87
T_J		3.37

TABLE 4.4: Pre-encounter orbital parameters expressed in the heliocentric ecliptic frame (*J2000*) and associated 1σ formal uncertainties.

test particles randomly selected using the radiant and speed uncertainties as explained above, as well as the major perturbating bodies (Sun, 8 planets, and Moon). The initial semi-major axis (Table 4.4) is close to the 7:2 (2.25 AU) and 10:3 (2.33 AU) mean motion resonances with Jupiter (MMRJ). These minor resonances start to scatter the eccentricity of a large number of test particles very early on, but neither are strong enough to decrease it significantly enough to take the meteoroid outside of Mars' orbit. Because of the interactions with the inner planets, the particle cloud rapidly spreads out, and particles gradually start falling into the two main dynamical pathways in this region: 3:1 MMRJ (2.5 AU) and the ν_6 secular resonance. These resonances rapidly expand the perihelia of particles out of the Earth's orbit initially, and eventually out of Mars' orbit and into the main belt.

During the integration over 1 million years, we count the number of particles that have converged close to stably populated regions of the main belt, and note which dynamical pathway they used to get there. This gives us the following statistics:

- ν_6: 12%

- 3:1 MMRJ: 82%

- 5:2 MMRJ: 6%
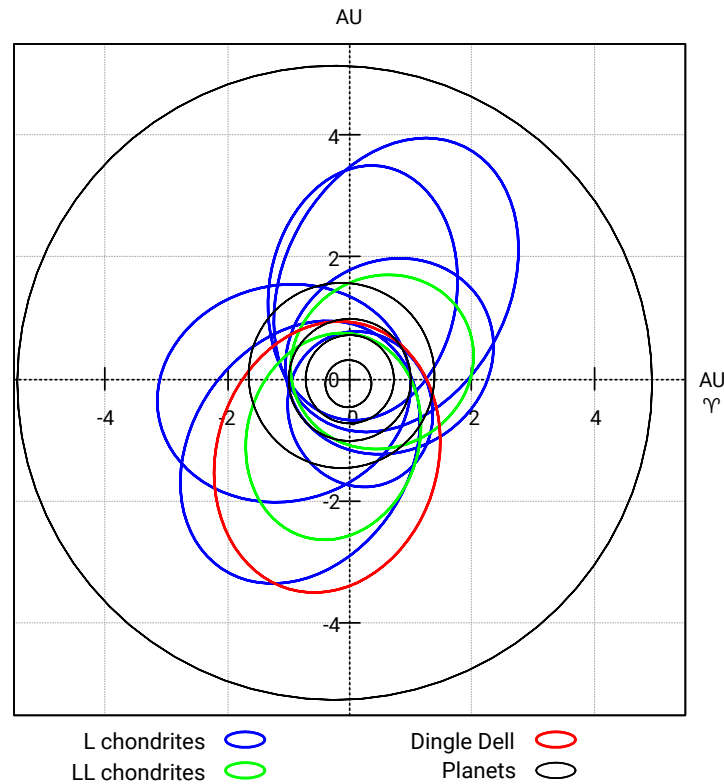
FIGURE 4.13: The orbit of Dingle Dell in context with other L and LL ordinary chondrite falls. References for L and LL orbits are in the introduction.

4.6. CONCLUSIONS

Dingle Dell is the fourth meteorite with an orbit recovered by the DFN in Australia. Its luminous trajectory was observed by 6 DFN camera stations up to 535 km away at 12:03:47.726 UTC on 31 October, 2016. Clouds severely affected the observations, but enough data was available to constrain the search area for a swift recovery, and determine one of the most precise orbits linked to a meteorite. The surviving rock was recovered within a week of its fall, without any precipitation contaminating the rock, confirming the DFN as a proficient sample recovery tool for planetary science. This recovery, in less than ideal

conditions, also validates various choices in the design and operations of the Desert Fireball Network:

- Use of high resolution digital cameras to enable reliable all-sky astrometry for events up to $300\,\text{km}$ away.

- Uninterrupted operation even when a large portion of the sky is cloudy for individual systems.

- Archiving of all raw data to mitigate event detection failures.

While the method of Sansom et al. (2017) was still in development at the time of the fall, the re-analysis of the fireball with this new technique is remarkably consistent with the main mass found, requiring just a small number of high quality astrometric data points. This validates the method, and will drastically reduce the search area for future observed falls.

After a 1 million year integration of 10,000 test particles, it is most likely that Dingle Dell was ejected from the main belt through the 3:1 mean motion resonance with Jupiter rather than the ν_6 resonance (82% for the 3:1 MMRJ compared to 12% probability for ν_6). This also means that L/LL Dingle Dell is unlikely to be associated with the Flora family, likely source of most LL chondrites (Vernazza et al., 2008), as the most efficient mechanism for getting Florian fragments to near-Earth space is the ν_6 secular resonance. This fall adds little insight into the Flora/LL link, but 2016 was rich in instrumentally observed LL falls, which might yield clues to help confirm this connection in the near future: Stubenberg (LL6) (Spurný et al., 2016; Bischoff et al., 2017), Hradec Králové (LL5) (Met, 2017), and Dishchii'bikoh (LL7) (Met, 2017; Palotai et al., 2018).

ACKNOWLEDGEMENTS

APPENDIX A. SUPPLEMENTARY FILES

We provide the raw astrometric tables for the 3 cameras used for computing the trajectory.

We also give the straight line trajectory solution (latitude, longitude, height), as well as the corresponding speeds calculated by the method of Sansom et al. (2015) using all the data available (this explains slight differences with the manuscript, as in the latter they were calculated separately for each camera).

Note that the number of decimals given in these tables is not necessarily representative of uncertainty.

To illustrate the meteorite searching strategy we provide the GPS tracks, as every member of the search team carried a GPS unit (see Fig. 4.11). Note that one GPS unit malfunctioned, this resulted in the loss of one of the tracks on the first afternoon of the search, and explains apparent gaps in the searching grid.

We include the preferred weather model used for dark flight integration (*W1*, from Fig. 4.9), extracted as a vertical profile.

4.7. References

The meteoritical bulletin, no. 106. *Meteoritics & Planetary Science*, 2017.

Astropy Collaboration, T. P. Robitaille, E. J. Tollerud, P. Greenfield, M. Droettboom, E. Bray, T. Aldcroft, M. Davis, A. Ginsburg, A. M. Price-Whelan, W. E. Kerzendorf, A. Conley, N. Crighton, K. Barbary, D. Muna, H. Ferguson, F. Grollier, M. M. Parikh, P. H. Nair, H. M. Unther, C. Deil, J. Woillez, S. Conseil, R. Kramer, J. E. H. Turner, L. Singer, R. Fox, B. A. Weaver, V. Zabalza, Z. I. Edwards, K. Azalee Bostroem, D. J. Burke, A. R. Casey, S. M. Crawford, N. Dencheva, J. Ely, T. Jenness, K. Labrie, P. L. Lim, F. Pierfederici, A. Pontzen, A. Ptak, B. Refsdal, M. Servillat, and O. Streicher. Astropy: A community Python package for astronomy. A&A, 558:A33, Oct. 2013. doi: 10.1051/0004-6361/201322068.

G. K. Benedix, L. V. Forman, L. Daly, B. Godel, L. Esteban, M. M. M. Meier, C. Maden, H. Busemann, Q. Z. Yin, M. Sanborn, K. Ziegler, J. W. Strasser, K. C. Welten, M. W. Caffee, D. P. Glavin, J. P. Dworkin, P. A. Bland, J. P. Paxman, M. C. Towner, M. Cupák, E. K. Sansom, R. M. Howie, H. A. R. Devillepoix, M. A. Cox, T. Jansen-Sturgeon, B. A. D. Hartig, and A. W. R. Bevan. Mineralogy, Petrology and Chronology of the Dingle Dell Meteorite. In *80th Annual Meeting of the Meteoritical Society 2017*, page 6229, 2017.

A. Bischoff, J.-A. Barrat, K. Bauer, C. Burkhardt, H. Busemann, S. Ebert, M. Gonsior, J. Hakenmüller, J. Haloda, D. Harries, D. Heinlein, H. Hiesinger, R. Hochleitner, V. Hoffmann, M. Kaliwoda, M. Laubenstein, C. Maden, M. M. M. Meier, A. Morlok, A. Pack, A. Ruf, P. Schmitt-Kopplin, M. SchöNbäChler, R. C. J. Steele, P. Spurný, and K. Wimmer. The Stubenberg

meteorite – An LL6 chondrite fragmental breccia recovered soon after precise prediction of the strewn field. *Meteoritics and Planetary Science*, 52:1683–1703, Aug. 2017. doi: 10.1111/maps.12883.

P. A. Bland, P. Spurný, M. C. Towner, A. W. R. Bevan, A. T. Singleton, W. F. Bottke, R. C. Greenwood, S. R. Chesley, L. Shrbený, J. Borovička, Z. Ceplecha, T. P. McClafferty, D. Vaughan, G. K. Benedix, G. Deacon, K. T. Howard, I. A. Franchi, and R. M. Hough. An Anomalous Basaltic Meteorite from the Innermost Main Belt. *Science*, 325:1525, Sept. 2009. doi: 10.1126/science. 1174787.

P. A. Bland, P. Spurný, A. W. R. Bevan, K. T. Howard, M. C. Towner, G. K. Benedix, R. C. Greenwood, L. Shrbený, I. A. Franchi, G. Deacon, J. Borovička, Z. Ceplecha, D. Vaughan, and R. M. Hough. The Australian Desert Fireball Network: a new era for planetary science. *Australian Journal of Earth Sciences*, 59:177–187, Mar. 2012. doi: 10.1080/08120099.2011.595428.

J. Borovička. The comparison of two methods of determining meteor trajectories from photographs. *Bulletin of the Astronomical Institutes of Czechoslovakia*, 41: 391–396, Dec. 1990.

J. Borovička, P. Spurný, P. Kalenda, and E. Tagliaferri. The Morávka meteorite fall: 1 Description of the events and determination of the fireball trajectory and orbit from video records. *Meteoritics and Planetary Science*, 38:975–987, July 2003. doi: 10.1111/j.1945-5100.2003.tb00293.x.

J. Borovička, P. Spurný, P. Brown, P. Wiegert, P. Kalenda, D. Clark, and L. Shrbený. The trajectory, structure and origin of the Chelyabinsk asteroidal impactor. Nature, 503:235–237, Nov. 2013. doi: 10.1038/nature12671.

J. Borovička, P. Spurný, and P. Brown. *Small Near-Earth Asteroids as a Source of Meteorites*, pages 257–280. University of Arizona Press, 2015. doi: 10.2458/ azu_uapress_9780816532131-ch014.

E. Bowell, J. Virtanen, K. Muinonen, and A. Boattini. *Asteroid Orbit Computation*, pages 27–43. University of Arizona Press, 2002.

V. A. Bronshten. *Physics of Meteoric Phenomena*. Geophysics and Astrophysics Monographs. Reidel, Dordrecht, Netherlands, 1983. ISBN 9789027716545.

P. Brown, D. Pack, W. N. Edwards, D. O. Revelle, B. B. Yoo, R. E. Spalding, and E. Tagliaferri. The orbit, atmospheric dynamics, and initial mass of the Park Forest meteorite. *Meteoritics and Planetary Science*, 39:1781–1796, Nov. 2004. doi: 10.1111/j.1945-5100.2004.tb00075.x.

P. Brown, P. J. A. McCausland, M. Fries, E. Silber, W. N. Edwards, D. K. Wong, R. J. Weryk, J. Fries, and Z. Krzeminski. The fall of the Grimsby meteorite I: Fireball dynamics and orbit from radar, video, and infrasound records. *Meteoritics and Planetary Science*, 46:339–363, Mar. 2011. doi: 10.1111/j.1945-5100.2010.01167.x.

P. G. Brown, J. D. Assink, L. Astiz, R. Blaauw, M. B. Boslough, J. Borovička, N. Brachet, D. Brown, M. Campbell-Brown, L. Ceranna, W. Cooke, C. de Groot-Hedlin, D. P. Drob, W. Edwards, L. G. Evers, M. Garces, J. Gill, M. Hedlin, A. Kingery, G. Laske, A. Le Pichon, P. Mialle, D. E. Moser, A. Saffer, E. Silber, P. Smets, R. E. Spalding, P. Spurný, E. Tagliaferri, D. Uren, R. J. Weryk, R. Whitaker, and Z. Krzeminski. A 500-kiloton airburst over Chelyabinsk and an enhanced hazard from small impactors. Nature, 503: 238–241, Nov. 2013. doi: 10.1038/nature12741.

Z. Ceplecha. Multiple fall of Příbram meteorites photographed. 1. Double-station photographs of the fireball and their relations to the found meteorites. *Bulletin of the Astronomical Institutes of Czechoslovakia*, 12:21, 1961.

H. A. R. Devillepoix, P. A. Bland, M. C. Towner, M. Cupák, E. K. Sansom, T. Jansen-Sturgeon, R. M. Howie, J. Paxman, and B. A. D. Hartig. Status of the Desert Fireball Network. In A. Roggemans and P. Roggemans, editors,

International Meteor Conference Egmond, the Netherlands, 2-5 June 2016, pages 60–62, Jan. 2016.

P. Farinella, D. Vokrouhlický, and W. K. Hartmann. Meteorite Delivery via Yarkovsky Orbital Drift. Icarus, 132:378–387, Apr. 1998. doi: 10.1006/icar.1997.5872.

M. Fries and J. Fries. Doppler weather radar as a meteorite recovery tool. *Meteoritics and Planetary Science*, 45:1476–1487, Sept. 2010. doi: 10.1111/j.1945-5100.2010.01115.x.

M. Fries, L. Le Corre, M. Hankey, J. Fries, R. Matson, J. Schaefer, and V. Reddy. Detection and rapid recovery of the Sutter's Mill meteorite fall as a model for future recoveries worldwide. *Meteoritics and Planetary Science*, 49:1989–1996, Nov. 2014. doi: 10.1111/maps.12249.

M. I. Gritsevich. Determination of parameters of meteor bodies based on flight observational data. *Advances in Space Research*, 44:323–334, Aug. 2009. doi: 10.1016/j.asr.2009.03.030.

I. Halliday, A. A. Griffin, and A. T. Blackwell. The Innisfree meteorite fall - A photographic analysis of fragmentation, dynamics and luminosity. *Meteoritics*, 16:153–170, June 1981.

I. Halliday, A. A. Griffin, and A. T. Blackwell. Detailed data for 259 fireballs from the Canadian camera network and inferences concerning the influx of large meteoroids. *Meteoritics and Planetary Science*, 31:185–217, Mar. 1996. doi: 10.1111/j.1945-5100.1996.tb02014.x.

M. Hankey and V. Perlerin. IMO's new online fireball form. *WGN, Journal of the International Meteor Organization*, 43:2–7, Feb. 2015.

J. Hoppe. Die physikalischen Vorgänge beim Eindringen meteoritischer Körper in die Erdatmosphäre. *Astronomische Nachrichten*, 262(10):169–198, 1937.

R. M. Howie, J. Paxman, P. A. Bland, M. C. Towner, M. Cupák, E. K. Sansom, and H. A. R. Devillepoix. How to build a continental scale fireball camera network. *Experimental Astronomy*, May 2017a. doi: 10.1007/s10686-017-9532-7.

R. M. Howie, J. Paxman, P. A. Bland, M. C. Towner, E. K. Sansom, and H. A. R. Devillepoix. Submillisecond fireball timing using de Bruijn time-codes. *Meteoritics and Planetary Science*, 52:1669–1682, Aug. 2017b. doi: 10.1111/maps.12878.

Z. Ivezic, T. Axelrod, W. N. Brandt, D. L. Burke, C. F. Claver, A. Connolly, K. H. Cook, P. Gee, D. K. Gilmore, S. H. Jacoby, R. L. Jones, S. M. Kahn, J. P. Kantor, V. V. Krabbendam, R. H. Lupton, D. G. Monet, P. A. Pinto, A. Saha, T. L. Schalk, D. P. Schneider, M. A. Strauss, C. W. Stubbs, D. Sweeney, A. Szalay, J. J. Thaler, J. A. Tyson, and LSST Collaboration. Large Synoptic Survey Telescope: From Science Drivers To Reference Design. *Serbian Astronomical Journal*, 176:1–13, June 2008. doi: 10.2298/SAJ0876001I.

P. Jenniskens. Recent documented meteorite falls, a review of meteorite - asteroid links. *Meteoroids 2013*, July 2014.

P. Jenniskens, M. H. Shaddad, D. Numan, S. Elsir, A. M. Kudoda, M. E. Zolensky, L. Le, G. A. Robinson, J. M. Friedrich, D. Rumble, A. Steele, S. R. Chesley, A. Fitzsimmons, S. Duddy, H. H. Hsieh, G. Ramsay, P. G. Brown, W. N. Edwards, E. Tagliaferri, M. B. Boslough, R. E. Spalding, R. Dantowitz, M. Kozubal, P. Pravec, J. Borovička, Z. Charvat, J. Vaubaillon, J. Kuiper, J. Albers, J. L. Bishop, R. L. Mancinelli, S. A. Sandford, S. N. Milam, M. Nuevo, and S. P. Worden. The impact and recovery of asteroid 2008 TC_3. Nature, 458: 485–488, Mar. 2009. doi: 10.1038/nature07920.

P. Jenniskens, M. D. Fries, Q.-Z. Yin, M. Zolensky, A. N. Krot, S. A. Sandford, D. Sears, R. Beauford, D. S. Ebel, J. M. Friedrich, K. Nagashima, J. Wimpenny, A. Yamakawa, K. Nishiizumi, Y. Hamajima, M. W. Caffee, K. C. Welten, M. Laubenstein, A. M. Davis, S. B. Simon, P. R. Heck, E. D. Young, I. E.

Kohl, M. H. Thiemens, M. H. Nunn, T. Mikouchi, K. Hagiya, K. Ohsumi, T. A. Cahill, J. A. Lawton, D. Barnes, A. Steele, P. Rochette, K. L. Verosub, J. Gattacceca, G. Cooper, D. P. Glavin, A. S. Burton, J. P. Dworkin, J. E. Elsila, S. Pizzarello, R. Ogliore, P. Schmitt-Kopplin, M. Harir, N. Hertkorn, A. Verchovsky, M. Grady, K. Nagao, R. Okazaki, H. Takechi, T. Hiroi, K. Smith, E. A. Silber, P. G. Brown, J. Albers, D. Klotz, M. Hankey, R. Matson, J. A. Fries, R. J. Walker, I. Puchtel, C.-T. A. Lee, M. E. Erdman, G. R. Eppich, S. Roeske, Z. Gabelica, M. Lerche, M. Nuevo, B. Girten, and S. P. Worden. Radar-Enabled Recovery of the Sutter's Mill Meteorite, a Carbonaceous Chondrite Regolith Breccia. *Science*, 338:1583, Dec. 2012. doi: 10.1126/science.1227163.

P. Jenniskens, A. E. Rubin, Q.-Z. Yin, D. W. G. Sears, S. A. Sandford, M. E. Zolensky, A. N. Krot, L. Blair, D. Kane, J. Utas, R. Verish, J. M. Friedrich, J. Wimpenny, G. R. Eppich, K. Ziegler, K. L. Verosub, D. J. Rowland, J. Albers, P. S. Gural, B. Grigsby, M. D. Fries, R. Matson, M. Johnston, E. Silber, P. Brown, A. Yamakawa, M. E. Sanborn, M. Laubenstein, K. C. Welten, K. Nishiizumi, M. M. M. Meier, H. Busemann, P. Clay, M. W. Caffee, P. Schmitt-Kopplin, N. Hertkorn, D. P. Glavin, M. P. Callahan, J. P. Dworkin, Q. Wu, R. N. Zare, M. Grady, S. Verchovsky, V. Emel'Yanenko, S. Naroenkov, D. L. Clark, B. Girten, and P. S. Worden. Fall, recovery, and characterization of the Novato L6 chondrite breccia. *Meteoritics and Planetary Science*, 49: 1388–1425, Aug. 2014. doi: 10.1111/maps.12323.

P. Jenniskens, J. Utas, Q.-Z. Yin, R. D. Matson, M. Fries, J. A. Howell, D. Free, J. Albers, H. Devillepoix, P. Bland, A. Miller, R. Verish, L. A. J. Garvie, M. E. Zolensky, K. Ziegler, M. E. Sanborn, K. L. Verosub, D. J. Rowland, D. R. Ostrowski, K. Bryson, M. Laubenstein, Q. Zhou, Q.-L. Li, X.-H. Li, Y. Liu, G.-Q. Tang, K. Welten, M. W. Caffee, M. M. M. Meier, A. A. Plant, C. Maden, H. Busemann, M. Granvik, and T. C. M. Consortium). The creston, california, meteorite fall and the origin of l chondrites. *Meteoritics & Planetary Science*,

in press, 2019. doi: 10.1111/maps.13235. URL `https://onlinelibrary.wiley.com/doi/abs/10.1111/maps.13235`.

C. S. Keay. Electrophonic sounds from large meteor fireballs. *Meteoritics & Planetary Science*, 27(2):144–148, 1992.

K. Keil, D. Stoeffler, S. G. Love, and E. R. D. Scott. Constraints on the role of impact heating and melting in asteroids. *Meteoritics and Planetary Science*, 32, May 1997. doi: 10.1111/j.1945-5100.1997.tb01278.x.

R. E. McCrosky and H. Boeschenstein. The Prairie Meteorite Network. *Optical Engineering*, 3(4):304127–304127, 1965.

A. Morbidelli, R. Gonczi, C. Froeschle, and P. Farinella. Delivery of meteorites through the nu_6 secular resonance. A&A, 282:955–979, Feb. 1994.

T. Nakamura, T. Noguchi, M. Tanaka, M. E. Zolensky, M. Kimura, A. Tsuchiyama, A. Nakato, T. Ogami, H. Ishida, M. Uesugi, T. Yada, K. Shirai, A. Fujimura, R. Okazaki, S. A. Sandford, Y. Ishibashi, M. Abe, T. Okada, M. Ueno, T. Mukai, M. Yoshikawa, and J. Kawaguchi. Itokawa Dust Particles: A Direct Link Between S-Type Asteroids and Ordinary Chondrites. *Science*, 333:1113, Aug. 2011. doi: 10.1126/science.1207758.

D. Nesvorný, D. Vokrouhlický, A. Morbidelli, and W. F. Bottke. Asteroidal source of L chondrite meteorites. Icarus, 200:698–701, Apr. 2009. doi: 10.1016/j.icarus.2008.12.016.

J. Oberst, S. Molau, D. Heinlein, C. Gritzner, M. Schindler, P. Spurny, Z. Ceplecha, J. Rendtel, and H. Betlem. The "European Fireball Network": Current status and future prospects. *Meteoritics and Planetary Science*, 33, Jan. 1998. doi: 10.1111/j.1945-5100.1998.tb01606.x.

C. Palotai, R. Sankar, D. L. Free, J. A. Howell, E. Botella, and D. Batcheldor. Analysis of June 2, 2016 bolide event. *ArXiv e-prints*, Jan. 2018.

J. Paxman and P. Bland. Fireballs in the sky: Improving the accuracy of crowd sourced fireball observation through the application of smartphone technology. In *Lunar and Planetary Science Conference*, volume 45, page 1731, 2014.

J. M. Picone, A. E. Hedin, D. P. Drob, and A. C. Aikin. NRLMSISE-00 empirical model of the atmosphere: Statistical comparisons and scientific issues. *Journal of Geophysical Research (Space Physics)*, 107:1468, Dec. 2002. doi: 10.1029/2002JA009430.

V. Reddy, J. A. Sanchez, W. F. Bottke, E. A. Cloutis, M. R. M. Izawa, D. P. O'Brien, P. Mann, M. Cuddy, L. Le Corre, M. J. Gaffey, and G. Fujihara. Chelyabinsk meteorite explains unusual spectral properties of Baptistina Asteroid Family. Icarus, 237:116–130, July 2014. doi: 10.1016/j.icarus.2014.04.027.

H. Rein and D. Tamayo. WHFAST: a fast and unbiased implementation of a symplectic Wisdom-Holman integrator for long-term gravitational simulations. MNRAS, 452:376–388, Sept. 2015. doi: 10.1093/mnras/stv1257.

E. Sansom, J. Ridgewell, P. Bland, and J. Paxman. Meteor reporting made easy-The Fireballs in the Sky smartphone app. In A. Roggemans and P. Roggemans, editors, *International Meteor Conference Egmond, the Netherlands, 2-5 June 2016*, pages 267–269, Jan. 2016.

E. K. Sansom. *Tracking Meteoroids in the Atmosphere: Fireball Trajectory Analysis*. PhD thesis, Curtin University, 2016. URL +http://hdl.handle.net/20.500.11937/55061.

E. K. Sansom, P. Bland, J. Paxman, and M. Towner. A novel approach to fireball modeling: The observable and the calculated. *Meteoritics and Planetary Science*, 50:1423–1435, Aug. 2015. doi: 10.1111/maps.12478.

E. K. Sansom, M. G. Rutten, and P. A. Bland. Analyzing Meteoroid Flights Using Particle Filters. AJ, 153:87, Feb. 2017. doi: 10.3847/1538-3881/153/2/87.

B. Schmitz, M. Tassinari, and B. Peucker-Ehrenbrink. A rain of ordinary chondritic meteorites in the early Ordovician. *Earth and Planetary Science Letters*, 194:1–15, Dec. 2001. doi: 10.1016/S0012-821X(01)00559-3.

W. C. Skamarock, J. B. Klemp, J. Dudhia, D. O. Gill, D. M. Barker, M. G. Duda, X. Y. Huang, W. Wang, and J. G. Powers. A description of the advanced research wrf version 3. Technical report, NCAR Technical Note NCAR/TN-475+STR, 2008.

R. B. Southworth and G. S. Hawkins. Statistics of meteor streams. *Smithsonian Contributions to Astrophysics*, 7:261, 1963.

P. Spurný, J. Borovička, J. Kac, P. Kalenda, J. Atanackov, G. Kladnik, D. Heinlein, and T. Grau. Analysis of instrumental observations of the Jesenice meteorite fall on April 9, 2009. *Meteoritics and Planetary Science*, 45:1392–1407, Aug. 2010. doi: 10.1111/j.1945-5100.2010.01121.x.

P. Spurný, P. A. Bland, L. Shrbený, M. C. Towner, J. Borovička, A. W. R. Bevan, and D. Vaughan. The Mason Gully Meteorite Fall in SW Australia: Fireball Trajectory and Orbit from Photographic Records. *Meteoritics and Planetary Science Supplement*, 74:5101, Sept. 2011.

P. Spurný, J. Haloda, J. Borovička, L. Shrbený, and P. Halodová. Reanalysis of the Benešov bolide and recovery of polymict breccia meteorites - old mystery solved after 20 years. A&A, 570:A39, Oct. 2014. doi: 10.1051/0004-6361/201424308.

P. Spurný, J. Borovička, J. Haloda, L. Shrbený, and D. Heinlein. Two Very Precisely Instrumentally Documented Meteorite Falls: Žďár nad Sázavou and Stubenberg - Prediction and Reality. In *79th Annual Meeting of the Meteoritical Society*, volume 1921 of *LPI Contributions*, page 6221, Aug. 2016.

J. M. Trigo-Rodríguez, J. Borovička, P. Spurný, J. L. Ortiz, J. A. Docobo, A. J. Castro-Tirado, and J. Llorca. The Villalbeto de la Peña meteorite fall: II.

Determination of atmospheric trajectory and orbit. *Meteoritics and Planetary Science*, 41:505–517, Apr. 2006. doi: 10.1111/j.1945-5100.2006.tb00478.x.

J. M. Trigo-Rodríguez, E. Lyytinen, M. Gritsevich, M. Moreno-Ibáñez, W. F. Bottke, I. Williams, V. Lupovka, V. Dmitriev, T. Kohout, and V. Grokhovsky. Orbit and dynamic origin of the recently recovered Annama's H5 chondrite. MNRAS, 449:2119–2127, May 2015. doi: 10.1093/mnras/stv378.

P. Vernazza, R. P. Binzel, C. A. Thomas, F. E. DeMeo, S. J. Bus, A. S. Rivkin, and A. T. Tokunaga. Compositional differences between meteorites and near-Earth asteroids. Nature, 454:858–860, Aug. 2008. doi: 10.1038/nature07154.

F. L. Whipple. Photographic meteor studies I. In *Publications of the American Astronomical Society*, volume 9 of *Publications of the American Astronomical Society*, page 136, 1939.

CHAPTER 5

TAURID METEOROID STREAM #628: A RESERVOIR OF LARGE IMPACTORS

Hadrien A. R. Devillepoix[a], Philip A. Bland[a], Petrus M. Jenniskens[c,d],
Eleanor K. Sansom[a], Martin C. Towner[a], Martin Cupák[a], Robert M. Howie[a],
Benjamin A. D. Hartig[a], Trent Jansen-Sturgeon[a],
Morgan A. Cox[a], Jonathan Paxman [b]

[a]School of Earth and Planetary Sciences, Curtin University, GPO Box U1987, Bentley, Perth, WA 6845, Australia

[b]School of Civil and Mechanical Engineering, Curtin University, GPO Box U1987, Bentley, Perth, WA 6845, Australia

[c]SETI Institute, 189 Bernardo Avenue, Mountain View, CA 94043, USA

[d]NASA Ames Research Center, Mail Stop 241-11, Moffett Field, CA 94035, USA

This chapter is laid out as a manuscript to be submitted to Astronomy & Astrophysics.

ABSTRACT

The Desert Fireball Network observed a significant outburst of fireballs between October 31 and November 10, 2015, associated with the Southern Taurid Complex meteor showers. While this returning outburst was predicted and observed in previous work, 2015 is the first year that the stream is observed and precisely described by fireball and low-light networks, providing an opportunity to better understand the nature and cause of this stream. The Desert Fireball Network of all-sky meteor camera detects centimetre to decimetre scale meteoroids. We combine this data with millimetre to centimetre scale observations by low-light video cameras of the Cameras for Allsky Meteor Surveillance (millimetre scale), and published data from metre-scale observations by spaceborne sensors. By calculating precise orbits we confirm that the outburst is due to meteoroids living near the 7:2 mean-motion resonance with Jupiter. The size distribution is exponential over a wide mass range and dominated by larger meteoroids compared to the regular Southern Taurid shower We show that the resonant meteoroids are consistently larger than regular Southern Taurid meteoroids. The stream contains metre-class objects. Even bright meteors do not survive below 50 km altitude (most show catastrophic fragmentation above 60 km), which suggests consistently weak material. The stream is the product of a relatively recent break up about 1500 years ago, of a body different from 2P/Encke. This supports a model for the Taurid Complex showers that involves an ongoing fragmentation cascade of comet 2P/Encke siblings that were created following a breakup some 20,000 years ago. Even large Southern Taurids meteoroids are unlikely to drop meteorites, but might generate dust that can be collected in the atmosphere.

5.1. INTRODUCTION

The Taurid Complex meteor showers are known to produce bright fireballs with a great variety of strengths (Jenniskens, 2006; Brown et al., 2013). Whipple (1940) first identified comet 2P/Encke as the likely parent body, but the wide dispersion of orbits (resulting in northern and southern branches as well as nighttime and daytime showers) required a formation age at least 20,000 years ago, the minimum time it takes to fully precess the node and disperse the longitude of perihelion of the orbits as wide as observed. Clube and Napier (1984) first suggested that the a large number of potential other parent body asteroids were part of a Taurid Complex that originated from a giant comet breakup 20,000 years ago. However, Jenniskens (2006) pointed out that most proposed parent bodies appeared to be S- or O-class stony asteroids, instead, which had evolved into Encke-like orbits via the ν_6 resonance. The same conclusion was also reached more recently by Popescu et al. (2014) and Tubiana et al. (2015). Jenniskens (2006); Jenniskens et al. (2016c) also noticed that there was no mirror image between Taurid shower component nodes in northern and southern branches, suggesting that meteoroids did not survive long enough to fully disperse their nodal line. Instead, it was proposed that the 20,000 year old stream reflected the current dispersion of a number of smaller parent bodies, including 2004 TG10, that continue to generate Taurid meteoroids. This idea that the Taurid complex is active as a whole, and is not just the remnant of a single 20,000+ years old break up, is supported by the orbital analysis done by Whipple and El-Din Hamid (1952). Long before modern orbital integrators and the introduction of orbital similarity criteria D_D (Drummond, 1981), they were able to identify a group of Southern Taurids that dynamically converged 1400 years in the past. To explain why Encke did not match the orbit of the group, they suggested that the stream of material could have come from a companion, which could have itself separated from Encke earlier. More recently,

Olech et al. (2016) reported two large bolides entering the skies of Poland on October 31, 2015. The meteoroids have very similar orbits ($D_D = 0.011$), and the authors identify two asteroids (2005 UR and 2005 TF50) as potential members of the stream. Using a backward integration, they show that these 4 objects (two meteoroids and two NEOs) have their orbital elements converge 1500 years ago, in good agreement with Whipple and El-Din Hamid (1952), after taking into account the 64 years that separates these publications. Because this disassociation event is relatively young in the history of the Taurids, can it tell us something about the Taurid complex as a whole? The 2015 bolides were part of an outburst of fireballs also detected by the European Network, from which Spurný et al. (2017) outlined a correlation between size and strength: larger bodies tend to be more fragile.

Similar enhanced Taurids activity has been observed in some other years, with no clear link to comet Encke perihelion passages. Froeschle and Scholl (1986) first suggested that mean motion resonances (MMR) could in some cases shape meteoroid streams by splitting or trapping shower material. Material trapped in a MMR is prevented from undergoing full nodal precession, explaining concentrations of dust on long periods of time. Asher et al. (1993) suggested that this occurred to some Taurids, trapped in 7:2 MMR with Jupiter. The expected periodic signature of outbursts was later verified by Asher and Izumi (1998). Their model is successful at explaining enhanced activity in years when the Earth comes within $\Delta_M \in \pm 30/40°$ of the resonance centre in mean anomaly. Asher and Izumi (1998) also published future year outburst predictions by his model (recent years are published on David Asher's personal website [1]), these predictions were subsequently verified:

- 1995 ($\Delta_M = +29°$): Spurný (1997)

- 1998 ($\Delta_M = -13°$): Beech et al. (2004)

---

[1] http://star.arm.ac.uk/~dja/taurid/swarmyears.html, accessed May 16, 2017

- 2005 ($\Delta_M = +11°$): Dubietis and Arlt (2007); Shrbený and Spurný (2012); Olech et al. (2017)

- 2008 ($\Delta_M = -30°$): SonotaCo (2009)

- 2012 ($\Delta_M = +35°$): Madiedo et al. (2014)

- 2015 ($\Delta_M = -07°$): this work; Spurný et al. (2017); Olech et al. (2017)

In this paper, we describe the enhanced 2015 Taurid fireball activity observed by the Desert Fireball Network (DFN) in Australia and by the Cameras for Allsky Meteor Surveillance (CAMS) network in California. Jenniskens et al. (2016a) have identified this shower in 2012 data as #628 in the IAU Working List of Meteor Showers, and called it the s Taurids (IAU code *STS*). We note that the "new stream" of Spurný et al. (2017) corresponds to IAU #628. Hereafter meteor showers IAU #2 (codenamed STA) refers to the "regular" Southern Taurids, IAU #628 (codenamed STS) designates the resonant Southern Taurid branch, and Southern Taurids encompass members from both sub-streams.

5.2. DATA AND METHODS

DFN and CAMS survey meteoroid impacts at different sizes ranges: CAMS has the sensitivity to detect large numbers of sub-millimetre size small grains, while the DFN takes advantage of a large collecting area to catch centimetre to decimetre scale meteoroids, at the cost of lower sensitivity. When it comes to observing a bright meteor shower like the Taurids, the two systems complement each other well.
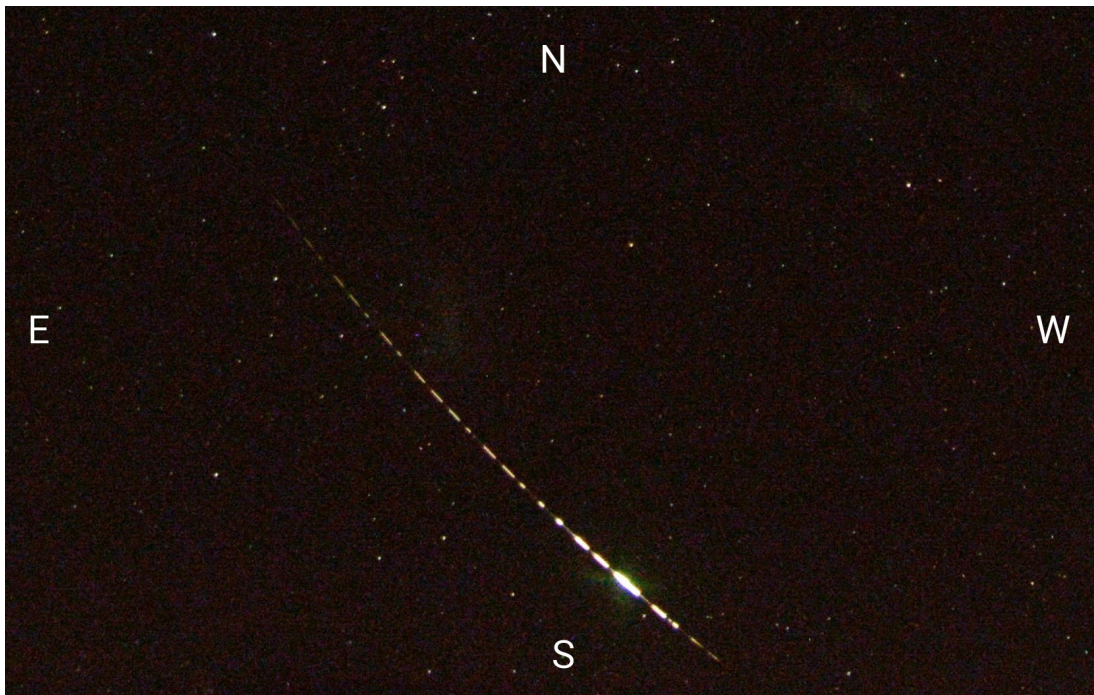
FIGURE 5.1: DN151104_01: a 2.6 s swarm Southern Taurid observed at Hughes siding in the Nullarbor plain, near the Magellanic clouds. This is a crop of the original all-sky picture. The meteoroid experiences a catastrophic fragmentation at 74 km altitude, shortly before disappearing.

5.2.1. DFN

The main goal of the Desert Fireball Network (DFN) is to observe meteorite falls in order to both have the necessary information to constrain a fall position, and to calculate where the meteoroid came from before crossing the Earth's path. To make such an instrument efficient, the following parameters must be optimised:

   i. good tracking accuracy of the object: constrain fall position and orbit well.

   ii. large collecting area: meteorite falls are rare.

   iii. favourable ground for meteorite recovery: low vegetation and good contrast.

   iv. favourable location for sky observations: good weather and dark skies.

Vast arid deserts such as the Nullarbor plain in Australia are ideal for (iii.) (Bland et al., 2012) and (iv.). The remoteness of such places, however, constrain how well (ii.) can be achieved: for logistical reasons the systems have to be autonomous, relatively cheap, and limited in numbers. Combined with (i.), this implies that each individual system must achieve high astrometric accuracy on the whole visible sky, which is not viable with current video camera technology.

Within its initial phase (starting 2005), the DFN used 4 large format film cameras (improving on the design of European Network technology), covering 150,000 km^2 of recoverable area. Over the first 5 years of science operations, this network yielded 2 meteorites (Bland et al., 2009; Spurný et al., 2011), at a time when the number meteorites with known orbit was still on the order of a dozen (Borovička et al., 2015). These successes prompted the upgrade for a much larger network, cheaper to build and to operate (Howie et al., 2017a). As of 2017, the Australian DFN covers 3 million km^2 of sky viewing

area (2.5 million km^2 of recoverable area), established around $30°$ S latitude. To some extend, operational and weather biases will be mitigated by the large collecting area and observation time. Each DFN observatory comprises of a high-resolution still imaging system: a 36 Mpixels digital camera (Nikon D800, D800E, or D810), associated with a Samyang 8 mm f/3.5 fish-eye lens, taking 25 seconds exposures at 6400 ISO. The cameras are sensitive to stellar magnitude 0.5 for meteors (7.5 for stars), and reliably detect meteors brighter than apparent magnitude -1.5. This upgraded design yielded its first meteorite recovery in late 2015, just over a year after starting science operations: Murrili (Devillepoix et al., 2016); followed by Dingle Dell (Devillepoix et al., 2018) in November 2016. These two rapid successes have proved the validity of using astrometric positions as main input for bright flight analysis (Sansom et al., 2015, 2016, 2017), as well as the benefits of encoding the absolute timing within the high-resolution images (Fig. 5.1) (Howie et al., 2017b) : automated data reduction is facilitated by not having to consolidate measurements from other instruments (such as a radiometer). A full description of the instrument can be found in Howie et al. (2017a), as well as the history of fireball networks and instrumentation used.

Meteor events are automatically detected in the images by the software procedures described by Towner and et al. (submitted). These algorithms reliably detect meteors as faint as visual magnitude -1.5 (3σ detection). The detection software is run on the on-board computer, and detections are sent to a central server. If successful triangulation is achieved, an email alert is issued for human review. Therefore, by design, single station events do not make it to the DFN data reduction pipeline. Calculating probing area as a function of time may be done accurately and relatively easily when a small number of narrow angle optics are used, such as described in Blaauw et al. (2016). Even at a basic level, this kind of work with all-sky cameras spaced on a continent-scale network, is more tricky, and de-biasing the DFN dataset to get precise
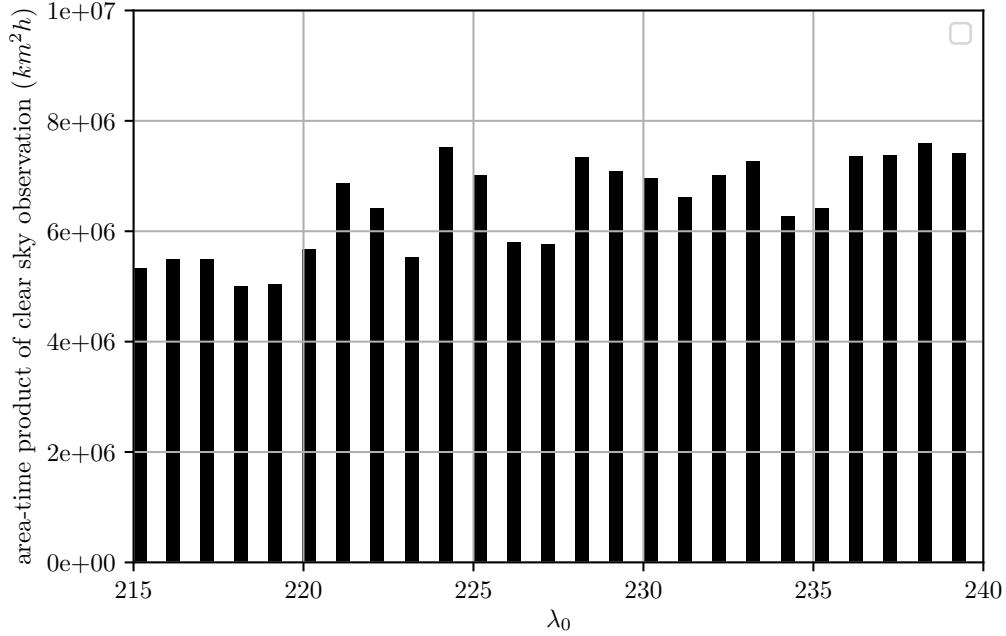
FIGURE 5.2: DFN clear sky logs in the $\lambda_\odot \in [215, 240]$ period, binned per year of observation. The double station coverage area is calculated using camera operation logs. This approximation comes with the limitations that partly cloudy sky conditions will be considered to be clear, thus slightly over-estimating the actual covering area. The total collecting time-area over the period amounts to $1.7 \times 10^8 \, km^2 h$.

fluxes will be the subject of a future paper. Here we use the operational log files as a proxy to get an estimate of coverage area. These analyses allow us to determine which cameras were observing at what time, as well as a zero-order approximate for cloud coverage (the cameras stop taking pictures at a defined level of cloudiness).

Fig. 5.2 allows a visualisation of how much space the DFN probes at any given time. However it does not make sense to calculate the activity rate on an hourly or even a daily basis, due to rarity of fireball events. Calculating overall activity for a broad stream on a specific year is valid for DFN data, as operational and weather biases will be mitigated by the large collecting area and observation time.

The cameras have sufficient resolution to provide accurate entry trajectories and pre-atmospheric orbits. The pixel coordinates of the meteors are transformed to celestial coordinates using stars as reference frame. The field of view observed by a camera for any given event is astrometrically calibrated using a different exposure, to avoid contamination problem by the meteor itself or a bright moon. The stability of the astrometric solution can be checked throughout the night. The agreement between star catalog positions and computed positions of this calibration are typically around 1 arcminute (Devillepoix et al., 2018).

The triangulation of meteor trajectories are performed using a weighted straight line least squares approach, similar to the one described in Borovička (1990). This method incorporates all the individual astrometric measurements and their corresponding angular uncertainties, from two or more camera locations to construct a best fit straight line trajectory that minimises the perpendicular distances between the meteors lines-of-sight from the cameras and this determined trajectory. While a straight line trajectory is assumed, this is not the reality due to gravitational and various aerodynamic forces. To lessen these effects on the following orbital and dark flight predictions for long trajectories, the start and end portions of the bright flight may be fitted separately.

In order to get an appropriate entry velocity for the meteoroid, an extended Kalman smoother may be applied to the positional data, throughout the visible bright flight (Sansom et al., 2015). This method also yields statistical uncertainties that encompass both model errors and measurement errors. These results are crucial for initialising orbit determination as orbital parameters, like the semi-major axis and eccentricity, are very sensitive to the errors in initial velocity. The heliocentric orbit of the meteoroids are determined using a backward integration from the start of the visible bright flight. The meteoroid is back-tracked through the upper layers of the atmosphere, and out of the sphere of influence of the Earth. Uncertainties on the orbital parameters are computed

using a Monte Carlo method based on the uncertainties of the first velocity vector observed.

The DFN reduction pipeline uses aperture photometry on the fireball track to calculate brightness. Doing photometry on the reference stars used for astrometry yield instrumental zero point of each camera, accounting for extinction and vignetting. Then fireball brightness is converted into magnitudes by accounting for the different exposure times: the effective exposure time for stars is typically 11.2 s (25 s exposure modulated by the liquid crystal shutter), and 0.06 s or 0.02 s for a fireball shutter break (see Howie et al. (2017b) for details on the action of the liquid crystal shutter). Apparent magnitude is converted to absolute after triangulation, using the observation range. The main limitation on this technique is the saturation of the sensor, which typically happens when the fireball exceeds apparent magnitude -8.

The main use of photometric measurement is to calculate meteoroid strength and to get a zero-order mass estimate. As thoroughly explained by Brown et al. (2016), the peak brightness instant of a fireball is a good indicator of catastrophic fragmentation, and therefore a reasonable proxy for calculating a general tensile strength for the entering body. This method is more robust to instrumental bias than the PE criterion introduced by Ceplecha and McCrosky (1976), and has the big advantage of being inferred directly from observable parameters (no mass involved). We therefore use the following relation from Bronshten (1981) to calculate tensile strength S: $S = \rho_{atm}.v^2$, where ρ_{atm} is the density of the atmosphere estimated using the *NRLMSISE-00* atmospheric model (Picone et al., 2002). v is the velocity at that instant calculated by the Kalman smoother described by Sansom et al. (2015). The main limitation of the method comes from the uncertainty on the instant of peak brightness, dominated by the sampling rate (10 Hz), which translates into 2 km of altitude for the average Taurid, or a $\simeq 1.3$ factor in strength.

5.2.2. CAMS

CAMS aims to map the presence of meteor showers throughout the year. CAMS methods are described in detail in Jenniskens et al. (2011). In brief, CAMS utilises a network of analog low-light video cameras, mostly Watec Wat902H2 Ultimate cameras with $30° \times 20°$ field of view each and +5.4 stellar limiting magnitude, and customized software that detects the meteors, calibrates the background star field to obtain astrometric positions, and then combines such data from two or more stations to triangulate the meteor trajectory. CAMS networks are established in California, Arizona, Florida, the BeNeLux, United Arab Emirates and New Zealand. CAMS yields more than 100,000 meteoroid orbits per year for mostly +4 to -4 magnitude meteors, and has proven to be a very efficient tool for studying meteor showers and linking them to possible parent objects (Jenniskens et al., 2016a,b,c). The high detection rate provides a baseline of sporadic meteor shower activity that can be used to calculate the effective observing time due to weather. As a result, a reliable record of activity of meteor showers is provided, while the global coverage provides some defense against bad weather.

5.3. RESULTS

Most CAMS networks are on the northern hemisphere, but they experienced a relatively small number of cloudy days. Fig. 5.3 plots the geocentric speed and time (solar longitude) of all meteors associated with the Southern Taurid complex. Vertical white bands are due to cloudy weather (no data). The data are split in two groups: the outburst years of 2012 and 2015, and the no-outburst years of 2010, 2011, 2013, 2014, and 2016. The outburst years show a component that produces a narrow range of geocentric entry speed at any given solar longitude, with a strong change in the speed as a function of time.
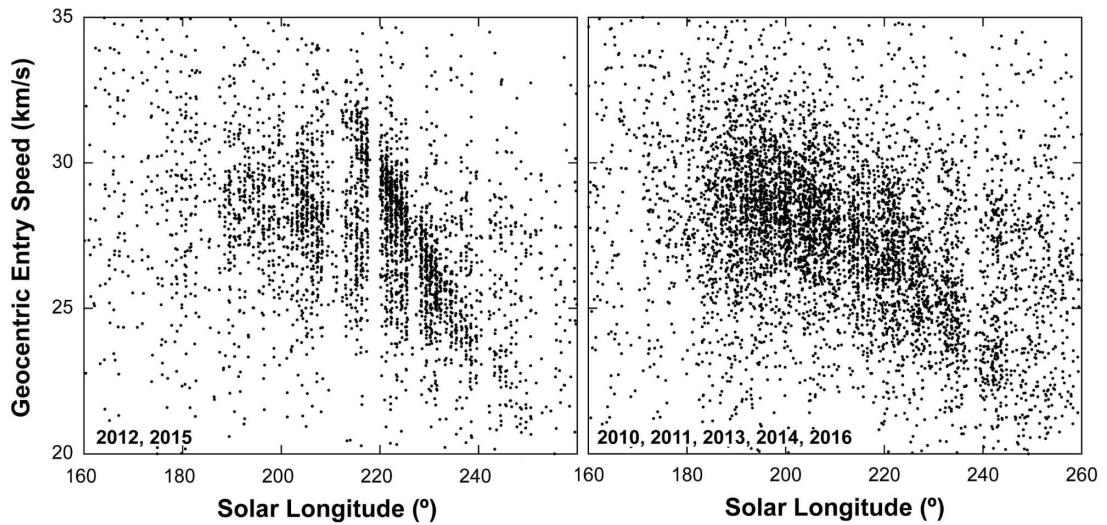
FIGURE 5.3: Southern Taurid meteor geocentric entry speed as a function of solar longitude in the years 2012 and 2015 (left) and other years (right), as observed by CAMS.

This component is only weakly present in non-outburst years (Fig. 5.3). This component was earlier identified as shower #628 (STS). The period of activity for this component is $\lambda_\odot \in [215, 240]$. The presence of this STS component is evident in the 2015 DFN data (Fig. 5.4), as the STS stream largely dominates the Southern Taurid activity at fireball sizes.

The speed increase for the STS component results in a larger semi-major axis. As already shown by Spurný et al. (2017), the measured semi-major axes for STS fireballs seem to cluster around 2.25 AU, which matches the location of the 7:2 mean-motion with Jupiter. This result is confirmed by DFN data (Fig. 5.5 and 5.7).

Fig. 5.8 shows the de-biased STS rates for CAMS, along with that of the remaining STA and NTA streams. The rates are normalised to that of all sporadic meteors with speeds $< 35\,\mathrm{km\,s^{-1}}$. This ensures that the total sporadic count reflects the observing conditions during that part of the night when the antihelion source is best observed. The sporadic apex and Toroidal sources have been removed from the count. The 2015 STS count was compared to the sporadic meteor rate in 2015 only. The multi-year de-biased distribution
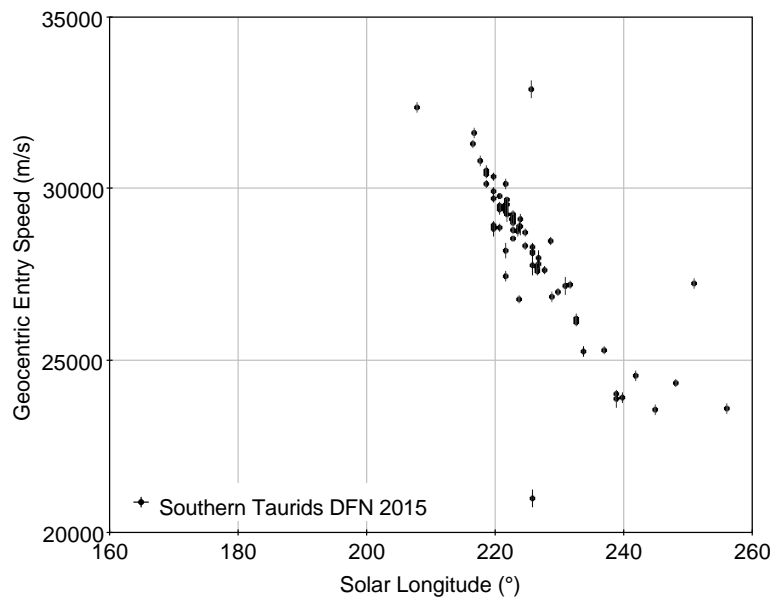
FIGURE 5.4: 2015 Southern Taurid fireball geocentric entry speed (with 1σ uncertainties error bars), as observed by the DFN. While CAMS observed both STAs and STSs in large numbers (Fig. 5.3), the STS stream dominates the STA stream at larger masses.

produced better define shower activity profiles than early results in Jenniskens et al. (2016b). The shower components identified in Jenniskens et al. (2016c) are still present. The STA and NTA shower profiles are different, an indication that the nodal line of individual meteoroid orbits did not fully rotate, as earlier pointed out.

Fig. 5.6 shows the distribution of peak magnitudes in 0.5 magnitude intervals for CAMS-detected NTA, STA and STS meteors. The count of all sporadic meteors was assumed to be exponential in shape of this magnitude interval, from which a detection probability function was derived by fitting an exponential slope to the bright-end of the magnitude distribution and then dividing observed counts by the fit-predicted count. This probability function was then applied to the detected count of shower meteors. The resulting curves show a distinctly different magnitude distribution for STA and NTA compared to STS meteors. The STS population is significantly more skewed towards brighter meteors. The magnitude size distribution index for STA is c = 3.0, NTA is c
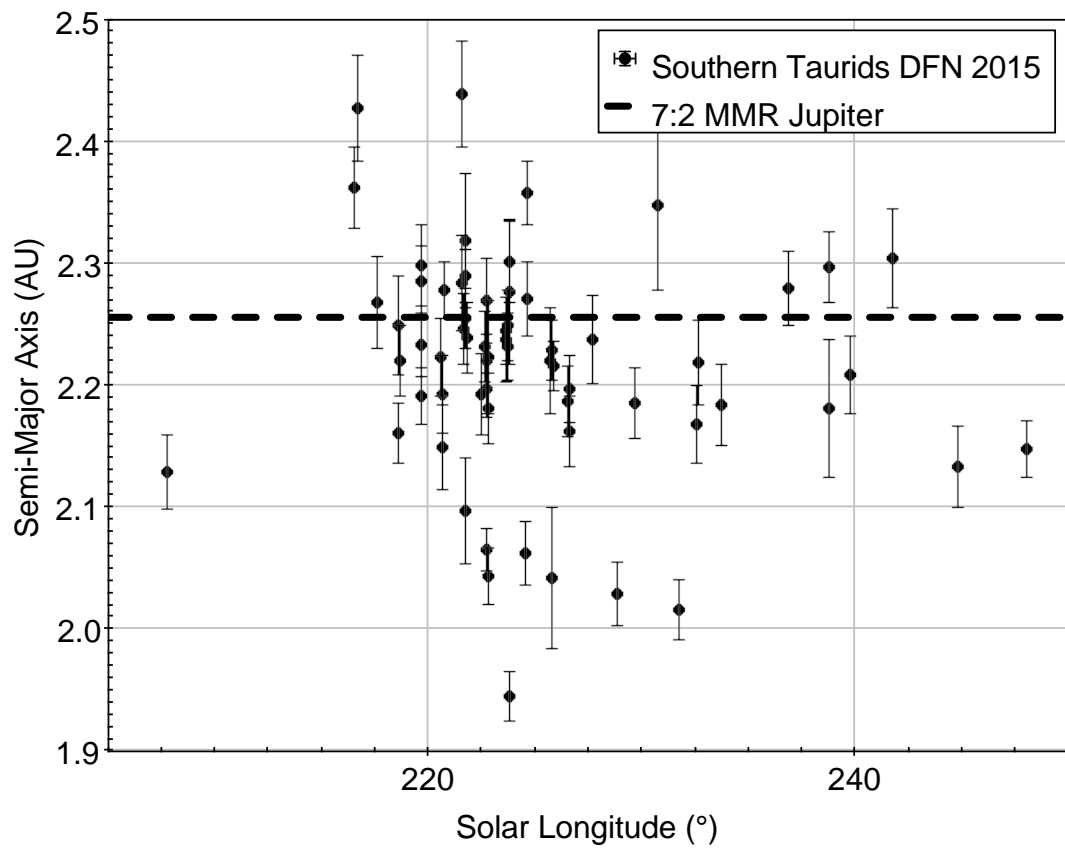
FIGURE 5.5: Semi-major axis measurements (with 1σ uncertainties error bars) of all Southern Taurid fireballs observed by the DFN 2015. Most are significantly higher than typical Southern Taurids, compatible with the a 7:2 mean-motion resonance with Jupiter (centered on 2.256 AU).
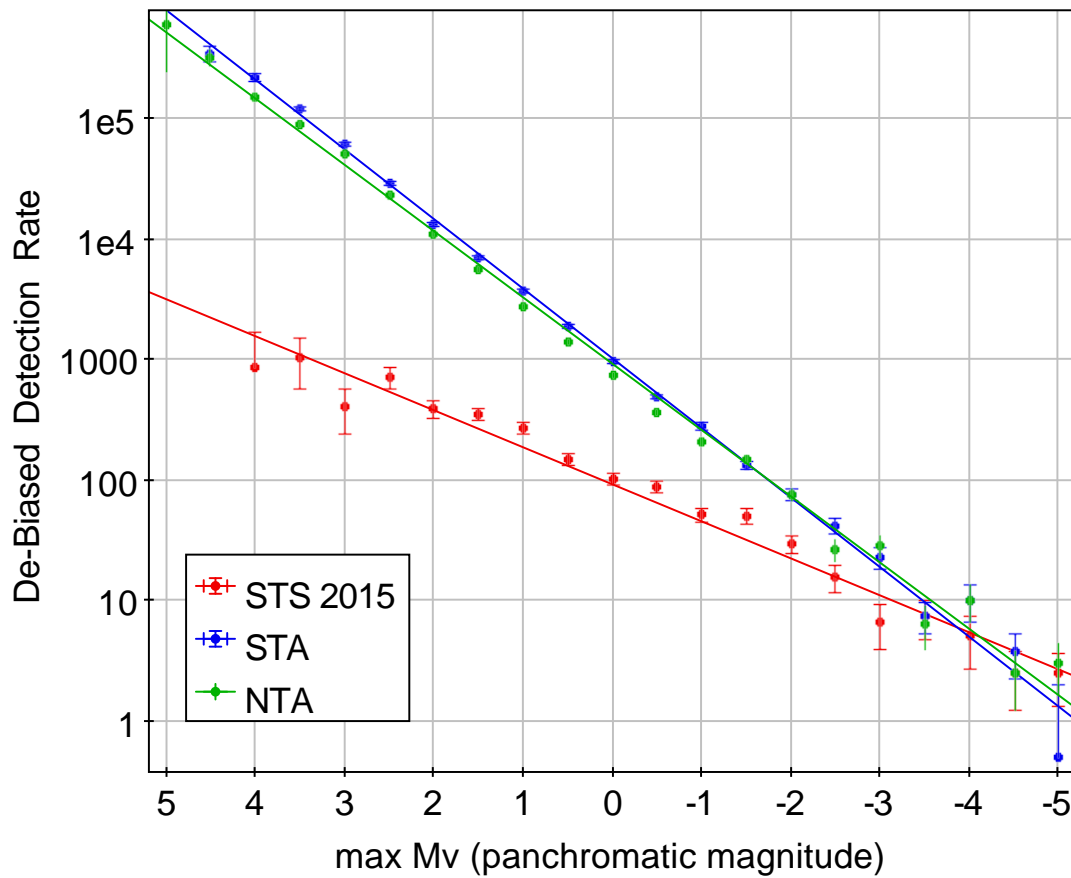
FIGURE 5.6: Peak magnitude frequency distribution for Southern Taurids substreams #2 STA, #17 NTA and #628 STS. Resonant Taurids (STS branch) are generally larger than regular Southern Taurids (STA).

= 3.0 and STS = c = 2.0 (assuming a sporadic c = 3.4). These meteors behave like weak matter. The s Taurids experience catastrophic disruption at very high altitudes (> 66 km, see Table 5.3).
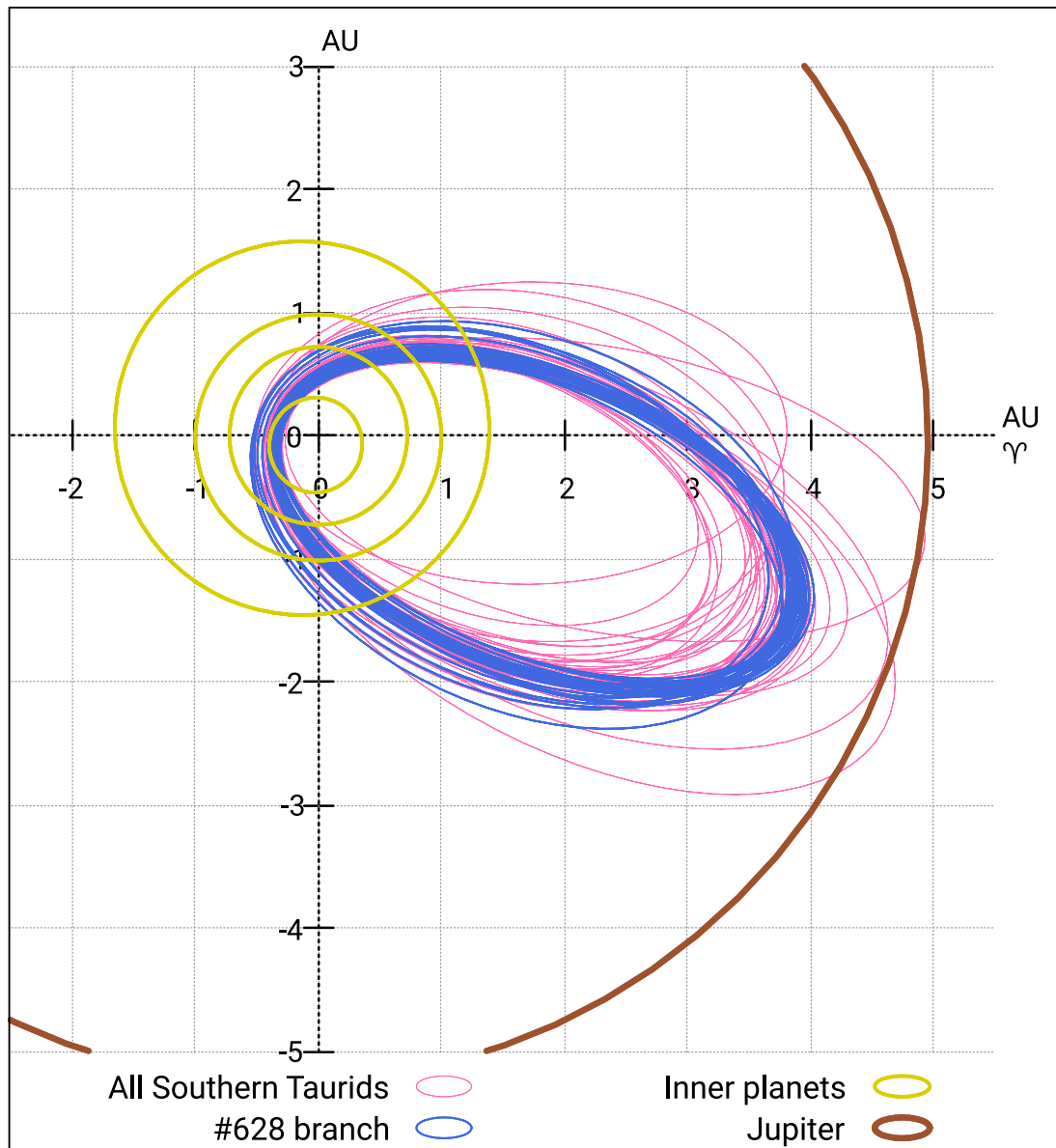
FIGURE 5.7: Ecliptic orbit plot of all Southern Taurids observed by the DFN in 2015 (pink), and the #628 branch (blue).
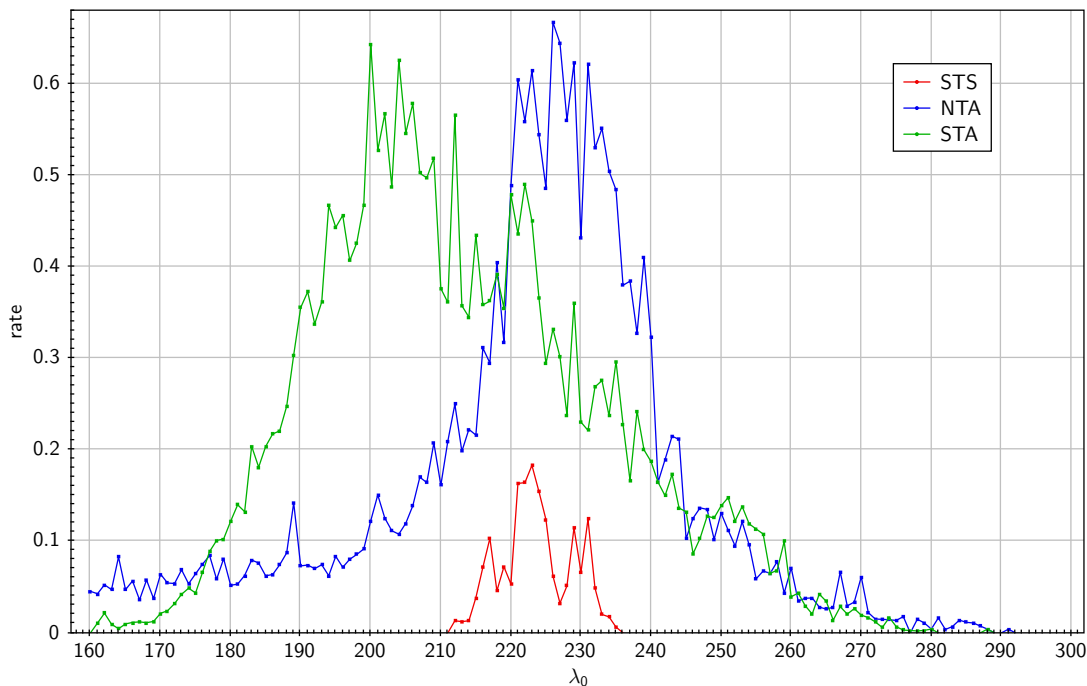
FIGURE 5.8: De-biased CAMS shower rates for shower 628 (STS), the Southern
Taurids (STA) and the Northern Taurids (NTA), as a function of solar longitude.

5.4. DISCUSSION

5.4.1. THE STS SIZE DISTRIBUTION IS VERY DIFFERENT THAN THAT OF NORMAL TAURIDS

The model by Asher and Izumi (1998) suggests a gradual concentration fall-off
for mean anomalies $|\Delta_M| \in [30, 40]°$. The 2012 encounter is $\Delta_M = 35°$ from
the centre of the resonance. The weak detection of the s Taurids in 2012 by
CAMS implies an extend of this component until at least mean anomaly $35°$, in
agreement.

A study by Soja et al. (2011) on radar meteor observed by the Canadian
Meteor Orbit Radar (CMOR) in 2005 (typical observed mass of 10^{-7} kg, which
roughly corresponds to optical magnitude +7), failed to identify the 7:2 reso-
nance from regular Southern Taurids. They discuss that this is partly due to the

poor constraints the radar observations put on the velocities (and therefore the semi-major axes), so it is not possible to distinguish STSs from STAs dynamically. Therefore unless the STS outburst is strong enough to significantly skew the overall Southern Taurids rates, it is not detectable. Soja et al. (2011) do no provide an upper constraint on the STS/STA activity, but even without hard numbers this analysis confirms the trend shown in Fig. 5.6: the STA branch dominates the STS branch at the low mass end ($Mv_{max} > -4$).

5.4.2. LARGE STREAM MEMBERS IN THE #628 STS STREAM

The DFN observations suggest that the size frequency distribution continues in a relatively shallow manner to brighter meteors. To catch those, a larger surface area is needed than monitored by DFN. The US government (USG) satellite sensors detect m-scale impactors in Earth's atmosphere over the entire planet as a collecting area. These data are reported online on the NASA JPL fireball website[2]. If any Taurids are among these impactors, we expect their penetration depth to be relatively shallow. We start by filtering the USG dataset by height 60km as a first pass to identify weak cometary impacts, as STS observed by the DFN break up $> 66\,\mathrm{km}$. We note that the stated peak brightness altitude from the sensors is generally reliable, as shown by Brown et al. (2016), and that these altitudes are reported for most events from the beginning of 2005 onwards. Detections are made at night, but also in daytime. As mentioned by Devillepoix et al. (2019), the typical energy report limit is $0.1\,kT\,TNT$, therefore we exclude event *2011-08-04 07:25:57* (0.098 kT reported yield) from our analysis for detection significance issues. We are left with 10 significant events that fit the height criterion (Table 5.1), however no velocities were reported for these events, so it is not possible to establish a dynamic link between any of these and the Taurid complex. Nevertheless, 3 out of these 10 very weak meteoroids fall within $\lambda_\odot \in [215, 240]$, and even more remarkable they happen in 2005 and 2015,

---

[2]`https://cneos.jpl.nasa.gov/fireballs/`, accessed May 16, 2017

two years during which strong STA activity has been reported and are predicted by the model of Asher and Izumi (1998). In 2005, two events occurred in short succession. All three events suggest the largest fragments in this stream are at solar longitude $[215, 240]°$. This combined with data in Fig. X, there may be a trend of larger matter to be more narrowly dispersed and peak earlier in time along Earth's path. For comparison, comet 2P/Encke would expected to cause meteoroid activity centred on $\lambda_\odot = 224.6°$, using method "H" of Hasegawa (1990), implemented by Neslusan et al. (1998).

We also confirm that these 3 events happened while the Southern Taurid radiant was above the local horizon. Considering the very low number of events observed, we need to build a statistical test to assess the significance of this apparent rate increase during a swarm episode. Let us test the hypothesis H_1: "*An airburst from weak material (main explosion ¿60 km) is more likely to happen during a STS activity period*" against the null hypothesis H_0: "*No increase in the rate of impacts from weak bodies can be observed during a STS activity episode*". We define a STS swarm episode as a period that happens on a year predicted by the model of Asher and Izumi (1998), within the interval where the USG sensors have consistently observed airbursts heights (2005, 2008, 2012, 2015), and within the activity period observed by CAMS (solar longitude $\in [215, 240]°$). We use the *rateratio.test R* package [3], that implements the methods described in Fay (2010) to carry out the statistical test. At 95% confidence, the background weak metre scale impact rate is $[0.001, 0.005]$, compared to $[0.009, 0.1]\, Earth^{-1}\lambda_\odot^{-1}$ when $\lambda_\odot \in [215, 240]$, which corresponds to an influx increase of $[2.1, 46]\times$ (see Table. 5.2 for full test test data and results). The small $p-value = 0.0071$ shows strong evidence against the null hypothesis (at 95% confidence). Although we cannot definitely link any individual events with the Taurids, the apparent rate increase in metre-scale weak impactors during the STS outburst is statistically significant, ans we can say that during an STS outburst episode the Earth is

---

[3]https://cran.r-project.org/package=rateratio.test

$10\times$ more likely to get impacted by a metre-scale STS than a sporadic meteoroid of the same size. This not only proves the presence of a significant number of metre scale bodies in the stream, but also implies that the stream is currently a major contributor to the overall population of large weak impactors. We also note that *USGS 1999-01-02 18:25:51* happened during the June daytime passage of the resonant swarm in 1999, predicted by the model of Asher and Izumi (1998). This daytime manifestation has not been reported by ground based optical network because of obvious observational issues.

TABLE 5.1: 14 high altitude (> 60 km) meteoroid airbursts observed by the USGS. No velocity information was provided for the events presented here. Highlighted rows show events that fall within the STS activity period. The 4 events at the bottom are excluded for statistical significance reasons (see in the text). +: Size calculated from the energy, assuming the velocity is equal to the mean STS velocity observed by the DFN at the same given solar longitude (see Table 5.3), and the 1600 kg m^{-3} bulk density estimated by (Babadzhanov and Kokhirova, 2009).

Peak brightness time ISO UTC	$\lambda_\odot$ °	Latitude ° (N+)	Longitude ° (E+)	Altitude km	Total Impact Energy kilotons TNT	Size+ m
2015-10-31 11:34:30	217.51	9.0	-138.0	71.0	0.29	1.5
2015-06-10 17:43:03	79.32	-11.5	-161.9	61.1	1.0	
2013-08-12 18:08:02	140.00	-34.4	118.2	66.6	0.15	
2012-02-12 05:25:52	322.72	-31.7	54.9	61.0	0.41	
2011-01-21 15:11:43	301.07	18.9	-44.6	61.0	0.23	
2010-12-09 02:54:07	256.76	-54.5	-169.7	66.0	0.2	
2005-12-24 15:30:26	272.85	-54.0	17.3	66.0	0.51	
2005-11-02 07:04:32	219.89	33.9	-154.9	68.5	0.11	1.1
2005-11-02 05:16:47	219.81	22.9	-123.8	74.0	0.21	1.3
2005-04-06 01:30:24	16.28	-42.7	154.6	70.0	0.1	
*2011-08-04 07:25:57	131.44	-40.7	-86.7	63.0	0.098	
2004-01-02 04:27:59	281.05	-28.2	3.2	63.0	0.39	
1999-06-25 06:27:41	93.30	50.0	121.0	69.0	0.37	
1999-01-02 18:25:51	281.93	47.0	103.0	65.0	0.12	

TABLE 5.2: Poisson test on the significance of the impact rate increase of metre-sized weak material (peak brightness $> 60\ km$) hitting the Earth observed by the USGS during STS outburst episodes ($\lambda_\odot \in [215, 240]$). Ranges given are at 2σ confidence. The influx increase factor during an STS outburst is $[2.1, 46]\times$.

population	surveyed years	observed events	$\lambda_\odot$ integrated	rate ($Earth^{-1}\lambda_\odot^{-1}$)
weak impactors population	[2005-2016]	10	3960	[0.001 - 0.005]
probable STS	2005, 2008, 2012, 2015	3	100	[0.006 - 0.09]

5.4.3. SIZE FREQUENCY DISTRIBUTION OF THE #628 STS STREAM

We have shown that the STS stream contains an unusual number of large members for a meteor shower. We aim to derive a frequency distribution for this population using observations at various size ranges.

As shown in Sec. 5.2.1 it is difficult to calculate the DFN shower activity with a small time step because of the small number of fireball events and the fact that the de-biasing information is not yet very precise. We can however work on the entire STS period using the activity pass-band derived from CAMS data. In 2015, the DFN observed 40 STS fireballs brighter than $MV_{max} = -7$, over a total collecting time-area of $1.7 \times 10^8 \, \text{km}^2$ hours. As of CAMS, the collecting area is discussed by Jenniskens et al. (2016a), the faint end of the distribution is de-biased using the sporadic counts and a magnitude population index of $c = 3.4$. This yields data points statistically significant for meteors between magnitude 2.5 to -4.

For these ground-based measurements, to relate localised observations to fluxes on the entire planet cross-section, we perform a zenithal correction, in order to account for low radiant angles. We convert the locally measured flux f to a corrected zenithal flux f_0, as if the cameras were sampling the area directly underneath the shower radiant: $f_0 = f / \sin(hR)$, with hR the mean altitude of the radiant.

As the USG samples the entire planet, we can just use the 2σ Poisson rates already calculate in Tab. 5.2. We must note that using the entry parameters calculated by Spurný et al. (2017), the *EN311015_180520* STS bolide should have been reported by the USG sensors. Its 0.2 kT TNT yield is within the reporting limit of the instrument (> 0.1 kT TNT, see Devillepoix et al. (2019)), this may be indicative of an unmodelled bias.

For this study, we note that we cannot use the European Network data from

Spurný et al. (2017), because de biasing information has not been reported. We also note that MORP reported on average just over 1 Taurid per year, except on 1981 where 8 Southern Taurids were reported, while only 2 STAs were observed in 1978, a likely indication that the MORP dataset contains STS. Unfortunately the de-biasing information is not available for each individual year (Ian Halliday, personal communication), so it is difficult to derive meteor shower fluxes for specific years with MORP.

The size-frequency distribution using CAMS, DFN, and USG is shown in Fig. 5.9. Using CAMS, DFN, and USG sensors, we define as a power law for the STS impacting population: $\log(N) = a - b\log(m)$, with N the cumulative number of objects colliding with the Earth on a swarm year with mass greater than m, we find $a = 2.4$ and $b = 0.9$.

The validity of extrapolating the established size frequency distribution to larger Potentially Hazardous Objects depends on the formation mechanism of Taurid meteoroids, more work is required to constrain this. If we make that assumption, the risk of the Earth getting impacted by a 140 m+ STS object would be around 10^{-8} on an outburst year.

5.4.4. Meteorite dropping Taurids?

Brown et al. (2013) identified the Taurid showers as a potential source of macroscopic meteorite dropping events. We have seen that the STS branch contains large members, do members of that population have a chance of surviving entry and falling as a meteorite? The deepest penetrating STS observed by the DFN ($DN151114\_04$) is not visible below 52 km. According to the criteria of Brown et al. (2013), which states that a height of 35 km and velocity of 10 km s^{-1} are approximate terminal dynamical criteria for a given event to have a chance of producing a meteorite fall, this is unlikely to produce a recoverable meteorite on the ground. It is worth noting that the two very bright STSs described by Olech
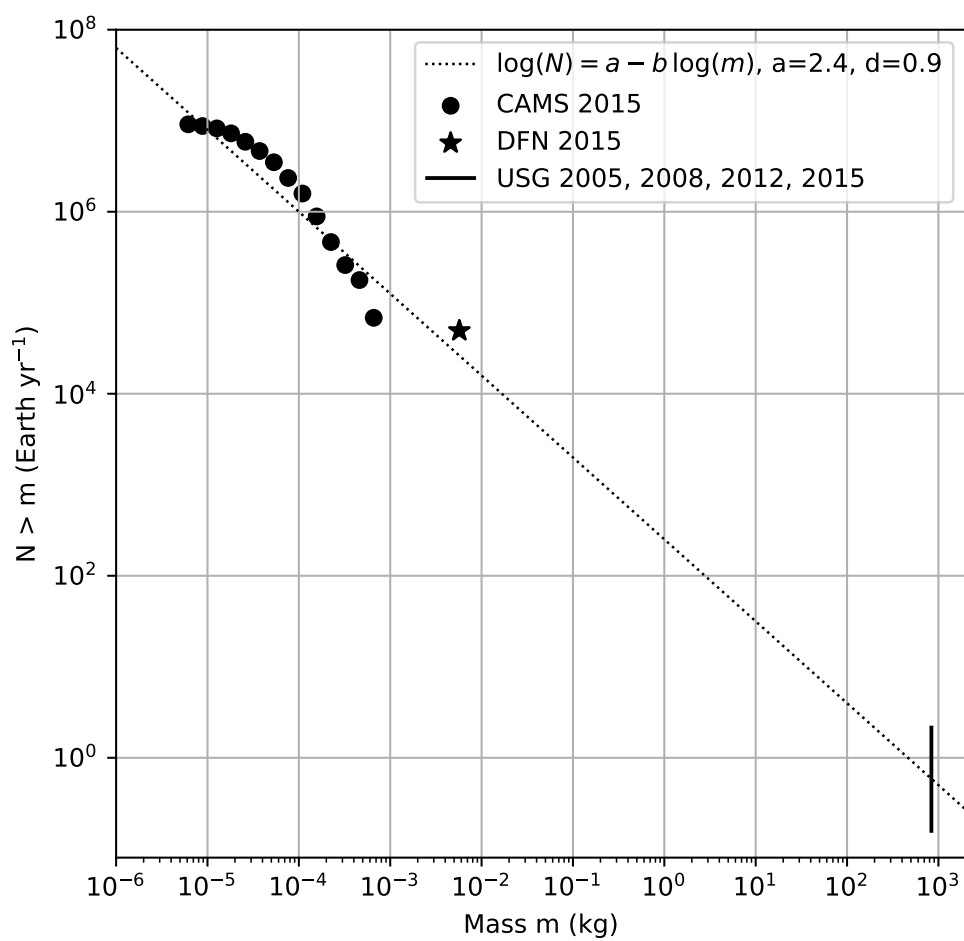
FIGURE 5.9: Size-frequency distribution of the #628 STS stream based on the $\lambda_\odot \in [215, 240]$ activity during the STS swarm years.

et al. (2016) also terminate at high altitudes of 57.86 and 60.20 km. The deepest penetrating Southern Taurid (MORP #715) described in the MORP dataset (Halliday et al., 1996), only penetrates to 54.8 km. As outlined by Brown et al. (2013), one of the EN fireballs in 1995 penetrated as deep as 30 km. Although this fireball was tentatively linked with the Taurid Complex, no definite association with either branch of the Taurids was reported, and the final velocity was not reported either. This analysis can be generalised to Southern Taurids in general, to our knowledge there is no report in the literature of a Southern Taurid that comes close to the terminal parameter of Brown et al. (2013). On the other hand, we have examples of Northern Taurids that are able to penetrate much lower than the 50 km ceiling that Southern Taurids seem to hit. For example, on October 9th, 2016, the DFN observed a Northern Taurid penetrating as deep as 36.4 km, slowing down to 9.7 km s^{-1}: the terminal parameters for this NTA are much closer to the cut-off criteria of Brown et al. (2013).

5.5. CONCLUSIONS

During the Southern Taurid #628 stream (STS) outburst years, the chance of the Earth being hit by a metre scale weak meteoroid is multiplied by 20. The Earth encounters the STS stream on average every 5 years, therefore the STS stream is responsible for as much as 20% of all weak (airburst > 60 km altitude) metre scale bodies.

We have established the size frequency distribution for the STS stream on 8 orders of magnitude in mass, this is unprecedented for a consistent stream of meteoroids. Using the modelled power law, we have calculated that the risk of Earth getting impacted by a potentially hazardous (> 140 m) is on the order of 10^{-8} on a swarm year, assuming the size frequency distribution scales from metre-scale to this class of objects. However there might be some issues

associated with with the reporting rate in USG data, which could underestimate this risk. When the stream next returns close to the Earth in 2022, the Large Synoptic Survey Telescope (Ivezic et al., 2008) will be able up and running and should be able to better constraint on the population of large STS. This could help get insights on the disruption mechanism that formed the stream.

The results presented here support the idea presented by Jenniskens (2006); Jenniskens et al. (2016b) that material is ejected as part of a continuous break up of the Taurid complex, in a sense that some features of the complex might be much younger than others, and have not had time to break up as much.

From the analysis of terminal parameters (heights and speeds) of the Taurid meteoroids observed by the DFN, a macroscopic meteorite from a Southern Taurid stream seems unlikely, on the other hand we have examples of Northern Taurids that approach the meteorite dropping terminal parameters discussed by (Brown et al., 2013).

ACKNOWLEDGEMENTS

APPENDIX

LIST OF SYMBOLS USED IN TABLE 5.3

- DFN: DFN event identification #
- datetime: UTC timestamp of the start of visible bright flight
- duration: duration of the observed bright flight
- $\lambda_\odot$: solar longitude
- a: semi-major axis
- e: eccentricity
- i: inclination
- ω: argument of periapsis
- Ω: longitude of the ascending node
- q: perihelion distance
- Q: aphelion distance
- ϖ: longitude of perihelion
- α_g, δ_g: corrected radiant
- v_g: geocentric speed
- T_J: Tisserand's criterion wrt. Jupiter
- slope: average entry angle wrt to local horizon
- v_∞, $\pm v_\infty$: observed speed at the top of the atmosphere and associated uncertainty
- v_e, $\pm v_e$:observed speed at the end of visible bright flight and associated uncertainty
- H_∞, λ_∞, ϕ_∞: height, longitude, latitude at start of visible bright flight
- Az_∞
- H_e, λ_e, ϕ_e: height, longitude, latitude at end of visible bright flight

- H_{max}: height at instant of peak brightness

- Q_c: best convergence angle between cameras observation planes

- R_∞: minimum slant range at the start of visible bright flight

TABLE 5.3: Key parameters for Southern Taurid meteors observed by the DFN in 2015

DFN #	datetime UTC (iso-8601)	duration s	$\lambda_\odot$ °	a AU	±a	e	±e	i °	±i	ω °	±ω	Ω °	±Ω	q AU	±q	Q AU	±Q	ϖ °	±ϖ	α_g j2000 °	±α_g	δ_g j2000 °	±δ_g	v_g m s⁻¹	T_J	slope	v_∞	±v_∞	H_∞	λ_∞ °	ϕ_∞ °	H_e m	H_{max} m	Q_e °	R_∞ km
DNI151021.02	2015-10-21T16:57:37.426	1.5	207.76	2.129	0.030	0.891	0.002	5.73	0.05	128.74	0.04	27.7950	0.0003	0.2329	0.0012	4.03	0.06	156.54	0.04	44.66	0.01	13.29	0.01	32374	3.02	47.7	34129	116	95800	135.4089	-27.7577	59659.4		46	138
DNI151030.01	2015-10-30T12:04:38.626	2.8	216.53	2.363	0.033	0.881	0.002	5.94	0.05	121.99	0.04	36.5508	0.0002	0.2814	0.0008	4.44	0.07	158.55	0.02	50.58	0.01	14.24	0.01	31325	2.84	21.6	33546	89	98405	136.1134	-31.9805	65552.6	77453.3	56	148
DNI151030.02	2015-10-30T14:53:34.286	1.0	216.64	2.427	0.043	0.886	0.003	5.51	0.05	122.46	0.05	36.6745	0.0011	0.2758	0.0011	4.58	0.09	159.14	0.04	50.75	0.02	14.67	0.02	31642	2.77	42.0	33700	132	96779	125.4614	-28.7875	74576.8		23	147
DNI151031.02	2015-10-31T12:51:50.926	1.9	217.56	2.268	0.038	0.872	0.003	5.20	0.05	121.37	0.07	37.5886	0.0003	0.2892	0.0012	4.25	0.08	158.96	0.07	51.22	0.04	14.83	0.02	30822	2.94	31.3	33006	118	93465	137.9136	-30.4063	63380.3	76239.6	72	113
DNI151101.04	2015-11-01T13:10:20.926	1.4	218.57	2.162	0.024	0.861	0.002	5.18	0.04	120.38	0.04	38.6033	0.0002	0.3010	0.0008	4.02	0.08	158.98	0.04	51.88	0.02	14.85	0.01	30155	3.06	32.6	32368	91	90564	136.6272	-31.9102	63322.8	71244.0	67	122
DNI151101.03	2015-11-01T14:17:53.226	1.4	218.62	2.249	0.040	0.868	0.003	5.54	0.05	120.54	0.03	38.6511	0.0003	0.2967	0.0013	4.20	0.08	159.20	0.02	52.04	0.01	14.70	0.02	30539	2.96	42.1	32603	151	93727	138.6748	-31.0368	64270.2	69455.5	9	103
DNI151101.01	2015-11-01T15:37:15.946	1.2	218.67	2.220	0.029	0.866	0.002	5.43	0.04	120.49	0.02	38.7095	0.0003	0.2981	0.0011	4.14	0.06	159.20	0.01	52.07	0.01	14.75	0.01	30418	3.00	45.0	32398	94	92692	135.1937	-31.4422	65784.9		68	115
DNI151102.05	2015-11-02T14:34:07.726	1.4	219.63	2.285	0.028	0.861	0.002	5.43	0.03	117.95	0.04	39.6622	0.0002	0.3179	0.0009	4.25	0.06	157.61	0.04	51.95	0.01	14.53	0.01	29927	2.95	40.2	32081	95	100733	135.9254	-29.9876	72191.7	79519.9	89	103
DNI151102.07	2015-11-02T14:34:07.886	1.2	219.63	2.233	0.026	0.861	0.003	5.46	0.03	117.87	0.03	39.6621	0.0009	0.3202	0.0009	4.15	0.05	157.53	0.03	51.95	0.01	14.46	0.01	29720	3.00	40.2	31905	85	97363	125.9022	-29.9873	73432.6		89	100
DNI151102.03	2015-11-02T15:05:32.947	1.4	219.65	2.191	0.023	0.845	0.002	5.30	0.03	115.82	0.02	39.6844	0.0002	0.3397	0.0008	4.04	0.05	155.50	0.02	51.09	0.01	14.15	0.01	28963	3.07	40.0	31206	85	94152	115.4520	-29.5975	67384.9	71180.6	37	130
DNI151102.04	2015-11-02T16:03:48.226	0.9	219.69	2.298	0.033	0.867	0.003	5.82	0.04	119.29	0.02	39.7232	0.0002	0.3059	0.0011	4.29	0.07	159.01	0.01	52.66	0.01	14.54	0.01	30372	2.92	46.4	32453	105	99668	113.5600	-27.0131	69517.3		33	275
DNI151102.02	2015-11-02T16:42:46.826	1.6	219.72	1.890	0.034	0.833	0.003	5.09	0.07	120.09	0.05	39.7581	0.0005	0.3148	0.0020	3.47	0.05	159.85	0.05	53.07	0.02	14.97	0.02	28838	3.42	46.1	30922	182	100665	116.8080	-27.1642	66994.1		52	136
DNI151103.04	2015-11-03T23:23:09.326	1.6	220.58	2.223	0.032	0.844	0.003	5.93	0.04	114.91	0.04	40.6104	0.0002	0.3465	0.0009	4.10	0.06	155.52	0.04	51.82	0.02	13.72	0.02	28859	3.04	35.0	31139	98	94626	132.4627	-30.8077	74292.1	77837.2	41	102
DNI151103.05	2015-11-03T15:14:18.126	0.8	220.66	2.193	0.032	0.852	0.003	5.70	0.04	117.62	0.05	40.6908	0.0002	0.3237	0.0011	4.06	0.06	158.31	0.05	52.97	0.02	14.47	0.01	29516	3.05	38.8	31700	119	99197	115.0323	-31.3095	75167.8	81877.4	61	145
DNI151103.02	2015-11-03T15:53:05.826	1.2	220.69	2.150	0.035	0.849	0.003	6.07	0.06	117.73	0.03	40.7197	0.0003	0.3243	0.0015	3.97	0.07	158.45	0.03	53.16	0.01	14.19	0.01	29395	2.96	44.7	31400	131	94168	136.6579	-30.0727	71415.1	79647.0	19	294
DNI151104.01	2015-11-03T17:08:17.326	1.6	220.74	2.277	0.022	0.858	0.002	6.62	0.04	117.32	0.03	40.7708	0.0003	0.3235	0.0009	4.23	0.05	158.09	0.03	53.13	0.01	13.80	0.01	29782	2.96	44.3	31645	83	93939	135.0416	-28.3737	67225.1	66188.0	85	96
DNI151104.10	2015-11-04T12:23:17.326	2.6	221.54	2.284	0.039	0.856	0.003	5.13	0.04	116.61	0.03	41.5724	0.0003	0.3294	0.0011	4.24	0.08	158.19	0.04	53.25	0.02	14.96	0.02	29548	3.04	22.5	31849	125	98988	130.5905	-31.7834	67992.5	73738.0	32	182
DNI151104.16	2015-11-04T12:23:17.386	2.5	221.54	2.439	0.043	0.867	0.003	5.92	0.04	116.80	0.02	41.5683	0.0002	0.3232	0.0011	4.55	0.09	158.37	0.02	53.16	0.01	14.49	0.01	30131	2.81	22.5	32413	117	96579	130.5995	-31.7923	68125.1	74229.5	12	275
DNI151104.09	2015-11-04T15:32:06.726	1.2	221.67	2.247	0.029	0.851	0.002	5.50	0.04	116.25	0.02	41.7099	0.0003	0.3337	0.0010	4.16	0.06	157.95	0.02	53.34	0.01	14.61	0.01	29328	3.00	43.9	31404	96	96860	129.2087	-32.1958	62719.6	71460.1	63	164
DNI151104.14	2015-11-04T15:43:03.826	1.6	221.68	2.255	0.024	0.853	0.002	6.13	0.03	116.02	0.03	41.7141	0.0002	0.3325	0.0009	4.18	0.06	158.07	0.03	53.57	0.01	14.17	0.01	29418	2.99	45.3	31484	86	91546	128.2807	-31.4342	62184.5	67864.4	81	133
DNI151104.15	2015-11-04T15:46:19.295	0.9	221.68	2.097	0.043	0.849	0.004	4.82	0.06	118.74	0.02	41.7247	0.0003	0.3173	0.0018	3.88	0.09	160.47	0.02	54.30	0.01	15.52	0.01	29437	3.15	41.0	31555	174	81275	122.2436	-33.5822	72672.4	76175.0	60	401
DNI151104.13	2015-11-04T15:48:31.026	0.3	221.68	1.881	0.026	0.811	0.004	4.88	0.05	116.58	0.01	41.7235	0.0004	0.3557	0.0014	3.41	0.05	157.30	0.01	53.10	0.01	14.71	0.02	27455	3.47	44.7	29734	133	86051	116.0805	-27.7748	75070.0	81191.8	38	88
DNI151104.11	2015-11-04T16:06:37.626	0.8	221.70	1.769	0.033	0.820	0.005	3.68	0.07	120.46	0.03	41.7532	0.0011	0.3180	0.0023	3.22	0.07	162.21	0.03	54.99	0.01	16.49	0.02	28218	3.61	40.0	30367	205	86051	123.0899	-34.8273	69911.4	76202.3	15	545
DNI151104.07	2015-11-04T16:11:41.626	1.5	221.70	2.290	0.021	0.857	0.002	5.75	0.03	116.91	0.04	41.7375	0.0006	0.3265	0.0008	4.25	0.04	158.65	0.04	53.70	0.02	14.59	0.01	29682	2.95	45.9	31624	77	98261	132.5929	-29.8542	82579.6	88854.0	89	158
DNI151104.12	2015-11-04T17:04:32.626	1.0	221.74	2.318	0.055	0.853	0.005	5.06	0.07	115.27	0.04	41.7800	0.0005	0.3399	0.0021	4.30	0.11	157.05	0.04	52.86	0.02	14.81	0.02	29281	2.94	43.3	31198	187	91865	132.5929	-29.8542	82579.6	82579.6	15	255
DNI151105.11	2015-11-04T18:30:51.826	1.2	221.80	2.239	0.029	0.854	0.003	6.34	0.06	116.96	0.04	41.8323	0.0003	0.3278	0.0010	4.15	0.06	158.80	0.04	54.00	0.03	14.16	0.03	29540	3.00	42.7	31393	113	91953	116.2984	-29.2938	66831.8	73048.4	85	93
DNI151105.12	2015-11-05T11:19:01.046	3.1	222.50	1.946	0.014	0.847	0.003	5.45	0.04	116.21	0.03	42.5260	0.0003	0.3359	0.0009	4.05	0.04	158.74	0.03	54.17	0.02	14.81	0.01	29119	3.06	14.1	31525	119	84690	133.9285	-26.6537	62819.5	77749.0	60	88
DNI151105.03	2015-11-05T14:57:32.726	1.1	222.65	2.232	0.028	0.850	0.003	5.68	0.04	116.11	0.03	42.6853	0.0003	0.3354	0.0010	4.13	0.06	158.79	0.03	54.33	0.01	14.68	0.01	29250	3.01	43.2	31395	114	88485	126.7332	-29.7805	70301.3	73001.3	30	130
DNI151105.02	2015-11-05T15:28:12.826	1.6	222.67	2.197	0.024	0.846	0.002	5.49	0.03	116.02	0.02	42.7090	0.0002	0.3374	0.0009	4.06	0.05	158.07	0.02	54.28	0.01	14.79	0.01	29250	3.06	44.6	31227	81	91880	125.1623	-30.2902	68142.3	75605.0	88	124
DNI151105.18	2015-11-05T15:28:49.726	1.1	222.67	2.269	0.035	0.850	0.003	5.75	0.05	115.30	0.01	42.7092	0.0003	0.3412	0.0012	4.20	0.07	158.01	0.01	54.02	0.01	14.49	0.01	29159	2.99	43.6	31253	136	98089	129.8792	-32.2867	73875.9	81438.9	45	241
DNI151105.13	2015-11-05T15:48:31.026	0.9	222.68	2.220	0.022	0.849	0.002	5.01	0.05	116.22	0.03	42.7224	0.0002	0.3348	0.0010	4.10	0.04	158.94	0.03	54.23	0.01	15.21	0.02	29213	3.01	48.2	31236	78	95421	116.0805	-27.7748	61676.2	72156.0	35	96
DNI151105.09	2015-11-05T17:16:17.726	1.6	222.75	2.065	0.018	0.835	0.003	4.72	0.03	112.58	0.03	42.7950	0.0003	0.3416	0.0010	3.79	0.03	155.34	0.03	55.10	0.01	15.34	0.01	28546	3.21	39.3	30466	83	85384	138.1836	-30.2134	63932.3	67853.0	53	191
DNI151106.05	2015-11-05T17:52:36.526	1.3	222.77	2.044	0.024	0.837	0.004	5.16	0.05	112.48	0.03	42.8159	0.0003	0.3416	0.0013	3.75	0.05	155.20	0.02	55.04	0.01	15.20	0.01	28802	3.23	42.4	30729	108	95119	123.3967	-29.7905	68524.0	75644.6	34	202
DNI151106.04	2015-11-05T18:03:17.026	1.5	222.77	2.181	0.029	0.845	0.003	5.39	0.04	123.08	0.03	42.8142	0.0004	0.3378	0.0012	4.02	0.06	158.85	0.03	54.37	0.01	14.88	0.02	29028	3.07	42.5	30951	119	96237	123.4073	-29.9084	67860.1		35	246
DNI151106.07	2015-11-05T18:33:10.826	2.3	222.58	2.238	0.046	0.847	0.004	5.72	0.05	116.04	0.03	42.8284	0.0006	0.3392	0.0021	4.11	0.09	158.52	0.06	54.14	0.02	15.07	0.02	29077	3.03	39.0	30944	170	96237	128.1129	-29.7731	74713.2	66874.6	78	97
DNI151106.06	2015-11-06T13:09:02.926	1.7	223.60	2.223	0.029	0.843	0.003	5.60	0.04	114.27	0.04	43.6104	0.0003	0.3513	0.0010	4.10	0.05	157.88	0.04	54.51	0.01	15.06	0.01	28754	3.03	33.0	31060	110	95606	134.7333	-31.8602	59735.8	69014.7	88	110
DNI151106.04	2015-11-06T13:34:34.726	1.4	223.62	2.249	0.031	0.846	0.003	5.17	0.04	114.67	0.03	43.6305	0.0002	0.3475	0.0011	4.15	0.06	158.30	0.03	54.66	0.01	15.06	0.01	28917	3.01	37.7	31130	97	97000	134.9376	-30.3879	66263.0	67749.0	61	135
DNI151106.08	2015-11-06T18:09:31.026	0.6	223.69	2.276	0.059	0.850	0.004	5.12	0.09	114.39	0.07	43.7140	0.0003	0.3488	0.0025	4.20	0.12	158.47	0.02	54.66	0.03	15.07	0.03	28905	3.01	45.8	30996	108	98427	134.5855	-27.9705	65427.6	66626.8	82	134
DNI151106.06	2015-11-06T18:36:46.826	1.1	223.81	2.301	0.033	0.846	0.002	5.77	0.03	116.00	0.02	43.8464	0.0003	0.3453	0.0011	4.26	0.07	158.54	0.01	54.91	0.01	14.64	0.01	29109	2.96	29.8	30889	127	96255	137.2734	-28.3491	73256.5		56	143
DNI151107.04	2015-11-07T12:44:13.926	1.2	224.56	2.063	0.025	0.836	0.003	6.52	0.04	115.89	0.05	44.5903	0.0003	0.3378	0.0012	3.79	0.05	161.15	0.02	56.77	0.01	14.43	0.01	29102	3.33	33.4	31102	90	80496	135.6323	-25.0326	72370.3	82983.5	88	216
DNI151107.03	2015-11-07T13:19:16.826	2.0	224.59	2.272	0.030	0.839	0.003	4.83	0.04	112.52	0.03	44.6283	0.0003	0.3655	0.0011	4.18	0.05	157.14	0.03	54.53	0.02	15.13	0.01	28354	3.01	34.1	30661	97	89164	134.6230	-32.2845	61676.2	73395.5	90	105
DNI151107.01	2015-11-07T13:51:20.626	1.7	224.61	2.357	0.027	0.846	0.002	6.70	0.04	112.48	0.03	44.6402	0.0002	0.3630	0.0010	4.35	0.05	157.12	0.02	55.04	0.01	13.66	0.01	28724	2.92	36.3	31002	75	93187	128.9981	-32.2269	65496.6	67265.1	24	152
DNI151108.06	2015-11-08T14:42:39.626	1.1	225.65	2.676	0.095	0.901	0.004	11.96	0.14	123.08	0.03	45.6684	0.0019	0.2649	0.0019	5.09	0.19	168.74	0.03	61.54	0.01	13.00	0.02	32894	2.55	41.9	34862	213	90315	129.7174	-30.3148	65832.4	69095.0	7	189
DNI151108.07	2015-11-08T16:39:03.074	1.3	225.73	2.220	0.043	0.834	0.004	3.00	0.09	110.89	0.07	45.7335	0.0013	0.3687	0.0016	4.07	0.09	156.70	0.04	55.65	0.04	15.75	0.04	28130	3.02	43.8	30379	151	100809	117.1038	-29.7731	66342.4		62	133
DNI151108.01	2015-11-08T18:07:12.826	1.4	225.79	2.229	0.029	0.837	0.003	5.07	0.04	112.81	0.01	45.8118	0.0004	0.3642	0.0011	4.09	0.06	158.65	0.01	55.96	0.01	15.24	0.01	28303	3.05	40.9	30172	91	96143	138.7517	-32.7809	72417.4		87	123
DNI151108.08	2015-11-08T18:07:13.426	0.7	225.82	2.301	0.057	0.855	0.007	4.38	0.11	111.10	0.03	45.8405	0.0024	0.3629	0.0015	3.72	0.12	159.66	0.11	56.29	0.04	15.88	0.05	27781	3.26	33.2	29687	251	86893	134.6747	-31.3127	73728.9	77428.8	39	216
DNI151108.03	2015-11-08T18:39:48.626	1.7	228.66	2.691	0.049	0.855	0.003	5.19	0.03	112.46	0.05	48.6966	0.0005	0.3906	0.0013	4.99	0.10	156.04	0.03	56.88	0.01	15.03	0.01	25268	2.68	46.9	27630	115	87342	134.7759	-31.4084	75654.9		29	155
DNI151109.03	2015-11-09T11:24:33.526	2.4	226.52	2.188	0.029	0.826	0.003	5.77	0.03	111.19	0.04	46.5462	0.0003	0.3802	0.0009	4.00	0.06	157.74	0.04	56.22	0.01	14.46	0.01	27716	3.11	19.6	29338	111	99375	115.2041	-29.0755	66281.5	79765.8	19	125
DNI151109.02	2015-11-09T13:05:15.526	2.3	226.59	2.162	0.034	0.824	0.003	5.39	0.04	111.16	0.05	46.6232	0.0003	0.3815	0.0011	3.94	0.06	157.79	0.05	56.18	0.01	14.78	0.04	27590	3.13	39.1	29290	116	94959	126.0290	-30.3934	73134.4	74104.5	71	172
DNI151109.04	2015-11-09T14:06:44.926	2.0	226.63	2.197	0.027	0.828	0.003	5.06	0.04	111.48	0.03	46.6712	0.0003	0.3772	0.0011	4.02	0.05	158.15	0.03	56.25	0.01	15.16	0.01	27806	3.09	44.3	29535	108	97254	138.4317	-28.0644	61473.5	81073.6	69	135
DNI151109.01	2015-11-09T16:28:12.126	1.2	226.73	2.801	0.094	0.854	0.006	4.05	0.06	105.86	0.03	46.7829	0.0022	0.4093	0.0022	5.19	0.19	152.64	0.03	53.46	0.03	15.30	0.04	28004	2.62	47.4	30130	187	92441	119.1299	-28.7472	62135.1		19	260
DNI151110.01	2015-11-10T13:59:05.726	1.7	227.63	2.237	0.037	0.827	0.003	5.01	0.04	110.29	0.28	47.6673	0.0007	0.3863	0.0013	4.09	0.07	157.96	0.28	56.72	0.14	15.22	0.01	26232	3.06	32.3	28689	116	87924	136.1785	-28.6125	70671.7	74306.8	90	113
DNI151111.03	2015-11-11T14:33:48.326	1.6	228.66	2.184	0.033	0.796	0.004	5.58	0.06	102.32	0.05	53.5746	0.0004	0.4593	0.0015	3.91	0.07	156.07	0.03	59.59	0.03	14.34	0.03	25268	3.17	48.7	27630	115	90677	136.5931	-28.5357	62347.9	67184.2	74	120
DNI151111.02	2015-11-11T17:19:32.626	1.6	236.84	2.280	0.031	0.790	0.003	4.75	0.05	101.10	0.07	56.8879	0.0004	0.4657	0.0014	4.09	0.07	157.99	0.07	61.91	0.01	15.66	0.04	25304	3.08	37.2	27438	106	94772	136.2386	-30.1176	66429.3	74721.3	74	99
DNI151112.01	2015-11-12T15:54:07.586	1.3	238.71	2.296	0.035	0.778	0.005	4.79	0.07	96.09	0.02	55.8755	0.0006	0.5094	0.0015	4.08	0.08	151.98	0.03	61.51	0.03	15.03	0.01	24025	3.10	44.4	26594	87	91028	132.9568	-28.2865	65142.6	71454.9	50	208
DNI151113.01	2015-11-12T17:35:40.726	1.6	238.71	2.181	0.057	0.769	0.007	4.93	0.08	97.28	0.05	58.7563	0.0008	0.5038	0.0023	3.86	0.12	156.04	0.05	62.15	0.02	14.99	0.04	23895	3.21	44.2	26474	191	89878	132.9350	-28.2952	65490.7	71388.7	45	212
DNI151114.04	2015-11-22T14:26:40.426	1.4	239.74	2.305	0.031	0.772	0.004	4.84	0.05	97.01	0.05	59.7893	0.0007	0.5247	0.0013	3.91	0.05	156.80	0.05	63.03	0.03	15.26	0.05	23953	3.18	42.4	26510	106	95479	139.8686	-31.5875	70371.9	80871.8	85	105
DNI151115.02	2015-11-24T13:10:46.426	1.2	241.71	2.148	0.041	0.786	0.006	4.65	0.11	97.90	0.05	61.7572	0.0006	0.4927	0.0014	4.12	0.08	159.65	0.03	65.36	0.03	16.08	0.04	27113	3.08	37.9	27113	115	92315	137.2536	-30.0513	73142.5	80491.0	38	261
DNI151115.03	2015-11-27T14:21:48.086	2.1	244.79	2.134	0.024	0.760	0.004	4.91	0.07	96.56	0.21	64.8401	0.0007	0.5116	0.0019	3.76	0.07	161.40	0.21	68.03	0.11	15.87	0.07	23583	3.27	44.6	26123	125	95451	137.2536	-30.0513	58380.9	80491.0	87	118
DNI151116.02	2015-11-28T06:00:03.886	1.4	248.00	2.148	0.024	0.772	0.005	5.27	0.05	98.97	0.04	68.0497	0.0014	0.4892	0.0014	3.81	0.05	167.02	0.04	72.57	0.02	16.33	0.05	24361	3.23	34.5	26531	97	95333	125.6163	-28.1596	63693.8	82399.9	74	201
DNI151119.01	2015-11-30T18:28:06.733	2.2	250.89	2.129	0.030	0.815	0.003	4.56	0.05	109.55	0.06	70.9474	0.0006	0.3948	0.0014	3.86	0.06	180.50	0.06	80.41	0.03	18.85	0.03	23480	3.18	41.7	25480	111	95107	134.4064	-30.0808	66917.9	80584.8	86	117
DNI151121.02	2015-12-08T13:13:48.446	2.2	255.90	2.176	0.032	0.762	0.004	5.21	0.04	95.52	0.05	75.9411	0.0004	0.5178	0.0011	3.83	0.07	171.46	0.05	79.13	0.02	16.67	0.02	23620	3.23	27.6	26399	115	92615	115.4893	-28.7417	66081.0	80584.8	28	146

5.6. REFERENCES

D. J. Asher and K. Izumi. Meteor observations in Japan: new implications for a Taurid meteoroid swarm. MNRAS, 297:23–27, June 1998. doi: 10.1046/j. 1365-8711.1998.01395.x.

D. J. Asher, S. V. M. Clube, and D. I. Steel. Asteroids in the Taurid Complex. MNRAS, 264:93, Sept. 1993. doi: 10.1093/mnras/264.1.93.

Astropy Collaboration, T. P. Robitaille, E. J. Tollerud, P. Greenfield, M. Droettboom, E. Bray, T. Aldcroft, M. Davis, A. Ginsburg, A. M. Price-Whelan, W. E. Kerzendorf, A. Conley, N. Crighton, K. Barbary, D. Muna, H. Ferguson, F. Grollier, M. M. Parikh, P. H. Nair, H. M. Unther, C. Deil, J. Woillez, S. Conseil, R. Kramer, J. E. H. Turner, L. Singer, R. Fox, B. A. Weaver, V. Zabalza, Z. I. Edwards, K. Azalee Bostroem, D. J. Burke, A. R. Casey, S. M. Crawford, N. Dencheva, J. Ely, T. Jenness, K. Labrie, P. L. Lim, F. Pierfederici, A. Pontzen, A. Ptak, B. Refsdal, M. Servillat, and O. Streicher. Astropy: A community Python package for astronomy. A&A, 558:A33, Oct. 2013. doi: 10.1051/0004-6361/201322068.

P. B. Babadzhanov and G. I. Kokhirova. Densities and porosities of meteoroids. A&A, 495:353–358, Feb. 2009. doi: 10.1051/0004-6361:200810460.

M. Beech, M. Hargrove, and P. Brown. The running of the bulls: a review of Taurid fireball activity since 1962. *The Observatory*, 124:277–284, Aug. 2004.

R. C. Blaauw, M. Campbell-Brown, and A. Kingery. Optical meteor fluxes and application to the 2015 Perseids. MNRAS, 463:441–448, Nov. 2016. doi: 10.1093/mnras/stw1979.

P. A. Bland, P. Spurný, M. C. Towner, A. W. R. Bevan, A. T. Singleton, W. F. Bottke, R. C. Greenwood, S. R. Chesley, L. Shrbený, J. Borovička, Z. Ceplecha, T. P. McClafferty, D. Vaughan, G. K. Benedix, G. Deacon, K. T. Howard, I. A. Franchi, and R. M. Hough. An Anomalous Basaltic Meteorite from the Innermost Main Belt. *Science*, 325:1525, Sept. 2009. doi: 10.1126/science. 1174787.

P. A. Bland, P. Spurný, A. W. R. Bevan, K. T. Howard, M. C. Towner, G. K. Benedix, R. C. Greenwood, L. Shrbený, I. A. Franchi, G. Deacon, J. Borovička, Z. Ceplecha, D. Vaughan, and R. M. Hough. The Australian Desert Fireball Network: a new era for planetary science. *Australian Journal of Earth Sciences*, 59:177–187, Mar. 2012. doi: 10.1080/08120099.2011.595428.

J. Borovička. The comparison of two methods of determining meteor trajectories from photographs. *Bulletin of the Astronomical Institutes of Czechoslovakia*, 41: 391–396, Dec. 1990.

J. Borovička, P. Spurný, and P. Brown. *Small Near-Earth Asteroids as a Source of Meteorites*, pages 257–280. University of Arizona Press, 2015. doi: 10.2458/azu_uapress_9780816532131-ch014.

V. A. Bronshten. The physics of meteoritic phenomena. *Moscow Izdatel Nauka*, 1981.

P. Brown, V. Marchenko, D. E. Moser, R. Weryk, and W. Cooke. Meteorites from meteor showers: A case study of the Taurids. *Meteoritics and Planetary Science*, 48:270–288, Feb. 2013. doi: 10.1111/maps.12055.

P. Brown, P. Wiegert, D. Clark, and E. Tagliaferri. Orbital and physical characteristics of meter-scale impactors from airburst observations. Icarus, 266: 96–111, Mar. 2016. doi: 10.1016/j.icarus.2015.11.022.

Z. Ceplecha and R. E. McCrosky. Fireball end heights - A diagnostic for the structure of meteoric material. J. Geophys. Res., 81:6257–6275, Dec. 1976. doi: 10.1029/JB081i035p06257.

S. V. M. Clube and W. M. Napier. The microstructure of terrestrial catastrophism. MNRAS, 211:953–968, Dec. 1984. doi: 10.1093/mnras/211.4.953.

H. A. R. Devillepoix, P. A. Bland, M. C. Towner, M. Cupák, E. K. Sansom, T. Jansen-Sturgeon, R. M. Howie, J. Paxman, and B. A. D. Hartig. Status of the Desert Fireball Network. In A. Roggemans and P. Roggemans, editors, *International Meteor Conference Egmond, the Netherlands, 2-5 June 2016*, pages 60–62, Jan. 2016.

H. A. R. Devillepoix, E. K. Sansom, P. A. Bland, M. C. Towner, M. CupáK, R. M. Howie, T. Jansen-Sturgeon, M. A. Cox, B. A. D. Hartig, G. K. Benedix,

and J. P. Paxman. The Dingle Dell meteorite: A Halloween treat from the Main Belt. *Meteoritics and Planetary Science*, 53:2212–2227, Oct. 2018. doi: 10.1111/maps.13142.

H. A. R. Devillepoix, P. A. Bland, E. K. Sansom, M. C. Towner, M. Cupák, R. M. Howie, B. A. D. Hartig, T. Jansen-Sturgeon, and M. A. Cox. Observation of metre-scale impactors by the Desert Fireball Network. MNRAS, 483:5166–5178, Mar 2019. doi: 10.1093/mnras/sty3442.

J. D. Drummond. A test of comet and meteor shower associations. Icarus, 45: 545–553, Mar. 1981. doi: 10.1016/0019-1035(81)90020-8.

A. Dubietis and R. Arlt. Taurid resonant-swarm encounters from two decades of visual observations. MNRAS, 376:890–894, Apr. 2007. doi: 10.1111/j. 1365-2966.2007.11488.x.

M. P. Fay. Two-sided Exact Tests and Matching Confidence Intervals for Discrete Data. *The R Journal*, 2(1):53–58, 2010.

C. Froeschle and H. Scholl. Gravitational splitting of Quadrantid-like meteor streams in resonance with Jupiter. A&A, 158:259–265, Apr. 1986.

I. Halliday, A. A. Griffin, and A. T. Blackwell. Detailed data for 259 fireballs from the Canadian camera network and inferences concerning the influx of large meteoroids. *Meteoritics and Planetary Science*, 31:185–217, Mar. 1996. doi: 10.1111/j.1945-5100.1996.tb02014.x.

I. Hasegawa. Predictions of the meteor radiant point associated with a comet. PASJ, 42:175–186, Feb. 1990.

R. M. Howie, J. Paxman, P. A. Bland, M. C. Towner, M. Cupák, E. K. Sansom, and H. A. R. Devillepoix. How to build a continental scale fireball camera network. *Experimental Astronomy*, May 2017a. doi: 10.1007/s10686-017-9532-7.

R. M. Howie, J. Paxman, P. A. Bland, M. C. Towner, E. K. Sansom, and H. A. R. Devillepoix. Submillisecond fireball timing using de Bruijn time-codes. *Meteoritics and Planetary Science*, 52:1669–1682, Aug. 2017b. doi: 10.1111/maps.12878.

Z. Ivezic, T. Axelrod, W. N. Brandt, D. L. Burke, C. F. Claver, A. Connolly, K. H. Cook, P. Gee, D. K. Gilmore, S. H. Jacoby, R. L. Jones, S. M. Kahn, J. P. Kantor, V. V. Krabbendam, R. H. Lupton, D. G. Monet, P. A. Pinto, A. Saha, T. L. Schalk, D. P. Schneider, M. A. Strauss, C. W. Stubbs, D. Sweeney, A. Szalay, J. J. Thaler, J. A. Tyson, and LSST Collaboration. Large Synoptic Survey Telescope: From Science Drivers To Reference Design. *Serbian Astronomical Journal*, 176:1–13, June 2008. doi: 10.2298/SAJ0876001I.

P. Jenniskens. *Meteor Showers and Their Parent Comets*. Cambridge University Press, 2006. ISBN 9780521853491.

P. Jenniskens, P. S. Gural, L. Dynneson, B. J. Grigsby, K. E. Newman, M. Borden, M. Koop, and D. Holman. CAMS: Cameras for Allsky Meteor Surveillance to establish minor meteor showers. Icarus, 216:40–61, Nov. 2011. doi: 10.1016/j.icarus.2011.08.012.

P. Jenniskens, Q. Nénon, J. Albers, P. S. Gural, B. Haberman, D. Holman, R. Morales, B. J. Grigsby, D. Samuels, and C. Johannink. The established meteor showers as observed by CAMS. Icarus, 266:331–354, Mar. 2016a. doi: 10.1016/j.icarus.2015.09.013.

P. Jenniskens, Q. Nénon, P. S. Gural, J. Albers, B. Haberman, B. Johnson, D. Holman, R. Morales, B. J. Grigsby, D. Samuels, and C. Johannink. CAMS confirmation of previously reported meteor showers. Icarus, 266:355–370, Mar. 2016b. doi: 10.1016/j.icarus.2015.08.014.

P. Jenniskens, Q. Nénon, P. S. Gural, J. Albers, B. Haberman, B. Johnson, R. Morales, B. J. Grigsby, D. Samuels, and C. Johannink. CAMS newly detected meteor showers and the sporadic background. Icarus, 266:384–409, Mar. 2016c. doi: 10.1016/j.icarus.2015.11.009.

J. M. Madiedo, J. L. Ortiz, J. M. Trigo-Rodríguez, J. Dergham, A. J. Castro-Tirado, J. Cabrera-Caño, and P. Pujols. Analysis of bright Taurid fireballs and their ability to produce meteorites. Icarus, 231:356–364, Mar. 2014. doi: 10.1016/j.icarus.2013.12.025.

L. Neslusan, J. Svoren, and V. Porubcan. A computer program for calculation of a theoretical meteor-stream radiant. A&A, 331:411–413, Mar. 1998.

A. Olech, P. Żołądek, M. Wiśniewski, R. Rudawska, M. Bęben, T. Krzyżanowski, M. Myszkiewicz, M. Stolarz, M. Gawroński, M. Gozdalski, T. Suchodolski, W. Węgrzyk, and Z. Tymiński. 2015 Southern Taurid fireballs and asteroids 2005 UR and 2005 TF50. MNRAS, 461:674–683, Sept. 2016. doi: 10.1093/mnras/stw1261.

A. Olech, P. Żołądek, M. Wiśniewski, Z. Tymiński, M. Stolarz, M. Bęben, D. Dorosz, T. Fajfer, K. Fietkiewicz, M. Gawroński, M. Gozdalski, M. Kałużny, M. Krasnowski, H. Krygiel, T. Krzyżanowski, M. Kwinta, T. Łojek, M. Maciejewski, S. Miernicki, M. Myszkiewicz, P. Nowak, K. Polak, K. Polakowski, J. Laskowski, M. Szlagor, G. Tissler, T. Suchodolski, W. Węgrzyk, P. Woźniak, and P. Zaręba. Enhanced activity of the Southern Taurids in 2005 and 2015. MNRAS, 469:2077–2088, Aug. 2017. doi: 10.1093/mnras/stx716.

J. M. Picone, A. E. Hedin, D. P. Drob, and A. C. Aikin. NRLMSISE-00 empirical model of the atmosphere: Statistical comparisons and scientific issues. *Journal of Geophysical Research (Space Physics)*, 107:1468, Dec. 2002. doi: 10.1029/2002JA009430.

M. Popescu, M. Birlan, D. A. Nedelcu, J. Vaubaillon, and C. P. Cristescu. Spectral properties of the largest asteroids associated with Taurid Complex. A&A, 572:A106, Dec. 2014. doi: 10.1051/0004-6361/201424064.

E. K. Sansom, P. Bland, J. Paxman, and M. Towner. A novel approach to fireball modeling: The observable and the calculated. *Meteoritics and Planetary Science*, 50:1423–1435, Aug. 2015. doi: 10.1111/maps.12478.

E. K. Sansom, P. A. Bland, M. G. Rutten, J. Paxman, and M. C. Towner. Filtering Meteoroid Flights Using Multiple Unscented Kalman Filters. AJ, 152:148, Nov. 2016. doi: 10.3847/0004-6256/152/5/148.

E. K. Sansom, M. G. Rutten, and P. A. Bland. Analyzing Meteoroid Flights Using Particle Filters. AJ, 153:87, Feb. 2017. doi: 10.3847/1538-3881/153/2/87.

L. Shrbený and P. Spurný. Precise Data on Photographic Fireballs Belonging to the Taurid Complex Observed within Czech Fireball Network. In *Asteroids, Comets, Meteors 2012*, volume 1667 of *LPI Contributions*, page 6436, May 2012.

R. H. Soja, W. J. Baggaley, P. Brown, and D. P. Hamilton. Dynamical resonant structures in meteoroid stream orbits. MNRAS, 414:1059–1076, June 2011. doi: 10.1111/j.1365-2966.2011.18442.x.

SonotaCo. A meteor shower catalog based on video observations in 2007-2008. *WGN, Journal of the International Meteor Organization*, 37:55–62, Apr. 2009.

P. Spurný. Exceptional fireballs photographed in central Europe during the period 1993-1996. Planet. Space Sci., 45:541–555, May 1997. doi: 10.1016/S0032-0633(97)00006-8.

P. Spurný, P. A. Bland, L. Shrbený, M. C. Towner, J. Borovička, A. W. R. Bevan, and D. Vaughan. The Mason Gully Meteorite Fall in SW Australia: Fireball Trajectory and Orbit from Photographic Records. *Meteoritics and Planetary Science Supplement*, 74:5101, Sept. 2011.

P. Spurný, J. Borovička, H. Mucke, and J. Svoreň. Discovery of a new branch of the Taurid meteoroid stream as a real source of potentially hazardous bodies. A&A, 605:A68, Sept. 2017. doi: 10.1051/0004-6361/201730787.

M. Towner and et al. Fireball streak detection with minimal CPU processing requirements for the Desert Fireball Network data processing pipeline. *PASA*, submitted.

C. Tubiana, C. Snodgrass, R. Michelsen, H. Haack, H. Böhnhardt, A. Fitzsimmons, and I. P. Williams. 2P/Encke, the Taurid complex NEOs and the Maribo and Sutter's Mill meteorites. A&A, 584:A97, Dec. 2015. doi: 10.1051/0004-6361/201425512.

F. Whipple. *Photographic Meteor Studies, III. The Taurid Shower*. Harvard reprint. Astronomical Observatory of Harvard College, 1940.

F. L. Whipple and S. El-Din Hamid. On the Origin of the Taurid Meteor Streams. *Helwan Institute of Astronomy and Geophysics Bulletins*, 41:3–30, 1952.

CHAPTER 6

THESIS CONCLUSIONS AND FUTURE WORK

The goal of this doctoral thesis was to make fireball data reduction more automated, and to explore the first science applications of the Desert Fireball Network.

The first task that was undertaken was building an automated data reduction pipeline from scratch (Chapter 2), handling 5 terabytes of images per night, turning them into scientifically usable data. This includes developing some of the core methods like the astrometric calibration, but also coordinating a team of 5 people also contributing to the project, as well as managing the development cycle associated with software operations in production. With the Global Fireball Observatory collaboration, expected to cover 2% of the Earth by 2020, the use of the software is about to be scaled several times.

The data reduction processes were successfully applied to the Creston, Murrili, and Dingle Dell (Chapter 4) meteorite fireballs. This in a way validates that the methods developed work.

Chapter 3 deals with metre-scale impactors, comparing ground-based ob-

servations of some these events with space borne sensors. Although the observations from orbit have a much larger collecting area, there are some accuracy issues with the data. This makes a coordinated ground-based effort even more relevant, as the Global Fireball Observatory is expected to observe one of these events per year on average.

Chapter 5 reports an unusual large number of Taurids fireball detections in 2015. Combining data with the CAMS meteor network as well as orbital sensors, covering 10 orders of magnitude in mass, this work revealed that the #628 branch of the Southern Taurids is a major contributor of cometary impactors up to at least metre-scale, a size range that is typically not represented in meteor showers.

In its next generation of observatories — tailored for the Global Fireball Observatory — the DFN is adding digital video cameras in parallel to the long-exposure high resolution imagers. This will notably allow daytime observation of very bright fireballs to be possible. A multispectral radiometer is also being developed, and will provide detailed fireballs light curves. The data reduction pipeline will need to be updated in order to fuse the data from these additional instruments together. Thanks to their Bayesian nature, the filtering methods that determine physical and dynamical entry parameters are naturally suited to accepting additional observations (Sec. 2.2.6).

Each new fresh ordinary chondrite recovered is a clue to understanding recent collisions in the asteroid main belt, while a sample of any other type of meteorite has the potential to be a game changer in our understanding of Solar System formation. As the DFN instrument's ability to recover meteorites is limited by the person time required to search for meteorites, the automation of this process using aerial sensors and sophisticated detection algorithms is a priority.

Future work will also include clear sky survey calculations, as described

in Sec. 2.6. The DFN is in a unique place to put strong constraints on the flux density of $10^1 - 10^4$ kg objects on Earth, a size range that is too small for telescopic survey but that requires a very large collecting area to get statistically significant numbers.

APPENDIX A

FIRST AUTHOR JOURNAL PUBLICATION REPRINTS

PAPER 1 – OBSERVATION OF METRE-SCALE IMPACTORS BY THE DESERT FIREBALL NETWORK

Hadrien A. R. Devillepoix, *Philip A. Bland, Eleanor K. Sansom, Martin C. Towner, Martin Cupák, Robert M. Howie, Benjamin A. D. Hartig, Trent Jansen-Sturgeon, Morgan A. Cox*

Statement of Authorship

Title of Paper: Observation of metre-scale impactors by the Desert Fireball Network.

Publication Status: Re-submitted to the Monthly Notices of the Royal Astronomical Society, after minor corrections following the review process.

Author Contributions

By signing the Statement of Authorship, each author certifies that their stated contribution to the publication is accurate and that permission is granted for the publication to be included in the candidate's thesis.

Name of Principal Author: Hadrien A. R. Devillepoix

Contribution to the Paper: Led the discussion. Contributed to astrometric, photometric, trajectory, and orbital analysis for both DFN and USG sensor data. Drafted and revised the manuscript for this publication.

Overall Percentage: 90%

Signature: *Date:*

Sept 19, 2018

Name of Co-Author: Philip A. Bland

Contribution to the Paper: Assisted with editing and revision of the manuscript.

Overall Percentage: 1%

Signature: *Date:*

Sept 19, 2018

Name of Co-Author: Eleanor K. Sansom

Contribution to the Paper: Contributed to mass and velocity modelling, and assisted with editing and revision of the manuscript.

Overall Percentage: 3%

Signature: *Date:*

Sept 19, 2018

Name of Co-Author: Martin C. Towner

Contribution to the Paper: Assisted with editing and revision of the manuscript.

Overall Percentage: 1%

Signature: *Date:*

Sept 19, 2018

Name of Co-Author: Martin Cupák

Contribution to the Paper: Assisted with editing and revision of the manuscript.

Overall Percentage: 1%

Signature: *Date:*

                                                                Sept 19, 2018

Name of Co-Author: Robert M. Howie

Contribution to the Paper: Assisted with editing and revision of the manuscript.

Overall Percentage: 1%

Signature: *Date:*

                                                                Sept 20, 2018

Name of Co-Author: Benjamin A. D. Hartig

Contribution to the Paper: Assisted with editing and revision of the manuscript.

Overall Percentage: 1%

Signature: *Date:*

                                                                Sept 19, 2018

Name of Co-Author: Trent Jansen-Sturgeon

Contribution to the Paper: Assisted with editing and revision of the manuscript.

Overall Percentage: 1%

Signature: *Date:*

Sept 19, 2018

Name of Co-Author: Morgan A. Cox

Contribution to the Paper: Assisted with editing and revision of the manuscript.

Overall Percentage: 1%

Signature: *Date:*

Sept 19, 2018

Observation of metre-scale impactors by the Desert Fireball Network

H. A. R. Devillepoix [ORCID],[*] P. A. Bland, E. K. Sansom, M. C. Towner, M. Cupák,
R. M. Howie, B. A. D. Hartig, T. Jansen-Sturgeon and M. A. Cox

School of Earth and Planetary Sciences, Curtin University, GPO Box U1987, Perth WA 6845, Australia

ABSTRACT

The Earth is impacted by 35–40 metre-scale objects every year. These meteoroids are the low-mass end of impactors that can do damage on the ground. Despite this they are very poorly surveyed and characterized, too infrequent for ground-based fireball observation efforts, and too small to be efficiently detected by NEO telescopic surveys whilst still in interplanetary space. We want to evaluate the suitability of different instruments for characterizing metre-scale impactors and where they come from. We use data collected over the first 3 yr of operation of the continent-scale Desert Fireball Network, and compare results with other published results as well as orbital sensors. We find that although the orbital sensors have the advantage of using the entire planet as collecting area, there are several serious problems with the accuracy of the data, notably the reported velocity vector, which is key to getting an accurate pre-impact orbit and calculating meteorite fall positions. We also outline dynamic range issues that fireball networks face when observing large meteoroid entries.

Key words: meteorites, meteors, meteoroids – minor planets, asteroids: general.

1 INTRODUCTION

The Earth is impacted by 35–40 metre-scale objects every year (Brown et al. 2002; Bland & Artemieva 2006). These large meteoroids are at the low-mass end of potentially damage-causing impacting asteroids like Chelyabinsk (Brown et al. 2013). The study of the atmospheric behaviour, physical nature, numbers, and dynamical origin of these objects is therefore important in order to assess the hazard they pose, and prepare an appropriate response should an asteroid be detected and determined to be on a collision course with Earth.

1.1 How frequently do these impacts happen?

One of the ways the size frequency distribution (SFD) of metre-scale has been surveyed is by using the so-called US Government (USG) sensors,[1] which are able to detect flashes all around the world, day and night, measure flash energy, and sometimes derive velocities and airburst heights. As outlined by Brown et al. (2013), there might be subtleties in the SFD, namely a larger number of 10–50 m objects. Indeed the 1–100 m size range is largely unobserved, with objects too small for telescopes and too infrequent for impact monitoring systems to get representative surveys. So far, there have been three cases of asteroids detected before atmospheric impact. These are

asteroids 2008 TC3 (Jenniskens et al. 2009; Farnocchia et al. 2017), 2014 AA (Farnocchia et al. 2016), and 2018 LA, all discovered by the Catalina Sky Survey only hours before impact. As large deep surveyors like LSST (Ivezic et al. 2008) come online these types of detections are going to become more common, and predicting the consequences of these impacts is going to be desirable. While the impact location of 2008 TC3 was well constrained to sub kilometre precision thanks to a very large number ($\simeq$900) of astrometric measurements, the prediction for 2014 AA was much more uncertain and covered a large area of the Atlantic ocean, as only a total of seven astrometric positions were available. The impact location of 2018 LA was very uncertain, until two extra observation by the Asteroid Terrestrial-impact Last Alert System (ATLAS) increased the observation arc length from 1.3 to 3.7 h, which narrowed down the impact location to South Africa. The number of astrometric observations and the length of the observation arc are therefore a critical factors to precisely determining the impact point. Well coordinated, large follow-up networks of telescopes can provide large numbers of such observations and will aid in future impact predictions (Lister et al. 2016).

1.2 How dangerous are these impacts?

The damage from an impact depends not only on dynamical parameters, but also on: size, rock type, structure, strength (s), and density (ρ). To illustrate this, we can use the equations of Collins, Melosh & Marcus (2005) to simulate the outcome of the impact of a 2 m object, with an entry angle of 18°, a velocity of 19 km s^{-1} at the top

of the atmosphere (same entry angle and velocity as Chelyabinsk), and various bulk strengths and densities corresponding to different classes of objects (from Chyba, Thomas & Zahnle 1993):

(i) a weak cometary body ($s = 10^5$ Pa, $\rho = 1000$ kg m^{-3}) will breakup at a high altitude (60 km), causing no significant direct damage because the predicted 0.18 kT TNT of energy released cannot be transferred efficiently to the ground due to the thin atmosphere (1 kT TNT $= 4.184 \times 10^{12}$ J).

(ii) a chondritic body ($s = 10^7$ Pa, $\rho = 3500$ kg m^{-3}) is likely going to airburst at relatively low altitudes (the model predicts an airburst at 27 km), releasing around 0.44 kT TNT of energy that can be propagated more efficiently by the denser atmosphere.

(iii) an iron ($s = 10^8$ Pa, $\rho = 7900$ kg m^{-3}) monolith will reach the surface at hypersonic velocity (3.8 km s^{-1}), causing important but very localized damage, as it only yields 10^{-1} kT TNT.

This is a simplistic example, but it shows how much the response to an imminent asteroid impact depends on both physical and dynamical characteristics of the impactor.

Several observation techniques can be levied while the asteroid is still in interplanetary space:

(i) Multiband photometry in Vis-NIR: size and rotation period, and lower constraint on cohesive strength as a consequence.

(ii) Spectroscopy: likely composition.

(iii) Astrometric observations: pre-encounter orbit, and predictions about the impact geometry, velocity, and location.

(iv) Radar observations: size, shape, rotation period, presence of satellites.

While the size and impacting velocity are well constrained factors using astrometric observations, determining the rock type and structure from remote sensing instruments is more challenging.

To some extent spectroscopy can provide insights on the mineralogy of the impactor, but this technique requires a good knowledge of how asteroid spectral types match meteorite types.

Another approach is the work of Mommert et al. (2014a, b) on small (metre-scale) asteroids for which spectroscopic work is generally impractical. They used a thermophysical model combined with an orbital model that takes non-gravitational forces into accounts. This model derives physical parameters (likely surface composition, size) by combining both astrometric observations and near-infrared photometry.

In order to be reliable on large scales, these techniques have to be qualified with direct sample analysis. This active area of research can be tackled in two ways: either direct sample return missions (like Stardust, Hayabusa, Hayabusa 2, OSIRIS-REx), or from a large number of meteorite recoveries with associated orbits that can link to asteroid families: the aim of ground-based efforts like the Desert Fireball Network (DFN).

The DFN is a fireball camera network currently operating in the Australian outback, designed for the detection and recovery of meteorite falls with associated orbits. Currently 52 observatories are deployed. On 2015 January 2, a particularly bright fireball was observed over South Australia, large enough to be simultaneously detected by the US government (USG) sensors, and by the DFN, which had just started science operation 2 months before. Another similarly bright event, also observed by both the DFN and the USG sensors, happened on 2017 June 30 over South Australia.

Over the 3 million km^2 that the DFN covers in Australia, the observation of a metre-scale impactor is only expected to happen once every 4–5 yr (Brown et al. 2002), and once every 8–10 yr

during night time when most dedicated fireball networks operate (without considering clear sky conditions). The observation of two such events during the first 3 yr of operation of the DFN, although outside the nominal collecting area, is somewhat lucky with respect to the size frequency distribution numbers of Brown et al. (2002). These two superbolides are described here and add to the small list of metre-scale impactors that have precisely determined trajectories:

(i) 13 events compiled and discussed by Brown et al. (2016).

(ii) the 'Romanian' bolide (Borovička et al. 2017).

(iii) the Dishchii'bikoh meteorite, for which initial trajectory details have been reported by Palotai et al. (2018).

(iv) the meteorite fall near Crawford Bay in British Columbia (Canada), for which initial trajectory details have been reported by Hildebrand et al. (2018).

1.3 Where do they come from?

The current state of the art for source region model for Near-Earth Objects (NEO) is detailed by Granvik et al. (2018). They report a significant size dependence of NEO origins, which had not been investigated by earlier similar works (Bottke et al. 2002; Binzel et al. 2004; Greenstreet, Ngo & Gladman 2012). Their work covers the absolute magnitude range $17 < H < 25$ (corresponds to diameter $1200 > D > 30$ m with an S-type albedo of 0.2), providing little insight on the metre-size region ($H = 32$).

Several outstanding issues show that it is not possible to simply interpolate the characteristics of the population of typical macroscopic meteorite dropper meteoroids (decimetre-scale) and the kilometre-scale well surveyed by telescopes. For instance, LL chondrites make up 8 per cent of meteorite falls, but it is generally thought that 1/3rd of observable near-Earth small body space is made up of LL compatible asteroids (Vernazza et al. 2008). Granvik et al. (2016) show that an unmodelled destructive effect prevents small bodies from stably populating the low perihelion region, further outlying the need to consider body size in the dynamical models.

Brown et al. (2016) are the first to perform a source region analysis on metre-class NEO bodies, using the Bottke et al. (2002) model on USG events. Considering the small number statistics they get intermediate source regions proportion that are comparable to previous works on kilometre-size NEO population (Bottke et al. 2002; Binzel et al. 2004; Greenstreet et al. 2012). However they also argue for a Halley-type comet (HTC) source region, comparable in importance to the Jupiter-family comets (JFC) source. This source has not been identified previously in NEO works, because of a near-complete lack of such objects in asteroid data bases. Their argument is based on three fireball events in the USG data set that have a Tisserand parameter with Jupiter, $T_J < 2$: identified as *20150102-133919*, *20150107-010559*, and *20150311-061859*, not associated with a meteor shower. Because the first two of these events have independently estimated trajectories, an issue that we are interested in is determining if this surprising outcome could be the results of limitations of USG data.

This work aims to compile independent information not just for these cases, but for several other metre-scale bodies, to determine the reliability of USG data in general, for population study, orbit determination, as well as undertaking meteorite searches based on these data. We also evaluate the suitability of hardware currently deployed by fireball networks to observe these particularly bright events.

5168 *H. A. R. Devillepoix et al.*

2 DATA AND METHODS

2.1 DFN

The DFN is the world's biggest fireball observation facility (3 million km^2 coverage), set-up in a desert environment where meteorites are more likely to be successfully recovered. The DFN is built to overcome the challenges of operating a distributed network of high technology devices in a harsh remote environment. The observatories operate completely autonomously for up to two years before maintenance is required: swapping the hard drives and replacing the mechanical shutter in the off-the-shelf camera. The systems can operate with network connectivity for event notifications, or completely offline. Due to their low power usage, simple solar photovoltaic systems ($\approx$160–240 W of solar panels) with 12 V deep-cycle lead acid battery storage are used to power most of the observatories across the network.

The main imaging system consists of a high-resolution digital camera and a fisheye all-sky lens, taking long exposures with shutter breaks embedded by the GNSS synchronized operation of a liquid crystal shutter. This mode of imaging has historically been the most successful method for determining positions of fallen meteorites from fireball observation, as shown in the compilation of Borovička, Spurný & Brown (2015). The DFN has recovered three meteorites in the first 3 yr of operation (Devillepoix et al. 2018). The automated observatories are more completely described by Howie et al. (2017a), and the encoding method used to record absolute and relative timing (to derive velocity information) is detailed by Howie et al. (2017b).

In 2017 June, the DFN initiated a firmware upgrade across the network to change the time encoding technique on the observatories' microcontroller. These were deployed to all online cameras remotely. The main new feature of this update was a new mode of operation for the liquid crystal shutter, different from the one described by Howie et al. (2017b). This new mode retained the absolute timing encoding through the use of a de Bruijn sequence, but made the pulses much shorter and equal in duration, replacing the 60 ms long dash with two 10 ms pulses and the short 20 ms dash into a single 10 ms pulse, in order to reduce saturation issues on bright fireballs, and make automated centroid determination easier. In Tables 2 and 5 we refer to this new method as pulse-frequency (PF), as opposed to the pulse-width (PW) method of Howie et al. (2017b).

Standard data reductions methods are detailed by Devillepoix et al. (2018). The DFN is optimized to observe macroscopic meteorite dropping events at the low-mass end. The observatories are sensitive to apparent magnitude 0, in order observe a small ($\sim$5 cm) meteoroid high enough before significant atmospheric deceleration happens, to derive a precise orbit. But they can also astrometrically observe the brightest phases of ablation of a half-metre size rock (magnitude 15), albeit with saturating the sensor.

Thanks to the large number of stars imaged by the long exposure, the cameras typically achieve their nominal arcmin astrometric precision down to 5° elevations above the horizon (Devillepoix et al. 2018). Typical kilogram scale meteorites usually ablate down to $\sim$20 km height, therefore the network is spaced in order to have three camera observation down to this height, which roughly corresponds to a 200 km slant range. Outside of these ideal observation conditions, fireballs are accurately imaged in the high-altitude phase of the flight (useful for orbital calculations), but getting precise meteorite fall positions becomes more difficult due to decreased astrometric precision.

Fireball trajectories are calculated using a modified version of the least-square method of Borovička (1990), and fireball dynamics are analysed using the methods of Sansom et al. (2015) and Gritsevich et al. (2017). Pre-encounter orbits are determined using numerical integration, as described by Jansen-Sturgeon, Sansom & Bland (2018).

The DFN observatories were designed with a low-resolution video system in parallel of the high-resolution still imager, initially as absolute timing device, but later kept on some systems for future daytime observations. These data are too low resolution to provide useful astrometric data, although they can be helpful in getting high temporal resolution photometric data. However the sensor gets saturated when the fireball gets brighter than $m_V = -5$, and the autogain on the cameras can only attenuate the signal by a factor of about four stellar magnitudes. Large fireballs still saturate the sensor, however Devillepoix et al. (2018) have successfully used the sum of all pixels in each field as a proxy for all sky brightness. This method is particularly successful at detecting large fragmentation events. The effect of autogain are corrected by performing traditional photometry on a non-saturated bright star, planet, or fixed light in the field of view. Unfortunately because of the lossy compression of the record and the sensor saturation, it is not possible to get a satisfying absolutely calibrated photometry from the video, and therefore the resulting light curve is only used qualitatively.

2.2 USG sensors

Large fireballs detected by the so-called 'USG sensors' are reported on the JPL website.[2] These sensors are apparently able to detect flashes all around the world, day and night, measure flash energy, and sometimes derive velocities and airburst heights. These data were used for size-frequency studies of metre-scale objects by Brown et al. (2002), and later to derive orbital and physical properties of this population (Brown et al. 2016).

In Table 1 we give the data for the subset of events for which all the parameters are reported (time, energy, location, velocity), and for which independent observations have been published (references in Table 7). The USG sensors data do not come with uncertainties, therefore we assume the last significant figure represents the precision of the measurement.

We calculate the radiant and pre-entry orbits for these meteoroids, based on USG data, using the numerical method of Jansen-Sturgeon et al. (2018). The various numbers reported in USG data relate to the instant of peak brightness, typically quite deep into the atmosphere. Since we are dealing with metre-scale bodies, we ignore deceleration due to the atmosphere and use a purely gravitational model from that point for calculating the orbit.

The online table converts the total radiated energy measured into an equivalent impact energy using an empirical relation determined by Brown et al. (2002). This total energy estimate, combined with the impacting speed, can be used to derive a photometric mass using the classical kinetic energy relation ($E = \frac{1}{2}mv^2$), and a rough size assuming a density. Only $>= 0.1$ kT TNT impacts are reported by the USG,[3] which roughly corresponds to a 1 m diameter object at typical impact speeds on Earth.

---

[2]https://cneos.jpl.nasa.gov/fireballs/accessed 2017 November 22.
[3]Johnson L. (2017) – SBAG meeting: https://www.lpi.usra.edu/sbag/meetings/jan2017/presentations/Johnson.pdf and remarks at 32 m and answer

Table 1. USG sensors fireball events that have reported velocities, and have been observed independently. Left of the table is from https://cneos.jpl.nasa.gov/fireballs/(accessed 2017 November 22). Apparent radiants and orbits have been calculated (angles are equinox J2000). The number of decimals is not representative of uncertainty. A similar work has been done by Brown et al. (2016) on the six older events in the list, in agreement. Corresponding ground-based observation details of the two highlighted events are presented in this work, references for the other events are in Table 7.

Peak brightness Date/Time UT	H km	V km s⁻¹	V_x km s⁻¹	V_y km s⁻¹	V_z ECEF	Radiated E. J	Impact E. KT TNT	Latitude °N+	Longitude °E+	α_{inf} °	δ_{inf} °	a au	e	i °	ω °	Ω °
2018-06-02 16:44:12	28.7	16.9	0.9	−16.4	3.9	3.8e+11	0.98	−21.2	23.3	235.0	−13.3	1.33	0.42	4.4	258.3	71.88
2017-09-05 05:11:27	36.0	14.7	12.7	−6.1	−4.2	3.8e+10	0.13	49.3	243.1	216.5	16.7	2.06	0.54	3.4	147.2	162.69
2017-06-30 14:26:45	20.0	15.2	10.9	−9.7	4.2	9.4e+10	0.29	−34.3	134.5	273.6	−16.1	1.24	0.35	3.6	259.7	98.80
2015-01-07 01:05:59	45.5	35.7	−35.4	1.8	−4.4	1.4e+11	0.4	45.7	26.9	119.7	7.1	4.78	0.93	20.7	111.9	106.19
2015-01-02 13:39:19	38.1	18.1	4.5	−14.4	−10.0	2.0e+10	0.073	−31.1	140.0	53.8	33.5	9.33	0.90	8.0	207.4	281.61
2013-02-15 03:20:33	23.3	18.6	12.8	−13.3	−2.4	3.8e+14	440.0	54.8	61.1	329.2	7.3	1.71	0.56	4.1	109.7	326.46
2010-02-28 22:24:50	37.0	15.1	−11.7	2.7	−9.1	1.5e+11	0.44	48.7	21.0	121.7	37.2	2.70	0.65	3.2	204.0	340.14
2008-11-21 00:26:44	28.2	12.9	3.9	−4.1	−11.6	1.4e+11	0.41	53.1	250.1	200.6	64.0	0.79	0.26	10.4	3.1	239.04
2008-10-07 02:45:45	38.9	13.3	−9.0	9.0	3.8	4.0e+11	1.0	20.9	31.4	12.4	−16.7	1.65	0.43	3.9	36.2	14.16

3 RESULTS

In this section we analyse in detail the atmospheric entry of two large meteoroids as observed by the DFN, these were also observed by the USG sensors (highlighted rows in Table 1).

3.1 DN150102_01 – Kalabity

On 2015 January 2 a bright bolide lit up the skies over lake Frome in South Australia (Fig. 1), starting at 2015-01-02T13:39:11.086 UTC (9 min after midnight ACDT) for 10.54 s. In early 2015 the DFN had just finished its initial expansion phase in South Australia with 16 cameras, unfortunately the bolide happened outside the standard network covering area at that time. Therefore a combination of cameras mostly over 300 km from the event had to be used to determine the trajectory (Table 2). The best convergence angle is 22° (between Gum Glen and William Creek). The convergence angle between the Billa Kalina and Ingomar stations is less than 1°, therefore the latter distant viewpoint does not help much in constraining the trajectory. The trajectory follows a relatively shallow slope of 20° to the horizon, visible on the images from 83.3 km altitude. Astrometric uncertainties vary between 1.5–3 arcmin (equates to 130–260 m once projected at 300 km). These are obtained by compounding astrometric calibration uncertainties (typically 1 arcmin) and fireball picking uncertainties (usually 0.5–1 pixel, depending on optics quality and fireball brightness). Most of the residuals to the straight line fit (Fig. 2) are then in agreement with astrometric uncertainties. As expected from an unconstrained astrometric solution under 5° elevation, the observation residuals to the straight line fit start diverging for observations below this elevation, this is visible on around the 52 km altitude mark on the Ingomar and William Creek viewpoints.

The all-sky light curves display early fragmentation events under 0.05 and 0.08 MPa and (peaks A and B in Fig. 3). The following part of the light curve is uneventful until the body encounters an order of magnitude higher dynamic pressures that eventually almost entirely destroys it (peaks C to G in Fig. 3). This adds to the list of large meteoroids (Popova et al. 2011) that undergo fragmentation under pressures several orders of magnitude smaller than the surviving material tensile strength on the ground, or pressures required to destroy the body in our case.

We note that the time reported by the USG sensor (2015-01-02T13:39:19 UTC) is in good agreement with the brightest peak (E) in our light curve determined to be 0.6 s later (Fig. 3 and Table 3). However the reported altitude is 38 km. This does not correspond to our brightest peak E at 40.2 km, but rather to the end of the very bright phase (peak G).

Only six shutter breaks are resolvable on the image after the explosion on the Billa Kalina image, all <4° on the horizon. Using the particle filter method of Sansom, Rutten & Bland (2017) on these data, we find that the main mass at this stage was only a couple of kilograms at the most. We are only able to track down to 33.4 km at 8.4 km s⁻¹. We suspect that this main mass is not visible down to ablation speed limit (≃3km s⁻¹), because of a sensitivity issue: at this stage the meteoroid is at a large distance from the observatory (>360 km), observed on an extreme elevation angle (≃ 3.5°), and the sky background is unusually bright because of the light from the main explosions (peaks E–G) raising the background. We suspect the reason this feature is not visible on the closer Gum

to questions at 56 m in online talk: https://ac.arc.nasa.gov/p98hreesxa9/, accessed August 24, 2018.
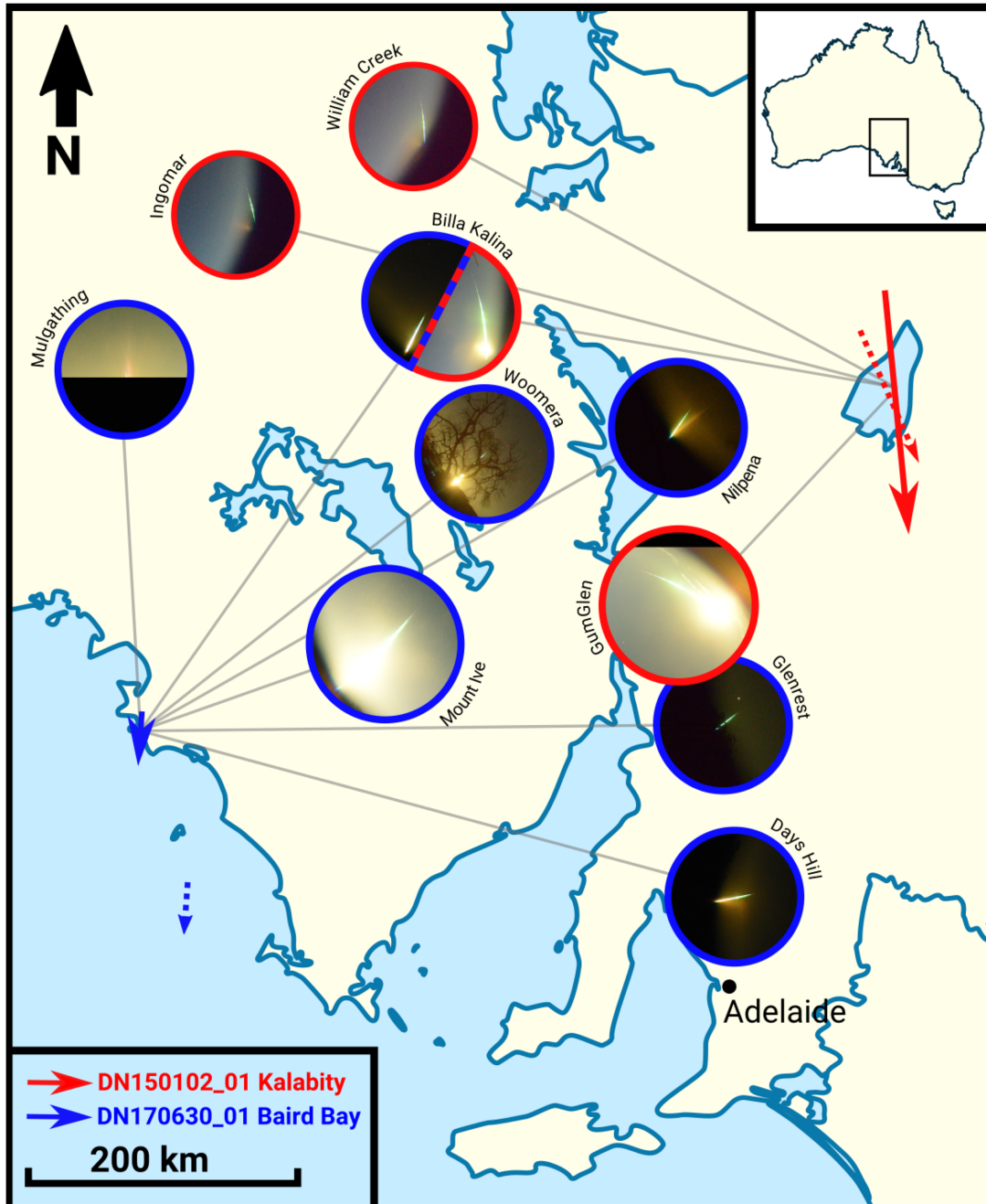
5170   *H. A. R. Devillepoix et al.*

Figure 1. Cropped all-sky images of the fireballs from the DFN observatories. Images are of the same pixel scale with the centre of each image positioned at the observatory location on the map. For the Kalabity fireball (red arrow, East), light from the main explosion is particularly scattered in the Gum Glen image because of clouds. For the Baird Bay event (blue arrow, West), the Mulgathing image is cropped because the sensor is not large enough to accommodate the full image circle on its short side. The fireball on the Woomera picture was partially masked by a tree. The O'Malley station only recorded video and is missing in this map, details are given in Table 5. The dashed arrows show the USG sensors trajectory solutions for both events (vectors are generated by backtracking the state vector at the time of peak brightness to $t - 5$ s).

Table 2. Locations and nature of instrumental records DN150102_01. P: Photographic record (long exposure high-resolution image), V: compressed PAL video (25 frames per second). PW designates the de Bruijn encoding method, as described in Section 2.1. Ranges are from the fireball at 70 km altitude. Photographic imaging system was out of order for Nilpena.

Observatory	Instruments	Latitude	Longitude	Altitude (m)	Range (km)
Gum Glen – DFNSMALL25	P_{PW}, V	32.20554 S	138.24121 E	242	246
Billa Kalina – DFNSMALL26	P_{PW}	30.23769 S	136.51565 E	114	328
William Creek – DFNSMALL30	P_{PW}	28.91566 S	136.33495 E	79	392
Ingomar – DFNSMALL27	P_{PW}	29.58556 S	135.03865 E	197	480
Nilpena – DFNSMALL42	V	31.02331 S	138.23256 E	112	175

Figure 2. Cross-track residuals of the straight line least squares fit to the trajectory from each view point. These distances correspond to astrometric residuals projected on a perpendicular plane to the line of sight, positive when the line of sight falls above the trajectory solution. The distances in the legend correspond to the observation range [highest point–lowest point]. The Ingomar and William Creek observation residuals start diverging after 52 km altitude, this corresponds to observation elevation angles of about 4° and 5°, respectively.

Glen image is because of the presence of clouds in the direction of the fireball, which efficiently scattered the light from the explosion and subsequently saturated the sensor on a much larger area than for Billa Kalina.

The particle filter method of Sansom et al. (2017) can also be used to put a lower bound on the initial mass of the meteoroid. The near lack of deceleration before the main explosion implies that the mass to cross-section area ratio was large. Using reasonable assumptions on shape (spherical), and density ($\rho = 3500$ kg m^{-3}, chondiric), we find that the meteoroid was >2600 kg (>1.1 m) before impact. We note that this assumes that the meteoroid is a single ablating body before the airbursts (peaks E–G). We know this assumption not to be well founded because some fragmentation happened early on (peaks A and B in Fig. 3), explaining why this number is given as a lower limit.

Using the velocity calculated at the brightest instant on DFN data (peak E in Table 3), and the impact energy measured by the USG sensors (Table 1), we derive a 3400 kg mass for this meteoroid, roughly equivalent to a 1.2 m diameter body, larger than the

Brown et al. (2016) estimate because of a different impact speed used.

The DFN dynamic initial size (>1.1 m) is in good agreement with the USG photometric mass (1.2 m).

The orbit of Kalabity is a typical main belt one with a semimajor axis of 1.80 au (Table 4 and Fig. 4), very different from the HTC type orbit derived from USG data (Table 1).

3.2 DN170630_01 – Baird bay

The Baird Bay meteoroid entered the atmosphere on a very steep trajectory (72° to the horizon), on a trajectory that starts over land in Sceale Bay, and ended in the Southern Ocean ∼10 km West of the Carca Peninsula (Fig. 1). The bolide was visible from 2017-06-30T14:26:41.50 UTC (3 min before midnight ACST) for 5.46 s on the DFN camera systems (Table 5). Several eye witnesses reported the bolide, notably from Adelaide, the closest densely populated area, 450 km away.
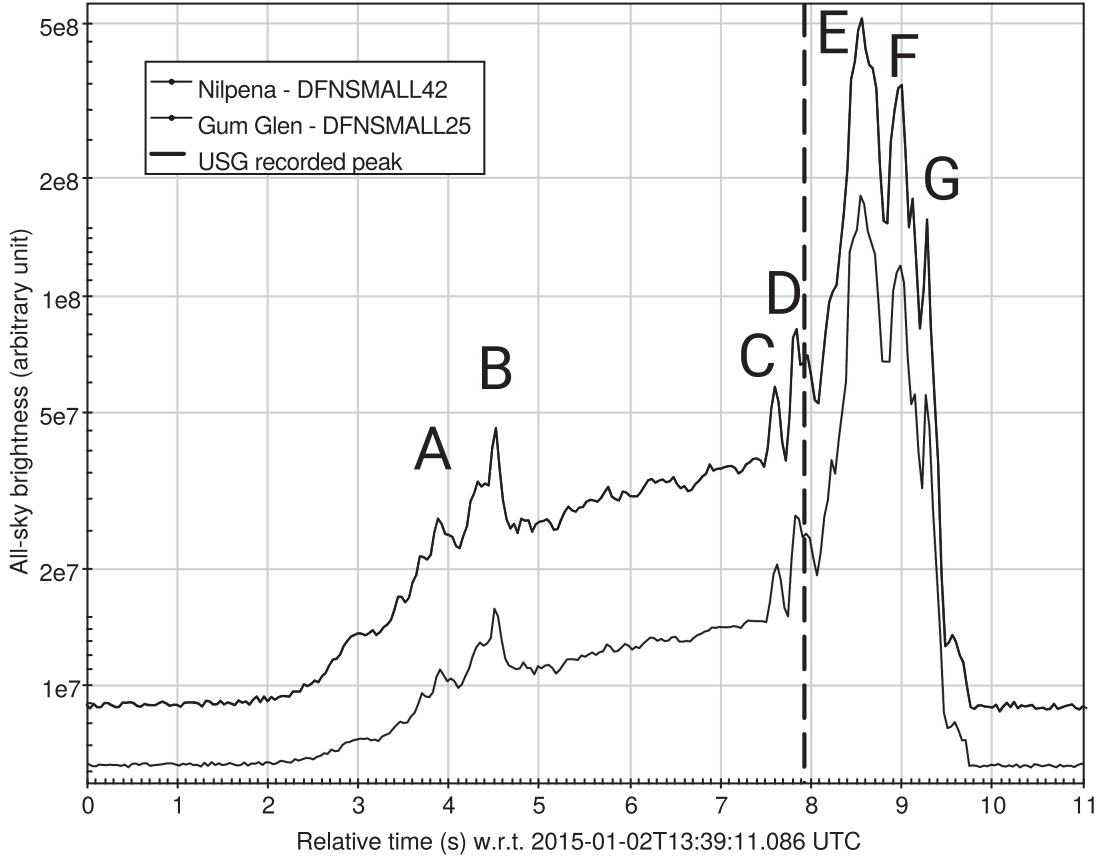
Figure 3. All-sky brightness (sum of all the pixels) from the Kalabity fireball, as recorded with the video cameras at the Gum Glen and Nilpena observatories. Using traditional PSF photometry on star Sirius the light curve is corrected to take into account the effect of autogain. The Nilpena curve has been shifted up for clarity. The peak brightness time recorded by the USG sensors (rounded to the nearest second) is marked by a vertical line.

Table 3. Summary table of bright flight events for DN150102_01 Kalabity. Fragmentation event letters are defined on the light curve (Fig. 3). Times are relative to 2015-01-02T13:39:11.086 UTC. Positions and speeds at the peaks are interpolated from astrometric data.

Event	Time s	Speed ms^{-1}	Height m	Longitude °E	Latitude °N	Dynamic pressure MPa
Beginning	0.0	15406 ± 79	83317	139.73897	−30.25421	
A	3.90	15351	62586	139.85081	−30.74874	0.05
B	4.50	15320	59453	139.86679	−30.82416	0.08
C	7.61	14487	43432	139.95010	−31.21547	0.52
D	7.83	14272	42571	139.95466	−31.23679	0.57
E – max	8.55	13463	40286	139.96683	−31.29360	0.69
F	8.95	13014	39017	139.97359	−31.32517	0.77
G	9.26	12665	38033	139.97883	−31.34963	0.83
End	10.54	8433	33420	140.00311	−31.46438	

The closest DFN camera is Mount Ive station (190 km away). The Mulgathing camera (250 km directly North from the event) only caught the top of the fireball (Fig. 5), as the image circle is cropped on the short side of the sensor (usually North and South).

Like Kalabity, Baird Bay experienced early fragmentation under pressure <1 MPa (peak A at 0.08 MPa), however a much larger pressure was required to destroy it (peak D, most likely between 1 and 2 MPa).

Table 4. Estimated orbital elements of DN150102_01 Kalabity and DN170630_01 Baird Bay, with 1σ formal uncertainties. (equinox J2000).

Parameter	Unit	DN150102_01 Kalabity	DN170630_01 Baird Bay
Epoch	TDB	2015-01-02T13:39:11	2017-06-30T14:26:41
a	au	1.80 ± 0.02	1.23 ± 0.01
e		0.498 ± 0.006	0.35 ± 0.01
i	$^\circ$	8.73 ± 0.02	3.57 ± 0.05
ω	$^\circ$	219.8 ± 0.09	259.06 ± 0.07
Ω	$^\circ$	281.619 ± 0.001	98.801 ± 0.002
q	au	0.908 ± 0.001	0.805 ± 0.004
Q	au	2.70 ± 0.04	1.66 ± 0.03
α_g	$^\circ$	64.3 ± 0.1	272.14 ± 0.02
δ_g	$^\circ$	51.7 ± 0.2	-12.5 ± 0.1
V_g	ms^{-1}	10776 ± 115	10007 ± 260
T_J		3.89	5.14
α_{inf}	$^\circ$	70.14 ± 0.02	271.74 ± 0.02
δ_{inf}	$^\circ$	38.05 ± 0.02	-15.89 ± 0.02

Using the same particle technique as in Section 3.1, with a reasonable assumptions on shape (spherical), and density ($\rho = 3500\,\text{kg m}^{-3}$, chondiric), we find that the meteoroid was $>9400\,\text{kg}$ ($>1.7\,\text{m}$) before impact. Using the particle filter we also find that the main mass was $\simeq 7000\,\text{kg}$ when it airburst at 26 km altitude. Unfortunately no astrometric data is available after the airburst, as the only camera close enough to image the bolide at the end, Mount Ive, has a large area of the sensor saturated because of the airburst (peak D in Fig. 6 and Table 6). The video record from the very distant O'Malley camera (410 km) shows that some material was still ablating for at least 0.85 s after the instant of peak brightness. This means that there is a distinct possibility that a main mass survived, and fell in the Southern Ocean, less than 10 km from the coast off Point Labatt.

The USG sensors locate the airburst $\lambda = 134.5^\circ$ $\phi = -34.3^\circ$ (WGS84) at $h = 20\,\text{km}$ altitude (Table 1). This position is $\sim 100\,\text{km}$ off to the South from our calculated entry parameters (Fig. 1).

On the other hand the USG geocentric velocity vector is consistent with our calculation. The radiant solutions are separated by only 0.4°, and the speeds are different only by $0.1\,\text{km s}^{-1}$, in agreement within uncertainties. This implies that even with the wrong position, the orbit calculated from USG data (Table 1) is in agreement with the DFN orbit (Table 4 and Fig. 4).

4 DISCUSSION

4.1 Reliability of USG fireball data

We have compiled in Table 7 how well USG events match independent observations of those events, using data both from the literature and the two fireballs described here.

It is possible to discuss the reliability of the USG data in terms of different desired outcomes.

4.1.1 For orbital studies

The factors that come into play to calculate a meteoroid orbit are the accuracy of the *location*, the absolute *time*, and the geocentric *velocity vector*.

All USG events in Table 7 agree in absolute time with independent records to within a few seconds.

Locations are correct in most cases, except for the Baird Bay event described in this work. However this $\sim 100\,\text{km}$ location issue in this case is not important for orbit calculation.

Hence the questions lie with the three geocentric Cartesian velocity components. Granvik & Brown (2018) show that in most cases a precision of $0.1\,\text{km s}^{-1}$ on the velocity is good enough for source region analysis, so we do not expect the lack of precision on the USG numbers to be an issue here. An accurate height can be useful to take into account the deceleration in the atmosphere, but it is not essential as we are looking at massive bodies that hardly decelerate before the airburst. Because radiant and speed are less likely to be correlated than the Cartesian velocity components, we have re-projected these velocity components as radiant and speed. The speeds are inconsistent in most cases (Table 7). The worst USG estimates are for the Buzzard Coulee meteorite (18.1 km s^{-1} calculated by Milley 2010 compared to 12.9 km s^{-1} USG), and the Romanian bolide (27.8 km s^{-1} calculated by Borovička et al. 2017 compared to 35.7 km s^{-1} USG). These were underestimated by 28 per cent, and overestimated by 28 per cent, respectively. The USG radiant vector is off for most events, sometimes by only a couple of degrees (which does not drastically affect the orbit), but sometimes by as much as 90°(Buzzard Coulee and Crawford Bay events). From these considerations, only 4 out of 10 events in Table 7 would have a reasonably accurate orbit if calculated from USG data: 2018 LA, Baird Bay, Chelyabinsk, and Košice. The USG orbits of some meteoroids are even misleadingly peculiar: Kalabity and Romanian would be on unusual HTC orbits (as already noted by Brown et al. 2016).

Therefore USG data can generally not be relied on for orbit determination, and there is no way to know for which events the data are reliable.

4.1.2 For material properties studies

The atmospheric behaviour of a meteoroid can yield some insights on what the meteoroid is made of and how it is held together. If no meteorite is recovered, the small set of USG sensors parameters contains very limited information regarding the rock itself, but it is nevertheless possible to derive the bulk strength of the body. A basic way of achieving this is to look at the dynamic pressure required to destroy the body (using $s = \rho_{atm}v^2$ from Bronshten 1981). This is not a perfect indicator as it does not show subtleties in the rock structure, but it should be able to distinguish iron, chondritic, and cometary material, as these differ in bulk strengths by orders of magnitude. The key parameters are then the *height* of peak brightness (to determine atmospheric density ρ_{atm}), and the *speed* v.

As shown by Brown et al. (2016; Table 4), the USG sensors tend to report reasonably accurate heights of peak brightness. We note that most of height inconsistencies are usually due to another peak in the light curve being recorded.

As seen in the previous paragraph, speeds can be wrong by as much as 28 per cent, which induce a factor of 2 error in strength. We conclude that the inaccuracy of USG numbers do not affect strengths by more than an order of magnitude, this is good enough with respect to our original aim.

4.1.3 For size-frequency studies

The USG data have the advantage of using the entire planet as a collector, yielding large sample sizes that ground-based networks
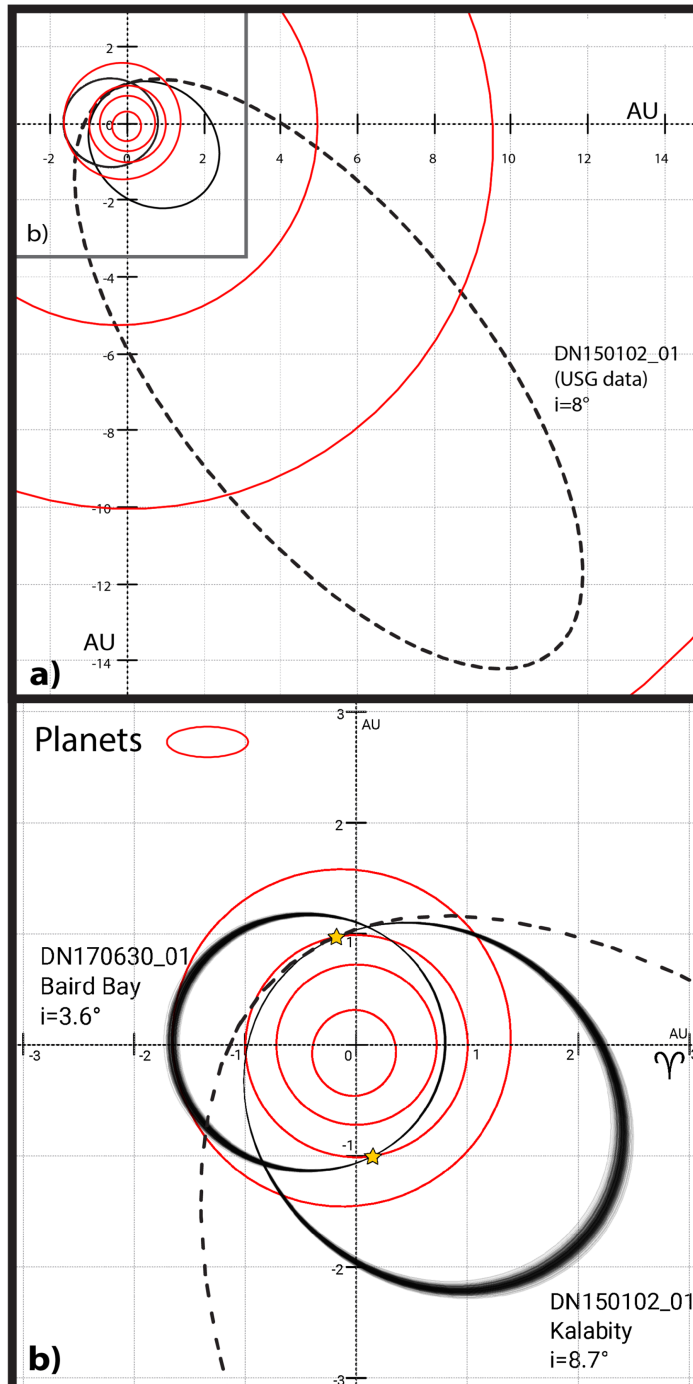
Figure 4. Ecliptic plot of the pre-atmospheric orbit of the Kalabity and Baird Bay meteoroids. **b** is limited to the inner Solar system, while **a** goes out all the way to the orbit of Uranus. The solid lines are orbits using DFN data (the shades of grey in **b** represent the confidence region as calculated by Monte Carlo simulations), whereas the dashed lines are using USG data. The orbit of Baird Bay calculated from USG data is indistinguishable from the DFN one. On the other hand the orbit of Kalabity is very different, mostly because of a speed issue with USG data.

Metre-scale Earth impactors 5175

Table 5. Locations and nature of instrumental records DN170630_01. P: Photographic record (long exposure high-resolution image), V: compressed PAL video (25 frames per second). PW and PF designate the de Bruijn encoding method, as described in Section 2.1. Ranges are from the fireball at 70 km altitude. Photographic imaging system was out of order for O'Malley. Note that the Mulgathing camera did not receive the PF firmware update immediately because of a temporary internet connectivity issue.

Observatory	Instruments	Latitude	Longitude	Altitude (m)	Range (km)
Mount Ive – DFNSMALL62	P_{PF}	32.45919 S	136.10332 E	293	201
Days Hill – DFNEXT005	P_{PF}	34.20749 S	138.66151 E	363	439
Nilpena – DFNSMALL12	P_{PF}	31.02328 S	138.23260 E	122	447
Glenrest – DFNSMALL06	P_{PF}	33.01963 S	138.57554 E	722	414
Billa Kalina – DFNSMALL43	P_{PF}	30.23759 S	136.51566 E	113	387
Mulgating – DFNSMALL15	P_{PW}	30.66078 S	134.18608 E	149	274
Woomera – DFNSMALL14	P_{PF}	31.19609 S	136.82682 E	163	329
O'Malley – DFNSMALL40	V	30.50663 S	131.19534 E	117	410

Figure 5. DN170630_01 Baird bay. Cross-track residuals of the straight line least squares fit to the trajectory from each view point. These distances correspond to astrometric residuals projected on a perpendicular plane to the line of sight, positive when the line of sight falls above the trajectory solution. The distances in the legend correspond to the observation range [highest point–lowest point].

will never be able to reach for this class of objects. Hence they can be a good tool for size-frequency studies, provided the *size* of the impacting bodies can be accurately determined, and the *detection efficiency* is well constrained.

As detailed in Section 2.2, using the empirical relation of Brown et al. (2002) and assuming a density, the radiated energy reported by the USG sensors can be converted into mass and size, with the caveat of speed accuracy. The energy estimates seem to match independent observation for the events presented here (Table 7).

As of the detection efficiency, Brown et al. (2002) mentions a 60–80 per cent Earth observation coverage by the USG sensors for their study on 1994–2002 data. If we subset the USG events in two different groups, before and after the study of Brown et al. (2002), we get on average 19 events per year before, and 26–27 events per year after 2002 September. This 40 per cent increase would suggest a 100 per cent Earth coverage after 2002. However it is interesting

to note that the 0.4 kT impact of *2014 AA* (Farnocchia et al. 2016) was not reported by the sensors.

USG data is therefore useful for size frequency studies (like the work done by Brown et al. (2002), Brown et al. (2013), as long as the sub-population grouping is done by other means than by the orbit calculated using the USG velocity data.

4.1.4 For meteorite searching

Although metre-scale impactors are usually too big to be able to decelerate enough before reaching dynamic pressures that destroy them, these objects still have a large chance of surviving as meteorites. We try to assess here the viability of initiating dark flight calculations using a weather model combined the USG entry vector. All the parameters in Table 7 (apart from time) need to be accurate.
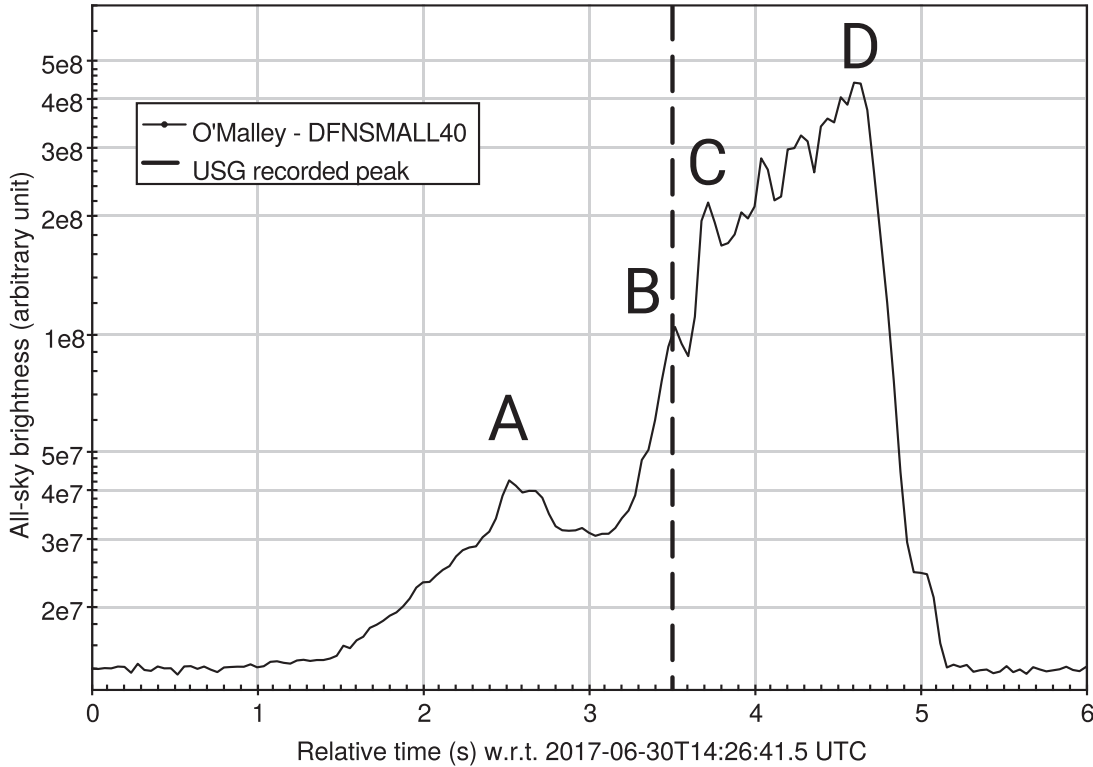
Figure 6. All-sky brightness (sum of all the pixels) from the Baird Bay fireball, as recorded with the video camera at the O'Malley observatory. Using traditional PSF photometry on star α Centauri the light curve is corrected to take into account the effect of autogain. The peak brightness time recorded by the USG sensors (rounded to the nearest second) is marked by a vertical line.

Table 6. Summary table of bright flight events for DN170630_01 Baird Bay. Fragmentation event letters are defined on the light curve (Fig. 6). Times are relative to 2017-06-30T14:26:41.50 UTC. ∗ marks figures that have been extrapolated. The end parameters have not been extrapolated as it is not possible to know what mass is left after the large explosion (peak D), and how this mass decelerated.

Event	Time s	Speed ms^{-1}	Height m	Longitude °E	Latitude °N	Dynamic pressure MPa
Beginning	0.0	15095 $\pm$ 61	86782	134.23858	− 32.99306	
A	2.51	14906	52111	134.21168	− 33.08981	0.08
B	3.51	13786	38817	134.20123	− 33.12718	0.42
C	3.71	13140	36240	134.19919	− 33.13445	0.58
Last astrometric data point	3.80	12783	35181	134.19836	− 33.13743	0.65
D − max	4.61	9568∗	25648∗	134.19083∗	− 33.16432∗	2.31∗
End	5.46					

Although the height of peak brightness is wrong for Chelyabinsk, the reported *(latitude, longitude, and height)* triplet is located near the ground truth track, hence the fall analysis would not significantly change for large masses. Therefore of the events compiled in Table 7, only two out of nine events (Košice and Chelyabinsk) would have reasonably accurate fall positions if computed from USG records.

But even worse, the 0.1° error on latitude/longitude translates into a ±5 km error on position on the ground, this is particularly large for undertaking meteorite searching activities.

From these considerations, it would be ill-advised to undertake meteorite searching solely based on USG data.

4.2 On the ground-based imaging capabilities of metre-scale impactors

With the help from collaborators outside Australia, the DFN is expanding into the Global Fireball Observatory, and will eventually cover 2 per cent of the Earth surface in the next few years. Metre-scale object will fall on the covered area every 1–2 yr on av-

Table 7. USG events that have their trajectory independently estimated. Note that the date/times of the events all match the independent measurements. The location is considered valid if the (latitude, longitude, height) is somewhere on the trajectory. CSS: Catalina Sky Survey, V: video, P: photographic, PE: photometer, CV: casual video, I: infrasound. ✓: correct within errors. ≈: incorrect, but not far off. ✗: incorrect. NR-U: not reported by USG. NR-L: not reported or yet published in literature. ∗: From light curve and infrasound data, [5] conclude that the impact kinetic energy for Košice is >0.1 kT, without an upper limit. References: (0) this work; (1) Hildebrand et al. (2018); (2) Brown et al. (2016); (3) Borovička et al. (2017); (4) Borovička et al. (2013b); (5) Borovička et al. (2013a); (6) Farnocchia et al. (2017); (7) Milley (2010); (8) Jenniskens et al. (2009); (9) Borovička & Charvát (2009); (10) Palotai et al. (2018); (+) JPL Horizons ephemeris service, using CSS and ATLAS astrometry.

Event	Date (UTC)	Instruments	Location	Airburst height	Speed	Radiant	Energy	Ref
2018 LA	2018-06-02T16:44:12	CSS	NR-L	NR-L	✓	✓	NR-L	+
Crawford Bay	2017-09-05T05:11:27	CV, I	≈	✓	✗	✗	✓	1
DN170630 – Baird Bay	2017-06-30T14:26:45	P, V	✗	✗	✓	✓	✓	0
Dishchii'bikoh	2016-06-02T10:56:32	V, CV	✗	NR-U	NR-U	NR-U	≈	10
Romanian	2015-01-07T01:05:59	CV, PE, P	✓	≈	✗	≈	✓	2, 3
DN150102 – Kalabity	2015-01-02T13:39:10	P, V	✓	✓	✗	✗	✓	0, 2
Chelyabinsk	2013-02-15T03:20:21	CV	≈	✗	≈	≈	✓	2, 4
Košice	2010-02-28T22:24:47	V, P, PE	✓	≈	✓	≈	✓∗	2, 5
Buzzard Coulee	2008-11-21T00:26:40	CV	✓	≈	✗	✗	NR-L	2, 7
Almahata Sita (2008 TC3)	2008-10-07T02:45:40	CSS	≈	✓	✗	✗	✓	2, 6, 8, 9

erage, but is the currently deployed technology fit to observe such events?

4.2.1 Night time observations

Fireball observatories are typically optimized to observe the behaviour of macroscopic meteorite droppers throughout their trajectory during the night. The challenge is mostly a dynamic range one: being sensitive enough to observe the smaller meteoroid at a high altitudes to get precise entry speed for orbit calculation, whilst not saturating the records of larger rocks shining 100 million times brighter when they reach the dense layers of the atmosphere.

So far no iron meteorite fall has been instrumentally observed, but it is expected that this class of objects contains the smallest meteoroids (i.e. the faintest fireball) that can drop a meteorite, as their large strength allows them to enter with limited mass-loss due to fragmentation. For instance, if we assume little to no gross fragmentation (Revelle & Ceplecha 1994), to produce a 100 g meteorite the parent meteoroid ($\rho = 7900 \, \mathrm{kg \, m^{-3}}$) can be as small as 0.5 kg $\equiv$ 5 cm diameter, assuming the most favourable entry conditions (vertical entry at $12 \, \mathrm{km \, s^{-1}}$). It is desirable to observe the meteor before the rock starts being affected by the atmosphere too much, 80 km altitude at which it would glow at magnitude $M_V = -1.5$ (assuming a luminous efficiency of 0.05).

On the bright end, we look at the compilation of Borovička et al. (2015) and see that metre-scale events usually approach $M_V^{max} = -18$, although this is highly dependent on their atmospheric behaviour, where and how important the fragmentation events are.

The set goal is then to have instruments that can cover 20 stellar magnitudes of effective dynamic range.

Long exposure high-resolution fireball camera systems have a long track record for yielding meteorite ground locations and orbits (listed as 'dedicated search from detailed computation of trajectory' by Borovička et al. 2015), compared to video systems. Thanks to their logarithmic response, film based imagers cover a very wide dynamic range (∼15 stellar magnitudes), but those systems are costly and impractical for large distributed autonomous fireball networks (Howie et al. 2017a), and do not achieve the 0 magnitude sensitivity objective. The DFN (Howie et al. 2017a) and the European Network (Spurný et al. 2016) have recently switched from film to digital camera technology. This shift has simplified some operational aspects (e.g. enhanced autonomy, better reliability, eased

data reduction), but it has come at the cost of a much limited dynamic range: ∼8 magnitudes without saturation. For astrometric purposes this range can be extended to 15 magnitudes (Devillepoix et al. 2018), but this is still quite far from the 20 magnitudes objective.

Video cameras are generally more sensitive than the still imagers, but suffer from the same limited dynamic range. Although a lot of events have been recorded, fixed frame rate TV systems have not been proficient in yielding meteorite fall positions. This is likely to be due to the low resolution offered by those systems (a PAL video system with a matching circular fisheye lens has an average pixel size over 10 × larger than the DFN cameras), and the difficulty of getting enough stars for astrometric calibration across the field of view (most of these cameras cannot shoot long exposures). However recent advances in digital video camera technology allow higher resolutions, long exposures for calibration, and higher bit depth, so we expect networks based on these systems to be more successful at meteorite recovery in the near future (e.g. the Fireball Recovery and InterPlanetary Observation Network (*FRIPON*) network of Colas et al. 2015).

4.2.2 Daytime observations

The easy exposure control on industrial digital cameras allows low-noise long exposure calibration shot to be taken at night, but also permits very short exposures to operate during the day. The *FRIPON* network endeavours to operate their cameras during both night time and daytime (Audureau et al. 2014), however fireball detection on daytime frames appears somewhat challenging (Egal et al. 2016). Even if calculating fall positions turns out to be difficult from daytime data, the prospects of being able to calculate orbits for meteorites that have been independently recovered are very interesting (9 out of 14 US meteorite falls in the last 10 yr do not have a trajectory solution published), as the astrometric calibration of casual footage can be very time consuming.

5 CONCLUSIONS

This work investigates the NEO impacting population around the metre-scale size range. Such events are relatively rare (35–40 per year), therefore a large collecting area is crucial in order to study them. The DFN is leading the effort as a ground-based instrument, covering over 3 million km².

5178   *H. A. R. Devillepoix et al.*

Meteoroids that have been observed by both the USG sensors and independent means comprises a small set of nine events. In this study we use a precise comparison of these events to assess the reliability of the USG sensors for NEO studies, yielding the following unequivocal conclusions:

(i) USG sensors data are generally unreliable for orbit calculations. The new metre-scale impactors source region of Brown et al. (2016; HTC) is based on three particular USG meteoroid orbits. We have shown that two of these are erroneous, seriously questioning the existence of this source region.

(ii) Size frequency distribution work relies on determining rough sizes and having a good knowledge of the probing time area. The USG seem to achieve both with reasonably good precision. This confirms the sound basis of the work done by Brown et al. (2002) and Brown et al. (2013).

(iii) Basic impactor physical properties (size and strength) can be well constrained with USG data. This validates the conclusions of Brown et al. (2016) that relate to physical properties of objects.

(iv) Based on how often the derived trajectories are wrong, it would be naive to invest large amounts of resources to undertake meteorite searching using USG data.

We also note that ground-based fireball networks must find solutions to increase the dynamic range of their observations, in order to get sound observation data when metre-scale objects impact the atmosphere.

REFERENCES

Astropy Collaboration, 2013, A&A, 558, A33
Audureau Y. et al., 2014, in Rault J.-L., Roggemans P., eds, Proceedings of the International Meteor Conference. Giron, France, p. 39
Binzel R. P., Rivkin A. S., Stuart J. S., Harris A. W., Bus S. J., Burbine T. H., 2004, Icarus, 170, 259
Bland P. A., Artemieva N. A., 2006, Meteorit. Planet. Sci., 41, 607
Borovička J. et al., 2013a, Meteorit. Planet. Sci., 48, 1757
Borovička J., 1990, Bull. Astron. Inst. Czech., 41, 391
Borovička J., Charvát Z., 2009, A&A, 507, 1015
Borovička J., Spurný P., Brown P., Wiegert P., Kalenda P., Clark D., Shrbený L., 2013b, Nature, 503, 235
Borovička J., Spurný P., Brown P., 2015, Small Near-Earth Asteroids as a Source of Meteorites. University of Arizona Press, p. 257
Borovička J., Spurný P., Grigore V. I., Svoreň J., 2017, Planet. Space Sci., 143, 147
Bottke W. F., Morbidelli A., Jedicke R., Petit J.-M., Levison H. F., Michel P., Metcalfe T. S., 2002, Icarus, 156, 399
Bronshten V. A., 1981, The Physics of Meteoritic Phenomena. Izdatel Nauka, Moscow
Brown P., Spalding R. E., ReVelle D. O., Tagliaferri E., Worden S. P., 2002, Nature, 420, 294
Brown P., Wiegert P., Clark D., Tagliaferri E., 2016, Icarus, 266, 96
Brown P. G. et al., 2013, Nature, 503, 238
Chyba C. F., Thomas P. J., Zahnle K. J., 1993, Nature, 361, 40
Colas F. et al., 2015, in Rault J.-L., Roggemans P., eds, International Meteor Conference Mistelbach. Austria, p. 37
Collins G. S., Melosh H. J., Marcus R. A., 2005, Meteorit. Planet. Sci., 40, 817
Devillepoix H. A. R. et al., 2018, Meteorit. Planet. Sci., 53, 2212
Egal A., Kwon M.-K., Colas F., Vaubaillon J., Marmo C., 2016, in Roggemans A., Roggemans P., eds, International Meteor Conference Egmond. the Netherlands, p. 73
Farnocchia D., Chesley S. R., Brown P. G., Chodas P. W., 2016, Icarus, 274, 327
Farnocchia D., Jenniskens P., Robertson D. K., Chesley S. R., Dimare L., Chodas P. W., 2017, Icarus, 294, 218
Granvik M. et al., 2016, Nature, 530, 303
Granvik M. et al., 2018, Icarus, 312, 181
Granvik M., Brown P., 2018, Icarus, 311, 271
Greenstreet S., Ngo H., Gladman B., 2012, Icarus, 217, 355
Gritsevich M. et al., 2017, in Assessment and Mitigation of Asteroid Impact Hazards, Astrophysics and Space Science Proceedings, Volume 46. Springer International Publishing, Switzerland, p. 153
Hildebrand A. H. et al., 2018, in Lunar and Planetary Science Conference. p. 3006
Howie R. M., Paxman J., Bland P. A., Towner M. C., Cupák M., Sansom E. K., Devillepoix H. A. R., 2017a, Exp. Astron., 43, 237
Howie R. M., Paxman J., Bland P. A., Towner M. C., Sansom E. K., Devillepoix H. A. R., 2017b, Meteorit. Planet. Sci., 52, 1669
Ivezic Z. et al., 2008, Serb. Astron. J., 176, 1
Jansen-Sturgeon T., Sansom E. K., Bland P. A., 2018, preprint (arXiv:1808.05768)
Jenniskens P. et al., 2009, Nature, 458, 485
Lister T., Greenstreet S., Gomez E., Christensen E. J., Larson S. M., 2016, AAS/Division for Planetary Sciences Meeting Abstracts, #405.06
Milley E. P., 2010, Master's thesis, University of Calgary
Mommert M. et al., 2014a, ApJ, 786, 148
Mommert M. et al., 2014b, ApJ, 789, L22
Palotai C., Sankar R., Free D. L., Howell J. A., Botella E., Batcheldor D., 2018, preprint (arXiv:1801.05072)
Popova O., Borovička J., Hartmann W. K., Spurný P., Gnos E., Nemtchinov I., Trigo-Rodríguez J. M., 2011, Meteorit. Planet. Sci., 46, 1525
Revelle D. O., Ceplecha Z., 1994, A&A, 292, 330
Sansom E. K., Bland P., Paxman J., Towner M., 2015, Meteorit. Planet. Sci., 50, 1423
Sansom E. K., Rutten M. G., Bland P. A., 2017, AJ, 153, 87
Spurný P., Borovička J., Haloda J., Shrbený L., Heinlein D., 2016, in 79th Annual Meeting of the Meteoritical Society, 6221
Vernazza P., Binzel R. P., Thomas C. A., DeMeo F. E., Bus S. J., Rivkin A. S., Tokunaga A. T., 2008, Nature, 454, 858

This paper has been typeset from a TEX/LATEX file prepared by the author.

Paper 2 – The Dingle Dell meteorite: a Halloween treat from the Main Belt

Statement of Authorship

Title of Paper: The Dingle Dell meteorite: a Halloween treat from the Main Belt.

Publication Status: Accepted for publication in Meteoritics and Planetary Science (April 21, 2018), in press.

Author Contributions

By signing the Statement of Authorship, each author certifies that their stated contribution to the publication is accurate and that permission is granted for the publication to be included in the candidate's thesis.

Name of Principal Author: Hadrien A. R. Devillepoix

Contribution to the Paper: Coordinated the data reduction. Contributed to astrometric, photometric, trajectory, and orbital analysis. Drafted and revised the manuscript for this publication. Was part of the team that recovered the meteorite.

Overall Percentage: 76%

Signature: *Date:*

Sept 19, 2018

Name of Co-Author: Eleanor K. Sansom

Contribution to the Paper: Contributed to mass and velocity modelling, and assisted with editing and revision of the manuscript.

Overall Percentage: 10%

Signature: *Date:*

Sept 19, 2018

Name of Co-Author: Philip A. Bland

Contribution to the Paper: Assisted with editing and revision of the manuscript.

Overall Percentage: 2%

Signature: *Date:*
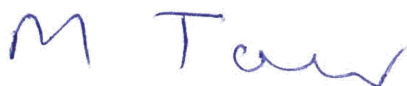
Sept 19, 2018

Name of Co-Author: Martin C. Towner

Contribution to the Paper: Contributed to dark flight calculations. Assisted with editing and revision of the manuscript. Was part of the team that recovered the meteorite.

Overall Percentage: 2%

Signature: *Date:*

Sept 19, 2018

Name of Co-Author: Martin Cupák

Contribution to the Paper: Contributed to weather modelling. Assisted with editing and revision of the manuscript.

Overall Percentage: 2%

Signature: *Date:*

Sept 19, 2018

Name of Co-Author: Robert M. Howie

Contribution to the Paper: Assisted with editing and revision of the manuscript.

Overall Percentage: 1%

Signature: *Date:*

Sept 20, 2018

Name of Co-Author: Trent Jansen-Sturgeon

Contribution to the Paper: Contributed to dark flight calculations, assisted with orbit determination. Assisted with editing and revision of the manuscript. Was part of the team that recovered the meteorite.

Overall Percentage: 3%

Signature: *Date:*

Sept 19, 2018

Name of Co-Author: Morgan A. Cox

Contribution to the Paper: Assisted with editing and revision of the manuscript.

Overall Percentage: 1%

Signature: *Date:*

Sept 19, 2018

Name of Co-Author: Benjamin A. D. Hartig

Contribution to the Paper: Assisted with editing and revision of the manuscript. Was part of the team that recovered the meteorite.

Overall Percentage: 1%

Signature: *Date:*

Sept 19, 2018

Name of Co-Author: Gretchen K. Benedix

Contribution to the Paper: Assisted with editing and revision of the manuscript.

Overall Percentage: 1%

Signature: *Date:*

Sept 19, 2018

Name of Co-Author: Jonathan Paxman

Contribution to the Paper: Compiled visual reports. Assisted with editing and revision of the manuscript.

Overall Percentage: 1%

Signature: *Date:*

Sept 19, 2018

The Dingle Dell meteorite: A Halloween treat from the Main Belt

Hadrien A. R. DEVILLEPOIX[1]*, Eleanor K. SANSOM[1], Philip A. BLAND[1], Martin C. TOWNER[1],
Martin CUPÁK[1], Robert M. HOWIE[1], Trent JANSEN-STURGEON[1], Morgan A. COX[1],
Benjamin A. D. HARTIG[1], Gretchen K. BENEDIX[1], and Jonathan P. PAXMAN[2]

[1]School of Earth and Planetary Sciences, Curtin University, Bentley, WA 6102, Australia
[2]School of Civil and Mechanical Engineering, Curtin University, Bentley, WA 6102, Australia
*Corresponding author. E-mail: h.devillepoix@postgrad.curtin.edu.au

Abstract–We describe the fall of the Dingle Dell (L/LL 5) meteorite near Morawa in Western Australia on October 31, 2016. The fireball was observed by six observatories of the Desert Fireball Network (DFN), a continental-scale facility optimized to recover meteorites and calculate their pre-entry orbits. The 30 cm meteoroid entered at 15.44 km s^{-1}, followed a moderately steep trajectory of 51° to the horizon from 81 km down to 19 km altitude, where the luminous flight ended at a speed of 3.2 km s^{-1}. Deceleration data indicated one large fragment had made it to the ground. The four person search team recovered a 1.15 kg meteorite within 130 m of the predicted fall line, after 8 h of searching, 6 days after the fall. Dingle Dell is the fourth meteorite recovered by the DFN in Australia, but the first before any rain had contaminated the sample. By numerical integration over 1 Ma, we show that Dingle Dell was most likely ejected from the Main Belt by the 3:1 mean motion resonance with Jupiter, with only a marginal chance that it came from the ν_6 resonance. This makes the connection of Dingle Dell to the Flora family (currently thought to be the origin of LL chondrites) unlikely.

INTRODUCTION

As of mid-2017, there are nearly 60k meteorite samples classified in the Meteoritical Bulletin Database.[1] However, aside from a handful of Lunar (≃300) and Martian (≃200) meteorites that have a well-known origin, the link with other solar system bodies is limited. From the instrumentally documented fall of the Příbram meteorite in 1959 (Ceplecha 1961), we learned that chondritic material comes from the asteroid Main Belt. The way this material evolves onto an Earth crossing orbit starts with a disruption in the Main Belt. The small members of the debris field can be strongly affected by the Yarkovsky effect (Farinella et al. 1998) and as a consequence their semimajor axis is continually altered. If the debris field is close to a powerful resonance (in semimajor axis, inclination, eccentricity space), the breakup event feeds material into that resonance, which will in turn push the debris' perihelia into the inner solar system. This can occur on a time scale of less than a million years in some cases (Morbidelli et al. 1994).

Calculating the orbit of a meteoroid using only the luminous trajectory as the observation arc is in most cases not precise enough to allow unequivocal backtracking into a specific region of the Main Belt, hence the statistical results reported by Bland et al. (2009); Brown et al. (2011); Jenniskens et al. (2014); and Trigo-Rodríguez et al. (2015). In order to understand the origin of the different groups of meteorites from the main asteroid belt, it is therefore essential to collect several dozen samples with orbits and look at source regions in a broader, statistical way.

Dedicated Networks to Recover Meteorites with Known Provenance

In the decade following 2000, the recovery rate of meteorites with determined orbits has dramatically increased (Borovička et al. 2015), without a significant increase in collecting area of the major dedicated fireball

[1]https://www.lpi.usra.edu/meteor/metbull.php

networks. While the initial phase of the Desert Fireball Network (DFN) started science operations in December 2005, covering 0.2×10^6 km^2 (Bland et al. 2012), other major networks ceased operations. The Prairie network in the United States (0.75×10^6 km^2 [McCrosky and Boeschenstein 1965]) shut down in 1975, the Canadian Meteorite Observation and Recovery Project (MORP)—1.3×10^6 km^2—stopped observing in 1985 (Halliday et al. 1996), and the European Network's covering area of $\sim 1 \times 10^6$ km^2 has not significantly changed (Oberst et al. 1998). If not due to a larger collecting area, this increase can be explained by other factors as follows.

1. Existing networks improving their data reduction techniques (Spurný et al. 2014).
2. Democratization and cheap operating cost of recording devices (surveillance cameras, consumer digital cameras, etc.) (Borovička et al. 2003).
3. Use of Doppler radar designed for weather observations to constrain the location of falling meteorites (Fries and Fries 2010; Jenniskens et al. 2012; Fries et al. 2014).
4. Deployment of the Desert Fireball Network expressly on favorable terrain to search for meteorites. In its early stage, within its first 5 years of science operation, the DFN yielded two meteorites (Bland et al. 2009; Spurný et al. 2011), while MORP only yielded one (Halliday et al. 1981) in 15 years of operations over a larger network.
5. To a lesser extent, development of NEO telescopic surveillance programs. One single case so far (the Catalina Sky Survey detecting the Almahata Sita meteoroid several hours before impact [Jenniskens et al. 2009]); however, this technique is likely to yield more frequent successes with new deeper and faster optical surveyors, like LSST, which comes online in 2021 (Ivezic et al. 2008).

The DFN started developing digital observatories to replace the film-based network in 2012 with the goal of covering 10^6 km^2, the more cost-effective than expected digital observatories allowed the construction of a continent-scale network covering over 2.5×10^6 km^2 (Howie et al. 2017a). This program rapidly yielded results, less than a year after starting science operation (in November 2014). One of the observatories lent to the SETI institute in California was a crucial viewpoint to calculating an orbit for the Creston fall in California in October 2015 (Meteoritical Bulletin 2015), and the first domestic success came 2 months later with the Murrili meteorite recovery on Kati Thanda–Lake Eyre (Devillepoix et al. 2016; Meteoritical Bulletin 2016). We report here the analysis of observations of a bright fireball that led to the fourth find by the Desert Fireball Network in Australia: the Dingle Dell meteorite. Dingle Dell was originally classified as an LL ordinary chondrite, petrographic type 6 (Meteoritical Bulletin 2017). However, further analysis revealed that it in fact sits on the L/LL boundary (Benedix et al. 2017). The sample has experienced a low level of shock, but has been heated enough to show recrystallization of minerals and matrix. There is no evidence of terrestrial weathering visible on the metal or sulfide grains, which is consistent with its extremely fast retrieval from the elements.

Current Understanding of the Origin of the Main Groups of L and LL Chondrites

L Chondrites

L chondrites represent 32% of total falls. Schmitz et al. (2001) first identified a large amount of fossil L chondrites meteorites in $\simeq 467$ Ma sedimentary rock, which suggests that a breakup happened not too long before, near an efficient meteorite transport route. From spectroscopic and dynamical arguments, Nesvorný et al. (2009) proposed that the Gefion family breakup event, close to the 5:2 MMR with Jupiter, might be the source of this bombardment, given the rapid delivery time, and a likely origin of L chondrite asteroids outside of the 2.5 AU. Most shocked L5 and L6 instrumentally observed falls also seem to come from this breakup, with an ^{39}Ar-^{40}Ar age around $\simeq 470$ Ma ago: Park Forest (Brown et al. 2004), Novato (Jenniskens et al. 2014), Jesenice (Spurný et al. 2010), and Innisfree (Halliday et al. 1981). Only the Villalbeto de la Peña L6 (Trigo-Rodríguez et al. 2006) does not fit in this story because of its large cosmic ray exposure age (48 Ma), inconsistent with a 8.9 Ma collisional lifetime (Jenniskens 2014).

LL Chondrites

Thanks to Vernazza et al. (2008), we know that S- and Q-type asteroids observed in NEO space are the most likely asteroidal analog to LL-type ordinary chondrites. The Hayabusa probe returned samples from S-type (25143) Itokawa, finally unequivocally matching the largest group of meteorites recovered on Earth (ordinary chondrites) with the most common spectral class of asteroids in the Main Belt (Nakamura et al. 2011). The sample brought back from Itokawa is compatible with LL chondrites. Indeed, LL compatible asteroids make up two thirds of near-Earth space. The spectrally compatible Flora family from the inner Main Belt can regenerate this population through the ν_6 secular resonance. But one large problem remains: only 8% of falls are LL chondrites (Vernazza et al. 2008). The orbits determined for some LL samples have so far not helped solve this issue. If we exclude Benešov (Spurný et al. 2014), which was a mixed fall, scientists had to wait until 2013 to get an LL sample with a

precisely calculated orbit: Chelyabinsk (Borovička et al. 2013; Brown et al. 2013). The preatmospheric orbit and composition of the Chelyabinsk meteorite seems to support the Flora family origin for LL chondrites, although a more recent impact could have reset the cosmic ray exposure age to 1.2 ± 0.2 Ma, and the presence of impact melts (very rare in ordinary chondrites due to the large impact velocities required [Keil et al. 1997]). Reddy et al. (2014) argued that an impact melt such as the one observed in the Chelyabinsk meteorites, or shock darkening, can alter the spectra of an S/Q-type asteroid to make it look like a C/X-type spectrally. The implication of this is that the Baptistina family members (C/X-type), which overlaps dynamically with the Flora (S-type), could be the remains of a large impact on a Florian asteroid, and meteorites from both families can be confused both in their spectral signature and dynamical origin. It must be noted however that Reddy et al. (2014) do not make any conclusions on the origin of Chelyabinsk from the Baptistina family. The Chelyabinsk meteorite is also not a typical LL sample found on Earth, because of its size ($\simeq$17 m) and the presence of impact melts.

Based on its classification, we put the orbit of the Dingle Dell meteorite in context with other calculated orbits from L and LL chondrites and discuss the resonances from which it may have originated.

FIREBALL OBSERVATION AND TRAJECTORY DATA

On Halloween night shortly after 8 PM local time, several reports of a large bolide were made via the *Fireballs In The Sky* smartphone app (Sansom et al. 2016) from the Western Australian Wheatbelt area. These were received a few hours prior to the daily DFN observatory reports, apprising the team of the event expeditiously. The DFN observatory sightings are routinely e-mailed after event detection has been completed on the night's data set. It revealed that six nearby DFN observatories simultaneously imaged a long fireball starting at 12:03:47.726 UTC on October 31, 2016 (Fig. 1).

Instrumental Records

The main imaging system of the DFN fireball observatories is a 36 MPixel sensor: Nikon D810 (or D800E on older models), combined with a Samyang lens 8 mm F/3.5. Long-exposure images are taken every 30 s. The absolute and relative timing (from which the fireball velocity is derived) is embedded into the luminous trail by use of a liquid crystal (LC) shutter between the lens and the sensor, modulated according to a de-Brujin sequence (Howie et al. 2017b). The LC
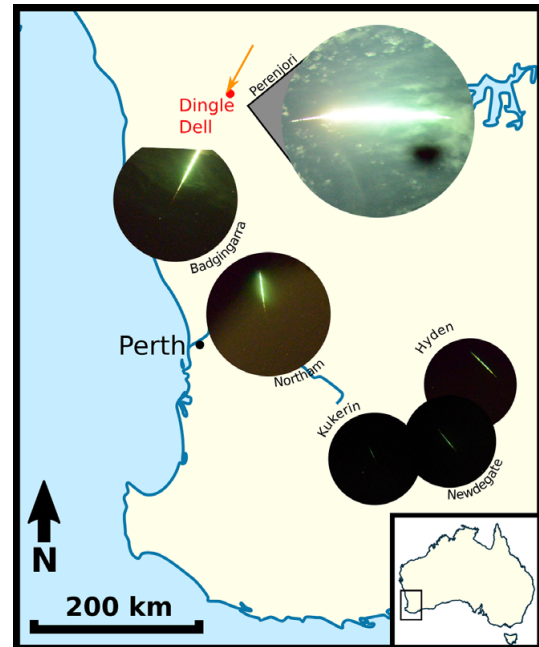
Fig. 1. Cropped all-sky images of the fireball from the six DFN observatories. Images are of the same pixel scale with the center of each image positioned at the observatory location on the map (with the exception of Perenjori, whose location is indicated). The Badgingarra image is cropped because the sensor is not large enough to accommodate the full image circle on its short side. The saturation issue is exacerbated by light scattered in the clouds on cameras close to the event, this is particularly visible on the Perenjori image. The black blotch in the Perenjori image is an artifact that thankfully did not extend far enough to affect the quality of the data. Approximate trajectory path shown by orange arrow. Location of the recovered meteorite is shown by the red dot.

shutter operation is tightly regulated by a microcontroller synced with a Global Navigation Satellite System (GNSS) module to ensure absolute timing accurate to ± 0.4 ms. For further details on DFN observatory specifications, see Howie et al. (2017a).

Some DFN observatories also include video systems operating in parallel with the long-exposure photographic imaging system (Table 1). The video cameras are Watec 902H2 Ultimate CCIR (8 bit 25 interlaced frames per second), with a Fujinon fisheye lens. Originally intended as a backup device for absolute timing, these video systems have been retained for future daytime observation capabilities. Here we make use of the video data to acquire a light curve, as the event saturated the still camera sensors. The closest camera system to this event was in Perenjori (Table 1),

4 H. A. R. Devillepoix et al.

located almost directly under the fireball, and was the only station to image the end of the luminous trajectory (Fig. 1). Other nearby camera sites were overcast and did not record the event. In order to triangulate the trajectory of the fireball, distant stations had to be used, all over 200 km away. The Hyden, Kukerin, and Newdegate systems were all around 500 km from the event and, although still managing to capture the fireball, were too low on the horizon for accurate calibration (Fig. 2).

Astrometry

All images captured by the DFN observatories are saved even when no fireball is detected. This is possible thanks to the availability of large-capacity hard drives

at reasonable costs. Not only does this mitigate event loss during initial testing of detection algorithms but it also gives a snapshot of the whole visible sky down to 7.5 point source limiting magnitude, every 30 s. The astrometric calibration allows the points picked along the fireball image to be converted to astrometric sky coordinates. The associated astrometric uncertainties are dominated by the uncertainty on identifying the centroids along the segmented fireball track.

We have carried out studies on the long-term camera stability by checking the camera pointing using astrometry. On the outback system tested, the pointing changed less than 1′ over the 3-month period assessed. The pointing is therefore remarkably stable, and the relevant fireball image can thus be astrometrically calibrated using a picture taken at a different epoch.

Table 1. Locations and nature of instrumental records. We use cameras <400 km away for trajectory determination.

Observatory	Instruments	Latitude	Longitude	Altitude (m)	Distance [a] (km)
Perenjori	P, V	29.36908 S	116.40654 E	242	91
Badgingarra	P	30.40259 S	115.55077 E	230	204
Northam	P	31.66738 S	116.66571 E	190	323
Hyden	P	32.40655 S	119.15325 E	390	484
Kukerin	P	33.25337 S	118.00628 E	340	520
Newdegate	P	33.05436 S	118.93534 E	302	534

P = Photographic record (exposures: 25 s, 6400 ISO, F/4.); V = video record.
[a]Distance from the meteoroid at 70 km altitude.

Fig. 2. Configuration of DFN station observations for the Dingle Dell fireball. White rays show observations used in triangulation of the trajectory (approximated to the yellow line, starting NE and terminating to the SW of Perenjori). Hyden, Newdegate, and Kukerin stations were all around 500 km away from the event and were not used in triangulation.

This is particularly useful when a bright fireball overprints nearby stars, and especially in this case where clouds are present. In general however, we aim to use a calibration frame taken as close as possible from the science frame, particularly when studying an important event, such as a meteorite fall. In the following paragraph, we present the methods used for astrometrically calibrating the still images, using as an example the Perenjori data. This technique is implemented in an automated way in the reduction pipeline for all detected events.

The astrometric solution for the Perenjori camera is obtained using an image taken a few hours after the event, once the clouds had cleared (2016-10-31T16:00:30 UTC), containing 1174 stars of apparent magnitude $mV \in [1.5, 5.5]$. A third-order polynomial fit is performed to match detected stars to the Tycho-2 star catalogue. The transformation is further corrected using a second-order polynomial on the radial component of the optics. The stability of the solution can be checked at regular intervals. The slight degradation in altitude precision for altitudes below 20° in Fig. 3 is due to a partly obstructed horizon from this camera (e.g., trees, roofs). This degradation usually starts around 10° on cameras with a clear horizon, as is the case for most outback systems.
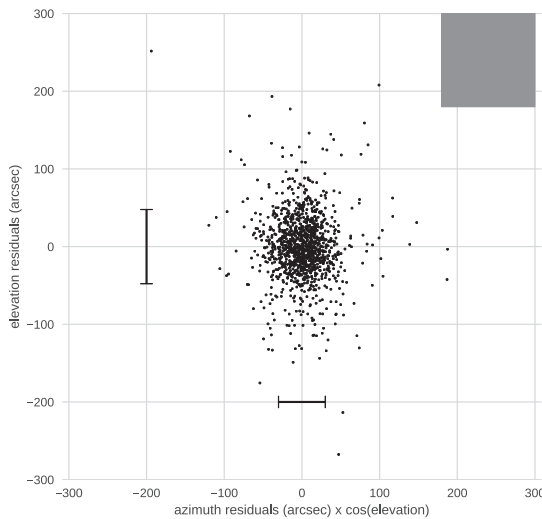
Fig. 3. Residuals on the global astrometric solution for the Perenjori camera. The pixel size at the center of the FoV is shown by the gray square in order to gauge the quality of the solution, as well as the 1σ residual bars on the stars. The azimuth residuals are artificially large around the pole of the spherical coordinate system, so we have multiplied them by *cos*(*elevation*) to cancel out this artifact.

The beginning of the fireball on the Perenjori image is partially masked by clouds, yielding only a handful of points. The middle section is not usable as the sensor was saturated in large blobs, rendering impossible timing decoding or even reliable identification of the center of the track. However, the Perenjori image provides a good viewpoint for the end of the fireball.

Well-calibrated data were also obtained from the Badgingarra camera, before it went outside the sensor area at 30.6 km altitude. Although the Northam camera was very cloudy, we were able to pick the track of the main meteoroid body without timing information, and use it as a purely geometric constraint. Hyden, Kukerin, and Newdegate also picked up the fireball; however, the astrometry so low on the horizon (<5°) was too imprecise (between 2 and 4 arcminutes) to refine the trajectory solution.

Photometry

The automated DFN data reduction pipeline routinely calculates brightness for nonsaturated fireball segments. For this bright event however, the brightness issue was exacerbated by large amounts of light scattered in the clouds (Fig. 1), so it was impossible to produce a useful light curve from the photograph. On the other hand, the Perenjori observatory recorded a low-resolution compressed video through the clouds. Although it is not possible to calibrate this signal, we can get a remarkably deep dynamic range reading of the all-sky brightness, thanks to the large amount of light scattered in the numerous clouds. By deinterlacing the analog video frames, we were able to effectively double the time resolution (25 interlaced frames per second to 50 fields per second, which are equally as precise for all-sky brightness measurements). To correct how the auto-gain affects the signal, we perform aperture photometry on Venus throughout the event. The analog video feed is converted to digital by the Commell MPX-885 capture card, and then processed by the compression algorithm (H264 VBR, FFmpeg *ultrafast* preset) (Howie et al. 2017a) before being written to disk, divided into 1 minute long segments. The PC clock is maintained by the Network Time Protocol (NTP) service, fed with both GNSS and network time sources. However, the timestamp on the file created by the PC suffers from a delay. We measured the average delay using a GPS video time inserter (IOTA-VTI) on a test observatory. This allowed us to match the light curve obtained from the video to astrometric data to within 20 ms. Peak *A* in Fig. 4 is visible on the photographs from both Badgingarra and Hyden. These are used to validate the absolute timing alignment of the video data.
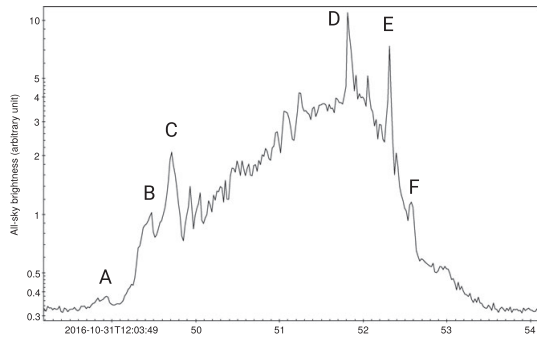
Fig. 4. All-sky brightness (sum of all the pixels) from the video camera at the Perenjori observatory. The light curve is corrected to take into account the effect of auto-gain.

Eye Witnesses

Three anecdotal reports of the fireball were received via the *Fireballs in the Sky* smartphone app (Paxman and Bland 2014; Sansom et al. 2016) within 2 hours of the event (Table 2). The free app is designed to enable members of the public to easily report fireball sightings. Phone GPS, compass, and accelerometers are utilized to report the direction of observations, while a fireball animation aids users in estimating the color, duration, and brightness of the event. This app is an interactive alternative to the popular web-based reporting tool of the International Meteor Organization (Hankey and Perlerin 2015).

The app reports were the first notification of the fireball received by the DFN team, even before the receipt of daily e-mails from the fireball observatories. The azimuth angles reported by the observers were not sufficiently consistent to enable a triangulation based on app reports alone.

The fireball was also reported by several nearby witnesses, and was described in detail by an eye witness only 7.4 km from the fall position (Table 2) who also reported hearing sounds, which due to the time of arrival may have been electrophonic in nature (Keay 1992).

FIREBALL TRAJECTORY ANALYSIS

Geometry

To determine the trajectory of the fireball through the atmosphere, we used a modified version of the Borovička (1990) straight-line least squares (SLLS) method. This involves creating a radiant in 3-D space that best fits all the observed lines of sight, minimizing the angular residuals between the radiant line and the observed lines of sight. While angular uncertainties will be similar across different camera systems, the effect of distance results in larger cross-track errors for more distant observatories (Fig. 5), and therefore less influence on the resulting radiant fit. The end of the fireball from the Perenjori image was used, along with Badgingarra and Northam camera data to triangulate the geometry of the fireball trajectory. The inclusion of astrometric data from Hyden, Kukerin, and Newdegate (see the Astrometry section) degraded the solution: the cross-track residuals from all viewpoints increased significantly, suggesting a systematic issue with the abovementioned camera data. Therefore, we only used the trajectory solution yielded by the three closest view points (Fig. 5). The best combination of viewpoints (Perenjori and Badgingarra) yields an excellent convergence angle of 86°. The trajectory solution points to a moderately steep entry with a slope of 51° from the horizon, with ablation starting at an altitude of 80.6 km and ending at 19.1 km (see Table 3).

Dynamic Modeling of the Trajectory, Including Velocity and Mass Determination

Filter Modeling

The method described in Chapter 4 of Sansom (2016) is an iterative Monte Carlo technique that aims to determine the path and physical characteristics such as shape (A: the cross section area to volume ratio), density (ρ_m), and ablation coefficient (σ) of a meteoroid from camera network data. In this approach, one is able to model meteoroid trajectories based on raw astrometric data. This avoids any preconceived constraints imposed on the trajectory, such as the

Table 2. Observer reports from eyewitness accounts and *Fireballs in the Sky* app (FITS).

Reporting means	Report time (UTC)	Location	Approx. distance from event (km)	Reported duration (s)	Reported brightness (stellar Mag)	Reported color
FITS	12:04	Perth region	300	2.6	−8	Orange
FITS	12:59	Ballidu	150	6.4	−7	Green
FITS	13:35	Dowerin	230	8.6	−9	Pink
Eye witness	N/A	Koolanooka Hills	7.4	>5	>−12.6 (full moon)	

The Dingle Dell meteorite fall   7
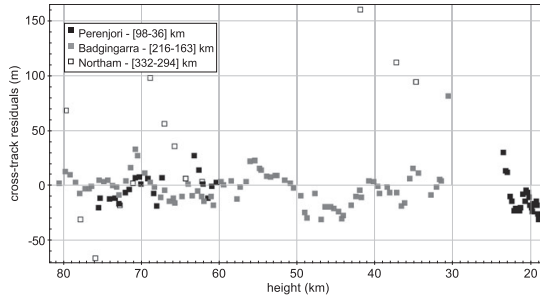
Fig. 5. Cross-track residuals of the straight-line least squares fit to the trajectory from each view point. These distances correspond to astrometric residuals projected on a perpendicular plane to the line of sight, positive when the line of sight falls above the trajectory solution. Note that the larger residuals on the Northam camera do not equate to larger astrometric uncertainties, but rather reflect a rather large distance from the observatory. The distances in the legend correspond to the observation range [highest point–lowest point].

straight-line assumption used in the Geometry section. Unfortunately, this requires multiple viewpoints with accurate absolute timing information to record the meteoroid position. For this event, timings encoded in the trajectory were distinguishable for only the initial 4.2 s by the Badgingarra system (before any significant deceleration) and for the final 1.1 s by the Perenjori system. In this case, we must rely on the straight-line least squares (SLLS) triangulation to determine meteoroid positions (see the Geometry section). We therefore applied the three-dimensional particle filter model outlined in Chapter 4 of Sansom (2016) using instead triangulated geocentric coordinates as observation measurements. Uncertainties associated with using pretriangulated positions based on an assumed straight-line trajectory are incorporated. The distribution of particle positions using such observations will be overall greater than if we had been able to use the raw measurements.

As a straight line may be an oversimplification of the trajectory to most reliably triangulate the end of the

luminous flight using the SLLS method, the final 1.1 s was isolated (this being after all major fragmentation events described in the Atmospheric Behavior section). The filter was run using these positions and initiated at t_0 = 5.0 s (2016-10-31T12:03:52.726 UTC). Particle mass values at this time would be more suitably initiated using a logarithmic distribution in the range from 0 kg to 1000 kg. The initiation of other filter parameters, including the multimodal density distribution, are described in Sansom et al. (2017) with ranges given in table 1 of their work. As a calibrated light curve was not attainable, brightness values were not included in this analysis, making it a purely dynamic solution. The adaptive particle filter technique applied here uses the same state vector and three-dimensional state equations as in Chapter 4 of Sansom (2016) to evaluate the meteoroid traveling through the atmosphere. As we are using pretriangulated geocentric positions as observations, the measurement function here is linear. The particles are still allowed to move in 3-D space, and an evaluation of the model fit is performed as the absolute distance between the pretriangulated SLLS point and the evaluated particle position. This is shown in Fig. 6 for all particles, with the distance to the mean value also shown. Mean particle positions show a good fit to the SLLS triangulated observations, with a maximum of 30 m differences early on, decreasing to 6 m at the end.

The filter estimates not only the position and velocity of the meteoroid at each observation time but also the mass; ablation coefficient, σ; and shape density coefficient, κ. At the final observation time t_f = 6.1 s (2016-10-31T12:03:53.826 UTC), the state estimate results in weighted median values of mass$_f$ = 1.49 ± 0.23 kg, speed$_f$ 3359 ± 72 m s^{-1}, σ_f = 0.0154 ± 0.0054 s^2 km^{-2}, and κ_f = 0.0027 ± 0.0001 (SI). Although κ may be used to calculate densities for a given shape and drag coefficient, to avoid introducing assumptions at this stage we may gauge its value by reviewing the density with which surviving particles were initiated. The distribution of final mass estimates is plotted against this initial density attributed to each given

Table 3. Summary table of bright flight events. Fragmentation event letters are defined on the light curve (Fig. 4).

Event	Time[a] (s)	Speed (m s^{-1})	Height (m)	Longitude (°E)	Latitude (°N)	Dynamic pressure (MPa)
Beginning	0.0	15443 ± 60	80594	116.41678	−28.77573	
A	1.20	15428	65819	116.36429	−28.86973	0.03
B	1.72	15401	59444	116.34151	−28.91045	0.08
C	1.96	15378	56531	116.33108	−28.92909	0.11
D	4.08	13240	32036	116.24270	−29.08672	2.28
E	4.58	10508	27302	116.22547	−29.11738	3.09
F	4.84	8988	25019	116.21716	−29.13217	3.27
Terminal	6.10	3243 ± 465	19122	116.19564	−29.17045	

[a]Past 2016-10-31T12:03:47.726 UTC.
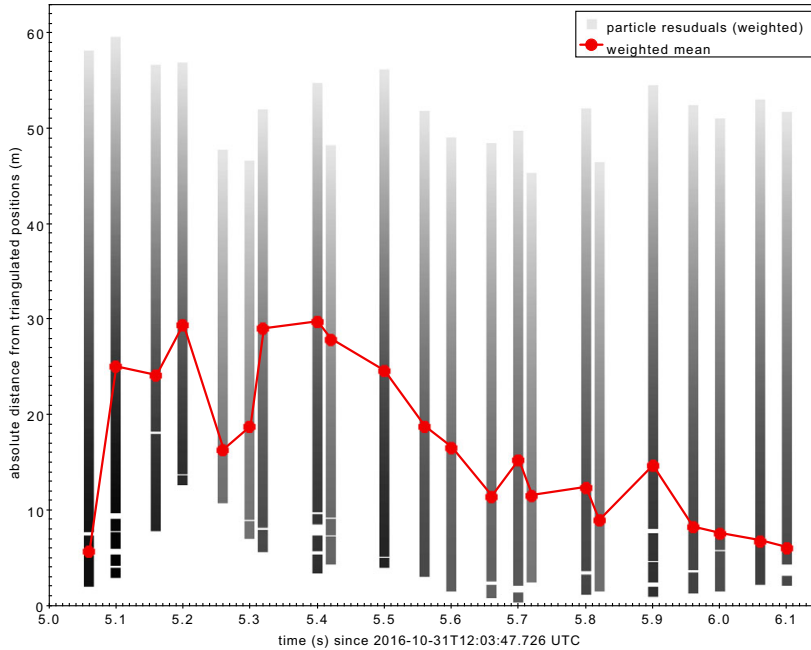
Fig. 6. Position residuals of the 3D particle filter fit to the SLLS triangulated observations for the final 1.1 *s* of the luminous trajectory. Individual particle weightings are shown in grayscales, with weighted mean values shown in red.

particle in Fig. 7, along with the recovered Dingle Dell meteorite mass of 1.150 kg and bulk density of 3450 kg m^{-3}. In this figure, the distribution of the main cluster of particles is consistent with the recovered mass; however, the initial densities are lower. The weighted median value of initial bulk densities (at $t_0 = 5.0$ s) for all particles resampled at t_f is 3306 kg m^{-3}. It is expected that the bulk density of a meteoroid body may slightly increase throughout the trajectory as lower density, more friable material is preferentially lost. This could justify the slightly lower bulk densities attributed at t_0.

In order to obtain the entry speed of the meteoroid with appropriate errors, we apply an extended Kalman smoother (Sansom et al. 2015) to the straight-line solution for the geometry, considering the timing of the points independently for each observatory. Of the two cameras that have timing data for the beginning of the trajectory, only Badgingarra caught the start, giving an entry speed of 15402 ± 60 m s^{-1} (1σ) at 80596 m altitude. To determine whether speeds calculated are consistent between observatories, the first speed calculated for Perenjori—15384 ± 64 m s^{-1} at 75548 m altitude—is compared to the Badgingarra solution at this same altitude -15386 ± 43 m s^{-1}. The results are

remarkably consistent, validating the use of a Kalman smoother for determining initial velocities.

Dimensionless Coefficient Method

As a comparison to the particle filter method, the dimensionless parameter technique described by Gritsevich (2009) was also applied. The ballistic parameter (α) and the mass loss parameter (β) were calculated for the event, resulting in $\alpha = 9.283$ and $\beta = 1.416$ (Fig. 8). As the particle filter technique in this case was not able to be performed on the first 5.0 s of the luminous trajectory, these parameters may be used to determine both initial,[2] and final[3] main masses, given assumed values of the shape and density of the body. Using the same parameters as Gritsevich (2009) ($c_d = 1$, $A = 1.55$) along with the density of the recovered meteorite, $\rho = 3450$ kg m^{-3} gives an entry mass, $m_e = 81.6$ kg, and a $m_f = 1.4$ kg. Varying the shape of the body to spherical values, $A = 1.21$ (Bronshten 1983) gives an initial mass of $m_e = 38.8$ kg. Instead of assuming values for c_d and A, we can also insert the κ value calculated by the particle filter to give

[2]See equation 14 in Gritsevich (2009).
[3]See equation 6 in Gritsevich (2009).

The Dingle Dell meteorite fall   9
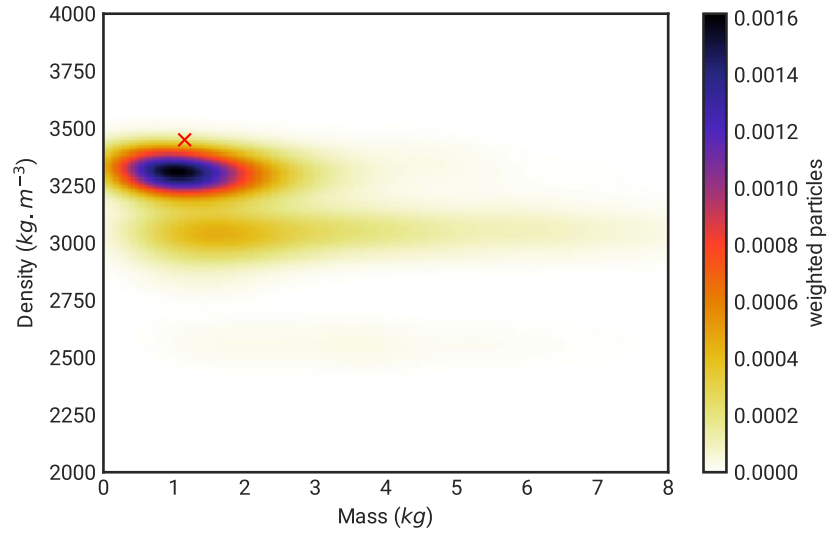
Fig. 7. Results of the 3D particle filter modeling, showing the distribution of final mass estimates along with the densities with which particles were initiated at $t_0 = 5$ s. Mass estimates are consistent with the recovered meteorite mass found (red cross), with initial densities slightly below the bulk rock value.

$m_e = 41.1$ kg. These results can be approximated to a 30 cm diameter initial body. Note that this method is the most reliable for calculating a minimum entry mass of the Dingle Dell meteoroid. The photometric method would require a calibrated light curve, and the particle filter method requires good astrometric data coverage

where significant deceleration occurs (the missing data between 4.2 and 5.0 s).

Atmospheric Behavior

In Table 3, we report the ram pressure ($P = \rho_a v^2$) required to initiate the major fragmentation events labeled on the light curve in Fig. 4. The density of the atmosphere, ρ_a, is calculated using the *NRLMSISE-00* model of Picone et al. (2002), and v is the calculated speed. The meteoroid started fragmenting quite early (events A, B, and C), starting at 0.03 MPa. These early fragmentation events suggest that the meteoroid had a much weaker lithology than the meteorite that was recovered on the ground. Then no major fragmentation happened until two very bright peaks in the light curve: D (2.28 MPa) and E (3.09 MPa). These large short-lived peaks suggest a release of a large number of small pieces that quickly burnt up. A small final flare (F −3.27 MPa) 1.26 s before the end is also noted.

DARK FLIGHT AND METEORITE RECOVERY

The results of the dynamic modeling (Fig. 7) are fed directly into the dark flight routine. By using the state vectors (both dynamical and physical parameters) from the cloud of possible particles, we ensure that there is no discontinuity between the bright flight and the dark flight, and we get a simulation of possible impact points
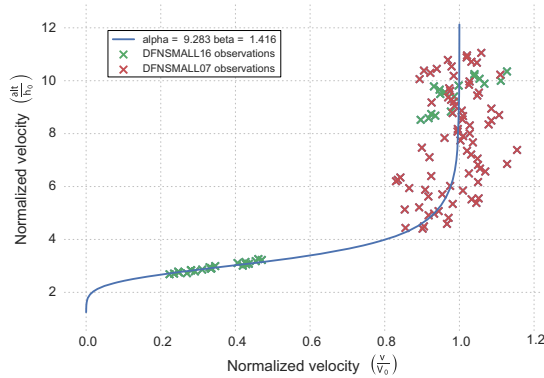
Fig. 8. Trajectory data from both Perenjori and Badgingarra observatories, with speeds normalized to the speed at the top of the atmosphere (15.443 km s^{-1}; Table 3), V_0, and altitudes normalized to the atmospheric scale height, $h_0 = 7.16$ km. The best fit to equation 10 of Gritsevich (2009) results in $\alpha = 9.283$ and $\beta = 1.416$ and is shown by the blue line. These dimensionless parameters can be used to determine the entry and terminal mass of the Dingle Dell meteoroid.

on the ground that is representative of the modeling work done on bright flight data.

Wind Modeling

The atmospheric winds were numerically modeled using the Weather Research and Forecasting (WRF) software package version 3.8.1 with the Advanced Research WRF (ARW) dynamic solver (Skamarock et al. 2008). The weather modeling was initialized using global 1° resolution National Centers for Environmental Prediction (FNL) Operational Model Global Tropospheric Analysis data. As a result, a 3 km resolution WRF product with 30 minutes history interval was created and weather profile at the end of the luminous flight for 2016-10-31T12:00 UTC was extracted (Fig. 9). The weather profile includes wind speed, wind direction, pressure, temperature, and relative humidity at heights ranging up to 30 km (Fig. 9), providing complete atmospheric data for the main mass from the end of the luminous phase to the ground, as well as for fragmentation events E and F (Table 3). Different wind profiles have been generated, by starting the WRF integration at different times: 2016 October 30d12h, 30d18h, 31d00h, 31d06h, and 31d12h UTC. Three of the resulting wind models converge to a similar solution in both speed and direction (30d12h, 31d00h, 31d12h) and will be hereafter referred to as solution $W1$ (Fig. 9). The other two models from 30d18h ($W2$) and 31d00h ($W3$) differ significantly. For example, the maximum jet stream strength is $\simeq 47$ m s^{-1} for $W1$, $\simeq 34$ m s^{-1} for $W3$, and $\simeq 29$ m s^{-1} for $W2$. To discriminate which wind profile is closer to the truth, we ran the model next to the Geraldton balloon launches of 2016 October 31d00h and 31d06h UTC, but no discrepancy was noticeable between all five scenarios. Considering that three model runs clump around $W1$, whereas $W3$ and $W2$ are isolated, we choose $W1$ as a preferred solution. The investigation of why $W3$ and $W2$ are different is beyond the scope of this paper, nonetheless we discuss how these differences affect the dark flight of the meteorites in the next section.

Dark Flight Integration

The dark flight calculations are performed using an eighth-order explicit Runge–Kutta integrator with adaptive step-size control for error handling. The physical model uses the single body equations for meteoroid deceleration and ablation (Hoppe 1937; Whipple 1939). In this model, rotation is accounted for such that the cross-sectional area to volume ratio (A) remains constant throughout the trajectory. The variation in flow regimes and Mach ranges passed through the body alter the values used for the drag coefficient, which can be approximated using table 1 in Sansom et al. (2015). The integration of all the particles from the Dynamic Modeling of the Trajectory, Including Velocity and Mass Determination section allows the generation of probability heat maps to maximize field searching efficiency. The ground impact speed for the mass corresponding to the recovered meteorite is evaluated at 67 m s^{-1}.

In calculating a fall line for an arbitrary range of masses, the assumed shape of the body and the wind model used both affect the final fall position. However for a given wind model, a change in shape only shifts the masses along the fall line.

We also calculate dark flight fall lines from fragmentation events that happened within the wind model domain: E and F. Unsurprisingly, the main masses from those events are a close match to the corresponding main mass started from the end of the visible bright flight. However, small fragments are unlikely to be found as they fell into the Koolanooka Hills bush land (Fig. 10).

Search and Recovery

Within 2 days, two of the authors (PB and MT) visited the predicted fall area, about 4 hours' drive from Perth, Western Australia to canvas local farmers for access and information. Having gained landowner permission to search, a team was sent to the area 3 days later. Searching was carried out by a team of four (MT, BH, TJS, and HD), mostly on foot and with some use of mountain biking in open fields. The open fields' searching conditions were excellent, although the field boundaries were vegetated. The team managed to cover about 12 ha per hour when looking for a >1 kg mass on foot. On the second day, a meteorite was found (Fig. 11) close to the Dingle Dell farm boundary, at coordinates $\lambda = 116.215439°$ $\varphi = -29.206106°$ (WGS84), about 130 m from the originally calculated fall line, after a total of 8 h of searching. The recovered meteorite weighs 1.15 kg, with a rounded brick shape of approximately $16 \times 9 \times 4$ cm, and a calculated bulk density of 3450 kg m^{-3} (Fig. 11). The condition of the meteorite is excellent, having only been on the ground for 6 days, 16 h. Discussion with the local landowner, and checking the weather on the nearest Bureau Of Meteorology observation station (Morawa Airport, 20 km away) showed that no precipitation had fallen between times of landing and recovery. The meteorite was collected and stored using a Teflon bag, and local soil samples were also collected in the same manner for comparison. No trace of impact on the ground was noticed. The meteorite was found intact (entirely
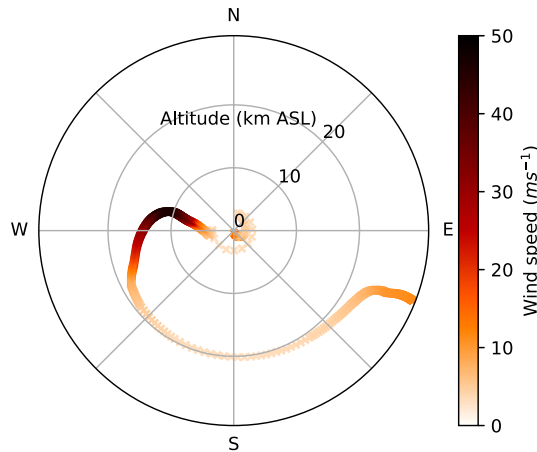
Fig. 9. Wind model profile *W1*, extracted as a vertical profile at the coordinates of the lowest visible bright flight measurement.

covered by fusion crust) on hard ground, resting upright (Fig. 11), and covered with dust. So it is possible that the meteorite fell a few meters away in softer ground and bounced or rolled to the recovered position.

PRE-ENCOUNTER ORBIT

The backward propagation of the observed trajectory into an orbit requires the calculation of the direction of the fireball (known as the radiant), and the position and speed at the top of the atmosphere. The associated uncertainties on these two components are mostly uncorrelated. In order to minimize issues associated with the oversimplified straight-line trajectory for orbit purposes, we retriangulate the observations using only points that fall >60 km altitude on the initial triangulation. In this case, as the trajectory is fairly steep, the difference in apparent radiant between the two solutions is less than 5 arcmin. To calculate the errors on the radiant, we use the covariance matrix from the least squares trajectory fit (see the Geometry section), this gives us the apparent radiant: slope to the horizontal = $51.562 \pm 0.002°$, azimuth of the radiant (East of North) = $206.17 \pm 0.03°$, which corresponds to ($\alpha = 173.38 \pm 0.02°$, $\delta = -6.34 \pm 0.01°$) in equatorial J2000 coordinates.

To calculate the formal uncertainty on the initial velocity, we apply the Kalman filter methods of Sansom et al. (2015) as outlined in the Dynamic Modeling of the Trajectory, Including Velocity and Mass Determination section. Using the time, position,

radiant, speed, and associated uncertainties, we determine the preatmospheric orbit by propagating the meteoroid trajectory back through time, considering the atmospheric effects, Earth's oblate shape effects (J2), and other major perturbing bodies (such as the Moon and planets), until the meteoroid has gone beyond $10\times$ the Earth's sphere of influence. From here, the meteoroid is propagated forward in time to the impact epoch, ignoring the effects of the Earth–Moon system. Uncertainties (Table 4) are calculated using a Monte Carlo approach on 1000 test particles randomly drawn using uncertainties on the radiant and the speed (Fig. 12).

We scanned the *Astorb*[4] asteroid orbital database (Bowell et al. 2002) for close matches in a, e, i, ω, Ω orbital space using the similarity criterion of Southworth and Hawkins (1963). The closest match is the small ($H = 24.6$) *2015 TD179* asteroid that came into light in November 2015 when it flew by Earth at $\simeq 10$ lunar distances. But the large difference between these orbits, $D = 0.04$, makes the dynamical connection between the two highly unlikely.

To calculate the likely source region and dynamical pathway that put the meteoroid on an Earth crossing orbit, we use the *Rebound* integrator (Rein and Tamayo 2015) to backward propagate the orbit of the meteoroid. We use 10,000 test particles randomly selected using the radiant and speed uncertainties as explained above, as well as the major perturbating bodies (Sun, eight planets, and Moon). The initial semimajor axis (Table 4) is close to the 7:2 (2.25 AU) and 10:3 (2.33 AU) mean motion resonances with Jupiter (MMRJ). These minor resonances start to scatter the eccentricity of a large number of test particles very early on, but neither are strong enough to decrease it significantly enough to take the meteoroid outside of Mars' orbit. Because of the interactions with the inner planets, the particle cloud rapidly spreads out, and particles gradually start falling into the two main dynamical pathways in this region: 3:1 MMRJ (2.5 AU) and the ν_6 secular resonance. These resonances rapidly expand the perihelia of particles out of the Earth's orbit initially, and eventually out of Mars' orbit and into the Main Belt.

During the integration over 1 Myr, we count the number of particles that have converged close to stably populated regions of the Main Belt, and note which dynamical pathway they used to get there. This gives us the following statistics:

1. ν_6: 12%
2. 3:1 MMRJ: 82%
3. 5:2 MMRJ: 6%

---

[4]ftp://ftp.lowell.edu/pub/elgb/astorb.html, downloaded June 24, 2017.
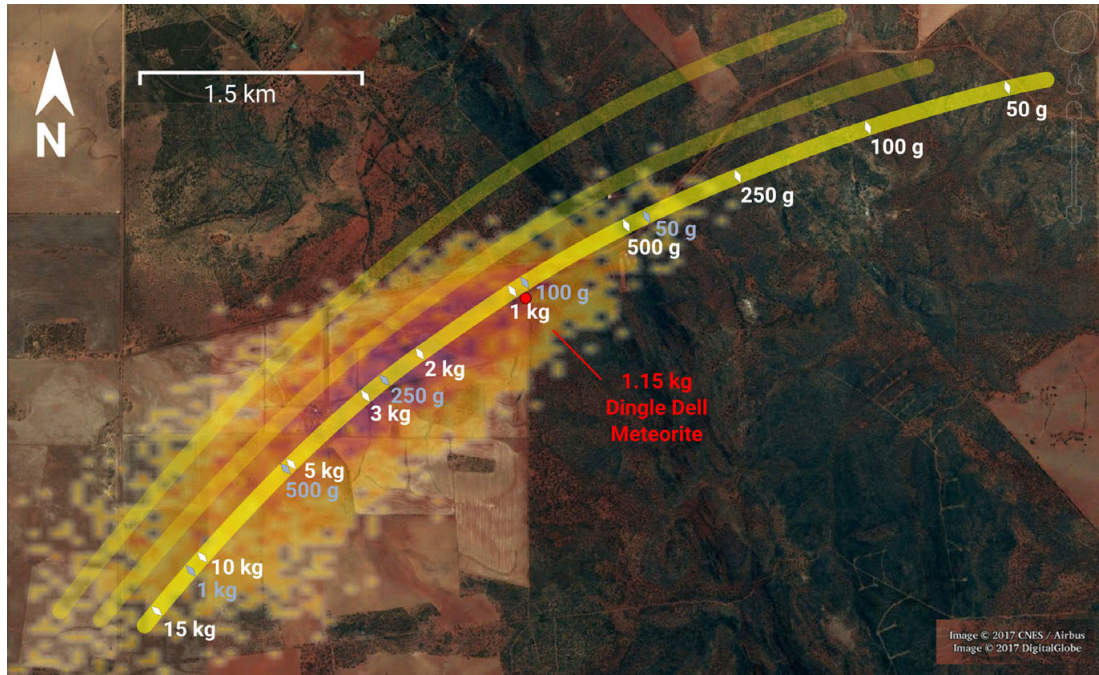
Fig. 10. Fall area around Dingle Dell farm and Koolanooka Hills. Fall lines in yellow represent different wind model solutions: *W1* (bottom), *W2* (middle), and *W3* (top). Mass predictions for the preferred wind model are shown for spherical (light blue markings; *A* = 1.21) and cylindrical (white markings; *A* = 1.5) assumptions. The particle filter results are propagated through dark flight using wind model *W1*, and are shown as a heat map. The location of the recovered meteorite (red dot) is ≃ 100 m from the *W1* fall line.

CONCLUSIONS

Dingle Dell is the fourth meteorite with an orbit recovered by the DFN in Australia. Its luminous trajectory was observed by six DFN camera stations up to 535 km away at 12:03:47.726 UTC on 31 October, 2016. Clouds severely affected the observations, but enough data were available to constrain the search area for a swift recovery, and determine one of the most precise orbits linked to a meteorite. The surviving rock was recovered within a week of its fall, without any precipitation contaminating the rock, confirming the DFN as a proficient sample recovery tool for planetary science. This recovery, in less than ideal conditions, also validates various choices in the design and operations of the Desert Fireball Network:

1. Use of high-resolution digital cameras to enable reliable all-sky astrometry for events up to 300 km away.
2. Uninterrupted operation even when a large portion of the sky is cloudy for individual systems.

3. Archiving of all raw data to mitigate event detection failures.

While the method of Sansom et al. (2017) was still in development at the time of the fall, the reanalysis of the fireball with this new technique is remarkably consistent with the main mass found, requiring just a small number of high-quality astrometric data points. This validates the method, and will drastically reduce the search area for future observed falls.

After a 1 million year integration of 10,000 test particles, it is most likely that Dingle Dell was ejected from the Main Belt through the 3:1 mean motion resonance with Jupiter rather than the ν_6 resonance (82% for the 3:1 MMRJ compared to 12% probability for ν_6). This also means that L/LL Dingle Dell is unlikely to be associated with the Flora family, likely source of most LL chondrites (Vernazza et al. 2008), as the most efficient mechanism for getting Florian fragments to near-Earth space is the ν_6 secular resonance. This fall adds little insight into the Flora/LL link (Fig. 13), but 2016 was rich in instrumentally

The Dingle Dell meteorite fall   13

Fig. 11. Dingle Dell meteorite as it was found. Image available at https://commons.wikimedia.org/wiki/File:Dingle_Dell_meteorite_as_it_was_found.jpg under a Creative Commons Attribution-ShareAlike 4.0 International.
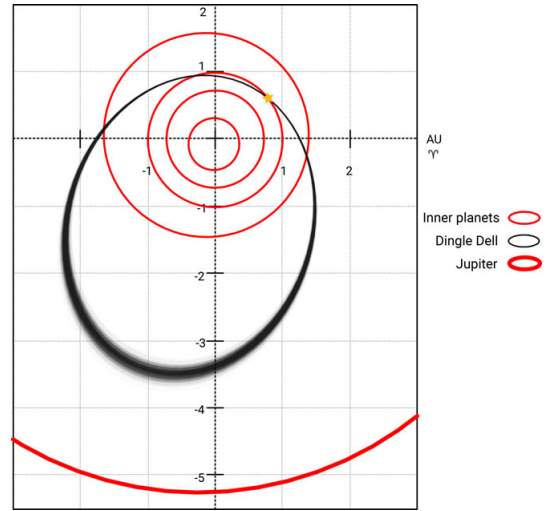
Fig. 12. Ecliptic projection of the pre-encounter orbit of Dingle Dell. The shades of gray represent the likelihood as calculated from 1000 Monte Carlo simulations based on formal uncertainties on the radiant and the speed.

Table 4. Pre-encounter orbital parameters expressed in the heliocentric ecliptic frame (*J2000*) and associated 1σ formal uncertainties.

Parameter	Unit	Value
a	AU	2.254 ± 0.034
e		0.5904 ± 0.0063
i	°	4.051 ± 0.012
ω	°	215.773 ± 0.049
Ω	°	218.252 ± 0.00032
q	AU	0.92328 ± 0.00032
Q	AU	3.586 ± 0.067
α_g	°	354.581 ± 0.037
δ_g	°	13.093 ± 0.081
V_g	m s^{-1}	10508 ± 87
T_J		3.37

observed LL falls, which might yield clues to help confirm this connection in the near future: Stubenberg (LL6) (Spurný et al. 2016; Bischoff et al. 2017), Hradec Králové (LL5) (Meteoritical Bulletin 2017), and Dishchííbikoh (LL7) (Meteoritical Bulletin 2017; Palotai et al. 2018).

Fig. 13. The orbit of Dingle Dell in context with other L and LL ordinary chondrite falls. References for L and LL orbits are in the introduction.

REFERENCES

Astropy Collaboration, Robitaille T. P., Tollerud E. J., Greenfield P., Droettboom M., Bray E., Aldcroft T., Davis M., Ginsburg A., Price-Whelan A. M., Kerzendorf W. E., Conley A., Crighton N., Barbary K., Muna D., Ferguson H., Grollier F., Parikh M. M., Nair P. H., Unther H. M., Deil C., Woillez J., Conseil S., Kramer R., Turner J. E. H., Singer L., Fox R., Weaver B. A., Zabalza V., Edwards Z. I., Azalee Bostroem K., Burke D. J., Casey A. R., Crawford S. M., Dencheva N., Ely J., Jenness T., Labrie K., Lim P. L., Pierfederici F., Pontzen A., Ptak A., Refsdal B., Servillat M., and Streicher O. 2013. Astropy: A community Python package for astronomy. *Astronomy & Astrophysics* 558:A33. https://doi.org/10.1051/0004-6361/201322068.

Benedix G. K., Forman L. V., Daly L., Godel B., Esteban L., Meier M. M. M., Maden C., Busemann H., Yin Q. Z., Sanborn M., Ziegler K., Welten K. C., Caffee M. W., Strasser J. W., Glavin D. P., Dworkin J. P., Bland P. A., Paxman J. P., Towner M. C., Cupak M., Sansom E. K., Howie R. M., Devillepoix H. A. R., Cox M. A., Jansen-Sturgeon T., Hartig B. A. D., and Bevan A. W. R. 2017. Mineralogy, petrology and chronology of the Dingle Dell meteorite (abstract #6229). 80th Annual Meeting of the Meteoritical Society 2017. Meteoritics & Planetary Science 52.

Bischoff A., Barrat J.-A., Bauer K., Burkhardt C., Busemann H., Ebert S., Gonsior M., Hakenmüller J., Haloda J., Harries D., Heinlein D., Hiesinger H., Hochleitner R., Hoffmann V., Kaliwoda M., Laubenstein M., Maden C., Meier M. M. M., Morlok A., Pack A., Ruf A., Schmitt-Kopplin P., Schönbächler M., Steele R. C. J., Spurný P., and Wimmer K. 2017. The Stubenberg meteorite—An LL6 chondrite fragmental breccia recovered soon after precise prediction of the strewn field. *Meteoritics & Planetary Science* 52:1683–1703. https://doi.org/10.1111/maps.12883.

Bland P. A., Spurný P., Towner M. C., Bevan A. W. R., Singleton A. T., Bottke W. F., Greenwood R. C., Chesley S. R., Shrbený L., Borovička J., Ceplecha Z., McClafferty T. P., Vaughan D., Benedix G. K., Deacon G., Howard K. T., Franchi I. A., and Hough R. M. 2009. An anomalous basaltic meteorite from the innermost Main Belt. *Science* 325:1525. https://doi.org/10.1126/science.1174787.

Bland P. A., Spurný P., Bevan A. W. R., Howard K. T., Towner M. C., Benedix G. K., Greenwood R. C., Shrbený L., Franchi I. A., Deacon G., Borovička J., Ceplecha Z., Vaughan D., and Hough R. M. 2012. The Australian Desert Fireball Network: A new era for planetary science. *Australian Journal of Earth Sciences* 59:177–187. https://doi.org/10.1080/08120099.2011.595428.

Borovička J. 1990. The comparison of two methods of determining meteor trajectories from photographs. *Bulletin of the Astronomical Institutes of Czechoslovakia* 41:391–396.

Borovička J., Spurný P., Kalenda P., and Tagliaferri E. 2003. The Moràvka meteorite fall: 1 Description of the events and determination of the fireball trajectory and orbit from video records. *Meteoritics & Planetary Science* 38:975–987. https://doi.org/10.1111/j.1945-5100.2003.tb00293.x.

Borovička J., Spurný P., Brown P., Wiegert P., Kalenda P., Clark D., and Shrbený L. 2013. The trajectory, structure and origin of the Chelyabinsk asteroidal impactor. *Nature* 503:235–237. https://doi.org/10.1038/nature12671.

Borovička J., Spurný P., and Brown P. 2015. Small near-Earth asteroids as a source of meteorites. In *Asteroids IV*, edited by Michel P., DeMeo F. E., and Bottke W. F. Tucson, Arizona: University of Arizona Press. pp. 257–280. https://10.2458/azu_uapress_9780816532131-ch014.

Bowell E., Virtanen J., Muinonen K., and Boattini A. 2002. *Asteroid orbit computation.* Tucson, Arizona: The University of Arizona Press. pp. 27–43.

Bronshten V. A. 1983. *Physics of meteoric phenomena.* Geophysics and Astrophysics Monographs. Dordrecht, Netherlands: Reidel. ISBN 9789027716545.

Brown P., Pack D., Edwards W. N., Revelle D. O., Yoo B. B., Spalding R. E., and Tagliaferri E. 2004. The orbit, atmospheric dynamics, and initial mass of the Park Forest meteorite. *Meteoritics & Planetary Science* 39:1781–1796. https://doi.org/10.1111/j.1945-5100.2004.tb00075.x.

Brown P., McCausland P. J. A., Fries M., Silber E., Edwards W. N., Wong D. K., Weryk R. J., Fries J., and Krzeminski Z. 2011. The fall of the Grimsby meteorite I: Fireball dynamics and orbit from radar, video, and infrasound records. *Meteoritics & Planetary Science* 46:339–363. https://doi.org/10.1111/j.1945-5100.2010.01167.x.

Brown P. G., Assink J. D., Astiz L., Blaauw R., Boslough M. B., Borovička J., Brachet N., Brown D., Campbell-Brown M., Ceranna L., Cooke W., de Groot-Hedlin C., Drob D. P., Edwards W., Evers L. G., Garces M., Gill J., Hedlin M., Kingery A., Laske G., Le Pichon A., Mialle P., Moser D. E., Saffer A., Silber E., Smets P., Spalding R. E., Spurný P., Tagliaferri E., Uren D., Weryk R. J., Whitaker R., and Krzeminski Z. 2013. A 500-kiloton airburst over Chelyabinsk and an enhanced hazard from small impactors. *Nature* 503:238–241. https://doi.org/10.1038/nature12741.

Ceplecha Z. 1961. Multiple fall of Příbram meteorites photographed. 1. Double-station photographs of the fireball and their relations to the found meteorites. *Bulletin of the Astronomical Institutes of Czechoslovakia* 12:21.

Devillepoix H. A. R., Bland P. A., Towner M. C., Cupák M., Sansom E. K., Jansen-Sturgeon T., Howie R. M., Paxman J., and Hartig B. A. D. 2016. Status of the Desert Fireball Network. In *International Meteor Conference Egmond, the Netherlands, 2–5 June 2016*, edited by Roggemans A. and Roggemans P. pp. 60–62.

The Dingle Dell meteorite fall   15

Farinella P., Vokrouhlický D., and Hartmann W. K. 1998. Meteorite delivery via Yarkovsky orbital drift. *Icarus* 132:378–387. https://doi.org/10.1006/icar.1997.5872.

Fries M. and Fries J. 2010. Doppler weather radar as a meteorite recovery tool. *Meteoritics & Planetary Science* 45:1476–1487. https://doi.org/10.1111/j.1945-5100.2010.01115.x.

Fries M., Le Corre L., Hankey M., Fries J., Matson R., Schaefer J., and Reddy V. 2014. Detection and rapid recovery of the Sutter's Mill meteorite fall as a model for future recoveries worldwide. *Meteoritics & Planetary Science* 49:1989–1996. https://doi.org/10.1111/maps.12249.

Gritsevich M. I. 2009. Determination of parameters of meteor bodies based on flight observational data. *Advances in Space Research* 44:323–334. https://doi.org/10.1016/j.asr.2009.03.030.

Halliday I., Griffin A. A., and Blackwell A. T. 1981. The Innisfree meteorite fall—A photographic analysis of fragmentation, dynamics and luminosity. *Meteoritics* 16:153–170.

Halliday I., Griffin A. A., and Blackwell A. T. 1996. Detailed data for 259 fireballs from the Canadian camera network and inferences concerning the influx of large meteoroids. *Meteoritics & Planetary Science* 31:185–217. https://doi.org/10.1111/j.1945-5100.1996.tb02014.x.

Hankey M. and Perlerin V. 2015. IMO's new online fireball form. *WGN, Journal of the International Meteor Organization* 43:2–7.

Hoppe J. 1937. Die physikalischen Vorgänge beim Eindringen meteoritischer Körper in die Erdatmosphäre. *Astronomische Nachrichten* 262:169–198.

Howie R. M., Paxman J., Bland P. A., Towner M. C., Cupàk M., Sansom E. K., and Devillepoix H. A. R. 2017a. How to build a continental scale fireball camera network. *Experimental Astronomy*. https://doi.org/10.1007/s10686-017-9532-7.

Howie R. M., Paxman J., Bland P. A., Towner M. C., Sansom E. K., and Devillepoix H. A. R. 2017b. Submillisecond fireball timing using de Bruijn timecodes. *Meteoritics & Planetary Science* 52:1669–1682. https://doi.org/10.1111/maps.12878.

Ivezic Z., Axelrod T., Brandt W. N., Burke D. L., Claver C. F., Connolly A., Cook K. H., Gee P., Gilmore D. K., Jacoby S. H., Jones R. L., Kahn S. M., Kantor J. P., Krabbendam V. V., Lupton R. H., Monet D. G., Pinto P. A., Saha A., Schalk T. L., Schneider D. P., Strauss M. A., Stubbs C. W., Sweeney D., Szalay A., Thaler J. J., and Tyson J. A., and Collaboration L. S. S. T. 2008. Large synoptic survey telescope: From science drivers to reference design. *Serbian Astronomical Journal* 176:1–13. https://doi.org/10.2298/SAJ0876001I.

Jenniskens P. 2014. Recent documented meteorite falls, a review of meteorite—Asteroid links. In *Proceedings of the Meteoroids 2013 Conference Aug 26–30, 2013*, edited by Jopek T. J., Rietmeijer F., Watanabe J., and Williams I. P. Poznan, Poland: A. M. University. pp. 57–68.

Jenniskens P., Shaddad M. H., Numan D., Elsir S., Kudoda A. M., Zolensky M. E., Le L., Robinson G. A., Friedrich J. M., Rumble D., Steele A., Chesley S. R., Fitzsimmons A., Duddy S., Hsieh H. H., Ramsay G., Brown P. G., Edwards W. N., Tagliaferri E., Boslough M. B., Spalding R. E., Dantowitz R., Kozubal M., Pravec P., Borovička J., Charvat Z., Vaubaillon J., Kuiper J., Albers J., Bishop J. L., Mancinelli R. L., Sandford S. A., Milam S. N., Nuevo M., and Worden S. P. 2009. The impact and recovery of asteroid 2008 TC$_3$. *Nature* 458:485–488. https://doi.org/10.1038/nature07920.

Jenniskens P., Fries M. D., Yin Q.-Z., Zolensky M., Krot A. N., Sandford S. A., Sears D., Beauford R., Ebel D. S., Friedrich J. M., Nagashima K., Wimpenny J., Yamakawa A., Nishiizumi K., Hamajima Y., Caffee M. W., Welten K. C., Laubenstein M., Davis A. M., Simon S. B., Heck P. R., Young E. D., Kohl I. E., Thiemens M. H., Nunn M. H., Mikouchi T., Hagiya K., Ohsumi K., Cahill T. A., Lawton J. A., Barnes D., Steele A., Rochette P., Verosub K. L., Gattacceca J., Cooper G., Glavin D. P., Burton A. S., Dworkin J. P., Elsila J. E., Pizzarello S., Ogliore R., Schmitt-Kopplin P., Harir M., Hertkorn N., Verchovsky A., Grady M., Nagao K., Okazaki R., Takechi H., Hiroi T., Smith K., Silber E. A., Brown P. G., Albers J., Klotz D., Hankey M., Matson R., Fries J. A., Walker R. J., Puchtel I., Lee C.-T. A., Erdman M. E., Eppich G. R., Roeske S., Gabelica Z., Lerche M., Nuevo M., Girten B., and Worden S. P. 2012. Radar-enabled recovery of the Sutter's Mill meteorite, a carbonaceous chondrite regolith breccia. *Science* 338:1583. https://doi.org/10.1126/science.1227163.

Jenniskens P., Rubin A. E., Yin Q.-Z., Sears D. W. G., Sandford S. A., Zolensky M. E., Krot A. N., Blair L., Kane D., Utas J., Verish R., Friedrich J. M., Wimpenny J., Eppich G. R., Ziegler K., Verosub K. L., Rowland D. J., Albers J., Gural P. S., Grigsby B., Fries M. D., Matson R., Johnston M., Silber E., Brown P., Yamakawa A., Sanborn M. E., Laubenstein M., Welten K. C., Nishiizumi K., Meier M. M. M., Busemann H., Clay P., Caffee M. W., Schmitt-Kopplin P., Hertkorn N., Glavin D. P., Callahan M. P., Dworkin J. P., Wu Q., Zare R. N., Grady M., Verchovsky S., Emel'Yanenko V., Naroenkov S., Clark D. L., Girten B., and Worden P. S. 2014. Fall, recovery, and characterization of the Novato L6 chondrite breccia. *Meteoritics & Planetary Science* 49:1388–1425. https://doi.org/10.1111/maps.12323.

Keay C. S. 1992. Electrophonic sounds from large meteor fireballs. *Meteoritics & Planetary Science* 27:144–148.

Keil K., Stoeffler D., Love S. G., and Scott E. R. D. 1997. Constraints on the role of impact heating and melting in asteroids. *Meteoritics & Planetary Science* 32:349–363. https://doi.org/10.1111/j.1945-5100.1997.tb01278.x.

McCrosky R. E. and Boeschenstein H. 1965. The Prairie meteorite network. *Optical Engineering* 3:304127.

Meteoritical Bulletin, 104, 2015.

Meteoritical Bulletin, 105, 2016.

Meteoritical Bulletin, 106, 2017.

Morbidelli A., Gonczi R., Froeschle C., and Farinella P. 1994. Delivery of meteorites through the nu$_6$ secular resonance. *Astronomy & Astrophysics* 282:955–979.

Nakamura T., Noguchi T., Tanaka M., Zolensky M. E., Kimura M., Tsuchiyama A., Nakato A., Ogami T., Ishida H., Uesugi M., Yada T., Shirai K., Fujimura A., Okazaki R., Sandford S. A., Ishibashi Y., Abe M., Okada T., Ueno M., Mukai T., Yoshikawa M., and Kawaguchi J. 2011. Itokawa dust particles: A direct link between S-type asteroids and ordinary chondrites. *Science* 333:1113. https://doi.org/10.1126/science.1207758.

Nesvorný D., Vokrouhlický D., Morbidelli A., and Bottke W. F. 2009. Asteroidal source of L chondrite meteorites. *Icarus* 200:698–701. https://doi.org/10.1016/j.icarus.2008.12.016.

Oberst J., Molau S., Heinlein D., Gritzner C., Schindler M., Spurny P., Ceplecha Z., Rendtel J., and Betlem H. 1998. The "European Fireball Network": Current status and future prospects. *Meteoritics & Planetary Science* 33:49–56. https://doi.org/10.1111/j.1945-5100.1998.tb01606.x.

Palotai C., Sankar R., Free D. L., Howell J. A., Botella E., and Batcheldor D. 2018. Analysis of June 2, 2016 bolide event. *ArXiv e-prints*.

Paxman J. and Bland P. 2014. Fireballs in the sky: Improving the accuracy of crowd sourced fireball observation through the application of smartphone technology (abstract #1731). 45th Lunar and Planetary Science Conference. CD-ROM.

Picone J. M., Hedin A. E., Drob D. P., and Aikin A. C. 2002. NRLMSISE-00 empirical model of the atmosphere: Statistical comparisons and scientific issues. *Journal of Geophysical Research (Space Physics)* 107:1468. https://doi.org/10.1029/2002JA009430.

Reddy V., Sanchez J. A., Bottke W. F., Cloutis E. A., Izawa M. R. M., O'Brien D. P., Mann P., Cuddy M., Le Corre L., Gaffey M. J., and Fujihara G. 2014. Chelyabinsk meteorite explains unusual spectral properties of Baptistina Asteroid Family. *Icarus* 237:116–130. https://doi.org/10.1016/j.icarus.2014.04.027.

Rein H. and Tamayo D. 2015. WHFAST: A fast and unbiased implementation of a symplectic Wisdom-Holman integrator for long-term gravitational simulations. *Monthly Notices of the Royal Astronomical Society* 452:376–388. https://doi.org/10.1093/mnras/stv1257.

Sansom E. K. 2016. Tracking meteoroids in the atmosphere: Fireball Trajectory Analysis. PhD thesis, Curtin University. http://hdl.handle.net/20.500.11937/55061.

Sansom E. K., Bland P., Paxman J., and Towner M. 2015. A novel approach to fireball modeling: The observable and the calculated. *Meteoritics & Planetary Science* 50:1423–1435. https://doi.org/10.1111/maps.12478.

Sansom E., Ridgewell J., Bland P., and Paxman J. 2016. Meteor reporting made easy—The Fireballs in the Sky smartphone app. In *International Meteor Conference Egmond, the Netherlands, 2-5 June 2016*, edited by Roggemans A. and Roggemans P. pp. 267–269.

Sansom E. K., Rutten M. G., and Bland P. A. 2017. Analyzing meteoroid flights using particle filters. *The Astronomical Journal* 153:87. https://doi.org/10.3847/1538-3881/153/2/87.

Schmitz B., Tassinari M., and Peucker-Ehrenbrink B. 2001. A rain of ordinary chondritic meteorites in the early Ordovician. *Earth and Planetary Science Letters* 194:1–15. https://doi.org/10.1016/S0012-821X(01)00559-3.

Skamarock W. C., Klemp J. B., Dudhia J., Gill D. O., Barker D. M., Duda M. G., Huang X. Y., Wang W., and Powers J. G. 2008. A description of the advanced research wrf version 3. Technical report, NCAR Technical Note NCAR/TN-475 + STR.

Southworth R. B. and Hawkins G. S. 1963. Statistics of meteor streams. *Smithsonian Contributions to Astrophysics* 7:261.

Spurný P., Borovička J., Kac J., Kalenda P., Atanackov J., Kladnik G., Heinlein D., and Grau T. 2010. Analysis of instrumental observations of the Jesenice meteorite fall on April 9, 2009. *Meteoritics & Planetary Science* 45:1392–1407. https://doi.org/10.1111/j.1945-5100.2010.01121.x.

Spurný P., Bland P. A., Shrbený L., Towner M. C., Borovička J., Bevan A. W. R., and Vaughan D. 2011. The Mason Gully Meteorite Fall in SW Australia: Fireball trajectory and orbit from photographic records. *Meteoritics & Planetary Science Supplement* 74:5101.

Spurný P., Haloda J., Borovička J., Shrbený L., and Halodovà P. 2014. Reanalysis of the Benešov bolide and recovery of polymict breccia meteorites—Old mystery solved after 20 years. *Astronomy & Astrophysics* 570:A39. https://doi.org/10.1051/0004-6361/201424308.

Spurný P., Borovička J., Haloda J., Shrbený L., and Heinlein D. 2016. Two very precisely instrumentally documented meteorite falls: Žďár nad Sázavou and Stubenberg—Prediction and reality (abstract #6221). In 79th Annual Meeting of the Meteoritical Society. *Meteoritics & Planetary Science* 51. LPI Contribution No. 1921.

Trigo-Rodríguez J. M., Borovička J., Spurný P., Ortiz J. L., Docobo J. A., Castro-Tirado A. J., and Llorca J. 2006. The Villalbeto de la Penã meteorite fall: II. Determination of atmospheric trajectory and orbit. *Meteoritics & Planetary Science* 41:505–517. https://doi.org/10.1111/j.1945-5100.2006.tb00478.x.

Trigo-Rodríguez J. M., Lyytinen E., Gritsevich M., Moreno-Ibáñez M., Bottke W. F., Williams I., Lupovka V., Dmitriev V., Kohout T., and Grokhovsky V. 2015. Orbit and dynamic origin of the recently recovered Annama's H5 chondrite. *Monthly Notices of the Royal Astronomical Society* 449:2119–2127. https://doi.org/10.1093/mnras/stv378.

Vernazza P., Binzel R. P., Thomas C. A., DeMeo F. E., Bus S. J., Rivkin A. S., and Tokunaga A. T. 2008. Compositional differences between meteorites and near-Earth asteroids. *Nature* 454:858–860. https://doi.org/10.1038/nature07154.

Whipple F. L. 1939. The Prairie meteorite network. In *Proceedings of the American Philosophical Society*. 79:499–548.

SUPPORTING INFORMATION

Additional supporting information may be found in the online version of this article:.

Table S1. Astrometric data for Badgingarra camera.

Table S2. Astrometric data for Perenjori camera.

Table S3. Astrometric data for Northam.

Table S4. Trajectory solution.

Table S5. Weather model profile W1.

File S6. Meteorite searching GPS tracks.

Manuscript − Taurid meteoroid stream #628: a reservoir of large impactors

Hadrien A. R. Devillepoix, Philip A. Bland, Eleanor K. Sansom, Martin C. Towner, Martin Cupák, Robert M. Howie, Benjamin A. D. Hartig, Trent Jansen-Sturgeon, Morgan A. Cox

This chapter is laid out as a manuscript to be submitted to Astronomy & Astrophysics

Statement of Authorship

Title of Paper: Taurid meteoroid stream #628: a reservoir of large impactors.

Publication Status: In preparation; publication style.

Author Contributions

By signing the Statement of Authorship, each author certifies that their stated contribution to the publication is accurate and that permission is granted for the publication to be included in the candidate's thesis.

Name of Principal Author: Hadrien A. R. Devillepoix

Contribution to the Paper: Led the discussion. Contributed to astrometric, photometric, trajectory, and orbital analysis for the DFN data. Drafted and revised the manuscript for this publication.

Overall Percentage: 71%

Signature: *Date:*

Sept 19, 2018

Name of Co-Author: Philip A. Bland

Contribution to the Paper: Contributed to the discussion, and assisted with editing and revision of the manuscript.

Overall Percentage: 5%

Signature: *Date:*

Sept 19, 2018
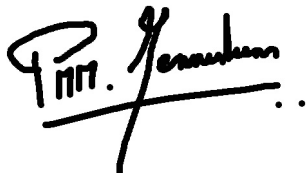
Name of Co-Author: Petrus M. M. Jenniskens

Contribution to the Paper: Reduced and interpreted the CAMS data, contributed to the results and the discussion, and assisted with editing and revision of the manuscript.

Overall Percentage: 15%

Signature: *Date:*

Sept 20, 2018

Name of Co-Author: Eleanor K. Sansom

Contribution to the Paper: Contributed to velocity modelling, and assisted with editing and revision of the manuscript.

Overall Percentage: 2%

Signature: *Date:*

Sept 19, 2018

Name of Co-Author:　Martin C. Towner

Contribution to the Paper:　Assisted with editing and revision of the manuscript.

Overall Percentage:　1%

Signature:　　　　　　　　　　　　　　*Date:*

Sept 19, 2018

Name of Co-Author:　Martin Cupák

Contribution to the Paper:　Assisted with editing and revision of the manuscript.

Overall Percentage:　1%

Signature:　　　　　　　　　　　　　　*Date:*

Sept 19, 2018

Name of Co-Author:　Robert M. Howie

Contribution to the Paper:　Assisted with editing and revision of the manuscript.

Overall Percentage:　1%

Signature:　　　　　　　　　　　　　　*Date:*

Sept 20, 2018

Name of Co-Author: Benjamin A. D. Hartig

Contribution to the Paper: Assisted with editing and revision of the manuscript.

Overall Percentage: 1%

Signature: *Date:*

Sept 19, 2018

Name of Co-Author: Trent Jansen-Sturgeon

Contribution to the Paper: Assisted with editing and revision of the manuscript.

Overall Percentage: 1%

Signature: *Date:*

Sept 19, 2018

Name of Co-Author: Morgan A. Cox

Contribution to the Paper: Assisted with editing and revision of the manuscript.

Overall Percentage: 1%

Signature: *Date:*

Sept 19, 2018

Name of Co-Author: Jonathan Paxman

Contribution to the Paper: Assisted with editing and revision of the manuscript.

Overall Percentage: 1%

Signature: *Date:*

Sept 19, 2018

APPENDIX B

CO-AUTHORED JOURNAL PUBLICATION REPRINTS

CO-AUTHORED PAPER 1 – PLUTO'S ATMOSPHERE FROM THE 2015 JUNE 29 GROUND-BASED STELLAR OCCULTATION AT THE TIME OF THE NEW HORIZONS FLYBY

B. Sicardy, J. Talbot, E. Meza, J. I. B. Camargo, J. Desmars, D. Gault, D. Herald, S. Kerr, H. Pavlov, F. Braga-Ribas, M. Assafin, G. Benedetti-Rossi, A. Dias- Oliveira, A. R. Gomes-Júnior, R. Vieira-Martins, D. Bérard, P. Kervella, J. Lecacheux, E. Lellouch, W. Beisker, D. Dunham, M. Jelınek, R. Duffard, J. L. Ortiz, A. J. Castro-Tirado, R. Cunniffe, R. Querel, P. C. Yock, A. A. Cole, A. B. Giles, K. M. Hill, J. P. Beaulieu, M. Harnisch, R. Jansen, A. Pennell, S. Todd, W. H. Allen, P. B. Graham, B. Loader, G. McKay, J. Milner, S. Parker, M. A. Barry, J. Bradshaw, J. Broughton, L. Davis, H. Devillepoix, J. Drummond, L. Field, M. Forbes, D. Giles, R. Glassey, R. Groom, D. Hooper, R. Horvat, G. Hudson, R. Idaczyk, D. Jenke, B. Lade, J. Newman, P. Nosworthy, P. Pur- cell, P. F. Skilton, M. Streamer, M. Unwin, H. Watanabe, G. L. White, and D. Watson.

CO-AUTHORED PAPER 2 — MULTI-MESSENGER OBSERVATIONS OF A BINARY NEUTRON STAR MERGER

LIGO Scientific Collaboration, Virgo Collaboration, Fermi GBM, INTEGRAL, IceCube Collaboration, AstroSat Cadmium Zinc Telluride Imager Team, IPN Collaboration, The Insight-HXMT Collaboration, ANTARES Collaboration, The Swift Collaboration, AGILE Team, The 1M2H Team, The Dark Energy Camera GW-EM Collaboration, the DES Collaboration, The DLT40 Collaboration, GRAWITA: GRAvitational Wave Inaf TeAm, The Fermi Large Area Telescope Collaboration, ATCA: Australia Telescope Compact Array, ASKAP: Australian SKA Pathfinder, Las Cumbres Observatory Group, OzGrav, DWF(Deeper, Wider, Faster Program), AST3, and CAASTRO Collaborations, The VINROUGE Collaboration, MASTER Collaboration, J-GEM GROWTH, JAGWAR, Caltech-NRAO, TTU-NRAO, and NuSTAR Collaborations, Pan-STARRS, TheMAXITeam, TZACConsortium, KU Collaboration, NordicOptical Telescope, ePESSTO, GROND, Texas Tech University, SALT Group, TOROS: Transient Robotic Observatory of the SouthCollaboration, The BOOTES Collaboration, MWA: Murchison Widefield Array, The CALET Collaboration, IKI-GW Follow-up Collaboration, H.E.S.S. Collaboration, LOFAR Collaboration, LWA: Long Wavelength Array, HAWC Collaboration, The Pierre Auger Collaboration, ALMA Collaboration, Euro VLBI Team, Pi of the Sky Collaboration, The Chandra Team at McGill University, **DFN: Desert Fireball Network**, *ATLAS, High Time Resolution Universe Survey, RIMAS, RATIR, and SKA South Africa/MeerKAT.* **3677 authors**, *including* **H. A. R. Devillepoix***).*

Multi-messenger Observations of a Binary Neutron Star Merger[*]

LIGO Scientific Collaboration and Virgo Collaboration, Fermi GBM, INTEGRAL, IceCube Collaboration, AstroSat Cadmium Zinc Telluride Imager Team, IPN Collaboration, The Insight-HXMT Collaboration, ANTARES Collaboration, The Swift Collaboration, AGILE Team, The 1M2H Team, The Dark Energy Camera GW-EM Collaboration and the DES Collaboration, The DLT40 Collaboration, GRAWITA: GRAvitational Wave Inaf TeAm, The Fermi Large Area Telescope Collaboration, ATCA: Australia Telescope Compact Array, ASKAP: Australian SKA Pathfinder, Las Cumbres Observatory Group, OzGrav, DWF (Deeper, Wider, Faster Program), AST3, and CAASTRO Collaborations, The VINROUGE Collaboration, MASTER Collaboration, J-GEM, GROWTH, JAGWAR, Caltech-NRAO, TTU-NRAO, and NuSTAR Collaborations, Pan-STARRS, The MAXI Team, TZAC Consortium, KU Collaboration, Nordic Optical Telescope, ePESSTO, GROND, Texas Tech University, SALT Group, TOROS: Transient Robotic Observatory of the South Collaboration, The BOOTES Collaboration, MWA: Murchison Widefield Array, The CALET Collaboration, IKI-GW Follow-up Collaboration, H.E.S.S. Collaboration, LOFAR Collaboration, LWA: Long Wavelength Array, HAWC Collaboration, The Pierre Auger Collaboration, ALMA Collaboration, Euro VLBI Team, Pi of the Sky Collaboration, The Chandra Team at McGill University, DFN: Desert Fireball Network, ATLAS, High Time Resolution Universe Survey, RIMAS and RATIR, and SKA South Africa/MeerKAT

(See the end matter for the full list of authors.)

Abstract

On 2017 August 17 a binary neutron star coalescence candidate (later designated GW170817) with merger time 12:41:04 UTC was observed through gravitational waves by the Advanced LIGO and Advanced Virgo detectors. The *Fermi* Gamma-ray Burst Monitor independently detected a gamma-ray burst (GRB 170817A) with a time delay of ~ 1.7 s with respect to the merger time. From the gravitational-wave signal, the source is initially localized to a sky region of 31 deg^2 at a luminosity distance of 40^{+8}_{-8} Mpc and with component masses consistent with neutron stars. The component masses were later measured to be in the range 0.86 to 2.26 $M_\odot$. An extensive observing campaign was launched across the electromagnetic spectrum leading to the discovery of a bright optical transient (SSS17a, now with the IAU identification of AT 2017gfo) in NGC 4993 (at ~ 40 Mpc) less than 11 hours after the merger by the One-Meter, Two Hemisphere (1M2H) team using the 1 m Swope Telescope. The optical transient was independently detected by multiple teams within an hour. Subsequent observations targeted the object and its environment. Early ultraviolet observations revealed a blue transient that faded within 48 hours. Optical and infrared observations showed a redward evolution over ~ 10 days. Following early non-detections, X-ray and radio emission were discovered at the transient's position ~ 9 and ~ 16 days, respectively, after the merger. Both the X-ray and radio emission likely arise from a physical process that is distinct from the one that generates the UV/optical/near-infrared emission. No ultra-high-energy gamma-rays and no neutrino candidates consistent with the source were found in follow-up searches. These observations support the hypothesis that GW170817 was produced by the merger of two neutron stars in NGC 4993 followed by a short gamma-ray burst (GRB 170817A) and a kilonova/macronova powered by the radioactive decay of *r*-process nuclei synthesized in the ejecta.

Key words: gravitational waves – stars: neutron

1. Introduction

Over 80 years ago Baade & Zwicky (1934) proposed the idea of neutron stars, and soon after, Oppenheimer & Volkoff (1939) carried out the first calculations of neutron star models. Neutron stars entered the realm of observational astronomy in the 1960s by providing a physical interpretation of X-ray emission from Scorpius X-1 (Giacconi et al. 1962; Shklovsky 1967) and of radio pulsars (Gold 1968; Hewish et al. 1968; Gold 1969).

The discovery of a radio pulsar in a double neutron star system by Hulse & Taylor (1975) led to a renewed interest in binary stars and compact-object astrophysics, including the development of a scenario for the formation of double neutron stars and the first population studies (Flannery & van den Heuvel 1975; Massevitch et al. 1976; Clark 1979; Clark et al. 1979; Dewey & Cordes 1987; Lipunov et al. 1987; for reviews see Kalogera et al. 2007; Postnov & Yungelson 2014). The Hulse-Taylor pulsar provided the first firm evidence (Taylor & Weisberg 1982) of the existence of gravitational waves (Einstein 1916, 1918) and sparked a renaissance of observational tests of general relativity (Damour & Taylor 1991, 1992; Taylor et al. 1992; Wex 2014). Merging binary neutron stars (BNSs) were quickly recognized to be promising sources of detectable gravitational waves, making them a primary target for ground-based interferometric detectors (see Abadie et al. 2010 for an overview). This motivated the development of accurate models for the two-body, general-relativistic dynamics (Blanchet et al. 1995; Buonanno & Damour 1999; Pretorius 2005; Baker et al. 2006; Campanelli et al. 2006; Blanchet 2014) that are critical for detecting and interpreting gravitational waves (Abbott et al. 2016c, 2016d, 2016e, 2017a, 2017c, 2017d).
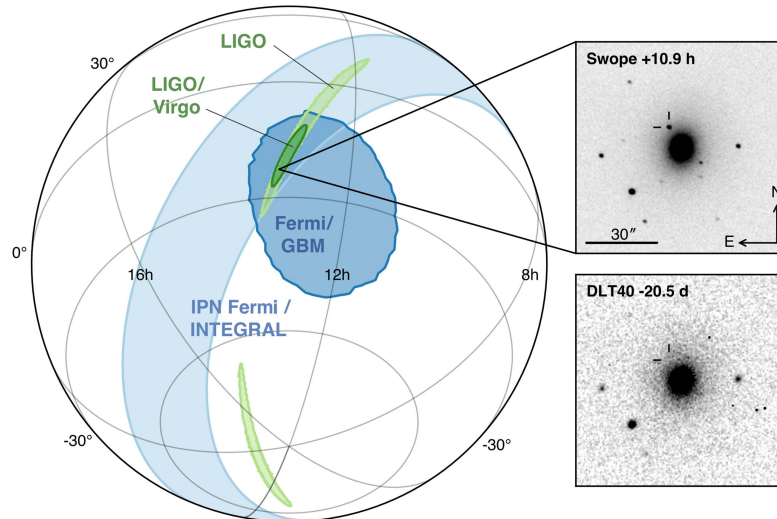

Figure 1. Localization of the gravitational-wave, gamma-ray, and optical signals. The left panel shows an orthographic projection of the 90% credible regions from LIGO (190 deg^2; light green), the initial LIGO-Virgo localization (31 deg^2; dark green), IPN triangulation from the time delay between *Fermi* and *INTEGRAL* (light blue), and *Fermi*-GBM (dark blue). The inset shows the location of the apparent host galaxy NGC 4993 in the Swope optical discovery image at 10.9 hr after the merger (top right) and the DLT40 pre-discovery image from 20.5 days prior to merger (bottom right). The reticle marks the position of the transient in both images.

In the mid-1960s, gamma-ray bursts (GRBs) were discovered by the Vela satellites, and their cosmic origin was first established by Klebesadel et al. (1973). GRBs are classified as *long* or *short*, based on their duration and spectral hardness (Dezalay et al. 1992; Kouveliotou et al. 1993). Uncovering the progenitors of GRBs has been one of the key challenges in high-energy astrophysics ever since (Lee & Ramirez-Ruiz 2007). It has long been suggested that short GRBs might be related to neutron star mergers (Goodman 1986; Paczynski 1986; Eichler et al. 1989; Narayan et al. 1992).

In 2005, the field of short gamma-ray burst (sGRB) studies experienced a breakthrough (for reviews see Nakar 2007; Berger 2014) with the identification of the first host galaxies of sGRBs and multi-wavelength observation (from X-ray to optical and radio) of their afterglows (Berger et al. 2005; Fox et al. 2005; Gehrels et al. 2005; Hjorth et al. 2005b; Villasenor et al. 2005). These observations provided strong hints that sGRBs might be associated with mergers of neutron stars with other neutron stars or with black holes. These hints included: (i) their association with both elliptical and star-forming galaxies (Barthelmy et al. 2005; Prochaska et al. 2006; Berger et al. 2007; Ofek et al. 2007; Troja et al. 2008; D'Avanzo et al. 2009; Fong et al. 2013), due to a very wide range of delay times, as predicted theoretically (Bagot et al. 1998; Fryer et al. 1999; Belczynski et al. 2002); (ii) a broad distribution of spatial offsets from host-galaxy centers (Berger 2010; Fong & Berger 2013; Tunnicliffe et al. 2014), which was predicted to arise from supernova kicks (Narayan et al. 1992; Bloom et al. 1999); and (iii) the absence of associated supernovae (Fox et al. 2005; Hjorth et al. 2005c, 2005a; Soderberg et al. 2006; Kocevski et al. 2010; Berger et al. 2013a). Despite these strong hints, proof that sGRBs were powered by neutron star mergers remained elusive, and interest intensified in following up gravitational-wave detections electromagnetically (Metzger & Berger 2012; Nissanke et al. 2013).

Evidence of beaming in some sGRBs was initially found by Soderberg et al. (2006) and Burrows et al. (2006) and confirmed by subsequent sGRB discoveries (see the compilation and analysis by Fong et al. 2015 and also Troja et al. 2016). Neutron star binary mergers are also expected, however, to produce isotropic electromagnetic signals, which include (i) early optical and infrared emission, a so-called kilonova/macronova (hereafter kilonova; Li & Paczyński 1998; Kulkarni 2005; Rosswog 2005; Metzger et al. 2010; Roberts et al. 2011; Barnes & Kasen 2013; Kasen et al. 2013; Tanaka & Hotokezaka 2013; Grossman et al. 2014; Barnes et al. 2016; Tanaka 2016; Metzger 2017) due to radioactive decay of rapid neutron-capture process (*r*-process) nuclei (Lattimer & Schramm 1974, 1976) synthesized in dynamical and accretion-disk-wind ejecta during the merger; and (ii) delayed radio emission from the interaction of the merger ejecta with the ambient medium (Nakar & Piran 2011; Piran et al. 2013; Hotokezaka & Piran 2015; Hotokezaka et al. 2016). The late-time infrared excess associated with GRB 130603B was interpreted as the signature of *r*-process nucleosynthesis (Berger et al. 2013b; Tanvir et al. 2013), and more candidates were identified later (for a compilation see Jin et al. 2016).

Here, we report on the global effort[958] that led to the first joint detection of gravitational and electromagnetic radiation from a single source. An ~ 100 s long gravitational-wave signal (GW170817) was followed by an sGRB (GRB 170817A) and an optical transient (SSS17a/AT 2017gfo) found in the host galaxy NGC 4993. The source was detected across the electromagnetic spectrum—in the X-ray, ultraviolet, optical, infrared, and radio bands—over hours, days, and weeks. These observations support the hypothesis that GW170817 was produced by the merger of two neutron stars in NGC4993, followed by an sGRB and a kilonova powered by the radioactive decay of *r*-process nuclei synthesized in the ejecta.

---

[958] A follow-up program established during initial LIGO-Virgo observations (Abadie et al. 2012) was greatly expanded in preparation for Advanced LIGO-Virgo observations. Partners have followed up binary black hole detections, starting with GW150914 (Abbott et al. 2016a), but have discovered no firm electromagnetic counterparts to those events.

2. A Multi-messenger Transient

On 2017 August 17 12:41:06 UTC the *Fermi* Gamma-ray Burst Monitor (GBM; Meegan et al. 2009) onboard flight software triggered on, classified, and localized a GRB. A Gamma-ray Coordinates Network (GCN) Notice (Fermi-GBM 2017) was issued at 12:41:20 UTC announcing the detection of the GRB, which was later designated GRB 170817A (von Kienlin et al. 2017). Approximately 6 minutes later, a gravitational-wave candidate (later designated GW170817) was registered in low latency (Cannon et al. 2012; Messick et al. 2017) based on a single-detector analysis of the Laser Interferometer Gravitational-wave Observatory (LIGO) Hanford data. The signal was consistent with a BNS coalescence with merger time, t_c, 12:41:04 UTC, less than 2 s before GRB 170817A. A GCN Notice was issued at 13:08:16 UTC. Single-detector gravitational-wave triggers had never been disseminated before in low latency. Given the temporal coincidence with the *Fermi*-GBM GRB, however, a GCN Circular was issued at 13:21:42 UTC (LIGO Scientific Collaboration & Virgo Collaboration et al. 2017a) reporting that a highly significant candidate event consistent with a BNS coalescence was associated with the time of the GRB[959]. An extensive observing campaign was launched across the electromagnetic spectrum in response to the *Fermi*-GBM and LIGO–Virgo detections, and especially the subsequent well-constrained, three-dimensional LIGO–Virgo localization. A bright optical transient (SSS17a, now with the IAU identification of AT 2017gfo) was discovered in NGC 4993 (at ∼40 Mpc) by the 1M2H team (August 18 01:05 UTC; Coulter et al. 2017a) less than 11 hr after the merger.

2.1. Gravitational-wave Observation

GW170817 was first detected online (Cannon et al. 2012; Messick et al. 2017) as a single-detector trigger and disseminated through a GCN Notice at 13:08:16 UTC and a GCN Circular at 13:21:42 UTC (LIGO Scientific Collaboration & Virgo Collaboration et al. 2017a). A rapid re-analysis (Nitz et al. 2017a, 2017b) of data from LIGO-Hanford, LIGO-Livingston, and Virgo confirmed a highly significant, coincident signal. These data were then combined to produce the first three-instrument skymap (Singer & Price 2016; Singer et al. 2016) at 17:54:51 UTC (LIGO Scientific Collaboration & Virgo Collaboration et al. 2017b), placing the source nearby, at a luminosity distance *initially* estimated to be 40^{+8}_{-8} Mpc in an elongated region of ≈31 deg² (90% credibility), centered around R.A. α(J2000.0) = $12^h 57^m$ and decl. δ(J2000.0) = $-17°51'$. Soon after, a coherent analysis (Veitch et al. 2015) of the data from the detector network produced a skymap that was distributed at 23:54:40 UTC (LIGO Scientific Collaboration & Virgo Collaboration et al. 2017c), consistent with the initial one: a ≃34 deg² sky region at 90% credibility centered around α(J2000.0) = $13^h 09^m$ and δ(J2000.0) = $-25°37'$.

The offline gravitational-wave analysis of the LIGO-Hanford and LIGO-Livingston data identified GW170817 with a false-alarm rate of less than one per 8.0×10^4 (Abbott et al. 2017c). This analysis uses post-Newtonian waveform models (Blanchet et al. 1995, 2004, 2006; Bohé et al. 2013) to construct a matched-filter search (Sathyaprakash & Dhurandhar 1991; Cutler et al. 1993; Allen et al. 2012) for gravitational waves from the coalescence of compact-object binary systems in the (detector frame) total mass range 2–500 $M_\odot$. GW170817 lasted for ∼100 s in the detector sensitivity band. The signal reached Virgo first,

then LIGO-Livingston 22 ms later, and after 3 ms more, it arrived at LIGO-Hanford. GW170817 was detected with a combined signal-to-noise ratio across the three-instrument network of 32.4. For comparison, GW150914 was observed with a signal-to-noise ratio of 24 (Abbott et al. 2016c).

The properties of the source that generated GW170817 (see Abbott et al. 2017c for full details; here, we report parameter ranges that span the 90% credible interval) were derived by employing a coherent Bayesian analysis (Veitch et al. 2015; Abbott et al. 2016b) of the three-instrument data, including marginalization over calibration uncertainties and assuming that the signal is described by waveform models of a binary system of compact objects in quasi-circular orbits (see Abbott et al. 2017c and references therein). The waveform models include the effects introduced by the objects' intrinsic rotation (spin) and tides. The source is located in a region of 28 deg² at a distance of 40^{+8}_{-14} Mpc, see Figure 1, consistent with the early estimates disseminated through GCN Circulars (LIGO Scientific Collaboration & Virgo Collaboration et al. 2017b, 2017c). The misalignment between the total angular momentum axis and the line of sight is ⩽56°.

The (source-frame[960]) masses of the primary and secondary components, m_1 and m_2, respectively, are in the range $m_1 \in (1.36–2.26)M_\odot$ and $m_2 \in (0.86–1.36)M_\odot$. The chirp mass,[961] $\mathcal{M}$, is the mass parameter that, at the leading order, drives the frequency evolution of gravitational radiation in the inspiral phase. This dominates the portion of GW170817 in the instruments' sensitivity band. As a consequence, it is the best measured mass parameter, $\mathcal{M} = 1.188^{+0.004}_{-0.002} M_\odot$. The total mass is $2.82^{+0.47}_{-0.09} M_\odot$, and the mass ratio m_2/m_1 is bound to the range 0.4–1.0. These results are consistent with a binary whose components are neutron stars. White dwarfs are ruled out since the gravitational-wave signal sweeps through 200 Hz in the instruments' sensitivity band, implying an orbit of size ∼100 km, which is smaller than the typical radius of a white dwarf by an order of magnitude (Shapiro & Teukolsky 1983). However, for this event gravitational-wave data *alone* cannot rule out objects more compact than neutron stars such as quark stars or black holes (Abbott et al. 2017c).

2.2. Prompt Gamma-Ray Burst Detection

The first announcement of GRB 170817A came from the GCN Notice (Fermi-GBM 2017) automatically generated by *Fermi*-GBM at 12:41:20 UTC, just 14 s after the detection of the GRB at T0 = 12:41:06 UTC. GRB 170817A was detected by the *International Gamma-Ray Astrophysics Laboratory* (*INTEGRAL*) spacecraft using the Anti-Coincidence Shield (von Kienlin et al. 2003) of the spectrometer on board *INTEGRAL* (SPI), through an offline search initiated by the LIGO-Virgo and *Fermi*-GBM reports. The final *Fermi*-GBM localization constrained GRB 170817A to a region with highest probability at α(J2000.0) = $12^h 28^m$ and δ(J2000.0) = $-30°$ and 90% probability region covering ∼1100 deg² (Goldstein et al. 2017a). The difference between the binary merger and the

---

[959] The trigger was recorded with LIGO-Virgo ID G298048, by which it is referred throughout the GCN Circulars.

[960] Any mass parameter $m^{(\mathrm{det})}$ derived from the observed signal is measured in the detector frame. It is related to the mass parameter, m, in the source frame by $m^{(\mathrm{det})} = (1 + z)m$, where z is the source's redshift. Here, we always report source-frame mass parameters, assuming standard cosmology (Ade et al. 2016) and correcting for the motion of the solar Ssystem barycenter with respect to the cosmic microwave background (Fixsen 2009). From the gravitational-wave luminosity distance measurement, the redshift is determined to be $z = 0.008^{+0.002}_{-0.003}$. For full details see Abbott et al. (2016b, 2017c, 2017e).

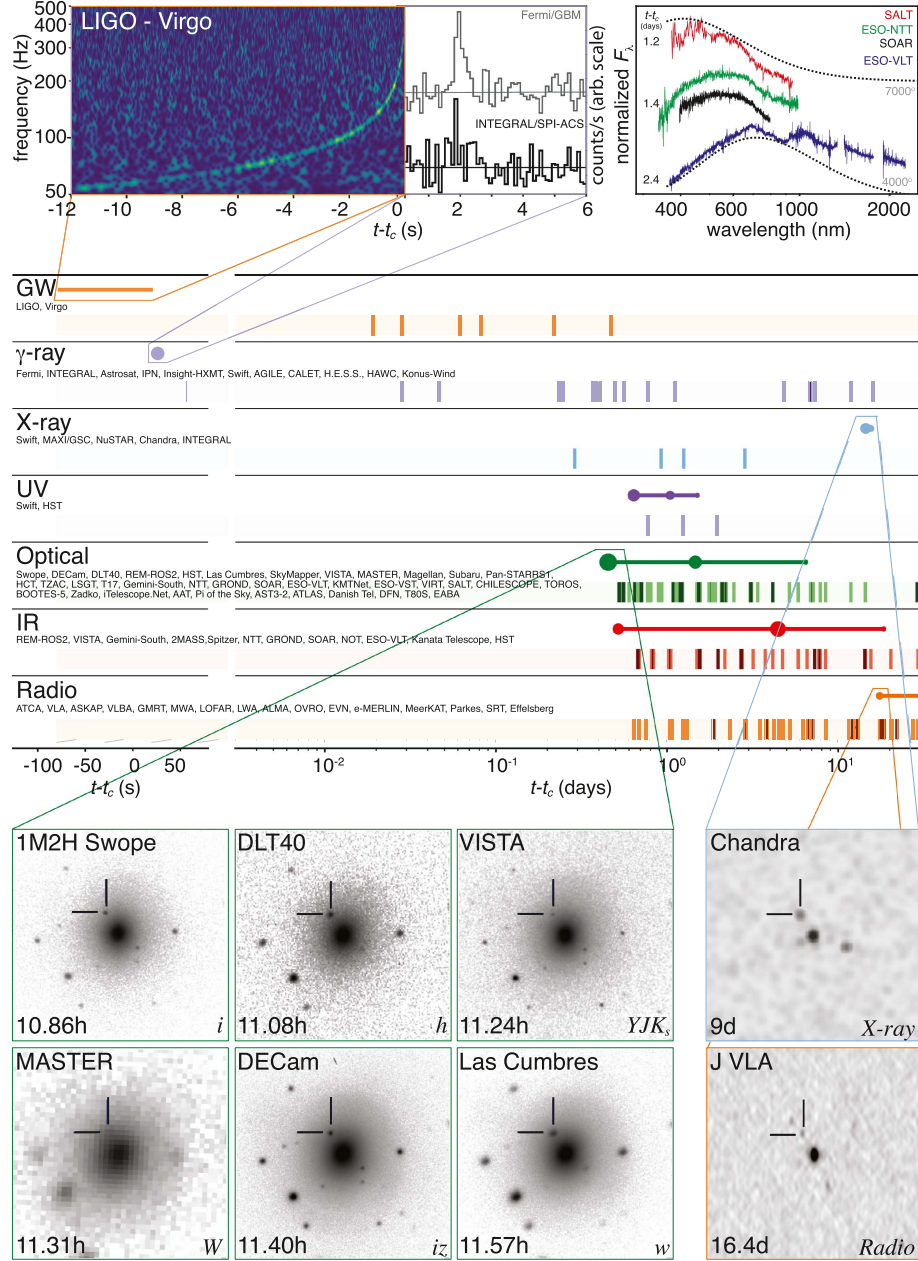[961] The binary's chirp mass is defined as $\mathcal{M} = (m_1 m_2)^{3/5}/(m_1 + m_2)^{1/5}$.

Figure 2. Timeline of the discovery of GW170817, GRB 170817A, SSS17a/AT 2017gfo, and the follow-up observations are shown by messenger and wavelength relative to the time t_c of the gravitational-wave event. Two types of information are shown for each band/messenger. First, the shaded dashes represent the times when information was reported in a GCN Circular. The names of the relevant instruments, facilities, or observing teams are collected at the beginning of the row. Second, representative observations (see Table 1) in each band are shown as solid circles with their areas approximately scaled by brightness; the solid lines indicate when the source was detectable by at least one telescope. Magnification insets give a picture of the first detections in the gravitational-wave, gamma-ray, optical, X-ray, and radio bands. They are respectively illustrated by the combined spectrogram of the signals received by LIGO-Hanford and LIGO-Livingston (see Section 2.1), the *Fermi*-GBM and *INTEGRAL*/SPI-ACS lightcurves matched in time resolution and phase (see Section 2.2), $1\rlap{.}'5 \times 1\rlap{.}'5$ postage stamps extracted from the initial six observations of SSS17a/AT 2017gfo and four early spectra taken with the SALT (at $t_c + 1.2$ days; Buckley et al. 2017; McCully et al. 2017b), ESO-NTT (at $t_c + 1.4$ days; Smartt et al. 2017), the SOAR 4 m telescope (at $t_c + 1.4$ days; Nicholl et al. 2017d), and ESO-VLT-XShooter (at $t_c + 2.4$ days; Smartt et al. 2017) as described in Section 2.3, and the first X-ray and radio detections of the same source by *Chandra* (see Section 3.3) and JVLA (see Section 3.4). In order to show representative spectral energy distributions, each spectrum is normalized to its maximum and shifted arbitrarily along the linear y-axis (no absolute scale). The high background in the SALT spectrum below 4500 Å prevents the identification of spectral features in this band (for details McCully et al. 2017b).

GRB is $T0 - t_c = 1.734 \pm 0.054$ s (Abbott et al. 2017g). Exploiting the difference in the arrival time of the gamma-ray signals at *Fermi*-GBM and *INTEGRAL* SPI-ACS (Svinkin et al. 2017c) provides additional significant constraints on the gamma-ray localization area (see Figure 1). The IPN localization capability will be especially important in the case of future gravitational-wave events that might be less well-localized by LIGO-Virgo.

Standard follow-up analyses (Goldstein et al. 2012; Paciesas et al. 2012; Gruber et al. 2014) of the *Fermi*-GBM trigger determined the burst duration to be $T_{90} = 2.0 \pm 0.5$ s, where T_{90} is defined as the interval over which 90% of the burst fluence is accumulated in the energy range of 50–300 keV. From the *Fermi*-GBM T_{90} measurement, GRB 170817A was classified as an sGRB with 3:1 odds over being a long GRB. The classification of GRB 170817A as an sGRB is further supported by incorporating the hardness ratio of the burst and comparing it to the *Fermi*-GBM catalog (Goldstein et al. 2017a). The SPI-ACS duration for GRB 170817A of 100 ms is consistent with an sGRB classification within the instrument's historic sample (Savchenko et al. 2012).

The GRB had a peak photon flux measured on a 64 ms timescale of 3.7 ± 0.9 photons s^{-1} cm^{-2} and a fluence over the T_{90} interval of $(2.8 \pm 0.2) \times 10^{-7}$ erg cm^{-2} (10–1000 keV; (Goldstein et al. 2017a). GRB 170817A is the closest sGRB with measured redshift. By usual measures, GRB 170817A is sub-luminous, a tantalizing observational result that is explored in Abbott et al. (2017g) and Goldstein et al. (2017a).

Detailed analysis of the *Fermi*-GBM data for GRB 170817A revealed two components to the burst: a main pulse encompassing the GRB trigger time from $T0 - 0.320$ s to $T0 + 0.256$ s followed by a weak tail starting at $T0 + 0.832$ s and extending to $T0 + 1.984$ s. The spectrum of the main pulse of GRB 170817A is best fit with a Comptonized function (a power law with an exponential cutoff) with a power-law photon index of -0.62 ± 0.40, peak energy $E_{peak} = 185 \pm 62$ keV, and time-averaged flux of $(3.1 \pm 0.7) \times 10^{-7}$ erg cm^{-2} s^{-1}. The weak tail that follows the main pulse, when analyzed independently, has a localization consistent with both the main pulse and the gravitational-wave position. The weak tail, at 34% the fluence of the main pulse, extends the T_{90} beyond the main pulse and has a softer, blackbody spectrum with $kT = 10.3 \pm 1.5$ keV (Goldstein et al. 2017a).

Using the *Fermi*-GBM spectral parameters of the main peak and T_{90} interval, the integrated fluence measured by *INTEGRAL* SPI-ACS is $(1.4 \pm 0.4) \times 10^{-7}$ erg cm^{-2} (75–2000 keV), compatible with the *Fermi*-GBM spectrum. Because SPI-ACS is most sensitive above 100 keV, it detects only the highest-energy part of the main peak near the start of the longer *Fermi*-GBM signal (Abbott et al. 2017f).

2.3. Discovery of the Optical Counterpart and Host Galaxy

The announcements of the *Fermi*-GBM and LIGO-Virgo detections, and especially the well-constrained, three-dimensional LIGO-Virgo localization, triggered a broadband observing campaign in search of electromagnetic counterparts. A large number of teams across the world were mobilized using ground- and space-based telescopes that could observe the region identified by the gravitational-wave detection. GW170817 was localized to the southern sky, setting in the early evening for the northern hemisphere

telescopes, thus making it inaccessible to the majority of them. The LIGO-Virgo localization region (LIGO Scientific Collaboration & Virgo Collaboration et al. 2017b, 2017c) became observable to telescopes in Chile about 10 hr after the merger with an altitude above the horizon of about 45°.

The One-Meter, Two-Hemisphere (1M2H) team was the first to discover and announce (August 18 01:05 UTC; Coulter et al. 2017a) a bright optical transient in an *i*-band image acquired on August 17 at 23:33 UTC ($t_c + 10.87$ hr) with the 1 m Swope telescope at Las Campanas Observatory in Chile. The team used an observing strategy (Gehrels et al. 2016) that targeted known galaxies (from White et al. 2011b) in the three-dimensional LIGO-Virgo localization taking into account the galaxy stellar mass and star formation rate (Coulter et al. 2017). The transient, designated Swope Supernova Survey 2017a (SSS17a), was $i = 17.057 \pm 0.018$ mag[962] (August 17 23:33 UTC, $t_c + 10.87$ hr) and did not match any known asteroid or supernova. SSS17a (now with the IAU designation AT 2017gfo) was located at α(J2000.0) = $13^{\rm h}09^{\rm m}48\overset{\rm s}{.}085 \pm 0.018$, δ(J2000.0) = $-23°22'53\overset{''}{.}343 \pm 0.218$ at a projected distance of $10\overset{''}{.}6$ from the center of NGC 4993, an early-type galaxy in the ESO 508 group at a distance of $\simeq$40 Mpc (Tully–Fisher distance from Freedman et al. 2001), consistent with the gravitational-wave luminosity distance (LIGO Scientific Collaboration & Virgo Collaboration et al. 2017b).

Five other teams took images of the transient within an hour of the 1M2H image (and before the SSS17a announcement) using different observational strategies to search the LIGO-Virgo sky localization region. They reported their discovery of the same optical transient in a sequence of GCNs: the Dark Energy Camera (01:15 UTC; Allam et al. 2017), the Distance Less Than 40 Mpc survey (01:41 UTC; Yang et al. 2017a), Las Cumbres Observatory (LCO; 04:07 UTC; Arcavi et al. 2017a), the Visible and Infrared Survey Telescope for Astronomy (VISTA; 05:04 UTC; Tanvir et al. 2017a), and MASTER (05:38 UTC; Lipunov et al. 2017d). Independent searches were also carried out by the Rapid Eye Mount (REM-GRAWITA, optical, 02:00 UTC; Melandri et al. 2017a), *Swift* UVOT/XRT (utraviolet, 07:24 UTC; Evans et al. 2017a), and Gemini-South (infrared, 08:00 UT; Singer et al. 2017a).

The Distance Less Than 40 Mpc survey (DLT40; L. Tartaglia et al. 2017, in preparation) team independently detected SSS17a/AT 2017gfo, automatically designated DLT17ck (Yang et al. 2017a) in an image taken on August 17 23:50 UTC while carrying out high-priority observations of 51 galaxies (20 within the LIGO-Virgo localization and 31 within the wider *Fermi*-GBM localization region; Valenti et al. 2017, accepted). A confirmation image was taken on August 18 00:41 UTC after the observing program had cycled through all of the high-priority targets and found no other transients. The updated magnitudes for these two epochs are $r = 17.18 \pm 0.03$ and 17.28 ± 0.04 mag, respectively.

SSS17a/AT 2017gfo was also observed by the VISTA in the second of two 1.5 deg^2 fields targeted. The fields were chosen to be within the high-likelihood localization region of GW170817 and to contain a high density of potential host galaxies (32 of the 54 entries in the list of Cook et al. 2017a). Observations began during evening twilight and were repeated twice to give a short temporal baseline over which to search for

---

[962] All apparent magnitudes are AB and corrected for the Galactic extinction in the direction of SSS17a ($E(B - V) = 0.109$ mag; Schlafly & Finkbeiner 2011).

variability (or proper motion of any candidates). The magnitudes of the transient source in the earliest images taken in the near-infrared were measured to be $K_s = 18.63 \pm 0.05$, $J = 17.88 \pm 0.03$, and $Y = 17.51 \pm 0.02$ mag.

On August 17 23:59 UTC, the MASTER-OAFA robotic telescope (Lipunov et al. 2010), covering the sky location of GW170817, recorded an image that included NGC 4993. The autodetection software identified MASTER OT J130948.10-232253.3, the bright optical transient with the unfiltered magnitude $W = 17.5 \pm 0.2$ mag, as part of an automated search performed by the MASTER Global Robotic Net (Lipunov et al. 2017a, 2017d).

The Dark Energy Camera (DECam; Flaugher et al. 2015) Survey team started observations of the GW170817 localization region on August 17 23:13 UTC. DECam covered 95% of the probability in the GW170817 localization area with a sensitivity sufficient to detect a source up to 100 times fainter than the observed optical transient. The transient was observed on 2017 August 18 at 00:05 UTC and independently detected at 00:42 UTC (Allam et al. 2017). The measured magnitudes of the transient source in the first images were $i = 17.30 \pm 0.02$, $z = 17.45 \pm 0.03$. A complete analysis of DECam data is presented in Soares-Santos et al. (2017).

Las Cumbres Observatory (LCO; Brown et al. 2013) surveys started their observations of individual galaxies with their global network of 1 and 2 m telescopes upon receipt of the initial *Fermi*-GBM localization. Approximately five hours later, when the LIGO-Virgo localization map was issued, the observations were switched to a prioritized list of galaxies (from Dalya et al. 2016) ranked by distance and luminosity (Arcavi et al. 2017, in preparation). In a 300 s *w*-band exposure beginning on August 18 00:15 UTC, a new transient, corresponding to AT 2017gfo/SSS17a/DLT17ck, was detected near NGC 4993 (Arcavi et al. 2017a). The transient was determined to have $w = 17.49 \pm 0.04$ mag (Arcavi et al. 2017e).

These early photometric measurements, from the optical to near-infrared, gave the first broadband spectral energy distribution of AT 2017gfo/SSS17a/DL17ck. They do not distinguish the transient from a young supernova, but they serve as reference values for subsequent observations that reveal the nature of the optical counterpart as described in Section 3.1. Images from the six earliest observations are shown in the inset of Figure 2.

3. Broadband Follow-up

While some of the first observations aimed to tile the error region of the GW170817 and GRB 170817A localization areas, including the use of galaxy targeting (White et al. 2011a; Dalya et al. 2016; D. Cook & M. Kasliwal 2017, in preparation; S. R. Kulkarni et al. 2017, in preparation), most groups focused their effort on the optical transient reported by Coulter et al. (2017) to define its nature and to rule out that it was a chance coincidence of an unrelated transient. The multi-wavelength evolution within the first 12–24 hr, and the subsequent discoveries of the X-ray and radio counterparts, proved key to scientific interpretation. This section summarizes the plethora of key observations that occurred in different wavebands, as well as searches for neutrino counterparts.

3.1. Ultraviolet, Optical, and Infrared

The quick discovery in the first few hours of Chilean darkness, and the possibility of fast evolution, prompted the need for the ultraviolet–optical–infrared follow-up community to have access to both space-based and longitudinally separated ground-based facilities. Over the next two weeks, a network of ground-based telescopes, from 40 cm to 10 m, and space-based observatories spanning the ultraviolet (UV), optical (O), and near-infrared (IR) wavelengths followed up GW170817. These observations revealed an exceptional electromagnetic counterpart through careful monitoring of its spectral energy distribution. Here, we first consider photometric and then spectroscopic observations of the source.

Regarding photometric observations, at $t_c + 11.6$ hr, the *Magellan*-Clay and *Magellan*-Baade telescopes (Drout et al. 2017a; Simon et al. 2017) initiated follow-up observations of the transient discovered by the Swope Supernova Survey from the optical (g band) to NIR (Ks band). At $t_c + 12.7$ hr and $t_c + 12.8$ hr, the Rapid Eye Mount (REM)/ROS2 (Melandri et al. 2017b) detected the optical transient and the Gemini-South FLAMINGO2 instrument first detected near-infrared Ks-band emission constraining the early optical to infrared color (Kasliwal et al. 2017; Singer et al. 2017a), respectively. At $t_c + 15.3$ hr, the *Swift* satellite (Gehrels 2004) detected bright, ultraviolet emission, further constraining the effective temperature (Evans et al. 2017a, 2017b). The ultraviolet evolution continued to be monitored with the *Swift* satellite (Evans et al. 2017b) and the *Hubble Space Telescope* (*HST*; Adams et al. 2017; Cowperthwaite et al. 2017b; Kasliwal et al. 2017).

Over the course of the next two days, an extensive photometric campaign showed a rapid dimming of this initial UV–blue emission and an unusual brightening of the near-infrared emission. After roughly a week, the redder optical and near-infrared bands began to fade as well. Ground- and space-based facilities participating in this photometric monitoring effort include (in alphabetical order): CTIO1.3 m, DECam (Cowperthwaite et al. 2017b; Nicholl et al. 2017a, 2017d), IRSF, the Gemini-South FLAMINGO2 (Singer et al. 2017a, 2017b; Chornock et al. 2017b; Troja et al. 2017b, 2017d), Gemini-South GMOS (Troja et al. 2017b), GROND (Chen et al. 2017; Wiseman et al. 2017), *HST* (Cowperthwaite et al. 2017b; Levan & Tanvir 2017; Levan et al. 2017a; Tanvir & Levan 2017; Troja et al. 2017a), iTelescope.Net telescopes (Im et al. 2017a, 2017b), the Korea Microlensing Telescope Network (KMTNet; Im et al. 2017c, 2017d), LCO (Arcavi et al. 2017b, 2017c, 2017e), the Lee Sang Gak Telescope (LSGT)/SNUCAM-II, the *Magellan*-Baade and *Magellan*-Clay 6.5 m telescopes (Drout et al. 2017a; Simon et al. 2017), the Nordic Optical Telescope (Malesani et al. 2017a), Pan-STARRS1 (Chambers et al. 2017a, 2017b, 2017c, 2017d), REM/ROS2 and REM/REMIR (Melandri et al. 2017a, 2017c), SkyMapper (Wolf et al. 2017), Subaru Hyper Suprime-Cam (Yoshida et al. 2017a, 2017b, 2017c, 2017d; Tominaga et al. 2017), ESO-VISTA (Tanvir et al. 2017a), ESO-VST/OmegaCAM (Grado et al. 2017a, 2017b), and ESO-VLT/FORS2 (D'Avanzo et al. 2017).

One of the key properties of the transient that alerted the worldwide community to its unusual nature was the rapid luminosity decline. In bluer optical bands (i.e., in the g band), the transient showed a fast decay between daily photometric measurements (Cowperthwaite et al. 2017b; Melandri et al. 2017c). Pan-STARRS (Chambers et al. 2017c) reported

photometric measurements in the optical/infrared *izy* bands with the same cadence, showing fading by 0.6 mag per day, with reliable photometry from difference imaging using already existing sky images (Chambers et al. 2016; Cowperthwaite et al. 2017b). Observations taken every 8 hr by LCO showed an initial rise in the *w* band, followed by rapid fading in all optical bands (more than 1 mag per day in the blue) and reddening with time (Arcavi et al. 2017e). Accurate measurements from Subaru (Tominaga et al. 2017), LSGT/SNUCAM-II and KMTNet (Im et al. 2017c), ESO-VLT/FORS2 (D'Avanzo et al. 2017), and DECam (Cowperthwaite et al. 2017b; Nicholl et al. 2017b) indicated a similar rate of fading. On the contrary, the near-infrared monitoring reports by GROND and Gemini-South showed that the source faded more slowly in the infrared (Chornock et al. 2017b; Wiseman et al. 2017) and even showed a late-time plateau in the Ks band (Singer et al. 2017b). This evolution was recognized by the community as quite unprecedented for transients in the nearby (within 100 Mpc) universe (e.g., Siebert et al. 2017).

Table 1 reports a summary of the imaging observations, which include coverage of the entire gravitational-wave sky localization and follow-up of SSS17a/AT 2017gfo. Figure 2 shows these observations in graphical form.

Concerning spectroscopic observations, immediately after discovery of SSS17a/AT 2017gfo on the Swope 1 m telescope, the same team obtained the first spectroscopic observations of the optical transient with the LDSS-3 spectrograph on the 6.5 m *Magellan*-Clay telescope and the MagE spectrograph on the 6.5 m *Magellan*-Baade telescope at Las Campanas Observatory. The spectra, just 30 minutes after the first image, showed a blue and featureless continuum between 4000 and 10000 Å, consistent with a power law (Drout et al. 2017a; Shappee et al. 2017). The lack of features and blue continuum during the first few hours implied an unusual, but not unprecedented transient since such characteristics are common in cataclysmic–variable stars and young core-collapse supernovae (see, e.g., Li et al. 2011a, 2011b).

The next 24 hr of observation were critical in decreasing the likelihood of a chance coincidence of SSS17a/ AT 2017gfo, GW170817, and GRB 170817A. The SALT-RSS spectrograph in South Africa (Buckley et al. 2017; McCully et al. 2017b; Shara et al. 2017), ePESSTO with the EFOSC2 instrument in spectroscopic mode at the ESO New Technology Telescope (NTT, in La Silla, Chile; Lyman et al. 2017), the X-shooter spectrograph on the ESO Very Large Telescope (Pian et al. 2017b) in Paranal, and the Goodman Spectrograph on the 4 m SOAR telescope (Nicholl et al. 2017c) obtained additional spectra. These groups reported a rapid fall off in the blue spectrum without any individual features identifiable with line absorption common in supernova-like transients (see, e.g., Lyman et al. 2017). This ruled out a young supernova of any type in NGC 4993, showing an exceptionally fast spectral evolution (Drout et al. 2017; Nicholl et al. 2017d). Figure 2 shows some representative early spectra (SALT spectrum is from Buckley et al. 2017; McCully et al. 2017b; ESO spectra from Smartt et al. 2017; SOAR spectrum from Nicholl et al. 2017d). These show rapid cooling, and the lack of commonly observed ions from elements abundant in supernova ejecta, indicating this object was unprecedented in its optical and near-infrared emission. Combined with the rapid fading, this was broadly indicative of a possible kilonova (e.g., Arcavi et al. 2017e; Cowperthwaite et al. 2017b; McCully et al. 2017b;

Kasen et al. 2017; Kasliwal et al. 2017; Kilpatrick et al. 2017b; Nicholl et al. 2017d; Smartt et al. 2017). This was confirmed by spectra taken at later times, such as with the Gemini Multi-Object Spectrograph (GMOS; Kasliwal et al. 2017; McCully et al. 2017b; Troja et al. 2017a, 2017b), the LDSS-3 spectrograph on the 6.5 m *Magellan*-Clay telescope at Las Campanas Observatory (Drout et al. 2017; Shappee et al. 2017), the LCO FLOYDS spectrograph at Faulkes Telescope South (McCully et al. 2017a, 2017b), and the AAOmega spectrograph on the 3.9 m Anglo-Australian Telescope (Andreoni et al. 2017), which did not show any significant emission or absorption lines over the red featureless continuum. The optical and near-infrared spectra over these few days provided convincing arguments that this transient was unlike any other discovered in extensive optical wide-field surveys over the past decade (see, e.g., Siebert et al. 2017).

The evolution of the spectral energy distribution, rapid fading, and emergence of broad spectral features indicated that the source had physical properties similar to models of kilonovae (e.g., Metzger et al. 2010; Kasen et al. 2013; Barnes & Kasen 2013; Tanaka & Hotokezaka 2013; Grossman et al. 2014; Metzger & Fernández 2014; Barnes et al. 2016; Tanaka 2016; Kasen et al. 2017; Kilpatrick et al. 2017b; Metzger 2017). These show a very rapid shift of the spectral energy distribution from the optical to the near-infrared. The FLAMINGOS2 near-infrared spectrograph at Gemini-South (Chornock et al. 2017c; Kasliwal et al. 2017) shows the emergence of very broad features in qualitative agreement with kilonova models. The ESO-VLT/X-shooter spectra, which simultaneously cover the wavelength range 3200–24800 Å, were taken over 2 weeks with a close to daily sampling (Pian et al. 2017a; Smartt et al. 2017) and revealed signatures of the radioactive decay of *r*-process nucleosynthesis elements (Pian et al. 2017a). Three epochs of infrared grism spectroscopy with the *HST* (Cowperthwaite et al. 2017b; Levan & Tanvir 2017; Levan et al. 2017a; Tanvir & Levan 2017; Troja et al. 2017a)[963] identified features consistent with the production of lanthanides within the ejecta (Levan & Tanvir 2017; Tanvir & Levan 2017; Troja et al. 2017a).

The optical follow-up campaign also includes linear polarimetry measurements of SSS17a/AT 2017gfo by ESO-VLT/FORS2, showing no evidence of an asymmetric geometry of the emitting region and lanthanide-rich late kilonova emission (Covino et al. 2017). In addition, the study of the galaxy with the MUSE Integral Field Spectrograph on the ESO-VLT (Levan et al. 2017b) provides simultaneous spectra of the counterpart and the host galaxy, which show broad absorption features in the transient spectrum, combined with emission lines from the spiral arms of the host galaxy (Levan & Tanvir 2017; Tanvir & Levan 2017).

Table 2 reports the spectroscopic observations that have led to the conclusion that the source broadly matches kilonovae theoretical predictions.

3.2. Gamma-Rays

The fleet of ground- and space-based gamma-ray observatories provided broad temporal and spectral coverage of the source location. Observations spanned ∼10 orders of magnitude in energy and covered the position of SSS17a/ AT 2017gfo from a few hundred seconds before the GRB 170817A trigger time (T0) to days afterward. Table 3 lists, in chronological order, the results reporting observation

---

[963] *HST* Program GO 14804 Levan, GO 14771 Tanvir, and GO 14850 Troja.

Table 1
A Partial Summary of Photometric Observations up to 2017 September 5 UTC with at Most Three Observations per Filter per Telescope/Group, i.e., the Earliest, the Peak, and the Latest in Each Case

Telescope/Instrument	UT Date	Band	References
DFN/–	2017 Aug 17 12:41:04	visible	Hancock et al. (2017),
MASTER/–	2017 Aug 17 17:06:47	Clear	Lipunov et al. (2017a, 2017b)
PioftheSky/PioftheSkyNorth	2017 Aug 17 21:46:28	visible wide band	Cwiek et al. (2017); Batsch et al. (2017); Zadrozny et al. (2017)
MASTER/–	2017 Aug 17 22:54:18	Visible	Lipunov et al. (2017b, 2017a)
Swope/DirectCCD	2017 Aug 17 23:33:17	i	Coulter et al. (2017a, 2017b, 2017)
PROMPT5(DLT40)/–	2017 Aug 17 23:49:00	r	Yang et al. (2017a), Valenti et al. (submitted)
VISTA/VIRCAM	2017 Aug 17 23:55:00	K	Tanvir & Levan (2017)
MASTER/–	2017 Aug 17 23:59:54	Clear	Lipunov et al. (2017d, 2017a)
Blanco/DECam/–	2017 Aug 18 00:04:24	i	Cowperthwaite et al. (2017b); Soares-Santos et al. (2017)
Blanco/DECam/–	2017 Aug 18 00:05:23	z	Cowperthwaite et al. (2017b); Soares-Santos et al. (2017)
VISTA/VIRCAM	2017 Aug 18 00:07:00	J	Tanvir & Levan (2017)
Magellan-Clay/LDSS3-C	2017 Aug 18 00:08:13	g	Simon et al. (2017); Drout et al. (2017b)
Magellan-Baade/FourStar	2017 Aug 18 00:12:19	H	Drout et al. (2017b)
LasCumbres1-m/Sinistro	2017 Aug 18 00:15:50	w	Arcavi et al. (2017a, 2017e)
VISTA/VIRCAM	2017 Aug 18 00:17:00	Y	Tanvir & Levan (2017)
MASTER/–	2017 Aug 18 00:19:05	Clear	Lipunov et al. (2017d, 2017a)
Magellan-Baade/FourStar	2017 Aug 18 00:25:51	J	Drout et al. (2017b)
Magellan-Baade/FourStar	2017 Aug 18 00:35:19	Ks	Drout et al. (2017b)
PROMPT5(DLT40)/–	2017 Aug 18 00:40:00	r	Yang et al. (2017a), Valenti et al. (submitted)
REM/ROS2	2017 Aug 18 01:24:56	g	Melandri et al. (2017a); Pian et al. (2017a)
REM/ROS2	2017 Aug 18 01:24:56	i	Melandri et al. (2017a); Pian et al. (2017a)
REM/ROS2	2017 Aug 18 01:24:56	z	Melandri et al. (2017a); Pian et al. (2017a)
REM/ROS2	2017 Aug 18 01:24:56	r	Melandri et al. (2017a); Pian et al. (2017a)
Gemini-South/Flamingos-2	2017 Aug 18 01:30:00	Ks	Singer et al. (2017a); Kasliwal et al. (2017)
PioftheSky/PioftheSkyNorth	2017 Aug 18 03:01:39	visible wide band	Cwiek et al. (2017); Batsch et al. (2017),
Swift/UVOT	2017 Aug 18 03:37:00	uvm2	Evans et al. (2017a, 2017b)
Swift/UVOT	2017 Aug 18 03:50:00	uvw1	Evans et al. (2017a, 2017b)
Swift/UVOT	2017 Aug 18 03:58:00	u	Evans et al. (2017a, 2017b)
Swift/UVOT	2017 Aug 18 04:02:00	uvw2	Evans et al. (2017a, 2017b)
Subaru/HyperSuprime-Cam	2017 Aug 18 05:31:00	z	Yoshida et al. (2017a, 2017b), Y. Utsumi et al. (2017, in preparation)
Pan-STARRS1/GPC1	2017 Aug 18 05:33:00	y	Chambers et al. (2017a); Smartt et al. (2017)
Pan-STARRS1/GPC1	2017 Aug 18 05:34:00	z	Chambers et al. (2017a); Smartt et al. (2017)
Pan-STARRS1/GPC1	2017 Aug 18 05:35:00	i	Chambers et al. (2017a); Smartt et al. (2017)
Pan-STARRS1/GPC1	2017 Aug 18 05:36:00	y	Chambers et al. (2017a); Smartt et al. (2017)
Pan-STARRS1/GPC1	2017 Aug 18 05:37:00	z	Chambers et al. (2017a); Smartt et al. (2017)
Pan-STARRS1/GPC1	2017 Aug 18 05:38:00	i	Chambers et al. (2017a); Smartt et al. (2017)
LasCumbres1-m/Sinistro	2017 Aug 18 09:10:04	w	Arcavi et al. (2017b, 2017e)
SkyMapper/–	2017 Aug 18 09:14:00	i	···
SkyMapper/–	2017 Aug 18 09:35:00	z	···
LasCumbres1-m/Sinistro	2017 Aug 18 09:37:26	g	Arcavi et al. (2017e)
SkyMapper/–	2017 Aug 18 09:39:00	r	···
SkyMapper/–	2017 Aug 18 09:41:00	g	···
LasCumbres1-m/Sinistro	2017 Aug 18 09:43:11	r	Arcavi et al. (2017e)
T17/–	2017 Aug 18 09:47:13	g	Im et al. (2017a, 2017b), Im et al. (2017, in preparation)
SkyMapper/–	2017 Aug 18 09:50:00	v	···
T17/–	2017 Aug 18 09:56:46	r	Im et al. (2017a, 2017b), Im et al. (2017, in preparation)
SkyMapper/–	2017 Aug 18 10:01:00	i	Wolf et al. (2017),
SkyMapper/–	2017 Aug 18 10:03:00	r	Wolf et al. (2017),
SkyMapper/–	2017 Aug 18 10:05:00	g	Wolf et al. (2017),
T17/–	2017 Aug 18 10:06:18	i	Im et al. (2017a, 2017b), Im et al. (2017, in preparation)
SkyMapper/–	2017 Aug 18 10:07:00	v	Wolf et al. (2017),
LSGT/SNUCAM-II	2017 Aug 18 10:08:01	m425	Im et al. (2017a, 2017b), Im et al. (2017, in preparation)
SkyMapper/–	2017 Aug 18 10:09:00	u	Wolf et al. (2017),
LSGT/SNUCAM-II	2017 Aug 18 10:12:48	m475	Im et al. (2017a, 2017b), Im et al. (2017, in preparation)
LSGT/SNUCAM-II	2017 Aug 18 10:15:16	m525	Im et al. (2017a, 2017b), Im et al. (2017, in preparation)
T17/–	2017 Aug 18 10:15:49	z	Im et al. (2017a, 2017b), Im et al. (2017, in preparation)
LSGT/SNUCAM-II	2017 Aug 18 10:21:14	m575	Im et al. (2017a, 2017b), Im et al. (2017, in preparation)
LSGT/SNUCAM-II	2017 Aug 18 10:22:33	m625	Im et al. (2017a, 2017b), Im et al. (2017, in preparation)
AST3-2/wide-fieldcamera	2017 Aug 18 13:11:49	g	Hu et al. (2017),
Swift/UVOT	2017 Aug 18 13:30:00	uvm2	Cenko et al. (2017); Evans et al. (2017b)
Swift/UVOT	2017 Aug 18 13:37:00	uvw1	Cenko et al. (2017); Evans et al. (2017b)

Table 1
(Continued)

Telescope/Instrument	UT Date	Band	References
Swift/UVOT	2017 Aug 18 13:41:00	u	Cenko et al. (2017); Evans et al. (2017b)
IRSF/SIRIUS	2017 Aug 18 16:34:00	Ks	Utsumi et al. (2017, in press)
IRSF/SIRIUS	2017 Aug 18 16:34:00	H	Utsumi et al. (2017, in press)
IRSF/SIRIUS	2017 Aug 18 16:48:00	J	Utsumi et al. (2017, in press)
KMTNet-SAAO/wide-fieldcamera	2017 Aug 18 17:00:36	B	Im et al. (2017d, 2017c); Troja et al. (2017a)
KMTNet-SAAO/wide-fieldcamera	2017 Aug 18 17:02:55	V	Im et al. (2017d, 2017c); Troja et al. (2017a)
KMTNet-SAAO/wide-fieldcamera	2017 Aug 18 17:04:54	R	Im et al. (2017d, 2017c); Troja et al. (2017a)
MASTER/–	2017 Aug 18 17:06:55	Clear	Lipunov et al. (2017e, 2017a)
KMTNet-SAAO/wide-fieldcamera	2017 Aug 18 17:07:12	I	Im et al. (2017d, 2017c); Troja et al. (2017a)
MASTER/–	2017 Aug 18 17:17:33	R	Lipunov et al. (2017c, 2017b, 2017a)
MASTER/–	2017 Aug 18 17:34:02	B	Lipunov et al. (2017b, 2017a)
1.5 m Boyden/–	2017 Aug 18 18:12:00	r	Smartt et al. (2017)
MPG2.2 m/GROND	2017 Aug 18 18:12:00	g	Smartt et al. (2017)
NOT/NOTCam	2017 Aug 18 20:24:08	Ks	Malesani et al. (2017a); Tanvir & Levan (2017)
NOT/NOTCam	2017 Aug 18 20:37:46	J	Malesani et al. (2017a); Tanvir & Levan (2017)
PioftheSky/PioftheSkyNorth	2017 Aug 18 21:44:44	visible wide band	Cwiek et al. (2017); Batsch et al. (2017),
LasCumbres1-m/Sinistro	2017 Aug 18 23:19:40	i	Arcavi et al. (2017e)
Blanco/DECam/–	2017 Aug 18 23:25:56	Y	Cowperthwaite et al. (2017b); Soares-Santos et al. (2017)
Magellan-Clay/LDSS3-C	2017 Aug 18 23:26:33	z	Drout et al. (2017b)
Blanco/DECam/–	2017 Aug 18 23:26:55	z	Cowperthwaite et al. (2017b); Soares-Santos et al. (2017)
Blanco/DECam/–	2017 Aug 18 23:27:54	i	Cowperthwaite et al. (2017b); Soares-Santos et al. (2017)
KMTNet-CTIO/wide-fieldcamera	2017 Aug 18 23:28:35	B	Im et al. (2017d, 2017c); Troja et al. (2017a)
Blanco/DECam/–	2017 Aug 18 23:28:53	r	Cowperthwaite et al. (2017b); Soares-Santos et al. (2017)
Blanco/DECam/–	2017 Aug 18 23:29:52	g	Cowperthwaite et al. (2017b); Soares-Santos et al. (2017)
KMTNet-CTIO/wide-fieldcamera	2017 Aug 18 23:30:31	V	Im et al. (2017d, 2017c); Troja et al. (2017a)
Blanco/DECam/–	2017 Aug 18 23:30:50	u	Cowperthwaite et al. (2017b); Soares-Santos et al. (2017)
Magellan-Clay/LDSS3-C	2017 Aug 18 23:30:55	i	Drout et al. (2017b)
REM/ROS2	2017 Aug 18 23:31:02	z	Melandri et al. (2017c); Pian et al. (2017a)
Magellan-Clay/LDSS3-C	2017 Aug 18 23:32:02	r	Drout et al. (2017b)
KMTNet-CTIO/wide-fieldcamera	2017 Aug 18 23:32:36	R	Im et al. (2017d, 2017c); Troja et al. (2017a)
Magellan-Baade/FourStar	2017 Aug 18 23:32:58	J	Drout et al. (2017b)
KMTNet-CTIO/wide-fieldcamera	2017 Aug 18 23:34:48	I	Im et al. (2017d, 2017c); Troja et al. (2017a)
Magellan-Clay/LDSS3-C	2017 Aug 18 23:35:20	B	Drout et al. (2017b)
VISTA/VIRCAM	2017 Aug 18 23:44:00	J	Tanvir & Levan (2017)
Magellan-Baade/FourStar	2017 Aug 18 23:45:49	H	Drout et al. (2017b)
PROMPT5(DLT40)/–	2017 Aug 18 23:47:00	r	Yang et al. (2017b), Valenti et al. (submitted)
VLT/FORS2	2017 Aug 18 23:47:02	Rspecial	Wiersema et al. (2017); Covino et al. (2017)
Swope/DirectCCD	2017 Aug 18 23:52:29	V	Kilpatrick et al. (2017a); Coulter et al. (2017)
VISTA/VIRCAM	2017 Aug 18 23:53:00	Y	Tanvir & Levan (2017)
TOROS/T80S	2017 Aug 18 23:53:00	g	Diaz et al. (2017a, 2017b), Diaz et al. (2017, in preparation)
TOROS/T80S	2017 Aug 18 23:53:00	r	Diaz et al. (2017a, 2017b), Diaz et al. (2017, in preparation)
TOROS/T80S	2017 Aug 18 23:53:00	i	Diaz et al. (2017a, 2017b), Diaz et al. (2017, in preparation)
MPG2.2 m/GROND	2017 Aug 18 23:56:00	i	Smartt et al. (2017)
MPG2.2 m/GROND	2017 Aug 18 23:56:00	z	Smartt et al. (2017)
MPG2.2 m/GROND	2017 Aug 18 23:56:00	J	Smartt et al. (2017)
MPG2.2 m/GROND	2017 Aug 18 23:56:00	r	Smartt et al. (2017)
MPG2.2 m/GROND	2017 Aug 18 23:56:00	H	Smartt et al. (2017)
MPG2.2 m/GROND	2017 Aug 18 23:56:00	Ks	Smartt et al. (2017)
Gemini-South/Flamingos-2	2017 Aug 19 00:00:19	H	Cowperthwaite et al. (2017b)
Magellan-Baade/FourStar	2017 Aug 19 00:02:53	J1	Drout et al. (2017b)
VLT/X-shooter	2017 Aug 19 00:08:58	r	Pian et al. (2017a, 2017a)
VLT/X-shooter	2017 Aug 19 00:10:46	z	Pian et al. (2017b, 2017b)
VLT/X-shooter	2017 Aug 19 00:14:01	g	Pian et al. (2017, 2017)
Swift/UVOT	2017 Aug 19 00:41:00	u	Evans et al. (2017b)
Swope/DirectCCD	2017 Aug 19 00:49:15	B	Kilpatrick et al. (2017a); Coulter et al. (2017)
Swope/DirectCCD	2017 Aug 19 01:08:00	r	Coulter et al. (2017)
NTT/–	2017 Aug 19 01:09:00	U	Smartt et al. (2017)
Swope/DirectCCD	2017 Aug 19 01:18:57	g	Coulter et al. (2017)
BOOTES-5/JGT/–	2017 Aug 19 03:08:14	clear	Castro-Tirado et al. (2017), Zhang et al. (2017, in preparation)
Pan-STARRS1/GPC1	2017 Aug 19 05:42:00	y	Chambers et al. (2017b); Smartt et al. (2017)
Pan-STARRS1/GPC1	2017 Aug 19 05:44:00	z	Chambers et al. (2017b); Smartt et al. (2017)

Table 1
(Continued)

Telescope/Instrument	UT Date	Band	References
Pan-STARRS1/GPC1	2017 Aug 19 05:46:00	i	Chambers et al. (2017b); Smartt et al. (2017)
MOA-II/MOA-cam3	2017 Aug 19 07:26:00	R	Utsumi et al. (2017, in press)
B&C61cm/Tripole5	2017 Aug 19 07:26:00	g	Utsumi et al. (2017, in press)
KMTNet-SSO/wide-fieldcamera	2017 Aug 19 08:32:48	B	Im et al. (2017d, 2017c); Troja et al. (2017a)
KMTNet-SSO/wide-fieldcamera	2017 Aug 19 08:34:43	V	Im et al. (2017d, 2017c); Troja et al. (2017a)
KMTNet-SSO/wide-fieldcamera	2017 Aug 19 08:36:39	R	Im et al. (2017d, 2017c); Troja et al. (2017a)
KMTNet-SSO/wide-fieldcamera	2017 Aug 19 08:38:42	I	Im et al. (2017d, 2017c); Troja et al. (2017a)
T27/–	2017 Aug 19 09:01:31	V	Im et al. (2017a, 2017b), Im et al. (2017, in preparation)
T30/–	2017 Aug 19 09:02:27	V	Im et al. (2017a, 2017b), Im et al. (2017, in preparation)
T27/–	2017 Aug 19 09:02:27	R	Im et al. (2017a, 2017b), Im et al. (2017, in preparation)
T31/–	2017 Aug 19 09:02:34	R	Im et al. (2017a, 2017b), Im et al. (2017, in preparation)
T27/–	2017 Aug 19 09:11:30	I	Im et al. (2017a, 2017b), Im et al. (2017, in preparation)
Zadko/CCDimager	2017 Aug 19 10:57:00	r	Coward et al. (2017a),
MASTER/–	2017 Aug 19 17:06:57	Clear	Lipunov et al. (2017b, 2017a)
MASTER/–	2017 Aug 19 17:53:34	R	Lipunov et al. (2017b, 2017a)
LasCumbres1-m/Sinistro	2017 Aug 19 18:01:26	V	Arcavi et al. (2017e)
LasCumbres1-m/Sinistro	2017 Aug 19 18:01:26	z	Arcavi et al. (2017e)
MASTER/–	2017 Aug 19 18:04:32	B	Lipunov et al. (2017b, 2017a)
1.5 m Boyden/–	2017 Aug 19 18:16:00	r	Smartt et al. (2017)
REM/ROS2	2017 Aug 19 23:12:59	r	Melandri et al. (2017c); Pian et al. (2017)
REM/ROS2	2017 Aug 19 23:12:59	i	Melandri et al. (2017c); Pian et al. (2017)
REM/ROS2	2017 Aug 19 23:12:59	g	Melandri et al. (2017c); Pian et al. (2017)
MASTER/–	2017 Aug 19 23:13:20	Clear	Lipunov et al. (2017b, 2017a)
Gemini-South/Flamingos-2	2017 Aug 19 23:13:34	H	Cowperthwaite et al. (2017b)
MPG2.2 m/GROND	2017 Aug 19 23:15:00	r	Smartt et al. (2017)
MPG2.2 m/GROND	2017 Aug 19 23:15:00	z	Smartt et al. (2017)
MPG2.2 m/GROND	2017 Aug 19 23:15:00	H	Smartt et al. (2017)
MPG2.2 m/GROND	2017 Aug 19 23:15:00	i	Smartt et al. (2017)
MPG2.2 m/GROND	2017 Aug 19 23:15:00	J	Smartt et al. (2017)
TOROS/EABA	2017 Aug 19 23:18:38	r	Diaz et al. (2017b), Diaz et al. (2017, in preparation)
Magellan-Baade/FourStar	2017 Aug 19 23:18:50	H	Drout et al. (2017b)
Etelman/VIRT/CCDimager	2017 Aug 19 23:19:00	R	Gendre et al. (2017), Andreoni et al. (2017, in preparation)
Blanco/DECam/–	2017 Aug 19 23:23:29	Y	Cowperthwaite et al. (2017b); Soares-Santos et al. (2017)
Blanco/DECam/–	2017 Aug 19 23:26:59	r	Cowperthwaite et al. (2017b); Soares-Santos et al. (2017)
Blanco/DECam/–	2017 Aug 19 23:27:59	g	Cowperthwaite et al. (2017b); Soares-Santos et al. (2017)
ChilescopeRC-1000/–	2017 Aug 19 23:30:33	clear	Pozanenko et al. (2017a, 2017b), Pozanenko et al. (2017, in preparation)
Magellan-Baade/FourStar	2017 Aug 19 23:31:06	J1	Drout et al. (2017b)
Blanco/DECam/–	2017 Aug 19 23:31:13	u	Cowperthwaite et al. (2017b); Soares-Santos et al. (2017)
Magellan-Baade/FourStar	2017 Aug 19 23:41:59	Ks	Drout et al. (2017b)
Magellan-Baade/IMACS	2017 Aug 20 00:13:32	r	Drout et al. (2017b)
Gemini-South/Flamingos-2	2017 Aug 20 00:19:00	Ks	Kasliwal et al. (2017)
LasCumbres1-m/Sinistro	2017 Aug 20 00:24:28	g	Arcavi et al. (2017e)
Gemini-South/Flamingos-2	2017 Aug 20 00:27:00	J	Kasliwal et al. (2017)
NTT/–	2017 Aug 20 01:19:00	U	Smartt et al. (2017)
Pan-STARRS1/GPC1	2017 Aug 20 05:38:00	y	Chambers et al. (2017c); Smartt et al. (2017)
Pan-STARRS1/GPC1	2017 Aug 20 05:41:00	z	Chambers et al. (2017c); Smartt et al. (2017)
Pan-STARRS1/GPC1	2017 Aug 20 05:45:00	i	Chambers et al. (2017c); Smartt et al. (2017)
T31/–	2017 Aug 20 09:20:38	R	Im et al. (2017a, 2017b), Im et al. (2017, in preparation)
MASTER/–	2017 Aug 20 17:04:36	Clear	Lipunov et al. (2017b, 2017a)
MASTER/–	2017 Aug 20 17:25:56	R	Lipunov et al. (2017b, 2017a)
MASTER/–	2017 Aug 20 17:36:32	B	Lipunov et al. (2017b, 2017a)
LasCumbres1-m/Sinistro	2017 Aug 20 17:39:50	i	Arcavi et al. (2017e)
LasCumbres1-m/Sinistro	2017 Aug 20 17:45:36	z	Arcavi et al. (2017e)
LasCumbres1-m/Sinistro	2017 Aug 20 17:49:55	V	Arcavi et al. (2017e)
MPG2.2 m/GROND	2017 Aug 20 23:15:00	g	Smartt et al. (2017)
Magellan-Baade/FourStar	2017 Aug 20 23:20:42	J	Drout et al. (2017b)
ChilescopeRC-1000/–	2017 Aug 20 23:21:09	clear	Pozanenko et al. (2017a)
VISTA/VIRCAM	2017 Aug 20 23:24:00	K	Tanvir & Levan (2017)
Blanco/DECam/–	2017 Aug 20 23:37:06	u	Cowperthwaite et al. (2017b); Soares-Santos et al. (2017)
Swope/DirectCCD	2017 Aug 20 23:44:36	V	Coulter et al. (2017)
Swope/DirectCCD	2017 Aug 20 23:53:00	B	Coulter et al. (2017)

Table 1
(Continued)

Telescope/Instrument	UT Date	Band	References
MASTER/–	2017 Aug 21 00:26:31	Clear	Lipunov et al. (2017b, 2017a)
Gemini-South/Flamingos-2	2017 Aug 21 00:38:00	H	Kasliwal et al. (2017); Troja et al. (2017a)
Pan-STARRS1/GPC1	2017 Aug 21 05:37:00	y	Chambers et al. (2017d); Smartt et al. (2017)
Pan-STARRS1/GPC1	2017 Aug 21 05:39:00	z	Chambers et al. (2017d); Smartt et al. (2017)
Pan-STARRS1/GPC1	2017 Aug 21 05:42:00	i	Chambers et al. (2017d); Smartt et al. (2017)
AST3-2/wide-fieldcamera	2017 Aug 21 15:36:50	g	…
MASTER/–	2017 Aug 21 17:08:14	Clear	Lipunov et al. (2017b, 2017a)
MASTER/–	2017 Aug 21 18:06:12	R	Lipunov et al. (2017b, 2017a)
MASTER/–	2017 Aug 21 19:20:23	B	Lipunov et al. (2017b, 2017a)
duPont/RetroCam	2017 Aug 21 23:17:19	Y	Drout et al. (2017b)
Etelman/VIRT/CCDimager	2017 Aug 21 23:19:00	Clear	Gendre et al. (2017); Andreoni et al. (2017, in preparation)
MPG2.2 m/GROND	2017 Aug 21 23:22:00	Ks	Smartt et al. (2017)
VLT/FORS2	2017 Aug 21 23:23:11	R	D'Avanzo et al. (2017); Pian et al. (2017)
ChilescopeRC-1000/–	2017 Aug 21 23:32:09	clear	Pozanenko et al. (2017c)
duPont/RetroCam	2017 Aug 21 23:34:34	H	Drout et al. (2017b)
LasCumbres1-m/Sinistro	2017 Aug 21 23:48:28	w	Arcavi et al. (2017e)
Swope/DirectCCD	2017 Aug 21 23:54:57	r	Coulter et al. (2017)
duPont/RetroCam	2017 Aug 21 23:57:41	J	Drout et al. (2017b)
Swope/DirectCCD	2017 Aug 22 00:06:17	g	Coulter et al. (2017)
VLT/FORS2	2017 Aug 22 00:09:09	z	D'Avanzo et al. (2017); Pian et al. (2017)
VLT/FORS2	2017 Aug 22 00:18:49	I	D'Avanzo et al. (2017); Pian et al. (2017)
Magellan-Clay/LDSS3-C	2017 Aug 22 00:27:40	g	Drout et al. (2017b)
VLT/FORS2	2017 Aug 22 00:28:18	B	D'Avanzo et al. (2017); Pian et al. (2017)
VLT/FORS2	2017 Aug 22 00:38:20	V	D'Avanzo et al. (2017); Pian et al. (2017)
HST/WFC3/IR	2017 Aug 22 07:34:00	F110W	Tanvir & Levan (2017); Troja et al. (2017a)
LasCumbres1-m/Sinistro	2017 Aug 22 08:35:31	r	Arcavi et al. (2017e)
HST/WFC3/IR	2017 Aug 22 10:45:00	F160W	Tanvir & Levan (2017); Troja et al. (2017a)
HubbleSpaceTelescope/WFC3	2017 Aug 22 20:19:00	F336W	Adams et al. (2017); Kasliwal et al. (2017)
Etelman/VIRT/CCDimager	2017 Aug 22 23:19:00	Clear	Gendre et al. (2017); Andreoni et al. (2017, in preparation)
VLT/VIMOS	2017 Aug 22 23:30:00	z	Tanvir & Levan (2017)
duPont/RetroCam	2017 Aug 22 23:33:54	Y	Drout et al. (2017b)
VLT/VIMOS	2017 Aug 22 23:42:00	R	Tanvir & Levan (2017)
VLT/VIMOS	2017 Aug 22 23:53:00	u	Evans et al. (2017b)
VLT/FORS2	2017 Aug 22 23:53:31	Rspecial	Covino et al. (2017)
VST/OmegaCam	2017 Aug 22 23:58:32	g	Grado et al. (2017a); Pian et al. (2017)
VLT/X-shooter	2017 Aug 23 00:35:20	r	Pian et al. (2017)
VLT/X-shooter	2017 Aug 23 00:37:08	z	Pian et al. (2017)
VLT/X-shooter	2017 Aug 23 00:40:24	g	Pian et al. (2017)
Zadko/CCDimager	2017 Aug 23 11:32:00	r	Coward et al. (2017a),
IRSF/SIRIUS	2017 Aug 23 17:22:00	Ks	Kasliwal et al. (2017)
IRSF/SIRIUS	2017 Aug 23 17:22:00	J	Kasliwal et al. (2017)
IRSF/SIRIUS	2017 Aug 23 17:22:00	H	Kasliwal et al. (2017)
VST/OmegaCam	2017 Aug 23 23:26:51	i	Grado et al. (2017a); Pian et al. (2017)
VLT/VISIR	2017 Aug 23 23:35:00	8.6um	Kasliwal et al. (2017)
VST/OmegaCam	2017 Aug 23 23:42:49	r	Grado et al. (2017a); Pian et al. (2017)
CTIO1.3 m/ANDICAM	2017 Aug 24 23:20:00	Ks	Kasliwal et al. (2017)
Swope/DirectCCD	2017 Aug 24 23:45:07	i	Coulter et al. (2017)
ChilescopeRC-1000/–	2017 Aug 24 23:53:39	clear	Pozanenko et al. (2017b),
Blanco/DECam/–	2017 Aug 24 23:56:22	g	Cowperthwaite et al. (2017b); Soares-Santos et al. (2017)
Magellan-Clay/LDSS3-C	2017 Aug 25 00:43:27	B	Drout et al. (2017b)
HST/WFC3/UVIS	2017 Aug 25 13:55:00	F606W	Tanvir & Levan (2017); Troja et al. (2017a)
HST/WFC3/UVIS	2017 Aug 25 15:28:00	F475W	Tanvir & Levan (2017); Troja et al. (2017a)
HST/WFC3/UVIS	2017 Aug 25 15:36:00	F275W	Levan & Tanvir (2017); Tanvir & Levan (2017),
Magellan-Clay/LDSS3-C	2017 Aug 25 23:19:41	z	Drout et al. (2017b)
Blanco/DECam/–	2017 Aug 25 23:56:05	r	Cowperthwaite et al. (2017b); Soares-Santos et al. (2017)
VLT/FORS2	2017 Aug 26 00:13:40	z	Covino et al. (2017)
duPont/RetroCam	2017 Aug 26 00:14:28	J	Drout et al. (2017b)
VLT/FORS2	2017 Aug 26 00:27:16	B	Pian et al. (2017)
IRSF/SIRIUS	2017 Aug 26 16:57:00	J	Kasliwal et al. (2017)
IRSF/SIRIUS	2017 Aug 26 16:57:00	Ks	Kasliwal et al. (2017)
IRSF/SIRIUS	2017 Aug 26 16:57:00	H	Kasliwal et al. (2017)

Table 1
(Continued)

Telescope/Instrument	UT Date	Band	References
VISTA/VIRCAM	2017 Aug 26 23:38:00	Y	Tanvir & Levan (2017)
ApachePointObservatory/NICFPS	2017 Aug 27 02:15:00	Ks	Kasliwal et al. (2017)
Palomar200inch/WIRC	2017 Aug 27 02:49:00	Ks	Kasliwal et al. (2017)
HST/WFC3/IR	2017 Aug 27 06:45:56	F110W	Cowperthwaite et al. (2017b)
HST/WFC3/IR	2017 Aug 27 07:06:57	F160W	Cowperthwaite et al. (2017b)
HST/WFC3/UVIS	2017 Aug 27 08:20:49	F336W	Cowperthwaite et al. (2017b)
HST/ACS/WFC	2017 Aug 27 10:24:14	F475W	Cowperthwaite et al. (2017b)
HST/ACS/WFC	2017 Aug 27 11:57:07	F625W	Cowperthwaite et al. (2017b)
HST/ACS/WFC	2017 Aug 27 13:27:15	F775W	Cowperthwaite et al. (2017b)
HST/ACS/WFC	2017 Aug 27 13:45:24	F850LP	Cowperthwaite et al. (2017b)
Gemini-South/Flamingos-2	2017 Aug 27 23:16:00	J	Kasliwal et al. (2017)
CTIO1.3 m/ANDICAM	2017 Aug 27 23:18:00	Ks	Kasliwal et al. (2017)
Blanco/DECam/–	2017 Aug 27 23:23:33	Y	Cowperthwaite et al. (2017b); Soares-Santos et al. (2017)
MPG2.2 m/GROND	2017 Aug 27 23:24:00	J	Smartt et al. (2017)
Gemini-South/Flamingos-2	2017 Aug 27 23:28:10	K_s	Cowperthwaite et al. (2017b)
Gemini-South/Flamingos-2	2017 Aug 27 23:33:07	H	Cowperthwaite et al. (2017b)
duPont/RetroCam	2017 Aug 27 23:36:25	H	Drout et al. (2017b)
Blanco/DECam/–	2017 Aug 27 23:40:57	z	Cowperthwaite et al. (2017b); Soares-Santos et al. (2017)
Blanco/DECam/–	2017 Aug 28 00:00:01	i	Cowperthwaite et al. (2017b); Soares-Santos et al. (2017)
VLT/FORS2	2017 Aug 28 00:07:31	R	Pian et al. (2017a)
VLT/FORS2	2017 Aug 28 00:15:56	V	Pian et al. (2017a)
MPG2.2 m/GROND	2017 Aug 28 00:22:00	H	Smartt et al. (2017)
HST/WFC3/IR	2017 Aug 28 01:50:00	F110W	Tanvir & Levan (2017); Troja et al. (2017a)
HST/WFC3/IR	2017 Aug 28 03:25:00	F160W	Tanvir & Levan (2017); Troja et al. (2017a)
HST/WFC3/UVIS	2017 Aug 28 20:56:00	F275W	Levan & Tanvir (2017); Tanvir & Levan (2017),
HST/WFC3/UVIS	2017 Aug 28 22:29:00	F475W	Tanvir & Levan (2017); Troja et al. (2017a)
HST/WFC3/UVIS	2017 Aug 28 23:02:00	F814W	Tanvir & Levan (2017); Troja et al. (2017a)
NTT/–	2017 Aug 28 23:03:00	H	Smartt et al. (2017)
HST/WFC3/UVIS	2017 Aug 28 23:08:00	F606W	Tanvir & Levan (2017); Troja et al. (2017a)
MPG2.2 m/GROND	2017 Aug 28 23:22:00	Ks	Smartt et al. (2017)
VISTA/VIRCAM	2017 Aug 28 23:33:00	J	Tanvir & Levan (2017)
Gemini-South/Flamingos-2	2017 Aug 28 23:36:01	K_s	Cowperthwaite et al. (2017b)
VLT/FORS2	2017 Aug 29 00:00:13	I	Pian et al. (2017a)
HubbleSpaceTelescope/WFC3/UVIS	2017 Aug 29 00:36:00	F275W	Kasliwal et al. (2017)
HubbleSpaceTelescope/WFC3/UVIS	2017 Aug 29 00:36:00	F225W	Kasliwal et al. (2017)
NTT/–	2017 Aug 29 22:56:00	Ks	Smartt et al. (2017)
VLT/VIMOS	2017 Aug 29 23:16:00	R	Tanvir & Levan (2017)
SkyMapper/–	2017 Aug 30 09:26:00	u	…
SkyMapper/–	2017 Aug 30 09:32:00	v	…
NTT/–	2017 Aug 30 23:03:00	Ks	Smartt et al. (2017)
VLT/FORS2	2017 Aug 31 23:34:46	z	Pian et al. (2017a)
VISTA/VIRCAM	2017 Aug 31 23:42:00	K	Tanvir & Levan (2017)
Gemini-South/Flamingos-2	2017 Aug 31 23:50:00	H	Singer et al. (2017b); Kasliwal et al. (2017)
SkyMapper/–	2017 Sep 01 09:12:00	i	…
SkyMapper/–	2017 Sep 01 09:14:00	z	…
SkyMapper/–	2017 Sep 03 09:21:00	g	…
SkyMapper/–	2017 Sep 03 09:23:00	r	…
NTT/–	2017 Sep 04 23:12:00	Ks	Smartt et al. (2017)
Gemini-South/Flamingos-2	2017 Sep 04 23:28:45	K_s	Cowperthwaite et al. (2017b)
VLT/VIMOS	2017 Sep 05 23:23:00	z	Tanvir & Levan (2017)
Gemini-South/Flamingos-2	2017 Sep 05 23:48:00	Ks	Kasliwal et al. (2017)
Magellan-Baade/FourStar	2017 Sep 06 23:24:28	Ks	Drout et al. (2017b)
VLT/HAWKI	2017 Sep 07 23:11:00	K	Tanvir & Levan (2017)
VLT/HAWKI	2017 Sep 11 23:21:00	K	Tanvir & Levan (2017)

Note. This is a subset of all the observations made in order to give a sense of the substantial coverage of this event.

time, flux upper limits, and the energy range of the observations, which are summarized here.

At the time of GRB 170817A, three out of six spacecraft of the Inter Planetary Network (Hurley et al. 2013) had a favorable orientation to observe the LIGO-Virgo skymap. However, based on the *Fermi*-GBM (Goldstein et al. 2017b) and *INTEGRAL* analyses, GRB 170817A was too weak to be detected by Konus-*Wind* (Svinkin et al. 2017a). Using the

Table 2
Record of Spectroscopic Observations

Telescope/Instrument	UT Date	Wavelengths (Å)	Resolution (R)	References
Magellan-Clay/LDSS-3	2017 Aug 18 00:26:17	3780–10200	860	Drout et al. (2017); Shappee et al. (2017)
Magellan-Clay/LDSS-3	2017 Aug 18 00:40:09	3800–6200	1900	Shappee et al. (2017)
Magellan-Clay/LDSS-3	2017 Aug 18 00:52:09	6450–10000	1810	Shappee et al. (2017)
Magellan-Baade/MagE	2017 Aug 18 01:26:22	3650–10100	5800	Shappee et al. (2017)
ANU2.3/WiFeS	2017 Aug 18 09:24:00	3200–9800	B/R 3000	…
SALT/RSS	2017 Aug 18 17:07:00	3600–8000	300	Shara et al. (2017),
NTT/EFOSC2Gr#11+16	2017 Aug 18 23:19:12	3330–9970	260/400	Smartt et al. (2017)
VLT/X-shooter	2017 Aug 18 23:22:25	3000–24800	4290/8150/5750	Pian et al. (2017b, 2017b)
SOAR/GHTS	2017 Aug 18 23:22:39	4000–8000	830	Nicholl et al. (2017d)
Magellan-Clay/LDSS-3	2017 Aug 18 23:47:37	3820–9120	860	Shappee et al. (2017)
VLT/MUSE	2017 Aug 18 23:49:00	4650–9300	3000	Levan & Tanvir (2017); Tanvir & Levan (2017)
Magellan-Clay/MIKE	2017 Aug 19 00:18:11	3900–9400	30000	Shappee et al. (2017)
Magellan-Baade/MagE	2017 Aug 19 00:35:25	3800–10300	4100	Shappee et al. (2017)
Gemini-South/FLAMINGOS2	2017 Aug 19 00:42:27	9100–18000	500	Chornock et al. (2017a)
LCOFaulkesTelescopeSouth/FLOYDS	2017 Aug 19 08:36:22	5500–9250	700	GC21908, McCully et al. (2017b)
ANU2.3/WiFeS	2017 Aug 19 09:26:12	3200–9800	B/R 3000	…
SALT/RSS	2017 Aug 19 16:58:00	3600–8000	300	Shara et al. (2017)
SALT/RSS	2017 Aug 19 16:58:32	3600–8000	300	Shara et al. (2017); Shara et al. 2017, McCully et al. (2017b)
NTT/EFOSC2Gr#11+16	2017 Aug 19 23:25:41	3330–9970	260/400	Smartt et al. (2017)
SOAR/GHTS	2017 Aug 19 23:28:32	4000–8000	830	Nicholl et al. (2017d)
VLT/Xshooterfixed	2017 Aug 19 23:28:46	3700–22790	4290/3330/5450	Smartt et al. (2017)
Gemini-South/FLAMINGOS2	2017 Aug 19 23:42:56	9100–18000	500	Chornock et al. (2017a)
Magellan-Baade/IMACS	2017 Aug 20 00:26:28	4355–8750	1000	Shappee et al. (2017)
GeminiSouth/GMOS	2017 Aug 20 01:01:54	4000–9500	400	McCully et al. (2017a, 2017b)
Gemini-South/GMOS	2017 Aug 20 01:08:00	6000–9000	1900	Kasliwal et al. (2017)
ANU2.3/WiFeS	2017 Aug 20 09:21:33	3200–9800	B/R 3000	…
NTT/EFOSC2Gr#11+16	2017 Aug 20 23:21:13	3330–9970	390/600	Smartt et al. (2017)
SOAR/GHTS	2017 Aug 20 23:23:17	5000–9000	830	Nicholl et al. (2017d)
VLT/X-shooter	2017 Aug 20 23:25:28	3000–24800	4290/8150/5750	Pian et al. (2017a)
Magellan-Clay/LDSS-3	2017 Aug 20 23:45:53	4450–10400	860	Shappee et al. (2017)
Gemini-South/GMOS	2017 Aug 21 00:15:00	3800–9200	1700	Troja et al. (2017b); Kasliwal et al. (2017); Troja et al. (2017a)
GeminiSouth/GMOS	2017 Aug 21 00:16:09	4000–9500	400	Troja et al. (2017b); McCully et al. (2017b); Troja et al. (2017a)
VLT/FORS2	2017 Aug 21 00:43:12	3500–8600	800–1000	Pian et al. (2017a)
ANU2.3/WiFeS	2017 Aug 21 09:13:00	3200–7060	B 3000 R 7000	…
NTT/SOFIBlueGrism	2017 Aug 21 23:11:37	9380–16460	550	Smartt et al. (2017)
SOAR/GHTS	2017 Aug 21 23:24:49	4000–8000	830	Nicholl et al. (2017d)
VLT/Xshooterfixed	2017 Aug 21 23:25:38	3700–22790	4290/3330/5450	Smartt et al. (2017)
VLT/FORS2	2017 Aug 21 23:31:12	3500–8600	800–1000	Pian et al. (2017a)
Gemini-South/FLAMINGOS2	2017 Aug 21 23:40:09	9100–18000	500	Chornock et al. (2017a)
Gemini-South/Flamingos-2	2017 Aug 22 00:21:00	12980–25070	600	Kasliwal et al. (2017)
Gemini-South/Flamingos-2	2017 Aug 22 00:47:00	9840–18020	600	Kasliwal et al. (2017)
Magellan-Clay/LDSS-3	2017 Aug 22 00:50:34	5010–10200	860	Shappee et al. (2017)
HST/WFC3/IR-G102	2017 Aug 22 09:07:00	8000–11150	210	Tanvir & Levan (2017); Troja et al. (2017a)
HST/WFC3/IR-G141	2017 Aug 22 10:53:00	10750–17000	130	Tanvir & Levan (2017); Troja et al. (2017a)
Magellan-Clay/LDSS-3	2017 Aug 22 23:34:00	5000–10200	860	Shappee et al. (2017)
HST/STIS	2017 Aug 23 02:51:54	1600–3200	700	Nicholl et al. (2017d)

Table 2
(Continued)

Telescope/Instrument	UT Date	Wavelengths (Å)	Resolution (R)	References
AAT/AAOmega2DF	2017 Aug 24 08:55:00	3750–8900	1700	Andreoni et al. (2017),
HST/WFC3/IR-G102	2017 Aug 24 18:58:00	8000–11150	210	Tanvir & Levan (2017); Troja et al. (2017a)
Magellan-Clay/LDSS-3	2017 Aug 24 23:33:51	6380–10500	1810	Shappee et al. (2017)
SOAR/GHTS	2017 Aug 24 23:34:31	5000–9000	830	Nicholl et al. (2017d)
Gemini-South/FLAMINGOS2	2017 Aug 24 23:56:32	9100–18000	500	Chornock et al. (2017a)
KeckI/LRIS	2017 Aug 25 05:45:00	2000–10300	1000	Kasliwal et al. (2017)
Magellan/Baade/IMACS	2017 Aug 25 23:37:59	4300–9300	1100	Nicholl et al. (2017d)
Magellan-Clay/LDSS-3	2017 Aug 25 23:39:18	6380–10500	1810	Shappee et al. (2017)
Gemini-South/FLAMINGOS2	2017 Aug 26 00:21:24	9100–18000	500	Chornock et al. (2017a)
HST/WFC3/IR-G141	2017 Aug 26 22:57:00	10750–17000	130	Tanvir & Levan (2017); Troja et al. (2017a)
Magellan/Baade/IMACS	2017 Aug 26 23:20:54	4300–9300	1100	Nicholl et al. (2017d)
Gemini-South/FLAMINGOS2	2017 Aug 27 00:12:20	9100–18000	500	Chornock et al. (2017a)
Gemini-South/FLAMINGOS2	2017 Aug 28 00:16:28	9100–18000	500	Chornock et al. (2017a)
HST/WFC3/IR-G102	2017 Aug 28 01:58:00	8000–11150	210	Tanvir & Levan (2017); Troja et al. (2017a)
HST/WFC3/IR-G141	2017 Aug 28 03:33:00	10750–17000	130	Tanvir & Levan (2017); Troja et al. (2017a)
Gemini-South/Flamingos-2	2017 Aug 29 00:23:00	12980–25070	600	Kasliwal et al. (2017)

Table 3
Gamma-Ray Monitoring and Evolution of GW170817

Observatory	UT Date	Time since GW Trigger	90% Flux Upper Limit ($erg\ cm^{-2}\ s^{-1}$)	Energy Band	GCN/Reference
Insight-HXMT/HE	Aug 17 12:34:24 UTC	−400 s	3.7×10^{-7}	0.2–5 MeV	Li et al. (2017)
CALET CGBM	Aug 17 12:41:04 UTC	0.0	1.3×10^{-7a}	10–1000 keV	Nakahira et al. (2017)
Konus-*Wind*	Aug 17 12:41:04.446 UTC	0.0	3.0×10^{-7} [erg cm^{-2}]	10 keV–10 MeV	Svinkin et al. (2017a)
Insight-HXMT/HE	Aug 17 12:41:04.446 UTC	0.0	3.7×10^{-7}	0.2–5 MeV	Li et al. (2017)
Insight-HXMT/HE	Aug 17 12:41:06.30 UTC	1.85 s	6.6×10^{-7}	0.2–5 MeV	Li et al. (2017)
Insight-HXMT/HE	Aug 17 12:46:04 UTC	300 s	1.5×10^{-7}	0.2–5 MeV	Li et al. (2017)
AGILE-GRID	Aug 17 12:56:41 UTC	0.011 days	3.9×10^{-9}	0.03–3 GeV	V. Verrecchia et al. (2017, in preparation)
Fermi-LAT	Aug 17 13:00:14 UTC	0.013 days	4.0×10^{-10}	0.1–1 GeV	Kocevski et al. (2017)
H.E.S.S.	Aug 17 17:59 UTC	0.22 days	3.9×10^{-12}	0.28–2.31 TeV	H. Abdalla et al. (H.E.S.S. Collaboration) (2017, in preparation)
HAWC	Aug 17 20:53:14—Aug 17 22:55:00 UTC	0.342 days + 0.425 days	1.7×10^{-10}	4–100 TeV	Martinez-Castellanos et al. (2017)
Fermi-GBM	Aug 16 12:41:06—Aug 18 12:41:06 UTC	±1.0 days	$(8.0–9.9) \times 10^{-10}$	20–100 keV	Goldstein et al. (2017a)
NTEGRAL IBIS/ISGRI	Aug 18 12:45:10—Aug 23 03:22:34 UTC	1–5.7 days	2.0×10^{-11}	20–80 keV	Savchenko et al. (2017)
INTEGRAL IBIS/ISGRI	Aug 18 12:45:10—Aug 23 03:22:34 UTC	1–5.7 days	3.6×10^{-11}	80–300 keV	Savchenko et al. (2017)
INTEGRAL IBIS/PICsIT	Aug 18 12:45:10—Aug 23 03:22:34 UTC	1–5.7 days	0.9×10^{-10}	468–572 keV	Savchenko et al. (2017)
INTEGRAL IBIS/PICsIT	Aug 18 12:45:10—Aug 23 03:22:34 UTC	1–5.7 days	4.4×10^{-10}	572–1196 keV	Savchenko et al. (2017)
INTEGRAL SPI	Aug 18 12:45:10—Aug 23 03:22:34 UTC	1–5.7 days	2.4×10^{-10}	300–500 keV	Savchenko et al. (2017)
INTEGRAL SPI	Aug 18 12:45:10—Aug 23 03:22:34 UTC	1–5.7 days	7.0×10^{-10}	500–1000 keV	Savchenko et al. (2017)
INTEGRAL SPI	Aug 18 12:45:10—Aug 23 03:22:34 UTC	1–5.7 days	1.5×10^{-9}	1000–2000 keV	Savchenko et al. (2017)
INTEGRAL SPI	Aug 18 12:45:10—Aug 23 03:22:34 UTC	1–5.7 days	2.9×10^{-9}	2000–4000 keV	Savchenko et al. (2017)
H.E.S.S.	Aug 18 17:55 UTC	1.22 days	3.3×10^{-12}	0.27–3.27 TeV	H. Abdalla et al. (H.E.S.S. Collaboration) (2017, in preparation)
H.E.S.S.	Aug 19 17:56 UTC	2.22 days	1.0×10^{-12}	0.31–2.88 TeV	H. Abdalla et al. (H.E.S.S. Collaboration) (2017, in preparation)
H.E.S.S.	Aug 21 + Aug 22 18:15 UTC	4.23 days + 5.23 days	2.9×10^{-12}	0.50–5.96 TeV	H. Abdalla et al. (H.E.S.S. Collaboration) (2017, in preparation)

Note.
[a] Assuming no shielding by the structures of ISS.

Earth Occultation technique (Wilson-Hodge et al. 2012), *Fermi*-GBM placed limits on persistent emission for the 48 hr period centered at the *Fermi*-GBM trigger time over the 90% credible region of the GW170817 localization. Using the offline targeted search for transient signals (Blackburn et al. 2015), *Fermi*-GBM also set constraining upper limits on precursor and extended emission associated with GRB 170817A (Goldstein et al. 2017b). *INTEGRAL* (Winkler et al. 2003) continued uninterrupted observations after GRB 170817A for 10 hr. Using the PiCSIT (Labanti et al. 2003) and SPI-ACS detectors, the presence of a steady source 10 times weaker than the prompt emission was excluded (Savchenko et al. 2017).

The High Energy telescope on board *Insight*-HXMT monitored the entire GW170817 skymap from T0 − 650 s to T0 + 450 s but, due to the weak and soft nature of GRB 170817A, did not detect any significant excess at T0 (Liao et al. 2017). Upper limits from 0.2–5 MeV for GRB 170817A and other emission episodes are reported in Li et al. (2017).

The Calorimetric Electron Telescope (CALET) Gamma-ray Burst Monitor (CGBM) found no significant excess around T0. Upper limits may be affected due to the location of SSS17a/AT 2017gfo being covered by the large structure of the International Space Station at the time of GRB 170817A (Nakahira et al. 2017). *AstroSat* CZTI (Singh et al. 2014; Bhalerao et al. 2017) reported upper limits for the 100 s interval centered on T0 (Balasubramanian et al. 2017); the position of SSS17a/AT 2017gfo was occulted by the Earth, however, at the time of the trigger.

For the AstroRivelatore Gamma a Immagini Leggero (AGILE) satellite (Tavani et al. 2009) the first exposure of the GW170817 localization region by the Gamma Ray Imaging Detector (GRID), which was occulted by the Earth at the time of GRB 170817A, started at T0 + 935 s. The GRID observed the field before and after T0, typically with 150 s exposures. No gamma-ray source was detected above 3σ in the energy range 30 MeV–30 GeV (V. Verrecchia et al. 2017, in preparation).

At the time of the trigger, *Fermi* was entering the South Atlantic Anomaly (SAA) and the Large Area Telescope (LAT) was not collecting science data (*Fermi*-GBM uses different SAA boundaries and was still observing). *Fermi*-LAT resumed data taking at roughly T0 + 1153 s, when 100% of the low-latency GW170817 skymap (LIGO Scientific Collaboration & Virgo Collaboration et al. 2017b) was in the field of view for $\sim$1000 s. No significant source of high-energy emission was detected. Additional searches over different timescales were performed for the entire time span of LAT data, and no significant excess was detected at the position of SSS17a/AT 2017gfo (Kocevski et al. 2017).

The High Energy Stereoscopic System (H.E.S.S.) array of imaging atmospheric Cherenkov telescopes observed from August 17 18:00 UTC with three pointing positions. The first, at T0 + 5.3 hr, covered SSS17a/AT 2017gfo. Observations repeated the following nights until the location moved outside the visibility window, with the last pointing performed on August 22 18:15 UTC. A preliminary analysis with an energy threshold of $\sim$500 GeV revealed no significant gamma-ray emission (de Naurois et al. 2017), confirmed by the final, offline analysis (see H. Abdalla et al. (H.E.S.S. Collaboration) 2017, in preparation, for more results).

For the High-Altitude Water Cherenkov (HAWC) Observatory (Abeysekara et al. 2017) the LIGO-Virgo localization

region first became visible on August 17 between 19:57 and 23:25 UTC. SSS17a/AT 2017gfo was observed for 2.03 hr starting at 20:53 UTC. Upper limits from HAWC for energies >40 TeV assuming an $E^{-2.5}$ spectrum are reported in Martinez-Castellanos et al. (2017).

INTEGRAL (3 keV–8 MeV) carried out follow-up observations of the LIGO-Virgo localization region, centered on the optical counterpart, starting 24 hr after the event and spanning 4.7 days. Hard X-ray emission is mostly constrained by IBIS (Ubertini et al. 2003), while above 500 keV SPI (Vedrenne et al. 2003) is more sensitive. Besides the steady flux limits reported in Table 3, these observations exclude delayed bursting activity at the level of giant magnetar flares. No gamma-ray lines from a kilonova or $e^{+/-}$ pair plasma annihilation were detected (see Savchenko et al. 2017).

3.3. Discovery of the X-Ray Counterpart

While the UV, optical, and IR observations mapped the emission from the sub-relativistic ejecta, X-ray observations probed a different physical regime. X-ray observations of GRB afterglows are important to constrain the geometry of the outflow, its energy output, and the orientation of the system with respect to the observers' line of sight.

The earliest limits at X-ray wavelengths were provided by the Gas Slit Camera (GSC) of the *Monitor of All-Sky X-ray Image* (*MAXI*; Matsuoka et al. 2009). Due to an unfavorable sky position, the location of GW170817 was not observed by *MAXI* until August 17 17:21 UTC (T0 + 0.19 days). No X-ray emission was detected at this time to a limiting flux of 8.6×10^{-9} erg cm^{-2} s^{-1} (2–10 keV; Sugita et al. 2017; S. Sugita 2017, in preparation). *MAXI* obtained three more scans over the location with no detections before the more sensitive pointed observations began.

In addition, the Super-*AGILE* detector (Feroci et al. 2007) on board the *AGILE* mission (Tavani et al. 2009) observed the location of GW170817 starting at August 18 01:16:34.84 UTC (T0 + 0.53 days). No X-ray source was detected at the location of GW170817, with a 3σ upper limit of 3.0×10^{-9} erg cm^{-2} s^{-1} (18–60 keV; V. Verrecchia et al. 2017, in preparation).

The first pointed X-ray observations of GW170817 were obtained by the X-Ray Telescope (Burrows et al. 2005) on the *Swift* satellite (Gehrels 2004) and the *NUclear Spectroscopic Telescope ARray* (*NuSTAR*; Harrison et al. 2013), beginning at T0 + 0.62 days and T0 + 0.70 days, respectively. No X-ray emission was detected at the location of GW170817 to limiting fluxes of 2.7×10^{-13} erg cm^{-2} s^{-1} (0.3–10.0 keV; Evans et al. 2017a, 2017b) and 2.6×10^{-14} erg cm^{-2} s^{-1} (3.0–10.0 keV; Evans et al. 2017a, 2017b). *Swift* continued to monitor the field, and after stacking several epochs of observations, a weak X-ray source was detected near the location of GW170817 at a flux of 2.6×10^{-14} erg cm^{-2} s^{-1} (Evans et al. 2017c).

INTEGRAL (see Section 3.2) performed pointed follow-up observations from one to about six days after the trigger. The X-ray monitor JEM-X (Lund et al. 2003) constrained the average X-ray luminosity at the location of the optical transient to be $<2 \times 10^{-11}$ erg cm^{-2} s^{-1} (3–10.0 keV) and $<7 \times 10^{-12}$ erg cm^{-2} s^{-1} (10–25 keV; Savchenko et al. 2017).

Chandra obtained a series of observations of GW170817 beginning at August 19 17:10 UTC (T0 + 2.2 days) and continuing until the emission from NGC 4993 became unobservable because of SSS17a/AT 2017gfo's proximity to

the Sun (Fong et al. 2017; Haggard et al. 2017b; Margutti et al. 2017a; Troja et al. 2017c, 2017e). Two days post-trigger, Margutti et al. (2017a) reported an X-ray non-detection for SSS17a/AT 2017gfo in a $\simeq$25 ks *Chandra* exposure,[964] along with the detection of an extended X-ray source whose position was consistent with the host NGC 4993 (Margutti et al. 2017b). Refined astrometry from subsequent *Swift* observations confirmed that the previously reported candidate was indeed associated with the host nucleus (Evans et al. 2017a, 2017b).

Nine days post-trigger, Troja et al. (2017c) reported the discovery of the X-ray counterpart with *Chandra*. In a 50 ks exposure observation, they detected significant X-ray emission at the same position of the optical/IR counterpart (Troja et al. 2017a; top right panel in Figure 2)[965]. Fifteen days post-trigger, two additional 50 ks *Chandra* observations were made, which confirmed the continued presence of X-ray emission. Based on the first of these two observations[966,967]: Fong et al. (2017) reported the detection of the X-ray counterpart and the presence of an additional X-ray point source in the near vicinity (Margutti et al. 2017b), and Troja et al. (2017e) reported a flux of 4.5×10^{-15} erg cm^{-2} s^{-1} for the X-ray counterpart. One day later, Haggard et al. (2017b) reported another deep observation showing continued distinct X-ray emission coincident with SSS17a/AT 2017gfo, NGC 4993, and the additional point source (Haggard et al. 2017a, 2017b).[10]

Neither *Swift* nor *Chandra* can currently observe GW170817 because it is too close to the Sun ($<47°$ for *Swift*, $<46°$ for *Chandra*). Hence, until early 2017 December, *NuSTAR* is the only sensitive X-ray observatory that can continue to observe the location of GW170817.

All X-ray observations of GW170817 are summarized in Table 4.

3.4. Discovery of the Radio Counterpart

Radio emission traces fast-moving ejecta from a neutron star coalescence, providing information on the energetics of the explosion, the geometry of the ejecta, as well as the environment of the merger. The spectral and temporal evolution of such emission, coupled with X-ray observations, are likely to constrain several proposed models (see, e.g., Nakar & Piran 2011; Piran et al. 2013; Hotokezaka & Piran 2015; Hotokezaka et al. 2016; Gottlieb et al. 2017).

Prior to detection of SSS17a/AT 2017gfo, a blind radio survey of cataloged galaxies in the gravitational-wave localization volume commenced with the Australia Telescope Compact Array (ATCA; Wilson et al. 2011), and observed the merger events' location on 2017 August 18 at 01:46 UTC (Kaplan et al. 2017a). In addition, the Long Wavelength Array 1 (LWA1; Ellingson et al. 2013) followed up the gravitational-wave localization with observations at $t_c + 6.5$ hr, then on 2017 August 23 and 30 (Callister et al. 2017a; Callister et al. 2017b) using four beams (one centered on NGC 4993, one off-center, and two off NGC 4993). These observations set 3σ upper limits for the appearance of a radio source in the beam centered on NGC 4993, about 8 hours after the GW event, as $\sim$200 Jy at 25 MHz and $\sim$100 Jy at 45 MHz.

The first reported radio observations of the optical transient SSS17a/AT 2017gfo's location occurred on August 18 at 02:09:00 UTC (T0+13.5 hr) with the Karl G. Jansky Very Large Array (VLA) by Alexander et al. (2017d).[968] Initially attributed to the optical transient, this radio source was later established to be an AGN in the nucleus of the host galaxy, NGC 4993 (Alexander et al. 2017e, 2017c). Subsequent observations with several radio facilities spanning a wide range of radio and millimeter frequencies continued to detect the AGN, but did not reveal radio emission at the position of the transient (Alexander et al. 2017f; Bannister et al. 2017b; Corsi et al. 2017a, 2017b, 2017c; De et al. 2017a, 2017b; Kaplan et al. 2017a; Lynch et al. 2017a, 2017b, 2017c; Mooley et al. 2017a; Resmi et al. 2017).

The first radio counterpart detection consistent with the *HST* position (refined by *Gaia* astrometry) of SSS17a/AT 2017gfo (Adams et al. 2017) was obtained with the VLA on 2017 September 2 and 3 at two different frequencies ($\approx$3 GHz and $\approx$6 GHz) via two independent observations: the Jansky VLA mapping of Gravitational Wave bursts as Afterglows in Radio (JAGWAR;[969] Mooley et al. 2017b) and VLA/16A-206[970] (Corsi et al. 2017d). Marginal evidence for radio excess emission at the location of SSS17a/AT 2017gfo was also confirmed in ATCA images taken on September 5 at similar radio frequencies ($\approx$7.25 GHz; Murphy et al. 2017). Subsequent repeated detections spanning multiple frequencies have confirmed an evolving transient (Hallinan et al. 2017a, 2017b; Corsi et al. 2017d; Mooley et al. 2017b). Independent observations carried out on 2017 September 5 with the same frequency and exposure time used by Corsi et al. (2017d) did not detect any emission to a 5σ limit[971] (Alexander et al. 2017a), but this group also subsequently detected the radio counterpart on 2017 September 25 (Alexander et al. 2017b, 2017c).

SSS17a/AT 2017gfo, as well as other parts of the initial gravitational-wave localization area, were and are also being continuously monitored at a multitude of different frequencies with the Atacama Large Millimeter/submillimeter Array (ALMA; Wootten & Thompson 2009; Schulze et al. 2017; Kim et al. 2017, in preparation; Alexander et al. 2017c; Williams et al. 2017a), the Australian Square Kilometre Array Pathfinder (ASKAP; Johnston et al. 2007), ASKAP-Fast Radio Burst (Bannister et al. 2017a, 2017c), ATCA, Effelsberg-100 m (Barr et al. 2013), the Giant Metrewave Radio Telescope (GMRT; Swarup et al. 1991), the Low-Frequency Array (LOFAR; van Haarlem et al. 2013), the Long Wavelength Array (LWA1), MeerKAT (Goedhart et al. 2017a), the Murchison Widefield Array (MWA; Tingay et al. 2013), Parkes-64 m (SUPERB; Bailes et al. 2017a; Keane et al. 2017), Sardinia Radio Telescope (SRT; Prandoni et al. 2017), VLA, VLA Low Band Ionosphere and Transient Experiment (VLITE; Clarke & Kassim 2016), and also using the very long baseline interferometry (VLBI) technique with e-MERLIN (Moldon et al. 2017a, 2017b), the European VLBI Network (Paragi et al. 2017a, 2017b), and the Very Long Baseline Array (VLBA; Deller et al. 2017a, 2017b). The latter have the potential to resolve (mildly) relativistic ejecta on a timescale of months.

Table 5 summarizes the radio observations of GW170817.

---

[964] *Chandra* OBSID-18955, PI: Fong.
[965] *Chandra* OBSID-19294, PI: Troja.
[966] *Chandra* OBSID-20728, PI: Troja (Director's Discretionary Time observation distributed also to Haggard, Fong, and Margutti).
[967] *Chandra* OBSID-18988, PI: Haggard.

[968] VLA/17A-218, PI: Fong.
[969] VLA/17A-374, PI: Mooley.
[970] VLA/16A-206, PI: Corsi.
[971] VLA/17A-231, PI: Alexander.

Table 4
X-Ray Monitoring and Evolution of GW170817

Observatory	UT Date (Start)	Time since GW trigger (days)	f_x (erg cm^{-2} s^{-1})	L_x (erg s^{-1})	Energy (keV)	GCN/Reference
MAXI	Aug 17 17:21:54 UTC	0.19	$<8.6 \times 10^{-9}$	$<1.65 \times 10^{45}$	2–10	S. Sugita et al. (2017, in preparation)
MAXI	Aug 17 18:54:27 UTC	0.26	$<7.7 \times 10^{-8}$	$<1.47 \times 10^{46}$	2–10	S. Sugita et al. (2017, in preparation)
MAXI	Aug 18 00:44:59 UTC	0.50	$<4.2 \times 10^{-9}$	$<8.0 \times 10^{44}$	2–10	S. Sugita et al. (2017, in preparation)
Super-*AGILE*	Aug 18 01:16:34 UTC	0.53	$<3.0 \times 10^{-9}$	$<5.4 \times 10^{44}$	18–60	V. Verrecchia et al. (2017, in preparation)
MAXI	Aug 18 02:18:08 UTC	0.57	$<2.2 \times 10^{-9}$	$<4.2 \times 10^{44}$	2–10	S. Sugita et al. (2017, in preparation)
Swift-XRT	Aug 18 03:34:33 UTC	0.62	$<2.74 \times 10^{-13}$	$<5.25 \times 10^{40}$	0.3–10	Evans et al. (2017b)
NuSTAR	Aug 18 05:25 UTC	0.7	$<2.62 \times 10^{-14}$	$<5.01 \times 10^{39}$	3–10	Evans et al. (2017b)
Swift-XRT	Aug 18 12:11:49 UTC	0.98	$<2.62 \times 10^{-12}$	$<5.01 \times 10^{41}$	0.3–10	Evans et al. (2017b)
INTEGRAL JEM-X	Aug 18 12:45:10 UTC	1–5.7	$<1.9 \times 10^{-11}$	$<3.6 \times 10^{42}$	3–10	Savchenko et al. (2017)
INTEGRAL JEM-X	Aug 18 12:45:10 UTC	1–5.7	$<7.0 \times 10^{-12}$	$<1.3 \times 10^{42}$	10–25	Savchenko et al. (2017)
Swift-XRT	Aug 18 13:29:43 UTC	1.03	$<1.77 \times 10^{-13}$	$<3.39 \times 10^{40}$	0.3–10	Evans et al. (2017b)
Swift-XRT	Aug 19 00:18:22 UTC	1.48	$<1.31 \times 10^{-13}$	$<2.51 \times 10^{40}$	0.3–10	Evans et al. (2017b)
Chandra	Aug 19 17:10:09 UTC	2.20	non-detection	…	0.3–10	Margutti et al. (2017a)
Swift-XRT	Aug 19 13:24:05 UTC	2.03	$<1.02 \times 10^{-13}$	$<1.95 \times 10^{40}$	0.3–10	Evans et al. (2017b)
Swift-XRT	Aug 19 18:30:52 UTC	2.24	$<1.34 \times 10^{-13}$	$<2.57 \times 10^{40}$	0.3–10	Evans et al. (2017b)
Swift-XRT	Aug 20 03:24:44 UTC	2.61	$<1.41 \times 10^{-13}$	$<2.69 \times 10^{40}$	0.3–10	Evans et al. (2017b)
Swift-XRT	Aug 20 08:28:05 UTC	2.82	$<3.87 \times 10^{-14}$	$<7.41 \times 10^{39}$	0.3–10	Evans et al. (2017b)
Swift-XRT	Aug 21 01:43:44 UTC	3.54	$<6.73 \times 10^{-14}$	$<1.29 \times 10^{40}$	0.3–10	Evans et al. (2017b)
NuSTAR	Aug 21 20:45:00 UTC	4.3	$<2.08 \times 10^{-14}$	$<3.98 \times 10^{39}$	3–10	Evans et al. (2017b)
Swift-XRT	Aug 22 00:05:57 UTC	4.48	$<6.28 \times 10^{-14}$	$<1.20 \times 10^{40}$	0.3–10	Evans et al. (2017b)
Swift-XRT	Aug 23 06:22:57 UTC	5.74	$<6.89 \times 10^{-14}$	$<1.32 \times 10^{40}$	0.3–10	Evans et al. (2017b)
Swift-XRT	Aug 23 23:59:57 UTC	6.47	$<7.21 \times 10^{-14}$	$<1.38 \times 10^{40}$	0.3–10	Evans et al. (2017b)
Chandra	Aug 26 10:33:50 UTC	8.9	Detection	…	0.5–8.0	Troja et al. (2017c, 2017a)
Swift-XRT	Aug 26 23:59:57 UTC	9.47	$<8.67 \times 10^{-14}$	$<1.66 \times 10^{40}$	0.3–10	Evans et al. (2017b)
Swift-XRT	Aug 28 10:46:17 UTC	10.92	$<1.41 \times 10^{-13}$	$<2.69 \times 10^{40}$	0.3–10	Evans et al. (2017b)
Swift-XRT	Aug 29 01:04:57 UTC	11.52	$<6.00 \times 10^{-14}$	$<1.15 \times 10^{40}$	0.3–10	Evans et al. (2017b)
Swift-XRT	Aug 30 01:00:57 UTC	12.51	$<5.47 \times 10^{-14}$	$<1.05 \times 10^{40}$	0.3–10	Evans et al. (2017b)
Swift-XRT	Aug 31 02:27:52 UTC	13.57	$<3.87 \times 10^{-14}$	$<7.41 \times 10^{39}$	0.3–10	Evans et al. (2017b)
Swift-XRT	Sep 01 05:53:04 UTC	14.72	$<4.45 \times 10^{-14}$	$<8.51 \times 10^{39}$	0.3–10	Evans et al. (2017b)
Chandra	Sep 01 15:22:22 UTC	15.1		…	…	Fong et al. (2017); Margutti et al. (2017b)
Chandra	Sep 01 15:22:22 UTC	15.1	4.5×10^{-15}	9×10^{38}	0.5–8.0	Troja et al. (2017e, 2017a)
Chandra	Sep 02 15:22:22 UTC	15.1	3.5×10^{-15}	2.7×10^{38}	0.3–10	Haggard et al. (2017b, 2017a)
Chandra	Sep 02 00:00:00 UTC	16.1	3.8×10^{-15}	3.0×10^{38}	0.3–10	Haggard et al. (2017b, 2017a)
Swift-XRT	Sep 02 08:40:56 UTC	15.83	$<1.51 \times 10^{-13}$	$<2.88 \times 10^{40}$	0.3–10	Evans et al. (2017b)
NuSTAR	Sep 04 17:56 UTC	18.2	$<6.58 \times 10^{-14}$	$<1.26 \times 10^{40}$	3–10	Evans et al. (2017b)
NuSTAR	Sep 05 14:51 UTC	19.1	$<4.15 \times 10^{-14}$	$<7.94 \times 10^{39}$	3–10	Evans et al. (2017b)
NuSTAR	Sep 06 17:56 UTC	20.1	$<3.30 \times 10^{-14}$	$<6.31 \times 10^{39}$	3–10	Evans et al. (2017b)
NuSTAR	Sep 21 11:10 UTC	34.9	$<1.65 \times 10^{-14}$	$<3.16 \times 10^{39}$	3–10	Evans et al. (2017b)

Table 5
Radio Monitoring and Evolution of GW170817

Telescope	UT Date	Time since GW Trigger (days)	Central Frequency (GHz)	Bandwidth (GHz)	Flux (μ Jy), 3σ	GCN/Reference
LWA1	Aug 17 13:09:51 UTC	0.02	0.02585	0.020	$\cdots$	Callister et al. (2017a)
LWA1	Aug 17 13:09:51 UTC	0.02	0.04545	0.020	$\cdots$	Callister et al. (2017a)
LWA1	Aug 17 19:15:00 UTC	0.27	0.02585	0.020	$<2 \times 10^8$	Callister et al. (2017a)
LWA1	Aug 17 19:15:00 UTC	0.27	0.04545	0.020	$<1 \times 10^8$	Callister et al. (2017a)
VLBA	Aug 17 19:58:00 UTC	0.30	8.7	0.26		Deller et al. (2017a)
VLA	Aug 18 02:18:00 UTC	0.57	10.0	$\cdots$		Alexander et al. (2017d, 2017e)
ATCA	Aug 18 01:00:00 UTC	1	8.5	2.049	<120	Bannister et al. (2017d)
						Kaplan et al. (2017a)
						Hallinan et al. (2017a)
ATCA	Aug 18 01:00:00 UTC	1	10.5	2.049	<150	Bannister et al. (2017d)
						Kaplan et al. (2017a)
						Hallinan et al. (2017a)
ATCA	Aug 18 01:00:00 UTC	1	16.7	2.049	<130	Kaplan et al. (2017a)
						Hallinan et al. (2017a)
ATCA	Aug 18 01:00:00 UTC	1	21.2	2.049	<140	Kaplan et al. (2017a)
						Hallinan et al. (2017a)
VLITE	Aug 18 22:23:31 UTC	1.44	0.3387	0.034	<34800	Hallinan et al. (2017a)
ASKAP	Aug 18 04:05:35 UTC	0.67	1.34	0.19		Bannister et al. (2017e, 2017c)
MWA	Aug 18 07:07:50 UTC	1	0. 185	0.03	$<51\,000$	Kaplan et al. (2017b)
ASKAP	Aug 18 08:57:33 UTC	0.86	1.34	0.19		Bannister et al. (2017e, 2017c)
VLA	Aug 18 22:04:57 UTC	1	10.0	3.8	<17.0	Alexander et al. (2017f)
ALMA	Aug 18 22:50:40 UTC	1.4	338.5	7.5	$\cdots$	Schulze et al. (2017)
GMRT	Aug 18 11:00:00 UTC	1	10.0	0.032	<195	De et al. (2017a)
						Hallinan et al. (2017a)
Parkes	Aug 18 00:00:00 UTC	1.38	1.34	0.34	$<1.4 \times 10^6$	Bailes et al. (2017a)
Parkes	Aug 18 00:00:00 UTC	1.46	1.34	0.34	$<1.4 \times 10^6$	Bailes et al. (2017a)
ASKAP	Aug 19 02:08:00 UTC	1.58	1.34	0.19		Bannister et al. (2017e)
ASKAP	Aug 19 05:34:33 UTC	2	1.345	$\cdots$	<900	Dobie et al. (2017a)
VLA	Aug 19 22:01:48 UTC	2	6.0	4	<22	Corsi et al. (2017a)
VLA	Aug 19 22:01:48 UTC	2	6.0	4	<22	Corsi et al. (2017a)
VLITE	Aug 19 22:29:29 UTC	2.44	0.3387	0.034	<28800	Hallinan et al. (2017a)
VLA	Aug 19 22:30:10 UTC	2.42	15.0	6	<22	Corsi et al. (2017e)
						Hallinan et al. (2017a)
VLA	Aug 19 23:04:06 UTC	2.44	10.0	4	<17	Corsi et al. (2017b)
						Hallinan et al. (2017a)
VLA	Aug 19 23:33:30 UTC	2.46	6.0	$\cdots$	<20	Corsi et al. (2017a)
						Hallinan et al. (2017a)
ALMA	Aug 19 22:31:43 UTC	2	97.5	$\cdots$	<50	Williams et al. (2017a)
Parkes	Aug 20 00:00:00 UTC	3.17	1.34	0.34	$<1.4 \times 10^6$	Bailes et al. (2017a)
Parkes	Aug 20 00:00:00 UTC	3.21	1.34	0.34	$<1.4 \times 10^6$	Bailes et al. (2017a)
VLITE	Aug 20 20:49:36 UTC	3.34	0.3387	0.034	<44700	Hallinan et al. (2017a)
VLA	Aug 20 00:01:24 UTC	3	9.7	4	<18	Corsi et al. (2017b)
GMRT	Aug 20 08:00:00 UTC	3	0.4	0.2	<780	De et al. (2017b)
GMRT	Aug 20 08:00:00 UTC	3	1.2	0.4	<98	De et al. (2017b)
VLA	Aug 20 21:07:00 UTC	3	6.2	4	<19	Corsi et al. (2017c)
VLA/JAGWAR	Aug 20 22:20:00 UTC	3	3.0	$\cdots$	<32	Mooley et al. (2017a)
ATCA	Aug 20 23:31:03 UTC	3	8.5	2.049	<20	Lynch et al. (2017a)

Table 5
(Continued)

Telescope	UT Date	Time since GW Trigger (days)	Central Frequency (GHz)	Bandwidth (GHz)	Flux (μ Jy), 3σ	GCN/Reference
ATCA	Aug 20 23:31:03 UTC	3	10.5	2.049	<135	Lynch et al. (2017a)
ALMA	Aug 20 22:40:16 UTC	3	338.5	7.5	⋯	Schulze et al. (2017)
VLBA	Aug 20 21:36:00 UTC	3	8.7	⋯	<48	Deller et al. (2017b)
ALMA	Aug 21 20:58:51 UTC	4.3	338.5	7.5	⋯	Schulze et al. (2017)
VLA	Aug 22 23:50:18 UTC	5.48	10.0	⋯		Alexander et al. (2017c)
e-MERLIN	Aug 23 12:00:00 UTC	6	5.0	0.512	<108	Moldon et al. (2017a)
e-MERLIN	Aug 24 12:00:00 UTC	7	5.0	0.512	<96	Moldon et al. (2017a)
LWA1	Aug 24 19:50:00 UTC	7	0.02585	0.016		Callister et al. (2017b)
LWA1	Aug 24 19:50:00 UTC	7	0.04545	0.016		Callister et al. (2017b)
e-MERLIN	Aug 25 12:00:00 UTC	8	5.0	512	<96	Moldon et al. (2017a)
VLITE	Aug 25 20:38:22 UTC	8.37	0.3387	0.034	<37500	Hallinan et al. (2017a)
GMRT	Aug 25 09:30:00 UTC	7.9	1.39	0.032	<130	Resmi et al. (2017)
VLA	Aug 25 19:15:12 UTC	8.29	10.0	⋯		Alexander et al. (2017c)
ALMA	Aug 25 22:35:17 UTC	8.4	338.5	7.5	⋯	Schulze et al. (2017)
MeerKAT	Aug 26 08:43:00 UTC	10	1.48	0.22	<70	Goedhart et al. (2017a)
ALMA	Aug 26 22:49:25 UTC	9.43	97.5	⋯		Williams et al. (2017a)
ALMA	Aug 26 22:58:41 UTC	9.4	338.5	7.5	⋯	Schulze et al. (2017); S. Kim et al. (2017, in preparation)
EVN	Aug 26 12:15:00 UTC	9	5.0	0.256	<96	Paragi et al. (2017a)
e-MERLIN	Aug 26 12:00:00 UTC	9	5.0	0.512	<114	Moldon et al. (2017a)
e-MERLIN	Aug 27 12:00:00 UTC	10	5.0	0.512	<90	Moldon et al. (2017a)
ATCA	Aug 27 23:26:25 UTC	10	8.5	2. 049	<54	Lynch et al. (2017b)
ATCA	Aug 27 23:26:25 UTC	10	10.5	2.049	<39	Lynch et al. (2017b)
e-MERLIN	Aug 28 12:00:00 UTC	11	5.0	0.512	<90	Moldon et al. (2017a)
VLITE	Aug 30 23:10:28 UTC	13.45	0.3387	0.034	<20400	Hallinan et al. (2017a)
LWA1	Aug 30 19:50:00 UTC	13	0.02585	0.016		Callister et al. (2017)
LWA1	Aug 30 19:50:00 UTC	13	0.04545	0.016		Callister et al. (2017)
VLA	Aug 30 22:09:24 UTC	13.41	10.0	⋯		Alexander et al. (2017c)
e-MERLIN	Aug 31 13:00:00 UTC	14	5.0	0.512	<109	Moldon et al. (2017b)
VLITE	Sep 1 20:44:59 UTC	15.37	0.3387	0.034	<11400	Hallinan et al. (2017a)
ATCA	Sep 1 12:00:00 UTC	15	16.7	⋯	<50	Troja et al. (2017f)
ATCA	Sep 1 12:00:00 UTC	15	21.2	⋯	<50	Troja et al. (2017f)
ATCA	Sep 1 12:00:00 UTC	15	43.0	⋯	<90	Troja et al. (2017f)
ATCA	Sep 1 12:00:00 UTC	15	45.0	⋯	<90	Troja et al. (2017f)
e-MERLIN	Sep 1 13:00:00 UTC	15	5.0	0.512	<114	Moldon et al. (2017b)
ALMA	Sep 120:22:05 UTC	15.33	97.5	⋯		Alexander et al. (2017c)
VLA/JAGWAR	Sep 2 00:00:00 UTC	16	3.0		Detection	Mooley et al. (2017b); Hallinan et al. (2017a)
e-MERLIN	Sep 2 13:00:00 UTC	16	5.0	0.512	<144	Moldon et al. (2017b)
VLITE	Sep 2 18:51:34 UTC	16.36	0.3387	0.034	<11700	Hallinan et al. (2017a)
e-MERLIN	Sep 3 13:00:00 UTC	17	5.0	0.512	<166	Moldon et al. (2017b)
VLA	Sep 3 23:30:00 UTC	17	6.0		Detection	Corsi et al. (2017d); Hallinan et al. (2017a)
VLITE	Sep 3 20:08:05 UTC	17.40	0.3387	0.034	<6900	Hallinan et al. (2017a)
e-MERLIN	Sep 4 13:00:00 UTC	18	5.0	0.512	<147	Moldon et al. (2017b)
ATCA	Sep 5 10:03:04 UTC	19	7.25		Detection	Murphy et al. (2017)
e-MERLIN	Sep 5 13:00:00 UTC	19	5.0	0.512	<162	Moldon et al. (2017b)
VLA	Sep 5 22:12:00 UTC	19.47	6.0	⋯		Alexander et al. (2017a)
VLA	Sep 5 23:26:06 UTC	19.43	10.0	⋯		Alexander et al. (2017c)
MeerKAT	Sep 6 03:22:00 UTC	20	1.48	0.22	<75	Goedhart et al. (2017a)

Table 5
(Continued)

Telescope	UT Date	Time since GW Trigger (days)	Central Frequency (GHz)	Bandwidth (GHz)	Flux (μ Jy), 3σ	GCN/Reference
VLITE	Sep 7 19:09:43 UTC	21.36	0.3387	0.034	<8100	Hallinan et al. (2017a)
SRT	Sep 7 10:41:00 UTC	20.92	7.2	0.68	<1200	Aresu et al. (2017)
ATCA	Sep 8 12:00:00 UTC	22	17.0	⋯	<35	Wieringa et al. (2017)
ATCA	Sep 8 12:00:00 UTC	22	21.0	⋯	<35	Wieringa et al. (2017)
SRT	Sep 8 11:00:00 UTC	21.93	7.2	0.68	<1500	Aresu et al. (2017)
VLITE	Sep 8 19:05:35 UTC	22.37	0.3387	0.034	<6300	Hallinan et al. (2017a)
SRT	Sep 9 10:37:00 UTC	22.92	7.2	0.68	<1800	Aresu et al. (2017)
VLITE	Sep 9 18:52:45 UTC	23.36	0.3387	0.034	<4800	Hallinan et al. (2017a)
GMRT	Sep 9 11:30:00 UTC	23.0	1.39	0.032	⋯	Resmi et al. (2017), S. Kim et al. (2017, in preparation)
e-MERLIN	Sep 10 13:00:00 UTC	24	5.0	0.512	<126	Moldon et al. (2017b)
Effelsberg	Sep 10 13:10 UTC	24	5	2	<30000	Kramer et al. (2017)
Effelsberg	Sep 10 13:35 UTC	24	32	2	<90000	Kramer et al. (2017)
VLITE	Sep 10 18:36:48 UTC	24.35	0.3387	0.034	<6600	Hallinan et al. (2017a)
e-MERLIN	Sep 11 13:00:00 UTC	25	5.0	0.512	<151	Moldon et al. (2017b)
e-MERLIN	Sep 12 13:00:00 UTC	26	5.0	0.512	<113	Moldon et al. (2017b)
e-MERLIN	Sep 14 13:00:00 UTC	28	5.0	0.512	<147	Moldon et al. 2017b
e-MERLIN	Sep 15 13:00:00 UTC	29	5.0	0.512	<106	Moldon et al. (2017b)
GMRT	Sep 16 07:30:00 UTC	29.8	1.39	0.032	⋯	Resmi et al. (2017); S. Kim et al. (2017, in preparation)
e-MERLIN	Sep 16 13:00:00 UTC	30	5.0	0.512	<118	Moldon et al. 2017b
ALMA	Sep 16 20:36:21 UTC	30.34	97.5	⋯		Alexander et al. (2017c)
MeerKAT	Sep 17 07:16:00 UTC	31	1.48	0.22	<60	Goedhart et al. (2017a)
e-MERLIN	Sep 17 13:00:00 UTC	31	5.0	0.512	<111	Moldon et al. (2017b)
e-MERLIN	Sep 18 13:00:00 UTC	32	5.0	0.512	111	Moldon et al. (2017b)
SRT	Sep 19 11:38:00 UTC	32.96	7.2	0.68	<1200	Aresu et al. (2017)
EVN	Sep 20 10:00:00 UTC	34	5.0	0.256	<84	Paragi et al. (2017b)
e-MERLIN	Sep 21 13:00:00 UTC	35	5.0	0.512	<132	Moldon et al. (2017b)
e-MERLIN	Sep 22 13:00:00 UTC	36	5.0	0.512	<121	Paragi et al. (2017b)
VLA	Sep 25 16:51:45 UTC	39.2	6.0 GHz		Detection	Alexander et al. (2017b)

Table 6
Gamma-ray Coordinates Network (GCN) Notices and Circulars related to GW170817 until 2017 October 1 UTC

Telescope	UT Date	Δt (days)	Obs. Wavelength	References
Fermi/GBM	2017 Aug 17 12:41:20	0.0	gamma-ray	GCN Notice 524666471, Fermi-GBM (2017)
LIGO-Virgo/–	2017 Aug 17 13:21:42	0.03	gw	GCN 21505, LIGO Scientific Collaboration & Virgo Collaboration et al. (2017a)
Fermi/GBM	2017 Aug 17 13:47:37	0.05	gamma-ray	GCN 21506, Connaughton et al. (2017)
INTEGRAL/SPI-ACS	2017 Aug 17 13:57:47	0.05	gamma-ray	GCN 21507, Savchenko et al. (2017a)
IceCube/–	2017 Aug 17 14:05:11	0.06	neutrino	GCN 21508, Bartos et al. (2017a)
LIGO-Virgo/–	2017 Aug 17 14:09:25	0.06	gw	GCN 21509, LIGO Scientific Collaboration & Virgo Collaboration et al. (2017d)
LIGO-Virgo/–	2017 Aug 17 14:38:46	0.08	gw	GCN 21510, LIGO Scientific Collaboration & Virgo Collaboration et al. (2017e)
IceCube/–	2017 Aug 17 14:54:58	0.09	neutrino	GCN 21511, Bartos et al. (2017c)
LIGO-Virgo/–	2017 Aug 17 17:54:51	0.22	gw	GCN 21513, LIGO Scientific Collaboration & Virgo Collaboration et al. (2017b)
Astrosat/CZTI	2017 Aug 17 18:16:42	0.23	gamma-ray	GCN 21514, Balasubramanian et al. (2017)
IPN/–	2017 Aug 17 18:35:12	0.25	gamma-ray	GCN 21515, Svinkin et al. (2017b)
–/–	2017 Aug 17 18:55:12	0.26		GCN 21516, Dalya et al. (2016)
Insight-HXMT/HE	2017 Aug 17 19:35:28	0.29	gamma-ray	GCN 21518, Liao et al. (2017)
–/–	2017 Aug 17 20:00:07	0.3		GCN 21519, Cook et al. (2017a)
Fermi/GBM	2017 Aug 17 20:00:07	0.3	gamma-ray	GCN 21520, von Kienlin et al. (2017)
–/–	2017 Aug 17 20:12:41	0.31		GCN 21521, Cook et al. (2017b)
ANTARES/–	2017 Aug 17 20:35:31	0.33	neutrino	GCN 21522, Ageron et al. (2017a)
Swift/BAT	2017 Aug 17 21:34:36	0.37	gamma-ray	GCN 21524, Barthelmy et al. (2017)
AGILE/MCAL	2017 Aug 17 22:01:26	0.39	gamma-ray	GCN 21525, Pilia et al. (2017)
AGILE/GRID	2017 Aug 17 22:22:43	0.4	gamma-ray	GCN 21526, Piano et al. (2017)
LIGO-Virgo/–	2017 Aug 17 23:54:40	0.47	gw	GCN 21527, LIGO Scientific Collaboration & Virgo Collaboration et al. (2017c)
Fermi/GBM	2017 Aug 18 00:36:12	0.5	gamma-ray	GCN 21528, Goldstein et al. (2017b)
Swope/–	2017 Aug 18 01:05:23	0.52	optical	GCN 21529, Coulter et al. (2017a)
DECam/–	2017 Aug 18 01:15:01	0.52	optical	GCN 21530, Allam et al. (2017)
DLT40/–	2017 Aug 18 01:41:13	0.54	optical	GCN 21531, Yang et al. (2017a)
REM-ROS2/–	2017 Aug 18 02:00:40	0.56	optical, IR	GCN 21532, Melandri et al. (2017a)
ASAS-SN/–	2017 Aug 18 02:06:30	0.56	optical	GCN 21533, Cowperthwaite et al. (2017a)
Fermi/LAT	2017 Aug 18 02:09:53	0.56	gamma-ray	GCN 21534, Kocevski et al. (2017)
–/–	2017 Aug 18 02:48:50	0.59		GCN 21535, Cook et al. (2017c)
HST/–	2017 Aug 18 03:01:20	0.6	optical	GCN 21536, Foley et al. (2017a)
ATCA/–	2017 Aug 18 04:04:00	0.64	radio	GCN 21537, Bannister et al. (2017d)
LasCumbres/–	2017 Aug 18 04:06:31	0.64	optical	GCN 21538, Arcavi et al. (2017a)
DLT40/–	2017 Aug 18 04:11:35	0.65	optical	GCN 21539, Yang et al. (2017c)
DECam/–	2017 Aug 18 04:44:32	0.67	optical	GCN 21541, Nicholl et al. (2017a)
SkyMapper/–	2017 Aug 18 04:46:27	0.67	optical	GCN 21542, Moller et al. (2017)
LasCumbres/–	2017 Aug 18 04:54:23	0.68	optical	GCN 21543, Arcavi et al. (2017d)
VISTA/VIRCAM	2017 Aug 18 05:03:48	0.68	optical, IR	GCN 21544, Tanvir et al. (2017a)
VLA/–	2017 Aug 18 05:07:58	0.69	radio	GCN 21545, Alexander et al. (2017d)
MASTER/–	2017 Aug 18 05:37:59	0.71	optical	GCN 21546, Lipunov et al. (2017d)
Magellan/–	2017 Aug 18 05:46:33	0.71	optical	GCN 21547, Drout et al. (2017)
VLA/–	2017 Aug 18 06:56:44	0.76	radio	GCN 21548, Alexander et al. (2017e)
Subaru/HSC	2017 Aug 18 07:07:07	0.77	optical	GCN 21549, Yoshida et al. (2017a)
Swift/UVOT,XRT	2017 Aug 18 07:24:04	0.78	x-ray, uv	GCN 21550, Evans et al. (2017a)
Magellan/LDSS-3	2017 Aug 18 07:54:23	0.8	optical	GCN 21551, Simon et al. (2017)
Gemini-South/Flamingos-2	2017 Aug 18 08:00:58	0.81	IR	GCN 21552, Singer et al. (2017a)
Pan-STARRS/–	2017 Aug 18 08:37:20	0.83	optical	GCN 21553, Chambers et al. (2017a)

Table 6
(Continued)

Telescope	UT Date	Δt (days)	Obs. Wavelength	References
HCT/HFOSC	2017 Aug 18 09:54:21	0.88	optical	GCN 21554, Pavana et al. (2017)
MAXI/GSC/–	2017 Aug 18 10:43:45	0.92	x-ray	GCN 21555, Sugita et al. (2017)
REM-ROS2/–	2017 Aug 18 10:54:42	0.93	optical	GCN 21556, Melandri et al. (2017b)
–/–	2017 Aug 18 12:15:23	0.98		GCN 21557, Foley et al. (2017b)
TZAC/TAROT-Reunion	2017 Aug 18 13:04:25	1.02	optical	GCN 21558, Klotz et al. (2017)
ATCA/–	2017 Aug 18 13:27:25	1.03	radio	GCN 21559, Bannister et al. (2017b)
SkyMapper/–	2017 Aug 18 13:54:11	1.05	optical	GCN 21560, Wolf et al. (2017)
Subaru/HSC	2017 Aug 18 14:27:26	1.07	optical	GCN 21561, Yoshida et al. (2017b)
ASKAP/–	2017 Aug 18 14:36:00	1.08	radio	GCN 21562, Bannister et al. (2017e)
LSGT,T17/SNUCAM-II	2017 Aug 18 14:45:33	1.09	optical	GCN 21563, Im et al. (2017a)
AGILE/GRID	2017 Aug 18 15:22:43	1.11	gamma-ray	GCN 21564, Bulgarelli et al. (2017)
LasCumbres/–	2017 Aug 18 15:58:41	1.14	optical	GCN 21565, Arcavi et al. (2017b)
LSGT,T17/SNUCAM-II	2017 Aug 18 17:15:43	1.19	optical	GCN 21566, Im et al. (2017b)
Swope/–	2017 Aug 18 17:19:22	1.19	optical	GCN 21567, Coulter et al. (2017b)
IceCube/–	2017 Aug 18 17:27:25	1.2	neutrino	GCN 21568, Bartos et al. (2017b)
Gemini-South/–	2017 Aug 18 17:44:26	1.21	optical, IR	GCN 21569, Singer et al. (2017c)
MASTER/–	2017 Aug 18 18:06:51	1.23	optical	GCN 21570, Lipunov et al. (2017e)
VLA/–	2017 Aug 18 18:16:30	1.23	radio	GCN 21571, Williams et al. (2017b)
Swift/UVOT,XRT	2017 Aug 18 18:32:37	1.24	x-ray, uv	GCN 21572, Cenko et al. (2017)
ATCA/–	2017 Aug 18 20:19:00	1.32	radio	GCN 21574, Kaplan et al. (2017a)
2MASS,Spitzer/–	2017 Aug 18 20:23:05	1.32	IR	GCN 21575, Eikenberry et al. (2017)
VISTA/VIRCam	2017 Aug 18 21:16:32	1.36	IR	GCN 21576, Tanvir et al. (2017b)
–/–	2017 Aug 18 23:00:31	1.43		GCN 21577, Malesani et al. (2017b)
–/–	2017 Aug 18 23:11:30	1.44		GCN 21578, Cowperthwaite et al. (2017c)
PROMPT5/–	2017 Aug 19 00:18:04	1.48	optical	GCN 21579, Yang et al. (2017b)
DECam/–	2017 Aug 19 00:22:23	1.49	optical	GCN 21580, Nicholl et al. (2017b)
LasCumbres/–	2017 Aug 19 01:26:07	1.53	optical	GCN 21581, Arcavi et al. (2017c)
NTT/–	2017 Aug 19 01:46:26	1.55	optical, IR	GCN 21582, Lyman et al. (2017)
Swope/–	2017 Aug 19 01:54:36	1.55	optical	GCN 21583, Kilpatrick et al. (2017a)
GROND/–	2017 Aug 19 01:58:14	1.55	optical, IR	GCN 21584, Wiseman et al. (2017)
SOAR/GoodmanSpectrograph	2017 Aug 19 03:10:19	1.6	IR, optical	GCN 21585, Nicholl et al. (2017c)
Subaru/HSC	2017 Aug 19 06:52:33	1.76	optical	GCN 21586, Yoshida et al. (2017c)
MASTER/–	2017 Aug 19 08:10:30	1.81	optical	GCN 21587, Lipunov et al. (2017c)
VLBA/–	2017 Aug 19 09:36:26	1.87	radio	GCN 21588, Deller et al. (2017a)
VLA/–	2017 Aug 19 09:51:33	1.88	radio	GCN 21589, Alexander et al. (2017f)
Pan-STARRS/–	2017 Aug 19 10:14:53	1.9	optical	GCN 21590, Chambers et al. (2017b)
NOT/NOTCam	2017 Aug 19 12:00:05	1.97	IR	GCN 21591, Malesani et al. (2017a)
ESO-VLT/X-shooter	2017 Aug 19 12:16:37	1.98	IR, optical	GCN 21592, Pian et al. (2017b)
ESO-VLT/FORS2	2017 Aug 19 14:13:15	2.06	optical	GCN 21594, Wiersema et al. (2017)
Subaru/HSC	2017 Aug 19 14:46:41	2.09	optical	GCN 21595, Tominaga et al. (2017)
REM-ROS2/–	2017 Aug 19 16:38:19	2.16	optical	GCN 21596, Melandri et al. (2017c)
KMTNet/wide-fieldcamera	2017 Aug 19 16:55:08	2.18	optical	GCN 21597, Im et al. (2017d)
ESO-VST/OmegaCam	2017 Aug 19 17:37:19	2.21	optical	GCN 21598, Grado et al. (2017c)
LaSilla-QUEST/–	2017 Aug 19 18:04:05	2.22	optical	GCN 21599, Rabinowitz et al. (2017)
GMRT/–	2017 Aug 19 21:18:21	2.36	radio	GCN 21603, De et al. (2017a)
PROMPT5/–	2017 Aug 19 23:31:25	2.45	optical	GCN 21606, Valenti et al. (2017)

Table 6
(Continued)

Telescope	UT Date	Δt (days)	Obs. Wavelength	References
GROND/–	2017 Aug 20 04:49:21	2.67	optical, IR	GCN 21608, Chen et al. (2017)
VIRT/–	2017 Aug 20 05:27:49	2.7	optical	GCN 21609, Gendre et al. (2017)
SALT/–	2017 Aug 20 06:14:37	2.73	optical	GCN 21610, Shara et al. (2017)
Swift/XRT	2017 Aug 20 08:42:40	2.83	x-ray	GCN 21612, Evans et al. (2017c)
VLA/–	2017 Aug 20 09:17:57	2.86	radio	GCN 21613, Corsi et al. (2017b)
VLA/–	2017 Aug 20 10:26:01	2.91	radio	GCN 21614, Corsi et al. (2017a)
Pan-STARRS/–	2017 Aug 20 13:59:50	3.05	optical	GCN 21617, Chambers et al. (2017c)
ChilescopeRC-1000/–	2017 Aug 20 14:24:47	3.07	optical	GCN 21618, Pozanenko et al. (2017d)
TOROS/–	2017 Aug 20 14:48:49	3.09	optical	GCN 21619, Diaz et al. (2017a)
TOROS/–	2017 Aug 20 15:03:42	3.1	optical	GCN 21620, Diaz et al. (2017c)
–/–	2017 Aug 20 15:40:35	3.12	⋯	GCN 21621, Lipunov (2017)
Kanata/HONIR	2017 Aug 20 16:37:38	3.16	IR	GCN 21623, Nakaoka et al. (2017)
BOOTES-5/–	2017 Aug 20 21:59:59	3.39	optical	GCN 21624, Castro-Tirado et al. (2017)
ASKAP/–	2017 Aug 21 00:58:33	3.51	radio	GCN 21625, Dobie et al. (2017b)
NuSTAR/–	2017 Aug 21 04:33:27	3.66	x-ray	GCN 21626, Harrison et al. (2017)
Zadko/–	2017 Aug 21 05:57:23	3.72	optical	GCN 21627, Coward et al. (2017b)
ATCA/–	2017 Aug 21 07:45:30	3.79	radio	GCN 21628, Lynch et al. (2017c)
ATCA/–	2017 Aug 21 09:02:12	3.85	radio	GCN 21629, Lynch et al. (2017d)
ANTARES/–	2017 Aug 21 15:08:00	4.1	neutrino	GCN 21631, Ageron et al. (2017b)
KMTNet,iTelescope.NET/–	2017 Aug 21 15:49:41	4.13	optical	GCN 21632, Im et al. (2017c)
Pan-STARRS/–	2017 Aug 21 16:03:52	4.14	optical	GCN 21633, Chambers et al. (2017d)
TOROS/CASLEO	2017 Aug 21 16:05:22	4.14	optical	GCN 21634, Diaz et al. (2017d)
ChilescopeRC-1000/–	2017 Aug 21 16:11:53	4.15	optical	GCN 21635, Pozanenko et al. (2017a)
VLA/–	2017 Aug 21 18:40:08	4.25	radio	GCN 21636, Corsi et al. (2017e)
MWA/–	2017 Aug 22 00:59:36	4.51	radio	GCN 21637, Kaplan et al. (2017c)
Gemini-South/Flamingos-2	2017 Aug 22 05:20:11	4.69	IR	GCN 21638, Chornock et al. (2017c)
ASKAP/–	2017 Aug 22 07:23:04	4.78	radio	GCN 21639, Dobie et al. (2017a)
CALET/CGBM	2017 Aug 22 09:36:51	4.87	gamma-ray	GCN 21641, Nakahira et al. (2017)
ChilescopeRC-1000/–	2017 Aug 22 15:23:04	5.11	optical	GCN 21644, Pozanenko et al. (2017c)
6dFGS/–	2017 Aug 22 16:55:17	5.18	optical	GCN 21645, Sadler et al. (2017)
Chandra/CXO	2017 Aug 22 18:06:23	5.23	x-ray	GCN 21648, Margutti et al. (2017b)
VLA/JAGWAR	2017 Aug 22 19:13:38	5.27	radio	GCN 21650, Mooley et al. (2017a)
ESO-VLT/FORS2	2017 Aug 23 07:52:38	5.8	optical	GCN 21653, D'Avanzo et al. (2017)
VLA/–	2017 Aug 23 18:25:07	6.24	radio	GCN 21664, Corsi et al. (2017c)
HST/Pan-STARRS1/GPC1	2017 Aug 24 01:39:20	6.54	optical	GCN 21669, Yu et al. (2017)
ATCA/–	2017 Aug 24 04:30:05	6.66	radio	GCN 21670, Lynch et al. (2017a)
ASKAP/–	2017 Aug 24 06:10:24	6.73	radio	GCN 21671, Bannister et al. (2017c)
INTEGRAL/SPI,IBIS,JEM-X,OMC	2017 Aug 24 09:03:02	6.85	gamma-ray, x-ray, optical	GCN 21672, Savchenko et al. (2017b)
H.E.S.S./–	2017 Aug 24 10:35:02	6.91	gamma-ray	GCN 21674, de Naurois et al. (2017)
LOFAR/ILT	2017 Aug 24 13:35:06	7.04	radio	GCN 21676, Broderick et al. (2017)
AAT/AAO	2017 Aug 24 15:31:25	7.12	optical	GCN 21677, Andreoni et al. (2017)
LWA/LWA1	2017 Aug 24 16:08:17	7.14	radio	GCN 21680, Callister et al. (2017a)
ESO-VLT/MUSEIntegralFieldUnit	2017 Aug 24 19:28:30	7.28	optical	GCN 21681, Levan et al. (2017b)
Gemini-South/Flamingos-2,GMOS	2017 Aug 24 19:31:19	7.28	optical, IR	GCN 21682, Troja et al. (2017b)
HAWC/–	2017 Aug 24 19:35:19	7.29	gamma-ray	GCN 21683, Martinez-Castellanos et al. (2017)
Gemini-South/Flamingos-2	2017 Aug 25 04:04:17	7.64	IR	GCN 21684, Chornock et al. (2017b)

Table 6
(Continued)

Telescope	UT Date	Δt (days)	Obs. Wavelength	References
Subaru/HSC	2017 Aug 25 07:38:17	7.79	optical	GCN 21685, Yoshida et al. (2017d)
Auger/SurfaceDetector	2017 Aug 25 08:13:23	7.81	neutrino	GCN 21686, Alvarez-Muniz et al. (2017)
MASTER/MASTER-II	2017 Aug 25 08:48:24	7.84	optical	GCN 21687, Lipunov et al. (2017b)
ESO-VST/OmegaCAM	2017 Aug 25 22:15:33	8.4	optical	GCN 21703, Grado et al. (2017a)
GMRT/–	2017 Aug 26 01:23:58	8.53	radio	GCN 21708, De et al. (2017b)
ATCA/–	2017 Aug 29 03:49:22	11.63	radio	GCN 21740, Lynch et al. (2017b)
Zadko/–	2017 Aug 29 08:29:39	11.83	optical	GCN 21744, Coward et al. (2017a)
Konus-Wind/–	2017 Aug 29 10:55:08	11.93	gamma-ray	GCN 21746, Svinkin et al. (2017a)
ALMA/–	2017 Aug 29 12:37:56	12.0	radio	GCN 21747, Schulze et al. (2017)
ALMA/–	2017 Aug 29 14:55:15	12.09	radio	GCN 21750, Williams et al. (2017a)
OVRO/–	2017 Aug 30 03:23:28	12.61	radio	GCN 21760, Pearson et al. (2017)
EVN/VLBI	2017 Aug 30 09:48:26	12.88	radio	GCN 21763, Paragi et al. (2017a)
Chandra/*CXO*	2017 Aug 30 12:07:12	12.98	x ray	GCN 21765, Troja et al. (2017c)
GMRT/–	2017 Aug 30 16:06:24	13.14	radio	GCN 21768, Resmi et al. (2017)
Gemini-South/–	2017 Aug 31 18:28:50	14.24	IR	GCN 21778, Troja et al. (2017d)
Gemini-South/Flamingos-2	2017 Aug 31 18:32:01	14.24	IR	GCN 21779, Singer et al. (2017b)
HST/–	2017 Aug 31 20:33:24	14.33	optical, IR	GCN 21781, Levan et al. (2017a)
PioftheSky/PioftheSkyNorth	2017 Sep 01 21:54:25	15.38	optical	GCN 21783, Cwiek et al. (2017)
AGILE/GRID	2017 Sep 02 16:54:59	16.18	gamma-ray	GCN 21785, Verrecchia et al. (2017)
Chandra/*CXO*	2017 Sep 02 16:57:54	16.18	x ray	GCN 21786, Fong et al. (2017)
Chandra/*CXO*	2017 Sep 02 17:06:21	16.18	x ray	GCN 21787, Troja et al. (2017e)
Chandra/*CXO*	2017 Sep 03 20:24:16	17.32	x ray	GCN 21798, Haggard et al. (2017b)
ATCA/–	2017 Sep 04 02:26:14	17.57	radio	GCN 21803, Troja et al. (2017f)
e-MERLIN/–	2017 Sep 04 07:48:43	17.8	radio	GCN 21804, Moldon et al. (2017a)
VLA/–	2017 Sep 04 22:14:55	18.4	radio	GCN 21814, Mooley et al. (2017b)
VLA/–	2017 Sep 04 22:14:59	18.4	radio	GCN 21815, Corsi et al. (2017d)
HST/*HST*,*Gaia*	2017 Sep 05 00:30:09	18.49	optical, IR, uv	GCN 21816, Adams et al. (2017)
ESO-VST/OMEGACam	2017 Sep 06 15:07:27	20.1	optical	GCN 21833, Grado et al. (2017b)
ATCA/–	2017 Sep 07 02:31:55	20.58	radio	GCN 21842, Murphy et al. (2017)
LWA/LWA1	2017 Sep 08 02:47:01	21.59	radio	GCN 21848, Callister et al. (2017b)
VLBA/–	2017 Sep 08 11:16:27	21.94	radio	GCN 21850, Deller et al. (2017b)
VLA/–	2017 Sep 08 13:23:16	22.03	radio	GCN 21851, Alexander et al. (2017a)
ATCA/–	2017 Sep 14 05:25:42	27.7	radio	GCN 21882, Wieringa et al. (2017)
AST3-2/–	2017 Sep 15 03:45:21	28.63	optical	GCN 21883, Hu et al. (2017)
ATLAS/–	2017 Sep 15 11:24:15	28.95	optical	GCN 21886, Tonry et al. (2017)
DanishTel/–	2017 Sep 15 16:40:07	29.17	optical	GCN 21889, Cano et al. (2017)
MeerKAT/–	2017 Sep 15 20:16:29	29.32	radio	GCN 21891, Goedhart et al. (2017b)
DFN/–	2017 Sep 18 13:45:29	32.04	optical	GCN 21894, Hancock et al. (2017)
T80S,EABA/–	2017 Sep 18 16:22:27	32.15	optical	GCN 21895, Diaz et al. (2017b)
VLBA/–	2017 Sep 19 07:51:22	32.8	radio	GCN 21897, Deller et al. (2017c)
ChilescopeRC-1000/–	2017 Sep 19 18:09:03	33.23	optical	GCN 21898, Pozanenko et al. (2017b)
Parkes/–	2017 Sep 21 02:38:29	34.58	radio	GCN 21899, Bailes et al. (2017a)
ATCA/–	2017 Sep 21 06:42:36	34.75	radio	GCN 21900, Ricci et al. (2017)
LasCumbres/FLOYDS,Gemini	2017 Sep 22 03:24:44	35.61	optical	GCN 21908, McCully et al. (2017a)
SRT/–	2017 Sep 22 19:06:44	36.27	radio	GCN 21914, Aresu et al. (2017)
Effelsberg/–	2017 Sep 23 20:34:41	37.33	radio	GCN 21920, Kramer et al. (2017)

Table 6
(Continued)

Telescope	UT Date	Δt (days)	Obs. Wavelength	References
MWA/–	2017 Sep 25 22:30:34	39.41	radio	GCN 21927, Kaplan et al. (2017b)
Parkes/–	2017 Sep 26 02:00:59	39.56	radio	GCN 21928, Bailes et al. (2017b)
VLA/–	2017 Sep 26 05:14:16	39.69	radio	GCN 21929, Hallinan et al. (2017b)
PioftheSky/PioftheSkyNorth	2017 Sep 26 21:17:49	40.36	optical	GCN 21931, Batsch et al. (2017)
MeerKAT/–	2017 Sep 27 13:19:14	41.03	radio	GCN 21933, Goedhart et al. (2017a)
VLA/–	2017 Sep 27 19:03:46	41.27	radio	GCN 21935, Alexander et al. (2017b)
EVN/–	2017 Sep 28 10:35:27	41.91	radio	GCN 21939, Paragi et al. (2017b)
e-MERLIN/–	2017 Sep 28 11:12:37	41.94	radio	GCN 21940, Moldon et al. (2017b)

3.5. Neutrinos

The detection of GW170817 was rapidly followed up by the IceCube (Aartsen et al. 2017) and Antares (Ageron et al. 2011) neutrino observatories and the Pierre Auger Observatory (Aab et al. 2015a) to search for coincident, high-energy (GeV– EeV) neutrinos emitted in the relativistic outflow produced by the BNS merger. The results from these observations, described briefly below, can be used to constrain the properties of relativistic outflows driven by the merger (A. Albert et al. 2017, in preparation).

In a search for muon–neutrino track candidates (Aartsen et al. 2016), and contained neutrino events of any flavor (Aartsen et al. 2015), IceCube identified no neutrinos that were directionally coincident with the final localization of GW170817 at 90% credible level, within ± 500 s of the merger (Bartos et al. 2017a, 2017b). Additionally, no MeV supernova neutrino burst signal was detected coincident with the merger. Following the identification via electromagnetic observations of the host galaxy of the event, IceCube also carried out an extended search in the direction of NGC 4993 for neutrinos within the 14 day period following the merger, but found no significant neutrino emission (A. Albert et al. 2017, in preparation).

A neutrino search for upgoing high-energy muon neutrinos was carried out using the online Antares data stream (Ageron et al. 2017a). No upgoing neutrino candidates were found over a $t_c \pm 500$ s time window. The final localization of GW170817 (LIGO Scientific Collaboration & Virgo Collaboration et al. 2017c) was above the Antares horizon at the time of the GW event. A search for downgoing muon neutrinos was thus performed, and no neutrinos were found over t_c 500 s (Ageron et al. 2017b). A search for neutrinos originating from below the Antares horizon, over an extended period of 14 days after the merger, was also performed, without yielding significant detection (A. Albert et al. 2017, in preparation).

The Pierre Auger Observatory carried out a search for ultra-high-energy (UHE) neutrinos above $\sim 10^{17}$ eV using its Surface Detector (Aab et al. 2015a). UHE neutrino-induced extensive air showers produced either by interactions of downward-going neutrinos in the atmosphere or by decays of tau leptons originating from tau neutrino interactions in the Earth's crust can be efficiently identified above the background of the more numerous ultra-high-energy cosmic rays (Aab et al. 2015b). Remarkably, the position of the transient in NGC 4993 was just between $0°\!.3$ and $3°\!.2$ below the horizon during $t_c \pm 500$ s. This region corresponds to the most efficient geometry for Earth-skimming tau neutrino detection at 10^{18} eV energies. No neutrino candidates were found in $t_c \pm 500$ s (Alvarez-Muniz et al. 2017) nor in the 14 day period after it (A. Albert et al. 2017, in preparation).

4. Conclusion

For the first time, gravitational and electromagnetic waves from a single source have been observed. The gravitational-wave observation of a binary neutron star merger is the first of its kind. The electromagnetic observations further support the interpretation of the nature of the binary, and comprise three components at different wavelengths: (i) a prompt sGRB that demonstrates that BNS mergers are the progenitor of at least a fraction of such bursts; (ii) an ultraviolet, optical, and infrared transient (kilonova), which allows for the identification of the host galaxy and is associated with the aftermath of the BNS merger; and (iii) delayed X-ray and radio counterparts that provide information on the environment of the binary. These observations, described in detail in the companion articles cited above, offer a comprehensive, sequential description of the physical processes related to the merger of a binary neutron star. Table 6 collects all of the Gamma-ray Coordinates Network (GCN) notices and circulars related to GW170817 through 2017 October 1 UTC. The results of this campaign demonstrate the importance of collaborative gravitational-wave, electromagnetic, and neutrino observations and mark a new era in multi-messenger, time-domain astronomy.

References

Aab, A., Abreu, P., Aglietta, M., et al. 2015a, NIMPA, 798, 172
Aab, A., Abreu, P., Aglietta, M., et al. 2015b, PhRvD, 91, 092008
Aartsen, M. G., Ackermann, M., Adams, J., et al. 2015, PhRvD, 91, 022001
Aartsen, M. G., Ackermann, M., Adams, J., et al. 2017, JInst, 12, P03012

Aartsen, M. G., Abraham, K., Ackermann, M., et al. 2016, JInst, 11, P11009
Abadie, J., Abbott, B. P., Abbott, R., et al. 2010, CQGra, 27, 173001
Abadie, J., Abbott, B. P., Abbott, R., et al. 2012, A&A, 541, A155
Abbott, B. P., Abbott, R., Abbott, T. D., et al. 2016a, ApJL, 826, L13
Abbott, B. P., Abbott, R., Abbott, T. D., et al. 2016b, PhRvL, 116, 241102
Abbott, B. P., Abbott, R., Abbott, T. D., et al. 2016c, PhRvL, 116, 061102
Abbott, B. P., Abbott, R., Abbott, T. D., et al. 2016d, PhRvL, 116, 241103
Abbott, B. P., Abbott, R., Abbott, T. D., et al. 2016e, PhRvX, 6, 041015
Abbott, B. P., Abbott, R., Abbott, T. D., et al. 2017a, PhRvL, 118, 221101
Abbott, B. P., Abbott, R., Abbott, T. D., et al. 2017b, PhRvL, 118, 221101
Abbott, B. P., Abbott, R., Abbott, T. D., et al. 2017c, PhRvL, 119, 161101
Abbott, B. P., Abbott, R., Abbott, T. D., et al. 2017d, PhRvL, 119, 141101
Abbott, B. P., Abbott, R., Abbott, T. D., et al. 2017e, Natur, https://doi.org/
    10.1038/nature24471
Abbott, B. P., Abbott, R., Abbott, T. D., et al. 2017f, ApJL, https://doi.org/
    10.3847/2041-8213/aa920c
Abbott, B. P., Abbott, R., Abbott, T. D., et al. 2017g, ApJL, https://doi.org/
    10.3847/2041-8213/aa91c9
Abeysekara, A. U., Albert, A., Alfaro, R., et al. 2017, ApJ, 843, 39
Adams, S. M., Kasliwal, M. M., Blagorodnova, N., et al. 2017, GCN, 21816
Ade, P. A. R., Aghanim, N., Arnaud, M., et al. 2016, A&A, 594, A13
Ageron, M., Aguilar, J. A., Al Samara, I., et al. 2011, NIMPA, 656, 11
Ageron, M., Baret, B., Coleiro, A., et al. 2017a, GCN, 21522
Ageron, M., Baret, B., Coleiro, A., et al. 2017b, GCN, 21631
Alexander, K. D., Berger, E., Eftekhari, T., et al. 2017a, GCN, 21851
Alexander, K., Berger , E., Fong, W., et al. 2017c, ApJL, https://doi.org/
    10.3847/2041-8213/aa905d
Alexander, K. D., Fong, W., Berger, E., et al. 2017d, GCN, 21545
Alexander, K. D., Fong, W., Berger, E., et al. 2017e, GCN, 21548
Alexander, K. D., Fong, W., Berger, E., et al. 2017f, GCN, 21589
Alexander, K. D., Fong, W., Williams, P. K. G., et al. 2017b, GCN, 21935
Allam, S., Annis, J., Berger, E., et al. 2017, GCN, 21530
Allen, B., Anderson, W. G., Brady, P. R., Brown, D. A., & Creighton, J. D. E.
    2012, PhRvD, 85, 122006
Alvarez-Muniz, J., Pedreira, F., Zas, E., et al. 2017, GCN, 21686
Andreoni, I., Cooke, J., Lidman, C., et al. 2017, GCN, 21677
Arcavi, I., Howell, D. A., McCully, C., et al. 2017a, GCN, 21538
Arcavi, I., Howell, D. A., McCully, C., et al. 2017b, GCN, 21565
Arcavi, I., Howell, D. A., McCully, C., et al. 2017c, GCN, 21581
Arcavi, I., Howell, D. A., McCully, C., et al. 2017d, GCN, 21543
Arcavi, I., Hosseinzadeh, G., Howell, D., et al. 2017e, Natur, https://doi.org/
    10.1038/nature24291
Aresu, G., Bachetti, M., Buffa, F., et al. 2017, GCN, 21914
Baade, W., & Zwicky, F. 1934, PhRv, 46, 76
Bagot, P., Portegies Zwart, S. F., & Yungelson, L. R. 1998, A&A, 332, L57
Bailes, M., Andreoni, I., et al. 2017a, GCN, 21899
Bailes, M., Andreoni, I., et al. 2017b, GCN, 21928
Baker, J. G., Centrella, J., Choi, D., Koppitz, M., & van Meter, J. 2006, PhRvL,
    96, 111102
Balasubramanian, A., Mate, S., Bhalerao, V., et al. 2017, GCN, 21514
Bannister, K., Lynch, C., Kaplan, D., et al. 2017b, GCN, 21559
Bannister, K., Lynch, C., Kaplan, D., et al. 2017d, GCN, 21537
Bannister, K., Shannon, R., Hotan, A., et al. 2017c, GCN, 21671
Bannister, K., Shannon, R., Hotan, A., et al. 2017e, GCN, 21562
Bannister, K. W., Shannon, R. M., Macquart, J.-P., et al. 2017a, ApJL,
    841, L12
Barnes, J., & Kasen, D. 2013, ApJ, 775, 18
Barnes, J., Kasen, D., Wu, M.-R., & Mart'inez-Pinedo, G. 2016, arXiv:1605.
    07218
Barr, E. D., Guillemot, L., Champion, D. J., et al. 2013, MNRAS, 429, 1633
Barthelmy, S. D., Chincarini, G., Burrows, D. N., et al. 2005, Natur, 438, 994
Barthelmy, S. D., Lien, A. Y., Palmer, D. M., et al. 2017, GCN, 21524
Bartos, I., Countryman, S., Finley, C., et al. 2017a, GCN, 21508
Bartos, I., Countryman, S., Finley, C., et al. 2017b, GCN, 21568
Bartos, I., Countryman, S., Finley, C., et al. 2017c, GCN, 21511
Batsch, T., Castro-Tirado, A. J., Czyrkowski, H., et al. 2017, GCN, 21931
Belczynski, K., Kalogera, V., & Bulik, T. 2002, ApJ, 572, 407
Berger, E. 2010, ApJ, 722, 1946
Berger, E. 2014, ARA&A, 52, 43
Berger, E., Fong, W., & Chornock, R. 2013a, ApJL, 774, L23
Berger, E., Fong, W., & Chornock, R. 2013b, ApJL, 774, L23
Berger, E., Fox, D. B., Price, P. A., et al. 2007, ApJ, 664, 1000
Berger, E., Price, P. A., Cenko, S. B., et al. 2005, Natur, 438, 988
Bhalerao, V., Bhattacharya, D., Vibhute, A., et al. 2017, JApA, 38, 31
Blackburn, L., Briggs, M. S., Camp, J., et al. 2015, ApJS, 217, 8
Blanchet, L. 2014, LRR, 17, 2

     Abbott et al.

Blanchet, L., Buonanno, A., & Faye, G. 2006, PhRvD, 74, 104034 (Erratum: 2007, PhRvD, 75, 049903; Erratum: 2010, PhRvD, 81, 089901)
Blanchet, L., Damour, T., Esposito-Farèse, G., & Iyer, B. R. 2004, PhRvL, 93, 091101
Blanchet, L., Damour, T., Iyer, B. R., Will, C. M., & Wiseman, A. G. 1995, PhRvL, 74, 3515
Bloom, J. S., Sigurdsson, S., & Pols, O. R. 1999, MNRAS, 305, 763
Bohé, A., Marsat, S., & Blanchet, L. 2013, CQGra, 30, 135009
Broderick, J. W., Rowlinson, A., Jonker, P. G., et al. 2017, GCN, 21676
Brown, T. M., Baliber, N., Bianco, F. B., et al. 2013, PASP, 125, 1031
Buckley, D. A. H., Andreoni, I., Barway, S., et al. 2017, MNRAS, submitted
Bulgarelli, A., Tavani, M., Verrecchia, F., et al. 2017, GCN, 21564
Buonanno, A., & Damour, T. 1999, PhRvD, 59, 084006
Burrows, D. N., Grupe, D., Capalbi, M., et al. 2006, ApJ, 653, 468
Burrows, D. N., Hill, J. E., Nousek, J. A., et al. 2005, SSRv, 120, 165
Callister, T., Dowell, J., Kanner, J., et al. 2017a, GCN, 21680
Callister, T., Dowell, J., Kanner, J., et al. 2017b, GCN, 21848
Campanelli, M., Lousto, C. O., Marronetti, & Zlochower, Y. 2006, PhRvL, 96, 111101
Cannon, K., Cariou, R., Chapman, A., et al. 2012, ApJ, 748, 136
Cano, Z., Jorgensen, U. G., Hodosan, G., et al. 2017, GCN, 21889
Castro-Tirado, A. J., Tello, J. C., Hu, Y., et al. 2017, GCN, 21624
Cenko, S. B., Emery, S. W. K., Campana, S., et al. 2017, GCN, 21572
Chambers, K. C., Huber, M. E., Smartt, S. J., et al. 2017a, GCN, 21553
Chambers, K. C., Huber, M. E., Smitch, K. W., et al. 2017c, GCN, 21617
Chambers, K. C., Huber, M. E., Smitch, K. W., et al. 2017d, GCN, 21633
Chambers, K. C., Magnier, E. A., Metcalfe, N., et al. 2016, arXiv:1612.05560
Chambers, K. C., Smartt, S. J., Huber, M. E., et al. 2017b, GCN, 21590
Chen, T. W., Wiseman, P., Greiner, J., et al. 2017, GCN, 21608
Chornock, R., Berger, E., et al. 2017b, GCN, 21684
Chornock, R., Berger, E., et al. 2017c, GCN, 21638
Chornock, R., Berger, E., Kasen, D., et al. 2017a, ApJL, https://doi.org/10.3847/2041-8213/aa905c
Clark, J. P. A. 1979, in Sources of Gravitational Radiation, ed. L. L. Smarr (Cambridge: Cambridge Univ. Press), 447
Clark, J. P. A., van den Heuvel, E. P. J., & Sutantyo, W. 1979, A&A, 72, 120
Clarke, T. E., Kassim, N. E., Brisken, W., et al. 2016, in Ground-based and Airborne Telescopes VI, Vol. 990699065B
Connaughton, V., Blackburn, L., Briggs, M. S., et al. 2017, GCN, 21506
Cook, D. O., Van Sistine, A., Singer, L., et al. 2017a, GCN, 21519
Cook, D. O., Van Sistine, A., Singer, L., et al. 2017b, GCN, 21521
Cook, D. O., Van Sistine, A., Singer, L., et al. 2017c, GCN, 21535
Corsi, A., Hallinan, G., Mooley, K., et al. 2017d, GCN, 21815
Corsi, A., Kasliwal, M. M., et al. 2017a, GCN, 21614
Corsi, A., Kasliwal, M. M., et al. 2017b, GCN, 21613
Corsi, A., Kasliwal, M. M., Frail, D., et al. 2017c, GCN, 21664
Corsi, A., Kasliwal, M. M., et al. 2017e, GCN, 21636
Coulter, D. A., Kilpatrick, C. D., Siebert, M. R., et al. 2017, Sci, https://doi.org/10.1126/science.aap9811
Coulter, D. A., Kilpatrick, C. D., Siebert, M. R., et al. 2017a, GCN, 21529
Coulter, D. A., Kilpatrick, C. D., Siebert, M. R., et al. 2017b, GCN, 21567
Covino, S., Wiersema, K., Fan, Y., & Toma, K. 2017, Natur, doi:10.1038/s41550-017-0285-z
Coward, D., Howell, E., Laugier, R., et al. 2017a, GCN, 21744
Coward, D., Howell, E., Laugier, R., et al. 2017b, GCN, 21627
Cowperthwaite, P. S., Berger, E., Villar, V. A., et al. 2017b, ApJL, https://doi.org/10.3847/2041-8213/aa8fc7
Cowperthwaite, P. S., Foley, R. J., & Berger, E. 2017a, GCN, 21533
Cowperthwaite, P. S., Nicholl, M., & Berger, E. 2017c, GCN, 21578
Cutler, C., Apostolos, T. A., Bildsten, L., et al. 1993, PhRvL, 70, 2984
Cwiek, A., Zarnecki, A. F., Mankiewicz, A., et al. 2017, GCN, 21783
Dalya, G., Frei, Z., Galgoczi, G., Raffai, P., & de Souza, R. 2016, yCat, 7275
Damour, T., & Taylor, J. H. 1991, ApJ, 366, 501
Damour, T., & Taylor, J. H. 1992, PhRvD, 45, 1840
D'Avanzo, P., Malesani, D., Covino, S., et al. 2009, A&A, 498, 711
D'Avanzo, P., Melandri, A., Covino, S., et al. 2017, GCN, 21653
De, K., Kasliwal, M. M., Bhalerao, V., et al. 2017a, GCN, 21603
De, K., Mooley, K. P., Chandra, P., et al. 2017b, GCN, 21708
de Naurois, M., Schussler, F., et al. 2017, GCN, 21674
Deller, A., Bailes, M., Andreoni, I., et al. 2017a, GCN, 21588
Deller, A., Bailes, M., Andreoni, I., et al. 2017b, GCN, 21850
Deller, A., Bailes, M., Andreoni, I., et al. 2017c, GCN, 21897
Dewey, R. J., & Cordes, J. M. 1987, ApJ, 321, 780
Dezalay, J.-P., Barat, C., Talon, R., et al. 1992, in AIP Conf. Proc. 265, Gamma-Ray Bursts, ed. W. S. Paciesas & G. J. Fishman (Melville, NY: AIP), 304

Diaz, M., Garcia Lambas, D., Macri, L., Nilo Castellon, J. L., & Bernoiz, M. 2017a, GCN, 21619
Diaz, M., Garcia Lambas, D., Macri, L., Nilo Castellon, J. L., & Bernoiz, M. 2017c, GCN, 21620
Diaz, M., Garcia Lambas, D., Macri, L., Nilo Castellon, J. L., & Bernoiz, M. 2017d, GCN, 21634
Diaz, M., Macri, L., Nilo Castellon, J. L., et al. 2017b, GCN, 21895
Dobie, D., Hotan, A., Bannister, K., et al. 2017a, GCN, 21639
Dobie, D., Hotan, A., Bannister, K., et al. 2017b, GCN, 21625
Drout, M. R., et al. 2017b, Sci, https://doi.org/10.1126/science.aaq0049
Drout, M. R., Simon, J. D., Shappee, B. J., et al. 2017a, GCN, 21547
Eichler, D., Livio, M., Piran, T., & Schramm, D. N. 1989, Natur, 340, 126
Eikenberry, S., Ackley, K., & Klimenko, S. 2017, GCN, 21575
Einstein, A. 1916, Sitzungsberichte der Königlich Preußischen Akademie der Wissenschaften (Berlin), 1, 688
Einstein, A. 1918, Sitzungsberichte der Königlich Preußischen Akademie der Wissenschaften (Berlin), 1, 154
Ellingson, S. W., Taylor, G. B., Craig, J., et al. 2013, ITAP, 61, 2540
Evans, P., Cenko, S., Kennea, J. A., et al. 2017a, Sci, https://doi.org/10.1126/science.aap9580
Evans, P., Kennea, J. A., Breeveld, A. A., et al. 2017b, GCN, 21550
Evans, P., Kennea, J. A., Cenko, S. B., et al. 2017c, GCN, 21612
Fermi-GBM 2017, GCN, 524666471
Feroci, M., Costa, E., Soffitta, P., et al. 2007, NIMPA, 581, 728
Fixsen, D. J. 2009, ApJ, 707, 916
Flannery, B. P., & van den Heuvel, E. P. J. 1975, A&A, 39, 61
Flaugher, B., Diehl, H. T., Honscheid, K., et al. 2015, AJ, 150, 150
Foley, R. J. 2017b, GCN, 21557
Foley, R. J., Kilpatrick, C. D., Nicholl, M., & Berger, E. 2017a, GCN, 21536
Fong, W., Berger, E., Chornock, R., et al. 2013, ApJ, 769, 56
Fong, W., Berger, E., Margutti, R., & Zauderer, B. A. 2015, ApJ, 815, 102
Fong, W., Margutti, R., Haggard, D., et al. 2017, GCN, 21786
Fong, W., Margutti, R., Haggard, D., et al. 2013, ApJ, 776, 18
Fox, D. B., Frail, D. A., Price, P. A., et al. 2005, Natur, 437, 845
Freedman, W. L., Madore, B. F., Gibson, B. K., et al. 2001, ApJ, 553, 47
Fryer, C. L., Woosley, S. E., & Hartmann, D. H. 1999, ApJ, 526, 152
Gehrels, N. 2004, in AIP Conf. Ser. 727, Gamma-Ray Bursts: 30 Years of Discovery, ed. E. Fenimore & M. Galassi (Melville, NY: AIP), 637
Gehrels, N., Cannizzo, J. K., Kanner, J., et al. 2016, ApJ, 820, 136
Gehrels, N., Sarazin, C. L., O'Brien, P. T., et al. 2005, Natur, 437, 851
Gendre, B., Cucchiara, A., Morris, D., et al. 2017, GCN, 21609
Giacconi, R., Gursky, H., Paolini, F. R., & Rossi, B. B. 1962, PhRvL, 9, 439
Goedhart, S., Mooley, K., et al. 2017a, GCN, 21933
Goedhart, S., Mooley, K., et al. 2017b, GCN, 21891
Gold, T. 1968, Natur, 218, 731
Gold, T. 1969, Natur, 221, 25
Goldstein, A., Burgess, J. M., Preece, R. D., et al. 2012, ApJS, 199, 19
Goldstein, A., Veres, P., Burns, E., et al. 2017a, ApJL, https://doi.org/10.3847/2041-8213/aa8f41
Goldstein, A., Veres, P., von Kienlin, A., et al. 2017b, GCN, 21528
Goodman, J. 1986, ApJL, 308, L47
Gottlieb, O., Nakar, E., & Piran, T. 2017, arXiv:1705.10797
Grado, A., Cappellaro, E., Greco, G., et al. 2017c, GCN, 21598
Grado, A., Getman, F., Limatola, L., et al. 2017a, GCN, 21703
Grado, A., Getman, F., Limatola, L., et al. 2017b, GCN, 21833
Grossman, D., Korobkin, O., Rosswog, S., & Piran, T. 2014, MNRAS, 439, 757
Gruber, D., Goldstein, A., Weller von Ahlefeld, V., et al. 2014, ApJS, 211, 12
Haggard, D., Nynka, M., Ruan, J. J., et al. 2017a, ApJL, https://doi.org/10.3847/2041-8213/aa8ede
Haggard, D., Nynka, M., Kalogera, V., et al. 2017b, GCN, 21798
Hallinan, G., et al. 2017a, Sci, https://doi.org/10.1126/science.aap9855
Hallinan, G., Corsi, A., Mooley, K., et al. 2017b, GCN, 21929
Hancock, P. J., Tingay, S. J., de Gois, J. S., et al. 2017, GCN, 21894
Harrison, F. A., Craig, W. W., Christensen, F. E., et al. 2013, ApJ, 770, 103
Harrison, F. A., Forster, K., Garcia, J., et al. 2017, GCN, 21626
Hewish, A., Bell, S. J., Pilkington, J. D. H., Scott, P. F., & Collins, R. A. 1968, Natur, 217, 709
Hjorth, J., Sollerman, J., Gorosabel, J., et al. 2005a, ApJL, 630, L117
Hjorth, J., Watson, D., Fynbo, J. P. U., et al. 2005b, Natur, 437, 859
Hjorth, J., Watson, D., Fynbo, J. P. U., et al. 2005c, Natur, 437, 859
Hotokezaka, K., Nissanke, S., Hallinan, G., et al. 2016, ApJ, 831, 190
Hotokezaka, K., & Piran, T. 2015, MNRAS, 450, 1430
Hu, L., Wang, L., Sun, T., et al. 2017, GCN, 21883

Hulse, R. A., & Taylor, J. H. 1975, ApJL, 195, L51
Hurley, K., Mitrofanov, I. G., Golovin, D., et al. 2013, in EAS Publications Ser. 61, Gamma-ray Bursts: 15 Years of GRB Afterglows – Progenitors, Environments and Host Galaxies from the Nearby to the Early Universe, ed. A. J. Castro-Tirado, J. Gorosabel, & I. H. Park (Les Ulis: EDP Sciences), 459
Im, M., Choi, C., Kim, J., et al. 2017a, GCN, 21563
Im, M., Choi, C., Kim, J., et al. 2017b, GCN, 21566
Im, M., Choi, C., Kim, J., et al. 2017c, GCN, 21632
Im, M., Choi, C., Kim, J., et al. 2017d, GCN, 21597
Jin, Z.-P., Hotokezaka, K., Li, X., et al. 2016, NatCo, 7, 12898
Johnston, S., Bailes, M., Bartel, N., et al. 2007, PASA, 24, 174
Kalogera, V., Belczynski, K., Kim, C., O'Shaughnessy, R., & Willems, B. 2007, PhR, 442, 75
Kaplan, D., Brown, I., Sokolowski, M., et al. 2017b, GCN, 21927
Kaplan, D., Murphy, T., Bannister, K., et al. 2017a, GCN, 21574
Kaplan, D., Sokolowski, M., Wayth, R., et al. 2017c, GCN, 21637
Kasen, D., Badnell, N. R., & Barnes, J. 2013, ApJ, 774, 25
Kasen, D., Metzger, B., Barnes, J., Quataert, E., & Ramirez-Ruiz, E. 2017, Natur, https://doi.org/10.1038/nature24453
Kasliwal, M., Nakar, E., Singer, L. P., & Kaplan, D. E. A. 2017, Sci, https://doi.org/10.1126/science.aap9455
Kilpatrick, C. D., Coulter, D. A., Siebert, M. R., et al. 2017a, GCN, 21583
Kilpatrick, C. D., Foley, R. J., Kasen, D., et al. 2017b, Science, https://doi.org/10.1126/science.aaq0073
Klebesadel, R. W., Strong, I. B., & Olson, R. A. 1973, ApJL, 182, L85
Klotz, A., Laugier, R., Boer, M., et al. 2017, GCN, 21558
Kocevski, D., Omodei, N., Buson, S., et al. 2017, GCN, 21534
Kocevski, D., Thöne, C. C., Ramirez-Ruiz, E., et al. 2010, MNRAS, 404, 963
Kouveliotou, C., Meegan, C. A., Fishman, G. J., et al. 1993, ApJL, 413, L101
Kramer, M., Kraus, A., Eatough, R., & Nissanke, S. 2017, GCN, 21920
Kulkarni, S. R. 2005, arXiv:astro-ph/0510256
Labanti, C., Di Cocco, G., Ferro, G., et al. 2003, A&A, 411, L149
Lattimer, J. M., & Schramm, D. N. 1974, ApJL, 192, L145
Lattimer, J. M., & Schramm, D. N. 1976, ApJ, 210, 549
Lee, W. H., & Ramirez-Ruiz, E. 2007, NJPh, 9, 17
Levan, A. J., Lyman, J. D., Tanvir, N. R., et al. 2017, ApJL, https://doi.org/10.3847/2041-8213/aa905f
Levan, A., Lyman, J. D., Steeghs, D. T. H., et al. 2017b, GCN, 21681
Levan, A., Troja, E., Tanvir, N. R., et al. 2017a, GCN, 21781
Li, L.-X., & Paczyński, B. 1998, ApJL, 507, L59
Li, T. P., Xiong, S. L., Zhang, S. N., et al. 2017, Science China Physics, Mechanics & Astronomy, https://doi.org/10.1007/s11433-017-9107-5
Li, W., Chornock, R., Leaman, J., et al. 2011a, MNRAS, 412, 1473
Li, W., Leaman, J., Chornock, R., et al. 2011b, MNRAS, 412, 1441
Liao, J. Y., Li, C. K., Ge, M. Y., et al. 2017, GCN, 21518
LIGO Scientific Collaboration & Virgo Collaboration et al. 2017a, GCN, 21505
LIGO Scientific Collaboration & Virgo Collaboration et al. 2017b, GCN, 21513
LIGO Scientific Collaboration & Virgo Collaboration et al. 2017c, GCN, 21527
LIGO Scientific Collaboration & Virgo Collaboration et al. 2017d, GCN, 21509
LIGO Scientific Collaboration & Virgo Collaboration et al. 2017e, GCN, 21510
Lipunov, V., Gorbovskoy, Kornilov, V., et al. 2017a, ApJL, https://doi.org/10.3847/2041-8213/aa92c0
Lipunov, V., Kornilov, V., Gorbovskoy, E., et al. 2010, AdAst, 2010, 349171
Lipunov, V. M. 2017, GCN, 21621
Lipunov, V. M., Gorbovskoy, E., Kornilov, V. G., et al. 2017b, GCN, 21687
Lipunov, V. M., Gorbovskoy, E., Kornilov, V. G., et al. 2017c, GCN, 21587
Lipunov, V. M., Gorbovskoy, E., Kornilov, V. G., et al. 2017d, GCN, 21546
Lipunov, V. M., Gorbovskoy, E., Kornilov, V. G., et al. 2017e, GCN, 21570
Lipunov, V. M., Postnov, K. A., & Prokhorov, M. E. 1987, A&A, 176, L1
Lund, N., Budtz-Jørgensen, C., Westergaard, N. J., et al. 2003, A&A, 411, L231
Lyman, J., Homan, D., Maguire, K., et al. 2017, GCN, 21582
Lynch, C., Murphy, T., Kaplan, D., et al. 2017a, GCN, 21670
Lynch, C., Murphy, T., Kaplan, D., et al. 2017b, GCN, 21740
Lynch, C., Murphy, T., Kaplan, D., et al. 2017c, GCN, 21628
Lynch, C., Murphy, T., Kaplan, D., et al. 2017d, GCN, 21629
Malesani, D., Pian, E., Hjorth, J., et al. 2017a, GCN, 21591
Malesani, D., Watson, D., & Hjorth, J. 2017b, GCN, 21577
Margutti, R., Berger, E., Fong, W., et al. 2017b, ApJL, https://doi.org/10.3847/2041-8213/aa9057
Margutti, R., Fong, W., Berger, E., et al. 2017a, GCN, 21648
Martinez-Castellanos, I., Smith, A. J., et al. 2017, GCN, 21683
Massevitch, A. G., Tutukov, A. V., & Iungelson, L. R. 1976, Ap&SS, 40, 115
Matsuoka, M., Kawasaki, K., Ueno, S., et al. 2009, PASJ, 61, 999
McCully, C., Hiramatsu, D., Howell, D. A., et al. 2017b, ApJL, https://doi.org/10.3847/2041-8213/aa9111
McCully, C., Howell, D. A., & Hosseinzadeh 2017a, GCN, 21908

Meegan, C., Lichti, G., Bhat, P. N., et al. 2009, ApJ, 702, 791
Melandri, A., Campana, S., Covino, S., et al. 2017a, GCN, 21532
Melandri, A., D'Avanzo, P., Campana, S., et al. 2017b, GCN, 21556
Melandri, A., D'Avanzo, P., Campana, S., et al. 2017c, GCN, 21596
Messick, C., Blackburn, K., Brady, P., et al. 2017, PhRvD, 95, 042001
Metzger, B. D. 2017, LRR, 20, 3
Metzger, B. D., & Berger, E. 2012, ApJ, 746, 48
Metzger, B. D., & Fernández, R. 2014, MNRAS, 441, 3444
Metzger, B. D., Martínez-Pinedo, G., Darbha, S., et al. 2010, MNRAS, 406, 2650
Moldon, J., Beswick, R., Paragi, Z., et al. 2017a, GCN, 21804
Moldon, J., Beswick, R., Paragi, Z., et al. 2017b, GCN, 21940
Möller, A., Chang, & Wolf, C. 2017, GCN, 21542
Mooley, K. P., Hallinan, G., et al. 2017a, GCN, 21650
Mooley, K. P., Hallinan, G., Corsi, A., et al. 2017b, GCN, 21814
Murphy, T., Lenc, E., Lynch, C., et al. 2017, GCN, 21842
Nakahira, S., Yoshida, A., Sakamota, T., et al. 2017, GCN, 21641
Nakaoka, T., Kawabata, K. S., Kawabata, M., et al. 2017, GCN, 21623
Nakar, E. 2007, PhR, 442, 166
Nakar, E., & Piran, T. 2011, Natur, 478, 82
Narayan, R., Paczynski, B., & Piran, T. 1992, ApJL, 395, L83
Nicholl, M., Berger, E., Kasen, D., et al. 2017d, ApJL, https://doi.org/10.3847/2041-8213/aa9029
Nicholl, M., Briceno, C., & Cowperthwaite 2017c, GCN, 21585
Nicholl, M., Cowperthwaite, P. S., Allam, S., et al. 2017a, GCN, 21541
Nicholl, M., Cowperthwaite, P. S., Berger, E., et al. 2017b, GCN, 21580
Nissanke, S., Kasliwal, M., & Georgieva, A. 2013, ApJ, 767, 124
Nitz, A. H., Dent, T., Dal Canton, T., Fairhurst, S., & Brown, D. A. 2017a, arXiv:1705.01513
Nitz, A., Harry, I., Brown, D., et al. 2017b, ligo-cbc/pycbc: O2 Production Release 20, doi:10.5281/zenodo.883086
Ofek, E. O., Cenko, S. B., Gal-Yam, A., et al. 2007, ApJ, 662, 1129
Oppenheimer, J. R., & Volkoff, G. M. 1939, PhRv, 55, 374
Paciesas, W. S., Meegan, C. A., von Kienlin, A., et al. 2012, ApJS, 199, 18
Paczynski, B. 1986, ApJL, 308, L43
Paragi, Z., Agudo, I., An, T., et al. 2017a, GCN, 21763
Paragi, Z., Yang, J., Marcote, B., et al. 2017b, GCN, 21939
Pavana, M., Kiran, B. S., Anupama, G. C., et al. 2017, GCN, 21554
Pearson, T. J., Readhead, A. C. S., et al. 2017, GCN, 21760
Pian, E., D'Avanzo, P., Bennetti, S., et al. 2017a, Natur, https://doi.org/10.1038/nature24298
Pian, E., D'Elia, V., Piranomonte, S., et al. 2017b, GCN, 21592
Piano, G., Verrecchia, F., Pilia, M., et al. 2017, GCN, 21526
Pilia, M., Cardillo, M., Piano, G., et al. 2017, GCN, 21525
Piran, T., Nakar, E., & Rosswog, S. 2013, MNRAS, 430, 2121
Postnov, K. A., & Yungelson, L. R. 2014, LRR, 17, 3
Pozanenko, A., Volnova, A., Mazaeva, E., et al. 2017a, GCN, 21635
Pozanenko, A., Volnova, A., Mazaeva, E., et al. 2017b, GCN, 21898
Pozanenko, A., Volnova, A., Mazaeva, E., et al. 2017c, GCN, 21644
Pozanenko, A., Volnova, A., Mazaeva, E., et al. 2017d, GCN, 21618
Prandoni, I., Murgia, M., Tarchi, A., et al. 2017, arXiv:1703.09673
Pretorius, F. 2005, PhRvL, 95, 121101
Prochaska, J. X., Bloom, J. S., Chen, H.-W., et al. 2006, ApJ, 642, 989
Rabinowitz, D., Baltay, C., et al. 2017, GCN, 21599
Resmi, L, Misra, K., Tanvir, N. R., et al. 2017, GCN, 21768
Ricci, R., Wieringa, M., Piro, L., & Troja, E. 2017, GCN, 21900
Roberts, L. F., Kasen, D., Lee, W. H., & Ramirez-Ruiz, E. 2011, ApJL, 736, L21
Rosswog, S. 2005, ApJ, 634, 1202
Sadler, E. M., Allison, J. R., Kaplan, D. L., et al. 2017, GCN, 21645
Sathyaprakash, B. S., & Dhurandhar, S. V. 1991, PhRvD, 44, 3819
Savchenko, V., Ferrigno, C., Kuulkers, E., et al. 2017, ApJL, https://doi.org/10.3847/2041-8213/aa8f94
Savchenko, V., Ferrigno, C., Kuulkers, E., et al. 2017b, GCN, 21672
Savchenko, V., Neronov, A., & Courvoisier, T. J.-L. 2012, A&A, 541, A122
Savchenko, V., Mereghetti, S., Ferrigno, C., et al. 2017a, GCN, 21507
Schlafly, E. F., & Finkbeiner, D. P. 2011, ApJ, 737, 103
Schulze, S., Kim, S., Martin, S., et al. 2017, GCN, 21747
Shapiro, S. L., & Teukolsky, S. A. 1983, Black Holes, White Dwarfs, and Neutron Stars: The Physics of Compact Objects (New York: Wiley)
Shappee, B. J., Simon, J. D., Drout, M. R., et al. 2017, Sci, https://doi.org/10.1126/science.aaq0186
Shara, M., Williams, T., Vaisanen, et al. 2017, GCN, 21610
Shklovsky, I. S. 1967, ApJL, 148, L1
Siebert, M. R., Foley, R. J., Drout, M. R., et al. 2017, ApJL, https://doi.org/10.3847/2041-8213/aa905e

Simon, J. D., Shappee, B. J., Drout, M. R., et al. 2017, GCN, 21551
Singer, L. P., et al. 2017c, GCN, 21569
Singer, L. P., Chen, H.-Y, Holz, D. E., et al. 2016, ApJL, 829, L15
Singer, L. P., Lau, R., Kasliwal, M. M., et al. 2017a, GCN, 21552
Singer, L. P., Lau, R., Kasliwal, M. M., et al. 2017b, GCN, 21779
Singer, L. P., & Price, L. 2016, PhRvD, 93, 024013
Singh, K. P., Tandon, S. N., Agrawal, P. C., et al. 2014, ASTROSAT Mission, doi:10.1117/12.2062667
Smartt, S. J., et al. 2017, Natur, https://doi.org/10.1038/nature24303
Soares-Santos, M., Holz, D., Annis, J., et al. 2017, ApJL, https://doi.org/10.3847/2041-8213/aa9059
Soderberg, A. M., Berger, E., Kasliwal, M., et al. 2006, ApJ, 650, 261
Sugita, S., Kawai, N., Serino, M., et al. 2017, GCN, 21555
Svinkin, D., Golenetskii, S., Aptekar, R., et al. 2017a, GCN, 21746
Svinkin, D., Hurley, K., von Kienlin, A., et al. 2017b, GCN, 21515
Svinkin, D., Hurley, K., von, K. A., et al. 2017c, GCN, 21515
Swarup, G., Ananthakrishnan, S., Kapahi, V. K., et al. 1991, CSci, 60, 95
Tanaka, M. 2016, AdAst, 2016, 634197
Tanaka, M., & Hotokezaka, K. 2013, ApJ, 775, 113
Tanvir, N. R., Levan, A. J., et al. 2017a, GCN, 21544
Tanvir, N. R., Levan, A. J., Fruchter, A. S., et al. 2013, Natur, 500, 547
Tanvir, N. R., Levan, A. J., González-Fernández, C., et al. 2017, ApJL, https://doi.org/10.3847/2041-8213/aa90b6
Tanvir, N. R., Levan, A. J., & Steeghs, D. 2017b, GCN, 21576
Tavani, M., Barbiellini, G., Argan, A., et al. 2009, A&A, 502, 995
Taylor, J. H., & Weisberg, J. M. 1982, ApJ, 253, 908
Taylor, J. H., Wolszczan, A., Damour, T., & Weisberg, J. M. 1992, Natur, 355, 132
Tingay, S. J., Goeke, R., Bowman, J. D., et al. 2013, PASA, 30, e007
Tominaga, N., Yoshida, M., Tanaka, M., et al. 2017, GCN, 21595
Tonry, J., Smith, K. W., Denneau, L., et al. 2017, GCN, 21886
Troja, E., Butler, N., Watson, A., et al. 2017d, GCN, 21778
Troja, E., King, A. R., O'Brien, P. T., Lyons, N., & Cusumano, G. 2008, MNRAS, 385, L10
Troja, E., Piro, L., Sakamota, T., et al. 2017c, GCN, 21765
Troja, E., Piro, L., Sakamota, T., et al. 2017e, GCN, 21787
Troja, E., Piro, L., van Eerten, H., et al. 2017a, Natur, doi:10.1038/nature24290

Troja, E., Sakamoto, T., Cenko, S. B., et al. 2016, ApJ, 827, 102
Troja, E., Watson, A., Covina, S., et al. 2017b, GCN, 21682
Troja, E., Ricci, R., Wieringa, M. L., & Piro, L. 2017f, GCN, 21803
Tunnicliffe, R. L., Levan, A. J., Tanvir, N. R., et al. 2014, MNRAS, 437, 1495
Ubertini, P., Lebrun, F., di Cocco, G., et al. 2003, A&A, 411, L131
Valenti, S., Yang, S., Sand, D., et al. 2017, GCN, 21606
van Haarlem, M. P., Wise, M. W., Gunst, A. W., et al. 2013, A&A, 556, A2
Vedrenne, G., Roques, J.-P., Schönfelder, V., et al. 2003, A&A, 411, L63
Veitch, J., Raymond, V., Farr, B., et al. 2015, PhRvD, 91, 042003
Verrecchia, F., Cardillo, M., Bulgarelli, A., et al. 2017, GCN, 21785
Villasenor, J. S., Lamb, D. Q., Ricker, G. R., et al. 2005, Natur, 437, 855
von Kienlin, A., Beckmann, V., Rau, A., et al. 2003, A&A, 411, L299
von Kienlin, A., Meegan, C., Goldstein, A., et al. 2017, GCN, 21520
Wex, N. 2014, arXiv:1402.5594
White, D. J., Daw, E., & Dhillon, V. 2011a, CQGra, 28, 085016
White, D. J., Daw, E. J., & Dhillon, V. S. 2011b, CQGra, 28, 085016
Wieringa, M., Ricci, R., & Piro Troja, E. 2017, GCN, 21882
Wiersema, K., Covino, S., Melandri, A., et al. 2017, GCN, 21594
Williams, P. K. G., Alexander, K. D., Berger, E., et al. 2017a, GCN, 21750
Williams, P. K. G., Alexander, K. D., Berger, E., et al. 2017b, GCN, 21571
Wilson, W. E., Ferris, R. H., Axtens, P., et al. 2011, MNRAS, 416, 832
Wilson-Hodge, C. A., Case, G. L., Cherry, M. L., et al. 2012, ApJS, 201, 33
Winkler, C., Courvoisier, T. J.-L., Di Cocco, G., et al. 2003, A&A, 411, L1
Wiseman, P., Chen, T. W., Greiner, J., et al. 2017, GCN, 21584
Wolf, C., Chang, S. W., & Möller, A. 2017, GCN, 21560
Wootten, A., & Thompson, A. R. 2009, IEEEP, 97, 1463
Yang, S., Valenti, S., Sand, D., et al. 2017a, GCN, 21531
Yang, S., Valenti, S., Sand, D., et al. 2017b, GCN, 21579
Yang, S., Valenti, S., Sand, D., et al. 2017c, GCN, 21539
Yoshida, M., Tanaka, M., Terai, T., et al. 2017a, GCN, 21549
Yoshida, M., Tanaka, M., Terai, T., et al. 2017b, GCN, 21561
Yoshida, M., Tanaka, M., Terai, T., et al. 2017c, GCN, 21586
Yoshida, M., Tanaka, M., Utsumi, Y., et al. 2017d, GCN, 21685
Yu, P.-C., Ngeow, C.-C., Ip, W.-H., et al. 2017, GCN, 21669
Zadrożny, A., Sokołowski, M., Mankiewicz, L., & Żarnecki, A. F. 2017, Pi of the Sky in LSC-Virgo's EM follow-up in O1 science, doi:10.1117/12.2281024

B. P. Abbott[1], R. Abbott[1], T. D. Abbott[2], F. Acernese[3,4], K. Ackley[5,6], C. Adams[7], T. Adams[8], P. Addesso[9], R. X. Adhikari[1], V. B. Adya[10], C. Affeldt[10], M. Afrough[11], B. Agarwal[12], M. Agathos[13], K. Agatsuma[14], N. Aggarwal[15], O. D. Aguiar[16], L. Aiello[17,18], A. Ain[19], P. Ajith[20], B. Allen[10,21,22], G. Allen[12], A. Allocca[23,24], P. A. Altin[25], A. Amato[26], A. Ananyeva[1], S. B. Anderson[1], W. G. Anderson[21], S. V. Angelova[27], S. Antier[28], S. Appert[1], K. Arai[1], M. C. Araya[1], J. S. Areeda[29], N. Arnaud[28,30], K. G. Arun[31], S. Ascenzi[32,33], G. Ashton[10], M. Ast[34], S. M. Aston[7], P. Astone[35], D. V. Atallah[36], P. Aufmuth[22], C. Aulbert[10], K. AultONeal[37], C. Austin[2], A. Avila-Alvarez[29], S. Babak[38], P. Bacon[39], M. K. M. Bader[14], S. Bae[40], P. T. Baker[41], F. Baldaccini[42,43], G. Ballardin[30], S. W. Ballmer[44], S. Banagiri[45], J. C. Barayoga[1], S. E. Barclay[46], B. C. Barish[1], D. Barker[47], K. Barkett[48], F. Barone[3,4], B. Barr[46], L. Barsotti[15], M. Barsuglia[39], D. Barta[49], S. D. Barthelmy[50], J. Bartlett[47], I. Bartos[51,5], R. Bassiri[52], A. Basti[23,24], J. C. Batch[47], M. Bawaj[53,43], J. C. Bayley[46], M. Bazzan[54,55], B. Bécsy[56], C. Beer[10], M. Bejger[57], I. Belahcene[28], A. S. Bell[46], B. K. Berger[1], G. Bergmann[10], J. J. Bero[58], C. P. L. Berry[59], D. Bersanetti[60], A. Bertolini[14], J. Betzwieser[7], S. Bhagwat[44], R. Bhandare[61], I. A. Bilenko[62], G. Billingsley[1], C. R. Billman[5], J. Birch[7], R. Birney[63], O. Birnholtz[10], S. Biscans[1,15], S. Biscoveanu[64,6], A. Bisht[22], M. Bitossi[30,24], C. Biwer[44], M. A. Bizouard[28], J. K. Blackburn[1], J. Blackman[48], C. D. Blair[1,65], D. G. Blair[65], R. M. Blair[47], S. Bloemen[66], O. Bock[10], N. Bode[10], M. Boer[67], G. Bogaert[67], A. Bohe[38], F. Bondu[68], E. Bonilla[52], R. Bonnand[8], B. A. Boom[14], R. Bork[1], V. Boschi[30,24], S. Bose[69,19], K. Bossie[7], Y. Bouffanais[39], A. Bozzi[30], C. Bradaschia[24], P. R. Brady[21], M. Branchesi[17,18], J. E. Brau[70], T. Briant[71], A. Brillet[67], M. Brinkmann[10], V. Brisson[28], P. Brockill[21], J. E. Broida[72], A. F. Brooks[1], D. A. Brown[44], D. D. Brown[73], S. Brunett[1], C. C. Buchanan[2], A. Buikema[15], T. Bulik[74], H. J. Bulten[75,14], A. Buonanno[38,76], D. Buskulic[8], C. Buy[39], R. L. Byer[52], M. Cabero[10], L. Cadonati[77], G. Cagnoli[26,78], C. Cahillane[1], J. Calderón Bustillo[77], T. A. Callister[1], E. Calloni[79,4], J. B. Camp[50], M. Canepa[60,80], P. Canizares[66], K. C. Cannon[81], H. Cao[73], J. Cao[82], C. D. Capano[10], E. Capocasa[39], F. Carbognani[30], S. Caride[83], M. F. Carney[84], J. Casanueva Diaz[28], C. Casentini[32,33], S. Caudill[14,21], M. Cavaglià[11], F. Cavalier[28], R. Cavalieri[30], G. Cella[24], C. B. Cepeda[1], P. Cerdá-Durán[85], G. Cerretani[23,24], E. Cesarini[33,86], S. J. Chamberlin[64], M. Chan[46], S. Chao[87], P. Charlton[88], E. Chase[89], E. Chassande-Mottin[39], D. Chatterjee[21], K. Chatziioannou[90], B. D. Cheeseboro[41], H. Y. Chen[91], X. Chen[65], Y. Chen[48], H.-P. Cheng[5], H. Chia[5], A. Chincarini[60], A. Chiummo[30], T. Chmiel[84], H. S. Cho[92], M. Cho[76], J. H. Chow[25], N. Christensen[72,67], Q. Chu[65], A. J. K. Chua[13], S. Chua[71], A. K. W. Chung[93], S. Chung[65], G. Ciani[5,54,55], R. Ciolfi[94,95], C. E. Cirelli[52], A. Cirone[60,80], F. Clara[47], J. A. Clark[77], P. Clearwater[96], F. Cleva[67], C. Cocchieri[11], E. Coccia[17,18], P.-F. Cohadon[71], D. Cohen[28], A. Colla[97,35], C. G. Collette[98],

L. R. Cominsky[99], M. Constancio Jr.[16], L. Conti[55], S. J. Cooper[59], P. Corban[7], T. R. Corbitt[2], I. Cordero-Carrión[100], K. R. Corley[51], N. Cornish[101], A. Corsi[83], S. Cortese[30], C. A. Costa[16], M. W. Coughlin[72,1], S. B. Coughlin[89], J.-P. Coulon[67], S. T. Countryman[51], P. Couvares[1], P. B. Covas[102], E. E. Cowan[77], D. M. Coward[65], M. J. Cowart[7], D. C. Coyne[1], R. Coyne[83], J. D. E. Creighton[21], T. D. Creighton[103], J. Cripe[2], S. G. Crowder[104], T. J. Cullen[29,2], A. Cumming[46], L. Cunningham[46], E. Cuoco[30], T. Dal Canton[50], G. Dálya[56], S. L. Danilishin[22,10], S. D'Antonio[33], K. Danzmann[22,10], A. Dasgupta[105], C. F. Da Silva Costa[5], V. Dattilo[30], I. Dave[61], M. Davier[28], D. Davis[44], E. J. Daw[106], B. Day[77], S. De[44], D. DeBra[52], J. Degallaix[26], M. De Laurentis[17,4], S. Deléglise[71], W. Del Pozzo[59,23,24], N. Demos[15], T. Denker[10], T. Dent[10], R. De Pietri[107,108], V. Dergachev[38], R. De Rosa[79,4], R. T. DeRosa[7], C. De Rossi[26,30], R. DeSalvo[109], O. de Varona[10], J. Devenson[27], S. Dhurandhar[19], M. C. Díaz[103], L. Di Fiore[4], M. Di Giovanni[110,95], T. Di Girolamo[51,79,4], A. Di Lieto[23,24], S. Di Pace[97,35], I. Di Palma[97,35], F. Di Renzo[23,24], Z. Doctor[91], V. Dolique[26], F. Donovan[15], K. L. Dooley[11], S. Doravari[10], I. Dorrington[36], R. Douglas[46], M. Dovale Álvarez[59], T. P. Downes[21], M. Drago[10], C. Dreissigacker[10], J. C. Driggers[47], Z. Du[82], M. Ducrot[8], P. Dupej[46], S. E. Dwyer[47], T. B. Edo[106], M. C. Edwards[72], A. Effler[7], P. Ehrens[1], J. Eichholz[1], S. S. Eikenberry[5], R. A. Eisenstein[15], R. C. Essick[15], D. Estevez[8], Z. B. Etienne[41], T. Etzel[1], M. Evans[15], T. M. Evans[7], M. Factourovich[51], V. Fafone[32,33,17], H. Fair[44], S. Fairhurst[36], X. Fan[82], S. Farinon[60], B. Farr[91], W. M. Farr[59], E. J. Fauchon-Jones[36], M. Favata[111], M. Fays[36], C. Fee[84], H. Fehrmann[10], J. Feicht[1], M. M. Fejer[52], A. Fernandez-Galiana[15], I. Ferrante[23,24], E. C. Ferreira[16], F. Ferrini[30], F. Fidecaro[23,24], D. Finstad[44], I. Fiori[30], D. Fiorucci[39], M. Fishbach[91], R. P. Fisher[44], M. Fitz-Axen[45], R. Flaminio[26,112], M. Fletcher[46], H. Fong[90], J. A. Font[85,113], P. W. F. Forsyth[25], S. S. Forsyth[77], J.-D. Fournier[67], S. Frasca[97,35], F. Frasconi[24], Z. Frei[56], A. Freise[59], R. Frey[70], V. Frey[28], E. M. Fries[1], P. Fritschel[15], V. V. Frolov[7], P. Fulda[5], M. Fyffe[7], H. Gabbard[46], B. U. Gadre[19], S. M. Gaebel[59], J. R. Gair[114], L. Gammaitoni[42], M. R. Ganija[73], S. G. Gaonkar[19], C. Garcia-Quiros[102], F. Garufi[79,4], B. Gateley[47], S. Gaudio[37], G. Gaur[115], V. Gayathri[116], N. Gehrels[50,954], G. Gemme[60], E. Genin[30], A. Gennai[24], D. George[12], J. George[61], L. Gergely[117], V. Germain[8], S. Ghonge[77], Abhirup Ghosh[20], Archisman Ghosh[20,14], S. Ghosh[66,14,21], J. A. Giaime[2,7], K. D. Giardina[7], A. Giazotto[24], K. Gill[37], L. Glover[109], E. Goetz[118], R. Goetz[5], S. Gomes[36], B. Goncharov[6], G. González[2], J. M. Gonzalez Castro[23,24], A. Gopakumar[119], M. L. Gorodetsky[62], S. E. Gossan[1], M. Gosselin[30], R. Gouaty[8], A. Grado[120,4], C. Graef[46], M. Granata[26], A. Grant[46], S. Gras[15], C. Gray[47], G. Greco[121,122], A. C. Green[59], E. M. Gretarsson[37], B. Griswold[70], P. Groot[66], H. Grote[10], S. Grunewald[38], P. Gruning[28], G. M. Guidi[121,122], X. Guo[82], A. Gupta[64], M. K. Gupta[105], K. E. Gushwa[1], E. K. Gustafson[1], R. Gustafson[118], O. Halim[18,17], B. R. Hall[69], E. D. Hall[15], E. Z. Hamilton[36], G. Hammond[46], M. Haney[123], M. M. Hanke[10], J. Hanks[47], C. Hanna[64], M. D. Hannam[36], O. A. Hannuksela[93], J. Hanson[7], T. Hardwick[2], J. Harms[17,18], G. M. Harry[124], I. W. Harry[38], M. J. Hart[46], C.-J. Haster[90], K. Haughian[46], J. Healy[58], A. Heidmann[71], M. C. Heintze[7], H. Heitmann[67], P. Hello[28], G. Hemming[30], M. Hendry[46], I. S. Heng[46], J. Hennig[46], A. W. Heptonstall[1], M. Heurs[10,22], S. Hild[46], T. Hinderer[66], D. Hoak[30], D. Hofman[26], K. Holt[7], D. E. Holz[91], P. Hopkins[36], C. Horst[21], J. Hough[46], E. A. Houston[46], E. J. Howell[65], A. Hreibi[67], Y. M. Hu[10], E. A. Huerta[12], D. Huet[28], B. Hughey[37], S. Husa[102], S. H. Huttner[46], T. Huynh-Dinh[7], N. Indik[10], R. Inta[83], G. Intini[97,35], H. N. Isa[46], J.-M. Isac[71], M. Isi[1], B. R. Iyer[20], K. Izumi[47], T. Jacqmin[71], K. Jani[77], P. Jaranowski[125], S. Jawahar[63], F. Jiménez-Forteza[102], W. W. Johnson[2], D. I. Jones[126], R. Jones[46], R. J. G. Jonker[14], L. Ju[65], J. Junker[10], C. V. Kalaghatgi[36], V. Kalogera[89], B. Kamai[1], S. Kandhasamy[7], G. Kang[40], J. B. Kanner[1], S. J. Kapadia[21], S. Karki[70], K. S. Karvinen[10], M. Kasprzack[2], M. Katolik[12], E. Katsavounidis[15], W. Katzman[7], S. Kaufer[22], K. Kawabe[47], F. Kéfélian[67], D. Keitel[46], A. J. Kemball[12], R. Kennedy[106], C. Kent[36], J. S. Key[127], F. Y. Khalili[62], I. Khan[17,33], S. Khan[36], Z. Khan[105], E. A. Khazanov[128], N. Kijbunchoo[25], Chunglee Kim[129], J. C. Kim[130], K. Kim[93], W. Kim[73], W. S. Kim[131], Y.-M. Kim[92], S. J. Kimbrell[77], E. J. King[73], P. J. King[47], M. Kinley-Hanlon[124], R. Kirchhoff[10], J. S. Kissel[47], L. Kleybolte[34], S. Klimenko[5], T. D. Knowles[41], P. Koch[10], S. M. Koehlenbeck[10], S. Koley[14], V. Kondrashov[1], A. Kontos[15], M. Korobko[34], W. Z. Korth[1], I. Kowalska[74], D. B. Kozak[1], C. Krämer[10], V. Kringel[10], B. Krishnan[10], A. Królak[132,133], G. Kuehn[10], P. Kumar[90], R. Kumar[105], S. Kumar[20], L. Kuo[87], A. Kutynia[132], S. Kwang[21], B. D. Lackey[38], K. H. Lai[93], M. Landry[47], R. N. Lang[134], J. Lange[58], B. Lantz[52], R. K. Lanza[15], S. L. Larson[89], A. Lartaux-Vollard[28], P. D. Lasky[6], M. Laxen[7], A. Lazzarini[1], C. Lazzaro[55], P. Leaci[97,35], S. Leavey[46], C. H. Lee[92], H. K. Lee[135], H. M. Lee[136], H. W. Lee[130], K. Lee[46], J. Lehmann[10], A. Lenon[41], M. Leonardi[110,95], N. Leroy[28], N. Letendre[8], Y. Levin[6], T. G. F. Li[93], S. D. Linker[109], T. B. Littenberg[137], J. Liu[65], R. K. L. Lo[93], N. A. Lockerbie[63], L. T. London[36], J. E. Lord[44], M. Lorenzini[17,18], V. Loriette[138], M. Lormand[7], G. Losurdo[24], J. D. Lough[10], C. O. Lousto[58], G. Lovelace[29], H. Lück[22,10], D. Lumaca[32,33], A. P. Lundgren[10], R. Lynch[15], Y. Ma[48], R. Macas[36], S. Macfoy[27], B. Machenschalk[10], M. MacInnis[15], D. M. Macleod[36], I. Magaña Hernandez[21], F. Magaña-Sandoval[44], L. Magaña Zertuche[44], R. M. Magee[64], E. Majorana[35], I. Maksimovic[138], N. Man[67], V. Mandic[45], V. Mangano[46], G. L. Mansell[25], M. Manske[21,25], M. Mantovani[30], F. Marchesoni[53,43], F. Marion[8], S. Márka[51], Z. Márka[51], C. Markakis[12], A. S. Markosyan[52], A. Markowitz[1], E. Maros[1], A. Marquina[100], P. Marsh[127], F. Martelli[121,122], L. Martellini[67], I. W. Martin[46], R. M. Martin[111], D. V. Martynov[15], K. Mason[15], E. Massera[106], A. Masserot[8], T. J. Massinger[1], M. Masso-Reid[46], S. Mastrogiovanni[97,35], A. Matas[45], F. Matichard[1,15], L. Matone[51], N. Mavalvala[15], N. Mazumder[69], R. McCarthy[47], D. E. McClelland[25], S. McCormick[7], L. McCuller[15], S. C. McGuire[139], G. McIntyre[1], J. McIver[1], D. J. McManus[25], L. McNeill[6], T. McRae[25], S. T. McWilliams[41], D. Meacher[64], G. D. Meadors[38,10], M. Mehmet[10],

J. Meidam[14], E. Mejuto-Villa[9], A. Melatos[96], G. Mendell[47], R. A. Mercer[21], E. L. Merilh[47], M. Merzougui[67], S. Meshkov[1], C. Messenger[46], C. Messick[64], R. Metzdorff[71], P. M. Meyers[45], H. Miao[59], C. Michel[26], H. Middleton[59], E. E. Mikhailov[140], L. Milano[79,4], A. L. Miller[5,97,35], B. B. Miller[89], J. Miller[15], M. Millhouse[101], M. C. Milovich-Goff[109], O. Minazzoli[67,141], Y. Minenkov[33], J. Ming[38], C. Mishra[142], S. Mitra[19], V. P. Mitrofanov[62], G. Mitselmakher[5], R. Mittleman[15], D. Moffa[84], A. Moggi[24], K. Mogushi[11], M. Mohan[30], S. R. P. Mohapatra[15], M. Montani[121,122], C. J. Moore[13], D. Moraru[47], G. Moreno[47], S. R. Morriss[103], B. Mours[8], C. M. Mow-Lowry[59], G. Mueller[5], A. W. Muir[36], Arunava Mukherjee[10], D. Mukherjee[21], S. Mukherjee[103], N. Mukund[19], A. Mullavey[7], J. Munch[73], E. A. Muñiz[44], M. Muratore[37], P. G. Murray[46], K. Napier[77], I. Nardecchia[32,33], L. Naticchioni[97,35], R. K. Nayak[143], J. Neilson[109], G. Nelemans[66,14], T. J. N. Nelson[7], M. Nery[10], A. Neunzert[118], L. Nevin[1], J. M. Newport[124], G. Newton[46,955], K. K. Y. Ng[93], P. Nguyen[70], T. T. Nguyen[25], D. Nichols[66], A. B. Nielsen[10], S. Nissanke[66,14], A. Nitz[10], A. Noack[10], F. Nocera[30], D. Nolting[7], C. North[36], L. K. Nuttall[36], J. Oberling[47], G. D. O'Dea[109], G. H. Ogin[144], J. J. Oh[131], S. H. Oh[131], F. Ohme[10], M. A. Okada[16], M. Oliver[102], P. Oppermann[10], Richard J. Oram[7], B. O'Reilly[7], R. Ormiston[45], L. F. Ortega[5], R. O'Shaughnessy[58], S. Ossokine[38], D. J. Ottaway[73], H. Overmier[7], B. J. Owen[83], A. E. Pace[64], J. Page[137], M. A. Page[65], A. Pai[116,145], S. A. Pai[61], J. R. Palamos[70], O. Palashov[128], C. Palomba[35], A. Pal-Singh[34], Howard Pan[87], Huang-Wei Pan[87], B. Pang[48], P. T. H. Pang[93], C. Pankow[89], F. Pannarale[36], B. C. Pant[61], F. Paoletti[24], A. Paoli[30], M. A. Papa[38,21,10], A. Parida[19], W. Parker[7], D. Pascucci[46], A. Pasqualetti[30], R. Passaquieti[23,24], D. Passuello[24], M. Patil[133], B. Patricelli[146,24], B. L. Pearlstone[46], M. Pedraza[1], R. Pedurand[26,147], L. Pekowsky[44], A. Pele[7], S. Penn[148], C. J. Perez[47], A. Perreca[1,110,95], L. M. Perri[89], H. P. Pfeiffer[90,38], M. Phelps[46], O. J. Piccinni[97,35], M. Pichot[67], F. Piergiovanni[121,122], V. Pierro[9], G. Pillant[30], L. Pinard[26], I. M. Pinto[9], M. Pirello[47], M. Pitkin[46], M. Poe[21], R. Poggiani[23,24], P. Popolizio[30], E. K. Porter[39], A. Post[10], J. Powell[46,149], J. Prasad[19], J. W. W. Pratt[37], G. Pratten[102], V. Predoi[36], T. Prestegard[21], L. R. Price[1], M. Prijatelj[10], M. Principe[9], S. Privitera[38], G. A. Prodi[110,95], L. G. Prokhorov[62], O. Puncken[10], M. Punturo[43], P. Puppo[35], M. Pürrer[38], H. Qi[21], V. Quetschke[103], E. A. Quintero[1], R. Quitzow-James[70], F. J. Raab[47], D. S. Rabeling[25], H. Radkins[47], P. Raffai[56], S. Raja[61], C. Rajan[61], B. Rajbhandari[83], M. Rakhmanov[103], K. E. Ramirez[103], A. Ramos-Buades[102], P. Rapagnani[97,35], V. Raymond[38], M. Razzano[23,24], J. Read[29], T. Regimbau[67], L. Rei[60], S. Reid[63], D. H. Reitze[1,5], W. Ren[12], S. D. Reyes[44], F. Ricci[97,35], P. M. Ricker[12], S. Rieger[10], K. Riles[118], M. Rizzo[58], N. A. Robertson[1,46], R. Robie[46], F. Robinet[28], A. Rocchi[33], L. Rolland[8], J. G. Rollins[1], V. J. Roma[70], R. Romano[3,4], C. L. Romel[47], J. H. Romie[7], D. Rosińska[150,57], M. P. Ross[151], S. Rowan[46], A. Rüdiger[10], P. Ruggi[30], G. Rutins[27], K. Ryan[47], S. Sachdev[1], T. Sadecki[47], L. Sadeghian[21], M. Sakellariadou[152], L. Salconi[30], M. Saleem[116], F. Salemi[10], A. Samajdar[143], L. Sammut[6], L. M. Sampson[89], E. J. Sanchez[1], L. E. Sanchez[1], N. Sanchis-Gual[85], V. Sandberg[47], J. R. Sanders[44], B. Sassolas[26], B. S. Sathyaprakash[64,36], P. R. Saulson[44], O. Sauter[118], R. L. Savage[47], A. Sawadsky[34], P. Schale[70], M. Scheel[48], J. Scheuer[89], J. Schmidt[205], P. Schmidt[1,66], R. Schnabel[34], R. M. S. Schofield[70], A. Schönbeck[34], E. Schreiber[10], D. Schuette[10,22], B. W. Schulte[10], B. F. Schutz[36,10], S. G. Schwalbe[37], J. Scott[46], S. M. Scott[25], E. Seidel[12], D. Sellers[7], A. S. Sengupta[153], D. Sentenac[30], V. Sequino[32,33,17], A. Sergeev[128], D. A. Shaddock[25], T. J. Shaffer[47], A. A. Shah[137], M. S. Shahriar[89], M. B. Shaner[109], L. Shao[38], B. Shapiro[52], P. Shawhan[76], A. Sheperd[21], D. H. Shoemaker[15], D. M. Shoemaker[77], K. Siellez[77], X. Siemens[21], M. Sieniawska[57], D. Sigg[47], A. D. Silva[16], L. P. Singer[50], A. Singh[38,10,22], A. Singhal[17,35], A. M. Sintes[102], B. J. J. Slagmolen[25], B. Smith[7], J. R. Smith[29], R. J. E. Smith[1,6], S. Somala[154], E. J. Son[131], J. A. Sonnenberg[21], B. Sorazu[46], F. Sorrentino[60], T. Souradeep[19], A. P. Spencer[46], A. K. Srivastava[105], K. Staats[37], A. Staley[51], M. Steinke[10], J. Steinlechner[34,46], S. Steinlechner[34], D. Steinmeyer[10], S. P. Stevenson[59,149], R. Stone[103], D. J. Stops[59], K. A. Strain[46], G. Stratta[121,122], S. E. Strigin[62], A. Strunk[47], R. Sturani[155], A. L. Stuver[7], T. Z. Summerscales[156], L. Sun[96], S. Sunil[105], J. Suresh[19], P. J. Sutton[36], B. L. Swinkels[30], M. J. Szczepańczyk[37], M. Tacca[14], S. C. Tait[46], C. Talbot[6], D. Talukder[70], D. B. Tanner[5], M. Tápai[117], A. Taracchini[38], J. D. Tasson[72], J. A. Taylor[137], R. Taylor[1], S. V. Tewari[148], T. Theeg[10], F. Thies[10], E. G. Thomas[59], M. Thomas[7], P. Thomas[47], K. A. Thorne[7], K. S. Thorne[48], E. Thrane[6], S. Tiwari[17,95], V. Tiwari[36], K. V. Tokmakov[63], K. Toland[46], M. Tonelli[23,24], Z. Tornasi[46], A. Torres-Forné[85], C. I. Torrie[1], D. Töyrä[59], F. Travasso[30,43], G. Traylor[7], J. Trinastic[5], M. C. Tringali[110,95], L. Trozzo[157,24], K. W. Tsang[14], M. Tse[15], R. Tso[1], L. Tsukada[81], D. Tsuna[81], D. Tuyenbayev[103], K. Ueno[21], D. Ugolini[158], C. S. Unnikrishnan[119], A. L. Urban[1], S. A. Usman[36], H. Vahlbruch[22], G. Vajente[1], G. Valdes[2], N. van Bakel[14], M. van Beuzekom[14], J. F. J. van den Brand[75,14], C. Van Den Broeck[14], D. C. Vander-Hyde[44], L. van der Schaaf[14], J. V. van Heijningen[14], A. A. van Veggel[46], M. Vardaro[54,55], V. Varma[48], S. Vass[1], M. Vasúth[49], A. Vecchio[59], G. Vedovato[55], J. Veitch[46], P. J. Veitch[73], K. Venkateswara[151], G. Venugopalan[1], D. Verkindt[8], F. Vetrano[121,122], A. Viceré[121,122], A. D. Viets[21], S. Vinciguerra[59], D. J. Vine[27], J.-Y. Vinet[67], S. Vitale[15], T. Vo[44], H. Vocca[42,43], C. Vorvick[47], S. P. Vyatchanin[62], A. R. Wade[1], L. E. Wade[84], M. Wade[84], R. Walet[14], M. Walker[29], L. Wallace[1], S. Walsh[38,10,21], G. Wang[17,122], H. Wang[59], J. Z. Wang[64], W. H. Wang[103], Y. F. Wang[93], R. L. Ward[25], J. Warner[47], M. Was[8], J. Watchi[98], B. Weaver[47], L.-W. Wei[10,22], M. Weinert[10], A. J. Weinstein[1], R. Weiss[15], L. Wen[65], E. K. Wessel[12], P. Wessels[10], J. Westerweck[10], T. Westphal[10], K. Wette[25], J. T. Whelan[58], S. E. Whitcomb[1], B. F. Whiting[5], C. Whittle[6], D. Wilken[10], D. Williams[46], R. D. Williams[1], A. R. Williamson[66], J. L. Willis[1,159], B. Willke[22,10], M. H. Wimmer[10], W. Winkler[10], C. C. Wipf[1], H. Wittel[10,22], G. Woan[46], J. Woehler[10], J. Wofford[58], K. W. K. Wong[93], J. Worden[47], J. L. Wright[46], D. S. Wu[10], D. M. Wysocki[58], S. Xiao[1], H. Yamamoto[1], C. C. Yancey[76], L. Yang[160], M. J. Yap[25],

M. Yazback[5], Hang Yu[15], Haocun Yu[15], M. Yvert[8], A. Zadrożny[132], M. Zanolin[37], T. Zelenova[30], J.-P. Zendri[55], M. Zevin[89], L. Zhang[1], M. Zhang[140], T. Zhang[46], Y.-H. Zhang[58], C. Zhao[65], M. Zhou[89], Z. Zhou[89], S. J. Zhu[38,10], X. J. Zhu[6], A. B. Zimmerman[90], M. E. Zucker[1,15], J. Zweizig[1],

(LIGO Scientific Collaboration and Virgo Collaboration),

C. A. Wilson-Hodge[137], E. Bissaldi[161,162], L. Blackburn[163,15], M. S. Briggs[164], E. Burns[50], W. H. Cleveland[165], V. Connaughton[165], M. H. Gibby[166], M. M Giles[166], A. Goldstein[165], R. Hamburg[164], P. Jenke[164], C. M. Hui[137], R. M. Kippen[167], D. Kocevski[137], S. McBreen[168], C. A. Meegan[164], W. S. Paciesas[165], S. Poolakkil[164], R. D. Preece[164], J. Racusin[50], O. J. Roberts[165], M. Stanbro[164], P. Veres[164], A. von Kienlin[169],

(Fermi GBM),

V. Savchenko[170], C. Ferrigno[170], E. Kuulkers[171], A. Bazzano[172], E. Bozzo[170], S. Brandt[173], J. Chenevez[173], T. J.-L. Courvoisier[170], R. Diehl[169], A. Domingo[174], L. Hanlon[168], E. Jourdain[175], P. Laurent[176,177], F. Lebrun[176], A. Lutovinov[178,179], A. Martin-Carrillo[168], S. Mereghetti[180], L. Natalucci[172], J. Rodi[172], J.-P. Roques[175], R. Sunyaev[178,181], P. Ubertini[172],

(INTEGRAL),

M. G. Aartsen[182], M. Ackermann[183], J. Adams[184], J. A. Aguilar[185], M. Ahlers[186], M. Ahrens[187], I. Al Samarai[188], D. Altmann[189], K. Andeen[190], T. Anderson[191], I. Ansseau[185], G. Anton[189], C. Argüelles[192], J. Auffenberg[193], S. Axani[192], H. Bagherpour[184], X. Bai[194], J. P. Barron[195], S. W. Barwick[196], V. Baum[197], R. Bay[198], J. J. Beatty[199,200], J. Becker Tjus[201], E. Bernardini[183], D. Z. Besson[202], G. Binder[198,203], D. Bindig[204], E. Blaufuss[205], S. Blot[183], C. Bohm[187], M. Börner[206], F. Bos[201], D. Bose[207], S. Böser[197], O. Botner[208], E. Bourbeau[186], J. Bourbeau[209], F. Bradascio[183], J. Braun[210], L. Brayeur[210], M. Brenzke[193], H.-P. Bretz[183], S. Bron[188], J. Brostean-Kaiser[183], A. Burgman[208], T. Carver[188], J. Casey[209], M. Casier[210], E. Cheung[205], D. Chirkin[209], A. Christov[188], K. Clark[211], L. Classen[212], S. Coenders[213], G. H. Collin[192], J. M. Conrad[192], D. F. Cowen[191,214], R. Cross[202], M. Day[209], J. P. A. M. de André[216], C. De Clercq[210], J. J. DeLaunay[191], H. Dembinski[217], S. De Ridder[218], P. Desiati[209], K. D. de Vries[210], G. de Wasseige[210], M. de With[219], T. DeYoung[216], J. C. Díaz-Vélez[209], V. di Lorenzo[197], H. Dujmovic[207], J. P. Dumm[187], M. Dunkman[191], E. Dvorak[194], B. Eberhardt[197], T. Ehrhardt[197], B. Eichmann[201], P. Eller[191], P. A. Evenson[217], S. Fahey[209], A. R. Fazely[220], J. Felde[205], K. Filimonov[198], C. Finley[187], S. Flis[187], A. Franckowiak[183], E. Friedman[205], T. Fuchs[206], T. K. Gaisser[217], J. Gallagher[221], L. Gerhardt[205], K. Ghorbani[209], W. Giang[195], T. Glauch[193], T. Glüsenkamp[189], A. Goldschmidt[205], J. G. Gonzalez[217], D. Grant[195], Z. Griffith[209], C. Haack[193], A. Hallgren[208], F. Halzen[209], K. Hanson[209], D. Hebecker[219], D. Heereman[185], K. Helbing[204], R. Hellauer[205], S. Hickford[204], J. Hignight[216], G. C. Hill[182], K. D. Hoffman[205], R. Hoffmann[204], B. Hokanson-Fasig[209], K. Hoshina[209,222], F. Huang[191], M. Huber[213], K. Hultqvist[187], M. Hünnefeld[206], S. In[207], A. Ishihara[223], E. Jacobi[183], G. S. Japaridze[224], M. Jeong[207], K. Jero[209], B. J. P. Jones[225], P. Kalaczynski[193], W. Kang[207], A. Kappes[212], T. Karg[183], A. Karle[209], M. Kauer[209], A. Keivani[191], J. L. Kelley[209], A. Kheirandish[209], J. Kim[207], M. Kim[223], T. Kintscher[183], J. Kiryluk[226], T. Kittler[189], S. R. Klein[205,198], G. Kohnen[227], R. Koirala[217], H. Kolanoski[219], L. Köpke[197], C. Kopper[195], S. Kopper[228], J. P. Koschinsky[193], D. J. Koskinen[186], M. Kowalski[219,183], K. Krings[213], M. Kroll[201], G. Krückl[197], J. Kunnen[210], S. Kunwar[183], N. Kurahashi[229], T. Kuwabara[223], A. Kyriacou[182], M. Labare[218], J. L. Lanfranchi[191], M. J. Larson[186], F. Lauber[204], M. Lesiak-Bzdak[226], M. Leuermann[193], Q. R. Liu[209], L. Lu[223], J. Lünemann[210], W. Luszczak[209], J. Madsen[230], G. Maggi[210], K. B. M. Mahn[216], S. Mancina[209], R. Maruyama[231], K. Mase[223], R. Maunu[205], F. McNally[209], K. Meagher[185], M. Medici[186], M. Meier[206], T. Menne[206], G. Merino[209], T. Meures[185], S. Miarecki[205,198], J. Micallef[216], G. Momenté[197], T. Montaruli[188], R. W. Moore[195], M. Moulai[192], R. Nahnhauer[183], P. Nakarmi[228], U. Naumann[204], G. Neer[216], H. Niederhausen[226], S. C. Nowicki[195], D. R. Nygren[203], A. Obertacke Pollmann[204], A. Olivas[205], A. O'Murchadha[185], T. Palczewski[203,198], H. Pandya[217], D. V. Pankova[191], P. Peiffer[197], J. A. Pepper[228], C. Pérez de los Heros[208], D. Pieloth[206], E. Pinat[185], P. B. Price[198], G. T. Przybylski[203], C. Raab[185], L. Rädel[193], M. Rameez[186], K. Rawlins[232], I. C. Rea[213], R. Reimann[193], B. Relethford[229], M. Relich[223], E. Resconi[213], W. Rhode[206], M. Richman[229], S. Robertson[182], M. Rongen[193], C. Rott[207], T. Ruhe[206], D. Ryckbosch[218], D. Rysewyk[216], T. Sälzer[193], S. E. Sanchez Herrera[195], A. Sandrock[206], J. Sandroos[197], M. Santander[228], S. Sarkar[186,233], S. Sarkar[195], K. Satalecka[183], P. Schlunder[206], T. Schmidt[205], A. Schneider[209], S. Schoenen[193], S. Schöneberg[201], L. Schumacher[193], D. Seckel[217], S. Seunarine[230], J. Soedingrekso[206], D. Soldin[204], M. Song[205], G. M. Spiczak[230], C. Spiering[183], J. Stachurska[183], M. Stamatikos[199], T. Stanev[217], A. Stasik[183], J. Stettner[193], A. Steuer[197], T. Stezelberger[203], R. G. Stokstad[203], A. Stössl[223], N. L. Strotjohann[183], T. Stuttard[186], G. W. Sullivan[205], M. Sutherland[199], I. Taboada[234], J. Tatar[203,198], F. Tenholt[201], S. Ter-Antonyan[220], A. Terliuk[183], G. Tešić[191], S. Tilav[217], P. A. Toale[228], M. N. Tobin[209], S. Toscano[210], D. Tosi[209], M. Tselengidou[189], C. F. Tung[234], A. Turcati[213], C. F. Turley[191], B. Ty[209], E. Unger[208], M. Usner[183], J. Vandenbroucke[209], W. Van Driessche[218], N. van Eijndhoven[210], S. Vanheule[218], J. van Santen[183], M. Vehring[193], E. Vogel[193], M. Vraeghe[218], C. Walck[187], A. Wallace[182], M. Wallraff[193], F. D. Wandler[195], N. Wandkowsky[209], A. Waza[193], C. Weaver[195], M. J. Weiss[191], C. Wendt[209], J. Werthebach[206], B. J. Whelan[182], K. Wiebe[197], C. H. Wiebusch[193], L. Wille[209], D. R. Williams[228], L. Wills[229], M. Wolf[209], T. R. Wood[195], E. Woolsey[195], K. Woschnagg[198], D. L. Xu[209], X. W. Xu[220], Y. Xu[226], J. P. Yanez[195], G. Yodh[196], S. Yoshida[223], T. Yuan[209], M. Zoll[187],

(IceCube Collaboration),

A. Balasubramanian[235,236], S. Mate[236], V. Bhalerao[236], D. Bhattacharya[19], A. Vibhute[19], G. C. Dewangan[19], A. R. Rao[119], S. V. Vadawale[237],

(AstroSat Cadmium Zinc Telluride Imager Team),

D. S. Svinkin[238], K. Hurley[239], R. L. Aptekar[238], D. D. Frederiks[238], S. V. Golenetskii[238], A. V. Kozlova[238], A. L. Lysenko[238], Ph. P. Oleynik[238], A. E. Tsvetkova[238], M. V. Ulanov[238], T. Cline[240],

(IPN Collaboration),

T. P. Li[241,82,242], S. L. Xiong[241], S. N. Zhang[241,242], F. J. Lu[241], L. M. Song[241], X. L. Cao[241], Z. Chang[241], G. Chen[241], L. Chen[243], T. X. Chen[241], Y. Chen[241], Y. B. Chen[82], Y. P. Chen[241], W. Cui[241,82], W. W. Cui[241], J. K. Deng[82], Y. W. Dong[241], Y. Y. Du[241], M. X. Fu[82], G. H. Gao[241,242], H. Gao[241,242], M. Gao[241], M. Y. Ge[241], Y. D. Gu[241], J. Guan[241], C. C. Guo[241,242], D. W. Han[241], W. Hu[241], Y. Huang[241], J. Huo[241], S. M. Jia[241], L. H. Jiang[241], W. C. Jiang[241], J. Jin[241], Y. J. Jin[82], B. Li[241], C. K. Li[241], G. Li[241], M. S. Li[241], W. Li[241], X. Li[241], X. B. Li[241], X. F. Li[241], Y. G. Li[241], Z. J. Li[241,242], Z. W. Li[241], X. H. Liang[241], J. Y. Liao[241], C. Z. Liu[241], G. Q. Liu[82], H. W. Liu[241], S. Z. Liu[241], X. J. Liu[241], Y. Liu[241], Y. N. Liu[82], B. Lu[241], X. F. Lu[241], T. Luo[241], X. Ma[241], B. Meng[241], Y. Nang[241,242], J. Y. Nie[241], G. Ou[241], J. L. Qu[241], N. Sai[241,242], L. Sun[241], Y. Tan[241], L. Tao[241], W. H. Tao[241], Y. L. Tuo[241,242], G. F. Wang[241], H. Y. Wang[241], J. Wang[241], W. S. Wang[241], Y. S. Wang[241], X. Y. Wen[241], B. B. Wu[241], M. Wu[241], G. C. Xiao[241,242], H. Xu[241], Y. P. Xu[241], L. L. Yan[241,242], J. W. Yang[241], S. Yang[241], Y. J. Yang[241], A. M. Zhang[241], C. L. Zhang[241], C. M. Zhang[241], F. Zhang[241], H. M. Zhang[241], J. Zhang[241], Q. Zhang[241], S. Zhang[241], T. Zhang[241], W. Zhang[241,242], W. C. Zhang[241], W. Z. Zhang[243], Y. Zhang[241], Y. Zhang[241,242], Y. F. Zhang[241], Y. J. Zhang[241], Z. Zhang[82], Z. L. Zhang[241], H. S. Zhao[241], J. L. Zhao[241], X. F. Zhao[241,242], S. J. Zheng[241], Y. Zhu[241], Y. X. Zhu[241], C. L. Zou[241],

(The Insight-HXMT Collaboration),

A. Albert[244], M. André[245], M. Anghinolfi[246,247], M. Ardid[247], J.-J. Aubert[248], J. Aublin[249], T. Avgitas[249], B. Baret[249], J. Barrios-Martí[250], S. Basa[251], B. Belhorma[252], V. Bertin[248], S. Biagi[253], R. Bormuth[14,254], S. Bourret[249], M. C. Bouwhuis[14], H. Brânzaş[255], R. Bruijn[14,256], J. Brunner[248], J. Busto[248], A. Capone[257,258], L. Caramete[255], J. Carr[248], S. Celli[257,258,259], R. Cherkaoui El Moursli[260], T. Chiarusi[261], M. Circella[262], J. A. B. Coelho[249], A. Coleiro[249,250], R. Coniglione[253], H. Costantini[248], P. Coyle[248], A. Creusot[249], A. F. Díaz[263], A. Deschamps[264], G. De Bonis[258], C. Distefano[253], I. Di Palma[257,258], A. Domi[246,265], C. Donzaud[249,266], D. Dornic[248], D. Drouhin[244], T. Eberl[189,260,267], I. El Bojaddaini[267], N. El Khayati[260], D. Elsässer[268], A. Enzenhöfer[248], A. Ettahiri[260], F. Fassi[260], I. Felis[247], L. A. Fusco[261,269], P. Gay[270,249], V. Giordano[271], H. Glotin[272,273], T. Grégoire[249], R. Gracia Ruiz[249], K. Graf[189], S. Hallmann[189], H. van Haren[274], A. J. Heijboer[14], Y. Hello[264], J. J. Hernández-Rey[250], J. Hössl[189], J. Hofestädt[189], C. Hugon[246,265], G. Illuminati[250], C. W. James[189], M. de Jong[14,254], M. Jongen[14], M. Kadler[268], O. Kalekin[189], U. Katz[189], D. Kiessling[189], A. Kouchner[249,273], M. Kreter[268], I. Kreykenbohm[275], V. Kulikovskiy[248,276], C. Lachaud[249], R. Lahmann[189], D. Lefèvre[277], E. Leonora[271,278], M. Lotze[250], S. Loucatos[279,249], M. Marcelin[251], A. Margiotta[261,269], A. Marinelli[280,281], J. A. Martínez-Mora[247], R. Mele[282,283], K. Melis[14,256], T. Michael[14], P. Migliozzi[282], A. Moussa[267], S. Navas[284], E. Nezri[251], M. Organokov[285], G. E. Păvălaş[255], C. Pellegrino[261,269], C. Perrina[257,258], P. Piattelli[253], V. Popa[255], T. Pradier[285], L. Quinn[248], C. Racca[244], G. Riccobene[253], A. Sánchez-Losa[262], M. Saldaña[247], I. Salvadori[248], D. F. E. Samtleben[14,254], M. Sanguineti[246,265], P. Sapienza[253], C. Sieger[189], M. Spurio[261,269], Th. Stolarczyk[279], M. Taiuti[246,265], Y. Tayalati[260], A. Trovato[253], D. Turpin[248], C. Tönnis[250], B. Vallage[279,249], V. Van Elewyck[249,273], F. Versari[261,269], D. Vivolo[282,283], A. Vizzoca[257,258], J. Wilms[275], J. D. Zornoza[250], J. Zúñiga[250],

(ANTARES Collaboration),

A. P. Beardmore[286], A. A. Breeveld[287], D. N. Burrows[288], S. B. Cenko[289,290], G. Cusumano[291], A. D'Aì[291], M. de Pasquale[292], S. W. K. Emery[287], P. A. Evans[286], P. Giommi[293], C. Gronwall[288,294], J. A. Kennea[288], H. A. Krimm[295,296], N. P. M. Kuin[287], A. Lien[297,298], F. E. Marshall[287], A. Melandri[299], J. A. Nousek[288], S. R. Oates[300], J. P. Osborne[286], C. Pagani[286], K. L. Page[286], D. M. Palmer[301], M. Perri[302,293], M. H. Siegel[288], B. Sbarufatti[288], G. Tagliaferri[299], A. Tohuvavohu[288,303],

(The Swift Collaboration),

M. Tavani[304,305,306], F. Verrecchia[307,308], A. Bulgarelli[309], Y. Evangelista[304], L. Pacciani[304], M. Feroci[304], C. Pittori[307,308], A. Giuliani[310], E. Del Monte[304], I. Donnarumma[311], A. Argan[304], A. Trois[312], A. Ursi[304], M. Cardillo[304], G. Piano[304], F. Longo[313], F. Lucarelli[307,308], P. Munar-Adrover[314], F. Fuschino[309], C. Labanti[309], M. Marisaldi[315], G. Minervini[304], V. Fioretti[309], N. Parmiggiani[309], F. Gianotti[309], M. Trifoglio[309], G. Di Persio[304], L. A. Antonelli[311], G. Barbiellini[313], P. Caraveo[310], P. W. Cattaneo[316], E. Costa[304], S. Colafrancesco[317], F. D'Amico[311], A. Ferrari[318], A. Morselli[319], F. Paoletti[320], P. Picozza[319], M. Pilia[312], A. Rappoldi[316], P. Soffitta[304], S. Vercellone[321],

(AGILE Team),

R. J. Foley[322], D. A. Coulter[322], C. D. Kilpatrick[322], M. R. Drout[323], A. L. Piro[323], B. J. Shappee[323,324], M. R. Siebert[322], J. D. Simon[323], N. Ulloa[325], D. Kasen[326,327], B. F. Madore[323], A. Murguia-Berthier[322], Y.-C. Pan[322], J. X. Prochaska[322], E. Ramirez-Ruiz[322,328], A. Rest[329,330], C. Rojas-Bravo[322],

(The 1M2H Team),

E. Berger[163], M. Soares-Santos[331,332], J. Annis[332], K. D. Alexander[163], S. Allam[332], E. Balbinot[333], P. Blanchard[163], D. Brout[334], R. E. Butler[335,332], R. Chornock[336], E. R. Cook[337,338], P. Cowperthwaite[163], H. T. Diehl[332], A. Drlica-Wagner[332], M. R. Drout[339], F. Durret[340], T. Eftekhari[163], D. A. Finley[332], W. Fong[341], J. A. Frieman[332], C. L. Fryer[342], J. García-Bellido[343], R. A. Gruendl[344], W. Hartley[345,346], K. Herner[332], R. Kessler[347], H. Lin[332], P. A. A. Lopes[348], A. C. C. Lourenço[348], R. Margutti[349], J. L. Marshall[337], T. Matheson[350], G. E. Medina[351], B. D. Metzger[352], R. R. Muñoz[351], J. Muir[353], M. Nicholl[163], P. Nugent[354], A. Palmese[345], F. Paz-Chinchón[344], E. Quataert[355], M. Sako[334], M. Sauseda[337], D. J. Schlegel[356], D. Scolnic[347], L. F. Secco[334], N. Smith[357], F. Sobreira[358,359], V. A. Villar[163], A. K. Vivas[360], W. Wester[332], P. K. G. Williams[163], B. Yanny[332], A. Zenteno[360], Y. Zhang[332], T. M. C. Abbott[360], M. Banerji[361,362], K. Bechtol[338], A. Benoit-Lévy[363,345,364], E. Bertin[363,364], D. Brooks[345], E. Buckley-Geer[332], D. L. Burke[365,366], D. Capozzi[367], A. Carnero Rosell[359,368], M. Carrasco Kind[369,344], F. J. Castander[370], M. Crocce[370], C. E. Cunha[365], C. B. D'Andrea[334], L. N. da Costa[359,368], C. Davis[365], D. L. DePoy[371], S. Desai[372], J. P. Dietrich[373,374], T. F. Eifler[375,376], E. Fernandez[377], B. Flaugher[332], P. Fosalba[370], E. Gaztanaga[370], D. W. Gerdes[378,379], T. Giannantonio[361,362,380], D. A. Goldstein[381,354], D. Gruen[365,366], J. Gschwend[359,368], G. Gutierrez[332], K. Honscheid[382,383], D. J. James[384], T. Jeltema[385], M. W. G. Johnson[344], M. D. Johnson[344], S. Kent[332,347], E. Krause[365], R. Kron[332,347], K. Kuehn[386], O. Lahav[345], M. Lima[387,359], M. A. G. Maia[359,368], M. March[334], P. Martini[382,388], R. G. McMahon[361,362], F. Menanteau[369,344], C. J. Miller[378,379], R. Miquel[389,377], J. J. Mohr[373,374,390], R. C. Nichol[367], R. L. C. Ogando[359,368], A. A. Plazas[376], A. K. Romer[391], A. Roodman[365,366], E. S. Rykoff[365,366], E. Sanchez[392], V. Scarpine[332], R. Schindler[366], M. Schubnell[379], I. Sevilla-Noarbe[392], E. Sheldon[393], M. Smith[394], R. C. Smith[360], A. Stebbins[332], E. Suchyta[395], M. E. C. Swanson[344], G. Tarle[379], R. C. Thomas[354], M. A. Troxel[382,383], D. L. Tucker[332], V. Vikram[396], A. R. Walker[360], R. H. Wechsler[397,365,366], J. Weller[373,390,380], J. L. Carlin[338], M. S. S. Gill[366], T. S. Li[332], J. Marriner[332], E. Neilsen[332],
(The Dark Energy Camera GW-EM Collaboration and the DES Collaboration),
J. B. Haislip[398], V. V. Kouprianov[398], D. E. Reichart[398], D. J. Sand[399], L. Tartaglia[399,400], S. Valenti[400], S. Yang[400,401,402],
(The DLT40 Collaboration),
S. Benetti[403], E. Brocato[404], S. Campana[405], E. Cappellaro[403], S. Covino[405], P. D'Avanzo[405], V. D'Elia[404,406], F. Getman[407], G. Ghirlanda[405], G. Ghisellini[405], L. Limatola[407], L. Nicastro[408], E. Palazzi[408], E. Pian[408], S. Piranomonte[404], A. Possenti[312], A. Rossi[408], O. S. Salafia[409,405], L. Tomasella[403], L. Amati[408], L. A. Antonelli[404], M. G. Bernardini[410,405], F. Bufano[411], M. Capaccioli[407,412], P. Casella[404], M. Dadina[408], G. De Cesare[408], A. Di Paola[404], G. Giuffrida[404], A. Giunta[404], G. L. Israel[404], M. Lisi[404], E. Maiorano[408], M. Mapelli[403,413], N. Masetti[408,414], A. Pescalli[415,405], L. Pulone[404], R. Salvaterra[416], P. Schipani[407], M. Spera[403], A. Stamerra[146,417], L. Stella[404], V. Testa[404], M. Turatto[403], D. Vergani[408], G. Aresu[312], M. Bachetti[312], F. Buffa[312], M. Burgay[312], M. Buttu[312], T. Caria[312], E. Carretti[312], V. Casasola[418], P. Castangia[312], G. Carboni[312], S. Casu[312], R. Concu[312], A. Corongiu[312], G. L. Deiana[312], E. Egron[312], A. Fara[312], F. Gaudiomonte[312], V. Gusai[312], A. Ladu[312], S. Loru[312], S. Leurini[312], L. Marongiu[312], A. Melis[312], G. Melis[312], Carlo Migoni[312], Sabrina Milia[312], Alessandro Navarrini[312], A. Orlati[312], P. Ortu[312], S. Palmas[312], A. Pellizzoni[312], D. Perrodin[312], T. Pisanu[312], S. Poppi[312], S. Righini[419], A. Saba[312], G. Serra[312], M. Serrau[312], M. Stagni[419], G. Surcis[312], V. Vacca[312], G. P. Vargiu[312], L. K. Hunt[418], Z. P. Jin[420], S. Klose[421], C. Kouveliotou[422,423], P. A. Mazzali[424,425], P. Møller[426], L. Nava[405,427], T. Piran[428], J. Selsing[328], S. D. Vergani[429,405], K. Wiersema[430], K. Toma[431,432], A. B. Higgins[430], C. G. Mundell[433], S. di Serego Alighieri[418], D. Götz[434], W. Gao[435], A. Gomboc[436], L. Kaper[437], S. Kobayashi[438], D. Kopac[439], J. Mao[440], R. L. C. Starling[430], I. Steele[441], A. J. van der Horst[442,423],
(GRAWITA: GRAvitational Wave Inaf TeAm),
F. Acero[443], W. B. Atwood[444], L. Baldini[445], G. Barbiellini[446,447], D. Bastieri[448,449], B. Berenji[450], R. Bellazzini[451], E. Bissaldi[452,453], R. D. Blandford[454], E. D. Bloom[454], R. Bonino[455,456], E. Bottacini[454], J. Bregeon[457], R. Buehler[469], S. Buson[50], R. A. Cameron[454], R. Caputo[459], P. A. Caraveo[180], E. Cavazzuti[460], A. Chekhtman[461], C. C. Cheung[462], J. Chiang[454], S. Ciprini[462,463], J. Cohen-Tanugi[457], L. R. Cominsky[465], D. Costantin[449], A. Cuoco[466,455], F. D'Ammando[466,467], F. de Palma[453,468], S. W. Digel[454], N. Di Lalla[445], M. Di Mauro[454], L. Di Venere[452,453], R. Dubois[454], S. J. Fegan[458], W. B. Focke[454], A. Franckowiak[458], Y. Fukazawa[471], S. Funk[189], P. Fusco[452,453], F. Gargano[453], D. Gasparrini[462,464], N. Giglietto[452,453], F. Giordano[452,453], M. Giroletti[466], T. Glanzman[454], D. Green[472,50], M.-H. Grondin[473], L. Guillemot[474,475], S. Guiriec[50,422], A. K. Harding[50], D. Horan[458], G. Jóhannesson[476,477], T. Kamae[478], S. Kensei[471], M. Kuss[451], G. La Mura[449], L. Latronico[455], M. Lemoine-Goumard[473], F. Longo[446,447], F. Loparco[452,453], M. N. Lovellette[462], P. Lubrano[463], J. D. Magill[472], S. Maldera[455], A. Manfreda[445], M. N. Mazziotta[453], J. E. McEnery[50,472], M. Meyer[454], P. F. Michelson[454], N. Mirabal[50], M. E. Monzani[454], E. Moretti[481], A. Morselli[479], I. V. Moskalenko[454], M. Negro[455,456], E. Nuss[457], R. Ojha[50], N. Omodei[454], M. Orienti[467], E. Orlando[454], M. Palatiello[446,446], V. S. Paliya[480], D. Paneque[481], M. Pesce-Rollins[451], F. Piron[457], T. A. Porter[454], G. Principe[189], S. Rainò[452,453], R. Rando[448,449], M. Razzano[451], S. Razzaque[482], A. Reimer[483,454], O. Reimer[483,454], T. Reposeur[473], L. S. Rochester[454], P. M. Saz Parkinson[444,484,485], C. Sgrò[451], E. J. Siskind[486], F. Spada[451], G. Spandre[451], D. J. Suson[487], M. Takahashi[481], Y. Tanaka[488], J. G. Thayer[454], J. B. Thayer[454], D. J. Thompson[50], L. Tibaldo[489,490], D. F. Torres[491,492], E. Torresi[493], E. Troja[50,472], T. M. Venters[50],

      Abbott et al.

G. Vianello[454], G. Zaharijas[446,447,494],

(The Fermi Large Area Telescope Collaboration),

J. R. Allison[495,496], K. W. Bannister[497], D. Dobie[495,497,498], D. L. Kaplan[499], E. Lenc[495,498], C. Lynch[495,498], T. Murphy[495,498], E. M. Sadler[495,498],

(ATCA: Australia Telescope Compact Array),

A. Hotan[500], C. W. James[501], S. Oslowski[502], W. Raja[497], R. M. Shannon[497,501], M. Whiting[497],

(ASKAP: Australian SKA Pathfinder),

I. Arcavi[503,504], D. A. Howell[503,504], C. McCully[503,504], G. Hosseinzadeh[503,504], D. Hiramatsu[503,504], D. Poznanski[505], J. Barnes[506], M. Zaltzman[505], S. Vasylyev[503,504], D. Maoz[505],

(Las Cumbres Observatory Group),

J. Cooke[507,508,509], M. Bailes[507,508], C. Wolf[510,509,508], A. T. Deller[507,508,509], C. Lidman[511,509], L. Wang[512,513,514], B. Gendre[515], I. Andreoni[507,508,511,509], K. Ackley[516], T. A. Pritchard[507], M. S. Bessell[510], S.-W. Chang[510,509], A. Möller[510,509], C. A. Onken[510,509], R. A. Scalzo[510,509,517], R. Ridden-Harper[510], R. G. Sharp[510,509], B. E. Tucker[510,509], T. J. Farrell[511], E. Elmer[518], S. Johnston[519,509], V. Venkatraman Krishnan[507,509], E. F. Keane[520,509], J. A. Green[519], A. Jameson[507,509], L. Hu[513,514], B. Ma[521,514], T. Sun[513,514], X. Wu[513,514], X. Wang[522], Z. Shang[521,523,514], Y. Hu[521,514], M. C. B. Ashley[524], X. Yuan[525,514], X. Li[525,514], C. Tao[522], Z. Zhu[526], H. Zhang[527], N. B. Suntzeff[512], J. Zhou[527], J. Yang[513], B. Orange[528], D. Morris[515], A. Cucchiara[515], T. Giblin[529], A. Klotz[530], J. Staff[515], P. Thierry[531], B. P. Schmidt[532,509],

(OzGrav, DWF (Deeper, Wider, Faster program), AST3, and CAASTRO Collaborations),

N. R. Tanvir[533], A. J. Levan[300], Z. Cano[52,534], A. de Ugarte-Postigo[527,534], C. González-Fernández[535], J. Greiner[536], J. Hjorth[328], M. Irwin[535], T. Krühler[536], I. Mandel[537], B. Milvang-Jensen[328], P. O'Brien[533], E. Rol[538], S. Rosetti[533], S. Rosswog[539], A. Rowlinson[540,541], D. T. H. Steeghs[300], C. C. Thöne[534], K. Ulaczyk[300], D. Watson[328], S. H. Bruun[328], R. Cutter[300], R. Figuera Jaimes[542], Y. I. Fujii[543,544], A. S. Fruchter[545], B. Gompertz[300], P. Jakobsson[546], G. Hodosan[534], U. G. Jèrgensen[543], T. Kangas[545], D. A. Kann[534], M. Rabus[547,548], S. L. Schrøder[328], E. R. Stanway[300], R. A. M. J. Wijers[540],

(The VINROUGE Collaboration),

V. M. Lipunov[549,550], E. S. Gorbovskoy[550], V. G. Kornilov[549,550], N. V. Tyurina[550], P. V. Balanutsa[550], A. S. Kuznetsov[550], D. M. Vlasenko[549,550], R. C. Podesta[551], C. Lopez[551], F. Podesta[551], H. O. Levato[552], C. Saffe[552], C. C. Mallamaci[553], N. M. Budnev[554], O. A. Gress[554,550], D. A. Kuvshinov[549,550], I. A. Gorbunov[549,550], V. V. Vladimirov[550], D. S. Zimnukhov[549,550], A. V. Gabovich[555], V. V. Yurkov[555], Yu. P. Sergienko[555], R. Rebolo[556], M. Serra-Ricart[556], A. G. Tlatov[557], Yu. V. Ishmuhametova[554],

(MASTER Collaboration),

F. Abe[558], K. Aoki[559], W. Aoki[560], Y. Asakura[558,956], S. Baar[561], S. Barway[562], I. A. Bond[563], M. Doi[564], F. Finet[559], T. Fujiyoshi[559], H. Furusawa[560], S. Honda[561], R. Itoh[565], N. Kanda[566], K. S. Kawabata[567], M. Kawabata[568], J. H. Kim[559], S. Koshida[559], D. Kuroda[569], C.-H. Lee[559], W. Liu[567,570], K. Matsubayashi[569], S. Miyazaki[571], K. Morihana[572], T. Morokuma[564], K. Motohara[564], K. L. Murata[565], H. Nagai[560], H. Nagashima[568], T. Nagayama[573], T. Nakaoka[568], F. Nakata[559], R. Ohsawa[564], T. Ohshima[561], K. Ohta[574], H. Okita[559], T. Saito[561], Y. Saito[565], S. Sako[564,575], Y. Sekiguchi[576], T. Sumi[571], A. Tajitsu[559], J. Takahashi[561], M. Takayama[561], Y. Tamura[572], I. Tanaka[559], M. Tanaka[560], T. Terai[559], N. Tominaga[577,578], P. J. Tristram[579], M. Uemura[567], Y. Utsumi[567], M. S. Yamaguchi[564], N. Yasuda[578], M. Yoshida[559], T. Zenko[574],

(J-GEM),

S. M. Adams[580], G. C. Anupama[581], J. Bally[582], S. Barway[583], E. Bellm[584], N. Blagorodnova[580], C. Cannella[580], P. Chandra[585], D. Chatterjee[586], T. E. Clarke[587], B. E. Cobb[588], D. O. Cook[580], C. Copperwheat[441], K. De[580], S. W. K. Emery[589], U. Feindt[591], K. Foster[580], O. D. Fox[592], D. A. Frail[593], C. Fremling[580], C. Frohmaier[594,595], J. A. Garcia[580], S. Ghosh[586], S. Giacintucci[587], A. Goobar[591], O. Gottlieb[596], B. W. Grefenstette[580], G. Hallinan[580], F. Harrison[580], M. Heida[580], G. Helou[597], A. Y. Q. Ho[580], A. Horesh[598], K. Hotokezaka[599], W.-H. Ip[600], R. Itoh[601], Bob Jacobs[66], J. E. Jencson[580], D. Kasen[602,603], M. M. Kasliwal[580], N. E. Kassim[587], H. Kim[604], B. S. Kiran[581], N. P. M. Kuin[589], S. R. Kulkarni[580], T. Kupfer[580], R. M. Lau[580], K. Madsen[580], P. A. Mazzali[441,605], A. A. Miller[606,607], H Miyasaka[580], K. Mooley[608], S. T. Myers[593], E. Nakar[596], C.-C. Ngeow[600], P. Nugent[602,354], E. O. Ofek[609], N. Palliyaguru[610], M. Pavana[581], D. A. Perley[611], W. M. Peters[587], S. Pike[580], T. Piran[598], H. Qi[586], R. M. Quimby[612,613], J. Rana[19], S. Rosswog[614], F. Rusu[615], E. M. Sadler[495,616], A. Van Sistine[586], J. Sollerman[614], Y. Xu[580], L. Yan[580,597], Y. Yatsu[601], P.-C. Yu[600], C. Zhang[586], W. Zhao[615],

(GROWTH, JAGWAR, Caltech-NRAO, TTU-NRAO, and NuSTAR Collaborations),

K. C. Chambers[617], M. E. Huber[617], A. S. B. Schultz[617], J. Bulger[617], H. Flewelling[617], E. A. Magnier[617], T. B. Lowe[617], R. J. Wainscoat[617], C. Waters[617], M. Willman[617],

(Pan-STARRS),

K. Ebisawa[618], C. Hanyu[619], S. Harita[620], T. Hashimoto[621], K. Hidaka[619], T. Hori[622], M. Ishikawa[623], N. Isobe[618], W. Iwakiri[624], H. Kawai[625], N. Kawai[620,624], T. Kawamuro[626], T. Kawase[627], Y. Kitaoka[621], K. Makishima[624], M. Matsuoka[624], T. Mihara[624], T. Morita[622], K. Morita[620], S. Nakahira[624], M. Nakajima[627], Y. Nakamura[625], H. Negoro[627], S. Oda[622], A. Sakamaki[627], R. Sasaki[625], M. Serino[621], M. Shidatsu[624], R. Shimomukai[618], Y. Sugawara[618], S. Sugita[620], M. Sugizaki[624], Y. Tachibana[620], Y. Takao[624], A. Tanimoto[622], H. Tomida[618], Y. Tsuboi[625], H. Tsunemi[628], Y. Ueda[622], S. Ueno[618], S. Yamada[622], K. Yamaoka[629], M. Yamauchi[619], F. Yatabe[624], T. Yoneyama[628], T. Yoshii[620],

(The MAXI Team),

D. M. Coward[630], H. Crisp[630], D. Macpherson[630], I. Andreoni[631], R. Laugier[632], K. Noysena[632,633], A. Klotz[633], B. Gendre[632,634], P. Thierry[635], D. Turpin[630],

(TZAC Consortium),

M. Im[636], C. Choi[636], J. Kim[636], Y. Yoon[636], G. Lim[636], S.-K. Lee[636], C.-U. Lee[637], S.-L. Kim[637], S.-W. Ko[637], J. Joe[637], M.-K. Kwon[637], P.-J. Kim[637], S.-K. Lim[637], J.-S. Choi[637],

(KU Collaboration),

J. P. U. Fynbo[328], D. Malesani[328], D. Xu[638],

(Nordic Optical Telescope),

S. J. Smartt[639], A. Jerkstrand[425], E. Kankare[639], S. A. Sim[639], M. Fraser[168], C. Inserra[640], K. Maguire[639], G. Leloudas[328], M. Magee[639], L. J. Shingles[639], K. W. Smith[639], D. R. Young[639], R. Kotak[639], A. Gal-Yam[641], J. D. Lyman[642], D. S. Homan[643], C. Agliozzo[644,645], J. P. Anderson[646], C. R. Angus[640], C. Ashall[611], C. Barbarino[647], F. E. Bauer[648,645,649], M. Berton[650,651], M. T. Botticella[652], M. Bulla[653], G. Cannizzaro[654], R. Cartier[640], A. Cikota[655], P. Clark[639], A. De Cia[655], M. Della Valle[652,656], M. Dennefeld[657], L. Dessart[658], G. Dimitriadis[640], N. Elias-Rosa[659], R. E. Firth[640], A. Flörs[655,425], C. Frohmaier[660], L. Galbany[661], S. González-Gaitán[662], M. Gromadzki[663], C. P. Gutiérrez[640], A. Hamanowicz[655,663], J. Harmanen[664], K. E. Heintz[546,328], M.-S. Hernandez[665], S. T. Hodgkin[666], I. M. Hook[667], L. Izzo[668], P. A. James[611], P. G. Jonker[654,66], W. E. Kerzendorf[655], Z. Kostrzewa-Rutkowska[654,66], M. Kromer[669,670], H. Kuncarayakti[671,664], A. Lawrence[643], I. Manulis[641], S. Mattila[664], O. McBrien[639], A. Müller[672], J. Nordin[673], D. O'Neill[639], F. Onori[654], J. T. Palmerio[674], A. Pastorello[675], F. Patat[655], G. Pignata[644,645], P. Podsiadlowski[676], A. Razza[646,677], T. Reynolds[664], R. Roy[647], A. J. Ruiter[678,532,679], K. A. Rybicki[663], L. Salmon[168], M. L. Pumo[680,675,681], S. J. Prentice[611], I. R. Seitenzahl[678,532], M. Smith[640], J. Sollerman[647], M. Sullivan[640], H. Szegedi[682], F. Taddia[647], S. Taubenberger[655,425], G. Terreran[349,675], B. Van Soelen[682], J. Vos[665], N. A. Walton[666], D. E. Wright[683], Ł. Wyrzykowski[663], O. Yaron[641],

(ePESSTO) ,

T.-W. Chen[684], T. Krühler[684], P. Schady[684], P. Wiseman[684], J. Greiner[684], A. Rau[684], T. Schweyer[684], S. Klose[685], A. Nicuesa Guelbenzu[685],

(GROND),

N. T. Palliyaguru[686],

(Texas Tech University),

M. M. Shara[687,361], T. Williams[688], P. Vaisanen[688,689], S. B. Potter[688], E. Romero Colmenero[688,689], S. Crawford[688,689], D. A. H. Buckley[688], J. Mao[440],

(SALT Group),

M. C. Díaz[690], L. M. Macri[691], D. García Lambas[692], C. Mendes de Oliveira[693], J. L. Nilo Castellón[694,695], T. Ribeiro[696], B. Sánchez[692], W. Schoenell[693,697], L. R. Abramo[698], S. Akras[699], J. S. Alcaniz[699], R. Artola[692], M. Beroiz[690], S. Bonoli[700], J. Cabral[692], R. Camuccio[690], V. Chavushyan[701], P. Coelho[693], C. Colazo[692], M. V. Costa-Duarte[693], H. Cuevas Larenas[695], M. Domínguez Romero[692], D. Dultzin[702], D. Fernández[703], J. García[690], C. Girardini[692], D. R. Gonçalves[704], T. S. Gonçalves[704], S. Gurovich[692], Y. Jiménez-Teja[699], A. Kanaan[697], M. Lares[692], R. Lopes de Oliveira[696,705], O. López-Cruz[701], R. Melia[692], A. Molino[693], N. Padilla[703], T. Peñuela[690,706], V. M. Placco[707,708], C. Quiñones[692], A. Ramírez Rivera[695], V. Renzi[692], L. Riguccini[704], E. Ríos-López[701], H. Rodriguez[692], L. Sampedro[693], M. Schneiter[692], L. Sodré[693], M. Starck[692], S. Torres-Flores[695], M. Tornatore[692], A. Zadrożny[690], M. Castillo[690],

(TOROS: Transient Robotic Observatory of the South Collaboration),

A. J. Castro-Tirado[709,710], J. C. Tello[709], Y.-D. Hu[709], B.-B. Zhang[709], R. Cunniffe[709], A. Castellón[711], D. Hiriart[712], M. D. Caballero-García[713], M. Jelínek[714], P. Kubánek[715], C. Pérez del Pulgar[710], I. H. Park[716], S. Jeong[716], J. M. Castro Cerón[717], S. B. Pandey[718], P. C. Yock[719], R. Querel[720], Y. Fan[721], C. Wang[721],

(The BOOTES Collaboration),

A Beardsley[722], I. S. Brown[499], B. Crosse[501], D. Emrich[501], T. Franzen[501], B. M. Gaensler[723], L. Horsley[501], M. Johnston-Hollitt[724], D. Kenney[501], M. F. Morales[725], D. Pallot[726], M. Sokolowski[501,498,727], K. Steele[501], S. J. Tingay[501,498], C. M. Trott[501,498], M. Walker[501], R. Wayth[501,498], A. Williams[501], C. Wu[726],

(MWA: Murchison Widefield Array),

A. Yoshida[728], T. Sakamoto[728], Y. Kawakubo[728], K. Yamaoka[729], I. Takahashi[730], Y. Asaoka[731], S. Ozawa[731], S. Torii[731], Y. Shimizu[732], T. Tamura[732], W. Ishizaki[733], M. L. Cherry[2], S. Ricciarini[734], A. V. Penacchioni[735], P. S. Marrocchesi[735],
(The CALET Collaboration),

A. S. Pozanenko[736,737,738], A. A. Volnova[736], E. D. Mazaeva[736], P. Yu. Minaev[736], M. A. Krugov[739], A. V. Kusakin[739], I. V. Reva[739], A. S. Moskvitin[740], V. V. Rumyantsev[741], R. Inasaridze[742], E. V. Klunko[743], N. Tungalag[744], S. E. Schmalz[745], O. Burhonov[746],
(IKI-GW Follow-up Collaboration),

H. Abdalla[747], A. Abramowski[748], F. Aharonian[749,750,751], F. Ait Benkhali[749], E. O. Angüner[752], M. Arakawa[753], M. Arrieta[754], P. Aubert[755], M. Backes[756], A. Balzer[757], M. Barnard[747], Y. Becherini[758], J. Becker Tjus[759], D. Berge[760], S. Bernhard[761], K. Bernlöhr[749], R. Blackwell[762], M. Böttcher[747], C. Boisson[754], J. Bolmont[763], S. Bonnefoy[183], P. Bordas[749], J. Bregeon[764], F. Brun[765], P. Brun[766], M. Bryan[757], M. Büchele[189], T. Bulik[767], M. Capasso[768], S. Caroff[470], A. Carosi[755], S. Casanova[752,746], M. Cerruti[763], N. Chakraborty[746], R. C. G. Chaves[764], A. Chen[769], J. Chevalier[755], S. Colafrancesco[769], B. Condon[765], J. Conrad[770], I. D. Davids[756], J. Decock[766], C. Deil[746], J. Devin[764], P. deWilt[762], L. Dirson[745], A. Djannati-Ataï[771], A. Donath[746], L. O'C. Drury[750], K. Dutson[772], J. Dyks[773], T. Edwards[746], K. Egberts[774], G. Emery[763], J.-P. Ernenwein[775], S. Eschbach[189], C. Farnier[770,758], S. Fegan[470], M. V. Fernandes[745], A. Fiasson[755], G. Fontaine[470], S. Funk[189], M. Füssling[183], S. Gabici[771], Y. A. Gallant[764], T. Garrigoux[744], F. Gaté[755], G. Giavitto[183], B. Giebels[470], D. Glawion[776], J. F. Glicenstein[766], D. Gottschall[768], M.-H. Grondin[765], J. Hahn[746], M. Haupt[183], J. Hawkes[762], G. Heinzelmann[745], G. Henri[777], G. Hermann[746], J. A. Hinton[746], W. Hofmann[746], C. Hoischen[774], T. L. Holch[778], M. Holler[761], D. Horns[745], A. Ivascenko[744], H. Iwasaki[753], A. Jacholkowska[763], M. Jamrozy[779], D. Jankowsky[189], F. Jankowsky[776], M. Jingo[769], L. Jouvin[771], I. Jung-Richardt[189], M. A. Kastendieck[745], K. Katarzyński[780], M. Katsuragawa[781,763], D. Kerszberg[763], D. Khangulyan[753], B. Khélifi[771], J. King[746], S. Klepser[183], D. Klochkov[768], W. Kluźniak[773], Nu. Komin[769], K. Kosack[766], S. Krakau[759], M. Kraus[189], P. P. Krüger[744], H. Laffon[765], G. Lamanna[755], J. Lau[762], J.-P. Lees[755], J. Lefaucheur[754], A. Lemière[771], M. Lemoine-Goumard[765], J.-P. Lenain[763], E. Leser[774], T. Lohse[778], M. Lorentz[766], R. Liu[746], I. Lypova[183], D. Malyshev[768], V. Marandon[746], A. Marcowith[764], C. Mariaud[470], R. Marx[746], G. Maurin[755], N. Maxted[762], M. Mayer[778], P. J. Meintjes[782], M. Meyer[770], A. M. W. Mitchell[746], R. Moderski[773], M. Mohamed[776], L. Mohrmann[189], K. Morå[770], E. Moulin[766], T. Murach[183], S. Nakashima[781], M. de Naurois[470], H. Ndiyavala[744], F. Niederwanger[761], J. Niemiec[752], L. Oakes[778], P. O'Brien[772], H. Odaka[781], S. Ohm[183], M. Ostrowski[779], I. Oya[183], M. Padovani[764], M. Panter[746], R. D. Parsons[746], N. W. Pekeur[744], G. Pelletier[777], C. Perennes[763], P.-O. Petrucci[777], B. Peyaud[766], Q. Piel[755], S. Pita[771], V. Poireau[755], H. Poon[746], D. Prokhorov[758], H. Prokoph[760], G. Pühlhofer[768], M. Punch[771,758], A. Quirrenbach[776], S. Raab[189], R. Rauth[761], A. Reimer[761], O. Reimer[761], M. Renaud[764], R. de los Reyes[746], F. Rieger[746,783], L. Rinchiuso[766], C. Romoli[750], G. Rowell[762], B. Rudak[773], C. B. Rulten[754], V. Sahakian[784,751], S. Saito[753], D. A. Sanchez[755], A. Santangelo[768], M. Sasaki[189], R. Schlickeiser[759], F. Schüssler[766], A. Schulz[183], U. Schwanke[778], S. Schwemmer[776], M. Seglar-Arroyo[766], M. Settimo[763], A. S. Seyffert[744], N. Shafi[769], I. Shilon[189], K. Shiningayamwe[756], R. Simoni[757], H. Sol[754], F. Spanier[744], M. Spir-Jacob[771], Ł. Stawarz[779], R. Steenkamp[756], C. Stegmann[774,183], C. Steppa[774], I. Sushch[744], T. Takahashi[781], J.-P. Tavernet[763], T. Tavernier[771], A. M. Taylor[183], R. Terrier[771], L. Tibaldo[746], D. Tiziani[189], M. Tluczykont[745], C. Trichard[775], M. Tsirou[764], N. Tsuji[753], R. Tuffs[746], Y. Uchiyama[753], D. J. van der Walt[744], C. van Eldik[189], C. van Rensburg[744], B. van Soelen[782], G. Vasileiadis[764], J. Veh[189], C. Venter[744], A. Viana[746], P. Vincent[763], J. Vink[757], F. Voisin[762], H. J. Völk[746], T. Vuillaume[755], Z. Wadiasingh[744], S. J. Wagner[776], P. Wagner[778], R. M. Wagner[770], R. White[746], A. Wierzcholska[752], P. Willmann[189], A. Wörnlein[189], D. Wouters[766], R. Yang[746], D. Zaborov[470], M. Zacharias[744], R. Zanin[746], A. A. Zdziarski[773], A. Zech[754], F. Zefi[470], A. Ziegler[189], J. Zorn[746], N. Żywucka[779],
(H.E.S.S. Collaboration),

R. P. Fender[785], J. W. Broderick[541], A. Rowlinson[786,541], R. A. M. J. Wijers[786], A. J. Stewart[785], S. ter Veen[541], A. Shulevski[541],
(LOFAR Collaboration),

M. Kavic[787], J. H. Simonetti[788], C. League[787], J. Tsai[788], K. S. Obenberger[789], K. Nathaniel[788], G. B. Taylor[790], J. D. Dowell[790], S. L. Liebling[791], J. A. Estes[787], M. Lippert[787], I. Sharma[787], P. Vincent[787], B. Farella[787],
(LWA: Long Wavelength Array),

A. U. Abeysekara[792], A. Albert[793], R. Alfaro[794], C. Alvarez[795], R. Arceo[795], J. C. Arteaga-Velázquez[796], D. Avila Rojas[794], H. A. Ayala Solares[797], A. S. Barber[792], J. Becerra Gonzalez[50], A. Becerril[794], E. Belmont-Moreno[794], S. Y. BenZvi[798], D. Berley[799], A. Bernal[800], J. Braun[801], C. Brisbois[797], K. S. Caballero-Mora[795], T. Capistrán[802], A. Carramiñana[802], S. Casanova[803], M. Castillo[796], U. Cotti[796], J. Cotzomi[804], S. Coutiño de León[802], C. De León[804], E. De la Fuente[805], R. Diaz Hernandez[802], S. Dichiara[800], B. L. Dingus[793], M. A. DuVernois[801], J. C. Díaz-Vélez[805,801], R. W. Ellsworth[806], K. Engel[799], O. Enríquez-Rivera[807], D. W. Fiorino[799], H. Fleischhack[797], N. Fraija[800], J. A. García-González[794], F. Garfias[800], M. Gerhardt[797], A. Gonzölez Muñoz[794], M. M. González[800], J. A. Goodman[799], Z. Hampel-Arias[801], J. P. Harding[793], S. Hernandez[794], A. Hernandez-Almada[794], B. Hona[797], P. Hüntemeyer[797], A. Iriarte[800], A. Jardin-Blicq[808], V. Joshi[808],

S. Kaufmann[795], D. Kieda[792], A. Lara[807], R. J. Lauer[809], D. Lennarz[810], H. León Vargas[794], J. T. Linnemann[811], A. L. Longinotti[802], G. Luis Raya[812], R. Luna-García[813], R. López-Coto[808], K. Malone[814], S. S. Marinelli[811], O. Martinez[804], I. Martinez-Castellanos[799], J. Martínez-Castro[813], H. Martínez-Huerta[815], J. A. Matthews[809], P. Miranda-Romagnoli[816], E. Moreno[804], M. Mostafá[814], L. Nellen[817], M. Newbold[792], M. U. Nisa[798], R. Noriega-Papaqui[816], R. Pelayo[813], J. Pretz[814], E. G. Pérez-Pérez[812], Z. Ren[809], C. D. Rho[798], C. Rivière[799], D. Rosa-González[802], M. Rosenberg[814], E. Ruiz-Velasco[794], H. Salazar[804], F. Salesa Greus[803], A. Sandoval[794], M. Schneider[818], H. Schoorlemmer[808], G. Sinnis[793], A. J. Smith[799], R. W. Springer[792], P. Surajbali[808], O. Tibolla[795], K. Tollefson[811], I. Torres[802], T. N. Ukwatta[793], T. Weisgarber[801], S. Westerhoff[801], I. G. Wisher[801], J. Wood[801], T. Yapici[811], G. B. Yodh[819], P. W. Younk[793], H. Zhou[793], J. D. Álvarez[796],

(HAWC Collaboration),

A. Aab[66], P. Abreu[820], M. Aglietta[821,822], I. F. M. Albuquerque[823], J. M. Albury[824], I. Allekotte[825], A. Almela[826,827], J. Alvarez Castillo[828], J. Alvarez-Muñiz[829], G. A. Anastasi[830,831], L. Anchordoqui[832], B. Andrada[826], S. Andringa[820], C. Aramo[833], N. Arsene[834], H. Asorey[825,835], P. Assis[820], G. Avila[836,837], A. M. Badescu[838], A. Balaceanu[839], F. Barbato[840,820], R. J. Barreira Luz[820], K. H. Becker[204], J. A. Bellido[824], C. Berat[841], M. E. Bertaina[822,842], X. Bertou[825], P. L. Biermann[843], J. Biteau[844], S. G. Blaess[824], A. Blanco[820], J. Blazek[845], C. Bleve[846,847], M. Boháčová[845], C. Bonifazi[848], N. Borodai[849], A. M. Botti[826,850], J. Brack[851], I. Brancus[839], T. Bretz[852], A. Bridgeman[853], F. L. Briechle[852], P. Buchholz[854], A. Bueno[855], S. Buitink[66], M. Buscemi[856,857], K. S. Caballero-Mora[795], L. Caccianiga[858], A. Cancio[827,826], F. Canfora[14,66], R. Caruso[856,857], A. Castellina[821,822], F. Catalani[859], G. Cataldi[847], L. Cazon[820], A. G. Chavez[860], J. A. Chinellato[861], J. Chudoba[845], R. W. Clay[824], A. C. Cobos Cerutti[862], R. Colalillo[840,833], A. Coleman[863], L. Collica[864], M. R. Coluccia[846,847], R. Conceição[820], G. Consolati[864,865], F. Contreras[836,837], M. J. Cooper[824], S. Coutu[863], C. E. Covault[866], J. Cronin[867,957], S. D'Amico[868,847], B. Daniel[861], S. Dasso[869,870], K. Daumiller[850], B. R. Dawson[824], J. A. Day[824], R. M. de Almeida[871], S. J. de Jong[14,66], G. De Mauro[14,66], J. R. T. de Mello Neto[848,872], I. De Mitri[846,847], J. de Oliveira[871], V. de Souza[873], J. Debatin[853], O. Deligny[844], M. L. Díaz Castro[861], F. Diogo[820], C. Dobrigkeit[861], J. C. D'Olivo[828], Q. Dorosti[854], R. C. Dos Anjos[874], M. T. Dova[875], A. Dundovic[876], J. Ebr[845], R. Engel[850], M. Erdmann[852], M. Erfani[854], C. O. Escobar[877], J. Espadanal[820], A. Etchegoyen[826,827], H. Falcke[14,66,878], J. Farmer[867], G. Farrar[879], A. C. Fauth[861], N. Fazzini[877], F. Feldbusch[880], F. Fenu[822,842], B. Fick[881], J. M. Figueira[826], A. Filipčič[494,882], M. M. Freire[883], T. Fujii[867], A. Fuster[826,827], R. Gaïor[884], B. García[862], F. Gaté[885], H. Gemmeke[880], A. Gherghel-Lascu[839], P. L. Ghia[844], U. Giaccari[848,886], M. Giammarchi[864], M. Giller[887], D. Głas[888], C. Glaser[852], G. Golup[825], M. Gómez Berisso[825], P. F. Gómez Vitale[836,837], N. González[826,850], A. Gorgi[821,822], M. Gottowik[204], A. F. Grillo[831,954], T. D. Grubb[824], F. Guarino[840,833], G. P. Guedes[889], R. Halliday[866], M. R. Hampel[826], P. Hansen[875], D. Harari[825], T. A. Harrison[824], V. M. Harvey[824], A. Haungs[850], T. Hebbeker[852], D. Heck[850], P. Heimann[854], A. E. Herve[853], G. C. Hill[824], C. Hojvat[877], E. Holt[850,826], P. Homola[849], J. R. Hörandel[14,66], P. Horvath[890], M. Hrabovský[890], T. Huege[850], J. Hulsman[826,850], A. Insolia[856,857], P. G. Isar[834], I. Jandt[204], J. A. Johnsen[891], M. Josebachuili[826], J. Jurysek[845], A. Kääpä[204], K. H. Kampert[204], B. Keilhauer[850], N. Kemmerich[823], J. Kemp[852], R. M. Kieckhafer[881], H. O. Klages[850], M. Kleifges[880], J. Kleinfeller[836], R. Krause[852], N. Krohm[204], D. Kuempel[204], G. Kukec Mezek[494], N. Kunka[880], A. Kuotb Awad[853], B. L. Lago[892], D. LaHurd[866], R. G. Lang[873], M. Lauscher[852], R. Legumina[887], M. A. Leigui de Oliveira[893], A. Letessier-Selvon[884], I. Lhenry-Yvon[844], K. Link[853], D. Lo Presti[856,857], L. Lopes[820], R. López[894], A. López Casado[829], R. Lorek[866], Q. Luce[844], A. Lucero[826], M. Malacari[867], M. Mallamaci[858,864], D. Mandat[845], P. Mantsch[877], A. G. Mariazzi[875], I. C. Maris[895], G. Marsella[846,847], D. Martello[846,847], H. Martinez[896], O. Martínez Bravo[894], J. J. Masías Meza[870], H. J. Mathes[850], S. Mathys[204], J. Matthews[2], G. Matthiae[897,898], E. Mayotte[204], P. O. Mazur[877], C. Medina[891], G. Medina-Tanco[828], D. Melo[826], A. Menshikov[880], K.-D. Merenda[891], S. Michal[890], M. I. Micheletti[883], L. Middendorf[852], L. Miramonti[858,864], B. Mitrica[839], D. Mockler[853], S. Mollerach[825], F. Montanet[841], C. Morello[821,822], G. Morlino[830,831], A. L. Müller[826,850], G. Müller[852], M. A. Muller[861,899], S. Müller[853,826], R. Mussa[822], I. Naranjo[825], P. H. Nguyen[824], M. Niculescu-Oglinzanu[839], M. Niechciol[854], L. Niemietz[204], T. Niggemann[852], D. Nitz[881], D. Nosek[900], V. Novotny[900], L. Nožka[890], L. A. Núñez[835], F. Oikonomou[863], A. Olinto[867], M. Palatka[845], J. Pallotta[901], P. Papenbreer[204], G. Parente[829], A. Parra[894], T. Paul[832], M. Pech[845], F. Pedreira[829], J. Pękala[849], J. Peña-Rodriguez[835], L. A. S. Pereira[861], M. Perlin[826], L. Perrone[846,847], C. Peters[852], S. Petrera[830,831], J. Phuntsok[863], T. Pierog[850], M. Pimenta[820], V. Pirronello[856,857], M. Platino[826], M. Plum[852], J. Poh[867], C. Porowski[849], R. R. Prado[873], P. Privitera[867], M. Prouza[845], E. J. Quel[901], S. Querchfeld[204], S. Quinn[866], R. Ramos-Pollan[835], J. Rautenberg[204], D. Ravignani[826], J. Ridky[845], F. Riehn[820], M. Risse[854], P. Ristori[901], V. Rizi[831,902], W. Rodrigues de Carvalho[823], G. Rodriguez Fernandez[897,898], J. Rodriguez Rojo[836], M. J. Roncoroni[826], M. Roth[850], E. Roulet[825], A. C. Rovero[869], P. Ruehl[854], S. J. Saffi[824], A. Saftoiu[839], F. Salamida[902,831], H. Salazar[894], A. Saleh[494], G. Salina[898], F. Sánchez[826], P. Sanchez-Lucas[855], E. M. Santos[823], E. Santos[845], F. Sarazin[891], R. Sarmento[820], C. Sarmiento-Cano[826], R. Sato[836], M. Schauer[204], V. Scherini[847], H. Schieler[850], M. Schimp[204], D. Schmidt[850,826], O. Scholten[903,904], P. Schovánek[845], F. G. Schröder[850], S. Schröder[204], A. Schulz[850], J. Schumacher[852], S. J. Sciutto[875], A. Segreto[857,905], A. Shadkam[2], R. C. Shellard[886], G. Sigl[876], G. Silli[826,850], R. Šmída[850], G. R. Snow[906], P. Sommers[863], S. Sonntag[854], J. F. Soriano[832], R. Squartini[836], D. Stanca[839], S. Stanič[494], J. Stasielak[849], P. Stassi[841], M. Stolpovskiy[841], F. Strafella[846,847], A. Streich[853],

     Abbott et al.

F. Suarez[826,827], M. Suarez-Durán[835], T. Sudholz[824], T. Suomijärvi[844], A. D. Supanitsky[869], J. Šupík[890], J. Swain[907],
Z. Szadkowski[888], A. Taboada[850], O. A. Taborda[825], C. Timmermans[14,66], C. J. Todero Peixoto[859], L. Tomankova[850],
B. Tomé[820], G. Torralba Elipe[829], P. Travnicek[845], M. Trini[494], M. Tueros[875], R. Ulrich[850], M. Unger[850], M. Urban[852],
J. F. Valdés Galicia[828], I. Valiño[829], L. Valore[840,833], G. van Aar[66], P. van Bodegom[824], A. M. van den Berg[903], A. van Vliet[66],
E. Varela[894], B. Vargas Cárdenas[828], R. A. Vázquez[829], D. Veberič[850], C. Ventura[872], I. D. Vergara Quispe[875], V. Verzi[898],
J. Vicha[845], L. Villaseñor[860], S. Vorobiov[494], H. Wahlberg[875], O. Wainberg[826,827], D. Walz[852], A. A. Watson[908], M. Weber[880],
A. Weindl[850], M. Wiedeński[888], L. Wiencke[891], H. Wilczyński[849], M. Wirtz[852], D. Wittkowski[204], B. Wundheiler[826],
L. Yang[494], A. Yushkov[845], E. Zas[829], D. Zavrtanik[494,882], M. Zavrtanik[494,882], A. Zepeda[896], B. Zimmermann[880],
M. Ziolkowski[854], Z. Zong[844], F. Zuccarello[909,857],
(The Pierre Auger Collaboration),
S. Kim[548,910], S. Schulze[911], F. E. Bauer[649,910,912], J. M. Corral-Santana[913], I. de Gregorio-Monsalvo[913,914],
J. González-López[910], D. H. Hartmann[915], C. H. Ishwara-Chandra[916], S. Martín[913,914], A. Mehner[913], K. Misra[917],
M. J. Michałowski[918], L. Resmi[919],
(ALMA Collaboration),
Z. Paragi[920], I. Agudo[921], T. An[922,923], R. Beswick[924], C. Casadio[925], S. Frey[926], P. Jonker[66,927], M. Kettenis[920],
B. Marcote[920], J. Moldon[924], A. Szomoru[920], H. J. van Langevelde[920,928], J. Yang[929],
(Euro VLBI Team),
A. Cwiek[727], M. Cwiok[930], H. Czyrkowski[930], R. Dabrowski[930], G. Kasprowicz[931], L. Mankiewicz[932], K. Nawrocki[727],
R. Opiela[932], L. W. Piotrowski[933], G. Wrochna[727], M. Zaremba[930], A. F. Żarnecki[930],
(Pi of the Sky Collaboration),
D. Haggard[934], M. Nynka[934], J. J. Ruan[934],
(The Chandra Team at McGill University),
P. A. Bland[935], T. Booler[501], H. A. R. Devillepoix[935], J. S. de Gois[501], P. J. Hancock[501], R. M. Howie[936], J. Paxman[936],
E. K. Sansom[935], M. C. Towner[935],
(DFN: Desert Fireball Network),
J. Tonry[617], M. Coughlin[937], C. W. Stubbs[938], L. Denneau[617], A. Heinze[617], B. Stalder[939], H. Weiland[617],
(ATLAS),
R. P. Eatough[940], M. Kramer[940], A. Kraus[940],
(High Time Resolution Universe Survey),
E. Troja[941,942], L. Piro[172], J. Becerra González[943,944], N. R. Butler[722], O. D. Fox[945], H. G. Khandrika[945], A. Kutyrev[941,942],
W. H. Lee[946,298], R. Ricci[947], R. E. Ryan Jr.[945], R. Sánchez-Ramírez[172], S. Veilleux[942,290], A. M. Watson[946],
M. H. Wieringa[948], J. M. Burgess[949], H. van Eerten[950], C. J. Fontes[951], C. L. Fryer[951], O. Korobkin[951], R. T. Wollaeger[951],
(RIMAS and RATIR),
and
F. Camilo[952], A. R. Foley[952], S. Goedhart[952], S. Makhathini[952], N. Oozeer[952], O. M. Smirnov[952],
R. P. Fender[66], and P. A. Woudt[953]
(SKA South Africa/MeerKAT)

[1] LIGO, California Institute of Technology, Pasadena, CA 91125, USA
[2] Louisiana State University, Baton Rouge, LA 70803, USA
[3] Università di Salerno, Fisciano, I-84084 Salerno, Italy
[4] INFN, Sezione di Napoli, Complesso Universitario di Monte S.Angelo, I-80126 Napoli, Italy
[5] University of Florida, Gainesville, FL 32611, USA
[6] OzGrav, School of Physics & Astronomy, Monash University, Clayton, VIC 3800, Australia
[7] LIGO Livingston Observatory, Livingston, LA 70754, USA
[8] Laboratoire d'Annecy-le-Vieux de Physique des Particules (LAPP), Université Savoie Mont Blanc, CNRS/IN2P3, F-74941 Annecy, France
[9] University of Sannio at Benevento, I-82100 Benevento, Italy and INFN, Sezione di Napoli, I-80100 Napoli, Italy
[10] Albert-Einstein-Institut, Max-Planck-Institut für Gravitationsphysik, D-30167 Hannover, Germany
[11] The University of Mississippi, University, MS 38677, USA
[12] NCSA, University of Illinois at Urbana-Champaign, Urbana, IL 61801, USA
[13] University of Cambridge, Cambridge CB2 1TN, UK
[14] Nikhef, Science Park, 1098 XG Amsterdam, The Netherlands
[15] LIGO, Massachusetts Institute of Technology, Cambridge, MA 02139, USA
[16] Instituto Nacional de Pesquisas Espaciais, 12227-010 São José dos Campos, São Paulo, Brazil
[17] Gran Sasso Science Institute (GSSI), I-67100 L'Aquila, Italy
[18] INFN, Laboratori Nazionali del Gran Sasso, I-67100 Assergi, Italy
[19] Inter-University Centre for Astronomy and Astrophysics, Pune 411007, India
[20] International Centre for Theoretical Sciences, Tata Institute of Fundamental Research, Bengaluru 560089, India
[21] University of Wisconsin-Milwaukee, Milwaukee, WI 53201, USA
[22] Leibniz Universität Hannover, D-30167 Hannover, Germany
[23] Università di Pisa, I-56127 Pisa, Italy

[24] INFN, Sezione di Pisa, I-56127 Pisa, Italy

[25] OzGrav, Australian National University, Canberra, ACT 0200, Australia

[26] Laboratoire des Matériaux Avancés (LMA), CNRS/IN2P3, F-69622 Villeurbanne, France

[27] SUPA, University of the West of Scotland, Paisley PA1 2BE, UK

[28] LAL, Univ. Paris-Sud, CNRS/IN2P3, Université Paris-Saclay, F-91898 Orsay, France

[29] California State University Fullerton, Fullerton, CA 92831, USA

[30] European Gravitational Observatory (EGO), I-56021 Cascina, Pisa, Italy

[31] Chennai Mathematical Institute, Chennai 603103, India

[32] Università di Roma Tor Vergata, I-00133 Roma, Italy

[33] INFN, Sezione di Roma Tor Vergata, I-00133 Roma, Italy

[34] Universität Hamburg, D-22761 Hamburg, Germany

[35] INFN, Sezione di Roma, I-00185 Roma, Italy

[36] Cardiff University, Cardiff CF24 3AA, UK

[37] Embry-Riddle Aeronautical University, Prescott, AZ 86301, USA

[38] Albert-Einstein-Institut, Max-Planck-Institut für Gravitationsphysik, D-14476 Potsdam-Golm, Germany

[39] APC, AstroParticule et Cosmologie, Université Paris Diderot, CNRS/IN2P3, CEA/Irfu, Observatoire de Paris, Sorbonne Paris Cité, F-75205 Paris Cedex 13, France

[40] Korea Institute of Science and Technology Information, Daejeon 34141, Korea

[41] West Virginia University, Morgantown, WV 26506, USA

[42] Università di Perugia, I-06123 Perugia, Italy

[43] INFN, Sezione di Perugia, I-06123 Perugia, Italy

[44] Syracuse University, Syracuse, NY 13244, USA

[45] University of Minnesota, Minneapolis, MN 55455, USA

[46] SUPA, University of Glasgow, Glasgow G12 8QQ, UK

[47] LIGO Hanford Observatory, Richland, WA 99352, USA

[48] Caltech CaRT, Pasadena, CA 91125, USA

[49] Wigner RCP, RMKI, Konkoly Thege Miklós út 29-33, H-1121 Budapest, Hungary

[50] NASA Goddard Space Flight Center, Greenbelt, MD 20771, USA

[51] Columbia University, New York, NY 10027, USA

[52] Stanford University, Stanford, CA 94305, USA

[53] Università di Camerino, Dipartimento di Fisica, I-62032 Camerino, Italy

[54] Università di Padova, Dipartimento di Fisica e Astronomia, I-35131 Padova, Italy

[55] INFN, Sezione di Padova, I-35131 Padova, Italy

[56] Institute of Physics, Eötvös University, Pázmány P. s. 1/A, H-1117 Budapest, Hungary

[57] Nicolaus Copernicus Astronomical Center, Polish Academy of Sciences, 00-716, Warsaw, Poland

[58] Rochester Institute of Technology, Rochester, NY 14623, USA

[59] University of Birmingham, Birmingham B15 2TT, UK

[60] INFN, Sezione di Genova, I-16146 Genova, Italy

[61] RRCAT, Indore MP 452013, India

[62] Faculty of Physics, Lomonosov Moscow State University, Moscow 119991, Russia

[63] SUPA, University of Strathclyde, Glasgow G1 1XQ, UK

[64] The Pennsylvania State University, University Park, PA 16802, USA

[65] OzGrav, University of Western Australia, Crawley, WA 6009, Australia

[66] Institute of Mathematics, Astrophysics and Particle Physics, Radboud University, 6525 AJ Nijmegen, The Netherlands

[67] Artemis, Université Côte d'Azur, Observatoire Côte d'Azur, CNRS, CS 34229, F-06304 Nice Cedex 4, France

[68] Institut FOTON, CNRS, Université de Rennes 1, F-35042 Rennes, France

[69] Washington State University, Pullman, WA 99164, USA

[70] University of Oregon, Eugene, OR 97403, USA

[71] Laboratoire Kastler Brossel, UPMC-Sorbonne Universités, CNRS, ENS-PSL Research University, Collège de France, F-75005 Paris, France

[72] Carleton College, Northfield, MN 55057, USA

[73] OzGrav, University of Adelaide, Adelaide, SA 5005, Australia

[74] Astronomical Observatory Warsaw University, 00-478 Warsaw, Poland

[75] VU University Amsterdam, 1081 HV Amsterdam, The Netherlands

[76] University of Maryland, College Park, MD 20742, USA

[77] Center for Relativistic Astrophysics, Georgia Institute of Technology, Atlanta, GA 30332, USA

[78] Université Claude Bernard Lyon 1, F-69622 Villeurbanne, France

[79] Università di Napoli "Federico II," Complesso Universitario di Monte S. Angelo, I-80126 Napoli, Italy

[80] Dipartimento di Fisica, Università degli Studi di Genova, I-16146 Genova, Italy

[81] RESCEU, University of Tokyo, Tokyo, 113-0033, Japan

[82] Tsinghua University, Beijing 100084, China

[83] Texas Tech University, Lubbock, TX 79409, USA

[84] Kenyon College, Gambier, OH 43022, USA

[85] Departamento de Astronomía y Astrofísica, Universitat de València, E-46100 Burjassot, València, Spain

[86] Museo Storico della Fisica e Centro Studi e Ricerche Enrico Fermi, I-00184 Roma, Italy

[87] National Tsing Hua University, Hsinchu City, 30013 Taiwan, Republic of China

[88] Charles Sturt University, Wagga Wagga, NSW 2678, Australia

[89] Center for Interdisciplinary Exploration & Research in Astrophysics (CIERA), Northwestern University, Evanston, IL 60208, USA

[90] Canadian Institute for Theoretical Astrophysics, University of Toronto, Toronto, ON M5S 3H8, Canada

[91] University of Chicago, Chicago, IL 60637, USA

[92] Pusan National University, Busan 46241, Korea

[93] The Chinese University of Hong Kong, Shatin, NT, Hong Kong

[94] INAF, Osservatorio Astronomico di Padova, I-35122 Padova, Italy

[95] INFN, Trento Institute for Fundamental Physics and Applications, I-38123 Povo, Trento, Italy

[96] OzGrav, University of Melbourne, Parkville, VIC 3010, Australia

[97] Università di Roma "La Sapienza," I-00185 Roma, Italy

[98] Université Libre de Bruxelles, Brussels 1050, Belgium

[99] Sonoma State University, Rohnert Park, CA 94928, USA

[100] Departamento de Matemáticas, Universitat de València, E-46100 Burjassot, València, Spain

[101] Montana State University, Bozeman, MT 59717, USA

[102] Universitat de les Illes Balears, IAC3—IEEC, E-07122 Palma de Mallorca, Spain

[103] The University of Texas Rio Grande Valley, Brownsville, TX 78520, USA

[104] Bellevue College, Bellevue, WA 98007, USA

[105] Institute for Plasma Research, Bhat, Gandhinagar 382428, India

[106] The University of Sheffield, Sheffield S10 2TN, UK

[107] Dipartimento di Scienze Matematiche, Fisiche e Informatiche, Università di Parma, I-43124 Parma, Italy

[108] INFN, Sezione di Milano Bicocca, Gruppo Collegato di Parma, I-43124 Parma, Italy

[109] California State University, Los Angeles, 5151 State University Drive, Los Angeles, CA 90032, USA

[110] Università di Trento, Dipartimento di Fisica, I-38123 Povo, Trento, Italy

[111] Montclair State University, Montclair, NJ 07043, USA

[112] National Astronomical Observatory of Japan, 2-21-1 Osawa, Mitaka, Tokyo 181-8588, Japan

[113] Observatori Astronòmic, Universitat de València, E-46980 Paterna, València, Spain

[114] School of Mathematics, University of Edinburgh, Edinburgh EH9 3FD, UK

[115] University and Institute of Advanced Research, Koba Institutional Area, Gandhinagar Gujarat 382007, India

[116] IISER-TVM, CET Campus, Trivandrum Kerala 695016, India

[117] University of Szeged, Dóm tér 9, H-6720 Szeged, Hungary

[118] University of Michigan, Ann Arbor, MI 48109, USA

[119] Tata Institute of Fundamental Research, Mumbai 400005, India

[120] INAF, Osservatorio Astronomico di Capodimonte, I-80131, Napoli, Italy

[121] Università degli Studi di Urbino "Carlo Bo," I-61029 Urbino, Italy

[122] INFN, Sezione di Firenze, I-50019 Sesto Fiorentino, Firenze, Italy

[123] Physik-Institut, University of Zurich, Winterthurerstrasse 190, CH-8057 Zurich, Switzerland

[124] American University, Washington, DC 20016, USA

[125] University of Białystok, 15-424 Białystok, Poland

[126] University of Southampton, Southampton SO17 1BJ, UK

[127] University of Washington Bothell, 18115 Campus Way NE, Bothell, WA 98011, USA

[128] Institute of Applied Physics, Nizhny Novgorod, 603950, Russia

[129] Korea Astronomy and Space Science Institute, Daejeon 34055, Korea

[130] Inje University Gimhae, South Gyeongsang 50834, Korea

[131] National Institute for Mathematical Sciences, Daejeon 34047, Korea

[132] NCBJ, 05-400 Świerk-Otwock, Poland

[133] Institute of Mathematics, Polish Academy of Sciences, 00656 Warsaw, Poland

[134] Hillsdale College, Hillsdale, MI 49242, USA

[135] Hanyang University, Seoul 04763, Korea

[136] Seoul National University, Seoul 08826, Korea

[137] NASA Marshall Space Flight Center, Huntsville, AL 35812, USA

[138] ESPCI, CNRS, F-75005 Paris, France

[139] Southern University and A&M College, Baton Rouge, LA 70813, USA

[140] College of William and Mary, Williamsburg, VA 23187, USA

[141] Centre Scientifique de Monaco, 8 quai Antoine Ier, MC-98000, Monaco

[142] Indian Institute of Technology Madras, Chennai 600036, India

[143] IISER-Kolkata, Mohanpur, West Bengal 741252, India

[144] Whitman College, 345 Boyer Avenue, Walla Walla, WA 99362 USA

[145] Indian Institute of Technology Bombay, Powai, Mumbai, Maharashtra 400076, India

[146] Scuola Normale Superiore, Piazza dei Cavalieri 7, I-56126 Pisa, Italy

[147] Université de Lyon, F-69361 Lyon, France

[148] Hobart and William Smith Colleges, Geneva, NY 14456, USA

[149] OzGrav, Swinburne University of Technology, Hawthorn, VIC 3122, Australia

[150] Janusz Gil Institute of Astronomy, University of Zielona Góra, 65-265 Zielona Góra, Poland

[151] University of Washington, Seattle, WA 98195, USA

[152] King's College London, University of London, London WC2R 2LS, UK

[153] Indian Institute of Technology, Gandhinagar Ahmedabad Gujarat 382424, India

[154] Indian Institute of Technology Hyderabad, Sangareddy, Khandi, Telangana 502285, India

[155] International Institute of Physics, Universidade Federal do Rio Grande do Norte, Natal RN 59078-970, Brazil

[156] Andrews University, Berrien Springs, MI 49104, USA

[157] Università di Siena, I-53100 Siena, Italy

[158] Trinity University, San Antonio, TX 78212, USA

[159] Abilene Christian University, Abilene, TX 79699, USA

[160] Colorado State University, Fort Collins, CO 80523, USA

[161] INFN Sezione di Bari, I-70126 Bari, Italy

[162] Politecnico di Bari, I-70126 Bari BA, Italy

[163] Harvard-Smithsonian Center for Astrophysics, 60 Garden Street, Cambridge, MA 02138, USA

[164] University of Alabama in Huntsville, Huntsville, AL 35899, USA

[165] Universities Space Research Association, Huntsville, AL 35805, USA

[166] Jacobs Technology, Inc., Huntsville, AL 35806, USA

[167] Los Alamos National Laboratory, Los Alamos, NM 87545, USA

[168] School of Physics, O'Brien Centre for Science North, University College Dublin, Belfield, Dublin 4, Ireland

[169] Max-Planck-Institut für extraterrestrische Physik, D-85748 Garching, Germany

[170] ISDC, Department of Astronomy, University of Geneva, Chemin d'Écogia, 16 CH-1290 Versoix, Switzerland

[171] European Space Research and Technology Centre (ESA/ESTEC), Keplerlaan 1, 2201 AZ Noordwijk, The Netherlands

[172] INAF, Istituto di Astrofisica e Planetologia Spaziali, via Fosso del Cavaliere 100, I-00133 Rome, Italy

[173] DTU Space, National Space Institute Elektrovej, Building 327 DK-2800 Kongens Lyngby Denmark
[174] Centro de Astrobiología (CAB-CSIC/INTA, ESAC Campus), Camino bajo del Castillo S/N, E-28692 Villanueva de la Cañada, Madrid, Spain
[175] IRAP, Université de Toulouse, CNRS, UPS, CNES, 9 Av. Roche, F-31028 Toulouse, France
[176] APC, AstroParticule et Cosmologie, Université Paris Diderot, CNRS/IN2P3, CEA/Irfu, Observatoire de Paris Sorbonne Paris Cité,
10 rue Alice Domont et Léonie Duquet, F-75205 Paris Cedex 13, France.
[177] DSM/Irfu/Service d'Astrophysique, Bat. 709 Orme des Merisiers CEA Saclay, F-91191 Gif-sur-Yvette Cedex, France
[178] Space Research Institute of Russian Academy of Sciences, Profsoyuznaya 84/32, Moscow, 117997, Russia
[179] Moscow Institute of Physics and Technology, Institutskiy per. 9, Dolgoprudny, Moscow Region, 141700, Russia
[180] INAF-Istituto di Astrofisica Spaziale e Fisica Cosmica Milano, via E. Bassini 15, I-20133 Milano, Italy
[181] Max Planck Institute for Astrophysics, Karl-Schwarzschild-Str. 1, Garching b. Munchen D-85741, Germany
[182] Department of Physics, University of Adelaide, Adelaide, 5005, Australia
[183] DESY, D-15738 Zeuthen, Germany
[184] Dept. of Physics and Astronomy, University of Canterbury, Private Bag 4800, Christchurch, New Zealand
[185] Université Libre de Bruxelles, Science Faculty CP230, B-1050 Brussels, Belgium
[186] Niels Bohr Institute, University of Copenhagen, DK-2100 Copenhagen, Denmark
[187] Oskar Klein Centre and Dept. of Physics, Stockholm University, SE-10691 Stockholm, Sweden
[188] Département de physique nucléaire et corpusculaire, Université de Genève, CH-1211 Genève, Switzerland
[189] Friedrich-Alexander-Universität Erlangen-Nürnberg, Erlangen Centre for Astroparticle Physics, Erwin-Rommel-Str. 1, D-91058 Erlangen, Germany
[190] Department of Physics, Marquette University, Milwaukee, WI, 53201, USA
[191] Dept. of Physics, Pennsylvania State University, University Park, PA 16802, USA
[192] Dept. of Physics, Massachusetts Institute of Technology, Cambridge, MA 02139, USA
[193] III. Physikalisches Institut, RWTH Aachen University, D-52056 Aachen, Germany
[194] Physics Department, South Dakota School of Mines and Technology, Rapid City, SD 57701, USA
[195] Dept. of Physics, University of Alberta, Edmonton, AB T6G 2E1, Canada
[196] Dept. of Physics and Astronomy, University of California, Irvine, CA 92697, USA
[197] Institute of Physics, University of Mainz, Staudinger Weg 7, D-55099 Mainz, Germany
[198] Dept. of Physics, University of California, Berkeley, CA 94720, USA
[199] Dept. of Physics and Center for Cosmology and Astro-Particle Physics, Ohio State University, Columbus, OH 43210, USA
[200] Dept. of Astronomy, Ohio State University, Columbus, OH 43210, USA
[201] Fakultät für Physik & Astronomie, Ruhr-Universität Bochum, D-44780 Bochum, Germany
[202] Dept. of Physics and Astronomy, University of Kansas, Lawrence, KS 66045, USA
[203] Lawrence Berkeley National Laboratory, Berkeley, CA 94720, USA
[204] Bergische Universität Wuppertal, Department of Physics, Germany
[205] Dept. of Physics, University of Maryland, College Park, MD 20742, USA
[206] Dept. of Physics, TU Dortmund University, D-44221 Dortmund, Germany
[207] Dept. of Physics, Sungkyunkwan University, Suwon 440-746, Korea
[208] Dept. of Physics and Astronomy, Uppsala University, Box 516, S-75120 Uppsala, Sweden
[209] Dept. of Physics and Wisconsin IceCube Particle Astrophysics Center, University of Wisconsin, Madison, WI 53706, USA
[210] Vrije Universiteit Brussel (VUB), Dienst ELEM, B-1050 Brussels, Belgium
[211] SNOLAB, 1039 Regional Road 24, Creighton Mine 9, Lively, ON P3Y 1N2, Canada
[212] Institut für Kernphysik, Westfälische Wilhelms-Universität Münster, D-48149 Münster, Germany
[213] Physik-department, Technische Universität München, D-85748 Garching, Germany
[214] Dept. of Astronomy and Astrophysics, Pennsylvania State University, University Park, PA 16802, USA
[215] Dept. of Physics and Astronomy, University of Rochester, Rochester, NY 14627, USA
[216] Dept. of Physics and Astronomy, Michigan State University, East Lansing, MI 48824, USA
[217] Bartol Research Institute and Dept. of Physics and Astronomy, University of Delaware, Newark, DE 19716, USA
[218] Dept. of Physics and Astronomy, University of Gent, B-9000 Gent, Belgium
[219] Institut für Physik, Humboldt-Universität zu Berlin, D-12489 Berlin, Germany
[220] Dept. of Physics, Southern University, Baton Rouge, LA 70813, USA
[221] Dept. of Astronomy, University of Wisconsin, Madison, WI 53706, USA
[222] Earthquake Research Institute, University of Tokyo, Bunkyo, Tokyo 113-0032, Japan
[223] Dept. of Physics and Institute for Global Prominent Research, Chiba University, Chiba 263-8522, Japan
[224] CTSPS, Clark-Atlanta University, Atlanta, GA 30314, USA
[225] Dept. of Physics, University of Texas at Arlington, 502 Yates Street, Science Hall Room 108, Box 19059, Arlington, TX 76019, USA
[226] Dept. of Physics and Astronomy, Stony Brook University, Stony Brook, NY 11794-3800, USA
[227] Université de Mons, B-7000 Mons, Belgium
[228] Dept. of Physics and Astronomy, University of Alabama, Tuscaloosa, AL 35487, USA
[229] Dept. of Physics, Drexel University, 3141 Chestnut Street, Philadelphia, PA 19104, USA
[230] Dept. of Physics, University of Wisconsin, River Falls, WI 54022, USA
[231] Dept. of Physics, Yale University, New Haven, CT 06520, USA
[232] Dept. of Physics and Astronomy, University of Alaska Anchorage, 3211 Providence Drive, Anchorage, AK 99508, USA
[233] Dept. of Physics, University of Oxford, 1 Keble Road, Oxford OX1 3NP, UK
[234] School of Physics and Center for Relativistic Astrophysics, Georgia Institute of Technology, Atlanta, GA 30332, USA
[235] Indian Institute of Science Education and Research, Dr. Homi Bhabha Road, Pashan, Pune 411008, India
[236] Department of Physics, Indian Institute of Technology Bombay, Mumbai 400076, India
[237] Physical Research Laboratory, Ahmedabad, India
[238] Ioffe Institute, Politekhnicheskaya 26, St. Petersburg 194021, Russia
[239] University of California-Berkeley, Space Sciences Lab, 7 Gauss Way, Berkeley, CA 94720, USA
[240] Emeritus, NASA Goddard Space Flight Center, Greenbelt, MD 20771, USA
[241] Key Laboratory Of Particle Astrophysics, Institute Of High Energy Physics, Chinese Academy Of Sciences, Beijing 100049, China
[242] University Of Chinese Academy Of Sciences, Chinese Academy Of Sciences, Beijing 100049, China
[243] Beijing Normal University, Beijing 100088, China
[244] GRPHE, Université de Haute Alsace, Institut universitaire de technologie de Colmar, 34 rue du Grillenbreit BP 50568, F-68008 Colmar, France
[245] Technical University of Catalonia, Laboratory of Applied Bioacoustics, Rambla Exposició, E-08800 Vilanova i la Geltrú, Barcelona, Spain
[246] INFN—Sezione di Genova, Via Dodecaneso 33, I-16146 Genova, Italy

[247] Institut d'Investigació per a la Gestió Integrada de les Zones Costaneres (IGIC), Universitat Politècnica de València. C/ Paranimf 1, E-46730 Gandia, Spain

[248] Aix Marseille Univ, CNRS/IN2P3, CPPM, Marseille, France

[249] APC, Univ Paris Diderot, CNRS/IN2P3, CEA/Irfu, Obs de Paris, Sorbonne Paris Cité, France

[250] IFIC, Instituto de Física Corpuscular (CSIC—Universitat de València), c/ Catedrático José Beltrán, 2 E-46980 Paterna, Valencia, Spain

[251] LAM—Laboratoire d'Astrophysique de Marseille, Pôle de l'Étoile Site de Château-Gombert, rue Frédéric Joliot-Curie 38, F-13388 Marseille Cedex 13, France

[252] National Center for Energy Sciences and Nuclear Techniques, B.P. 1382, R. P. 10001 Rabat, Morocco

[253] INFN—Laboratori Nazionali del Sud (LNS), Via S. Sofia 62, I-95123 Catania, Italy

[254] Huygens-Kamerlingh Onnes Laboratorium, Universiteit Leiden, The Netherlands

[255] Institute for Space Science, RO-077125 Bucharest, Măgurele, Romania

[256] Universiteit van Amsterdam, Instituut voor Hoge-Energie Fysica, Science Park 105, 1098 XG Amsterdam, The Netherlands

[257] INFN—Sezione di Roma, P.le Aldo Moro 2, I-00185 Roma, Italy

[258] Dipartimento di Fisica dell'Università La Sapienza, P.le Aldo Moro 2, I-00185 Roma, Italy

[259] Gran Sasso Science Institute, Viale Francesco Crispi 7, I-00167 L'Aquila, Italy

[260] University Mohammed V in Rabat, Faculty of Sciences, 4 av. Ibn Battouta, B.P. 1014, 10000, Rabat, Morocco

[261] INFN—Sezione di Bologna, Viale Berti-Pichat 6/2, I-40127 Bologna, Italy

[262] INFN—Sezione di Bari, Via E. Orabona 4, I-70126 Bari, Italy

[263] Department of Computer Architecture and Technology/CITIC, University of Granada, E-18071 Granada, Spain

[264] Géoazur, UCA, CNRS, IRD, Observatoire de la Côte d'Azur, Sophia Antipolis, France

[265] Dipartimento di Fisica dell'Università, Via Dodecaneso 33, I-16146 Genova, Italy

[266] Université Paris-Sud, F-91405 Orsay Cedex, France

[267] University Mohammed I, Laboratory of Physics of Matter and Radiations, B.P. 717, Oujda 6000, Morocco

[268] Institut für Theoretische Physik und Astrophysik, Universität Würzburg, Emil-Fischer Str. 31, D-97074 Würzburg, Germany

[269] Dipartimento di Fisica e Astronomia dell'Università, Viale Berti Pichat 6/2, I-40127 Bologna, Italy

[270] Laboratoire de Physique Corpusculaire, Clermont Université, Université Blaise Pascal, CNRS/IN2P3, BP 10448, F-63000 Clermont-Ferrand, France

[271] INFN—Sezione di Catania, Viale Andrea Doria 6, I-95125 Catania, Italy

[272] LSIS, Aix Marseille Université CNRS ENSAM LSIS UMR 7296 F-13397 Marseille, France; Université de Toulon CNRS LSIS UMR 7296, F-83957 La Garde, France

[273] Institut Universitaire de France, F-75005 Paris, France

[274] Royal Netherlands Institute for Sea Research (NIOZ) and Utrecht University, Landsdiep 4, 1797 SZ 't Horntje (Texel), The Netherlands

[275] Dr. Remeis-Sternwarte and ECAP, Universität Erlangen-Nürnberg, Sternwartstr. 7, D-96049 Bamberg, Germany

[276] Moscow State University, Skobeltsyn Institute of Nuclear Physics, Leninskie gory, 119991 Moscow, Russia

[277] Mediterranean Institute of Oceanography (MIO), Aix-Marseille University, F-13288, Marseille, Cedex 9, France; Université du Sud Toulon-Var, CNRS-INSU/IRD UM 110, 83957, La Garde Cedex, France

[278] Dipartimento di Fisica ed Astronomia dell'Università, Viale Andrea Doria 6, I-95125 Catania, Italy

[279] Direction des Sciences de la Matière, Institut de recherche sur les lois fondamentales de l'Univers, Service de Physique des Particules, CEA Saclay, F-91191 Gif-sur-Yvette Cedex, France

[280] INFN—Sezione di Pisa, Largo B. Pontecorvo 3, I-56127 Pisa, Italy

[281] Dipartimento di Fisica dell'Università, Largo B. Pontecorvo 3, I-56127 Pisa, Italy

[282] INFN—Sezione di Napoli, Via Cintia I-80126 Napoli, Italy

[283] Dipartimento di Fisica dell'Università Federico II di Napoli, Via Cintia I-80126, Napoli, Italy

[284] Dpto. de Física Teórica y del Cosmos & C.A.F.P.E., University of Granada, E-18071 Granada, Spain

[285] Université de Strasbourg, CNRS, IPHC UMR 7178, F-67000 Strasbourg, France

[286] University of Leicester, X-ray and Observational Astronomy Research Group, Leicester Institute for Space and Earth Observation, Department of Physics & Astronomy, University Road, Leicester, LE1 7RH, UK

[287] University College London, Mullard Space Science Laboratory, Holmbury St. Mary, Dorking, RH5 6NT, UK

[288] Department of Astronomy and Astrophysics, The Pennsylvania State University, University Park, PA 16802, USA

[289] Astrophysics Science Division, NASA Goddard Space Flight Center, Greenbelt, MD 20771 USA

[290] Joint Space-Science Institute, University of Maryland, College Park, MD 20742, USA

[291] Istituto Nazionale di Astrofisica – Istituto di Astrofisica Spaziale e Fisica Cosmica Palermo, Via Ugo La Malfa 153, I-90146, Palermo, Italy

[292] Department of Astronomy and Space Sciences, University of Istanbul, Beyzıt 34119, Istanbul, Turkey

[293] Space Science Data Center—Agenzia Spaziale Italiana, I-00133 Roma, Italy

[294] Institute for Gravitation and the Cosmos, The Pennsylvania State University, University Park, PA 16802, USA

[295] Universities Space Research Association, 7178 Columbia Gateway Drive, Columbia, MD 21046, USA

[296] National Science Foundation, 2415 Eisenhower Avenue, Alexandria, VA 22314, USA

[297] Center for Research and Exploration in Space Science and Technology (CRESST) and NASA Goddard Space Flight Center, Greenbelt MD, 20771 USA

[298] Department of Physics, University of Maryland, Baltimore County, 1000 Hilltop Circle, Baltimore, MD 21250, USA

[299] Istituto Nazionale di Astrofisica – Osservatorio Astronomico di Brera, Via Bianchi 46, I-23807 Merate, Italy

[300] Department of Physics, University of Warwick, Coventry CV4 7AL, UK

[301] Los Alamos National Laboratory, B244, Los Alamos, NM, 87545, USA

[302] Istituto Nazionale di Astrofisica – Osservatorio Astronomico di Roma, Via Frascati 33, I-00040 Monteporzio Catone, Italy

[303] Department of Physics and Astronomy, University of Maryland, College Park, MD 20742-4111, USA

[304] INAF-IAPS, via del Fosso del Cavaliere 100, I-00133 Roma, Italy

[305] Dip. di Fisica, Univ. di Roma "Tor Vergata," via della Ricerca Scientifica 1, I-00133 Roma, Italy

[306] Gran Sasso Science Institute, viale Francesco Crispi 7, I-67100 L'Aquila, Italy

[307] INAF-OAR, via Frascati 33, I-00078 Monte Porzio Catone (Roma), Italy

[308] ASI Space Science Data Center (SSDC), via del Politecnico, I-00133 Roma, Italy

[309] INAF-IASF-Bologna, via Gobetti 101, I-40129 Bologna, Italy

[310] INAF-IASF Milano, via E.Bassini 15, I-20133 Milano, Italy

[311] Agenzia Spaziale Italiana, via del Politecnico, I-00133 Roma, Italy

[312] INAF, Osservatorio Astronomico di Cagliari, Via della Scienza 5, I-09047 Selargius (CA), Italy

[313] Dip. di Fisica, Università di Trieste and INFN, via Valerio 2, I-34127 Trieste, Italy

[314] Unitat de Física de les Radiacions, Departament de Física, and CERES-IEEC, Universitat Autònoma de Barcelona, E-08193 Bellaterra, Spain

[315] Birkeland Centre for Space Science, Department of Physics and Technology, University of Bergen, Bergen, Norway

[316] INFN-Pavia, via Bassi 6, I-27100 Pavia, Italy

[317] University of Witwatersrand, Johannesburg, South Africa

[318] CIFS, c/o Physics Department, University of Turin, via P. Giuria 1, I-10125, Torino, Italy
[319] INFN Roma Tor Vergata, via della Ricerca Scientifica 1, I-00133 Roma, Italy
[320] East Windsor RSD, 25A Leshin Lane, Hightstown, NJ 08520, USA
[321] Osservatorio Astronomico di Brera, via Emilio Bianchi 46, I-23807 Merate (LC), Italy
[322] Department of Astronomy and Astrophysics, University of California, Santa Cruz, CA 95064, USA
[323] The Observatories of the Carnegie Institution for Science, 813 Santa Barbara Street, Pasadena, CA 91101, USA
[324] Institute for Astronomy, University of Hawai'i, 2680 Woodlawn Drive, Honolulu, HI 96822, USA
[325] Departamento de Física y Astronomía, Universidad de La Serena, La Serena, Chile
[326] Nuclear Science Division, Lawrence Berkeley National Laboratory, Berkeley, CA 94720, USA
[327] Departments of Physics and Astronomy, University of California, Berkeley, CA 94720, USA
[328] Dark Cosmology Centre, Niels Bohr Institute, University of Copenhagen, Juliane Maries Vej 30, DK-2100 Copenhagen Ø, Denmark
[329] Space Telescope Science Institute, 3700 San Martin Drive, Baltimore, MD 21218, USA
[330] Department of Physics and Astronomy, The Johns Hopkins University, 3400 North Charles Street, Baltimore, MD 21218, USA
[331] Department of Physics, Brandeis University, Waltham, MA, USA
[332] Fermi National Accelerator Laboratory, P. O. Box 500, Batavia, IL 60510, USA
[333] Department of Physics, University of Surrey, Guildford GU2 7XH, UK
[334] Department of Physics and Astronomy, University of Pennsylvania, Philadelphia, PA 19104, USA
[335] Department of Astronomy, Indiana University, 727 E. Third Street, Bloomington, IN 47405, USA
[336] Astrophysical Institute, Department of Physics and Astronomy, 251B Clippinger Lab, Ohio University, Athens, OH 45701, USA
[337] George P. and Cynthia Woods Mitchell Institute for Fundamental Physics and Astronomy, and Department of Physics and Astronomy, Texas A&M University,
College Station, TX 77843, USA
[338] LSST, 933 North Cherry Avenue, Tucson, AZ 85721, USA
[339] The Observatories of the Carnegie Institution for Science, 813 Santa Barbara St., Pasadena, CA 91101, USA
[340] Institut d'Astrophysique de Paris (UMR7095: CNRS & UPMC), 98 bis Bd Arago, F-75014, Paris, France
[341] Center for Interdisciplinary Exploration and Research in Astrophysics (CIERA) and Department of Physics and Astronomy, Northwestern University,
Evanston, IL 60208, USA
[342] Center for Theoretical Astrophysics, Los Alamos National Laboratory, Los Alamos, NM 87544, USA
[343] Instituto de Fisica Teorica UAM/CSIC, Universidad Autonoma de Madrid, E-28049 Madrid, Spain
[344] National Center for Supercomputing Applications, 1205 West Clark Street, Urbana, IL 61801, USA
[345] Department of Physics & Astronomy, University College London, Gower Street, London WC1E 6BT, UK
[346] Department of Physics, ETH Zurich, Wolfgang-Pauli-Strasse 16, CH-8093 Zurich, Switzerland
[347] Kavli Institute for Cosmological Physics, University of Chicago, Chicago, IL 60637, USA
[348] Observatòrio do Valongo, Universidade Federal do Rio de Janeiro, Ladeira do Pedro Antônio 43, Rio de Janeiro, RJ, 20080-090, Brazil
[349] Center for Interdisciplinary Exploration and Research in Astrophysics (CIERA) and Department of Physics and Astronomy, Northwestern University,
Evanston, IL 60208, USA
[350] National Optical Astronomy Observatory, 950 North Cherry Avenue, Tucson, AZ 85719, USA
[351] Departamento de Astronomonía, Universidad de Chile, Camino del Observatorio 1515, Las Condes, Santiago, Chile
[352] Department of Physics and Columbia Astrophysics Laboratory, Columbia University, New York, NY 10027, USA
[353] Department of Physics, University of Michigan, 450 Church Street, Ann Arbor, MI 48109-1040, USA
[354] Lawrence Berkeley National Laboratory, 1 Cyclotron Road, Berkeley, CA 94720, USA
[355] Department of Astronomy & Theoretical Astrophysics Center, University of California, Berkeley, CA 94720-3411, USA
[356] Physics Division, Lawrence Berkeley National Laboratory, Berkeley, CA 94720-8160, USA
[357] Steward Observatory, University of Arizona, 933 N. Cherry Avenue, Tucson, AZ 85721, USA
[358] Instituto de Física Gleb Wataghin, Universidade Estadual de Campinas, Campinas, SP—13083-859, Brazil
[359] Laboratório Interinstitucional de e-Astronomia—LIneA, Rua Gal. José Cristino 77, Rio de Janeiro, RJ—20921-400, Brazil
[360] Cerro Tololo Inter-American Observatory, National Optical Astronomy Observatory, Casilla 603, La Serena, Chile
[361] Institute of Astronomy, University of Cambridge Madingley Road, Cambridge CB3 0HA, UK
[362] Kavli Institute for Cosmology, University of Cambridge, Madingley Road, Cambridge CB3 0HA, UK
[363] CNRS, UMR 7095, Institut d'Astrophysique de Paris, F-75014, Paris, France
[364] Sorbonne Universités, UPMC Univ Paris 06, UMR 7095, Institut d'Astrophysique de Paris, F-75014, Paris, France
[365] Kavli Institute for Particle Astrophysics & Cosmology, P. O. Box 2450, Stanford University, Stanford, CA 94305, USA
[366] SLAC National Accelerator Laboratory, Menlo Park, CA 94025, USA
[367] Institute of Cosmology & Gravitation, University of Portsmouth, Portsmouth PO1 3FX, UK
[368] Observatório Nacional, Rua Gal. José Cristino 77, Rio de Janeiro, RJ—20921-400, Brazil
[369] Department of Astronomy, University of Illinois, 1002 W. Green Street, Urbana, IL 61801, USA
[370] Institute of Space Sciences, IEEC-CSIC, Campus UAB, Carrer de Can Magrans, s/n, E-08193 Barcelona, Spain
[371] George P. and Cynthia Woods Mitchell Institute for Fundamental Physics and Astronomy, and Department of Physics and Astronomy, Texas A&M University,
College Station, TX 77843, USA
[372] Department of Physics, IIT Hyderabad, Kandi, Telangana 502285, India
[373] Excellence Cluster Universe, Boltzmannstr. 2, D-85748 Garching, Germany
[374] Faculty of Physics, Ludwig-Maximilians-Universität, Scheinerstr. 1, D-81679 Munich, Germany
[375] Department of Physics, California Institute of Technology, Pasadena, CA 91125, USA
[376] Jet Propulsion Laboratory, California Institute of Technology, 4800 Oak Grove Drive, Pasadena, CA 91109, USA
[377] Institut de Física d'Altes Energies (IFAE), The Barcelona Institute of Science and Technology, Campus UAB, 08193 Bellaterra (Barcelona), Spain
[378] Department of Astronomy, University of Michigan, Ann Arbor, MI 48109, USA
[379] Department of Physics, University of Michigan, Ann Arbor, MI 48109, USA
[380] Universitäts-Sternwarte, Fakultät für Physik, Ludwig-Maximilians Universität München, Scheinerstr. 1, D-81679 München, Germany
[381] Department of Astronomy, University of California, Berkeley, 501 Campbell Hall, Berkeley, CA 94720, USA
[382] Center for Cosmology and Astro-Particle Physics, The Ohio State University, Columbus, OH 43210, USA
[383] Department of Physics, The Ohio State University, Columbus, OH 43210, USA
[384] Astronomy Department, University of Washington, Box 351580, Seattle, WA 98195, USA
[385] Santa Cruz Institute for Particle Physics, Santa Cruz, CA 95064, USA
[386] Australian Astronomical Observatory, North Ryde, NSW 2113, Australia
[387] Departamento de Física Matemática, Instituto de Física, Universidade de São Paulo, CP 66318, São Paulo, SP—05314-970, Brazil
[388] Department of Astronomy, The Ohio State University, Columbus, OH 43210, USA

[389] Institució Catalana de Recerca i Estudis Avançats, E-08010 Barcelona, Spain
[390] Max Planck Institute for Extraterrestrial Physics, Giessenbachstrasse, D-85748 Garching, Germany
[391] Department of Physics and Astronomy, Pevensey Building, University of Sussex, Brighton BN1 9QH, UK
[392] Centro de Investigaciones Energéticas, Medioambientales y Tecnológicas (CIEMAT), Madrid, Spain
[393] Brookhaven National Laboratory, Building 510, Upton, NY 11973, USA
[394] School of Physics and Astronomy, University of Southampton, Southampton SO17 1BJ, UK
[395] Computer Science and Mathematics Division, Oak Ridge National Laboratory, Oak Ridge, TN 37831, USA
[396] Argonne National Laboratory, 9700 South Cass Avenue, Lemont, IL 60439, USA
[397] Department of Physics, Stanford University, 382 Via Pueblo Mall, Stanford, CA 94305, USA
[398] Department of Physics and Astronomy, University of North Carolina at Chapel Hill, Chapel Hill, NC 27599, USA
[399] Department of Astronomy and Steward Observatory, University of Arizona, 933 N Cherry Avenue, Tucson, AZ 85719, USA
[400] Department of Physics, University of California, 1 Shields Avenue, Davis, CA 95616-5270, USA
[401] Department of Physics and Astronomy, University of Padova, Via 8 Febbraio, I-35122 Padova, Italy
[402] INAF—Osservatorio Astronomico di Padova, Vicolo della Osservatorio 5, I-35122 Padova, Italy
[403] INAF—Osservatorio Astronomico di Padova, Vicolo dell'Osservatorio 5, I-35122 Padova, Italy
[404] INAF—Osservatorio Astronomico di Roma, Via di Frascati, 33, I-00078 Monteporzio Catone, Italy
[405] INAF—Osservatorio Astronomico di Brera, Via E. Bianchi 46, I-23807 Merate (LC), Italy
[406] Space Science Data Center, ASI, Via del Politecnico, s.n.c., I-00133, Roma, Italy
[407] INAF—Osservatorio Astronomico di Capodimonte, salita Moiariello 16, I-80131, Napoli, Italy
[408] INAF—Istituto di Astrofisica Spaziale e Fisica Cosmica di Bologna, Via Gobetti 101, I-40129 Bologna, Italy
[409] Dipartimento di Fisica "G. Occhialini," Università degli Studi di Milano-Bicocca, P.za della Scienza 3, I-20126 Milano, Italy
[410] Laboratoire Univers et Particules de Montpellier, Université Montpellier 2, 34095, Montpellier, France
[411] INAF—Osservatorio Astronomico di Catania, Via S. Sofia 78, I-95123, Catania, Italy
[412] Department of physics, University of Naples Federico II, Corso Umberto I, 40, I-80138 Napoli, Italy
[413] Institute for Astrophysics and Particle Physics, University of Innsbruck, Technikerstrasse 25/8, A-6020 Innsbruck, Austria
[414] Departamento de Ciencias Físicas, Universidad Andrés Bello, Fernández Concha 700, Las Condes, Santiago, Chile
[415] Università degli Studi dell'Insubria, via Valleggio 11, I-22100, Como, Italy
[416] INAF—Istituto di Astrofisica Spaziale e Fisica Cosmica di Milano, via E. Bassini 15, I-20133 Milano, Italy
[417] INAF—Osservatorio Astrofisico di Torino, Pino Torinese, Italy
[418] INAF—Osservatorio Astrofisico di Arcetri, Largo Enrico Fermi 5, I-50125, Florence, Italy
[419] INAF—Istituto di Radioastronomia di Bologna, Bologna Italy
[420] Key Laboratory of dark Matter and Space Astronomy, Purple Mountain Observatory, Chinese Academy of Science, Nanjing 210008, China
[421] Thüringer Landessternwarte Tautenburg, Sternwarte 5, D-07778 Tautenburg, Germany
[422] Department of Physics, The George Washington University, Corcoran Hall, Washington, DC 20052, USA
[423] Astronomy, Physics, and Statistics Institute of Sciences (APSIS)
[424] Astrophysics Research Institute, Liverpool John Moores University, Liverpool Science Park, IC2, 146 Brownlow Hill, Liverpool L3 5RF, UK
[425] Max-Planck-Institut für Astrophysik, Karl-Schwarzschild-Str. 1, D-85748 Garching bei München, Germany
[426] European Southern Observatory, Karl-Schwarzschild-Strasse 2, D-85748 Garching bei München, Germany
[427] INAF—Osservatorio Astronomico di Trieste, Via G.B. Tiepolo 11, I-34143 Trieste, Italy
[428] Racah Institute of Physics, The Hebrew University of Jerusalem, Jerusalem 91904, Israel
[429] GEPI, Observatoire de Paris, PSL Research University, CNRS, Place Jules Janssen, F-92190, Meudon, France
[430] Department of Physics and Astronomy, University of Leicester, Leicester LE1 7RH, UK
[431] Frontier Research Institute for Interdisciplinary Sciences, Tohoku University, Sendai 980-8578, Japan
[432] Astronomical Institute, Tohoku University, Sendai 980-8578, Japan
[433] Department of Physics, University of Bath Claverton Down, Bath, BA2 7AY, UK
[434] CEA Saclay—DRF/Irfu/Département d'Astrophysique, F-91191 Gif-sur-Yvette, France
[435] Department of Physics and Institute of Theoretical Physics, Nanjing Normal University, Nanjing 210046, China
[436] Center for Astrophysics and Cosmology (CAC), University of Nova Gorica, Nova Gorica, Slovenia
[437] Anton Pannekoek Institute, University of Amsterdam, Science Park 904, 1098XH Amsterdam, The Netherlands
[438] Astrophysics Research Institute, Liverpool John Moores University, ic2, Liverpool Science Park, 146 Brownlow Hill, Liverpool L3 5RF, UK
[439] Faculty of Mathematics and Physics, University of Ljubljana, Jadranska 19, 1000 Ljubljana, Slovenia
[440] Yunnan Observatories, Chinese Academy of Sciences, 650011 Kunming, Yunnan Province, China
[441] Astrophysics Research Institute, Liverpool John Moores University, Liverpool, L3 5RF, UK
[442] Department of Physics, The George Washington University, 725 21st Street NW, Washington, DC 20052, USA
[443] Laboratoire AIM, CEA-IRFU/CNRS/Université Paris Diderot, Service d'Astrophysique, CEA Saclay, F-91191 Gif-sur-Yvette, France
[444] Santa Cruz Institute for Particle Physics, Department of Physics and Department of Astronomy and Astrophysics, University of California at Santa Cruz, Santa Cruz, CA 95064, USA
[445] Università di Pisa and Istituto Nazionale di Fisica Nucleare, Sezione di Pisa, I-56127 Pisa, Italy
[446] Istituto Nazionale di Fisica Nucleare, Sezione di Trieste, and Università di Trieste, I-34127 Trieste, Italy
[447] Dipartimento di Fisica, Università di Trieste, I-34127 Trieste, Italy
[448] Istituto Nazionale di Fisica Nucleare, Sezione di Padova, I-35131 Padova, Italy
[449] Dipartimento di Fisica e Astronomia "G. Galilei," Università di Padova, I-35131 Padova, Italy
[450] California State University, Los Angeles, Department of Physics and Astronomy, Los Angeles, CA 90032, USA
[451] Istituto Nazionale di Fisica Nucleare, Sezione di Pisa, I-56127 Pisa, Italy
[452] Dipartimento di Fisica "M. Merlin" dell'Università e del Politecnico di Bari, I-70126 Bari, Italy
[453] Istituto Nazionale di Fisica Nucleare, Sezione di Bari, I-70126 Bari, Italy
[454] W. W. Hansen Experimental Physics Laboratory, Kavli Institute for Particle Astrophysics and Cosmology, Department of Physics and SLAC National Accelerator Laboratory, Stanford University, Stanford, CA 94305, USA
[455] Istituto Nazionale di Fisica Nucleare, Sezione di Torino, I-10125 Torino, Italy
[456] Dipartimento di Fisica, Università degli Studi di Torino, I-10125 Torino, Italy
[457] Laboratoire Univers et Particules de Montpellier, Université Montpellier, CNRS/IN2P3, F-34095 Montpellier, France
[458] Deutsches Elektronen Synchrotron DESY, D-15738 Zeuthen, Germany
[459] Center for Research and Exploration in Space Science and Technology (CRESST) and NASA Goddard Space Flight Center, Greenbelt, MD 20771, USA
[460] Italian Space Agency, Via del Politecnico, snc, I-00133 Roma, Italy
[461] College of Science, George Mason University, Fairfax, VA 22030; Resident at Naval Research Laboratory, Washington, DC 20375, USA

[462] Space Science Division, Naval Research Laboratory, Washington, DC 20375-5352, USA
[463] Space Science Data Center—Agenzia Spaziale Italiana, Via del Politecnico, snc, I-00133, Roma, Italy
[464] Istituto Nazionale di Fisica Nucleare, Sezione di Perugia, I-06123 Perugia, Italy
[465] Department of Physics and Astronomy, Sonoma State University, Rohnert Park, CA 94928-3609, USA
[466] RWTH Aachen University, Institute for Theoretical Particle Physics and Cosmology (TTK), D-52056 Aachen, Germany
[467] INAF Istituto di Radioastronomia, I-40129 Bologna, Italy
[468] Dipartimento di Astronomia, Università di Bologna, I-40127 Bologna, Italy
[469] Università Telematica Pegaso, Piazza Trieste e Trento, 48, I-80132 Napoli, Italy
[470] Laboratoire Leprince-Ringuet, École polytechnique, CNRS/IN2P3, F-91128 Palaiseau, France
[471] Department of Physical Sciences, Hiroshima University, Higashi-Hiroshima, Hiroshima 739-8526, Japan
[472] Department of Physics and Department of Astronomy, University of Maryland, College Park, MD 20742, USA
[473] Centre d'Études Nucléaires de Bordeaux Gradignan, IN2P3/CNRS, Université Bordeaux 1, BP120, F-33175 Gradignan Cedex, France
[474] Laboratoire de Physique et Chimie de l'Environnement et de l'Espace, Université d'Orléans/CNRS, F-45071 Orléans Cedex 02, France
[475] Station de radioastronomie de Nançay, Observatoire de Paris, CNRS/INSU, F-18330 Nançay, France
[476] Science Institute, University of Iceland, IS-107 Reykjavik, Iceland
[477] Nordita, Roslagstullsbacken 23, 106 91 Stockholm, Sweden
[478] Department of Physics, Graduate School of Science, University of Tokyo, 7-3-1 Hongo, Bunkyo-ku, Tokyo 113-0033, Japan
[479] Istituto Nazionale di Fisica Nucleare, Sezione di Roma "Tor Vergata," I-00133 Roma, Italy
[480] Department of Physics and Astronomy, Clemson University, Kinard Lab of Physics, Clemson, SC 29634-0978, USA
[481] Max-Planck-Institut für Physik, D-80805 München, Germany
[482] Department of Physics, University of Johannesburg, PO Box 524, Auckland Park 2006, South Africa
[483] Institut für Astro- und Teilchenphysik and Institut für Theoretische Physik, Leopold-Franzens-Universität Innsbruck, A-6020 Innsbruck, Austria
[484] Department of Physics, The University of Hong Kong, Pokfulam Road, Hong Kong, China
[485] Laboratory for Space Research, The University of Hong Kong, Hong Kong, China
[486] NYCB Real-Time Computing Inc., Lattingtown, NY 11560-1025, USA
[487] Purdue University Northwest, Hammond, IN 46323, USA
[488] Hiroshima Astrophysical Science Center, Hiroshima University, Higashi-Hiroshima, Hiroshima 739-8526, Japan
[489] CNRS, IRAP, F-31028 Toulouse cedex 4, France
[490] GAHEC, Universit de Toulouse, UPS-OMP, IRAP, F-31400 Toulouse, France
[491] Institute of Space Sciences (CSICIEEC), Campus UAB, Carrer de Magrans s/n, E-08193 Barcelona, Spain
[492] Institució Catalana de Recerca i Estudis Avançats (ICREA), E-08010 Barcelona, Spain
[493] INAF-Istituto di Astrofisica Spaziale e Fisica Cosmica Bologna, via P. Gobetti 101, I-40129 Bologna, Italy
[494] Centre for Astrophysics and Cosmology, University of Nova Gorica, Vipavska 11c, 5270 Ajdovščina, Slovenia
[495] Sydney Institute for Astronomy, School of Physics, The University of Sydney, Sydney, NSW 2006, Australia
[496] ARC Centre of Excellence for All-sky Astrophysics in 3 Dimensions (ASTRO 3D)
[497] ATNF, CSIRO Astronomy and Space Science, PO Box 76, Epping, NSW 1710, Australia
[498] ARC Centre of Excellence for All-sky Astrophysics (CAASTRO)
[499] University of Wisconsin–Milwaukee, Milwaukee, WI 53201, USA
[500] ATNF, CSIRO Astronomy and Space Science, 26 Dick Perry Avenue, Kensington, WA 6152, Australia
[501] International Centre for Radio Astronomy Research, Curtin University, Bentley, WA 6102, Australia
[502] Centre for Astrophysics and Supercomputing, Swinburne University of Technology, Mail H30, PO Box 218, VIC 3122, Australia
[503] Department of Physics, University of California, Santa Barbara, CA 93106-9530, USA
[504] Las Cumbres Observatory, 6740 Cortona Drive, Suite 102, Goleta, CA 93117-5575, USA
[505] School of Physics and Astronomy, Tel Aviv University, Tel Aviv 69978, Israel
[506] Columbia Astrophysics Laboratory, Columbia University, New York, NY, 10027, USA
[507] Centre for Astrophysics and Supercomputing, Swinburne University of Technology, PO Box 218, H29, Hawthorn, VIC 3122, Australia
[508] The Australian Research Council Centre of Excellence for Gravitational Wave Discovery (OzGrav), Australia
[509] The Australian Research Council Centre of Excellence for All-Sky Astrophysics (CAASTRO), Australia
[510] Research School of Astronomy and Astrophysics, The Australian National University, Canberra, ACT 2611, Australia
[511] Australian Astronomical Observatory, 105 Delhi Road, North Ryde, NSW 2113, Australia
[512] George P. and Cynthia Woods Mitchell Institute for Fundamental Physics & Astronomy, Texas A. & M. University,
Department of Physics and Astronomy, 4242 TAMU, College Station, TX 77843, USA
[513] Purple Mountain Observatory, Chinese Academy of Sciences, Nanjing 210008, China
[514] Chinese Center for Antarctic Astronomy, Nanjing 210008, China
[515] The University of the Virgin Islands, 2 John Brewer's Bay, St. Thomas 00802, USVI
[516] Monash Centre for Astrophysics, Monash University, VIC 3800, Australia
[517] Centre for Translational Data Science, University of Sydney, Sydney, NSW 2006, Australia
[518] School of Physics and Astronomy, University of Nottingham, Nottingham, UK
[519] CSIRO Astronomy & Space Science, Australia Telescope National Facility, P.O. Box 76, Epping, NSW 1710, Australia
[520] SKA Organisation, Jodrell Bank Observatory, SK11 9DL, UK
[521] National Astronomical Observatories, Chinese Academy of Sciences, Beijing 100012, China
[522] Physics Department and Tsinghua Center for Astrophysics (THCA), Tsinghua University, Beijing, 100084, China
[523] Tianjin Normal University, Tianjin 300074, China
[524] School of Physics, University of New South Wales, NSW 2052, Australia
[525] Nanjing Institute of Astronomical Optics and Technology, Nanjing 210042, China
[526] Department of Astronomy, Beijing Normal University, Beijing 100875, China
[527] School of Astronomy and Space Science and Key Laboratory of Modern Astronomy and Astrophysics in Ministry of Education, Nanjing University,
Nanjing 210093, China
[528] Orangewave Innovation Science, 2113 Old Highway 52, Moncks Corner, SC 29461, USA
[529] Department of Physics, 2354 Fairchild Drive, U.S. Air Force Academy, CO 80840, USA
[530] Universite de Toulouse, IRAP 14 Av. Edouard Belin, F-31000 Toulouse France
[531] Auragne Observatory, France
[532] Research School of Astronomy and Astrophysics, The Australian National University, Canberra, ACT 2611, Australia
[533] Department of Physics and Astronomy, University of Leicester, University Road, Leicester, LE1 7RH, UK
[534] Instituto de Astrofísica de Andalucía (IAA-CSIC), Glorieta de la Astronomía s/n, E-18008 Granada, Spain

[535] Institute of Astronomy, University of Cambridge, Madingley Road, Cambridge, CB3 0HA, UK

[536] Max-Planck-Institut für extraterrestrische Physik, Giessenbachstr. 1, D-85740 Garching, Germany

[537] Birmingham Institute for Gravitational Wave Astronomy and School of Physics and Astronomy, University of Birmingham, Birmingham B15 2TT, UK

[538] School of Physics and Astronomy and Monash Centre for Astrophysics, Monash University, VIC 3800, Australia

[539] The Oskar Klein Centre, Department of Astronomy, AlbaNova, Stockholm University, SE-106 91 Stockholm, Sweden

[540] Anton Pannekoek Institute, University of Amsterdam, Science Park 904, 1098 XH Amsterdam, the Netherlands

[541] ASTRON, the Netherlands Institute for Radio Astronomy, Postbus 2, 7990 AA Dwingeloo, the Netherlands

[542] SUPA, School of Physics & Astronomy, University of St Andrews, North Haugh, St Andrews KY16 9SS, UK

[543] Niels Bohr Institute & Centre for Star and Planet Formation, University of Copenhagen Øster Voldgade 5, DK-1350—Copenhagen, Denmark

[544] Institute for Advanced Research, Nagoya University, Furo-cho, Chikusa-ku, Nagoya 464-8601, Japan

[545] Space Telescope Science Institute, 3700 San Martin Drive, Baltimore, MD 21218, USA

[546] Centre for Astrophysics and Cosmology, Science Institute, University of Iceland, Dunhagi 5, 107 Reykjavík, Iceland

[547] Instituto de Astrofísica, Pontificia Universidad Católica de Chile, Av. Vicuña Mackenna 4860, 7820436 Macul, Santiago, Chile

[548] Max-Planck-Institut für Astronomie Königstuhl 17, D-69117 Heidelberg, Germany

[549] Lomonosov Moscow State University, Physics Department, Vorobievy gory, 1 Moscow, 119991, Russia

[550] Lomonosov Moscow State University,SAI, Universitetsky prospekt, 13 Moscow, 119234, Russia

[551] Observatorio Astronomico Felix Aguilar (OAFA), Avda Benavides s/n, Rivadavia, El Leonsito, Argentina

[552] Instituto de Ciencias Astronomicas de la Tierra y del Espacio, Casilla de Correo 49, 5400 San Juan, Argentina

[553] Universidad Nacional de San Juan, Av. Ignacio de la Roza 391, San Juan, 5400, Argentina

[554] Irkutsk State University Applied Physics Institute, 20, Boulevard, 664003, Irkutsk, Russia

[555] Blagoveschenk State Pedagogical University, Lenin str., 104, Blagoveschensk, 675000, Russia

[556] Instituto de Astrofsica de Canarias, C/Via Lctea, s/n E-38205, La Laguna, Tenerife, Spain

[557] Kislovodsk Solar Station, Pulkovo Observatory RAS, Gagarina str. 100, Kislovodsk, 357700, Russia

[558] Institute for Space-Earth Environmental Research, Nagoya, 464-8601, Japan

[559] Subaru Telescope, Hilo, HI 96720, USA

[560] National Astronomical Observatory of Japan, Mitaka, Tokyo 181-8588, Japan

[561] University of Hyogo, Sayo 679-5313, Japan

[562] South African Astronomical Observatory, Cape Town, South Africa

[563] Massey University, Auckland 0745, New Zealand

[564] Institute of Astronomy, Graduate School of Science, Mitaka 181-0015, Japan

[565] Tokyo Institute of Technology, Tokyo 152-8551, Japan

[566] Osaka City University, Osaka 558-8585, Japan

[567] Hiroshima Astrophysical Science Center, Higashi-Hiroshima 739-8526, Japan

[568] Hiroshima University, Higashi-Hiroshima, 739-8526, Japan

[569] Okayama Astrophysical Observatory, Asakuchi 719-0232, Japan

[570] Purple Mountain Observatory, Nanjing 210008, China

[571] Osaka University, Toyonaka 560-0043, Japan

[572] Nagoya University, Nagoya 464-8602, Japan

[573] Kagoshima University, Kogoshima 890-0065, Japan

[574] Kyoto University, Kyoto 606-8502, Japan

[575] Precursory Research for Embryonic Science and Technology, Mitaka, Tokyo 181-0015, Japan

[576] Toho University, Funabashi 274-8510, Japan

[577] Konan University, Kobe 658-8501, Japan

[578] Kavli Institute for the Physics and Mathematics of the Universe (WPI), Kashiwa 277-8583, Japan

[579] University of Canterbury, Mt John Observatory, Lake Tekapo 7945, New Zealand

[580] Division of Physics, Math and Astronomy, California Institute of Technology, Pasadena, CA 91125, USA

[581] Indian Institute of Astrophysics, Bangalore-560034, India

[582] University of Colorado, Boulder, CO 80309, USA

[583] South African Astronomical Observatory (SAAO), Cape Town 7935, South Africa

[584] Department of Astronomy, University of Washington, Seattle, WA 98195, USA

[585] National Center for Radio Astrophysics, Tata Institute of Fundamental Research, Pune University Campus, Ganeshkhind Pune 411007, India

[586] Department of Physics, University of Wisconsin, Milwaukee, WI 53201, USA

[587] Remote Sensing Division, Naval Research Laboratory, Code 7213, Washington, DC 20375, USA

[588] Department of Physics, George Washington University,Washington, DC 20052, USA

[589] University College London, Mullard Space Science Laboratory, RH5 6NT, UK

[590] X-ray and Observational Astronomy Research Group, Leicester Institute for Space and Earth Observation, Department of Physics & Astronomy, University of Leicester, Leicester LE1 7RH, UK

[591] The Oskar Klein Centre, Department of Physics, Stockholm, University, AlbaNova, SE-106 91 Stockholm, Sweden

[592] Space Telescope Science Institute, Baltimore, MD 21218, USA

[593] National Radio Astronomy Observatory, Socorro, NM, USA

[594] Department of Physics and Astronomy, University of Southampton, Southampton, Hampshire SO17 1BJ, UK

[595] Institute of Cosmology and Gravitation, University of Portsmouth, Portsmouth PO1 3FX, UK

[596] The Raymond and Beverly Sackler School of Physics and Astronomy, Tel Aviv University, Tel Aviv 69978, Israel

[597] Infrared Processing and Analysis Center, California Institute of Technology, Pasadena, CA 91125, USA

[598] Racah Institute of Physics, The Hebrew University of Jerusalem, Jerusalem, 91904, Israel

[599] Center for Computational Astrophysics, Simons Foundation, New York, NY 10010, USA

[600] Graduate Institute of Astronomy, National Central University, Taoyuan City 32001, Taiwan

[601] Department of Physics, Tokyo Institute of Technology, Tokyo 152-8551, Japan

[602] Department of Astronomy, University of California, Berkeley, CA 94720-3411, USA

[603] Department of Physics, University of California, Berkeley, CA 94720, USA

[604] Gemini Observatory, Casilla 603, La Serena, Chile

[605] Max-Planck Institute for Astrophysics, Garching, Germany

[606] Center for Interdisciplinary Exploration and Research in Astrophysics (CIERA), Department of Physics and Astronomy, Northwestern University, Evanston, IL 60208, USA

[607] The Adler Planetarium, Chicago, IL 60605, USA

54

Abbott et al.

[608] Astrophysics, Department of Physics, University of Oxford, Oxford OX1 3RH, UK
[609] Department of Particle Physics & Astrophysics, Weizmann Institute of Science, Rehovot 7610001, Israel
[610] Department of Physics and Astronomy, Texas Tech University, Lubbock, TX 79409-1051, USA
[611] Astrophysics Research Institute, Liverpool John Moores University, IC2, Liverpool Science Park, 146 Brownlow Hill, Liverpool L3 5RF, UK
[612] Department of Astronomy, San Diego State University, CA 92182, USA
[613] Kavli Institute for the Physics and Mathematics of the Universe (WPI), The University of Tokyo Institutes for Advanced Study, The University of Tokyo, Kashiwa, Chiba 277-8583, Japan
[614] The Oskar Klein Centre, Department of Astronomy, Stockholm University, AlbaNova, SE-106 91 Stockholm, Sweden
[615] University of California Merced, Merced, CA, USA
[616] Australian Research Council Centre of Excellence for All-sky Astrophysics (CAASTRO), Sydney Institute for Astronomy, School of Physics, The University of Sydney, Sydney, NSW 2006, Australia
[617] Institute for Astronomy, University of Hawaii, 2680 Woodlawn Drive, Honolulu, Hawaii 96822, USA
[618] ISAS/JAXA, Sagamihara, Kanagawa 229-8510, Japan
[619] University of Miyazaki, Miyazaki, Miyazaki 889-2192, Japan
[620] Tokyo Institute of Technology, Meguro-ku, Tokyo 152-8551, Japan
[621] Aoyama Gakuin University, Sagamihara, Kanagawa 229-8558, Japan
[622] Kyoto University, Kyoto, Kyoto, 606-8502, Japan
[623] JAXA, Tsukuba, Ibaraki 305-8505, Japan
[624] RIKEN, Wako, Saitama, 351-0198, Japan
[625] Chuo University, Bunkyo-ku, Tokyo 112-8551, Japan
[626] National Astronomical Observatory of Japan, Mitaka, Tokyo 181-8588, Japan
[627] Nihon University, Chiyoda-ku, Tokyo 101-8308, Japan
[628] Osaka University, Toyonaka, Osaka 560-0043, Japan
[629] Nagoya University, Nagoya, Aichi 464-8601, Japan
[630] The University of Western Australia, 35, Stirling Highway, Perth, WA 6009, Australia
[631] Swinburne University, John Street, Hawthorn, VIC 3122, Australia
[632] ARTEMIS (UCA, CNRS, OCA), boulevard de l'Observatoire, CS 34229, F-06304 Nice, France
[633] IRAP (CNRS, UPS), 14 avenue Edouard Belin, F-31029 Toulouse, France
[634] The University of the Virgin Islands, 2 John Brewer's Bay, St Thomas 00802, USVI
[635] The Auragne Observatory, F-31190 Auragne, France
[636] Center of the Exploration of the Origin of the Universe, Astronomy Program, Dept. of Physics & Astronomy, Seoul National University, 1 Gwanak-rho, Gwanak-gu, Seoul 08826, Korea
[637] Korea Astronomy and Space Science Institute, 776 Daedeokdae-ro, Yuseong-gu, Daejeon 34055, Korea
[638] CAS Key Laboratory of Space Astronomy and Technology, National Astronomical Observatories, Chinese Academy of Sciences, Beijing 100012, China
[639] Astrophysics Research Centre, School of Mathematics and Physics, Queens University Belfast, Belfast BT7 1NN, UK
[640] Department of Physics and Astronomy, University of Southampton, Southampton SO17 1BJ, UK
[641] Department of Particle Physics and Astrophysics, Weizmann Institute of Science, Rehovot 76100, Israel
[642] Department of Physics, University of Warwick, Coventry CV4 7AL, UK
[643] Institute for Astronomy, SUPA (Scottish Universities Physics Alliance), University of Edinburgh, Royal Observatory, Blackford Hill, Edinburgh EH9 3HJ, UK
[644] Departamento de Ciencias Fisicas, Universidad Andres Bello, Avda. Republica 252, Santiago, 8320000, Chile
[645] Millennium Institute of Astrophysics (MAS), Nuncio Monseñor Sótero Sanz 100, Providencia, Santiago, Chile
[646] European Southern Observatory, Alonso de Córdova 3107, Casilla 19, Santiago, Chile
[647] The Oskar Klein Centre, Department of Astronomy, Stockholm University, SE-10691 Stockholm, Sweden
[648] Instituto de Astrofísica and Centro de Astroingeniería, Facultad de Física, Pontificia Universidad Católica de Chile, Casilla 306, Santiago 22, Chile
[649] Space Science Institute, 4750 Walnut Street, Suite 205, Boulder, CO 80301, USA
[650] Dipartimento di Fisica e Astronomia "G. Galilei," Università di Padova, Vicolo dell'Osservatorio 3, I-35122, Padova, Italy
[651] INAF—Osservatorio Astronomico di Brera, via E. Bianchi 46, I-23807 Merate (LC), Italy
[652] INAF—Osservatorio Astronomico di Capodimonte, via Salita Moiariello 16, I-80131 Napoli, Italy
[653] The Oskar Klein Centre, Department of Physics, Stockholm University, AlbaNova, SE-10691 Stockholm, Sweden
[654] SRON, Netherlands Institute for Space Research, Sorbonnelaan 2, NL-3584 CA Utrecht, The Netherlands
[655] European Southern Observatory, Karl-Schwarzschild-Str. 2, D-85748 Garching b. München, Germany
[656] ICRANet-Pescara, Piazza della Repubblica 10, I-65122 Pescara, Italy
[657] IAP/CNRS and Université Pierre et Marie Curie, Paris, France
[658] Unidad Mixta Internacional Franco-Chilena de Astronomía (CNRS UMI 3386), Departamento de Astronomía, Universidad de Chile, Camino El Observatorio 1515, Las Condes, Santiago, Chile
[659] Istituto Nazionale di Astrofisica, Viale del Parco Mellini 84, I-00136 Roma, Italy
[660] Institute of Cosmology and Gravitation, Dennis Sciama Building, University of Portsmouth, Burnaby Road, Portsmouth PO1 3FX, UK
[661] PITT PACC, Department of Physics and Astronomy, University of Pittsburgh, Pittsburgh, PA 15260, USA
[662] CENTRA, Instituto Superior Técnico, Universidade de Lisboa, Portugal
[663] Warsaw University Astronomical Observatory, Al. Ujazdowskie 4, 00-478 Warszawa, Poland
[664] Tuorla Observatory, Department of Physics and Astronomy, University of Turku, Väisäläntie 20, FI-21500 Piikkiö, Finland
[665] Instituto de Física y Astronomía, Universidad de Valparaiso, Gran Bretaña 1111, Playa Ancha, Valparaíso 2360102, Chile
[666] Institute of Astronomy, University of Cambridge, Madingley Road, Cambridge, CB3 0HA, UK
[667] Department of Physics, Lancaster University, Lancaster LA1 4YB, UK
[668] Instituto de Astrofísica de Andalucía (IAA-CSIC), Glorieta de la Astronomía s/n, E-18008, Granada, Spain
[669] Zentrum für Astronomie der Universität Heidelberg, Institut für Theoretische Astrophysik, Philosophenweg 12, D-69120 Heidelberg, Germany
[670] Heidelberger Institut für Theoretische Studien, Schloss-Wolfsbrunnenweg 35, D-69118 Heidelberg, Germany
[671] Finnish Centre for Astronomy with ESO (FINCA), University of Turku, Väisäläntie 20, 21500 Piikkiö, Finland
[672] Max Planck Institute for Astronomy, Königstuhl 17, D-69117 Heidelberg, Germany
[673] Institut für Physik, Humboldt-Universitat zu Berlin, Newtonstr. 15, D-12489 Berlin, Germany
[674] Sorbonne Universités, UPMC Univ. Paris 6 and CNRS, UMR 7095, Institut d'Astrophysique de Paris, 98 bis bd Arago, F-75014 Paris, France
[675] INAF-Osservatorio Astronomico di Padova, Vicolo dell'Osservatorio 5, I-35122 Padova, Italy
[676] Department of Astrophysics, University of Oxford, Oxford OX1 3RH, UK
[677] Department of Astronomy, Universidad de Chile, Camino El Observatorio 1515, Las Condes, Santiago de Chile, Chile

[678] School of Physical, Environmental, and Mathematical Sciences, University of New South Wales, Australian Defence Force Academy, Canberra, ACT 2600, Australia

[679] ARC Centre of Excellence for All-sky Astrophysics (CAASTRO), Canberra, ACT 2611, Australia

[680] Università degli studi di Catania, DFA & DIEEI, Via Santa Sofia 64, I-95123 Catania, Italy

[681] INFN—Laboratori Nazionali del Sud, Via Santa Sofia 62, I-95123 Catania, Italy

[682] Department of Physics, University of the Free State, Bloemfontein, 9300 South Africa

[683] School of Physics and Astronomy, University of Minnesota, 116 Church Street SE, Minneapolis, MN 55455-0149, USA

[684] Max-Planck-Institut für Extraterrestrische Physik, Giessenbachstraße 1, D-85748, Garching, Germany

[685] Thüringer Landessternwarte Tautenburg, Sternwarte 5, D-07778 Tautenburg, Germany

[686] Texas Tech University, Lubbock, TX 79409, USA

[687] Department of Astrophysics, American Museum of Natural History, Central Park West and 79th Street, New York, NY 10024, USA

[688] South African Astronomical Observatory, PO Box 9, 7935 Observatory, South Africa

[689] Southern African Large Telescope Foundation, P.O. Box 9, 7935 Observatory, South Africa.

[690] Center for Gravitational Wave Astronomy and Department of Physics & Astronomy, University of Texas—Río Grande Valley, Brownsville, TX, USA

[691] George P. and Cynthia W. Mitchell Institute for Fundamental Physics & Astronomy, Department of Physics & Astronomy, Texas A&M University, College Station, TX, USA

[692] IATE-OAC, Universidad Nacional de Córdoba-CONICET, Córdoba, Argentina

[693] Instituto de Astronomia, Geofísica e Ciências Atmosféricas da U. de São Paulo, São Paulo, SP, Brazil

[694] Instituto de Investigación Multidisciplinario en Ciencia y Tecnología, Universidad de La Serena, La Serena, Chile

[695] Departamento de Física y Astronomía, Universidad de La Serena, La Serena, Chile

[696] Departamento de Física, Universidade Federal de Sergipe, São Cristóvão, SE, Brazil

[697] Departamento de Física, Universidade Federal de Santa Catarina, Florianópolis, SC, Brazil

[698] Departamento de Física Matemática, Instituto de Física, Universidade de São Paulo, São Paulo, SP, Brazil

[699] Departamento de Astronomia, Observatório Nacional, Rio de Janeiro, RJ, Brazil

[700] Centro de Estudios de Física del Cosmos de Aragón, E-44001 Teruel, Spain

[701] Instituto Nacional de Astrofísica, Óptica y Electrónica, Tonantzintla, Puebla, México

[702] Instituto de Astronomía, Universidad Nacional Autónoma de México, Ciudad de México, México

[703] Instituto de Astrofísica, Pontificia Universidad Católica de Chile, Santiago, Chile

[704] Observatorio do Valongo, Universidade Federal do Rio de Janeiro, Río de Janeiro, RJ, Brazil

[705] X-ray Astrophysics Laboratory and CRESST, NASA Goddard Space Flight Center, Greenbelt, MD, USA

[706] Ludwig Maximilian Universität Munich, Faculty of Physics, Munich, Germany

[707] Department of Physics, University of Notre Dame, Notre Dame, IN, USA

[708] Joint Institute for Nuclear Astrophysics—Center for the Evolution of the Elements, USA

[709] Instituto de Astrofísica de Andalucía del Consejo Superior de Investigaciones Científicas (IAA-CSIC), Granada, Apdo. 03004, E-18080 Granada, Spain

[710] Departamento de Ingeniería de Sistemas y Automática, Escuela de Ingenierías (Unidad Asociada al IAA-CSIC), Universidad de Málaga, Dr. Pedro Ortiz Ramos, E-29071 Málaga, Spain

[711] Departamento de Álgebra, Geometría y Topología, Facultad de Ciencias, Universidad de Málaga, Málaga, Campus de Teatinos, E-29071 sn, Málaga, Spain

[712] Instituto de Astronomía, Universidad Nacional Autónoma de México, Apdo. Postal 870, 2800 Ensenada, Baja California, México

[713] Astronomical Institute, Academy of Sciences of the Czech Republic, Boční II 1401, CZ-141 00 Prague, Czech Republic

[714] Astronomical Institute, Academy of Sciences of the Czech Republic, 251 65 Ondřejov, Czech Republic

[715] Institute of Physics of the Czech Academy of Sciences, Na Slovance 1999/2, 182 21 Praha 8, Czech Republic

[716] Department of Physics, Sungkyunkwan University, 2066, Seobu-ro, Jangan-gu, Suwon, Gyeonggi-do, 16419, Korea

[717] ISDEFE for ESA, ESAC, E-28692 Villanueva de la Cañada (Madrid), Spain

[718] Aryabhatta Research Institute of Observational Sciences, Manora Peak, Nainital 263 002, India

[719] Department of Physics, University of Auckland, Private Bag 92019, Auckland, New Zealand

[720] National Institute of Water and Atmospheric Research (NIWA), Lauder, New Zealand

[721] Yunnan Astronomical Observatory, CAS, Kunming 650011, Yunnan, China

[722] School of Earth and Space Exploration, Arizona State University, Tempe, AZ 85287, USA

[723] Dunlap Institute for Astronomy and Astrophysics, University of Toronto, Toronto, ON M5S 3H4, Canada

[724] Peripety Scientific Ltd., PO Box 11355 Manners Street, Wellington, 6142, New Zealand

[725] Department of Physics, University of Washington, Seattle, WA 98195, USA

[726] International Centre for Radio Astronomy Research, University of Western Australia, Crawley, WA 6009, Australia

[727] National Centre for Nuclear Research, 00-681 Warsaw, Poland

[728] Aoyama Gakuin University, 5-10-1 Fuchinobe, Chuo, Sagamihara, Kanagawa 252-5258, Japan

[729] Nagoya University, Furo, Chikusa, Nagoya 464-8601, Japan

[730] Kavli Institute for the Physics and Mathematics of the Universe, The University of Tokyo, 5-1-5 Kashiwanoha, Kashiwa 277-8583, Japan

[731] Waseda University, 3-4-1 Okubo, Shinjuku, Tokyo 169-8555, Japan

[732] Kanagawa University, 3-27-1 Rokkakubashi, Kanagawa, Yokohama, Kanagawa 221-8686, Japan

[733] Institute for Cosmic Ray Research, The University of Tokyo, 5-1-5 Kashiwa-no-Ha, Kashiwa, Chiba 277-8582, Japan

[734] Institute of Applied Physics (IFAC), National Research Council (CNR), Via Madonna del Piano, 10, I-50019 Sesto, Fiorentino, Italy

[735] University of Siena, Rettorato, via Banchi di Sotto 55, I-53100 Siena, Italy

[736] Space Research Institute, Moscow, 117997, Russia

[737] National Research University Higher School of Economics, Moscow, 101000, Russia

[738] National Research Nuclear University MEPhI, Moscow, 115409, Russia

[739] Fesenkov Astrophysical Institute, Almaty, 050020, Kazakhstan

[740] Special Astrophysical Observatory of Russian Academy of Sciences, Nizhniy Arkhyz, 369167, Russia

[741] Crimean Astrophysical Observatory, Nauchny, Crimea 298409

[742] Kharadze Abastumani Astrophysical Observatory, Ilia State University, Tbilisi, 0162, Georgia

[743] Institute of Solar Terrestrial Physics, Irkutsk, 664033 Russia

[744] Institute of Astronomy and Geophysics, Mongolian Academy of Sciences, 13343, Ulaanbaatar, Mongolia

[745] Keldysh Institute of Applied Mathematics, Russian Academy of Sciences, Miusskaya 4, 125047, Moscow, Russia

[746] Ulugh Beg Astronomical Institute, Astronomicheskaya st., 33, Tashkent, 100052, Uzbekistan

[747] Centre for Space Research, North-West University, Potchefstroom 2520, South Africa

[748] Universität Hamburg, Institut für Experimentalphysik, Luruper Chaussee 149, D 22761 Hamburg, Germany

[749] Max-Planck-Institut für Kernphysik, P.O. Box 103980, D-69029 Heidelberg, Germany

[750] Dublin Institute for Advanced Studies, 31 Fitzwilliam Place, Dublin 2, Ireland

[751] National Academy of Sciences of the Republic of Armenia, Marshall Baghramian Avenue, 24, 0019 Yerevan, Republic of Armenia

[752] Instytut Fizyki Jądrowej PAN, ul. Radzikowskiego 152, 31-342 Kraków, Poland

[753] Department of Physics, Rikkyo University, 3-34-1 Nishi-Ikebukuro, Toshima-ku, Tokyo 171-8501, Japan

[754] LUTH, Observatoire de Paris, PSL Research University, CNRS, Université Paris Diderot, 5 Place Jules Janssen, F-92190 Meudon, France

[755] Laboratoire d'Annecy-le-Vieux de Physique des Particules, Université Savoie Mont-Blanc, CNRS/IN2P3, F-74941 Annecy-le-Vieux, France

[756] University of Namibia, Department of Physics, Private Bag 13301, Windhoek, Namibia

[757] GRAPPA, Anton Pannekoek Institute for Astronomy, University of Amsterdam, Science Park 904, 1098 XH Amsterdam, The Netherlands

[758] Department of Physics and Electrical Engineering, Linnaeus University, 351 95 Växjö, Sweden

[759] Institut für Theoretische Physik, Lehrstuhl IV: Weltraum und Astrophysik, Ruhr-Universität Bochum, D 44780 Bochum, Germany

[760] GRAPPA, Anton Pannekoek Institute for Astronomy and Institute of High-Energy Physics, University of Amsterdam, Science Park 904, 1098 XH Amsterdam, The Netherlands

[761] Institut für Astro- und Teilchenphysik, Leopold-Franzens-Universität Innsbruck, A-6020 Innsbruck, Austria

[762] School of Physical Sciences, University of Adelaide, Adelaide 5005, Australia

[763] Sorbonne Universités, UPMC Université Paris 06, Université Paris Diderot, Sorbonne Paris Cité, CNRS, Laboratoire de Physique Nucléaire et de Hautes Energies (LPNHE), 4 place Jussieu, F-75252, Paris Cedex 5, France

[764] Laboratoire Univers et Particules de Montpellier, Université Montpellier, CNRS/IN2P3, CC 72, Place Eugène Bataillon, F-34095 Montpellier Cedex 5, France

[765] Université Bordeaux, CNRS/IN2P3, Centre d'Études Nucléaires de Bordeaux Gradignan, F-33175 Gradignan, France

[766] IRFU, CEA, Université Paris-Saclay, F-91191 Gif-sur-Yvette, France

[767] Astronomical Observatory, The University of Warsaw, Al. Ujazdowskie 4, 00-478 Warsaw, Poland

[768] Institut für Astronomie und Astrophysik, Universität Tübingen, Sand 1, D 72076 Tübingen, Germany

[769] School of Physics, University of the Witwatersrand, 1 Jan Smuts Avenue, Braamfontein, Johannesburg 2050, South Africa

[770] Oskar Klein Centre, Department of Physics, Stockholm University, Albanova University Center, SE-10691 Stockholm, Sweden

[771] APC, AstroParticule et Cosmologie, Université Paris Diderot, CNRS/IN2P3, CEA/Irfu, Observatoire de Paris, Sorbonne Paris Cité, 10, rue Alice Domon et Léonie Duquet, 75205 Paris Cedex 13, France

[772] Department of Physics and Astronomy, The University of Leicester, University Road, Leicester LE1 7RH, UK

[773] Nicolaus Copernicus Astronomical Center, Polish Academy of Sciences, ul. Bartycka 18, 00-716 Warsaw, Poland

[774] Institut für Physik und Astronomie, Universität Potsdam, Karl-Liebknecht-Strasse 24/25, D 14476 Potsdam, Germany

[775] Aix Marseille Université, CNRS/IN2P3, CPPM, Marseille, France

[776] Landessternwarte, Universität Heidelberg, Königstuhl, D 69117 Heidelberg, Germany

[777] Univ. Grenoble Alpes, CNRS, IPAG, F-38000 Grenoble, France

[778] Institut für Physik, Humboldt-Universität zu Berlin, Newtonstr. 15, D 12489 Berlin, Germany

[779] Obserwatorium Astronomiczne, Uniwersytet Jagielloński, ul. Orla 171, 30-244 Kraków, Poland

[780] Centre for Astronomy, Faculty of Physics, Astronomy and Informatics, Nicolaus Copernicus University, Grudziadzka 5, 87-100 Torun, Poland

[781] Japan Aerpspace Exploration Agency (JAXA), Institute of Space and Astronautical Science (ISAS), 3-1-1 Yoshinodai, Chuo-ku, Sagamihara, Kanagawa 229-8510, Japan

[782] Department of Physics, University of the Free State, PO Box 339, Bloemfontein 9300, South Africa

[783] Heisenberg Fellow (DFG), ITA Universität Heidelberg, Germany

[784] Yerevan Physics Institute, 2 Alikhanian Brothers Street, 375036 Yerevan, Armenia

[785] Astrophysics, Department of Physics, University of Oxford, Keble Road, Oxford OX1 3RH, UK

[786] Anton Pannekoek Institute, University of Amsterdam, Science Park 904, 1098 XH Amsterdam, The Netherlands

[787] Long Island University, New York, NY 11201, USA

[788] Virginia Tech, Blacksburg, VA 24061, USA

[789] Air Force Research Laboratory, NM 87117, USA

[790] University of New Mexico, Albuquerque, NM 87131, USA

[791] Long Island University, Brookville, NY 11548, USA

[792] Department of Physics and Astronomy, University of Utah, Salt Lake City, UT, USA

[793] Physics Division, Los Alamos National Laboratory, Los Alamos, NM, USA

[794] Instituto de Física, Universidad Nacional Autónoma de México, Ciudad de México, México

[795] Universidad Autónoma de Chiapas, Tuxtla Gutiérrez, Chiapas, México

[796] Universidad Michoacana de San Nicolas de Hidalgo, Morelia, Mexico

[797] Department of Physics, Michigan Technological University, Houghton, MI, USA

[798] Department of Physics & Astronomy, University of Rochester, Rochester, NY, USA

[799] Department of Physics, University of Maryland, College Park, MD, USA

[800] Instituto de Astronomía, Universidad Nacional Autónoma de México, Ciudad de México, México

[801] Department of Physics, University of Wisconsin-Madison, Madison, WI, USA

[802] Instituto Nacional de Astrofísica, Optica y Electrónica, Puebla, Mexico

[803] Instytut Fizyki Jadrowej im Henryka Niewodniczanskiego Polskiej Akademii Nauk, IFJ-PAN, Krakow, Poland

[804] Facultad de Ciencias Físico Matematicas, Benemérita Universidad Autónoma de Puebla, Puebla, Mexico

[805] Departamento de Física, Centro Universitario de Ciencias Exactase Ingenierias, Universidad de Guadalajara, Guadalajara, Mexico

[806] School of Physics, Astronomy, and Computational Sciences, George Mason University, Fairfax, VA, USA

[807] Instituto de Geofísica, Universidad Nacional Autónoma de México, Ciudad de México, México

[808] Max-Planck Institute for Nuclear Physics, 69117 Heidelberg, Germany

[809] Department of Physics and Astronomy, University of New Mexico, Albuquerque, NM, USA

[810] School of Physics and Center for Relativistic Astrophysics—Georgia Institute of Technology, Atlanta, GA, USA 30332

[811] Department of Physics and Astronomy, Michigan State University, East Lansing, MI, USA

[812] Universidad Politecnica de Pachuca, Pachuca, Hgo, Mexico

[813] Centro de Investigación en Computación, Instituto Politécnico Nacional, México City, México.

[814] Department of Physics, Pennsylvania State University, University Park, PA, USA

[815] Physics Department, Centro de Investigacion y de Estudios Avanzados del IPN, México City, DF, México

[816] Universidad Autónoma del Estado de Hidalgo, Pachuca, Mexico

[817] Instituto de Ciencias Nucleares, Universidad Nacional Autónoma de Mexico, Ciudad de México, México

[818] Santa Cruz Institute for Particle Physics, University of California, Santa Cruz, Santa Cruz, CA, USA

[819] Department of Physics and Astronomy, University of California, Irvine, Irvine, CA, USA

[820] Laboratório de Instrumentação e Física Experimental de Partículas – LIP and Instituto Superior Técnico – IST, Universidade de Lisboa – UL, Lisboa, Portugal

[821] Osservatorio Astrofisico di Torino (INAF), Torino, Italy

[822] INFN, Sezione di Torino, Torino, Italy

[823] Universidade de São Paulo, Instituto de Física, São Paulo, SP, Brazil

[824] University of Adelaide, Adelaide, SA, Australia

[825] Centro Atómico Bariloche and Instituto Balseiro (CNEA-UNCuyo-CONICET), San Carlos de Bariloche, Argentina

[826] Instituto de Tecnologías en Detección y Astropartículas (CNEA, CONICET, UNSAM), Buenos Aires, Argentina

[827] Universidad Tecnológica Nacional, Facultad Regional Buenos Aires, Buenos Aires, Argentina

[828] Universidad Nacional Autónoma de México, México, D.F., México

[829] Universidad de Santiago de Compostela, Santiago de Compostela, Spain

[830] Gran Sasso Science Institute (INFN), L'Aquila, Italy

[831] INFN Laboratori Nazionali del Gran Sasso, Assergi (L'Aquila), Italy

[832] Department of Physics and Astronomy, Lehman College, City University of New York, New York, NY, USA

[833] INFN, Sezione di Napoli, Napoli, Italy

[834] Institute of Space Science, Bucharest-Magurele, Romania

[835] Universidad Industrial de Santander, Bucaramanga, Colombia

[836] Observatorio Pierre Auger, Malargüe, Argentina

[837] Observatorio Pierre Auger and Comisión Nacional de Energía Atómica, Malargüe, Argentina

[838] University Politehnica of Bucharest, Bucharest, Romania

[839] "Horia Hulubei" National Institute for Physics and Nuclear Engineering, Bucharest-Magurele, Romania

[840] Università di Napoli "Federico II", Dipartimento di Fisica "Ettore Pancini," Napoli, Italy

[841] Laboratoire de Physique Subatomique et de Cosmologie (LPSC), Université Grenoble-Alpes, CNRS/IN2P3, Grenoble, France

[842] Università Torino, Dipartimento di Fisica, Torino, Italy

[843] Max-Planck-Institut für Radioastronomie, Bonn, Germany

[844] Institut de Physique Nucléaire d'Orsay (IPNO), Université Paris-Sud, Univ. Paris/Saclay, CNRS-IN2P3, Orsay, France

[845] Institute of Physics of the Czech Academy of Sciences, Prague, Czech Republic

[846] Università del Salento, Dipartimento di Matematica e Fisica "E. De Giorgi," Lecce, Italy

[847] INFN, Sezione di Lecce, Lecce, Italy

[848] Universidade Federal do Rio de Janeiro, Instituto de Física, Rio de Janeiro, RJ, Brazil

[849] Institute of Nuclear Physics PAN, Krakow, Poland

[850] Karlsruhe Institute of Technology, Institut für Kernphysik, Karlsruhe, Germany

[851] Colorado State University, Fort Collins, CO 80523

[852] RWTH Aachen University, III. Physikalisches Institut A, Aachen, Germany

[853] Karlsruhe Institute of Technology, Institut für Experimentelle Kernphysik (IEKP), Karlsruhe, Germany

[854] Universität Siegen, Fachbereich 7 Physik – Experimentelle Teilchenphysik, Siegen, Germany

[855] Universidad de Granada and C.A.F.P.E., Granada, Spain

[856] Università di Catania, Dipartimento di Fisica e Astronomia, Catania, Italy

[857] INFN, Sezione di Catania, Catania, Italy

[858] Università di Milano, Dipartimento di Fisica, Milano, Italy

[859] Universidade de São Paulo, Escola de Engenharia de Lorena, Lorena, SP, Brazil

[860] Universidad Michoacana de San Nicolás de Hidalgo, Morelia, Michoacán, México

[861] Universidade Estadual de Campinas, IFGW, Campinas, SP, Brazil

[862] Instituto de Tecnologías en Detección y Astropartículas (CNEA, CONICET, UNSAM), and Universidad Tecnológica Nacional – Facultad Regional Mendoza (CONICET/CNEA), Mendoza, Argentina

[863] Pennsylvania State University, University Park, PA, USA

[864] INFN, Sezione di Milano, Milano, Italy

[865] Politecnico di Milano, Dipartimento di Scienze e Tecnologie Aerospaziali, Milano, Italy

[866] Case Western Reserve University, Cleveland, OH, USA

[867] University of Chicago, Enrico Fermi Institute, Chicago, IL, USA

[868] Università del Salento, Dipartimento di Ingegneria, Lecce, Italy

[869] Instituto de Astronomía y Física del Espacio (IAFE, CONICET-UBA), Buenos Aires, Argentina

[870] Departamento de Física and Departamento de Ciencias de la Atmósfera y los Océanos, FCEyN, Universidad de Buenos Aires and CONICET, Buenos Aires, Argentina

[871] Universidade Federal Fluminense, EEIMVR, Volta Redonda, RJ, Brazil

[872] Universidade Federal do Rio de Janeiro (UFRJ), Observatório do Valongo, Rio de Janeiro, RJ, Brazil

[873] Universidade de São Paulo, Instituto de Física de São Carlos, São Carlos, SP, Brazil

[874] Universidade Federal do Paraná, Setor Palotina, Palotina, Brazil

[875] IFLP, Universidad Nacional de La Plata and CONICET, La Plata, Argentina

[876] Universität Hamburg, II. Institut für Theoretische Physik, Hamburg, Germany

[877] Fermi National Accelerator Laboratory, USA

[878] Stichting Astronomisch Onderzoek in Nederland (ASTRON), Dwingeloo, The Netherlands

[879] New York University, New York, NY, USA

[880] Karlsruhe Institute of Technology, Institut für Prozessdatenverarbeitung und Elektronik, Karlsruhe, Germany

[881] Michigan Technological University, Houghton, MI, USA

[882] Experimental Particle Physics Department, J. Stefan Institute, Ljubljana, Slovenia

[883] Instituto de Física de Rosario (IFIR) – CONICET/U.N.R. and Facultad de Ciencias Bioquímicas y Farmacéuticas U.N.R., Rosario, Argentina

[884] Laboratoire de Physique Nucléaire et de Hautes Energies (LPNHE), Universités Paris 6 et Paris 7, CNRS-IN2P3, Paris, France

[885] SUBATECH, École des Mines de Nantes, CNRS-IN2P3, Université de Nantes, France

[886] Centro Brasileiro de Pesquisas Fisicas, Rio de Janeiro, RJ, Brazil

[887] University of Łódź, Faculty of Astrophysics, Łódź, Poland

[888] University of Łódź, Faculty of High-Energy Astrophysics, Łódź, Poland

[889] Universidade Estadual de Feira de Santana, Feira de Santana, Brazil

[890] Palacky University, RCPTM, Olomouc, Czech Republic

[891] Colorado School of Mines, Golden, CO, USA

[892] Centro Federal de Educação Tecnológica Celso Suckow da Fonseca, Nova Friburgo, Brazil

[893] Universidade Federal do ABC, Santo André, SP, Brazil
[894] Benemérita Universidad Autónoma de Puebla, Puebla, México
[895] Université Libre de Bruxelles (ULB), Brussels, Belgium
[896] Centro de Investigación y de Estudios Avanzados del IPN (CINVESTAV), México, D.F., México
[897] Università di Roma "Tor Vergata," Dipartimento di Fisica, Roma, Italy
[898] INFN, Sezione di Roma "Tor Vergata", Roma, Italy
[899] Also at Universidade Federal de Alfenas, Brasília, Brazil
[900] Charles University, Faculty of Mathematics and Physics, Institute of Particle and Nuclear Physics, Prague, Czech Republic
[901] Centro de Investigaciones en Láseres y Aplicaciones, CITEDEF and CONICET, Villa Martelli, Argentina
[902] Università dell'Aquila, Dipartimento di Scienze Fisiche e Chimiche, L'Aquila, Italy
[903] KVI – Center for Advanced Radiation Technology, University of Groningen, Groningen, The Netherlands
[904] Also at Vrije Universiteit Brussels, Brussels, Belgium
[905] INAF – Istituto di Astrofisica Spaziale e Fisica Cosmica di Palermo, Palermo, Italy
[906] University of Nebraska, Lincoln, NE, USA
[907] Northeastern University, Boston, MA, USA
[908] School of Physics and Astronomy, University of Leeds, Leeds, UK
[909] Universitá di Catania, Dipartimento di Fisica e Astronomia, Catania, Italy
[910] Instituto de Astrofísica and Centro de Astroingeniería, Facultad de Física, Pontificia Universidad Católica de Chile, Casilla 306, Santiago 22, Chile
[911] Department of Particle Physics and Astrophysics, Weizmann Institute of Science, Rehovot 761000, Israel
[912] Millennium Institute of Astrophysics (MAS), Nuncio Monseñor Sótero Sanz 100, Providencia, Santiago, Chile
[913] European Southern Observatory, Alonso de Córdova 3107, Vitacura, Santiago 763-0355, Chile
[914] Joint ALMA Observatory, Alonso de Córdova 3107, Vitacura, Santiago 763-0355, Chile
[915] Department of Physics & Astronomy, Clemson University, Clemson, SC 29634, USA
[916] National Center for Radio Astrophysics, Pune 411007, India
[917] ARIES, Manora Peak, Nainital 263 001, India
[918] Astronomical Observatory Institute, Faculty of Physics, Adam Mickiewicz University, ul. Słoneczna 36, 60-286 Poznań, Poland
[919] Indian Institute of Space Science & Technology, Trivandrum 695547, India
[920] Joint Institute for VLBI ERIC (JIVE), 7991 PD Dwingeloo, The Netherlands
[921] Instituto de Astrofísica de Andalucía-CSIC, Granada, Spain
[922] Shanghai Astronomical Observatory (ShAO), Key Laboratory of Radio Astronomy, CAS, Shanghai 200030 China
[923] Guilin University of Electronic Technology (GUET), Guilin 541004, China
[924] JBCA, The University of Manchester, Manchester M13 9PL, UK
[925] Max Planck Institut für Radioastronomie, D-53121, Bonn, Germany
[926] Konkoly Observatory, MTA CSFK, H-1121 Budapest, Hungary
[927] SRON Netherlands Institute for Space Research, 3584 CA Utrecht, The Netherlands
[928] Leiden Observatory, Leiden University, 2300 RA Leiden, The Netherlands.
[929] Onsala Space Observatory, 439 92 Onsala, Sweden
[930] University of Warsaw, Faculty of Physics, 02-093 Warsaw, Poland
[931] Warsaw University of Technology, Institute of Electronic Systems, 00-665 Warsaw, Poland
[932] Center for Theoretical Physics, Polish Academy of Sciences, 02-668 Warsaw, Poland
[933] RIKEN, Wako, 351-0198 Saitama, Japan
[934] McGill Space Institute and Department of Physics, McGill University, 3600 rue University, Montreal, QC H3A 2T8, Canada
[935] Department of Applied Geology, Curtin University, GPO Box U1987, Perth, WA 6845, Australia
[936] Department of Mechanical Engineering, Curtin University, GPO Box U1987, Perth, WA 6845, Australia
[937] LIGO Laboratory West Bridge, California Institute of Technology, MC 100-36, Room 257, Pasadena, CA 91125
[938] Department of Physics, Harvard University, Cambridge, MA 02138, USA
[939] LSST, 950 N. Cherry Avenue, Tucson, AZ 85719, USA
[940] Max-Planck-Institut für Radioastronomie, Auf dem Hügel 69, D-53177 Bonn, Germany
[941] NASA Goddard Space Flight Center, 8800 Greenbelt Road, Greenbelt, MD 20771, USA
[942] Department of Astronomy, University of Maryland, College Park, MD 20742-4111, USA
[943] Inst. de Astrofísica de Canarias, E-38200 La Laguna, Tenerife, Spain
[944] Universidad de La Laguna, Dpto. Astrofísica, E-38206 La Laguna, Tenerife, Spain
[945] Space Telescope Science Institute, Baltimore MD, 21218
[946] Instituto de Astronomía, Universidad Nacional Autónoma de México, Apartado Postal 70-264, 04510 México, CDMX, Mexico
[947] INFN—Istituto di Radioastronomia, Via Gobetti 101, I-40129, Italy
[948] CSIRO Astronomy and Space Science, P.O. Box 76, Epping, NSW 1710, Australia
[949] Max-Planck-Institut für extraterrestrische Physik, Giessenbachstrasse, D-85748 Garching, Germany
[950] Department of Physics, University of Bath, Claverton Down, Bath BA2 7AY, UK
[951] Center for Theoretical Astrophysics, Los Alamos National Laboratory, Los Alamos, NM 87545, USA
[952] SKA South Africa, Pinelands, 7405, South Africa
[953] Department of Astronomy, Astrophysics, Cosmology and Gravity Centre, University of Cape Town, Private Bag X3 Rondebosch, 7701 South Africa
[954] Deceased 2017 February.
[955] Deceased 2016 December.
[956] Deceased 2017 August 18.
[957] Deceased 2016 August.

CO-AUTHORED PAPER 3 — FOLLOW UP OF GW170817 AND ITS ELECTROMAGNETIC COUNTERPART BY AUSTRALIAN-LED OBSERVING PROGRAMMES

I. Andreoni, K. Ackley, J. Cooke, A. Acharyya, J. R. Allison, G. E. Anderson, M. C. B. Ashley, D. Baade, M. Bailes, K. Bannister, A. Beardsley, M. S. Bessell, F. Bian, P. A. Bland, M. Boer, T. Booler, A. Brandeker, I. S. Brown, D. A. H. Buckley, S. W. Chang, D. M. Coward, S. Crawford, H. Crisp, B. Crosse, A. Cucchiara, M. Cupák, J. S. de Gois, A. Deller, **H. A. R. Devillepoix**, *D. Dobie, E. Elmer, D. Emrich, W. Farah, T. J. Farrell, T. Franzen, B. M. Gaensler, D. K. Galloway, B. Gendre, T. Giblin, A. Goobar, J. Green, P. J. Hancock, B. A. D. Hartig, E. J. Howell, L. Horsley, A. Hotan, R. M. Howie, L. Hu, Y. Hu, C. W. James, S. Johnston, M. Johnston-Hollitt, D. L. Kaplan, M. Kasliwal, E. F. Keane, D. Kenney, A. Klotz, R. Lau, R. Laugier, E. Lenc, X. Li, E. Liang, C. Lidman, L. C. Luvaul, C. Lynch, B. Ma, D. Macpherson, J. Mao, D. E. McClelland, C. McCully, A. Möller, M. F. Morales, D. Morris, T. Murphy, K. Noysena, C. A. Onken, N. B. Orange, S. Osłowski, D. Pallot, J. Paxman, S. B. Potter, T. Pritchard, W. Raja, R. Ridden- Harper, E. Romero-Colmenero, E. M. Sadler, E. K. Sansom, R. A. Scalzo, B. P. Schmidt, S. M. Scott, N. Seghouani, Z. Shang, R. M. Shannon, L. Shao, M. M. Shara, R. Sharp, M. Sokolowski, J. Sollerman, J. Staff, K. Steele, T. Sun, N. B. Suntzeff, C. Tao, S. Tingay, M. C. Towner, P. Thierry, C. Trott, B. E. Tucker, P. Väisänen, V. V. Krishnan, M. Walker, L. Wang, X. Wang, R. Wayth, M. Whiting, A. Williams, T. Williams, C. Wolf, C. Wu, X. Wu, J. Yang, X. Yuan, H. Zhang, J. Zhou, and H. Zovaro.*

Follow Up of GW170817 and Its Electromagnetic Counterpart by Australian-Led Observing Programmes

I. Andreoni[1,2,3,54], K. Ackley[2,4,5], J. Cooke[1,2,6], A. Acharyya[7], J. R. Allison[8,9], G. E. Anderson[10], M. C. B. Ashley[11], D. Baade[12], M. Bailes[1,2], K. Bannister[13], A. Beardsley[14], M. S. Bessell[7], F. Bian[7], P. A. Bland[15], M. Boer[16], T. Booler[10], A. Brandeker[17], I. S. Brown[18], D. A. H. Buckley[19], S.-W. Chang[7,6], D. M. Coward[20], S. Crawford[19], H. Crisp[20], B. Crosse[10], A. Cucchiara[21], M. Cupák[15], J. S. de Gois[10], A. Deller[1], H. A. R. Devillepoix[15], D. Dobie[8,13,6], E. Elmer[22], D. Emrich[10], W. Farah[1], T. J. Farrell[3], T. Franzen[23], B. M. Gaensler[24], D. K. Galloway[2,4,5], B. Gendre[21,16], T. Giblin[25], A. Goobar[26], J. Green[13], P. J. Hancock[10], B. A. D. Hartig[15], E. J. Howell[20], L. Horsley[10], A. Hotan[23], R. M. Howie[27], L. Hu[28,29], Y. Hu[30,29], C. W. James[8], S. Johnston[13], M. Johnston-Hollitt[31], D. L. Kaplan[18], M. Kasliwal[32], E. F. Keane[33], D. Kenney[10], A. Klotz[34], R. Lau[32], R. Laugier[16], E. Lenc[6,8], X. Li[35,29], E. Liang[36], C. Lidman[3], L. C. Luvaul[7], C. Lynch[8,6], B. Ma[30], D. Macpherson[20], J. Mao[37], D. E. McClelland[38,2], C. McCully[39,40], A. Möller[7,6], M. F. Morales[41], D. Morris[21], T. Murphy[8,6], K. Noysena[16,34], C. A. Onken[7,6], N. B. Orange[42], S. Osłowski[1], D. Pallot[20], J. Paxman[27], S. B. Potter[19], T. Pritchard[1], W. Raja[13], R. Ridden-Harper[7], E. Romero-Colmenero[19,43], E. M. Sadler[8,6], E. K. Sansom[15], R. A. Scalzo[7,6,44], B. P. Schmidt[7,6], S. M. Scott[38,2], N. Seghouani[45], Z. Shang[30,46,29], R. M. Shannon[13,10,2], L. Shao[7,47], M. M. Shara[48,49], R. Sharp[7,6], M. Sokolowski[10,6], J. Sollerman[17], J. Staff[21], K. Steele[10], T. Sun[28,29], N. B. Suntzeff[50], C. Tao[51,52], S. Tingay[10,6], M. C. Towner[15], P. Thierry[53], C. Trott[10,6], B. E. Tucker[7,6], P. Väisänen[19,43], V. Venkatraman Krishnan[1,6], M. Walker[10], L. Wang[50,28,29], X. Wang[52], R. Wayth[10,6], M. Whiting[13], A. Williams[10], T. Williams[19], C. Wolf[7,6,2], C. Wu[20], X. Wu[28,29], J. Yang[28], X. Yuan[35,29], H. Zhang[36], J. Zhou[36] and H. Zovaro[7]

[1]Centre for Astrophysics and Supercomputing, Swinburne University of Technology, PO Box 218, H29, Hawthorn, VIC 3122, Australia
[2]The Australian Research Council Centre of Excellence for Gravitational Wave Discovery (OzGrav)
[3]Australian Astronomical Observatory, 105 Delhi Rd, North Ryde, NSW 2113, Australia
[4]Monash Centre of Astrophysics, Monash University, VIC 3800, Australia
[5]School of Physics & Astronomy, Monash University, VIC 3800, Australia
[6]The Australian Research Council Centre of Excellence for All-Sky Astrophysics (CAASTRO)
[7]Research School of Astronomy and Astrophysics, The Australian National University, Canberra ACT 2611, Australia
[8]Sydney Institute for Astronomy, School of Physics, University of Sydney, NSW 2006, Australia
[9]The Australian Research Council Centre of Excellence for All-sky Astrophysics in 3 Dimensions (ASTRO 3D)
[10]International Centre for Radio Astronomy Research, Curtin University, Bentley WA 6102, Australia
[11]School of Physics, University of New South Wales, NSW 2052, Australia
[12]European Organisation for Astronomical Research in the Southern Hemisphere (ESO), Karl-Schwarzschild-Str. 2, 85748 Garching bei München, Germany
[13]ATNF, CSIRO Astronomy and Space Science, PO Box 76, Epping, NSW 1710, Australia
[14]School of Earth and Space Exploration, Arizona State University, Tempe, AZ 85287, USA
[15]Department of Applied Geology, Curtin University, GPO Box U1987, Perth, WA 6845, Australia
[16]Artémis/Observatoire de la Cote d'Azur/CNRS, Boulevard de l'Observatoire CS 34229 - F 06304 NICE Cedex 4, France
[17]Department of Astronomy, Stockholm University, Albanova, SE 10691 Stockholm, Sweden
[18]Department of Physics, University of Wisconsin–Milwaukee, Milwaukee, WI 53201, USA
[19]South African Astronomical Observatory, PO Box 9, 7935 Observatory, South Africa
[20]School of Physics, University of Western Australia, Crawley, WA 6009, Australia
[21]University of the Virgin Islands, 2 John Brewer's Bay, 00802 St Thomas, US Virgin Islands, USA
[22]School of Physics and Astronomy, University of Nottingham, Nottingham, UK
[23]ATNF, CSIRO Astronomy and Space Science, 26 Dick Perry Avenue, Kensington WA 6152, Australia
[24]Dunlap Institute for Astronomy and Astrophysics, University of Toronto, ON, M5S 3H4, Canada
[25]Department of Physics, 2354 Fairchild Drive, U.S. Air Force Academy, CO 80840, USA
[26]The Oskar Klein Centre, Department of Physics, Stockholm University, Albanova, SE 106 91 Stockholm, Sweden
[27]Department of Mechanical Engineering, Curtin University, GPO Box U1987, Perth, WA 6845, Australia
[28]Purple Mountain Observatory, Chinese Academy of Sciences, Nanjing 210008, China
[29]Chinese Center for Antarctic Astronomy, Nanjing 210008, China
[30]National Astronomical Observatories, Chinese Academy of Sciences, Beijing 100012, China
[31]Peripety Scientific Ltd., PO Box 11355 Manners Street, Wellington, 6142, New Zealand
[32]Division of Physics, Mathematics and Astronomy, California Institute of Technology, Pasadena, CA 91125, USA
[33]SKA Organisation, Jodrell Bank Observatory, SK11 9DL, UK
[34]IRAP (CNRS/UPS) 34 ave. Edouard Belin, 31400 Toulouse, France
[35]Nanjing Institute of Astronomical Optics and Technology, Nanjing 210042, China

1

2   *Andreoni et al.*

[36]School of Astronomy and Space Science and Key Laboratory of Modern Astronomy and Astrophysics in Ministry of Education, Nanjing University, Nanjing 210093, China
[37]Yunnan Observatories, Chinese Academy of Sciences, 650011 Kunming, Yunnan Province, China
[38]Research School of Physics and Engineering, The Australian National University, Canberra ACT 2611, Australia
[39]Las Cumbres Observatory, 6740 Cortona Dr., Suite 102, Goleta, CA 93117-5575, USA
[40]Department of Physics, University of California, Santa Barbara, CA 93106-9530, USA
[41]Department of Physics, University of Washington, Seattle, WA 98195, USA
[42]OrangeWave Innovative Science LLC, Moncks Corner, SC 29461, USA
[43]Southern African Large Telescope Foundation, P.O. Box 9, 7935 Observatory, South Africa
[44]Centre for Translational Data Science, University of Sydney, NSW 2006, Australia
[45]Centre de Recherche en Astronomie, Astrophysique et Géophysique, BP 63, Route de l'Observatoire, Bouzareah, 16340, Alger, Algeria
[46]Tianjin Normal University, Tianjin 300074, China
[47]Kavli Institute for Astronomy and Astrophysics, Peking University, 5 Yiheyuan Road, Haidian District, Beijing 100871, P. R. China
[48]Department of Astrophysics, American Museum of Natural History, Central Park West and 79th Street, New York, NY 10024, USA
[49]Institute of Astronomy, University of Cambridge, Madingley Road, Cambridge CB3 0HA, UK
[50]George P. and Cynthia Woods Mitchell Institute for Fundamental Physics & Astronomy, Texas A. & M. University, Department of Physics and Astronomy, 4242 TAMU, College Station, TX 77843, USA
[51]Aix Marseille Univ, CNRS/IN2P3, CPPM, Marseille 13288, France
[52]Physics Department and Tsinghua Center for Astrophysics, Tsinghua University, Beijing, 100084, China
[53]Observatoire d'Auragne, 31190 Auragne, France
[54]Email: igor.andreoni@gmail.com

Abstract

The discovery of the first electromagnetic counterpart to a gravitational wave signal has generated follow-up observations by over 50 facilities world-wide, ushering in the new era of multi-messenger astronomy. In this paper, we present follow-up observations of the gravitational wave event GW170817 and its electromagnetic counterpart SSS17a/DLT17ck (IAU label AT2017gfo) by 14 Australian telescopes and partner observatories as part of Australian-based and Australian-led research programs. We report early- to late-time multi-wavelength observations, including optical imaging and spectroscopy, mid-infrared imaging, radio imaging, and searches for fast radio bursts. Our optical spectra reveal that the transient source emission cooled from approximately 6 400 K to 2 100 K over a 7-d period and produced no significant optical emission lines. The spectral profiles, cooling rate, and photometric light curves are consistent with the expected outburst and subsequent processes of a binary neutron star merger. Star formation in the host galaxy probably ceased at least a Gyr ago, although there is evidence for a galaxy merger. Binary pulsars with short (100 Myr) decay times are therefore unlikely progenitors, but pulsars like PSR B1534+12 with its 2.7 Gyr coalescence time could produce such a merger. The displacement ($\sim$2.2 kpc) of the binary star system from the centre of the main galaxy is not unusual for stars in the host galaxy or stars originating in the merging galaxy, and therefore any constraints on the kick velocity imparted to the progenitor are poor.

Keywords: gamma-ray burst: individual: GRB170817A – gravitational waves – stars: neutron – supernovae: general – supernovae: individual: AT2017gfo

1 INTRODUCTION

The first detection of an electromagnetic (EM) counterpart to a gravitational wave (GW) event has led to the new era of GW multi-messenger astrophysics. The close coordination of LIGO data analysis groups and multiple observational teams worldwide via the restricted Gamma-Ray Coordinates Network (GCN) reports under confidential Memoranda of Understanding (MoU), were key to the prompt identification and detailed multi-wavelength follow up of the counterpart.

On 2017 August 17 12:41:04[1], the Advanced Laser Interferometer Gravitational-Wave Observatory (aLIGO) interferometers detected a GW signal G298048, now referred to as GW170817 (Abbott et al. 2017c, 2017d, 2017e, 2017f, 2017g, 2017a). The Advanced-Virgo (aVirgo) interferometer was online at the time of the discovery and also con-

tributed to the localisation of the GW event. On 2017 August 17 12:41:06, about 2 s after the GW detection, the Gamma-ray Burst Monitor (GBM) instrument on board the *Fermi* satellite independently detected a short gamma-ray burst, labelled as GRB 170817A (Connaughton et al. 2017; Goldstein et al. 2017a; Goldstein et al. 2017b; von Kienlin et al. 2017). The INTErnational Gamma-Ray Astrophysics Laboratory (INTEGRAL) also detected GRB 170817A (Savchenko et al. 2017a; Savchenko et al. 2017b), providing unique information especially when the data were combined with those obtained with *Fermi* (Abbott et al. 2017b). The close temporal coincidence of the gamma-ray burst and GW event made it a compelling target for follow-up observations at other wavelengths.

The One-Meter, Two-Hemisphere project (1M2H) first announced the discovery of a transient in an image acquired with the 1-m Swope telescope at Las Campanas Observatory in Chile on 2017 August 17 at 23:33, 10.87 h

---

[1] All dates in this paper are UT, unless a different time reference is explicitly specified.

after the LIGO detection. However, the optical counterpart to GW170817 (and GRB 170817A) was already imaged independently by six other programmes before this report. The 1M2H team referred to the transient with the name Swope Supernova Survey 2017a (SSS17a, Coulter et al. 2017b, 2017a). Details about the other independent detections can be found in Allam et al. (2017) for the Dark Energy Camera, Valenti et al. (2017) and Yang et al. (2017) for the Distance Less Than 40 Mpc survey (DLT40), Arcavi et al. (2017a) and Arcavi et al. (2017b) for the Las Cumbres Observatory, Tanvir et al. (2017a) and (2017b) for the Visible and Infrared Survey Telescope for Astronomy, Lipunov et al. (2017a) and (2017b) for the MASTER discoveries.

Lipunov et al. (2017b) offer an extensive review of the world-wide follow up. The optical transient is located at RA = 13:09:48.089 DEC = −23:22:53.350 (Adams et al. 2017; Kasliwal et al. 2017), approximately 2.2 kpc from the centre of its host galaxy NGC 4993. The host is a nearby E/S0 galaxy at $z = 0.009727$, corresponding to a distance of ∼39.5 Mpc (Freedman et al. 2001). Hereafter, we refer to the EM counterpart of GW170817 with the IAU label AT2017gfo.

Short-duration GRBs (sGRBs, a class first identified by Kouveliotou et al. 1993) were previously suggested to be associated with merging compact objects, such as a binary neutron star (BNS) system or neutron star-black hole (NSBH) system (e.g., Paczynski 1986; Goodman 1986; Eichler et al. 1989). Electromagnetically, such mergers are also postulated to generate a relatively rapidly evolving optical/infrared transient—referred to as kilonova or macronova (e.g., Li & Paczyński 1998; Metzger et al. 2010; Roberts et al. 2011; Barnes & Kasen 2013; Tanaka & Hotokezaka 2013; Kasen, Fernández, & Metzger 2015; Metzger et al. 2015; Barnes et al. 2016). The combination of an sGRB and kilonova is considered the 'smoking gun' signature of such mergers. Kilonova candidates were previously identified during the follow up of sGRBs, for example, GRB 080503 (Perley et al. 2009; Gao et al. 2015), GRB 130603B (Berger, Fong, & Chornock 2013; Tanvir et al. 2013; Hotokezaka et al. 2013), and GRB 050709 (Jin et al. 2016). However, no kilonova candidates have been discovered unrelated to GRB triggers, despite their anticipated isotropic emission, unlike that of sGRBs. BNS, and NSBH mergers, thus sGRBs, and subsequent kilonovae, are expected to be the most promising GW events to exhibit EM counterparts.

Previous work has discussed the importance of rapid response (e.g., Chu et al. 2016) and collaborative strategies to maximise the chances of success in the EM follow up of aLIGO and Virgo triggers. Specifically, Howell et al. (2015) presents the role that Australia can play in this context. The association of GW170817 to GRB 170817A, detected during the LIGO and Virgo Collaboration (LVC) 'O2' run, has enabled the first multi-messenger (EM multi-wavelength, neutrino, and GW observations) study of an astrophysical event (Lipunov et al. 2017b).

This paper presents and discusses the data acquired during the search for an EM counterpart to GW170817 and the follow up of the now confirmed counterpart, AT2017gfo, by 14 observing programmes led by Australian institutions and researchers. The observing programmes include facilities and collaborators associated with the Australia Research Council (ARC) Centre of Excellence for All-sky Astrophysics (CAASTRO[2]), the ARC Centre of Excellence for Gravitational Wave Discovery (OzGrav[3]), and the multi-wavelength, multi-facility Deeper, Wider, Faster (DWF[4]) programme. In Section 2, we summarise the observations from the telescopes/instruments that participated in the GW170817 follow up, including optical, mid-infrared, and radio imaging and spectroscopic observations. In Section 3, we provide an overview of the spectroscopic observations of the event and host galaxy and preliminary comparisons of our observations with theoretical sGRB afterglow and kilonova models. Finally, we present a discussion and summary and in Section 4.

2 FACILITIES INVOLVED IN THE EM FOLLOW UP OF GW170817

The following sections describe the optical, mid-infrared (mIR), and radio telescopes, instruments, and relevant observations involved in the follow up of the GW170817 EM counterpart by Australian or Australian-led programmes.

Shortly after the LVC community was alerted to the GW event, many of the facilities discussed here were triggered into action for follow-up observations. However, NGC 4993 and the bulk of the LVC error ellipse had set in Eastern Australia and the Zadko telescope in Western Australia was temporarily not operational. On the following day, the location of the optical counterpart AT2017gfo was known. Radio telescopes were on the field that day and optical facilities were on the field shortly after sunset. Figure 1 presents the broad temporal coverage of the GW event by our spectroscopic, radio, and optical/mIR observations that extend from early to late times. The general characteristics of each facility is presented in Table 1 and details of the corresponding observations are listed in Tables 2–15.

2.1. Optical/near-infrared imaging

2.1.1. SkyMapper

SkyMapper (Keller et al. 2007) is a 1.35-m modified-Cassegrain telescope located at Siding Spring Observatory in New South Wales, Australia, which is owned and operated by the Australian National University (ANU). The camera has a 5.7 deg^2 field of view, a pixel scale of 0.5 arcsec/pixel and six photometric filters in the *uvgriz* system, which span the visible and ultraviolet bands from 325 to 960 nm. Typical single-epoch 5σ limiting magnitudes for each filter are

---

[2] http://www.caastro.org
[3] http://www.ozgrav.org
[4] http://www.dwfprogram.altervista.org

Table 1. Facilities participating in the follow-up observations summarised in this paper. Principal references for the relevant data from each facility are indicated in the right-most column. We specify under which programme the observations were taken when multiple groups used the same telescope to follow up GW170817 and AT2017gfo.

OIR imaging	Band	FoV	Aperture (m)	References
SkyMapper	u,v,g,r,i,z	5.7 deg^2	1.35	This work
AST3-2[a]	i	4.14 deg^2	0.5	This work Hu et al. (2017b)
Zadko	r, Clear	0.15 deg^2	1	This work
UVI Etelman[a]	R, Clear	0.11 deg^2	0.5	This work
ESO VLT/NACO[a]	L3.8 µm	784 arcsec^2	8.2	This work
ESO VLT/VISIR[a]	J8.9 µm	1 arcmin^2	8.2	Kasliwal et al. (2017)
DFN	V	full-sky	2×8 mm	This work
OIR spectroscopy	Range (Å)	R	Aperture (m)	References
ANU2.3/WiFeS	3 300–9 200	3 000, 7 000	2.3	This work This work
SALT/RSS[a]	3 600–9 700	∼300	10	McCully et al. (2017) Buckley et al. (2017)
AAT/2dF+AAOmega[a]	3 700–8 800	1 700	3.9	This work
Radio	Band	FoV (deg^2)	Mode	References
ATCA[b]	5.5–21.2 GHz	$0.037 - 0.143$	Imaging	Hallinan et al. (2017) Kasliwal et al. (2017)
ASKAP	0.7–1.8 GHz	30	Imaging	This work
ASKAP	0.7–1.8 GHz	210	FRB	This work
MWA[c]	185 MHz	400	Imaging	This work
VLBA	8.7 GHz	0.04	Imaging	This work
Parkes	1.2–1.6 GHz	0.55	FRB	This work

[a]Observations initiated, or proposed for, via collaboration with DWF programme.
[b] Programme CX391.
[c] Programme BD218.
[d] Programme D0010.
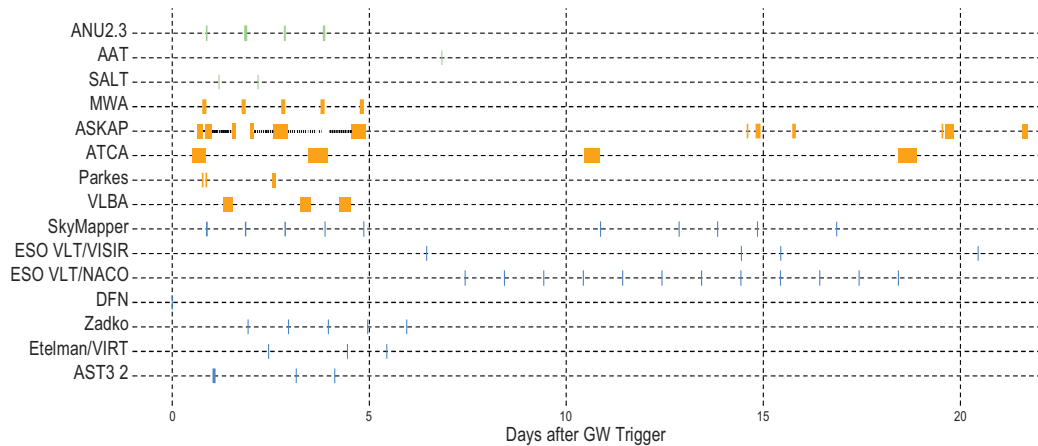
Figure 1. Observation timeline for the facilities presented in this paper showing the time of observation offset from the GW event and the nominal length of the reported observations. Spectroscopic observations are shown in green, radio observations in orange, and optical and mid-infrared are in blue.

$u = 19.5$, $v = 19.5$, $g = 21$, $r = 21$, $i = 20$, and $z = 19$, over 100 s exposure times. Since 2014, SkyMapper has conducted a full-hemisphere Southern sky survey in all six bands (see Wolf et al. in preparation; http://skymapper.anu.edu.au). Alongside this survey, the SkyMapper Transient Survey

(SMT) has been performing a survey dedicated to supernovae and other transients (Scalzo et al. 2017).

SkyMapper first received the GW trigger when the target area had recently set in Eastern Australia and began observing relevant target ranges shortly after sunset the following night.

Follow Up of GW170817 and Its Electromagnetic Counterpart by Australian-Led Observing Programmes 5

Table 2. AST3-2 observations of GW170817 and AT2017gfo.

	AST3-2		
UT obs date	Band	Mag	Mag error
2017-08-18 13:11:42.72	i	17.23	0.22(−0.21)
2017-08-18 14:15:54.29	i	17.61	0.16
2017-08-18 15:00:16.24	i	17.72	0.18(−0.17)
2017-08-20 16:07:27.71	i	>18.67	
2017-08-21 15:36:49.65	i	>18.38	

Figure 2. Footprints of SkyMapper observations in two different follow-up modes: one using the blind search of new transient sources where fields overlap with GW localisation map (grey squares) and the other using the targeted observation of the optical counterpart, AT2017gfo, discovered by other EM follow-up groups (yellow square). The positions of AT2017gfo and its host galaxy (NGC 4993) are indicated on the figure. The red dots are target galaxies from the 6dFGS catalogue that were prioritised by their position and spectroscopic redshift.
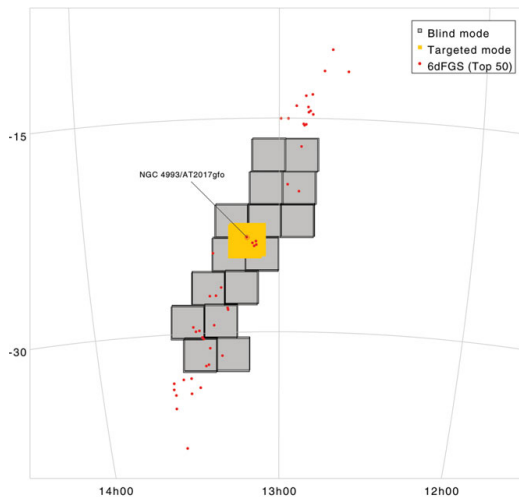
The follow-up strategy included two components: (1) to obtain *uvgriz* photometry of the field containing AT2017gfo, in the event that the transient was the correct counterpart to the GW trigger, and (2) to image the 90% probability region (85 deg^2) of the LVC sky-map to search for other counterpart candidates (Figure 2).

Archival images at the coordinates of AT2017gfo were found from the SkyMapper Southern Sky Survey and the SMT from 2015 August 8 to 2017 July 22. We found no evidence of a pre-existing source or variability in the images coincident with AT2017gfo to a 95% upper limit of $i \sim 19.6$ and $r \sim 20.5$ (Figure 3; Möller et al. 2017).

Imaging of the LVC skymap started at 2017-08-18 09:04:56 in the *uvgriz* filters with $t_{exp} = 100$ s. The images of AT2017gfo were taken between 2017-08-18 09:16:58 and
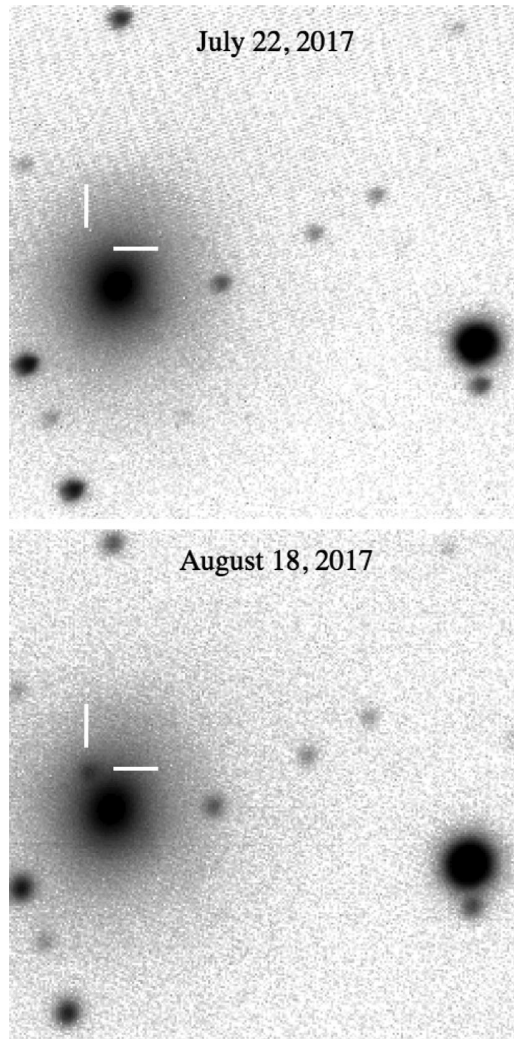
Figure 3. SkyMapper optical images of NGC 4993 (left centre) ~26 d before and ~1 d after the detection of AT2017gfo. The images are oriented with North up and East to the left and are cropped to 2 arcmin on a side, with the position of AT2017gfo marked. The image taken on 2017 July 22 is in *i*-band, the image taken on 2017 August 18 (where the transient is visible) is in *r*-band.

2017-08-18 10:00 UT in all bands (Figure 4). The observations were taken at an airmass above 2 and roughly half of the primary mirror was vignetted by the telescope dome. As a result of dome seeing and high airmass, the images have a seeing FWHM of 3.5–6 arcsec in *ilz*-bands to *u*-band. Nevertheless, the transient AT2017gfo was immediately confirmed visually on raw frames in all six bands. Preliminary

6 *Andreoni et al.*

Figure 4. Optical light curve of AT2017gfo for the first week after the GW detection obtained with the AST3-2, SkyMapper (SM), Zadko, and Etelman/VIRT telescopes. Down arrows indicate upper limits. Note that the evolution at bluer bands is faster than the evolution at redder bands. Dashed vertical lines indicate epochs when spectroscopy was acquired. Spectra analysed in this work and presented in Figures 7 and 8 are indicated in black, whereas spectra marked in grey were obtained but are to be published at a later time, as they were acquired in a different mode than the first and require a different analysis.

Table 3. Zadko observations of GW170817 and AT2017gfo.

Zadko			
UT obs date	Band	Mag	Mag error
2017-08-19 10:57:00	*r*	18.46	0.17
2017-08-20 11:30:00	*r*	19.18	0.12
2017-08-21 11:52:00	*r*	19.86	0.21
2017-08-22 11:46:00	*r*	20.20	0.23
2017-08-23 11:32:00	*r*	>20.6	

Table 4. Etelman/VIRT observations of GW170817 and AT2017gfo.

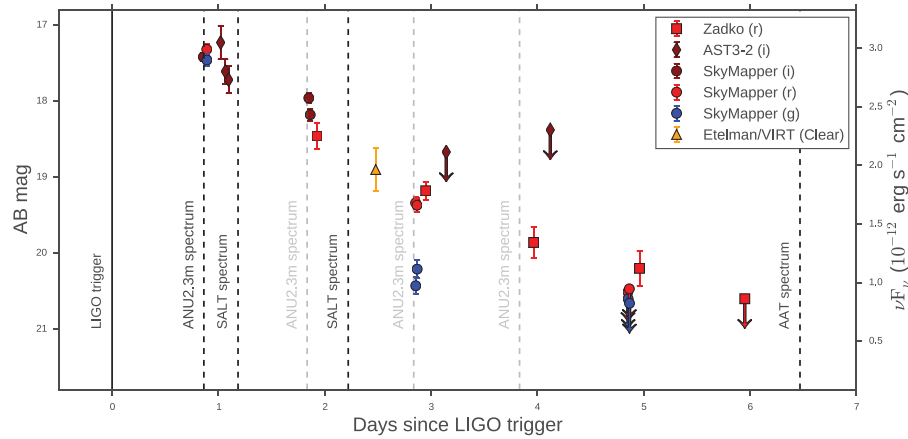| Etelman/VIRT			
UT obs date	Band	Mag	Mag error
2017-08-20 00:12	Clear	18.90	0.28

photometric AB magnitudes are given as $u = 17.9 \pm 0.15$, $v = 17.9 \pm 0.10$, $g = 17.76 \pm 0.05$, $r = 17.20 \pm 0.05$, and $i = 16.0 \pm 0.30$, respectively (Wolf et al. 2017a).

Observations of the source continued between 2017-08-18 and 2017-08-22, at which point AT2017gfo could no longer be visually identified in *uvg* bands. Imaging was attempted again between 2017-08-28 and 2017-09-03 to obtain images for host galaxy subtraction, but was unsuccessful. A total of 83 successful exposures were taken with exposure times of 100 s for bands *griz* and up to 300 s, for *uv*. Host galaxy images in all filters are planned when the target re-appears from behind the Sun.

2.1.2. AST3-2

The Antarctic Schmidt Telescope (AST3) project comprises three 68 cm (50 cm non-vignetted aperture) equatorial-mount telescopes located at the Kunlun Station at Dome A, Antarctica (Cui, Yuan, & Gong 2008).

The second of the AST3 telescopes, AST3-2, employs a 10 K×10 K STA1600FT camera with a pixel scale of 1 arcsec pixel^{-1} and a 4.14° field of view. The AST3-2 observations presented in this paper were performed as part of the DWF programme (PI Cooke). Most facilities following AT2017gfo were only able to monitor the source for 1–2 h per night as a result of its position near the Sun. The location of AST3-2 is advantageous in that it can monitor the source over longer periods of time as the source moved low along the horizon. The disadvantages are that the source was always at high airmass and the dark Antarctic winter was ending.

Observations targeting the GW counterpart AT2017gfo span from 2017-08-18 to 2017-08-28 in SDSS-*i* filter. A total of 262 exposures were acquired, each with an exposure time of 300 s per image, except for the initial five images having exposure time of 60 s, with approximately 54 s between exposures. AST3-2 detected AT2017gfo on 2017-08-18 with an average *i*-band magnitude of $17.23^{+0.22}_{-0.21}$, $17.61^{+0.16}_{-0.16}$, and $17.72^{+0.18}_{-0.17}$ from co-added images. The uncertainties of these measurements include the 0.088 mag errors of the zero-point calibration. The AST3-2 circular, Hu et al. (2017a), reports

Table 5. ESO VLT observations of GW170817 and AT2017gfo (Kasliwal et al. in preparation).

	ESO VLT		
Instrument	UT obs date	Band	Mag
NACO	2017-08-25 22:45	L'3.8	>14.5
NACO	2017-08-26 22:45	L'3.8	>14.8
NACO	2017-08-27 22:45	L'3.8	>14.5
NACO	2017-09-01 22:45	L'3.8	>14.3
VISIR	2017-08-23 23:35	J8.9	>8.26
VISIR	2017-08-31 23:18	J8.9	>7.74
VISIR	2017-09-01 23:18	J8.9	>7.57
VISIR	2017-09-06 23:33	J8.9	>7.42

Table 6. SkyMapper Observations of GW170817 and AT2017gfo with photometric measurements. The SkyMapper follow up is not limited to the data points presented in this table. The results from the analysis of the complete dataset will be discussed in future publications.

	SkyMapper		
UT obs date	Band	Mag	Mag error
2017-08-18 09:16:58	i	17.42	0.05
2017-08-18 10:03:44	r	17.32	0.07
2017-08-18 10:05:44	g	17.46	0.08
2017-08-19 09:06:17	i	17.96	0.07
2017-08-19 09:24:57	i	18.18	0.08
2017-08-20 09:12:57	r	19.34	0.08
2017-08-20 09:14:58	g	20.43	0.11
2017-08-20 09:31:44	r	19.37	0.09
2017-08-20 09:33:45	g	20.21	0.12
2017-08-22 09:09:22	r	>20.51	95%
2017-08-22 09:11:24	g	>20.60	95%
2017-08-22 09:28:08	r	>20.47	95%
2017-08-22 09:30:08	g	>20.66	95%
2017-08-28 09:17:13	r	>19.36	95%
2017-08-28 09:19:13	g	>19.53	95%
2017-08-28 09:35:52	r	>19.39	95%
2017-08-28 09:37:53	g	>19.50	95%
2017-08-30 09:18:53	g	>19.36	95%
2017-08-30 09:20:52	r	>19.32	95%
2017-08-30 09:37:33	g	>19.24	95%

g-band magnitudes, however, this must be corrected to the i-band magnitudes that we report here. Detections and upper limits estimated in the following observations are presented in Figure 4 and Table 2.

2.1.3. Zadko

The 1-m Zadko Telescope (Coward et al. 2010) is located just north of Perth in Western Australia. The CCD imager has a pixel scale of 0.69 arcsec pixel^{-1} (binning 1 × 1) resulting in a field of view of 0.15 deg^2 and reaches an approximate limiting magnitude of 21 in the R-band in 180 s.

The TAROT–Zadko–Aures–C2PU collaboration (TZAC) joins the efforts of partners located in Australia (Zadko), France (with TAROT telescopes in France, Chile and La Réunion Island, C2PU in France), and Algeria (Aurès Observatory, under construction). The initial position of GW 170817 was monitored using the TCH (TAROT-Chile) 25-cm rapid robotic telescope prior to Zadko imaging.

Zadko observations of AT2017gfo commenced on 2017-08-19 10:57 and extended until 2017-08-26 11:43 in the Clear (C) and r filters, with 120 s exposures and 2 × 2 binning. The object was observed for ∼1 h at the onset of dusk each night, until its low elevation precluded observations.

We stacked all images taken each night to increase the signal-to-noise ratio under the assumption that the brightness of the object does not vary significantly during 1 h. As AT2017gfo is located at 10 arcsec from the nucleus of NGC 4993 (i.e. 7 pixels), the background varies steeply. For accurate photometry, a galaxy reference image without AT2017gfo was subtracted to retrieve a flat background. The reference image was created from the stack of images taken on the last night (i.e., nine nights after the GW trigger) when the source was no longer visible. The photometry was performed on the subtracted image taking the point spread function (PSF) of the star NOMAD-1 0666-0296321 (RA=197^{h}28^{m}44.96^s, Dec=−23°21′49.70″ J2000.0, m_R=15.580). Photometric results are presented in Coward et al. (2017), Figure 4, and Table 3.

2.1.4. University of virgin islands Etelman observatory

The Virgin Islands Robotic Telescope (VIRT) is a 0.5-m Cassegrain telescope located at the Etelman Observatory in the U. S. Virgin Islands. The observations with VIRT presented in this paper were performed in association with the DWF programme. VIRT is equipped with a Marconi 42-20 CCD imager that has a pixel scale of 0.5 arcsec pixel^{-1}, a field of view of 0.11 deg^2, and imaging in the UBVRI and ND filters.

Observations of AT2017gfo commenced on 2017-08-19 23:19 in the R and Clear (C) filters. At approximately 2017-08-19 23:54, a potential counterpart was observed in the C filter. Calculation of the precise source magnitude is limited due to the galaxy contamination in the observing band (Gendre et al. 2017). Additional observations were carried out on 2017-08-20 00:12 and 2017-08-22 00:00 with the C filter, where a possible first detection of the source was made on 2017-08-20 m_C = 18.90 ± 0.28 (Figure 4). Inclement tropical weather (hurricane Irma, followed by hurricane Maria) delayed full analysis of the observations, however, the measurements made to date are listed in Table 4.

2.1.5. The desert fireball network

The Desert Fireball Network (DFN, Day & Bland 2016) is a network of 50 remote cameras located in the Western and South Australian desert designed for the detection and triangulation of Fireballs and bright meteors. Each DFN camera consists of a Nikon D800E camera equipped with a Samyang

8   *Andreoni et al.*

Table 7. ASKAP Observations of GW170817 and AT2017gfo.

			ASKAP		
UT obs date	Mode	Frequency (MHz)	Bandwidth (MHz)	$N_{\text{ant.}}$	N_{beams}
2017-08-18 04:05–07:36	FRB	1 320	336	7	108
2017-08-18 08:57–13:03	FRB	1 320	336	7	108
2017-08-19 02:08–13:08	FRB	1 320	336	7	108
2017-08-19 05:34–07:58	Imaging	1 344	192	10	36
2017-08-20 02:21–11:21	Imaging	1 344	192	10	36
2017-08-21 07:21–12:28	Imaging	1 344	192	10	36
2017-08-22 01:44–10:52	Imaging	1 344	192	10	36
2017-09-01 02:33–03:28	Imaging	888	192	12	1
2017-09-01 07:59–10:59	Imaging	888	192	12	1
2017-09-02 06:21–08:28	Imaging	888	192	16	1
2017-09-06 01:16–02:17	Imaging	1 344	192	12	1
2017-09-06 03:36–08:36	Imaging	1 344	192	12	1
2017-09-08 02:32–06:00	Imaging	1 344	192	16	1
2017-09-09 03:34–08:41	Imaging	1 344	192	16	1
2017-09-10 03:52–04:52	Imaging	1 344	192	16	1
2017-09-15 08:17–11:17	Imaging	1 344	192	15	1
2017-09-21 05:30–06:30	Imaging	1 344	192	12	1
2017-09-22 08:35–10:35	Imaging	1 368	240	12	1
2017-09-29 23:21–2017-09-30 03:21	Imaging	1 320	240	12	36
2017-09-30 23:32–2017-10-01 03:32	Imaging	1 320	240	12	36
2017-10-01 23:32–2017-10-02 03:32	Imaging	1 320	240	12	36

Table 8. ATCA Observations of GW170817 and AT2017gfo.

	ATCA (Imaging)		
UT obs date	Frequency (GHz)	Bandwidth (GHz)	Flux (μJy)
2017-08-18 01:00–09:07	8.5	2.049	<120
2017-08-18 01:00–09:07	10.5	2.049	<150
2017-08-18 01:00–09:07	16.7	2.049	<130
2017-08-18 01:00–09:07	21.2	2.049	<140
2017-08-20 23:31–2017-08-21 11:16	8.5	2.049	<135
2017-08-20 23:31–2017-08-21 11:16	10.5	2.049	<99
2017-08-27 23:31–2017-08-28 09:00	8.5	2.049	<54
2017-08-27 23:31–2017-08-28 09:00	10.5	2.049	<39
2017-08-27 23:31–2017-08-28 09:00	10.5	2.049	<39
2017-09-04 22:48–2017-09-05 10:04	7.25	4.098	25±6

8 mm f/3.5 UMC Fish-eye CS II lens. The cameras capture full sky images with a cadence of 30 s from sunset to sunrise every night of the year.

Observations from Wooleen Station are available from 2 min before the GW170817 trigger and, as a result, DFN is the only optical facility imaging the source during the GW detection. Between 12:39:28 and 12:49:28, the host galaxy was observed at an elevation of 20°. Initial analysis of the images finds no persistent or transient sources in a 3° radius of NGC 4993, to a limiting magnitude of mag$_v$= 4 (Hancock et al. 2017). Further calibration and analysis have brought this limiting magnitude down to mag$_v$ = 6.

2.1.6. ESO VLT/NACO mid-IR

The ESO Very Large Telescope (VLT) consists of four 8.2-m telescopes located at the Paranal Observatory in Chile. Ob-

servations were made with the NACO instrument (Lenzen et al. 2003; Rousset et al. 2003) on the VLT UT1 Antu telescope. The system allows for adaptive-optics and natural seeing imaging over J, H, Ks, L', and M' filters, as well as providing Wollaston polarimetry and coronography in L'. The 5σ limiting magnitudes are given as $J = 24.05$, $H = 24.05$, $Ks = 23.35$, $L' = 18.55$, and $M' = 15.15$ in 1 h. These observations were initially proposed as Director's Discretionary Time (PI Cooke, Baade) as part of the DWF programme to be made immediately available to the LVC community. However, the observations were finalised and executed by ESO, and made available to the LVC community.

Observations in the L'-band (3.8 μm) were attempted on each night between 2017-08-24 and 2017-09-04. Due to the proximity to the Sun and scheduling constraints, the target was observed during twilight (at UT 22:45–23:20) at
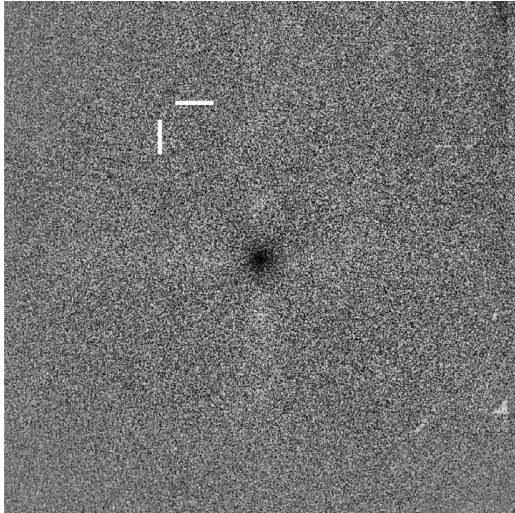
Figure 5. Stacked NACO image of NGC 4993 (27 arcsec × 27 arcsec), with the location of AT2017gfo marked. The image is oriented with North up and East to the left. The image is the combination of observations taken over four nights and no significant source was found to the detection limits of $L' = 15.3, 5\sigma$.

airmass 1.5–1.6. Weather and inaccurate pointing during the first nights resulted in the data from the four nights of August 25, 26, 27, and September 1 being analysed. A pixel scale of 27 mas pix^{-1} was used for a total field of view of 27×27 arcsec. Observations were made in natural seeing mode with integration times 126 × 0.2 s per jitter point (with a 3 arcsec throw per axis), for a total of 15, 19, 14, and 11 min per night. HD 205772 was observed as a flux standard on August 28. The data were reduced by a custom script in a standard way, correcting for sky variance by combining the jittered observations and de-striping by median filtering each detector quadrant separately.

No sources apart from the NGC 4993 nucleus were detected in the field (Figure 5). The detection limits were estimated from the background noise assuming a conservative PSF corresponding to the detected galactic nucleus at approximately 0.5 arcsec FWHM, using a circular aperture of 1 arcsec (40 pix) radius. For the nights of August 25, 26, 27, and September 1, the 5σ detection limits in L' are 14.5, 14.8, 14.5, and 14.3 mag, respectively, with a combined limit of 15.3 mag.

2.1.7. ESO VLT/VISIR mid-IR

Imaging observations in the mid-IR were also made with the VISIR instrument (Lagage et al. 2004) on the ESO VLT UT3 Melipal telescope. Similar to NACO above, the observations were executed by ESO and made available to the LVC community. VISIR provides an imaging field of view of 38 arcsec × 38 arcsec with a plate scale of 0.045 arcsec per

Table 9. ATCA measured flux densities for NGC 4993.

Observation date (UTC)	Frequency (GHz)	Flux density (µJy)
2017-08-18.04 – 2017-08-18.38	8.5	420±50
2017-08-20.98 – 2017-08-21.47	8.5	360±20
2017-08-27.98 – 2017-08-28.37	8.5	460±30
2017-08-18.04 – 2017-08-18.38	10.5	500±40
2017-08-20.98 – 2017-08-21.47	10.5	550±60
2017-08-27.98 – 2017-08-28.37	10.5	400±20
2017-08-18.04 – 2017-08-18.38	16.7	300±50
2017-08-18.04 – 2017-08-18.38	21.2	210±70

Table 10. MWA Observations of GW170817 and AT2017gfo.

MWA (Imaging)		
UT obs date	Frequency (MHz)	Bandwidth (MHz)
2017-08-18 07:07:52–09:40:00	185	30.72
2017-08-19 07:04:00–09:38:00	185	30.72
2017-08-20 07:00:08–09:34:08	185	30.72
2017-08-21 06:56:08–09:28:08	185	30.72
2017-08-22 06:52:16–09:26:16	185	30.72

Table 11. Parkes observations of GW170817 and AT2017gfo searching for FRBs.

Parkes (FRB)		
UT obs date	Frequency (GHz)	Bandwidth (MHz)
2017-08-18 06:49:31	1.341	340
2017-08-18 08:50:36	1.341	340
2017-08-20 01:44:32	1.341	340
2017-08-20 02:50:14	1.341	340

pixel. AT2017gfo was observed on 2017 August 23, 2017 August 31, September 1, 2017, and 2017 September 6, 2017 with the J8.9 filter (central wavelength 8.72 µm). Total on-source integration times were 44.8, 17.5, 12.2, and 44.8 min, respectively. Chopping and nodding in perpendicular directions with 8 arcsec amplitudes were used to remove the sky and telescope thermal background. No source was detected to a limiting mag of J8.9 ∼7–8 (Table 5). Details of the observations can be found in Kasliwal et al. (2017).

2.2. Optical/near-infrared spectroscopy

Observations of AT2017gfo and the galaxy NGC 4993 were taken in the optical via longslit, fibre, and integral field unit (IFU) spectroscopic modes. Both Australian and Australian partner observational programmes participated in the spectroscopic follow up of AT2017gfo. Details of the instruments and observations are provided below.

10   *Andreoni et al.*

Table 12. VLBA observations of GW170817 and AT2017gfo.

VLBA (Imaging)			
UT obs date	Frequency (GHz)	Bandwidth (MHz)	Flux (μJy)
2017-08-18 19:58–2017-08-19 01:34	8.7	256	<125
2017-08-20 18:31–2017-08-21 01:13	8.7	256	<125
2017-08-21 18:26–2017-08-22 01:08	8.7	256	<120

Table 13. ANU2.3/WiFeS observations of GW170817 and AT2017gfo.

ANU2.3/WiFeS		
UT obs date	Spectral range (Å)	Exposure (s)
2017-08-18 09:24:25	3 300–9 800	900
2017-08-18 09:40:25	3 300–9 800	900
2017-08-19 08:43:15	3 300–9 800	900
2017-08-19 08:59:42	3 300–9 800	900
2017-08-19 09:16:06	3 300–9 800	900
2017-08-19 09:36:18	3 300–9 800	900
2017-08-19 09:55:38	3 300–9 800	900
2017-08-20 08:47:28	3 200–7 060	1 800
2017-08-20 09:21:33	3 300–9 800	1 800
2017-08-21 08:40:58	3 300–9 800	900
2017-08-21 09:13	3 300–9 800	900
2017-08-21 09:29	3 300–9 800	900

Table 14. SALT/RSS observations of GW170817 and AT2017gfo.

SALT/RSS		
UT obs date	Spectral range (Å)	Exposure (s)
2017-08-18 17:07:19.703	3 600–8 000	433
2017-08-19 16:58:32.76	3 600–8 000	716

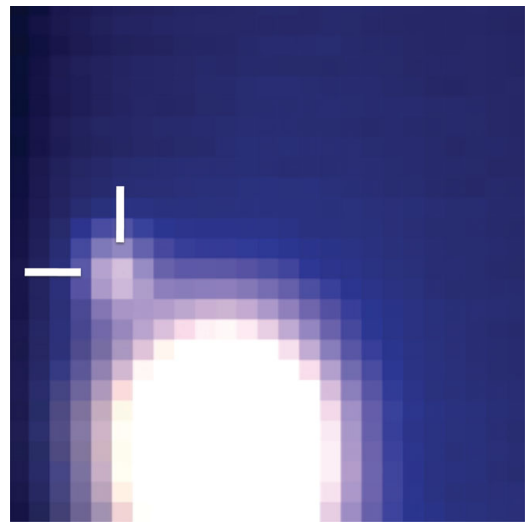**Figure 6.** WiFeS IFU collapsed data cube image (cropped to ∼25 arcsec × 25 arcsec) of NGC 4993 and AT2017gfo (marked). The image combines the data from both beams taken on 2017-08-18. The transient is noticeably bluer than the host galaxy.

2.2.1. ANU2.3/WiFeS

The ANU 2.3-m telescope is located at Siding Spring Observatory in New South Wales, Australia. It includes the dual-beam, image-slicing, integral-field echelle spectrograph (WiFeS, Dopita et al. 2007) which can simultaneously observe spectra over a 25 arcsec × 38 arcsec field of view. WiFeS has a spectral range extending from 3 300 to 9 800 Å, which can be observed either in a single exposure with a resolution of $R = 3\,000$, or in two exposures with $R = 7\,000$, depending on the choice of low- or high-resolution grating configurations, respectively. The observations were done using Director's Discretionary Time.

Spectroscopic observations began on 2017-08-18 at 09:24:25 and 09:40:25 with a wavelength range of 3 200–9 800 Å. Each observation had an exposure time of 15 min. The reduced spectrum shows a blue, featureless continuum peaking near 4 500 Å (Figure 7). The observations con-

tinued for two further nights with the same configuration but a larger number of exposures to increase signal for the fading source. The last exposures were taken on 2017-08-21 at times 08:40:58, 09:13, and 09:29 with a wavelength range of 3 200–7 060 Å, again with exposure times of 15 min. A WiFeS collapsed data cube image is shown in Figure 6.

2.2.2. SALT/RSS

Optical spectroscopy of AT2017gfo was obtained using the Robert Stobie Spectrograph (RSS, Burgh et al. 2003) on the 10-m-class Southern African Large Telescope (SALT) located in Sutherland, South Africa. The observations were taken with Director's Discretionary Time initiated as part of the DWF programme. The RSS is a spectrograph covering the range 3 200–9 000 Å with spectroscopic resolutions of $R = 500$–$10\,000$. The observations were performed using the PG0300 grating at an angle of 5.75° and the 2 arcsec slit. Data taken on 2017-08-18 at 17:07 and 2017-08-19 at 16:59
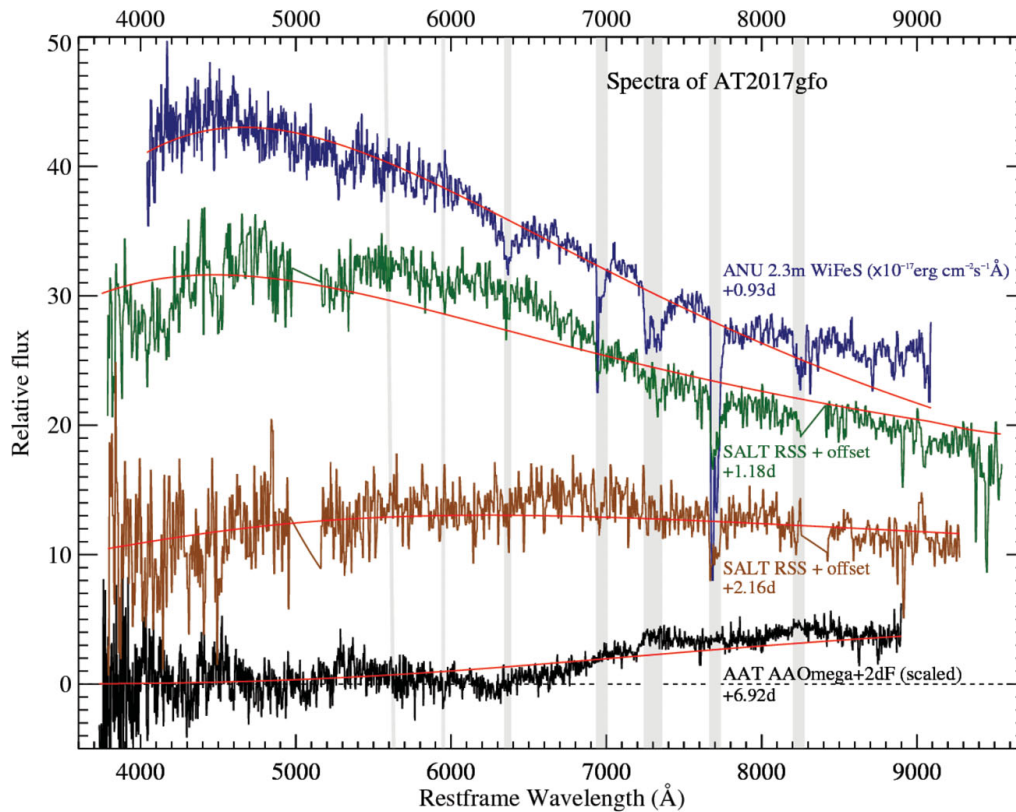
Figure 7. The rapid spectral evolution of AT2017gfo. The ANU 2.3-m WiFeS, SALT RSS (2 spectra), and AAT AAOmega+2dF spectra obtained at 0.93, 1.18, 2.16, and 6.92 d, respectively, after GW detection are shown and labelled. Vertical grey bands denote telluric features that are not well removed in some spectra. Blackbody model fits (red curves) over the full spectra result in temperatures of 6 275 K (WiFeS), 6 475 and 4 700 K (RSS), and 2 080 K (AAOmega). Peaks in the WiFeS, RSS, and AAOmega continua correspond to ~6 400 K, ~5 600 K, ~4 400 K, and <3 200 K, respectively.

(Shara et al. 2017) had exposure times of 433 and 716 s, respectively. Due to the visibility limitations of SALT, the data were acquired in early twilight and are heavily contaminated with a high sky background. Spectral flux calibration standards were also observed on the same night.

Basic CCD reductions, cosmic ray cleaning, wavelength calibration, and relative flux calibration were carried out with the PySALT package (Crawford et al. 2010). Because of the changing pupil during SALT observations, only a relative flux calibration can be achieved. In order to de-blend the sources, the flux from the host galaxy, the atmospheric sky lines, and the GW source were fit simultaneously using the astropy modelling package (Astropy Collaboration et al. 2013). The reduced spectra appears to have a relatively blue, featureless continua as seen in Figure 7. The data are also presented and interpreted in McCully et al. (2017) and Buckley et al. (2017).

2.2.3. AAT/2dF+AAOmega

The Anglo-Australian Telescope (AAT) is a 3.9-m Equatorial-mount optical telescope located in New South Wales, Australia. AAOmega is a dual-beam optical fibre spectrograph with 3 700 to 8 800 Å wavelength coverage and a spectroscopic resolution of $R = 1\,700$ (Smith et al. 2004). We used AAOmega combined with the Two Degree Field (2dF) multi-object system which allows for simultaneous spectroscopic observations of up to 392 objects within a 2° diameter field of view. The observations were done as part of the DWF programme and granted via Director's Discretionary Time while activating the newly commissioned AAT 2dF Target Of Opportunity (ToO) mode. Fully configuring all 392 fibres takes ~40 min and is too long for rapid follow up of short-lived transient phenomena. In rapid ToO mode, the 2dF software determines, from an existing fibre configuration, which fibres need to move to place a single fibre on the target and one
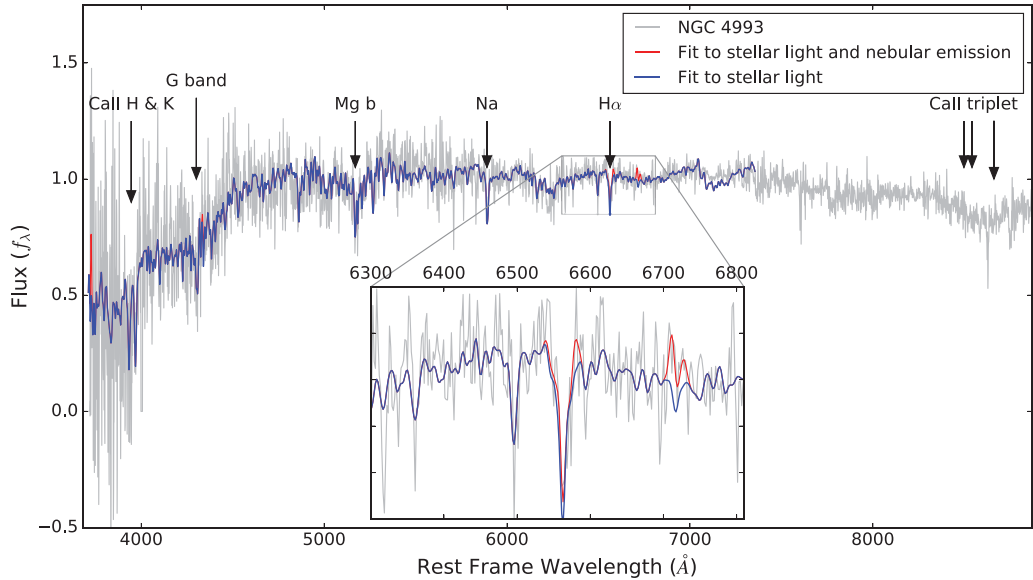
Figure 8. AAT fibre spectrum of NGC 4993 in a 2-arcsec region at the position of AT2017gfo. A fit to the stellar light (blue) and the stellar light and nebular emission (red) are shown. The fits include the flux of AT2017gfo (at +6.92 d) and the galaxy. Several common atomic transitions are marked and a zoom-in of the Hα region is shown. The spectrum is corrected for line-of-sight Milky Way extinction.

Table 15. AAT/AAOmega+2dF observations of GW170817 and AT2017gfo.

AAT/AAOmega+2dF		
UT obs date	Spectral range (Å)	Exposure (s)
2017-08-24 08:55:07	3 750–8 900	2 400

on a guide star. This capability enables configuration and observation within a few minutes and, in the case of AT2017gfo, 5 min between ToO activation and the commencement of the observations.

AT2017gfo observations began on 2017-08-24 at 08:55:07 to 09:41:28 with exposure times of 600 s each (Table 15). The data were processed using the OzDES pipeline (Childress et al. 2017). Four exposures were analysed, revealing an E/S0-like galaxy spectrum (Figure 8) with a weak red flux enhancement (Andreoni et al. 2017b). The source was isolated by subtracting the host galaxy using the SALT host galaxy spectrum (McCully et al. 2017) extracted from the region of the galaxy near the source. The SALT spectrum was cleaned over chip gaps and telluric line regions using the average value on either edge of each feature. Finally, the SALT host and AAT AAOmega host+event spectra were scaled and subtracted (Figure 7). Subtracting two spectra with relative flux calibrations introduces uncertainties in the scalar offset. Such subtractions do not significantly affect the form of the residual

spectrum, but can provide a small affect on blackbody model fit results. Although care was taken in the subtraction process, the two spectra introduce possible flux calibration differences from the different instruments and extraction techniques. As a result, we stress that the spectrum presented here is meant to be indicative of the behaviour and temperature of the event at 6.92 d, and suffers from the above caveats. A proper host galaxy subtraction with the AAT AAOmega+2dF is planned when NGC 4993 becomes visible.

2.3. Radio

Five Australian and international radio facilities participated in this follow-up campaign. In this section we describe the role of each radio observatory that performed the follow up of GW170817 and/or AT2017gfo under Australian-led observing programs.

2.3.1. ATCA

The Australia Telescope Compact Array (ATCA) is located at the Paul Wild Observatory in New South Wales, Australia. It is an array of six 22-m radio antennas, which can be configured with antenna spacings up to 6 km. The array can observe in one of five observing bands spread between 1.1 and 105 GHz.

We carried out ATCA observations on August 18, 21, 28, and September 5, 2017 under a ToO programme (CX391; PI: T. Murphy). During the August observations, we targeted

53 galaxies identified to be located within the 90% containment volume of GW170817 (Bannister et al. 2017b, 2017c). The September 5 observation targeted only the optical counterpart, AT2017gfo and its host galaxy NGC 4993. Table 8 presents a summary of the observations.

The August observations used two 2 GHz frequency bands with central frequencies of 8.5 and 10.5 GHz and observed NGC 4993 using two frequency bands centred on 16 and 21 GHz on August 18, For the September observations, we centred these two frequency bands on 5.5 and 9.0 GHz. The configuration of the ATCA changed over the course of the observations, with ATCA in the EW352 configuration for the August 18 observation and in the 1.5 A configuration for all other observations.

For all epochs and all frequencies, the flux scale was determined using the ATCA primary calibrator PKS B1934-638. The bandpass response at 8.5 and 10.5 GHz was determined using PKS B1934-638 and observations of QSO B1245-197 were used to calibrate the complex gains. We used QSO B1921-293 to solve for the bandpass at 16.7 and 21.2 GHz and observations of QSO B1256-220 were used to solve for the complex gains at these frequencies. All of the visibility data were reduced using the standard routines in the MIRIAD environment (Sault et al. 1995).

We used the MIRIAD tasks INVERT, CLEAN, and RESTOR to invert and clean the calibrated visibility data from the August observations of the 53 targeted galaxies. We fit a single Gaussian to each of the 53 galaxies detected in our August observing epochs (Lynch et al. LVC GCN 21628, Lynch et al. LVC GCN 21629). Comparing these observations, we find no transient emission above a 3σ limit between 36 and 640 μJy. The measured flux densities for host galaxy NGC 4993 are listed in Table 9. The results from our observations of AT2017gfo are described in Hallinan et al. (2017), including a detection on September 5 at 7.25 GHz, with measured flux density of 25±6 μJy (Murphy et al. 2017).

2.3.2. ASKAP

The Australian Square Kilometre Array Pathfinder (ASKAP) is a system of 36 12-m phased-array feed receiver radio telescopes located in Western Australia. The instrument covers a frequency range of 0.7 to 1.8 GHz with a bandwidth of 300 MHz. The field of view of is 30 deg^2 at 1.4 GHz, with a resolution of ∼30 arcsec.

ASKAP performed imaging observations on 2017-08-19 05:34:32 (LVC GCN 21513) with 12 of the 36 antennas[5]. The 90% LVC contour region (The LIGO Scientific Collaboration and the Virgo Collaboration 2017d) was covered with three pointings using an automated algorithm (Dobie et al. in preparation) observed over the following 4 d. We place an upper limit of ∼1 mJy on emission from AT2017gfo and its host galaxy NGC4993.

At the time of publication, 14 further single-beam observations of the AT2017gfo location were carried out with varying

numbers of beams and antennas at different frequencies and bandwidths (subject to commissioning constraints). These observations are undergoing processing, while further observations are ongoing.

ASKAP also searched the 90% LVC uncertainty region at high-time resolution for fast radio bursts (FRBs Lorimer et al. 2007) using the search algorithms described in Section 2.3.5 to cover a dispersion measure range of 0–2 000 pc cm^{-3}. The observations were in "fly's-eye" mode with seven antennas at a central frequency of 1 320 MHz (Bannister et al. 2017a). Observation times were 2017-08-18 04:05, 2017-08-18 08:57, and 2017-08-19 02:08, for a total duration of 3.6, 4.1, and 11.0 h, respectively. Above a flux density threshold of ∼40 Jy/$\sqrt{w}$, there were no FRB detections (GCN21671), where w is the observed width of the FRB in milliseconds.

2.3.3. MWA

The Murchison Widefield Array (MWA) is a system of 2048 dual-polarisation dipole antennas organised into 128 tiles of 4×4 antennas located in Western Australia. MWA operates between 80 and 300 MHz (Tingay et al. 2013) and has a resolution of several arcmin. Operations with the original array (baselines up to 3 km) with a compact configuration with maximum redundancy ceased in 2016. The reduced baseline was used until mid-2017 at which point tiles with extended baselines up to 5 km were installed for MWA Phase II.

The telescope responded automatically to the LVC GCN (Kaplan et al. 2015) but the initial LVC notice only included information from a single detector of LIGO, so the telescope pointing was not useful. Later, we manually pointed the telescope and began observations on 2017-08-18 at 07:07 with only 40 tiles in a hybrid array with elements of the maximally redundant array and the original array. Observations occurred daily from 2017-08-18 to 2017-08-22 with 75 × 2 min exposures and then continued weekly. The observations cover a 400 deg^2 field of view at a central frequency of 185 MHz and a bandwidth of 30 MHz (Kaplan et al. 2017b). We see no emission at the position of NGC 4993 with a flux density limit of 51 mJy beam^{-1} (3σ confidence) from the data taken on 2017 August 18 (Kaplan et al. 2017c). Later, observations with more functioning tiles and longer baselines should have considerably improved performance. Kaplan et al. (2016) discuss in detail the strategies to use MWA for finding prompt radio counterparts to GW events.

2.3.4. VLBA

The Very Long Baseline Array (VLBA) is a radio interferometer consisting of 10 25-m radio telescopes spread across the United States, and is capable of observing in one of 10 bands at frequencies between 1.2 and 96 GHz.

The counterpart AT2017gfo and its host galaxy NGC 4993 were observed on three occasions under the Director's Discretionary Time project BD218, each with 6.5 h duration. The observations were performed from 2017-08-18 19:58 to 2017-08-19 01:34, 2017-08-20 18:31 to

---

[5] As a result of ongoing commissioning.

14 *Andreoni et al.*

2017-08-21 01:13, and 017-08-21 18:26 to 2017-08-22 01:09. The central observing frequency was 8.7 GHz, with a bandwidth of 256 MHz and dual polarisation. The source VCS1 J1258-2219, with a position uncertainty of 0.2 mas, was used as a primary phase reference calibrator, with NVSS J131248-235046 as a secondary calibrator. An observing failure rendered the first epoch unusable, but the second and third epochs provided good data.

No source was detected within 0.5 arcsec of the position of AT2017gfo, consistent with the findings of both the VLA and ATCA instruments (e.g., Bannister et al. 2017c; Kaplan et al. 2017a; Lynch et al. 2017). However, we are able to provide 5.5σ upper limits of 125 and 120 μJy beam^{-1} at 2017 August 20 21:36 and 2017 August 21 21:36, respectively, while stacking the two images produces an upper limit of 88 μJy beam^{-1} (Deller et al. 2017a, 2017b).

Imaging the core region of NGC 4993 identifies a sub-mJy radio source at the centre with coordinates RA = $13^h09^m47.69398^s$ Dec = $-23°23'02.3195''$ (J2000). The detection is consistent with either an unresolved source or a marginally resolved source on a scale smaller than the VLBA synthesised beam (2.5×1.0 mas). The systematic uncertainties of our position are $\leqslant 1$ mas in both RA and DEC. We find a 9σ flux density of 0.22 mJy, and the *a priori* amplitude calibration available to the VLBA is accurate to the 20% level. If we assume the synthesised beam size of 2.5×1.0 mas to represent a conservative upper limit on the size of the source, we infer a lower limit for the brightness temperature of 1.6×10^6 K. An initial interpretation suggests the recovered brightness temperature is consistent with an AGN (Deller et al. 2017c). Comparison of the flux densities estimated by ATCA and VLA (see Table 9 and Hallinan et al. 2017) to the VLBA value indicates that a considerable amount ($\sim 50\%$) of the total source flux is contained within this mass scale component.

2.3.5. Parkes

The Parkes Radio Telescope (Parkes) is a 64-m telescope located in Parkes, New South Wales, Australia. Parkes operated in FRB search mode with the Multibeam receiver (Staveley-Smith et al. 1996) and the BPSR backend (Keith et al. 2010). The usable bandwidth is 340 MHz, in the range of 1182–1582 MHz. If the neutron star merger produced a massive ($> 2 \, M_\odot$) neutron star instead of a black hole, it would be expected to possess a spin period close to the break-up velocity of ~ 1 ms and potentially a large magnetic field generated during its formation. Such objects (millisecond magnetars) are a potential source of FRBs or possibly even repeating FRBs (Spitler et al. 2016; Metzger, Berger, & Margalit 2017). The FRB should be detectable at S/N > 100 with Parkes at the distance of NGC 4993, if appropriately beamed and not hidden by the ejecta from the merger.

A dedicated search for FRBs (Keane et al. 2018) with dispersion measures ranging from 0–2 000 pc cm^{-3} associated with AT2017gfo was performed on 2017-08-18 at 06:49:31 and 08:50:36 with 2-h and 1-h integration times, respectively,

and again on 2017-08-20 at 01:44:32 and 02:50:14 with 1-h integration times (Bailes et al. 2017a, 2017b). No FRBs were detected with a 7σ limiting flux density of 1.4 sqrt(w/0.064) Jy sqrt(ms), where *w* is the observed pulse width of the FRB in ms.

3 ANALYSIS

The observations presented here identified the optical transient on multiple epochs for the first ~ 7 d after the LIGO trigger, starting from about 21 h after the event. In Figure 4, we present the multi-band photometric light curve of AT2017gfo, observed in *g*-band (SkyMapper), *r*-band (SkyMapper, Zadko, Etelman/VIRT), and *i*-band (AST3-2, SkyMapper). The multi-band measurements indicate a decay faster in *g*-band than in the *r*- and *i*-bands. We processed and analysed four optical spectra acquired with ANU2.3m/WiFeS, SALT/RSS, AAT/2dF+AAOmega. The subtraction of the host galaxy allows the signature of the transient to be identified and the spectral evolution to be assessed (Figure 7). In this section, we review the spectral evolution of AT2017gfo, describe the properties of the host galaxy NGC 4993, and assess the photometric evolution of the event compared to sGRB and kilonova models.

3.1. Spectral evolution of AT2017gfo

The ANU 2.3m (WiFeS), SALT (RSS), and AAT (AAOmega+2dF) spectra reveal a rapid evolution of the transient over ~ 7 d while maintaining relatively featureless continua. As a coarse measure of the evolving spectral energy distribution, we fit a blackbody model to the spectra (Figure 7). Continuum blackbody temperatures were calculated by fitting the observed spectra using the python `scipy` package implementation of the non-linear least-squares Levenberg–Marquadt algorithm. Spectra are corrected to rest-frame and for Milky Way line-of-sight extinction using the Cardelli, Clayton, & Mathis (1989) prescription and adopting $R_V = 3.1$ and $E(B - V) = 0.12$ and based on the dust maps of Schlegel, Finkbeiner, & Davis (1998).

The model fits result in a temperature evolution from $\sim 6\,400$ K to $\sim 2\,100$ K in ~ 7 d. The WiFeS spectrum is reasonably well fit by a $\sim 6\,300$ K blackbody, with the peak in the spectrum continuum corresponding to $\sim 6\,400$ K. The curvature of the SALT spectrum is not well fit by a blackbody model, with the model fit producing a temperature of $\sim 6\,500$ K, whereas the peak in the spectrum roughly corresponds to $\sim 5\,600$ K. The second SALT spectrum, taken at +2.16 d, is reasonably well fit, producing a blackbody model fit of ~ 4700 K, while the continuum peak corresponds to roughly 4 400 K. By day ~ 7, the source is quite faint and host galaxy subtraction is less reliable. The AAOmega+2dF spectrum at +6.92 d is best fit by a blackbody model at $\sim 2\,080$ K, but has the caveats stated in Section 2.2.3.

3.2. The host galaxy

The AAT/2dF+AAOmega spectrum (Figure 8, Andreoni et al. 2017b) was acquired 6.92 d after the LIGO trigger. The fibre was centred on the transient position, but the spectrum is dominated by the light of the host galaxy. Figure 7 shows the galaxy-subtracted transient spectrum from the same observation.

We use pPXF (Cappellari 2017) to fit the spectrum to 7 300 Å (the extent of the MILES spectral template library) to estimate the metallicity, age, r-band mass-to-light ratio, and velocity dispersion of stars in the region immediately surrounding AT2017gfo. At the redshift of the host galaxy, the 2-arcsec diameter of a 2dF fibre corresponds to a linear size of 400 parsec. Assuming a spectral resolution of 4.5 Å (measured using night sky lines), the pPXF fit yields a velocity dispersion of 100 km s^{-1}, a stellar age of 10 billion yrs, a metallicity of [M/H] $= -0.2$, and an r-band mass-to-light ratio of 4. Evidence for Hα emission in the pPXF fit is very weak, measured at EW $= -0.2$ Å, but is consistent with zero. The environment in the location of the transient is consistent with an old, passively evolving stellar population with no ongoing star formation.

The above assessment of NGC 4993 in the region of the source is consistent with the report of Sadler et al. (2017) for the central 6-arcsec region of the galaxy based on spectroscopy from the 6dFGS (Jones et al. 2009). The central stellar velocity dispersion of 163 km s^{-1} (Ogando et al. 2008) predicts a central black hole mass of $M_{BH} = 10^{7.7}$ M$_\odot$ (Yu et al. 2017), which can be compared against estimates based on the radio properties of the central source. The compact radio emission detected by VLBA in the central region of NGC 4993 with a brightness temperature exceeding 10^6 K indicates the presence of a low-luminosity active galactic nucleus (LLAGN), allowing us to estimate the black hole mass using the fundamental plane of black hole activity (e.g. Plotkin et al. 2012; Merloni, Heinz, & di Matteo 2003; Falcke, Körding, & Markoff 2004). The VLBA flux density was measured to be 0.22 ± 0.04 mJy at 8.7 GHz, which (assuming a flat spectral index) gives a 5-GHz radio luminosity of $(2.1 \pm 0.04) \times 10^{36}$ erg s^{-1}, while the X-ray luminosity as measured by *SWIFT* is $5.6^{+2.4}_{-1.9} \times 10^{39}$ erg s^{-1} (Evans et al. 2017). The radio spectral index is consistent with being flat or slightly negative (as can be seen from the ATCA results shown in Table 9); the results are insensitive to small variations in this parameter. Using the relationship described in Plotkin et al. (2012), we obtain a predicted central black hole mass of $10^{7.8 \pm 0.3}$ M$_\odot$, in good agreement with the velocity dispersion estimate.

Sadler et al. (2017) also state that the nuclear dust lanes evident in the *HST* ACS images (Foley et al. 2017; Pan et al. 2017) may be the product of a galaxy–galaxy merger that occurred as long as several Gyr ago. We note that a wet galaxy merger (to produce the visible dust) implies that the binary progenitor of AT2017gfo might have originated in the merging galaxy and not necessarily in the main early-type

host. Such an origin could permit a shorter BNS inspiral time than would be plausible for a massive galaxy with no recent star formation. Previous sGRB hosts with possible kilonovae are often low-mass, blue star-forming galaxies (Tanvir et al. 2013; Fong & Berger 2013), though 20–40% of sGRBs occur in early-type galaxies (Fong et al. 2013). The diversity of possible host galaxies for neutron star merger events therefore needs to be kept in mind when searching for the counterparts of future GW events.

3.3. Comparison with GRB afterglow and kilonova models

The optical data we acquired, alone, can give insight on the nature of the transient event. First, we explore the GRB afterglow scenario in order to test the possibility that AT2017gfo behaves as a 'standard' on-axis GRB in the optical, specifically using the Granot, Piran, & Sari (1999) and Granot & Sari (2002) models. Second, we investigate the kilonova scenario by comparing the data we acquired with three possible models (Tanaka & Hotokezaka 2013; Hotokezaka et al. 2013; Barnes & Kasen 2013; Metzger et al. 2015). In Figure 9, we overlay the results we obtain to our data.

3.3.1. GRB afterglow

We investigate the GRB afterglow scenario using the Granot and Sari (Granot et al. 1999; Granot & Sari 2002, G02) formulation for a relativistic blast wave in an ISM environment. Far from the sites of the break frequencies of the GS02 spectra, each power-law segment becomes asymptotic. In particular, we can assume that the frequency of our optical observations, ν_{opt}, relates to other characteristic frequencies as $\nu_{sa} < \nu_m < \nu_{opt} < \nu_c$, where ν_{sa} is the self-absorption frequency, ν_m is the minimal electron synchrotron (or peak) frequency, and ν_c is the frequency at which an electron cools over the dynamical time span of the system. In this region of the spectrum, we can approximate the spectral flux density as $F_\nu \propto t^\alpha$. Simultaneous X-ray or radio measurements would help to constrain the locations of the break frequencies of the spectrum.

We calculate the index α by χ^2 minimisation of the Zadko telescope r-band data points and we find $\alpha = -1.73 \pm 0.10$; in addition, we derive an electron power-law index $p = 1 + \frac{4}{3}\alpha$ (G02) to determine $p = 3.31 \pm 0.13$. This value is higher than historical sGRBS (see Fong et al. 2015, for a decadal review), where the median value of p is found to be $\langle p \rangle = 2.43^{+0.36}_{-0.28}$. In a classical sGRB scenario, our calculated p could be interpreted as (i) emission is not a spherically isotropic blast wave (Sari, Piran, & Halpern 1999) giving a larger temporal decay slope than historical sGRBs (Fong et al. 2015) or (ii) evidence that the jet itself may be structured (Rossi, Lazzati, & Rees 2002; Granot & Kumar 2003).

We use the isotropic gamma-ray energy measured with *Fermi* $\langle E_{\gamma,\,iso} \rangle \approx (5.35 \pm 1.26) \times 10^{46}$ erg (Goldstein et al. 2017a) to constrain our parameter space, assuming that $E_{\gamma,\,iso} \approx E_{K,\,iso}$ (Frail et al. 2001). In this way, we find an unphysically high circumburst number density (in the order of
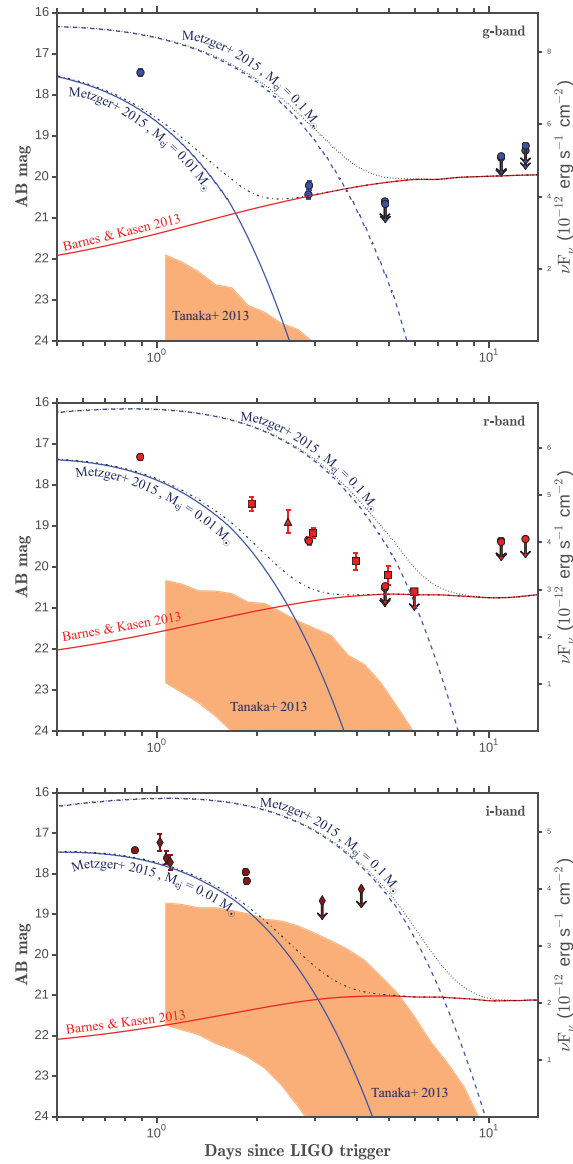
Figure 9. Comparison of models to optical photometry with Zadko (squares, *r*-band), AST3-2 (diamonds, *i*-band), Etelman/VIRT (triangles, *C*-filter presented in the central panel), and SkyMapper (circles, *gri*-bands). The solid black line is the GS02 model of a short GRB afterglow. The dark orange region represents the kilonova model by Tanaka & Hotokezaka (2013). The solid red line represents the Barnes & Kasen (2013) model for ^{56}Ni+r-process opacities. The blue lines represent the free neutron-powered blue precursor (solid: $v_{ej} = 0.2c$, $M_{ej} = 0.01\,M_{\odot}$; dashed: $v_{ej} = 0.2c$, $M_{ej} = 0.1\,M_{\odot}$ Metzger et al. 2015), while the black dashed and dot–dashed lines represent the Metzger et al. (2015) and Barnes & Kasen (2013) models together. The figure is organised in three panels, presenting photometry and overlaid models in *g*-band (top), *r*-band (centre), and *i*-band (bottom).

$n \sim 10^{13}$ cm^{-3}). In addition, placing such high values for the circumburst number density back into the GS02 models, we come across results that contradict our assumption that $\nu_{sa} < \nu_m < \nu_{opt} < \nu_c$, i.e. that $\nu_c < \nu_{opt}$. Contradictory results are also obtained considering any other assumption for the relation between the spectral breaks and for any spectra given in Granot & Sari (2002). Therefore, we rule out the optical emission being the afterglow of a 'standard' on-axis sGRB. This conclusion is supported by the lack of any prompt X-ray afterglow detection (Cenko et al. 2017), which usually follow on-axis-GRB discoveries.

3.3.2. Kilonova models

We compare our data with three standard models describing inherent kilonova emission. In particular, we consider the case of r-processes in the ejecta from BNS mergers in the 'TH13' formulation (Tanaka & Hotokezaka 2013; Hotokezaka et al. 2013) for a range of NS equations of state, the 'B&K13' model (Barnes & Kasen 2013), and free neutron-powered blue precursor to the kilonova emission ('M15', Metzger et al. 2015). We plot the expected *gri*-bands light curves for all these models in Figure 9.

TH13 model: We calculate the expected light curves using the TH13 kilonova *gri*-bands light curves for a source located at D_L=40 Mpc and for a variety of NS equations of state, specifically APR4-1215, H4-1215, Sly-135, APR4-1314, and H4-1314. We calculate the light curves for polar view angles, where the magnitudes are *K*-corrected in the rest frame using a standard ΛCDM cosmology with $H_0 = 70$ km s^{-1} Mpc^{-1}, $\Omega_m = 0.3$, and $\Omega_\Lambda = 0.7$ (Hotokezaka et al. 2013). The results lie within the solid orange regions in Figure 9 and show a fainter emission than we observed. The results are to be expected, as the spectra (Figure 7) are characteristic of a blue transient—at least in the first few days after the merger—while the TH13 model predicts a transient peaking at near-IR wavelengths. The 'mismatch' between our measurements and the TH13 models reduces at late times and at redder bands (from *g* to *i*), but only a longer monitoring of the source could indicate whether the transient can be dominated by r-processes at late times.

BK13 model: In the BK13 model, the ejecta have an opacity similar to r-process material, made up of heavier lanthanide-group elements generated from dynamical ejection, and material made up of ^{56}Ni that is ejected via disk winds. These cases predict an emission peaking in the near-IR and optical, respectively (Barnes & Kasen 2013). We show the results for the emission expected from ^{56}Ni in Figure 9 as a dashed grey line. At late times ($t \approx 6$ days), we find an upper limit magnitude consistent with this model.

M15 precursor model: The photometry and spectroscopy acquired here show a high optical luminosity and hot, blue continua during the first $\sim$1 d (see Section 3.1). Therefore, we explore the M15 model that predicts an energetic blue precursor. This model is based on the idea that a small fraction (i.e. $M_n \sim 10^{-4}$M$_\odot$; Metzger 2017) of the ejected mass in the outer shell is rapidly expanded after shock heating during the merger. Thus, the neutrons in the outer shell avoid capture by the nuclei in the dense inner ejecta during the r-process. The unbound neutrons are then subject to β-decay, which gives rise to a precursor to the kilonova which, at the distance to AT2017gfo, would peak at mag$_r \sim 17.5$ after a few hours, and consistent with the photometry. The peak luminosity of the neutron layer can be approximated by $L_{peak} \propto v_{ej} \times M_{ej}^{1/3}$ (Metzger 2017) We overlay the *gri*-bands plots to our data in Figure 9 for lanthanide-free ejecta and for two sets of values for the velocity and mass of the ejecta ($v_{ej} = 0.2c$, $M_{ej} = 0.01$ M$_\odot$; and $v_{ej} = 0.2c$, $M_{ej} = 0.1$ M$_\odot$).

The M15 model seems to match our observations with a greater accuracy than the TH13 and BK13 models in the first $\sim$2 d after the merger. However, this model alone predicts a steeper decay of the light curve than the observations. The SkyMapper *g*-band upper limits place a mild constraint in favour of a scenario with only an M13-type precursor. Nevertheless, the combination of the M15 and BK13 models, represented with black dashed lines in Figure 9, is a better match to our data and, particularly, for the *r*-band measurements shown in the central panel.

4 DISCUSSION

The first detection of the EM counterpart to a GW event is a milestone in the history of modern astronomy. Australian teams contributed to both the search and the follow up of the transient AT2017gfo, the EM counterpart to GW170817. In this paper, we present the observations, follow-up strategies, and data acquired by 14 radio, infrared, and optical facilities led by Australian observing programmes.

It is interesting to discuss the progenitor of this event. Our own galaxy contains at least seven BNS pairs that will coalesce in less than a Hubble time, see Özel & Freire (2016). For some, like the double pulsar PSR J0737-3039A/B (Burgay et al. 2003), the 'remaining time' before merger is short ($\sim$80 Myr), whereas for others, like PSR B1534+12 the (remaining) coalescence time is 2.7 Gyr (Arzoumanian, Cordes, & Wasserman 1999). The latter would appear to be a more likely progenitor for this event as it could have formed when the last episode of star formation in NGC 4993 was still underway. It will be fascinating to see how many binary star mergers are ultimately observed in active star-forming galaxies from 'ultra-relativistic' progenitors with short lifetimes compared to those from wider systems like PSR B1534+12.

The location in NGC 4993 is also of some interest. At 40 Mpc, the projected distance of AT2017gfo from the centre is 2.2 kpc. Such a displacement could be achieved during a galaxy merger, so constraints on any kick received by the binary are poor.

No radio source is detected down to 40 μJy with the ATCA, ASKAP, VLBA, and MWA telescopes within 10 d from the GW detection. However, past sGRBs that were detected in the radio despite being 30–60 times more distant than this event (Berger et al. 2005; Soderberg et al. 2006; Fong et al. 2014;

18   *Andreoni et al.*

Zhang et al. 2017) imply that future neutron star mergers at these (40 Mpc) distances could reach flux densities of 0.1 to 1 Jy. The Parkes and ASKAP radio telescopes searched for FRBs in NGC 4993 after the BNS merger for a total of 5 and 18.7 h, respectively. No FRB was detected: a signal from a source at ∼40 Mpc with similar properties of the repeating FRB 121102 (Spitler et al. 2016) would have resulted in a highly significant detection.

We compared 'standard' sGRB afterglow models (GS02) with the optical light curve obtained with the measurements of the Zadko, AST3-2, SkyMapper, and Etelman/VIRT telescopes. The AT2017gfo transient was proven to be the EM counterpart to GW170817 and GRB 170817A (Lipunov et al. 2017b), but its optical light curve does not match the sGRB afterglow models. The continuum profiles and evolution of the spectra of AT2017gfo are unlike sGRBs and argue for a kilonova-like explosion, with a blackbody-like event cooling rapidly over the ∼7 d of our spectral coverage. No features are identifiable in the optical spectra acquired in the first week after the trigger, which prevents us from performing velocity measurements. We cannot rule out that the emission is collisionally dominated. Tidally energised winds may have existed just prior to the merger, however the lack of any strong X-ray emission and the exotic composition required for such winds make this scenario unlikely. We compared three kilonova models (T&H13, B&K13, and M15) with our photometric data and the plots, combined with the spectral evolution of the transient, make the combination of a neutron-powered blue precursor and a r-process red emission at later time a plausible scenario.

5 FUTURE PERSPECTIVES

Several facilities discussed here have existing reactive programmes to follow-up GW alerts, while others perform observations as part of DWF and/or OzGrav.

DWF coordinates ∼30 major observatories worldwide and in space to provide simultaneous, fast-cadenced, deep (m ∼ 23–25, optical), radio to gamma-ray coverage of fast transients and GW events[6] (Cooke et al. in preparation). As a result, DWF is on-source before, during, and after fast transients and has been in full operation since 2016. Moreover, DWF performs real-time (seconds) supercomputing data analysis and transient identification (Andreoni et al. 2017a; Vohl et al. 2017; Meade et al. 2017) and triggers rapid-response, conventional ToO, and long-term spectroscopy and imaging with our network of 1–10-m class telescopes. DWF operates several weeks a year and was not on sky during this GW event. However, 10 DWF participating facilities provided data for AT2017gfo. GW event detections during future DWF observing runs will provide complete, densely sampled, multiwavelength imaging, and spectroscopy of the event and host galaxy.

The intent of the EM component of OzGrav is to help oversee a number of collaborating facilities, including the DWF programme, in an effort to optimise the follow up of GW events by Australian and Australian-led programs at all wavelengths. By the time of LIGO/Virgo 'O3' run, OzGrav will be fully optimised to provide complete and dense coverage of GW events at all wavelengths via imaging, spectroscopy, interferometry, and FRB searches.

The DFN is being augmented with cameras designed to detect bright optical transients. The first such station consists of a Nikon D810 Camera with a Samyang 14 mm f/2.8 IF ED UMC Lens, giving a field of view of $80 \times 100°$, an imaging cadence of 15 s, and a limiting magnitude of $mag_v = 10$. Successor astronomy stations have been developed to have a greater sky coverage and increased sensitivity, via multiple cameras to tile the sky with a <5 s imaging cadence and limiting magnitude of $ag_v = 12$. The current and future DFN network is the only facility that can provide continuous monitoring for half of the Southern sky.

The future of the OzGrav facilities network also includes the Gravitational-wave Optical Transient Observer (GOTO[7]), a planned wide-field robotic optical telescope optimised for following up LVC triggers. GOTO is supported by a collaboration between Monash University; Warwick, Sheffield, Leicester, and Armagh University in the UK; and the National Astronomical Research Institute of Thailand (NARIT). Each instrument consists of eight 40-cm astrographs on a single mount, with fields of view arranged to achieve a total coverage of order 40 deg^2. The prototype instrument, with four astrographs, was deployed in 2017 June, although full robotic operation was not achieved before the end of O2. Funding has now been secured for an additional four astrographs, and the instrument is expected to commence operations in 2018.

Australia will further be able to support the search for and characterisation of GW sources with GLUV, a 30-cm ultraviolet survey telescope under development at ANU (Sharp et al. 2016) for a high altitude balloon platform. It will feature a 7 deg^2 field of view and a limiting magnitude in near-UV of ∼22. Ridden-Harper et al. (2017) explores the application of GLUV to GW source characterisation, showing that early UV observations could provide a powerful diagnostic to identify merger pathways. The system is expected to fly in 2019 and build towards a constellation of telescopes flying in observation campaigns.

---

[6] http://www.dwfprogram.altervista.org

---

[7] http://goto-observatory.org

References

Abbott, B. P., et al. 2017a, PhRvL, 119, 161101
Abbott, B. P., et al. 2017b, ApJL, 848, L13
Abbott, B. P., et al. 2017c, GCN, 21505, 1
Abbott, B. P., et al. 2017d, GCN, 21509, 1
Abbott, B. P., et al. 2017e, GCN, 21510, 1
Abbott, B. P., et al. 2017f, GCN, 21513, 1
Abbott, B. P., et al. 2017g, GCN, 21527, 1
Adams, S. M., et al. 2017, GCN, 21816, 1
Allam, S., et al. 2017, GCN, 21530, 1
Andreoni, I., Jacobs, C., Hegarty, S., Pritchard, T., Cooke, J., & Ryder, S. 2017a, PASA, 34, 37
Andreoni, I., et al. 2017b, GCN, 21677, 1
Arcavi, I., et al,. 2017a, Nature, 551, 64
Arcavi, I., et al. 2017b, GCN, 21538, 1
Arzoumanian, Z., Cordes, J. M., & Wasserman, I. 1999, ApJ, 520, 696
Astropy Collaboration, et al. 2013, A&A, 558, A33
Bailes, M., et al. 2017a, GCN, 21899, 1
Bailes, M., et al. 2017b, GCN, 21928, 1
Bannister, K. W., et al. 2017a, ApJ, 841, L12
Bannister, K., et al. 2017b, GCN, 21537, 1
Bannister, K., et al. 2017c, GCN, 21559, 1
Barnes, J., & Kasen, D. 2013, ApJ, 775, 18
Barnes, J., Kasen, D., Wu, M.-R., & Martínez-Pinedo, G. 2016, ApJ, 829, 110
Berger, E., et al. 2005, Nature, 438, 988
Berger, E., Fong, W., & Chornock, R. 2013, ApJL, 774, L23
Buckley, D., et al. 2017, MNRAS, accepted
Burgay, M., et al. 2003, Nature, 426, 531
Burgh, E. B., Nordsieck, K. H., Kobulnicky, H. A., Williams, T. B., O'Donoghue, D., Smith, M. P., & Percival, J. W. 2003, in Proc. SPIE, Vol. 4841, Instrument Design and Performance for Optical/Infrared Ground-based Telescopes, eds. M. Iye & A. F. M. Moorwood (Bellingham: SPIE), 1463
Cappellari, M. 2017, MNRAS, 466, 798
Cardelli, J. A., Clayton, G. C., & Mathis, J. S. 1989, ApJ, 345, 245
Cenko, S. B., et al. 2017, GCN, 21572, 1
Childress, M. J., et al. 2017, MNRAS, 472, 273
Chu, Q., Howell, E. J., Rowlinson, A., Gao, H., Zhang, B., Tingay, S. J., Boër, M., & Wen, L. 2016, MNRAS, 459, 121

20 *Andreoni et al.*

Connaughton, V., et al. 2017, GCN, 21506, 1
Coulter, D. A., et al. 2017a, Science, aap9811
Coulter, D. A., et al. 2017b, GCN, 21529, 1
Coward, D. M., et al. 2010, PASA, 27, 331
Coward, D., et al. 2017, GCN, 21744, 1
Crawford, S. M., et al. 2010, in Proc. SPIE, Vol. 7737, Observatory Operations: Strategies, Processes, and Systems III eds. D. R. Silva, A. B. Peck, & B. T. Soifer (Bellingham: SPIE), 773725
Cui, X., Yuan, X., & Gong, X. 2008, in Proc. SPIE, Vol. 7012, Ground-based and Airborne Telescopes II eds. L. M. Stepp & R. Gilmozzi (Bellingham: SPIE), 70122D
Day, B. H., & Bland, P. 2016, AGU Fall Meeting Abstracts, P53C-2234
Deller, A., et al. 2017a, GCN, 21588, 1
Deller, A., et al. 2017b, GCN, 21850, 1
Deller, A., et al. 2017c, GCN, 21897, 1
Dopita, M., Hart, J., McGregor, P., Oates, P., Bloxham, G., & Jones, D. 2007, Ap&SS, 310, 255
Eichler, D., Livio, M., Piran, T., & Schramm, D. N. 1989, Nature, 340, 126
Evans, P., et al. 2017, GCN, 21612, 1
Falcke, H., Körding, E., & Markoff, S. 2004, A&A, 414, 895
Foley, R. J., et al. 2017, GCN, 21536, 1
Fong, W., & Berger, E. 2013, ApJ, 776, 18
Fong, W., Berger, E., Margutti, R., & Zauderer, B. A. 2015, ApJ, 815, 102
Fong, W., et al. 2013, ApJ, 769, 56
Fong, W., et al. 2014, ApJ, 780, 118
Frail, D. A., et al. 2001, ApJL, 562, L55
Freedman, W. L., et al. 2001, ApJ, 553, 47
Gao, H., Ding, X., Wu, X.-F., Dai, Z.-G., & Zhang, B. 2015, ApJ, 807, 163
Gendre, B., et al. 2017, GCN, 21609, 1
Goldstein, A., et al. 2017a, ApJ, 848, L14
Goldstein, A., et al. 2017b, GCN, 21528, 1
Goodman, J. 1986, ApJ, 308, L47
Granot, J., & Kumar, P. 2003, ApJ, 591, 108s6
Granot, J., Piran, T., & Sari, R. 1999, ApJ, 527, 236
Granot, J., & Sari, R. 2002, ApJ, 568, 820
Hallinan, G., et al. 2017, Science, aap9885
Hancock, P. J., et al. 2017, GCN, 21894, 1
Hotokezaka, K., Kyutoku, K., Tanaka, M., Kiuchi, K., Sekiguchi, Y., Shibata, M., & Wanajo, S. 2013, ApJ, 778, L16
Howell, E. J., et al. 2015, PASA, 32, 46
Hu, L., et al. 2017a, GCN, 21883, 1
Hu, L., et al. 2017b, Science Bulletin, 62, 1433
Jin, Z.-P., et al. 2016, NatCo, 7, 128s98
Jones, D. H., et al. 2009, MNRAS, 399, 683
Kaplan, D. L., Murphy, T., Rowlinson, A., Croft, S. D., Wayth, R. B., & Trott, C. M. 2016, PASA, 33, e050
Kaplan, D. L., et al. 2015, ApJ, 814, L25
Kaplan, D., et al. 2017a, GCN, 21574, 1
Kaplan, D., et al. 2017b, GCN, 21637, 1
Kaplan, D., et al. 2017c, GCN, 21927, 1
Kasen, D., Fernández, R., & Metzger, B. D. 2015, MNRAS, 450, 1777
Kasliwal, M. M., et al. 2017, Science, aap9455
Keane, E. F., et al. 2018, MNRAS, 473, 116
Keith, M. J., et al. 2010, MNRAS, 409, 619
Keller, S. C., et al. 2007, PASA, 24, 1

Kouveliotou, C., Meegan, C. A., Fishman, G. J., Bhat, N. P., Briggs, M. S., Koshut, T. M., Paciesas, W. S., & Pendleton, G. N. 1993, ApJ, 413, L101
Lagage, P. O., et al. 2004, Msngr, 117, 12
Lenzen, R., et al. 2003, in Proc. SPIE, Vol. 4841, Instrument Design and Performance for Optical/Infrared Ground-based Telescopes, eds. M. Iye & A. F. M. Moorwood (Bellingham: SPIE), 944
Li, L.-X., & Paczyński, B. 1998, ApJ, 507, L59
Lipunov, V. M., et al. 2017a, ApJ, 850, L1
Lipunov, V., et al. 2017b, GCN, 21546, 1
Lorimer, D. R., Bailes, M., McLaughlin, M. A., Narkevic, D. J., & Crawford, F. 2007, Science, 318, 777
Lynch, C., et al. 2017, GCN, 21670, 1
McCully, C., et al. 2017, ApJL, 848, L32
Meade, B., et al. 2017, PASA, 34, 23
Merloni, A., Heinz, S., & di Matteo, T. 2003, MNRAS, 345, 1057
Metzger, B. D. 2017, LRR, 20, 3
Metzger, B. D., Bauswein, A., Goriely, S., & Kasen, D. 2015, MNRAS, 446, 1115
Metzger, B. D., Berger, E., & Margalit, B. 2017, ApJ, 841, 14
Metzger, B. D., et al. 2010, MNRAS, 406, 2650
Möller, A., et al. 2017, GCN, 21542, 1
Murphy, T., et al. 2017, GCN, 21842, 1
Ogando, R. L. C., Maia, M. A. G., Pellegrini, P. S., & da Costa, L. N. 2008, AJ, 135, 2424
Özel, F., & Freire, P. 2016, ARA&A, 54, 401
Paczynski, B. 1986, ApJ, 308, L43
Pan, Y.-C., et al. 2017, ApJ, 848, L30
Perley, D. A., et al. 2009, ApJ, 696, 1871
Plotkin, R. M., Markoff, S., Kelly, B. C., Körding, E., & Anderson, S. F. 2012, MNRAS, 419, 267
Ridden-Harper, R., Tucker, B., Sharp, R., Gilbert, J., & Petkovic, M. 2017, MNRAS, 472, 4521
Roberts, L. F., Kasen, D., Lee, W. H., & Ramirez-Ruiz, E. 2011, ApJ, 736, L21
Rossi, E., Lazzati, D., & Rees, M. J. 2002, MNRAS, 332, 945
Rousset, G., et al. 2003, in Proc. SPIE, Vol. 4839, Adaptive Optical System Technologies II, eds. P. L. Wizinowich, & D. Bonaccini (Bellingham: SPIE), 140
Sadler, E. M., et al. 2017, GCN, 21645, 1
Sari, R., Piran, T., & Halpern, J. P. 1999, ApJL, 519, L17
Sault, R. J., Teuben, P. J., & Wright, M. C. H. 1995, in ASP Conf. Ser., Vol. 77, Astronomical Data Analysis Software and Systems IV, eds. R. A. Shaw, H. E. Payne, & J. J. E. Hayes (San Francisco: ASP), 433
Savchenko, V., et al. 2017a, ApJ, 848, L15
Savchenko, V., et al. 2017b, GCN, 21507, 1
Scalzo, R. A., et al. 2017, PASA, 34, 30
Schlegel, D. J., Finkbeiner, D. P., & Davis, M. 1998, ApJ, 500, 525
Shara, M., et al. 2017, GCN, 21610, 1
Sharp, R., Tucker, B., Ridden-Harper, R., Bloxham, G., & Petkovic, M. 2016, in Proc. SPIE, Vol. 9908, Ground-based and Airborne Instrumentation for Astronomy VI, eds. C. J. Evans, L. Simard, & H. Takami (Bellingham: SPIE), 99080V
Smith, G. A., et al. 2004, in Proc. SPIE, Vol. 5492, Ground-based Instrumentation for Astronomy, eds. A. F. M. Moorwood, & M. Iye (Bellingham: SPIE), 410
Soderberg, A. M., et al. 2006, ApJ, 650, 261
Spitler, L. G., et al. 2016, Nature, 531, 202
Staveley-Smith, L., et al. 1996, PASA, 13, 243
Tanaka, M., & Hotokezaka, K. 2013, ApJ, 775, 113

Tanvir, N. R., Levan, A. J., Fruchter, A. S., Hjorth, J., Hounsell, R. A., Wiersema, K., & Tunnicliffe, R. L. 2013, Nature, 500, 547

Tanvir, N. R., et al. 2017a, ApJ, 848, L27

Tanvir, N. R., et al. 2017b, GCN, 21544, 1

Tingay, S. J., et al. 2013, PASA, 30, 7

Valenti, S., et al. 2017, ApJ, 848, L24

Vohl, D., Pritchard, T., Andreoni, I., Cooke, J., & Meade, B. 2017, PASA, 34, 38

von Kienlin, A., et al. 2017, GCN, 21520, 1

Wolf, C., et al. 2017a, GCN, 21560, 1

Yang, S., et al. 2017, GCN, 21531, 1

Yu, P.-C., et al. 2017, GCN, 21669, 1

Zhang, S., Jin, Z.-P., Wang, Y.-Z., & Wei, D.-M. 2017, ApJ, 835, 73

CO-AUTHORED PAPER 4 – HOW TO BUILD A CONTINENTAL SCALE FIREBALL CAMERA NETWORK

CrossMark

ORIGINAL ARTICLE

How to build a continental scale fireball camera network

Robert M. Howie[1] · **Jonathan Paxman[1]** · **Philip A. Bland[2]** ·
Martin C. Towner[2] · **Martin Cupak[2]** · **Eleanor K. Sansom[2]** ·
Hadrien A. R. Devillepoix[2]

Abstract The expansion of the Australian Desert Fireball Network has been enabled by the development of a new digital fireball observatory based around a consumer digital camera. The observatories are more practical and much more cost effective than previous solutions whilst retaining high imaging performance. This was made possible through a flexible concurrent design approach, a careful focus on design for manufacture and assembly, and by considering installation and maintenance early in the design process. A new timing technique for long exposure fireball observatories was also developed to remove the need for a separate timing subsystem and data integration from multiple instruments. A liquid crystal shutter is used to modulate light transmittance during the long exposure which embeds a timecode into the fireball images for determining fireball arrival times and velocities. Using these observatories, the Desert Fireball Network has expanded to cover approximately 2.5 million square kilometres (around one third of Australia). The observatory and network design has been validated via the recovery of the Murrili Meteorite in South Australia through a systematic search at the end of 2015 and the calculation of a pre-atmospheric entry orbit. This article presents an overview of the design, implementation and performance of the new fireball observatories.

✉ Robert M. Howie
robert.howie@curtin.edu.au

1   Department of Mechanical Engineering, Curtin University, Perth, Australia

2   Department of Applied Geology, Curtin University, Perth, Australia

1 Introduction

Meteorites provide insight into the formation and current state of the solar system, but the value of most of these (more than 50,000 worldwide) is limited because the origin of the sample, the heliocentric orbit, is unknown. The scientific value of samples with known origins is one of the motivations for sample return missions such as Stardust [1] and Hayabusa [2]. Meteorites with a known pre-atmospheric entry orbit determined by a fireball camera network allow us to constrain the origin of the rock in the main asteroid belt, and possibly in some cases, even the specific asteroid parent body. As of mid 2016, only about 29 [3–8] recovered meteorites have orbits determined through fireball camera networks or other observational means.

Fireball camera networks continuously monitor the night sky for fireballs (meteors magnitude -4 or brighter) produced as larger meteoroids enter the Earth's atmosphere at high speeds (tens of kilometres per second). These larger meteoroids are more likely to produce meteorites on the ground instead of completely burning up during the luminous trajectory (bright flight). The bright fireballs produced during the ablation process can be tracked as they move through the atmosphere using optical means. The observed trajectory (consisting of both position and timing data) allows the calculation of the heliocentric orbit of the meteoroid and a fall position estimate of the meteorite. The fall position must be known with sufficient certainty to recover the meteorite via a ground search, and orbital precision must allow meaningful comparison with the orbits of known Solar System bodies. These constraints inform the observational requirements of a fireball camera network.

The Australian Nullarbor plain is an exemplary site for a fireball camera network due to its dark skies, minimal cloud cover, low rainfall, lack of vegetation and pale geology [9]. The light coloured featureless terrain contrasts well with (usually) black recent meteorites for a visual search. The Australian Desert Fireball Network (DFN) aims to cover the Nullarbor and a significant fraction of the entire Australian Outback with fireball cameras in order to produce the first consistent source of meteorites with orbits (delivering multiple meteorites with orbits per year). The original goal was one million square kilometres of coverage [10], but that has since been revised upwards due to the performance of the new observatories exceeding initial expectations. The new goal is to cover as much good meteorite searching terrain as possible in Australia. The network recovered two meteorites with orbits during its initial phase using large format film cameras (see Section 2.5): Bunburra Rockhole, an anomalous basaltic meteorite [11] in 2008, and Mason Gully, an H5 ordinary chondrite [12, 13] in 2010. A third meteorite (Murrili) has now been recovered using the new digital observatories detailed in this work.

Meteorite recovery rates are determined by network coverage area which is limited by the per observatory cost relative to the imaging performance. Reducing this cost to expand the network is the driving motivation behind the development of a new cost effective fireball observatory for the DFN. The fully autonomous digital observatory (Fig. 1) is designed to record high resolution fireball trajectories in the harsh conditions of the remote Australian Outback and is based on commodity off-the-shelf digital imaging and computing hardware to minimise costs.

Fig. 1 Digtal DFN observatory installation at Mt Ive Station in South Australia

2 Fireball camera networks

The first meteor photograph was captured in 1885 [14], and systematic photographic meteor observations have taken place since 1936 [15]. Three large fireball camera networks with the aim of meteorite recovery were constructed in the latter half of the 20th century. The European Fireball Network (originally the Czechoslovak Fireball Network) and the US Prairie Meteorite Network started operations in the mid '60's, and the Canadian Meteorite Observation and Recovery Project (MORP) followed in the early '70's [16]. These networks used large format film based camera systems to achieve the required resolution and sensitivity to image fireballs for orbit determination and meteorite recovery. The observatories typically take one exposure per camera per night; an additional exposure is sometimes started after a bright fireball is detected (depending on network capability) [17].

Estimating fall positions of meteorites from fireball data requires camera networks to capture fireball trajectories with high spatial and temporal precision from multiple geographically distinct locations. The spatial precision of the cameras determines the accuracy of the trajectory path triangulation, and relative timing data is required to determine the velocity and deceleration of the meteoroid for mass estimation [18]. Absolute timing (time of appearance) is also required to calculate the pre-atmospheric entry orbit due to the constant orbital motion and rotation of the Earth. Previous networks have employed different approaches to determining absolute timing, ranging from relying on chance observations of the general public (no timing) to high precision sky brightness loggers [16].

2.1 Czechoslovak fireball network

Ondřejov Observatory has a long history of meteor observation, and commenced double station observations using multiple narrow angle meteor cameras in 1951 [19]. These employed a rotating shutter mounted in front of the objective lens to create periodic breaks (at 68 and 98 breaks per second [20]) in the meteor trails created as the shutter arms pass in front of the objective lens to indicate meteoroid velocity (once observations were triangulated with the secondary station). Since this technique only determines the relative timing (velocity) of the meteors and not the arrival times necessary for orbits, sidereal tracking cameras following the relative motion of the sky throughout the night were added alongside the fixed cameras by 1958 [21]. Meteor arrival times were determined by comparing the unguided (fixed pointing) and sidereal tracking guided images [22]. These meteor cameras captured the fireball that lead to the recovery of the Příbram meteorite fragments in 1959, providing the first recovered meteorite with a known heliocentric orbit [23, 24].

The successful recovery of the Příbram chondrite spurred the creation of the Czechoslovak Fireball network—with the goal of meteorite recovery in addition to the previous objectives of meteor observation, trajectory analysis and orbit determination. This new network started operations with five stations in autumn 1963 [25]. These fireball cameras used a single all-sky camera per station instead of multiple narrow angle cameras used by the meteor photography stations; this reduced the workload for the operators manually initiating the night long exposures. The camera and rotating shutter were mounted above a convex mirror to collect all sky imagery. The rotating shutter in the fireball cameras was driven to produce 12.5 breaks per second—slower than the rate used on the previous meteor cameras. The observatories gathered the data required for trajectory triangulation and fall position estimation (trajectory spatial and relative timing data) but employed no method of determining the arrival times of fireballs; the network originally relied on chance fireball observations by the public for arrival times and therefore orbits. Driven sidereal tracking cameras were added to three of the fireball camera sites at a later date to calculate arrival times in the same method used by the original meteor cameras with an accuracy usually within 5 seconds [22].

2.2 Prairie meteorite network

The US Prairie Meteorite Network was established in 1964 with sixteen stations in the Midwest [26]. Each station consisted of four cameras using repurposed rectilinear large format aerial imaging cameras integrated into small buildings with ancillary instrumentation. The Prairie Network observatories also periodically occulted the fireballs (20 times per second) to allow velocity measurement of triangulated events, but departed from the rotating shutter design of previous fireball and meteor cameras. The Prairie observatories utilised a switching shutter constructed from a bistable electromechanical relay attached to a lightweight blade which oscillated in and out of the optical path in the centre of the lens breaking meteor trail images according to a pre-programmed pattern. The pattern embedded into the fireball trail image recorded

the fireball's arrival time. The system used repeating sequences which limited the timing precision to a 10.4 second window.

The Prairie systems were also equipped with sky photomultiplier tube (PMT) based photometers alongside each camera to extend the capabilities of the observatory. The photometer controlled the film exposure in response to sky brightness during normal operation, and during extremely bright fireball events, it could reduce the lens aperture and insert a neutral density filter to protect the exposure. The photometer also stamped arrival times (more accurately than the switching shutter timecode) of bright meteors by re-illuminating the data chamber (containing the clock) when meteors brighter than magnitude -4 (fireballs) were detected [26]. The Prairie network recovered the Lost City meteorite with an orbit in 1971 [27] and ceased operation in 1975.

2.3 Meteorite observation and recovery project

The Canadian Meteorite Observation and Recovery Project (MORP) was created after a number of Canadian meteorite falls were recovered in the 1960's, stimulating regional interest in the field. The network started routine operation in 1971 and took a similar approach in observatory design to the Prairie Network, with observatories consisting of five rectilinear cameras housed in a purpose built pentagonal building. The cameras used a rotating shutter with a unique three sector design, consisting of one transparent sector and two neutral density sectors (of densities 2.0 and 5.0) designed to image meteors across a large range of brightnesses [17]. Due their unique design, the rotating shutters in the MORP observatories were driven more slowly than previous designs to produce four dashes per second.

The MORP observatories used innovative PMT based meteor detectors for the precise recording of meteor arrival times. In order to detect fireballs, and reject other common bright transients, two concentric perforated cones were mounted over the PMT. A light source moving at typical fireball speeds would produce a signal in a particular frequency range as the light was periodically blocked and admitted through the holes in the interleaved cones. Signals in this frequency range were detected via electronic filtering, and this commanded the observatory to print the time of the meteor event and advance the film after an appropriate delay. The project operated from 1971 to 1985, recovering the Innisfree [17] meteorite with an orbit in 1977 and produced a sizeable fireball dataset [28–30].

2.4 European fireball network

The Czechoslovak network became the European Fireball Network in 1968 when a number of cameras were installed in southern Germany to work in conjunction with the Czechoslovak cameras. This coverage was again expanded in 1988 when the German cameras were redistributed to cover a larger area including Austria, Belgium and Switzerland [31]. The Czechoslovak part of the network has undergone considerable expansion and modernisation since its inception. The cameras have been upgraded multiple times, first, moving from the manual mirror based all sky cameras to manual

large format fisheye lenses providing significantly better precision (angular resolution of approximately one arc minute) and sensitivity. Additional stations with guided cameras for absolute timing were added, and more recently (2003-2008) the manual observatories have been replaced with automated observatories [32]. These contain the same larger format film fisheye imaging configuration but are automated for 32 exposures providing five to seven weeks of autonomous observing, depending on conditions, by way of a magazine equipped film handling system [32]. The cameras monitor observing conditions using precipitation sensors and video camera based star counters. If conditions are favourable, the observatories commence night long exposures and continue to monitor the observing conditions throughout the night (pausing or ending observations as required). The automated observatories are also equipped with PMTs to measure sky brightness during fireball events. The brightness is logged at 500 Hz, (later upgraded to 5000 Hz [7]) producing detailed brightness curves for mass estimation via the photometric method [33]. The automated observatories are networked through a central server and can rapidly alert researchers of the occurrence of bright fireballs. The European Network has recovered a number of meteorites through systematic search campaigns (including Neuschwanstein [34], Košice [35], Žďár nad Sázavou [6] and Stubenberg [6]) and provided orbital or trajectory data for a number of other meteorites found by members of the public in Europe (including Jesenice [36] and Križevci [37]); the network continues to operate to this day. Recently the European Network has also started the transition to digital observatories [6].

2.5 Desert fireball network — initial phase

The excellent searching terrain in the Australian Nullarbor was the motivation for the development of the Australian Desert Fireball Network; the initial phase was conducted using four fireball observatories [10] based on the automated Czech design [32]. The design was modified to deal with the extreme heat of the Australian Outback with the addition of side panels and a retractable sunshield to shade the system during the day, a modified thermal management system, and special high reflectance paint to minimise solar heating. The solar powered observatories were installed on pastoral stations, network connectivity was provided by geostationary satellite data links, and the generous volunteer hosts changed the film magazines as required.

The initial DFN observatories track fireballs well, but are expensive, difficult to install and costly to run and maintain; the £60,000 120kg observatories (Fig. 2) required a truck and three days of work by a small team to install. The systems required monthly film magazine changes were powered by eighteen 80 Watt solar panels. Storage was provided by a small shed of flooded lead acid batteries. Maintenance was complicated by the size and weight of the observatory.

The initial phase of the DFN commenced routine operation in 2005 and produced two meteorites with orbits: Bunburra Rockhole [11, 38] in 2008 and Mason Gully [12, 13] in 2010. This proved the viability of a fireball camera network based in the Australian Outback and laid the groundwork for the expanded digital DFN. Operation of the initial film based observatories ceased in 2015 once the expanded digital network using the observatories described in this work commenced operations.

Fig. 2 DFN large format film based observatory — used in initial phase, prototype digital observatory visible in background

One aspect common to all of the custom engineered observatories used by these previous networks is their high cost and complexity. It would be cost prohibitive and impractical (due to the maintenance requirements) to cover an extremely large area like the Australian Outback with these designs. A substantial reduction in observatory cost and complexity whilst retaining high imaging performance was required to meet the DFN coverage goals.

3 The need for a more practical and cost effective photographic fireball observatory

The meteorite recovery rate of a fireball camera network depends on the size of the coverage area and nature of the meteorite searching terrain. The southern half of the Australian Outback, and the Nullarbor in particular, is excellent terrain for meteorite recovery, so the primary factor influencing the number of meteorite recoveries is the observational capability of the DFN. With nearly ideal night time observing conditions in this region due to low light pollution and minimal cloud cover to interrupt observations, this capability is primarily dependant upon the double station (triangulable) coverage area.

Network coverage depends on the number and spacing of observatory stations which is constrained by observatory imaging capabilities and the logistics of installation and maintenance. The number of stations is directly determined by the costs

and maintenance requirements of the fireball camera design. The ideal fireball observatory has a low upfront cost, low ongoing costs, simple installation, infrequent and minimal maintenance and high imaging performance.

Two types of fireball networks exist today: video networks and long exposure photographic networks. Video networks (such as the Southern Ontario All-sky Meteor Camera Network [39], the Slovak Video Meteor Network [40], the Finnish Fireball Network [41], and the French FRIPON network [42]) use analogue or digital video cameras to record meteor trajectories at a high frame rate (usually around 30 frames per second) but at low resolutions (0.3-1 megapixel (MP)). Photographic networks (such as those previously mentioned in Section 2 or the Tajikistan Fireball Network [43]) capture long exposure fireball photographs using high resolution (20+ MP digital or large format film) cameras to record meteor trajectories in a long exposure. The exposures can be up to a few hours in length, so these networks also utilise at least one method of determining meteor arrival times within the long exposure (see Section 4.3).

The video based approach has become popular in recent years due to the increased availability and affordability of sensitive video cameras. Observatories can be constructed from widely available off-the-shelf hardware and software, and the per station cost is low, making them an attractive approach for amateur and collaborative networks. Sensitive video cameras are well suited for recording meteor trajectories to determine geophysical properties by examining ablation and fragmentation and for characterising meteoroid flux and orbital population distributions. However, low resolution cameras do not, generally, record trajectories with sufficient precision to refine fall position distributions to the point where meteorites can be reliably recovered through systematic search campaigns at specific locations (with the exception of more advanced multi camera systems such as [44]). All sky video networks do indicate the general region where meteorites may fall, and these are sometimes then recovered by the public (*cf.* [36, 45, 46]).Video networks also offer limited orbital precision (due to the spatial precision of trajectory observations) which can make matching sporadic fireballs (those not part of a known meteor stream) to parent bodies with high confidence more difficult.

Much higher resolution photographic cameras do offer the spatial precision required to determine fall positions with sufficient accuracy to reliably recover meteorites through systematic search campaigns. Large format film has been traditionally used to achieve spatial precision of approximately one arcminute (limited by film scanning techniques). Long exposure fireball observatories are more complex due to the need to periodically occult the exposure for velocity determination and—traditionally—the need for a separate absolute timing system. Digital photographic cameras now offer the necessary resolution, but are expensive and require custom camera control solutions to function as fireball cameras. For these reasons, the design and construction of high resolution long exposure fireball observatories have typically been out of reach for amateur and collaborative networks.

Reaching the DFN's original goals would be difficult using previous high precision fireball observatories. Modern digital still cameras present an opportunity to develop a smaller, lighter, more power efficient and less costly fireball observatory.

This type of design, constructed around a high resolution consumer digital camera and off-the-shelf components, could satisfy the operational requirements and be constructed for a much lower cost than previously possible.

4 The new automated digital fireball observatory

4.1 Requirements

The main design goals of the new Desert Fireball Network observatory are sufficient spatial and temporal precision to enable meteorite recovery by small teams on foot; the ability to operate reliably and unattended in the Australian Outback for long periods; compatibility with an automated data reduction pipeline; low per-system costs relative to the imaging performance; and simple, fast and inexpensive manufacture, assembly and deployment.

The observatories must be capable of withstanding the extremes of the Australian Outback including temperatures over 50 °C, wind gusts carrying sand and dust in excess of 100 km/hr, thunderstorms bringing occasional torrential rain, and must operate unattended for long periods between servicing and data download visits (ideally at least one year). This requires a robust design with the capability to recover from minor malfunctions such as software or subsystem crashes. Connectivity to enable remote access for administration, troubleshooting and fireball event data download is also desirable.

Small teams on foot in the Outback can cover 2-6 km^2 per week depending on the terrain; trips are usually limited to to around two weeks and 5-12 people due to logistical constraints. This drives the spatial and temporal precision requirements of the network. In order to reduce the uncertainty of the fall position estimate to the point where recovery within these constraints is probable, the trajectory triangulation should be accurate to ±100 metres (triangulation final vector should be accurate to ± 0.05 degrees) and the mass estimation should be within one order of magnitude. Absolute temporal precision should be 0.01 seconds or better in order to obtain accurate pre-atmospheric entry orbits, enable independent point by point triangulation along the trajectory and allow straightforward alignment with measurements taken by any other instruments. Relative timing precision (for velocity determination and mass estimation) must be significantly more precise.

Camera spacing influences the choice of imaging system; around 100-150 km between sites is a good compromise between coverage density and servicing effort, and suits the spacing of availably installation sites (mostly pastoral stations) in the Outback. A high resolution imaging system is required in order to meet the trajectory precision requirements at this spacing; 36 MP image sensors are readily available in consumer digital cameras and exceed this requirement (even when used with all sky lenses).

In order to deploy a continental scale network, the upfront and ongoing per station costs must be minimised relative to the imaging performance. The upfront costs include materials, manufacturing, assembly and installation while the ongoing costs include maintenance and data connection costs. The move to digital imaging yields

both cost reductions compared to film based systems and an automated data reduction capability. The cost and capability of digital imaging has greatly improved in the last decade to the point where commodity consumer cameras have the resolution and sensitivity required to capture fireball imagery with enough precision to produce orbits and recover meteorites. Basing the observatory around off-the-shelf components where possible enables significant cost reductions compared to the highly customised approach of previous observatories.

It is not possible to manually process the large volume of fireball events generated by a continental scale network. To process the huge amount of data generated, the new observatories must be compatible with an automated data reduction pipeline. Consumer digital cameras integrate well into this approach because they allow automatic data download to a computer in a readily accessible format.

The size, weight and power draw of the observatories needed to be reduced compared to previous designs in order to make deployment and observatory maintenance fast and simple. On site maintenance is difficult in the Outback due to the dusty and sometimes harsh conditions. Ideally, the observatory would be small and light enough for spares to be carried on servicing trips. This would allow the observatories to be exchanged in the field and serviced in the lab (for more serious problems), allowing simpler and more time efficient network maintenance.

4.2 Concept design

The proven approach of a long exposure fireball camera with an optical occulter was selected to satisfy the design requirements but implemented with a high resolution digital camera instead of large format film. The long exposures would be limited to around 30 seconds (instead of an entire night) to prevent star trails that hamper lens calibration and astrometry. These 30 second exposures would be collected continuously throughout the night during good observing conditions. A mechanical shutter, of the rotating or switching type, was eliminated early in the design process to reduce the number of expensive and failure prone precision mechanical components. A number of different electro-optic modulators, or shutters, were tested for suitability, and a LC-Tec X-FOS liquid crystal (LC) shutter was selected for it's ease of implementation, proven reliability and long lifetime (http://www.lc-tec.se/products/fast-optical-shutters/). (Liquid crystal displays have been operating in consumer devices for decades.) The LC shutter is driven via a microcontroller through an H-bridge driver. The microcontroller also triggers the camera exposures via the camera's remote release port. The operation of the microcontroller is tightly synchronised with highly precise global navigation satellite service (GNSS) time through a GNSS receiver module. The long exposure images captured by the camera throughout the night are downloaded via an embedded PC using the camera's USB connection; see Fig. 3 for system topology. Images are then automatically analysed by the computer for fireball events before being moved from the solid state drive to the archival disk drives. As a part of the event detection, the observatories communicate with the network's central server via an Internet connection (where available) to corroborate potential fireball events with a preliminary approximate triangulation excluding single station false positives.
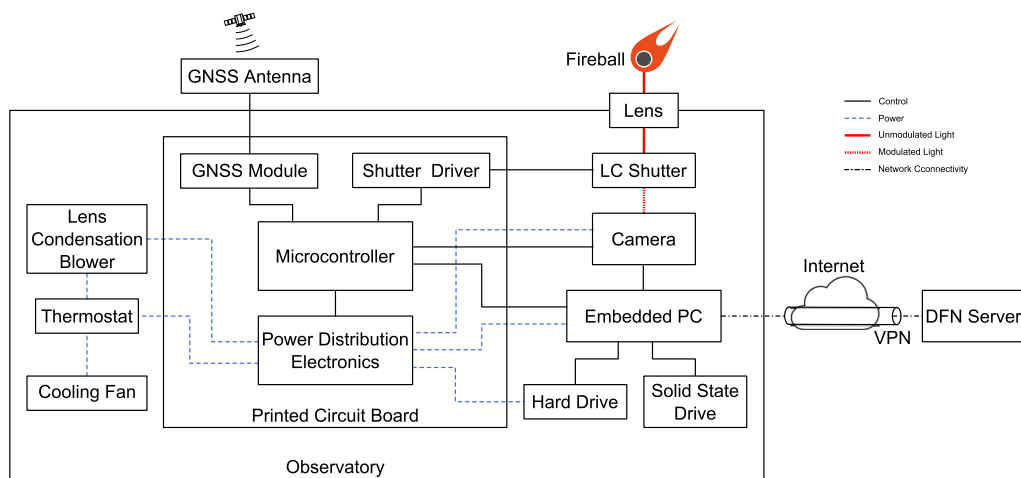
Fig. 3 Digital Desert Fireball Network observatory block diagram showing data and power connections

Rapid development of the fireball observatory was prioritised to get the digital network operational as quickly as possible. A number of cameras and all-sky lenses were tested for suitability. The Samyang 8mm f/3.5 UMC Fish-eye CS II was selected due to the favourable (stereographic) projection and acceptable image quality. The Nikon D800E (later replaced with the D810) digital single lens reflex camera (DSLR) was selected for its weather resistance, high resolution and good noise performance, as well as the ability to control it from a Linux computer via gPhoto2 (http://gphoto.sourceforge.net/). In order to determine the viability of a fireball observatory based around an off-the-shelf consumer camera, four prototypes were rapidly built and deployed for the 2012/13 summer to test the durability of the DSLRs in the hot Australian climate.

The decision to archive all images (instead of only fireball images) was made early in the concept design phase. This eliminated the chance of losing fireball images due to false negatives in the event detection algorithms and allows us to collect a complete wide field optical night sky dataset taken from multiple geographically distinct locations. This dataset is offered to interested researchers for investigation of optical counterparts to radio transients, meteorology, animal behaviour and other fields (contact the authors for access).

To keep the observatory cost low, the primary components (camera, lens, computer, data storage) are commercial off-the-shelf products with small modifications where necessary. The electronics to drive and synchronise the shutter with GNSS time and manage subsystem power are custom designed. The number of moving parts has been minimised to keep costs low and reduce the potential points of failure.

4.3 Fireball timing

A photomultiplier tube is too large and expensive of a solution to fireball timing if the design goals were to be achieved (mostly due to the high voltage power supply required). The flexibility of the microcontroller controlled shutter driver makes

it possible to drive the LC shutter to modulate the exposure according to a pattern or sequence. This can be used to embed a unique timecode into the fireball trail recorded by the camera as it travels across the frame during the (30 s) long exposure. This imprinted sequence shows the arrival time (absolute timing) and the velocity information (relative timing) of the meteoroid allowing the calculation of both a fall position and orbit. The ideal sequence is as long as possible while requiring the smallest part of the sequence to be known in order to identify a unique arrival time for the fireball. A longer sequence permits an extended exposure time, reducing the data rate of the camera and wear on the camera's shutter mechanism. This permits less frequent data download and maintenance visits, reducing operating demands and cost. It is desirable to be able to decode the timing from a short part of the sequence because short meteors are more abundant, and statistical analysis of meteoroid populations is another objective of the DFN.

The sequence that optimally satisfies these requirements is a De Bruijn sequence, defined as the shortest possible sequence containing all possible *n*-element subsequences [47–49]. The microcontroller is precisely synchronised with UTC time via a GNSS receiver to maintain timing precision. The technique eliminates the separate absolute timing subsystem required by most previous designs, reducing, size complexity, and cost. It is the main innovation allowing the new DFN digital fireball observatories to be so compact and cost effective; the approach is detailed in Howie et al. [50]. The Prairie Meteorite Network film cameras also used coded operation of the (mechanical) shutter to record fireball arrival times directly into the fireball image (on film), but this time was only known to within a 10.4 second window which doesn't meet the timing precision requirements of the DFN. For more accurate times the Prairie Network systems depended on the same complex and expensive PMT used in other designs, and this was limited to only bright meteors (fireballs, magnitude -4 and brighter).

The De Bruijn sequence technique used in the DFN observatories encodes absolute and relative timing for all meteors and fireballs that are clearly imaged by the cameras; The absolute timing precision is better than one millisecond and the relative timing is significantly more precise.

Figure 4 shows a good meteorite dropping fireball candidate (DN141129_01) with clearly visible time encoding as observed from the Perenjori DFN station.

The absolute timing precision allows independent triangulation of the fireball data points (two per dash, twenty per second) along the trajectory. This three dimensional point by point triangulation method eschews the straight line assumption used in the traditional methods (intersection of planes [51], least-squares [52] and multiparameter fit [53]).

4.4 Observatory design

In order to rapidly develop the digital fireball observatory, we adopted a concurrent engineering design approach, prototyping early and often. This allowed us to quickly prove the viability of a digital fireball observatory based around commodity imaging hardware and discover the key areas of difficulty early on in the design process.
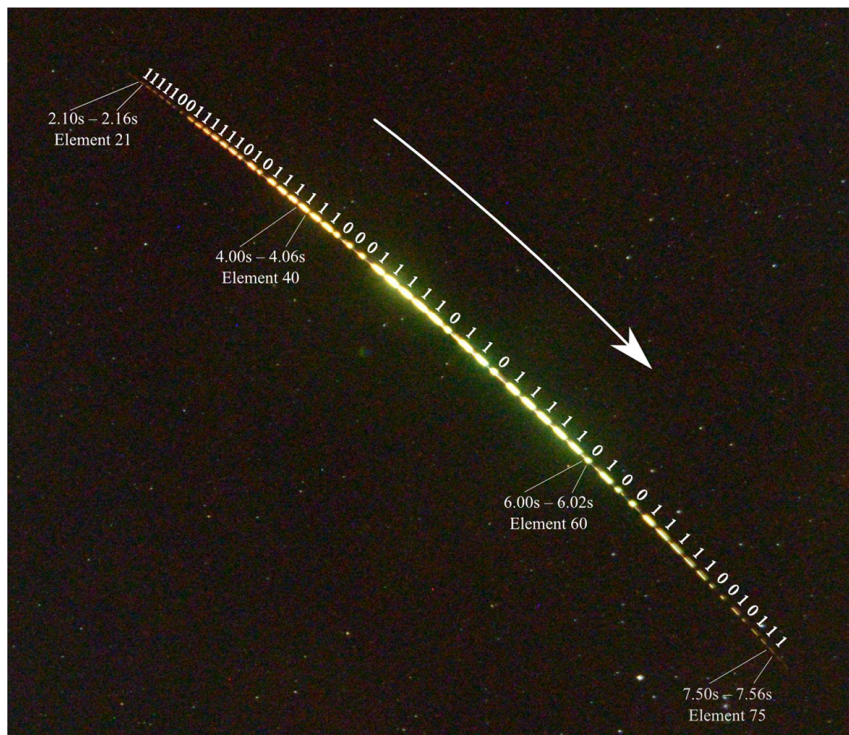
Fig. 4 Enlarged view of DFN fireball event DN141129_01 with de Bruijn sequence time encoding clearly visible. Times relative to exposure start time at 14:31:30 UTC on 29 November 2014

Discovering these problems early on significantly accelerated the design process, and ensured design effort was targeted towards the aspects of the observatory that most required it. Areas where this additional effort was required included the lens environmental sealing and power supply reliability. Care was taken to devise and test simple and creative solutions to design challenges adding minimal cost and complexity before implementing more complex solutions. For example, instead of developing a mechanised lens cover, an inexpensive hydrophobic surface treatment was successfully tested on the prototypes to allow self cleaning of accumulated dust on the lenses during rainfall.

The observatory was designed with manufacture, assembly and maintenance in mind. The number of manual manufacturing steps had to be minimised to construct the significant number of observatories (more than 75) without contracting out the manufacture. This was achieved by modelling the design in a 3D computer aided design (CAD) package and then using affordable and flexible computer aided manufacturing (CAM) techniques including computer numeric control (CNC) laser cutting, CNC water jet cutting, 3D printing and CNC turning for the majority of the manufacturing operations. This computer aided approach allowed us to minimise the number of design revisions by examining the fit and alignment of components in the computer model without waiting for the manufacture of prototype components. Most of the (few) manufacturing steps were performed with these flexible and cost effective manufacturing processes (with minimal or no tooling cost) using the CAD

model geometry directly resulting in short lead times. This made rapid design iterations and the short development time possible. Minimal manufacturing processes were performed in-house; the majority of in-house work was semi-skilled assembly performed by casual workers on an as needed basis. This flexibility allowed us to easily respond to design variations and respond to the changing demand as the network roll-out progressed.

Off-the-shelf components were used wherever possible, resulting in significant reductions in up front costs compared to previous fireball observatories (by a factor of about 12). Care was taken to keep the design modular to simplify field and lab based maintenance. The various subassemblies are interconnected using pluggable connectors and, for the most part, can be removed and replaced without removing or disassembling the adjacent subassemblies.

The first observatory prototypes proved the reliability of the selected DSLR and LC shutter in the harsh conditions of the Australian summer as well as the operation of the De Bruijn encoding; the design was revised a number of times adding functionality and refining the existing systems. Care was taken whilst refining the design to ensure complexity was minimised.

The initial observatory prototypes contained a fisheye lens, LC shutter, camera, low powered PC with a system drive, power supplies and a basic circuit with the GNNS module, microcontroller, and shutter driver. The four prototypes were installed at the original film observatory sites (which were still operating at the time). Data was stored on a small dual 3.5 inch drive network attached storage (NAS) device located in the film camera's battery shed and connected via Ethernet. These prototypes successfully proved the concept, and underwent two major revisions to produce the final design: Figs. 5 and 6.

The first major revision added a video camera to provide additional imagery of the fireballs—especially of fragmentation events, increased computing power for image processing, moved the data storage inside the observatory enclosure and integrated more flexible power management.

Lens condensation blowers for the main and video lenses were added to prevent condensation obscuring the images when the temperature of the glass front elements dropped below the dewpoint at night. The design works particularly well because the airflow cools the internal components and then transfers heat to the lenses, reliably defogging them with minimal power usage (compared to lens heaters). Subsystem power management is controlled by the microcontroller and directed via the PC for a flexible system making fine grained power management possible. The subsystems can be powered on and off as required; allowing the solar powered observatory to achieve the desired low power usage. Figure 3 shows the power and control connections between the different observatory subsystems.

The archival data storage consists of two 3.5 inch hard drives (WD Red models with an extended operating temperature range) in a dual drive enclosure connected via USB. Over time the total capacity has increased as larger drives (6 and 8 TB) have become available.

A small number of these second revision prototypes were constructed, and, after testing, the PCB was re-implemented with surface mount components to accelerate production and save board space. A serial level converter was added to allow the PC
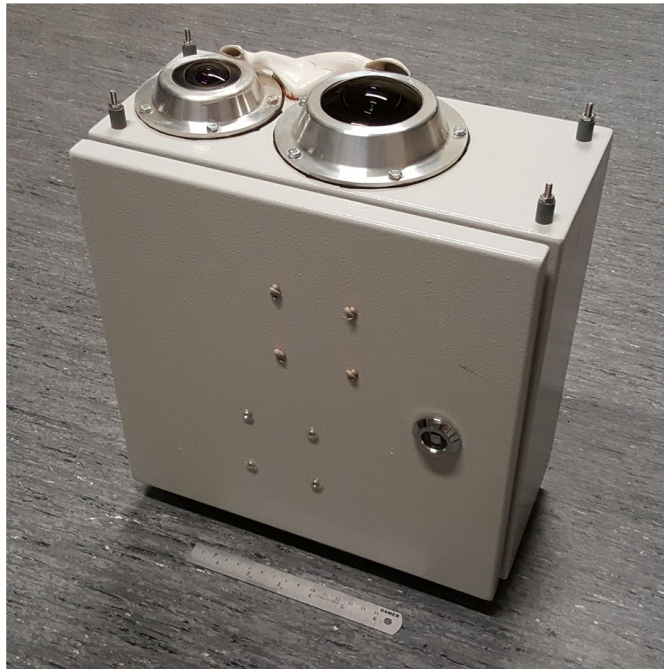
Fig. 5 The exterior of the fireball observatory showing the door, lenses, outer blower ducting and sunshield mounting bolts with a 15 cm ruler for scale

to also receive accurate time information from the GNSS module, and the self reset functionality was also slightly modified. The design as a whole has not changed since this revision, but minor changes have been made to the self reset circuitry and some modifications have been made for production reasons (e.g.: swapping IC packages for more reliable reflow soldering).

The the other components in the observatory have evolved a little over the three years the design has been in use. The camera was upgraded to the Nikon D810 when it was released due to the slightly increased performance and lower cost compared to the D800E. The embedded PC was upgraded to a Commell LE-37D model equipped with USB 3.0 enabling faster image download from the camera, a wider input voltage range, more powerful CPU, additional expansion ports, and a more reliable power connector. The initial observatories had some reliability issues due to power supply problems, but these were eliminated by the PC upgrade, swapping to higher rated solar charge regulators and swapping the DC-DC converter regulating the power to the PC and hard disk drives (HDDs) to a more capable model with a wider input voltage range. The modular design of the observatory allowed most of these changes to be easily retrofitted to the existing systems in the field.

5 Notable design aspects

The observatory has a number of notable features and inventive solutions to problems encountered.

Fig. 6 Fireball observatory internals. Showing (clockwise from top left): video camera and lens, blower ducting, camera and lens (LC shutter inside), embedded PC, observatory management PCB (microcontroller, GNSS module), hard drive enclosure

5.1 3D printed blower ducting

Directing airflow from the lens blower mounted inside the box over the lenses to remove condensation during the night was a significant challenge due to the tight space constraints. A two piece duct was designed in software from the geometry and layout of the box, blower and lenses. The duct is a complex organic shape designed to direct the airflow evenly over the two lenses without sharp turns and provide multiple drain locations for any accumulated water. The part was designed in CAD (see Fig. 7a) and produced on two different 3D printers. This allowed the production of the complicated shape without the significant tooling expense of injection moulding. A simple coat of paint provides UV resistance to the printed plastic part. The final blower and ducting assembly is shown in Fig. 7b.

5.2 Lasercut interlocking stand

Installation of the film observatories was a laborious, time consuming and expensive three day exercise requiring a truck, a large team and pouring of a concrete foundation. A faster and smaller scale installation procedure was required for the rapid deployment of the digital DFN; a semi-permanent support structure would allow this faster deployment and uncomplicated camera relocations if required. The semi-permanent nature of the installation, leaving little to no trace after removal, allowed simpler negotiation of installation sites enabling rapid network deployment.

Fig. 7 Lens condensation blower and ducting. **a** The CAD design showing the complex ducting geometry. **b** The manufactured ducting assembly removed from the observatory with the blower

The stand (Fig. 8) is constructed from interlocking laser cut steel plate which is cut to order with low lead times and machining costs. The interlocking plates fit together like a three dimensional jigsaw puzzle and are affixed with inexpensive steel wedges hammered into specially design slots in the interlocking tabs. This design packs flat and allows rapid installation in approximately thirty minutes. Torsional stability is provided by tensioned wire stays visible in Fig. 1.

5.3 Weather sealed lens flanges and hydrophobic coating

To weatherproof the lenses against the infrequent but sometimes torrential rain, they are sealed into custom designed Aluminium flanges (clearly visible in Fig. 5). The flanges also support the lenses and attached cameras. The flange meets the glass front element of the lens with a thin metal protrusion which is bonded to the glass with a small amount of precisely applied waterproof and flexible silicone sealant. The weather sealing on a few flanges failed initially; the sealant application procedure was modified and no further failures have occurred. The design is versatile and has been adapted to the Samyang 14mm f/2.8 rectilinear and Canon 8-15mm f/4 fisheye zoom lenses for testing and special purpose DFN observatories.

The open flange design does not protect the lens from dust which can lower the contrast and sensitivity of the imaging system. To minimise the accumulation of dirt and ensure water droplets run off the dome shaped front element (instead of evaporating in place leaving a precipitate) the lenses are coated with a consumer hydrophobic surface treatment. This is intended to make the lenses self cleaning; accumulated dust and dirt should be cleaned off when rain droplets bead up and run off the lens. The coating seems to perform as intended, as the lenses remain clean between servicing trips.

Image quality is not affected at all by the flanges making them preferred to protective domes. The weather sealed flanges are also much simpler and less costly than retractable lens covers. They are not susceptible to mechanical or electronic failure helping to increase reliability.
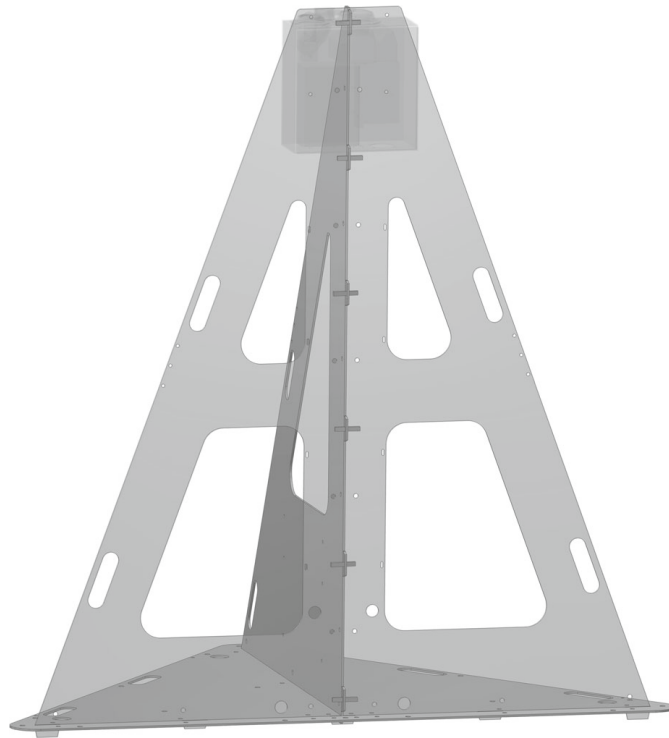
Fig. 8 Stand made from interlocking lasercut steel plates which packs flat and can be assembled on site with steel wedges in about 30 minutes

5.4 Flexible network connectivity

The observatories are networked via an Internet connection where available. This links them to the central server for status reporting and allows event detection to incorporate observations from multiple stations to increase reliability. The observatories support a wide variety of different connection types including: 3G mobile data from two different service providers, Ethernet, WiFi and satellite data. This versatility allows the installation of DFN observatories nearly anywhere, and allows the use of the lowest cost connection on a per-site basis. A virtual private network (VPN) is used to bridge the heterogeneous architecture creating a connection agnostic and seamless network. The majority of the network is connected through 3G mobile data. The connected observatories use a few hundred megabytes of data per month on logs and event detection notifications (which include small image tiles). The observatory is also capable of operating without a network connection; event detection is run on the data from these offline cameras when the hard drives are collected and ingested into the central data store. This mode of operation is used at some remote sites where satellite connections are currently prohibitively expensive.

5.5 Other notable aspects

Some other notable design aspects include the ability to power cycle all of the sub-systems including the cameras, PC, HDD's and microcontroller. This allows recovery

from occasional software glitches including frozen cameras or dropped USB connections. The observatory enclosure is an off-the-shelf steel hinged enclosure CNC water jet cut to accommodate the observatory fittings. This provides a high quality durable enclosure that meets the requirements without the expense and complication of designing and manufacturing a custom enclosure. CNC cutting makes improvements and new prototypes simple to implement by modifying the CAD software design. Enclosure temperature is regulated by a thermostat controlled cooling fan. (Heating is not necessary at the current observatory sites.) A fixed sunshield mounted on top of the observatory reduces solar heating during the day. The shield is mounted below the protruding lenses and does not obscure the field of view.

5.6 Design for manufacture and assembly

Considerable design effort was focused on the ease of assembly of the observatory to make it possible to produce the design quickly and easily in-house. The manufacturing steps are automated from the CAD design, including the laser cutting of the backplane, HDD support, stand and sunshield; the water jet cutting of the enclosure, gasket, and flange rings; the CNC turning of the lens flanges; and the 3d printing of the blower ducting. The observatory is modular and easy to assemble; the in-house assembly is performed in small batches and takes approximately six hours per observatory.

6 Observatory operation

The observatory is controlled by the embedded PC (Commell LE-37D); flexible scripting allows it to adapt to the operational conditions as required including: position, date, time of day, weather and remaining drive capacity. Online observatories regularly file status reports with the central server and relay fireball event detections, so potentially meteorite dropping fireballs can be analysed before HDD collection. Full size images can be downloaded from online cameras for analysis if required. This is only performed for significant potentially meteorite dropping fireball events due to the high data transfer costs of downloading large raw image files.

The PC is connected to the Atmel ATmega32U4 microcontroller via a USB virtual serial connection (using the LUFA library—http://www.fourwalledcubicle.com/LUFA.php) which controls the observatory subsystems. The PC directs operations with high level commands (e.g.: start camera triggering) that are sent to the microcontroller and then implemented at a low level (e.g.: triggering the DSLR every 30 seconds through the remote release port). This approach avoids tying the observatory to a specific embedded PC; any PC with USB connections for the microcontroller, camera and hard drives would be compatible. Subsystems are only powered by the power distribution electronics when required. This results in substantial power savings for the solar powered observatory as many subsystems are only required for a portion of the day or night (e.g.: camera and video camera at night during good observing conditions, hard drives for 30-60 minutes in the morning while data is archived). The operational and exposure parameters are listed in Table 1.

Table 1 Nominal DFN operational parameters

Parameter	Value	Note:
Exposure Period	30 s	time between exposure starts
Exposure Duration	29 s	shutter open time
Deadtime	1 s (out of every 30 s)	time where shutter is not open
Observing Time	8-14 hours per night	depending on latitude and season
Camera	Nikon D810	older systems use D800/D800E
Sensor Size	35.9 x 24.0 mm	35 mm "full frame"
Image Resolution	36 MP (7360 x 4912)	69 % pixel utilisation, see Fig. 14
Bit Depth	14 bits	
Colour Filter	RGGB Bayer array	
Image Size	45 MB	$\approx$45-75 GB per cloudless night
Image Format	Nikon lossless compressed raw	(.NEF)
Embedded PC	Commell LE-37D	Intel Bay Trail based single board computer
Operating System	Debian GNU/Linux	
Camera Control Library	gPhoto2	
ISO Speed	6400	most stations
Lens Aperture Setting	f/4	most stations
Lens	Samyang 8mm F3.5 Fish-eye CS II	Nikon F mount
Lens Projection	stereographic fisheye	
Image Circle	$\approx$28.7 mm	slight crop at top and bottom of image circle
Field of view	180 degrees	5 % of hemisphere area cropped
Limiting Magnitude, Fireballs	$\approx$0.5 stellar magnitude	
Limiting Magnitude, Stars	$\approx$7.5 stellar magnitude	
Optical Modulator	LC-Tec X-FOS LC Shutter	twisted nematic type liquid crystal shutter
Open state transmittance	36%	
Closed state transmittance	0.1%	
Shutter Operation	de Bruijn time-code	
Shutter Rate	10 dashes per second, $t_e = 100$ ms	10 elements per second sequence rate
Data Point Rate	20 data points per second	dash starts and ends
Particular Sequence	prefer high de Bruijn sequence	$k = 2$ (binary), $n = 9$ (subsequence length)
Encoding	pulse width	$t_0 = 20$ ms, $t_1 = 60$ ms (dash length)

Observations are automatically controlled by local sunset and sunrise times at each site depending on season and location; observations start and stop when the Sun is six degrees below the horizon. Each exposure is modulated by the LC shutter between the lens and the image sensor to encode the arrival time of any fireballs.

The microcontroller precisely synchronises the start and end of the exposure as well as the modulation of the LC shutter with GNSS time to ensure sub-millisecond timing precision. Images are captured in the Nikon raw format. Every fifteen minutes, an image is analysed to determine the quality of observing conditions. Which are quantified using a star counting algorithm comparing the count to a dynamically adjusted threshold that compensates for the presence of the Moon and other bright light sources within the image. Observations are paused in poor conditions to save storage space and shutter actuations (wear on the camera). Analysis of the observing conditions continues at 15 minute intervals, and normal operation is resumed if conditions improve.

The video camera operates at night in parallel with the still camera. One minute segments are saved to the SSD throughout the night and retained on the HDDs where a corresponding event is detected in the still images. The operational parameters for the video camera are shown in Table 2. The video camera observations are not currently incorporated into the automated data pipeline. Expanded video capabilities, including photometry, will be incorporated into the data pipeline in the future.

In the morning, still images are downloaded from the camera's CF card over the USB connection using gPhoto2 and stored on a solid state drive (SSD). Custom automated event detection software then searches the sequence of images for meteor events which are then relayed back to the central server (for online cameras). The server attempts to corroborate the events across multiple observatories by performing a rough triangulation which eliminates most false positives: satellites, aircraft, stray lights. Data is periodically archived from the SSD to the larger HDDs to be collected during servicing and then ingested into the central data store.

When a significant fireball event is detected, the images are processed through the centralised data pipeline—Fig. 9.

Table 2 Nominal DFN video camera operational parameters

Parameter	Value	Note:
Video camera	Watec WAT-902H2 CCIR ULTIMATE	some older systems using EIA equivalent
Video camera resolution	795 x 582	
Colour Filter	none	panchromatic camera
Bit depth	8 bit, YUV colourspace	
Frame rate	25 fps, interlaced	
Exposure time	1/50 s	
Gain control	auto gain	
Capture card	Commell MPX-885	
Compression	H264 variable bit rate	FFmpeg "ultrafast" preset
Nominal bit rate	$\approx$ 27 Mbps	
Lens	Fujinon FE185C046HA-1	1/2" format 5 MP 185 degree fisheye
Lens aperture setting	f/1.4	
Limiting magnitude	$\approx$2 stellar magnitude	(fireballs and stars)
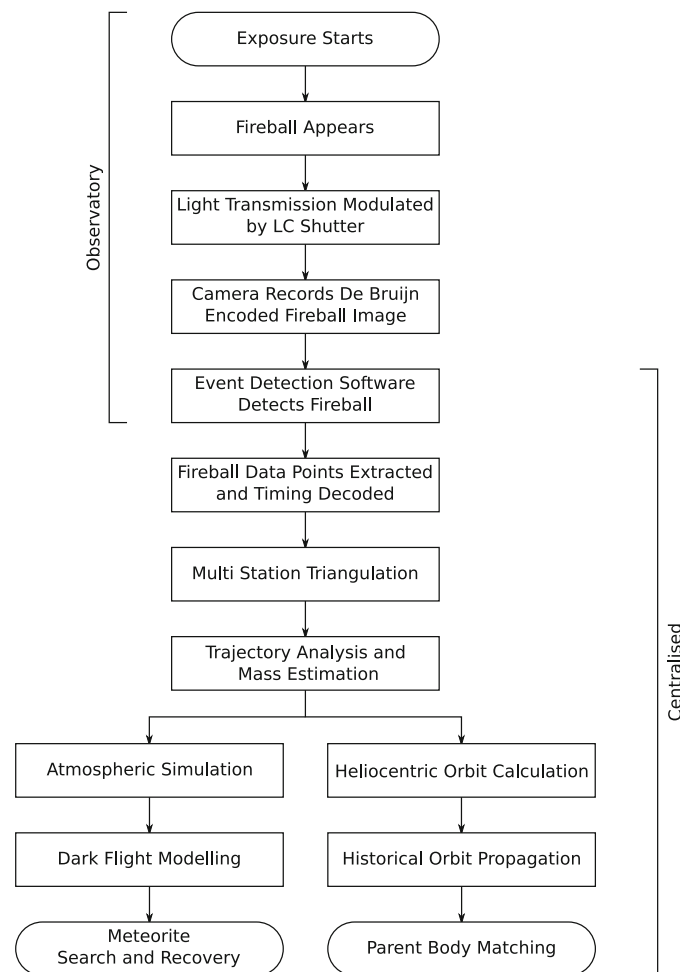
Fig. 9 Stages in the data processing pipeline for a fireball event

7 Data pipeline

When a promising fireball event is flagged by the event detection, the relevant images are downloaded from the cameras or recalled from the data store. Event metadata is tracked throughout the entire pipeline. First, pixel coordinates are selected with timing from the fireball dashes; this is performed manually with a workflow optimised custom software tool (Fig. 10) allowing the points to be selected quickly and reviewed or edited if required. This process takes approximately five minutes per image on average. The luminous trajectory is triangulated using these points and the camera calibration data which characterises the relationship between each observatory's pixel coordinates and the corresponding altitude and azimuth coordinates from each site. This relationship is dependant on the all-sky lens projection, atmospheric refraction, lens distortion (intrinsic parameters) and camera orientation (extrinsic parameters). Calibration is determined by analysing the starfield as imaged by the DLSR. Visible stars are matched to a catalogue iteratively from the centre of the image until the entire field of view is described by a polynomial fit.
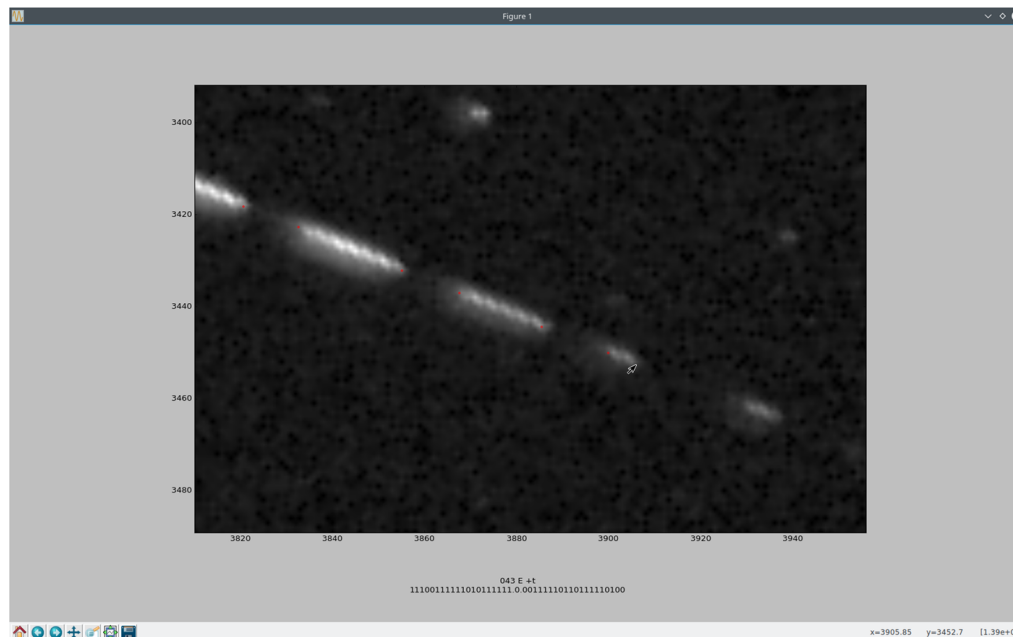
Fig. 10 Fireball data point extraction tool. Times for the data points (in *red*) are automatically calculated from the corresponding de Bruijn sequence element. A partial preview of the sequence, as well as the currently selected element, is displayed to the user at the bottom of the window

Triangulation is currently performed using the least-squares method [52] which makes a straight line assumption, but we are currently developing a independent point by point three dimensional triangulation method that doesn't rely on this assumption. This is only possible due to the absolute timing precision of the observations that is maintained by the GNSS synchronised operation.

The triangulated trajectory is analysed using the dynamic method as described by [18], which uses the observations to estimate meteoroid position, velocity and mass. This method calculates the likely errors based on the uncertainties of the observations and the single body dynamic model. This approach is advantageous because these uncertainties, and in particular the uncertainty of the final mass, can then be factored into the dark flight modelling and incorporated into search and recovery decisions.

The final vector and mass distribution is used to model the dark flight of the meteoroid once it has decelerated to the point where ablation ceases and it is no longer visible to the camera network. The first step of this process is high resolution (3km grid) WRF ARW (http://www.wrf-model.org/index.php) atmospheric modelling of the relevant volume initialised from a regional model incorporating local ground and weather balloon flight data. The fall position distribution is determined by simulation of meteoroid motion through this volume (dark flight) using the Monte Carlo method to incorporate uncertainties (mostly in the mass, final velocity, and the atmospheric model). This fall position distribution is then used to plan the search and recovery of the single meteorite or multiple meteorite fragments. The ideal fireball has a long visible trajectory at a steep angle, a slow final velocity at a low altitude, a final mass estimate of one kilogram or more and a search area in accessible featureless terrain with a stable hard surface [54–56].

The heliocentric meteoroid orbit is calculated from the initial atmospheric entry vector refined in the trajectory analysis using an numerical propagation technique, which can then be back propagated (in time) and possibly matched to a parent body or asteroid family. Where a link can be made and a meteorite recovered, the sample—now of known origin—can be analysed with the proper context; which may, in turn, contribute to new understanding about the formation and current state of the Solar System.

The data processing pipeline, in it's current state, is semi-automated; the individual steps (apart from fireball coordinate extraction) are automated but, for now, the process is manually coordinated. Automation of the image analysis for coordinate extraction is a priority. While the problem is not difficult for the ideal case (a fast, unsaturated fireball in the higher resolution central area of the fisheye lens), it is challenging in many real world cases where the fireball is obstructed, slow or toward the edge of the lens. In the long term, all of the steps and the coordination of the pipeline will be fully automated to produce masses, fall positions and orbits from detected events without manual intervention.

8 Performance

The digital fireball observatory has satisfied the design requirements and enabled the rapid deployment of the digital Australian Desert Fireball Network. The observatories are so cost effective and easy to deploy that the coverage goal has been revised upwards to cover as much good searching terrain as possible within Australia—and this is well under way.

The system has proven to be reliable, suitable for harsh Australian conditions, compatible with a (semi-)automated data pipeline, and easy to install and maintain. The observatories successfully operate for long periods between data download and maintenance trips, but the desired goal of one year between download intervals has not been met yet. The cameras fill two 6TB drives after 8-10 months, but some configuration changes are planned to reduce the filesize of the images, by cropping them to just the region of the sensor used by the fisheye lens. This should extend the download interval to approximately one year when combined with drive upgrades (8 TB drives with suitable temperature ratings are now available and in use at some stations).

The spatial precision of the observatories is approximately one arcminute (down to 5 degrees above the horizon) which is similar to the precision of the previous film based observatories. This allows trajectory triangulation to within several tens of metres. Improvements past this point would do little to refine search areas on the ground due to the dark flight (wind profile) and mass uncertainties. The de Bruijn timecode has performed well: absolute timing precision on the trajectory is better than one millisecond and the techniques has even produced good results for visibly fragmented meteors. The spatial and timing precision achieved more than satisfy the requirements for orbits and ground searches.

The observatories can be fully deployed and commissioned in four hours by two people. The observatories are are small (370x300x150 mm) and light (12 kg). This makes it simple to bring spare observatories on maintenance trips; for more serious problems, they can be exchanged in the field and serviced back in the clean laboratory with more capable equipment. Maintenance in the field and in the lab is made easier by the modular construction. Routine maintenance includes inspection, exchanging hard drives, cleaning the lenses, examining the power systems and connections, operations testing, replacement of the outer blower ducting if required and extracting the occasional spider. The periodic replacement of some parts is planned: the DSLR's mechanical focal plane shutter has a limited lifetime; the outer blower ducting usually lasts for one to two years, and lenses are predicted to degrade at some point from UV exposure and dust storms. Nikon rates the D800/D810 as tested to 200,000 shutter actuations; in practise, the cameras seem to last significantly longer than this: very few have failed to date. One D800 has taken more than 890,000 exposures to date and is still operating, but more time is required to determine the average shutter lifetime under observatory conditions. The cameras can be returned to the manufacturer for a focal plane shutter replacement when required.

A graphical summary of the performance and characteristics of the new digital fireball observatory compared to the previous large format film observatories is presented in Fig. 11.
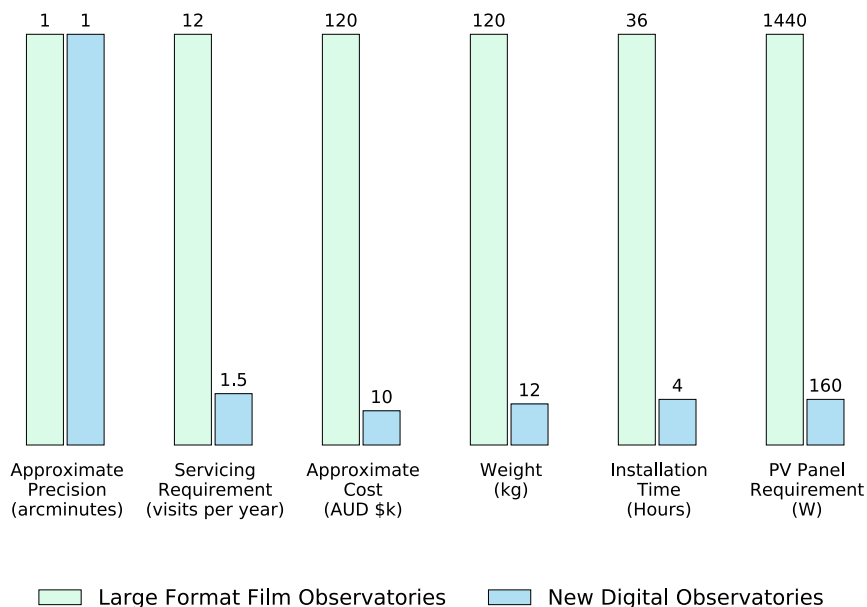
Fig. 11 A comparison of the new digital DFN observatories and the previous film based observatories used in the initial phase

8.1 Network deployment

The first four production observatories were installed in December 2012, and, as of December 2016, the Desert Fireball Network has expanded to 49 stations in three main regions: Western Australia (Wheatbelt and Mid-west), The Nullarbor and South Australia. A new southern Queensland region is also being established. Nominal camera spacing is about 130 km, and the current network coverage (Fig. 12) is ≈2.5 million km^2 (approximate double station coverage — where fireball triangulation is possible), which is roughly one third of Australia.

8.2 First recovery — murrili meteorite

The DFN recovered the Murrili Meteorite at the end of 2015 (Fig. 13) using observations from four of the new digital observatories. This is the third meteorite recovered by the DFN and the first using the new digital network. The 6.1 second fireball (Fig. 14) appeared on 27 November 2015 on a steep trajectory into Kati Thanda—Lake Eyre South in South Australia. The heliocentric orbit has also been calculated, and will be presented in a future publication. The 1.7 kg meteorite was located through a systematic search by a small team of three researchers and excavated from
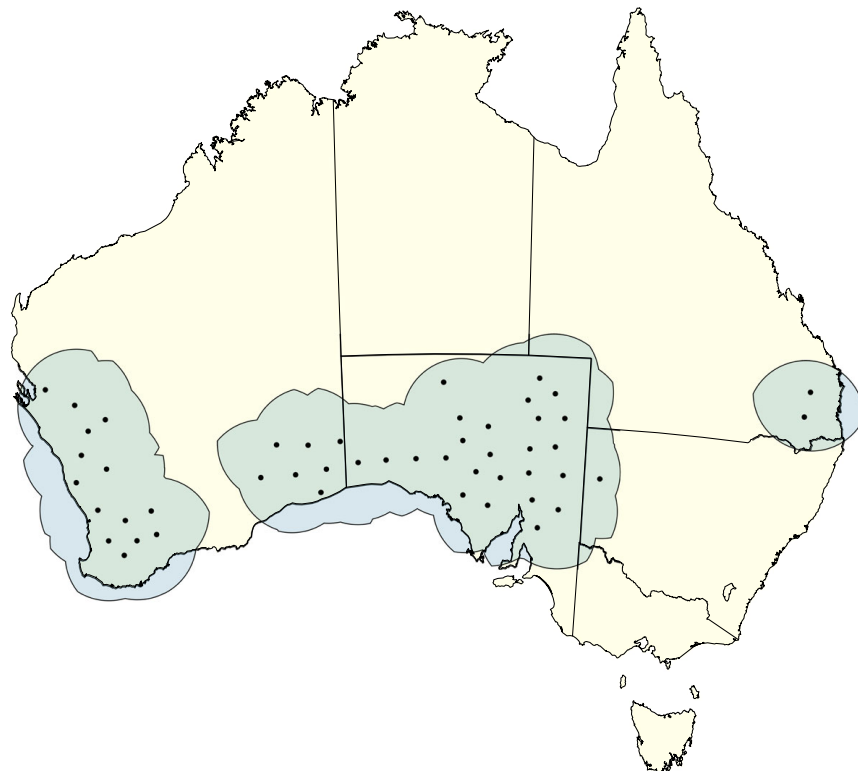
Fig. 12 Current DFN deployment of 49 stations showing approximate double-station coverage (triangulable area)
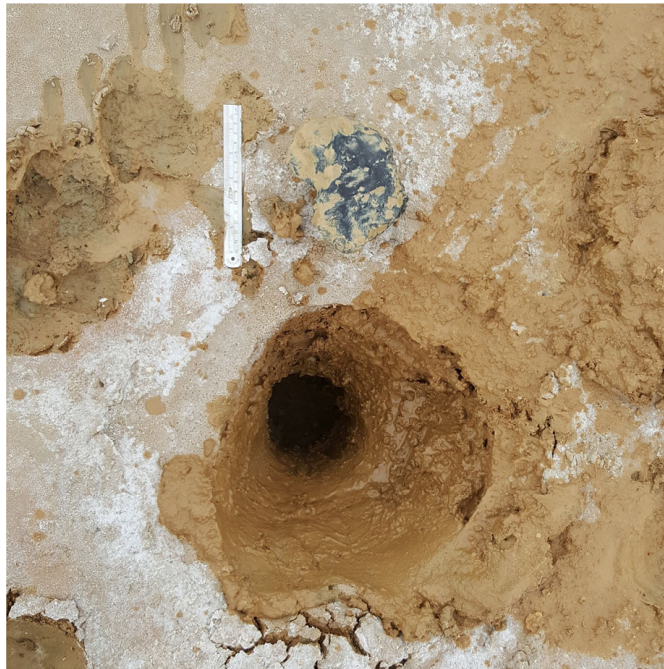
Fig. 13 The Murrilli Meteorite — the first recovered using the new digital DFN observatories

the thick salt lake mud by hand from a depth of 42 cm. The Arabana People, the local indigenous people, assisted with the recovery and naming of the meteorite. This result demonstrates the success of the digital DFN and the viability of the new observatory design.

Fig. 14 The 6.2 second Murrili Meteorite Fireball, 27 November 2015 10:43:44.50 UTC as observed by the Billa Kalina DFN observatory

9 Future work

Network expansion is ongoing in Australia and internationally through partner networks managed by collaborators. A new version of the camera designed for simple rooftop installation at mains powered sites is under development.

The extreme dynamic range of fireball events pose a problem for all imaging systems. The DFN observatories are well suited for imaging the vast majority of meteorite dropping fireballs, but extremely bright superbolides can saturate large areas of the image sensor, obscuring the trajectory and timing. While events like this are rare (a couple per year at the current network size), they are particularly interesting. Work to improve the dynamic range at both ends of the spectrum is currently under way.

The current (dynamic) mass estimation method [18] does not require brightness, so fireball photometry is not regularly performed. As the data processing pipeline is further developed, fireball photometry will be automatically derived from video camera data using local brightness reference stars to be incorporated in future models.

More than a dozen good meteorite dropping fireball candidates have been observed to date. Fieldwork to recover some of these will be conducted in the future.

References

1. Brownlee, D., Tsou, P., Aléon, J., Alexander, C.M., Araki, T., Bajt, S., Baratta, G.A., Bastien, R., Bland, P., Bleuet, P., et al.: Comet 81p/wild 2 under a microscope. Science **314**, 1711–1716 (2006)
2. Yoshikawa, M., Fujiwara, A., Kawaguchi, J.: Hayabusa and its adventure around the tiny asteroid Itokawa. Highlights Astron. **14**, 323–324 (2007)
3. Borovička, J., Spurný, P., Brown, P.: Small near-Earth asteroids as a source of meteorites, others, Asteroids IV, University of Arizona, Tucson, pp. 257–280 (2015)
4. Trigo-Rodriguez, J.M., Lyytinen, E., Gritsevich, M., Moreno-Ibáñez, M., Bottke, W.F., Williams, I., Lupovka, V., Dmitriev, V., Kohout, T., Grokhovsky, V.: Orbit and dynamic origin of the recently recovered annama's h5 chondrite. Mon. Not. R. Astron. Soc. **449**, 2119–2127 (2015)
5. Meteoritical Society, Creston (2015)
6. Spurný, P., Borovička, J., Haloda, J., Shrbený, L., Heinlein, D.: Two Very Precisely Instrumentally Documented Meteorite Falls: Žďar nad Sázavou and Stubenberg-Prediction and Reality. LPI Contrib. **1921** (2016)
7. Spurný, P., Borovička, J., Baumgarten, G., Haack, H., Heinlein, D., Sørensen, A.: Atmospheric trajectory and heliocentric orbit of the Ejby meteorite fall in Denmark on February 6, 2016 Planetary and Space Science (2016)
8. Bland, P., Towner, M., Sansom, E., Devillepoix, H., Howie, R., Paxman, J., Cupak, M., Benedix, G., Cox, M., Jansen-Sturgeon, T., et al.: Fall and recovery of the murrili meteorite, and an update on the desert fireball network. LPI Contributions **1921** (2016)
9. Bevan, A., Binns, R.: Meteorites from the Nullarbor Region, Western Australia: I. A review of past recoveries and a procedure for naming new finds. Meteoritics **24**, 127–133 (1989)

10. Bland, P., Spurný, P., Bevan, A., Howard, K., Towner, M., Benedix, G., Greenwood, R., Shrbený, L., Franchi, I., Deacon, G., et al.: The Australian Desert Fireball Network: a new era for planetary science. Aust. J. Earth Sci. **59**, 177–187 (2012)

11. Bland, P.A., Spurný, P., Towner, M.C., Bevan, A.W., Singleton, A.T., Bottke, W.F., Greenwood, R.C., Chesley, S.R., Shrbený, L., Borovička, J., et al.: An anomalous basaltic meteorite from the innermost main belt. Science **325**, 1525–1527 (2009)

12. Towner, M., Bland, P., Spurný, P., Benedix, G., Dyl, K., Greenwood, R., Gibson, J., Franchi, I., Shrbený, L., Bevan, A., et al.: Mason Gully: The second meteorite recovered by the Desert Fireball Network. Meteorit. Planet Sci. Suppl. **74**, 5124 (2011)

13. Dyl, K.A., Benedix, G.K., Bland, P.A., Friedrich, J.M., Spurný, P., Towner, M.C., O'Keefe, M.C., Howard, K., Greenwood, R., Macke, R.J., et al.: Characterization of Mason Gully (H5): The second recovered fall from the Desert Fireball Network. Meteorit. Planet. Sci. **51**, 596–613 (2016)

14. Hughes, S.: Catchers of the Light: The Forgotten Lives of the Men and Women Who First Photographed the Heavens. Stefan Hughes (2012)

15. Jacchia, L.G., Whipple, F.L.: The Harvard photographic meteor programme. Vistas Astron. **2**, 982–994 (1956)

16. Halliday, I.: Photographic fireball networks. In: Evolutionary and physical properties of meteoroids: The proceedings of the International Astronomical Union's colloquium # 13. held at the State University of New York, Albany, NY. pp. 14–17, 1971, NASA SP, edited by C. Hemenway, P. Millman, A. Cook, and I. A. Union (Scientific and Technical Information Office, National Aeronautics and Space Administration; [for sale by the Supt. of Docs., U.S. Govt. Print. Off.], 1973)

17. Halliday, I., Blackwell, A., Griffin, A.: The Innisfree meteorite and the Canadian camera network. J. Royal Astron. Soc. Can. **72**, 15–39 (1978)

18. Sansom, E.K., Rutten, M.G., Bland, P.A.: Analysing Meteoroid Flights Using Particle Filters, The Astronomical Journal (in press)

19. Ceplecha, Z.: Statistical observations of meteors 1951. Bullet. Astron. Instit. Czechoslovakia **3**, 53 (1952)

20. Ceplecha, Z.: Photographic Geminids 1955. Bullet. Astron. Instit. Czechoslovakia **8**, 51 (1957)

21. Ceplecha, Z., Rajchl, J., Sehnal, L.: Complete data on bright meteor 15761. Bullet. Astron. Instit. Czechoslovakia **10**, 204 (1959)

22. Spurný, P.: Photographic monitoring of fireballs in central europe, in Optical Science, Engineering and Instrumentation'97, pp. 144–155. International Society for Optics and Photonics (1997)

23. Ceplecha, Z., Rajchl, J., Sehnal, L.: New Czechoslovak meteorite "Luhy". Bullet. Astron. Instit. Czechoslovakia **10**, 147 (1959)

24. Ceplecha, Z.: Multiple fall of Přiribram meteorites photographed. 1. Doublestation photographs of the fireball and their relations to the found meteorites. Bullet. Astron. Instit. Czechoslovakia **12**, 21 (1961)

25. Ceplecha, Z., Rajchl, J.: Programme of fireball photography in CzechoSlovakia. Bullet. Astron. Instit. Czechoslovakia **16**, 15 (1965)

26. McCrosky, R.E., Boeschenstein, J.H.: The prairie meteorite network. Opt. Eng. **3**, 304127 (1965)

27. McCrosky, R., Posen, A., Schwartz, G., Shao, C.-Y.: Lost City meteorite—Its recovery and a comparison with other fireballs. J. Geophys. Res. **76**, 4090–4108 (1971)

28. Halliday, I., Griffin, A.A., Blackwell, A.T.: Detailed data for 259 fireballs from the Canadian camera network and inferences concerning the in ux of large meteoroids. Meteorit. Planet. Sci. **31**, 185–217 (1996)

29. Halliday, I.: Geminid fireballs and the peculiar asteroid 3200 Phaethon. Icarus **76**, 279294 (1988)

30. Campbell-Brown, M., Hildebrand, A.: A new analysis of data from the meteorite observation and recovery project. Bullet. Amer. Astron. Soc. **36**, 1142 (2004)

31. Oberst, J., Molau, S., Heinlein, D., Gritzner, C., Schindler, M., Spurný, P., Ceplecha, Z., Rendtel, J., Betlem, H.: The European Fireball Network: current status and future prospects. Meteorit. Planet. Sci. **33**, 49–56 (1998)

32. Spurný, P., Borovička, J., Shrbený, L.: Automation of the Czech part of the European fireball network: equipment, methods and first results. Proc. Int. Astron. Union **2**, 121–130 (2006)

33. Ceplecha, Z., Revelle, D.O.: Fragmentation model of meteoroid motion, mass loss, and radiation in the atmosphere. Meteorit. Planet. Sci. **40**, 35–54 (2005)

34. Spurný, P., Oberst, J., Heinlein, D.: Photographic observations of Neuschwanstein, a second meteorite from the orbit of the Příbram chondrite. Nature **423**, 151–153 (2003)

35. Borovička, J., Tóth, J., Igaz, A., Spurný, P., Kalenda, P., Haloda, J., Svoreň, J., Kornoš, L., Silber, E., Brown, P., et al.: The Košice meteorite fall: Atmospheric trajectory, fragmentation, and orbit. Meteorit. Planet. Sci. **48**, 1757–1779 (2013)

36. Spurný, P., Borovička, J., Kac, J., Kalenda, P., Atanackov, J., Kladnik, G., Heinlein, D., Grau, T.: Analysis of instrumental observations of the Jesenice meteorite fall on April 9, 2009. Meteorit. Planet. Sci. **45**, 1392–1407 (2010)

37. Borovička, J., Spurný, P., Šegon, D., Andreič, v., Kac, J., Korlevič, K., Atanackov, J., Kladnik, G., Mucke, H., Vida, D., et al.: The instrumentally recorded fall of the Križevci meteorite, Croatia, February 4, 2011. Meteorit. Planet. Sci. **50**, 1244–1259 (2015)

38. Spurný, P., Bland, P.A., Shrbený, L., Borovička, J., Ceplecha, Z., Singelton, A., Bevan, A.W., Vaughan, D., Towner, M.C., McClafferty, T.P., et al.: The Bunburra Rockhole meteorite fall in SW Australia: fireball trajectory, luminosity, dynamics, orbit, and impact position from photographic and photoelectric records. Meteorit. Planet. Sci. **47**, 163–185 (2012)

39. Weryk, R., Brown, P., Domokos, A., Edwards, W., Krzeminski, Z., Nudds, S., Welch, D.: The Southern Ontario all-sky meteor camera network. Earth Moon, Planets **102**, 241–246 (2008)

40. Toth, J., Kornos, L., Piffl, R., Koukal, J., Gajdos, S., Popek, M., Majchrovic, I., Zima, M., Vilagi, J., Kalmancok, D., et al.: Slovak video meteor networkstatus and results: Lyrids 2009, geminids 2010, quadrantids 2011. In: Proceedings of the International Meteor Conference, 30th IMC, pp. 82–84, Sibiu, Romania, 2011 (2012)

41. Gritsevich, M., Lyytinen, E., Moilanen, J., Kohout, T., Dmitriev, V., Lupovka, V., Midtskogen, S., Kruglikov, N., Ischenko, A., Yakovlev, G., et al.: First meteorite recovery based on observations by the Finnish Fireball Network. In: Proceedings of the International Meteor Conference pp. 162–169 (2014)

42. Colas, F., Zanda, B., Vaubaillon, J., Bouley, S., Marmo, C., Audureau, Y., Kwon, M.K., Rault, J.-L., Caminade, S., Vernazza, P., et al.: French fireball network FRIPON. In: Rault, J.-L., Roggemans, P. (eds.) Proceedings of the International Meteor Conference, Mistelbach, Austria (2015). International Meteor Organization, ISBN 978-2-87355-029-5, pp. 37–40, Vol. 1

43. Kokhirova, G., Babadzhanov, P., Khamroev, U.K.: Tajikistan fireball network and results of photographic observations. Solar Syst. Res. **49**, 275–283 (2015)

44. Jenniskens, P., Gural, P., Dynneson, L., Grigsby, B., Newman, K., Borden, M., Koop, M., Holman, D.: CAMS: Cameras for Allsky Meteor Surveillance to establish minor meteor showers. Icarus **216**, 40–61 (2011)

45. Brown, P., McCausland, P., Fries, M., Silber, E., Edwards, W., Wong, D., Weryk, R., Fries, J., Krzeminski, Z.: The fall of the Grimsby meteorite— I: Fireball dynamics and orbit from radar, video, and infrasound records. Meteorit. Planet. Sci. **46**, 339–363 (2011)

46. Jenniskens, P., Rubin, A.E., Yin, Q.-Z., Sears, D.W., Sandford, S.A., Zolensky, M.E., Krot, A.N., Blair, L., Kane, D., Utas, J., et al.: Fall, recovery, and characterization of the Novato L6 chondrite breccia. Meteorit. Planet. Sci. **49**, 1388–1425 (2014)

47. Flye-Sainte Marie, C.: Solution to problem number 48. L'Intermédiaire des Mathématiciens **1**, 107–110 (1894)

48. De Bruijn, N.G., Erdos, P.: A combinatorial problem, Koninklijke Nederlandse Akademie v. Wetenschappen **49**, 758–764 (1946)

49. Van Aardenne-Ehrenfest, T., De Bruijn, N.G.: Circuits and trees in oriented linear graphs. Simon Stevin: Wis-en Natuurkundig Tijdschr. **28**, 203 (1951)

50. Howie, R.M., Paxman, J., Bland, P.A., Towner, M.C., Sansom, E.K., Devillepoix, H.A.R.: Submillisecond fireball timing using de Bruijn timecodes. Meteoritics and Planetary Science (2017)

51. Ceplecha, Z.: Geometric, dynamic, orbital and photometric data on meteoroids from photographic fireball networks. Bullet. Astron. Instit. Czechoslovakia **38**, 222–234 (1987)

52. Borovicka, J.: The comparison of two methods of determining meteor trajectories from photographs. Bullet. Astron. Instit. Czechoslovakia **41**, 391–396 (1990)

53. Gural, P.S.: A new method of meteor trajectory determination applied to multiple unsynchronized video cameras. Meteorit. Planet. Sci. **47**, 1405–1418 (2012)

54. Wetherill, G., ReVelle, D.: Which fireballs are meteorites? A study of the Prairie Network photographic meteor data. Icarus **48**, 308–328 (1981)

55. Brown, P., Marchenko, V., Moser, D.E., Weryk, R., Cooke, W.: Meteorites from meteor showers: A case study of the Taurids. Meteorit. Planet. Sci. **48**, 270–288 (2013)

56. Halliday, I., Blackwell, A.T., Griffin, A.A.: The typical meteorite event, based on photographic records of 44 fireballs. Meteoritics **24**, 65–72 (1989)

CO-AUTHORED PAPER 5 — SUBMILLISECOND FIREBALL TIMING USING DE BRUIJN TIMECODES

Submillisecond fireball timing using de Bruijn timecodes

Robert M. HOWIE[1]* ⓘ, Jonathan PAXMAN[1], Philip A. BLAND[2], Martin C. TOWNER[2],
Eleanor K. SANSOM[2], and Hadrien A. R. DEVILLEPOIX[2]

[1]Department of Mechanical Engineering, Curtin University, Perth, Western Australia 6845, Australia
[2]Department of Applied Geology, Curtin University, Perth, Western Australia 6845, Australia
*Corresponding author. E-mail: robert.howie@curtin.edu.au

Abstract–Long-exposure fireball photographs have been used to systematically record meteoroid trajectories, calculate heliocentric orbits, and determine meteorite fall positions since the mid-20th century. Periodic shuttering is used to determine meteoroid velocity, but up until this point, a separate method of precisely determining the arrival time of a meteoroid was required. We show it is possible to encode precise arrival times directly into the meteor image by driving the periodic shutter according to a particular pattern—a de Bruijn sequence—and eliminate the need for a separate subsystem to record absolute fireball timing. The Desert Fireball Network has implemented this approach using a microcontroller driven electro-optic shutter synchronized with GNSS UTC time to create small, simple, and cost-effective high-precision fireball observatories with submillisecond timing accuracy.

INTRODUCTION

Meteorites provide valuable insight into the formation and history of the solar system and have remained relatively undisturbed since the formation of their parent bodies. There is no shortage of recovered meteorites available for study, but interpreting the results of the physical and chemical analysis is constrained by a lack of knowledge of the precise origins of the samples; this lack of context also limits the conclusions that can be drawn from a single meteorite. The solution is to study planetary materials of known origins. Sample return and rendezvous space missions to asteroids and comets are expensive and high-risk approaches to solving this problem; fireball camera networks which record atmospheric trajectories of bright meteors can provide a cost-effective alternative.

Fireball camera networks traditionally use long-exposure photography from multiple stations to produce a triangulated trajectory with sufficient precision to recover meteorites and calculate heliocentric orbits that can be compared to the orbits of potential parent bodies (Halliday 1973). Long-exposure images are occulted by a periodic shutter in order to determine meteoroid velocity during the observable trajectory

(Jacchia and Whipple 1956; Ceplecha 1957). Traditionally, these systems have required separate timing subsystems to record absolute arrival times for orbit calculation (McCrosky and Boeschenstein 1965; Halliday et al. 1978). We present a technique using timecodes constructed from de Bruijn sequences (Flye Sainte-Marie 1894; de Bruijn 1946) to embed the arrival time into the fireball trail image using an electro-optic shutter with no moving parts. This approach enables much smaller, lower power, and more cost-effective fireball cameras than previously possible, and has allowed the rapid deployment of the Desert Fireball Network (DFN) (Bland et al. 2012) in the Australian Outback. The development is significant in that it allows off-the-shelf cameras to be turned into high-precision fireball observatories without the need for additional sensors. The design also significantly simplifies data reduction. The motivation and development will be outlined along with a demonstration of the results produced using the technique to gather all required trajectory data from a single long-exposure image per station.

Using this technique, the Desert Fireball Network has achieved spatial precision of approximately 1 arcminute and submillisecond timing precision at a fraction of the cost of previous observatories. The

technique could also be applied to other areas where high-precision motion-time data are required, including spacecraft, particle image velocimetry, and tracking other objects or phenomena.

FIREBALL CAMERA NETWORKS

Fireball camera networks continuously observe the night sky for rare bright meteors known as fireballs or bolides, which may result in single or multiple meteorite falls. The bright flight or observable luminous trajectory of the fireball (as the meteoroid ablates in the atmosphere) is recorded on a highly accurate imaging device from multiple geographically distinct stations. The meteoroid's trajectory through the Earth's atmosphere is triangulated from these multiple observations in order to determine the estimated fall location and the meteoroid's preatmospheric entry orbit. In addition to the path through the atmosphere, the distributed observatories must also accurately record timing of the trajectory. The relative timing is vital for determining meteoroid velocity and deceleration, which, in combination with the path geometry, allows the estimation of its mass and hence a fall position distribution. The absolute arrival time of the fireball is required to accurately determine the heliocentric orbit of the meteoroid due to the constant orbital motion and rotation of the Earth.

Three large fireball networks were developed in the 1960s and 1970s. The Czechoslovak Fireball Network (now the European Fireball Network) commenced operations with all-sky cameras in 1963 (Ceplecha and Rajchl 1965), shortly followed by the Prairie Meteorite Network in the Midwest United States in 1964 (McCrosky and Boeschenstein 1965) and the Canadian Meteorite Observation and Recovery Project (MORP) in 1971 (Halliday et al. 1978). The Desert Fireball Network (DFN), located in the remote Australian Outback, commenced operation in 2003 with the testing of a large-format film-based observatory based on the recent European Network automated design (Spurný et al. 2006) with modifications for the Australian climate (Bland et al. 2012). The network became operational with three stations in 2005, and a fourth station was added in 2007 (Spurný et al. 2012a). The trial network successfully recovered two meteorites: Bunburra Rockhole (Bland et al. 2009; Spurný et al. 2012a) and Mason Gully (Spurný et al. 2012b; Dyl et al. 2016). This success paved the way for the development and deployment of the first all digital fireball camera network designed for meteorite recovery.

Fireball trajectories must be recorded with high accuracy and precision to ensure meteorites can be located and meteoroid orbits can be meaningfully compared to the orbits of potential parent bodies. Due to the extremely low population density and remoteness of the region, meteorite searches in the Australian Outback are typically conducted by small teams (5–12 persons) on foot, for up to 2 weeks. This places an upper limit on the area of searchable terrain for each predicted meteorite fall (approximately 2–6 km^2), which informs the precision requirements for the network (DFN precision goals for bright flight observations: meteoroid trajectory: ±50 m, triangulation final vector: ±0.05°, mass: 1 order of magnitude). The relative timing along the bright flight trajectory provides the velocity information required to calculate a fall position probability distribution, while the precise absolute arrival time is required for the orbital calculation. Trajectory analysis and mass estimation are performed using the dynamic method detailed in Sansom et al. (2015), giving a robust analysis of the observational and modeling errors involved. After the mass distribution has been estimated, dark flight modeling simulates the meteoroid behavior as it falls to the ground after ablation ceases and it is no longer visible to the camera network; the atmospheric conditions are modeled in the relevant volume from a climate model based on the best available local meteorological data including ground-based measurements and balloon flight data.

Uncertainties in the observed position and velocity of the meteoroid during the trajectory increase the area of the ground search; for this reason, meteor camera networks have previously used large-format film-based cameras to achieve high spatial precision (approximately 1 arcminute, limited by film developing and scanning techniques [Spurný et al. 2006]). The DFN uses high-resolution (36 megapixel), full-frame (24 × 36 mm) digital sensors with fisheye all-sky lenses to achieve similar spatial precision. The digital observatories are constructed from off-the-shelf components where possible to simplify manufacturing and reduce costs (Howie et al. 2017). They are significantly smaller and easier to manufacture and install than previous designs and integrate with an automated data processing pipeline to greatly reduce the data reduction workload of a large network.

RELATIVE FIREBALL TRAJECTORY TIMING

Relative fireball timing is determined by periodically occulting the sensor or film plane during a long-exposure fireball image. This chops the meteor trail (Fig. 1a) into small segments (Fig. 1b) at a known rate, allowing the calculation of meteoroid velocity throughout the luminous trajectory after triangulation from multiple stations. The first purpose-built fireball observatories in the Czechoslovak network used a
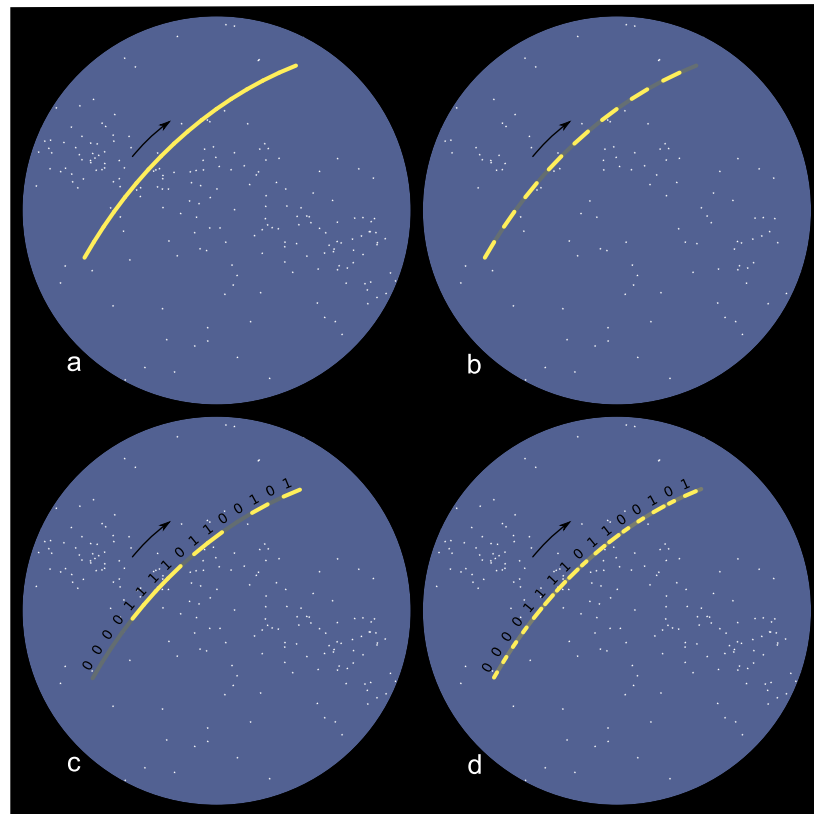
Fig. 1. Long-exposure fireball encoding using a light modulator. a) Long exposure, no encoding. b)Traditional periodic occultation for velocity determination. c) de Bruijn sequence encoded as shutter opacity (0: closed, 1: open). d) de Bruijn sequence encoded as pulse width (0: short, 1: long). (Color figure can be viewed at wileyonlinelibrary.com.)

mechanical rotating shutter to periodically obstruct the film plane similar to previous meteor camera designs (Ceplecha et al. 1959; Ceplecha and Rajchl 1965). The rotational position of the shutter is tightly controlled with respect to time. As the shutter rotates throughout the exposure, the open sectors in the disk create the visible dashes, and the opaque sectors create blanks in the trail where the light path from the fireball to the film plane is obstructed. This relative timing data enables the estimation of fall site distributions but not heliocentric orbits. The Prairie Network replaced the rotating mechanical shutter with a solenoid-controlled switching shutter that moved a lightweight blade in and out of the optical path within the lens (McCrosky and Boeschenstein 1965). This switching shutter operated at 20 cycles per second to produce regular dashes in fireball trails for relative timing similar to the rotating approach. The Canadian MORP network used modified

slow-rotating shutters with three different sectors producing four dashes per second, one transparent and two different neutral density filters to allow the imaging of very bright fireballs that would otherwise overexpose the film (Halliday et al. 1978).

Absolute Fireball Trajectory Timing (Arrival Time)

The absolute arrival time of a meteoroid is required in addition to the path and velocity of the meteor's luminous trajectory in order to calculate the meteoroid's preatmospheric orbit due to the constant orbital motion and rotation of the Earth. Because photographs in long-exposure fireball camera networks can be up to one night in length, a method of determining the arrival time of a fireball within the exposure is required. The three large networks took different approaches to the absolute timing problem. The Czechoslovak network

initially relied on chance human observations for arrival times, but was then upgraded to determine absolute timing by comparing images from the fixed fireball cameras with rotating shutters to concurrent images from identical sidereal-guided cameras on equatorial mounts (Ceplecha et al. 1959). The difference in position of the meteor trail image between the two cameras is determined by the position of the guided camera when the meteor arrives. This allows the calculation of the arrival time due to the precise relationship between time of day and the guided camera's position. This method is theoretically simple but relies on very precise movement of the equatorial mount to achieve the specified timing precision of ± 5 s (Spurný 1997). The Prairie Network recorded absolute timing by modifying the switching shutter's pattern of operation. A break was extended to denote the beginning of a timing window. Different dashes were omitted in each window by holding the switching shutter closed to indicate which 10.4 s window in the 4 h exposure a fireball appeared (McCrosky and Boeschenstein 1965). A photomultiplier tube (PMT) was also used to timestamp arrivals, but only for meteors brighter than magnitude -4 (fireballs). The MORP observatories were also equipped with a PMT—this time behind interleaved perforated masks to detect motion in the appropriate (angular) velocity range for meteors via an electronic filter circuit. This meteor detector printed the arrival time on the current sheet of film in the camera and then advanced the film to the next frame. The Czechoslovak design (now operating within the European Fireball Network) was updated in the late 1990s with the addition of a PMT to record meteor light curves at a high sample rate and remove the need for guided cameras operating alongside the fixed cameras (Oberst et al. 1998); this Czech design was later automated to reduce the labor demand (Spurný et al. 2006).

Standard video cameras are also used in some fireball networks (Finnish Fireball Network [Gritsevich et al. 2014], Spanish Fireball Network [Trigo-Rodríguez et al. 2005], Polish Fireball Network [Olech et al. 2006], the Croatian Meteor Network [Andreić and Šegon 2010], and others). These video cameras can offer good timing precision, do not require data integration from multiple sensors, and are often used in amateur and collaborative networks where the low per station cost makes them an attractive option. However, the poor spatial resolution offered by systems built around commonly available video cameras paired with all-sky lenses produces significant uncertainty in the fall position and orbit, reducing the likelihood of successful meteorite recovery and the chance of matching an orbit to a potential parent body. Video systems based on expensive high-resolution industrial imaging cameras or using multiple video cameras with rectilinear lenses (such as Cameras for Allsky Meteor Surveillance [CAMS] [Jenniskens et al. 2011]) can achieve similar spatial precision to still cameras. However, the high data rates can make the overall solution complex.

The absolute timing precision required for accurate orbit determination depends on the spatial precision of the observatory. Absolute timing precision of 1 s is sufficient for orbit determination by networks similar to the DFN (high-resolution still cameras with all-sky lenses). More precise timing will not result in more precise orbits due to the spatial uncertainty. The submillisecond timing precision offered by this technique becomes more useful for orbit determination when higher spatial precision instruments such as traditional telescopes and fireball observatories incorporating narrow angle rectilinear lenses are used. The technique can be applied in these higher spatial precision instruments without additional difficulty.

High absolute timing precision is also useful for other purposes aside from orbit determination. The ability to precisely align camera network fireball observations with other timed data sources such as Doppler RADAR (which can provide meteoroid positions at lower altitudes than camera networks) can be beneficial for the recovery of meteorites in more difficult situations. Accurate absolute timing of the data points in fireball images also makes a wider range of triangulation techniques possible because the trajectory data points can be individually triangulated.

A NEW APPROACH

The primary objective during the development of a new fireball observatory for the DFN was to reduce the per station cost in order to deploy the largest network possible on a finite budget while maintaining the precision required for meteorite recovery. The expected number of meteorite dropping fireballs observed by the network per year depends primarily on the network coverage area, and the likelihood of recovery depends on the suitability of the meteorite searching terrain. The primary factors contributing to the high cost of previous designs were the custom large-format film-based imaging system, the precision manufacturing and assembly required to produce the mechanical shutter, and the expensive and complex photomultiplier tube subsystem. The new DFN observatories are based around off-the-shelf consumer digital cameras in order to significantly reduce the per station cost and utilize an automatic data pipeline for triangulation, fall position estimation, and orbit

Fireball timing using de Bruijn timecodes   1673

calculation. After testing a number of camera and lens options, the Nikon D810 (offering high resolution and good low-light noise performance) and Samyang 8 mm f/3.5 II (offering a favorable projection and good value) were selected. A mechanical shutter of the rotating or switching type presents an obstacle to reducing the per observatory cost; the tight manufacturing tolerances and difficult assembly required to implement a precisely controlled mechanical shutter between the lens and sensor plane would significantly contribute to the overall cost of each observatory.

An electro-optic shutter does not require such tight manufacturing tolerances and significantly reduces complexity with no moving parts, resulting in greatly reduced manufacturing and assembly costs. Liquid crystal, polymer-dispersed liquid crystal, and switchable liquid crystal mirror shutter technologies were tested; the liquid crystal (LC) shutter option was selected for its proven track record in long-lasting consumer products (liquid crystal displays), ease of implementation, low cost, and availability. The LC shutter also has the added advantage of global operation, where the transmittance changes across the whole frame with the same timing and hence timing is position independent. This is in contrast to a rotating shutter where the sweeping motion of the rotating shutter across the frame over time must be considered (Ceplecha 1987). The drawback of LC shutters is the limited open state transmittance—approximately 36% for the LC-Tec X-FOS shutters used by the DFN (LC-Tec 2013); this drives the need for good low-light performance from the camera. The LC shutter is mounted between the lens and the sensor plane to periodically obstruct the light path like the mechanical shutters of previous designs, but without moving parts. The shutter must be as thin as possible to minimize focus shift and optical aberrations. The LC shutter is simply mounted over the rear element of the all-sky lens (Fig. 2), and the thin drive wires are routed out through the side of the lens.

A New Technique for Absolute Timing

The previous techniques for determining arrival time in long-exposure fireball images are not ideal for a low-cost fireball camera network deployed in the Australian Outback where the observatories must operate in harsh conditions without manual intervention for periods up to 1 yr. The dust and high winds prevalent in the outback make it difficult and expensive to design and construct precision mechanical systems that operate reliably without frequent maintenance; the dual guided and unguided camera configuration of the
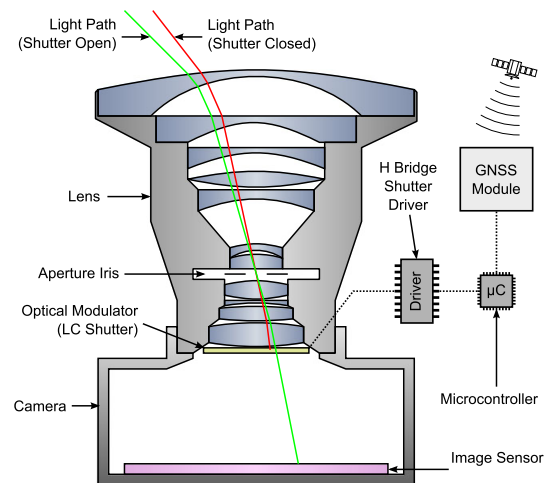
Fig. 2. Imaging system showing all-sky lens, camera, LC shutter, shutter driver, microcontroller, and GNSS receiver. (Color figure can be viewed at wileyonlinelibrary.com.)

original Czechoslovak system was not considered for this reason. The photomultiplier tubes of the recent European network design provide fireball timing along with well-resolved brightness data but are expensive and require high voltage power supplies, complex supporting electronics, a separate optical window or cover, and constant drive voltage adjustments in order to capture a high dynamic range and prevent destruction of the PMT. Processing the brightness curve data is not simple due to the changing drive voltage (affecting gain) and the angle-dependent response of the PMT. Avoiding the added cost and complexity of a separate absolute timing subsystem enables a more cost-effective, smaller, and more power efficient fireball camera. The coded shutter approach of the Prairie Meteorite Network (McCrosky and Boeschenstein 1965) partly achieves this as it records absolute timing in the fireball's trail as it travels across the frame of the long-exposure image, but the precision of the system is too low (within a 10.4 s window) to meet the DFN's objectives for high orbital accuracy.

Time Encoding

Electro-optic shutters make more advanced time encoding straightforward: the devices have fast response times compared to mechanical alternatives and are simple to drive electronically. The flexibility of a microcontroller-driven LC shutter makes it possible to encode absolute timing data (arrival time) by slightly varying the pattern used for relative timing

data (velocity) according to a timecode without requiring any additional hardware. Higher precision than previous attempts at using timecodes—in absolute timing and therefore orbits—is achieved with a constantly changing sequence that does not repeat during the exposure and by synchronizing the operation with highly accurate GNSS time. GNSS or global navigation satellite systems use constellations of satellites (including GPS, GLONASS, QZSS, Galileo, and Compass/BeiDou) to provide users with precise positioning and timing data.

When a meteor or fireball appears, the image of the meteor trail is embedded with a part of this timecode as the meteor moves across the frame, while the LC shutter modulates the light transmittance according to the timecode sequence. The part of the timecode sequence visible in the meteor trail corresponds to the time within the long exposure where the fireball was visible. This records the absolute timing data including the arrival time, and makes the calculation of the heliocentric orbit possible. The recording of the relative and absolute timing data is inherent in the image and does not require the integration of data from multiple subsystems, therefore simplifying the data processing problem.

The ideal timecode should be as long as possible in order to maximize the possible exposure length, but require as few elements visible as possible for time decoding in order to capture the arrival times of short fireballs. While short fireballs are less likely to drop recoverable meteorites, they appear more frequently and are important for the statistical analysis of meteoroid orbits, a secondary goal of the DFN.

A number of different types of sequences were considered as timecodes. The characters in the sequence produce uniquely recognizable image features (e.g., brightness, or dash length—depending on the encoding used); the absolute timing of the trajectory can be determined when the pattern of features visible in the image can be matched with a section of the timecode sequence. The conceptually simplest is a counter sequence with each digit encoded as a different shutter opacity (the first approach in Table 1). This type of sequence is not optimal because the start of each subsequence is not defined and the number of elements that must be visible to decode the unique arrival time varies throughout the sequence. An alternate encoding with a character reserved to define the start of each subsequence could be used (the second approach in Table 1), but this is an inefficient usage of a character in the sequence alphabet that could otherwise be used to extend the sequence. A longer sequence allows a longer exposure on the fireball observatory; this extends the camera lifetime and reduces the amount of data

Table 1. A simplistic comparison of three timecode approaches using the three character alphabet {0,1,2}. Each sequence requires three elements to be known for the unique position within the sequence (time within the timecode) to be discovered (for all positions in the sequence).

Approach	Resulting sequence	Sequence length
Counter sequence	000102101112202122	18
Counter sequence with reserved start character	200201210211	12
de Bruijn sequence	000222122021121020120011101	27

collected per night resulting in longer periods between visits for maintenance and drive changes.

The optimal solution for this type of problem is a sequence that includes every subsequence exactly once for a given subsequence length (the third approach in Table 1). This type of sequence is known as a full-length cycle or de Bruijn sequence (Flye Sainte-Marie 1894; de Bruijn 1946).

DE BRUIJN SEQUENCES

De Bruijn sequences are the shortest cyclic sequences containing all possible subsequences for a given alphabet and subsequence length. Their existence was formally described in Flye Sainte-Marie (1894) and then independently described again several times in the 20th century (de Bruijn 1975). de Bruijn (1946) is the best known of these rediscoveries and the reason they are often referred to as de Bruijn sequences today. Interestingly, their use dates at least as far back as an ancient Sanskrit sutra for memorizing rhythms around 1000 AD (Kak 2000; Stein 2010). As an example, the de Bruijn sequence "00011101" contains all of the eight possible three element subsequences "000," "001," "011," "111," "110," "101," "010," and "100" for the binary alphabet A={0, 1} when considered cyclically (the last three digit subsequence is formed by the last digit and the first two). As a window three elements in length is slid along the cyclical sequence, each subsequence is revealed. In the fireball camera application, the sequence is encoded by the electro-optic shutter over time and the window revealing a particular subsequence is the appearance of a fireball in the frame. The elements visible in the fireball's trail indicate the position in the timecode and therefore the fireball's time of arrival. Subsequences are also referred to as *n*-tuples, where *n* is the subsequence length; de Bruijn sequences are also known as full-length cycles because they contain all possible *n*-tuples.

Given an alphabet A with size k (a k-ary alphabet) and a subsequence length of n, there are number of different particular de Bruijn sequences that satisfy the above criteria. The number $|B|$ distinct sequences B_i for the case $B(k, n)$ can be calculated from de Bruijn's Theorem generalized for k-ary alphabets (Van Aardenne-Ehrenfest and de Bruijn 1951) (Equation 1).

$$|B| = \frac{(k!)^{k^{n-1}}}{k^n} \qquad (1)$$

For many applications such as meteor trajectory encoding, it is not important to know all of these sequences, or even the number of distinct sequences. What is required, however, is the ability to procedurally generate at least one of these sequences for all relevant cases of n and k. There are various algorithms for developing de Bruijn sequences, many of which are discussed in Fredricksen (1982) and Mitchell et al. (1996). Memory usage and computation speed of these algorithms are of interest to users in the fields of communication and genetics where sequences can be billions of elements long (Compeau et al. 2011); these factors are unimportant for fireball cameras where only relatively short sequences (several hundred elements in length) are required for encoding meteor trajectory data. The length of the de Bruijn sequences N depends on the subsequence length n and the alphabet size k (Equation 2).

$$N = k^n \qquad (2)$$

This length refers to the size of the cyclic sequence where the subsequence beginning with the last element in the sequence is completed by the first n-1 elements. The number of possible sequences increases rapidly as the alphabet size or subsequence lengths increase. There are 24 possible distinct sequences of nine elements in length for $B(k = 3, n = 2)$, but this increases to 373,248 distinct sequences of 27 elements in length for the case $B(k = 3, n = 3)$.

de Bruijn Sequence Generation

A repeatable method of generating de Bruijn sequences is required to implement the encoding on the observatory and the decoding in the image processing pipeline; one of the simpler ways to construct a de Bruijn sequence is the prefer high method which is a generalization of the prefer one method for binary alphabets detailed in Fredricksen (1982). The construction starts with n zeros. Then the highest number in the alphabet (k-1) is inserted unless this

```
algorithm prefer high de Bruijn sequence generation:
  set n to sequence length
  set k to alphabet size
  make empty list sequence
  for n times:
    append 0 to sequence
  while length of sequence is less than or equal to k^n:
    set i to k-1
    set element added to false
    while element added is false:
      set test n-tuple to last n-1 elements of sequence concatenated with i
      if sequence does not contain test n-tuple:
        append i to sequence
        set element added to true
      else:
        decrement i by 1
  return sequence
```

would produce an n-tuple already present in the sequence. In this case, the next highest element is tried and the process continues until the sequence is complete. An implementation of this algorithm is presented above in pseudocode.

This method is simple to implement, but there is no methodical way to know where a particular subsequence appears in the sequence without generating it and performing a search. This requirement can become quite computationally expensive for longer sequences. Others have focused on constructing decodable de Bruijn sequences that do not require this brute force approach (Mitchell et al. 1996), but this is unnecessary for meteor time encoding as the short sequences only take fractions of a second to generate and search.

SEQUENCE ENCODING

The sequence encoding defines the way in which the de Bruijn sequence is used to modulate the transmittance of the electro-optic shutter. The state of the shutter is changed over time according to the elements of the sequence; two options were tested on the DFN observatories. In the initial method, the sequence was encoded in shutter opacity. A "0" was encoded with a fully darkened shutter, a "1" was encoded with a partially opened shutter, and a "2" was encoded with a fully opened shutter. This encoding is simple to implement, even with an alphabet of arbitrary size, but has two main drawbacks for meteor trajectory timing. First, it can be difficult to distinguish between the fully and partially open shutter states for fireballs with rapidly changing brightness due to fragmentation. This

is especially true when examining dim fireballs at the edges of all-sky images where resolution is decreased and optical aberrations are more prevalent. The problem can be alleviated by only using a binary alphabet with the shutter open and closed, producing the encoding as in Fig. 1c. The second problem with the opacity encoding approach is the ambiguity when velocity is uncertain. If only a few sequence elements are visible, it can be impossible to decode the sequence because the dash length is unknown. For example, the subsequence "222000111," which would be encoded as a bright dash, a blank of equal length, and then a dim dash of equal length, appears identical to the subsequences "220011" and "201" if the velocity is completely unknown. A related problem is that the data points from the dash endpoints are not generated at a consistent rate. Areas of the de Bruijn sequence where elements are repeated have a lower data point density than locations where elements are not repeated. This is undesirable and can increase trajectory velocity uncertainty for fireballs arriving at certain times.

A more appropriate encoding method would eliminate this velocity ambiguity and provide data points at a constant rate. Encoding the sequence elements as pulse width instead of opacity (Fig. 1d) is simple with the flexible shutter driver and accomplishes this goal. The encoding has only been implemented for a binary alphabet for ease of decoding with high sequence rates, but could be generalized to larger alphabets. A "0" is encoded with a short dash length and a "1" is encoded with a longer dash length; there is no velocity ambiguity and data points have a consistent density throughout the sequence. Pulse width encoding also clearly shows the direction of a fireball even when only a couple of dashes are visible.

Sequence Parameters for Fireball Observation

The appropriate parameters of the de Bruijn sequence depend on the imaging configuration and target meteor characteristics. The appropriate sequence rate (in elements per second) depends on the expected velocity of the target meteor and the amount of halation or blurring caused by optical aberrations in the imaging system and meteor trail length. If the sequence rate is too high for a particular scenario, the elements (dashes) in the sequence will smear together making the decoding difficult or impossible. A sequence rate near the upper limit is desirable to provide as many trajectory timing data points as possible and therefore, a more accurate meteoroid mass estimation—using the dynamic method (Sansom et al. 2015)—and fall position distribution. Faster meteors can be imaged with a higher sequence rate than slower meteors

because each dash and blank of the meteor trail is projected across more pixels on the sensor making it easier to discern between the individual segments. The DFN is currently optimized for slower fireballs operating at a rate of 10 sequence elements per second with 8 mm all-sky lenses and 36 megapixel full frame (36×24 mm) sensors. If the targets of interest are faster, dimmer meteors from a known shower instead of slower, brighter fireballs, the operating parameters could be tuned to produce as many trajectory data points as possible by increasing the sequence rate. The DFN plans to add this capability of switching into an alternate mode of operation during peak periods of known showers in the future.

The sequence duration (t_S) must be greater than the exposure time to avoid duplicating subsequences during the exposure, thereby ensuring a meteor's arrival time during the exposure is unambiguous. The sequence duration depends on the sequence length and the sequence rate (Equation 3); extending the exposure time with a longer sequence duration is desirable due to the corresponding reduction in data rate and storage requirements. If star trails are not a concern, the exposure length is limited by the long-exposure noise performance of the camera.

The minimum time a fireball must be visible for, in order to be decoded, t_{Min} is equal to the subsequence length divided by the sequence rate (Equation 3). t_{Min} has a large impact on t_s and therefore the corresponding data rate of the observatories, all other parameters being equal (Equation 3).

$$t_s = \frac{N}{r_s} = \frac{k^n}{r_s} = \frac{k^{t_{Min} r_s}}{r_s} \tag{3}$$

$$t_{Min} = \frac{n}{r_s} \tag{4}$$

The alphabet size is determined by the number of distinguishable distinct patterns using the chosen encoding and sequence rate. A binary alphabet ($k = 2$) with pulse width modulation at 10 elements per second is used by the DFN ($r_S = 10$). The subsequence length currently used is nine elements ($n = 9$), and hence the minimum decodable meteor duration (t_{Min}) is 0.9 s. This limits the exposure length to 52.0 s. Zeros in the sequence are represented by a short dash where the LC shutter is open for 0.02 s, and ones are represented by a long 0.06 s dash. The starts of the dashes are aligned (every 0.1 s). The DFN observatories take 25 s exposures every 30 s during operation. However, work to extend the open time to 29.0–29.5 s out of 30 is underway. The approximate exposure start time is recorded in the image file by the camera. The de Bruijn

sequence and the camera exposure start every 30 s at the top and bottom of the UTC minute and are precisely (better than 1 ms) synchronized with UTC time through a global navigation satellite system (GNSS) receiver.

Decoding Arrival Time

The DFN currently uses a semiautomated approach to de Bruijn sequence decoding. If the automated event processing routines detect a large fireball appearing simultaneously at multiple stations, the images are downloaded for analysis and decoding. The camera's sequences are synchronized (via the GNSS receivers) so points in the sequence from multiple cameras can be matched. Trajectory triangulation is possible without any knowledge of the de Bruijn sequence.

The search for the subsequence in the overall de Bruijn sequence revealed by each fireball can be performed in a few seconds, either manually or with the assistance of a DFN software tool designed for matching partially obscured de Bruijn sequences. The sequence of long and short dashes are manually translated into the corresponding sequence of "0"s and "1"s; this string is then either found manually within the sequence (usually using a text editor) or fed into the error tolerant search tool. The Hamming distance (Hamming 1950) provides a good metric for finding the location of the subsequence within the complete de Bruijn sequence in a fault tolerant manner. The fault tolerant search is possible because each additional element visible past the required n elements provides a degree of error checking. The current search tool also permits searching for partially obstructed sequences by entering unknown elements. In this situation, the Levenshtein distance (Levenshtein 1966) is used because it also accounts for insertions and deletions unlike the Hamming distance. This is important if the number of elements obstructed is unknown.

Once the subsequence is located within the overall de Bruijn sequence, the absolute timing of the trajectory is simply calculated from the element length t_E, location found in the sequence search, and the dash lengths. The propagation delay due to the operation of the microcontroller and the shutter driver as well as the time response of the LC shutter are also accounted for (these can be determined experimentally and should be less than a millisecond). The approximate time in the image metadata is examined to determine the precisely synchronized sequence start time (hh: mm:00.000 or hh:mm:30.000 UTC) and this is added to the time within the sequence to produce the absolute timing for the trajectory (including the arrival time).

IMPLEMENTATION

The first four prototype long-exposure fireball cameras using LC shutters with de Bruijn timecodes were deployed to The Nullarbor in December 2012. The design has since been revised to expand storage, increase computing power for image processing, and optimize power management. The network now consists of more than 49 observatories covering a double station triangulable area of over 2.5 million square kilometers —approximately one-third of Australia.

The operation of the de Bruijn timecode has been verified in the laboratory with a phototransistor ($\approx$10 μs time response) and a data logging digital oscilloscope. The precision—relative to the GNSS time source—is better than 1 ms, and the time response of the LC shutter is the limiting factor.

This technique, combined with the use of digital off-the-shelf hardware where possible, has enabled the development of smaller, lighter (10×), more cost-effective (20×) fireball observatories for the DFN (compared to the initial film systems) and enabled the rapid roll-out of the digital network. The initial digital DFN observatory for solar-powered operation in remote locations proved the viability of the technique and core imaging system. The observatory hardware is presented in detail in Howie et al. (2017). Recently, an even smaller and lower cost mains powered rooftop variant of the autonomous digital fireball observatory has been developed for powered sites that can be attended more frequently (twice per year).

The LC shutters have proven reliable and long-lasting, and the de Bruijn sequence time encoding has been used to capture precise timing data for over 1,000 fireballs including at least one nine station event and one meteorite recovery with an orbit (Murrili) (Bland et al. 2016). Approximately a dozen of the fireballs observed as of February 2016 have been classified as meteorite dropping by the data processing pipeline, and searches will be conducted for many of these in the future.

Limitations

The technique is validated by the large number of successfully imaged and processed fireballs with timing as well as the recovery of the Murrili meteorite but has a few limitations. Under some conditions, it can be hard to decode the sequence. Extremely bright fireballs pose problems for a few reasons. The all-sky lenses in the DFN's implementation perform best at the image center, but optical aberrations become more prevalent toward the edge of the image. These imperfections can cause the brighter dashes to smear together, becoming

hard to distinguish. Extremely bright fireballs have the potential to saturate large areas of the sensor at the high sensitivity settings used to image as much of the fading fireball at the end of its luminous trajectory as possible. This obstacle is present in all imaging systems because of the limited dynamic range of digital sensors and film. This problem will be reduced as higher dynamic range sensors are developed and become available. The other limitation with respect to bright fireballs is the transmittance of the shutter in the closed state. The shutter still allows a small percentage of the incoming light (approximately 0.45%) (LC-Tec 2013) through in the closed state. This light bleed can complicate the time decoding of extremely bright fireballs. Fireball tails and fragmentation also present some problems for the implementation of timecodes in long-exposure images. Very long tails can be visible in the space where the image of the fireball head was darkened by the shutter. This is the downside of this sort of spatial-time encoding used for the de Bruijn sequence time encoding and previous long-exposure meteor camera techniques (rotating and switching shutters). If the tail is long enough to completely cover the break between dashes, decoding timing can become difficult or impossible. Video networks solve this timing problem by eliminating the long exposures, but compromise on spatial precision. The precise positioning of the data points can be degraded by the tail effect in both video and photographic networks if a simple data point extraction algorithm (such as finding the centroid) is used. The tail has the effect of dragging the apparent data point away from the true point at the head of the fireball.

Another limitation inherent in any long exposure system employing a periodic shutter is that part of the fireball trail is obscured. Flares due to fragmentation and other variations in brightness during breaks where the shutter is closed can be missed. For this reason, radiometers such as PMTs are used where the mass estimation is performed using the photometric method (Gritsevich and Koschny 2011). The dynamic method used as part of the DFN's data pipeline (Sansom et al. 2016) incorporates these fragmentation events by the corresponding observed deceleration, but most DFN observatories also employ a video camera so that data can be collected on these fragmentation events more directly.

Fragmentation performance of the de Bruijn sequence time encoding has been better than expected. While fragmentation of the fireball into multiple heads does make the (currently manual) point picking process take longer, it is possible to distinguish between the main mass and smaller fragments in almost every case. These fragments have been processed separately on a
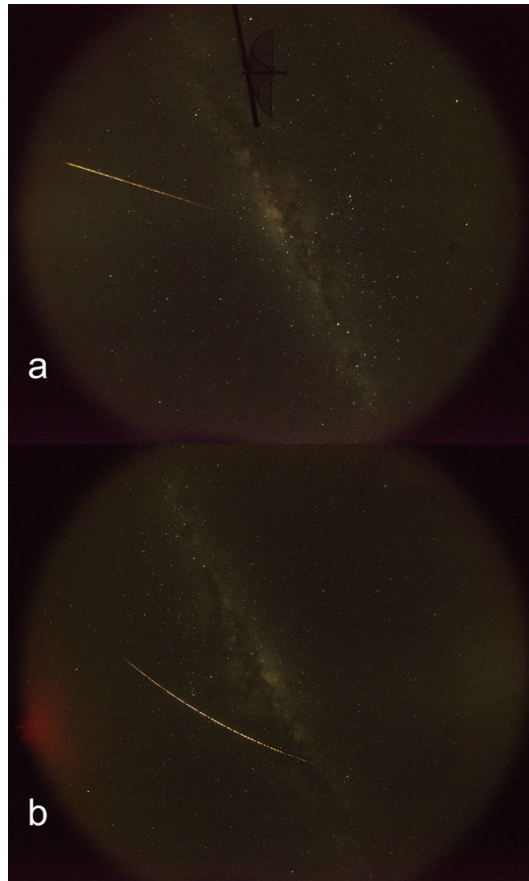
Fig. 3. DN150417_01 Fireball seen from DFN observatories at Kybo (a) and Forrest (b). (Color figure can be viewed at wileyonlinelibrary.com.)

number of fireballs to produce separate fall position estimates for the fragments and main mass.

These limitations are present in all long-exposure meteor camera systems that interrupt the meteor image for relative or absolute timing. In its current state, the approach is suitable for imaging the vast majority of meteorite dropping fireballs, but as lens designs and sensor technologies improve (with reduced optical aberrations and increased sensor dynamic range), the results for very faint and extremely bright fireballs will only improve.

RESULTS IN PRACTICE: DN150417_01

On April 17, 2015, a fireball event in the upper atmosphere above the West Australian Nullarbor

Fireball timing using de Bruijn timecodes   1679

Fig. 4. DN150417_01 fireball observed from Forrest observatory showing de Bruijn sequence encoded timing (alphabet size $k = 2$, subsequence length $n = 9$, rate $r_s = 10$ elements per second, generated using the prefer high method). Element 0 is at 2015-04-07 20:04.00 UTC. Sequence: 000000000111111111011111111001111110101111110011110111001011110100**111100101111000 011110111011110110011110101011110100011110**0110111100100111100010111100001110111001101101011110100111010110110 101010011101001011101000011100110011100101011100010011100011011110001001110000101110000001011 011010011011001011100011101011001101010101011010100011010010011010000101101000001001100011001001011001100 11000011010110011010101011010101000110100100110100001011010000011001100011001010011001001011001000010101100010 001100001001100000101100000001010101001010101000010100100010100010010 100000010010010000010001000011 (labeled elements in bold). (Color figure can be viewed at wileyonlinelibrary.com.)

Fig. 5. Observed versus modeled position residuals along the straight-line trajectory, dashed lines indicate $\pm 1\sigma$ range. (Color figure can be viewed at wileyonlinelibrary.com.)

designated as DN150417_01 was recorded by five DFN observatories and is presented here to demonstrate the use of de Bruijn timecodes in long-exposure fireball photography; the object became visible to the camera network at UTC20:04:04.3270 $\pm$ 0.0006 s traveling eastwards and remained observable for 10.4590 $\pm$ 0.0007 s without visible flares or fragmentation until observable ablation ceased at UTC20:04:14.7864 $\pm$ 0.0001 s.

The best observations were made from the closest DFN cameras at Kybo (Fig. 3a) and Forrest (Fig. 3b), adjacent settlements located along the Trans-Australian Railway. The sites are separated by nearly 150 km and each have a permanent population of approximately two persons (giving an indication of the population density in the coverage area of the DFN). The trajectory triangulation was performed using four of the five observations (Kybo, Forrest, Deakin North, and Kanandah). Hughes was excluded because distant and low to the horizon observations result in reduced

Fig. 6. Heliocentric orbit for DN_15041701 meteoroid. (Color figure can be viewed at wileyonlinelibrary.com.)

precision (compared to the closer cameras with better triangulation geometry).

Trajectory timing was recorded by the DFN observatories using the de Bruijn timecode approach. The timing embedded by the GNSS synchron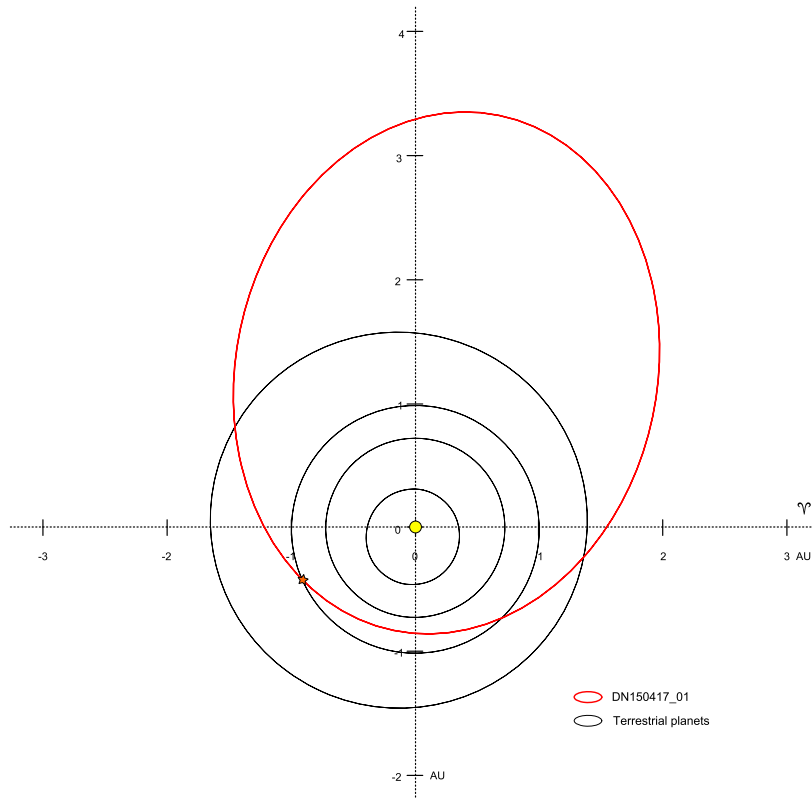ized LC shutter into the Forrest observatory image is illustrated in Fig. 4. The trajectory was triangulated according to the straight least squares method (Borovička 1990) and analyzed using the dynamic method described previously (Sansom et al. 2015), which uses the observations to estimate the position, mass, and velocity of a meteoroid while statistically constraining the uncertainties in these parameters introduced by observation and dynamic model errors. The object appeared at a height of 85.80 ± 0.05 km at $126.7166 \pm 0.0003°E$ $31.02550 \pm 0.00022°S$ (WSG 84) with an initial velocity of 17.98 ± 0.07 km s^{-1} and an entry angle of $15.14 \pm 0.05°$ from the horizontal. The object gradually decelerated over the 143.31 ± 0.01 km luminous trajectory, which ceased at a height of 45.70 ± 0.03 km at $128.23950 \pm 0.00017°E$ $30.57766 \pm$

$0.00015°S$ (WSG 84) and a final velocity of 4.4 ± 0.7 km s^{-1}. The trajectory analysis indicates the fireball event was the result of a small meteoroid with an initial mass of 32 ± 4 kg entering the atmosphere at a shallow angle before completely burning up. The position residuals from the trajectory analysis (Fig. 5) show a good fit between the observations and the dynamic model.

The heliocentric orbit (Fig. 6) was calculated from the initial entry vector using a numerical propagation technique that accounts for perturbations caused by a number of small solar system bodies. The eccentric and slightly inclined orbit has its aphelion inside the Main Belt and its perihelion between the orbits of Earth and Venus ($e = 0.5992$, $a = 2.132$ AU, $i = 6.960°$, $\Omega = 207.59011°$, $\omega = 51.06°$ J2000).

These data were entirely derived from the four images taken by the DFN observatories with the relative timing for trajectory analysis and the absolute timing for orbit calculation embedded by the de Briujn sequence timecode.

Fireball timing using de Bruijn timecodes   1681

FUTURE WORK

Extraction of fireball data points from images with timing is currently performed manually with the assistance of a custom software tool. It is the only time-consuming step remaining in the DFN's data pipeline that has not been automated. The development of image-processing software to handle this task is a priority. The problem is simple in the ideal case (a fast-moving fireball in the center of the lens with no blown highlights and minimal fragmentation and tail), but significantly more difficult when the fireball is partially obstructed, close to the extreme edge of the image, or contains bright flares. Once the data points can be precisely located automatically in most conditions, the automatic decoding of de Bruijn sequence timing is simple. Newer trajectory triangulation techniques that take advantage of the fact that each data point along the trajectory can be independently triangulated are currently being developed and will be tested against more traditional techniques that make the straight line assumption.

Other aspects warranting further study include the viability of larger ternary and quaternary alphabets (three or four different pulse lengths), higher sequence rates for imaging known meteor showers, real-time adjustment of the LC shutter in response to very bright fireballs to prevent sensor saturation, and the testing of other higher transmittance electro-optic shutter technologies. The method may also be useful in other fields where precise motion-time data are required such as spacecraft, fluid dynamics, and high speed tracking of other (nonmeteoroid) objects.

Editorial Handling—Dr. Josep M. Trigo-Rodríguez

REFERENCES

Andreić Ž. and Šegon D. 2010. The first year of Croatian Meteor Network. In *Proceedings of the International Meteor Conference 27th IMC, Sachticka, Slovakia, 2008* pp. 16–23.

Bland P. A., Bland P. A., Spurny P., Towner M. C., Bevan A. W., Singleton A. T., Bottke W. F. Jr ., Greenwood R. C., Chesley S. R., Shrbeny L., Borovicka J., Ceplecha Z., McClafferty T. P., Vaughan D., Benedix G. K., Deacon G., Howard K. T., Franchi I. A., and Hough R. M. 2009. An anomalous basaltic meteorite from the innermost Main Belt. *Science* 325:1525–1527.

Bland P., Spurny P., Bevan A. W. R., Howard K. T., Towner M. C., Benedix G. K., Greenwood R. C., Shrbený L., Franchi I. A., Deacon G., Borovicka J., Ceplecha Z., Vaughan D., and Hough R. M. 2012. The Australian Desert Fireball Network: A new era for planetary science. *Australian Journal of Earth Sciences* 59:177–187.

Bland P. A., Towner M. C., Sansom E. K., Devillepoix H., Howie R. M., Paxman J. P., Cupak M., Benedix G. K., Cox M. A., Jansen-Sturgeon T., Stuart D., and Strangway D. 2016. Fall and recovery of the Murrili meteorite, and an update on the desert fireball network (abstract #6265). *Meteoritics & Planetary Science* 51:A144–A692.

Borovička J. 1990. The comparison of two methods of determining meteor trajectories from photographs. *Bulletin of the Astronomical Institutes of Czechoslovakia* 41:391–396.

de Bruijn N. G. 1946. A combinatorial problem. *Koninklijke Nederlandse Akademie v. Wetenschappen* 49:758–764.

de Bruijn N. G. 1975. Acknowledgement of priority to C. Flye Sainte-Marie on the counting of circular arrangements of 2n zeros and ones that show each n-letter word exactly once. *EUT report. WSK, Deptartment of Mathematics and Computing Science, Volume 75-WSK-06*. Eindhoven, the Netherlands: Technische Hogeschool Eindhoven.

Ceplecha Z. 1957. Photographic Geminids 1955. *Bulletin of the Astronomical Institutes of Czechoslovakia* 8:51.

Ceplecha Z. 1987. Geometric, dynamic, orbital and photometric data on meteoroids from photographic fireball networks. *Bulletin of the Astronomical Institutes of Czechoslovakia* 38:222–234.

Ceplecha Z. and Rajchl J. 1965. Programme of fireball photography in Czechoslovakia. *Bulletin of the Astronomical Institutes of Czechoslovakia* 16:15.

Ceplecha Z., Rajchl J., and Sehnal L. 1959. Complete data on bright meteor 15761. *Bulletin of the Astronomical Institutes of Czechoslovakia* 10:204.

Compeau P. E., Pevzner P. A., and Tesler G. 2011. How to apply de Bruijn graphs to genome assembly. *Nature Biotechnology* 29:987–991.

Dyl K. A., Benedix G. K., Bland P. A., Friedrich J. M., Spurný P., Towner M. C., O'Keefe M. C., Howard K., Greenwood R., Macke R. J., Britt D. T., Halfpenny A., Thostenson J. O., Rudolph Rebecca A., Rivers M. L., and Bevan A. W. R. 2016. Characterization of Mason Gully (H5): The second recovered fall from the Desert Fireball Network. *Meteoritics & Planetary Science* 51:596–613.

Flye Sainte-Marie C. 1894. Solution to question nr. 48. *L'intermédiaire des Mathématiciens* 1:107–110.

Fredricksen H. 1982. A survey of full length nonlinear shift register cycle algorithms. *SIAM Review* 24:195–221.

Gritsevich M. and Koschny D. 2011. Constraining the luminous efficiency of meteors. *Icarus* 212:877–884.

Gritsevich M. Lyytinen E., Moilanen J., Kohout T., Dmitriev V., Lupovka V., Midtskogen V., Kruglikov N., Ischenko A., Yakovlev G., Grokhovsky V., Haloda J., Halodova P., Peltoniemi J., Aikkila A., Taavitsainen A., Lauanne J., Pekkola M., Kokko P., Lahtinen P., and Larionov M. 2014. First meteorite recovery based on observations by the Finnish Fireball Network. In *Proceedings of the*

International Meteor Conference, Giron, France, 18-21 September 2014, edited by Rault J.-L. and Roggemans P. International Meteor Organization.

Halliday I. 1973. Photographic fireball networks. In *Evolutionary and physical properties of meteoroids: The proceedings of the International Astronomical Union's colloquium # 13, held at the State University of New York, Albany, NY, on June 14-17, 1971*, edited by Hemenway C. L., Millman P. M. K., Cook A. F., and Union I. A. Washington, D.C.: Scientific and Technical Information Office, National Aeronautics and Space Administration. p. 1.

Halliday I., Blackwell A., and Griffin A. 1978. The Innisfree meteorite and the Canadian camera network. *Journal of the Royal Astronomical Society of Canada* 72:15–39.

Hamming R. W. 1950. Error detecting and error correcting codes. *Bell System Technical Journal* 29:147–160.

Howie R. M., Paxman J., Bland P. A., Towner M. C., Cupak M., Sansom E. K., and Devillepoix H. A. R. 2017. How to build a continental scale fireball camera network. *Experimental Astronomy*, doi:10.1007/s10686-017-9532-7

Jacchia L. G. and Whipple F. L. 1956. The Harvard photographic meteor programme. *Vistas in Astronomy* 2:982–994.

Jenniskens P., Gural P. S., Dynneson L., Grigsby B. J., Newman K. E., Borden M., Koop M., and Holman D. 2011. CAMS: Cameras for Allsky Meteor Surveillance to establish minor meteor showers. *Icarus* 216:40–61.

Kak S. 2000. An interesting combinatoric sutra. *Indian Journal of History of Science* 35:123–127.

LC-Tec. 2013. Fast optical shutter series, http://www.lc-tec.com/UserFiles/Products/FOS_Products-130121.pdf.

Levenshtein V. I. 1966. Binary codes capable of correcting deletions, insertions, and reversals. *Soviet Physics Doklady* 10:707–710.

McCrosky R. E. and Boeschenstein H. Jr. 1965. The prairie meteorite network. *Optical Engineering* 3:304127.

Mitchell C. J., Etzion T., and Paterson K. G. 1996. A method for constructing decodable de Bruijn sequences. *IEEE Transactions on Information Theory* 42:1472–1478.

Oberst J., Molau S., Heinlein D., Gritzner C., Schindler M., Spurný P., Ceplecha Z., Rendtel J., and Betlem H. 1998. The "European Fireball Network": Current status and future prospects. *Meteoritics & Planetary Science* 33:49–56.

Olech A., Zoladek P., Wisniewski M., Krasnowski M., Kwinta M., Fajfer T., Fietkiewicz K., Dorosz D., Kowalski L., Olejnik J., Mularczyk K., and Zloczewski K. 2006. Polish fireball network. In *Proceedings of the International Meteor Conference, 24th IMC, Oostmalle, Belgium 2005*, edited by Bastiaens L., Verbert J., Wislez J.-M., and Verbeeck C. International Meteor Organization. pp. 53–62.

Sansom E. K., Bland P., Paxman J., and Towner M. 2015. A novel approach to fireball modeling: The observable and the calculated. *Meteoritics & Planetary Science* 50:1423–1435.

Sansom E., Bland P., Rutten M., Paxman J., and Towner M. 2016. Filtering meteoroid flights using multiple unscented kalman filters. *The Astronomical Journal* 152:148.

Spurný P. 1997. Photographic monitoring of fireballs in Central Europe. In *Optical science, engineering and instrumentation'97*. San Diego, California: International Society for Optics and Photonics. pp. 144–155.

Spurný P., Borovička J., and Shrbený L. 2006. Automation of the Czech part of the European fireball network: Equipment, methods and first results. *Proceedings of the International Astronomical Union* 2:121–130.

Spurný P., Bland P. A., Shrbený L., Borovička J., Ceplecha Z., Singleton A., Bevan A. W. R., Vaughan D., Towner M. C., McClafferty T. P., Toumi R., and Deacon G. 2012a. The Bunburra Rockhole meteorite fall in SW Australia: Fireball trajectory, luminosity, dynamics, orbit, and impact position from photographic and photoelectric records. *Meteoritics & Planetary Science* 47:163–185.

Spurný P., Bland P., Borovička J., Towner M., Shrbený L., Bevan A. W., and Vaughan D. 2012b. The Mason Gully meteorite fall in SW Australia: Fireball trajectory, luminosity, dynamics, orbit and impact position from photographic records (abstract #6369). LPI Contributions 1677. Houston, Texas: Lunar and Planetary Institute.

Stein S. K. 2010. *Mathematics: The man-made universe*. New York: Dover Publications.

Trigo-Rodríguez J., Castro-Tirado A. J., Llorca J., Fabregat J., Martínez V. J., Reglero V., Jelínek M., Kubánek P., Mateo T., and Postigo A. D. U. 2005. The development of the Spanish Fireball Network using a new all-sky CCD system. *Earth, Moon, and Planets* 95:553–567.

Van Aardenne-Ehrenfest T. and de Bruijn N. G. 1951. Circuits and trees in oriented linear graphs. *Simon Stevin: Wis-en Natuurkundig Tijdschrift* 28:203.

CO-AUTHORED PAPER 6 – LIMITS ON RADIO EMISSION FROM METEORS USING THE MWA

*X. Zhang, P. Hancock, **H. A. R. Devillepoix**, R. B. Wayth, A. Beardsley, B. Crosse, D. Emrich, T. M. O. Franzen, B. M. Gaensler, L. Horsley, M. Johnston-Hollitt, D. L. Kaplan, D. Kenney, M. F. Morales, D. Pallot, K. Steele, S. J. Tingay, C. M. Trott, M. Walker, A. Williams, C. Wu, J. Ji, and Y. Ma*

Limits on radio emission from meteors using the MWA

X. Zhang,[1,2,3,4]★ P. Hancock,[3,4]★ H. A. R. Devillepoix,[5] R. B. Wayth,[3,4] A. Beardsley,[6]
B. Crosse,[3] D. Emrich,[3] T. M. O. Franzen,[3] B. M. Gaensler,[4,7,8] L. Horsley,[3]
M. Johnston-Hollitt,[3,9] D. L. Kaplan,[10] D. Kenney,[3] M. F. Morales,[11] D. Pallot,[12]
K. Steele,[3] S. J. Tingay,[3,4] C. M. Trott,[3,4,13] M. Walker,[3] A. Williams,[3] C. Wu,[12]
Jianghui Ji[1] and Yuehua Ma[1]

[1]*CAS Key Laboratory of Planetary Sciences, Purple Mountain Observatory, Chinese Academy of Sciences, Nanjing 210008, China*
[2]*University of Chinese Academy of Sciences, Beijing 100049, China*
[3]*International Centre for Radio Astronomy Research, Curtin University, Bentley, WA 6102, Australia*
[4]*ARC Centre of Excellence for All-Sky Astrophysics (CAASTRO), Sydney, NSW 2006, Australia*
[5]*School of Earth and Planetary Sciences, Curtin University, Bentley, WA 6102, Australia*
[6]*School of Earth and Space Exploration, Arizona State University, Tempe, AZ 85287, USA*
[7]*Sydney Institute for Astronomy, School of Physics, The University of Sydney, NSW 2006, Australia*
[8]*Dunlap Institute for Astronomy and Astrophysics, University of Toronto, ON M5S 3H4, Canada*
[9]*Peripety Scientific Ltd., PO Box 11355 Manners Street, Wellington 6142, New Zealand*
[10]*Department of Physics, University of Wisconsin–Milwaukee, Milwaukee, WI 53201, USA*
[11]*Department of Physics, University of Washington, Seattle, WA 98195, USA*
[12]*International Centre for Radio Astronomy Research, University of Western Australia, Crawley, WA 6009, Australia*
[13]*ARC Centre of Excellence for All Sky Astrophysics in 3 Dimensions (ASTRO 3D), Bentley, W 6102, Australia*

ABSTRACT

Recently, low-frequency, broad-band radio emission has been observed accompanying bright meteors by the Long Wavelength Array (LWA). The broad-band spectra between 20 and 60 MHz were captured for several events, while the spectral index (dependence of flux density on frequency, with $S_\nu \propto \nu^\alpha$) was estimated to be -4 ± 1 during the peak of meteor afterglows. Here we present a survey of meteor emission and other transient events using the Murchison Wide Field Array (MWA) at 72–103 MHz. In our 322 h survey, down to a 5σ detection threshold of 3.5 Jy beam^{-1}, no transient candidates were identified as intrinsic emission from meteors. We derived an upper limit of -3.7 (95 per cent confidence limit) on the spectral index in our frequency range. We also report detections of other transient events, such as reflected FM broadcast signals from small satellites, conclusively demonstrating the ability of the MWA to detect and track space debris on scales as small as 0.1 m in low Earth orbits.

Key words: plasmas – instrumentation: interferometers – meteorites, meteors, meteoroids.

1 INTRODUCTION

When a rocky or a metallic object (meteoroid) plunges into the atmosphere and is heated to incandescence, a meteor can be observed. Very bright meteors are referred to as fireballs. The meteor is heated by radiation from the atmospheric shock front that it produces (De Pater & Lissauer 2015), causing iron and silicates to melt and vapourize. The vapourized atoms are ionized in collisions with air atoms, producing a cloud of quasi-neutral plasma, which is referred to as the ionized trail (Dokuchaev 1960). The ionized trails are known to reflect radio waves, and radio echoes are used to measure the orbits of meteors and radiants of meteor showers (Ceplecha et al. 1998).

Detailed investigations of radio emission from meteors began in the 1950s, when astronomers proposed that plasma resonance in meteor trails might produce radio noise (Hawkins 1958). Detections of low-frequency emission were reported to be coincident with large meteors in the past several decades (Beech, Brown & Jones 1995; Guha et al. 2012). Sometimes bright meteors were observed accompanied by acoustic propagation, which might be caused by radio emission converting into electrophonic sounds (Keay 1980, 1992; Keay & Ceplecha 1994).

Recently, scientists working with the LWA (Taylor et al. 2012; Ellingson et al. 2013a) made some interesting discoveries of radio emission from meteors. In 2014, two transient events were reported

5168   *X. Zhang et al.*

in a search for prompt low-frequency emission from gamma-ray bursts (GRBs) with the first station of the Long Wavelength Array (LWA1; Obenberger et al. 2014a). The LWA1 was operating in the narrow transient buffer mode, with a usable bandwidth of 75 kHz tunable to any centre frequency between 10 and 88 MHz. These two events lasted for 75 and 100 s, respectively at 37.9 and 29.9 MHz. They were not coincident with any known GRBs. Further observations revealed more similar long-duration (tens of seconds) transients. Many of these transients were coincident with optical meteors, both spatially and temporally. Between 2014 April and 2016 April, a total of 20 000 h data were collected, in which 154 radio transients were detected (Obenberger et al. 2016a). Optical meteor counterparts were coincident with 44 of these radio transients.

The transients correlated with meteors are different from the well-studied radio echoes from meteor trails (Obenberger et al. 2014b). First, most radio transmitters are polarized, thus the reflections from meteor trails are also polarized (Close et al. 2011; Helmboldt et al. 2014). However, no significant amount of polarization has shown up in these transient cases, either linear or circular. Secondly, transmitters often broadcast in very narrow radio bands, and spectral lines are visible in meteor reflection, but spectral features are not found anywhere in the LWA1 transients. Thirdly, power profiles of these transients resemble each other, but are quite different from meteor reflections. All these differences led Obenberger et al. (2014b) to suggest that meteors emit a previously undiscovered low-frequency, non-thermal pulse.

Broad-band measurements were also made with the beamformer mode of the LWA1 in order to obtain the dynamic spectra of the transient events (Obenberger et al. 2016b). Three beams were formed and pointed around zenith at azimuths of $60°$, $180°$, and $240°$, all with elevations of $87°$. The field of view for each beam is $\sim$50 deg^2. Compared with the all-sky imager mode, the beamformer mode's field of view is much smaller, leading to fewer detections. The broad-band spectra of four events were captured between 22.0 and 55.0 MHz. The frequency-dependent flux densities of these events were fit to a power law, and the spectral indices were found to be time variable, with the spectrum steepening overtime.

Obenberger et al. (2016b) also discussed the potential for other observatories to measure meteor spectra, including the Murchison Wide Field Array (MWA; Tingay et al. 2013a) in Australia, the Amsterdam-ASTRON Radio Transients Facility and Analysis Center (AARTFAAC; Prasad et al. 2014) based on the Low-Frequency Array (LOFAR; Van Haarlem et al. 2013) in the Netherlands, and two additional LWA stations. It was concluded that the MWA, with its exceptionally high sensitivity, had the best opportunity to test the high-frequency predictions of meteor radio afterglows. However, there are several factors that might prevent the MWA from detecting radio emission from meteors: the high spatial resolution of the MWA will lead to a drop in peak flux density, thus the meteors might still be undetectable for the MWA; the uncertain and time variable spectral index may cause a lower flux density than predicted.

Based on the research above, we carried out a 322 h survey for meteor afterglows with the MWA. Our work aims to detect the radio afterglow from ionized meteor trails at higher frequencies and put some limits on the meteor radiation spectra.

In this paper, we begin in Section 2 with a description of our observations, both radio and optical. The data reduction process is given in Section 3, including pre-processing, imaging, and source finding. A brief description of results is given in Section 4. In Section 5, we discuss the relation between meteor event rates and flux density, followed by an estimated upper limit on meteor radiation spectra. Section 5 also contains some other transient events detected in our survey and a discussion of future work. The conclusion is presented in Section 6.

2 OBSERVATIONS

Both radio and optical observations were carried out in this work. Radio observations were made by the MWA, while optical observations were performed by the Desert Fireball Network (DFN; Bland et al. 2012). The implementation of optical observations allows us to compare radio transient events with optical meteors and investigate possible emission from meteors.

2.1 Radio observations using the MWA

The MWA is one of the Square Kilometre Array Precursor telescopes. It is located at the Murchison Radio-astronomy Observatory in Western Australia, where the Radio Frequency Interference (RFI) is extremely low (Offringa et al. 2015). The MWA consists of 128 aperture array antennas (referred to as tiles) distributed over a $\sim$3 km diameter area. It is optimized for the 80–300 MHz frequency range, with a processed bandwidth of 30.72 MHz for both linear polarizations (Tingay et al. 2013a).

In this project, radio observations were carried out under two modes, one targeted and another opportunistic. For both observations, all the tiles of the MWA were pointed to the zenith, and the lowest band of the MWA (72.3–103.0 MHz) was used. The choice of observational band was based on two reasons: first, previously detected radio emission from meteors was below 60 MHz; secondly, the chosen band partly overlapped with the FM broadcast band in Australia (87.5–108 MHz), making it possible for us to observe reflection and intrinsic emission from meteors at the same time.

Under the targeted mode, we observed several known meteor showers listed in the International Meteor Organization (IMO) Meteor shower calendar (Rendtel, Ogawa & Sugimoto 2017), which are given in Table 1. The α-Centaurids, γ-Normids, π-Puppids, and η-Aquariids showers were observed because they all have radiants in the Southern hemisphere. We observed each of these showers for 2 h around midnight. The Geminids shower, however, was chosen due to its especially high zenithal hourly rate (ZHR). We observed the Geminids three times – in 2014, 2015, and 2016. Each time the observation lasted about 9 h, from dusk to dawn.

For all the meteor showers listed in Table 1, a series of 112 s observations were obtained with a temporal resolution of 0.5 s, which is the highest temporal resolution of the MWA. The frequency resolution was 40 kHz. The drift of the sky during each 112 s scan was accounted for during imaging processing by fixing the phase centre for each observation to be at a certain RA/Dec.

Since we were not able to predict when and where meteors occur, we also performed some opportunistic observations when the MWA was not occupied by other projects. An example of the opportunistic observations is the filling observations carried out in 2016 March, when some of the MWA tiles failed to point due to lightning damage. Since these tiles pointed up by default, we pointed all tiles to the zenith and observed the sky with the entire array. The filling observations were carried out with a duration of 232 s and a temporal resolution of 2 s. A list of the opportunistic observations is given in Table 2. The total radio observational time from both dedicated and opportunistic campaigns adds up to approximately 322 h.

Table 1. Meteor showers observed by the MWA. ZHR stands for zenithal hourly rate, for a calculated maximum number of meteors per hour, an ideal observer would see in perfectly clear skies with the shower radiant overhead. Velocities listed in this table are apparent meteoric velocities.

Date	Name	Total observation length (h)	Radiant (RA, Dec.)	ZHR	Velocity in km s^{-1}
2014–2016 December 14	Geminids	28	112°, +30°	120	35
2016 Feburary 8	α-Centaurids	2	210°, −59°	6	56
2016 March 14	γ-Normids	2	239°, −50°	6	56
2016 April 23	π-Puppids	2	110°, −45°	Variable	18
2016 May 5	η-Aquariids	2	338°, −01°	40	66

Table 2. Opportunistic observations, performed when the MWA was not occupied by other projects.

Date	Total observation length (h)
2015 March 14–22	15
2016 March 17–29	103
2016 April 2–14	49
2016 May 1–3	22
2016 May 10–June 1	93
2016 September 8–9	4

2.2 Optical observations using the DFN

The DFN is a camera network with dozens of cameras in Western Australia and South Australia. It is designed to detect meteors and triangulate their trajectories, in order to recover the meteorite (debris of a meteor, which impacts the Earth's surface) and trace the meteor back to its origin. Since 2015 September, some DFN cameras have been installed at Wooleen station, 70 km away from the MWA, thus these cameras share a significant portion of the sky with the MWA. For our 322 h radio observations, 297 h were also covered by optical observations.

The Wooleen DFN node includes a standard meteor camera, as well as a specially designed camera for astronomical work (Howie et al. 2017). Both cameras are pointed to the zenith. The standard meteor camera has a fish-eye lens that can see the entire sky. The limiting magnitude for a meteor to be detected by the camera is about 0.5 mag. A modulated liquid crystal shutter is used to determine the angular speed of meteors, which leads to gaps in meteor trails in the images (see Fig. 1). The standard meteor camera is operated autonomously, taking images with a 29 s exposure time when the Sun is down, and the sky is clear. The astronomical camera, on the other hand, has a much improved sensitivity with a smaller field of view (80° × 100°). The exposure duration of the astronomical camera is 13 s.

3 DATA REDUCTION

For radio observations, the data reduction pipeline is composed of four steps: pre-processing via COTTER (Offringa et al. 2015), calibration using bright radio sources, imaging with WSCLEAN (Offringa et al. 2014), and source finding via AEGEAN (Hancock et al. 2012; Hancock, Trott & Hurley-Walker 2018). However, in our 322 h observation, not all the data were of good quality. Therefore, only 308 h of observational data were processed with the pipeline and used for the analysis.

The optical data were captured as an independent verification of the presence of a meteor. These images were used in their original form (coloured JPEGs). Recently a calibration scheme has been
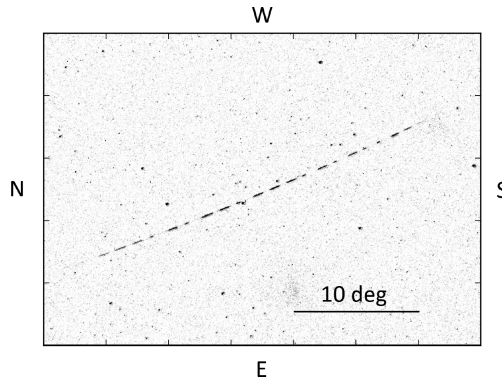

Figure 1. Optical image of a meteor captured by the DFN camera at Wooleen station, on 2015 December 14. The exposure duration was 25 s. The gaps in the meteor trail were caused by the coded shutter to measure its apparent speed.

created to correct astrometry and photometry of these images, but such calibraion was not required in this project.

3.1 Pre-processing and calibration

We pre-processed the raw visibility data through the MWA pre-processing pipeline, COTTER, to average the data and convert it into Common Astronomy Software Applications (CASA; McMullin et al. 2007) measurement set format. COTTER can also flag RFI with a c++ library provided by the RFI detector, AOFLAGGER (Offringa et al. 2010; Offringa, Van de Gronde & Roerdink 2012).

For each observation, we made two measurement sets with 8 s integration: we flagged RFI in one measurement set (referred to as *emission* data), and kept RFI in another (referred to as *reflection* data). Since ionized meteor trails are known to reflect RFI, the emission data can show intrinsic emission from meteors, while the reflection data are able to reveal reflected radio signal from meteors. However, the RFI flagging process is not able to exclude all the RFI in the FM band, so we only used emission data outside the FM band to make emission images, as described in Section 3.2.

After pre-processing, the measurement sets were calibrated using bright point sources with well-modelled emission for the MWA. Based on the models of the calibrators, we derived time-independent, frequency-dependent phase, and amplitude calibration solutions, which were applied to the measurement sets.

Calibrators were observed for 112 s at the phase centre of the telescope, before or after our scheduled observations for one night.

5170   *X. Zhang et al.*

Table 3. The WSCLEAN settings used to image the meteor observations. All other settings were set to default.

Setting	Value
UV range (λ)	<32
Channel range for emission images (MHz)	72.3–86.4
Channel range for reflection images (MHz)	72.3–103.0
Image integration time (s)	8
Maximum number of clean iterations	4000
Size of image (pixel)	240
Size of one pixel (arcmin)	20
Briggs weighting	0.5
Polarization	XX, YY

The quality of drift scan data is always limited by the ionosphere, so in calm conditions a single calibration solution can be applied to all the data from the same night (Hurley-Walker et al. 2014). The most commonly used calibrator was Hydra A. For several nights without useful calibrator observations, we either used a common observation in which a bright radio source was close to the zenith, or used catalogued radio resources from the GaLactic and Extragalactic All-sky MWA survey (GLEAM; Wayth et al. 2015; Hurley-Walker et al. 2017) for calibration.

3.2 Imaging

The calibrated measurement sets were imaged and deconvolved using WSCLEAN (Offringa et al. 2014), a fast wide-field imager for radio astronomy. For each observation, the reflection and emission measurement sets were separately made into 8 s integrated *reflection* and *emission* all-sky images. In this process, only short baselines were used, and only frequency channels below the FM band were used for the emission images. Precise limits on baselines and frequency channels were decided via a few tests with a simulated meteor, which are described in Section 3.3. The detailed settings of WSCLEAN are listed in Table 3.

The selection of image integration time (8 s) was based on the detected meteor dynamic spectra from Obenberger et al. (2015). Meteor emission can last for more than 1 min at 20–40 MHz, but the spectral index drops significantly after the first 20 s. Thus meteor emission at MWA frequencies may be shorter in duration.

In order to exclude background sources and reduce noise, we subtracted adjacent 8 s snapshots to make difference images, as shown in Fig. 2. Dirty (un-deconvolved) images were used for subtraction, because cleaning may create artefacts in difference images. In the imaging process, the phase centre of each observation was fixed in RA/Dec., so sky rotation did not introduce artefacts into the difference images.

3.3 Baseline and channel limits in imaging process

There are two reasons why we only have used short baselines. First, like most radio telescopes, the MWA is focused in the far field, since most objects included in the MWA science are effectively at an infinite distance from the telescope. The MWA correlator assumes incoming waves from these sources as plane waves. However, for objects close to the telescope (in the near field), the incoming waves are spherical rather than planar. In antenna design, the widely accepted transition between near field and far field is the Fraunhofer distance $d = 2D^2/\lambda$, where D is the diameter of the telescope and λ is the wavelength. For the MWA with its longest baselines at 80 MHz, the Fraunhofer distance is 4800 km. Since the typical height of meteors is 80–120 km, using the longest baselines will put meteors in the near field. In order to place the meteors in the far field at 80 km, we can only use baselines shorter than 387 m.

Another reason to use the short baselines is to improve the detectability for meteors. A typical meteor trail is tens of kilometres long, several metres wide, and about 100 km above the ground. In MWA observational images, that corresponds to an extended source which is tens of degrees in length and less than 1 arcmin in width, we excluded baselines longer than 120 m to get a lower spatial resolution (2.15°) and higher peak flux density for meteors. Since the MWA has a 100 m diameter dense core containing 50 tiles (Tingay et al. 2013a), excluding these baselines increases the thermal noise by just 16 per cent.

We limited the channel ranges (72.3–86.4 MHz) for emission images mostly due to RFI contamination, since our observational band (72.3–103 MHz) overlapped with the FM broadcasting band in Australia (87.5–108 MHz). Although AOFLAGGER was used to flag RFI, a small amount of RFI was still left within the FM band. Using the channels below, the FM band also brought another advantage: the meteor emission is much brighter at lower frequencies, thus only using the lower band can improve the detectability of meteors.

In order to determine the precise baseline and channel limits to be used in the imaging process, we did tests by adding a simulated meteor to the visibility data of a blank sky observation, and made difference emission images with several baseline and channel range settings.

According to the four meteor events described by Obenberger et al. (2016b), the spectrum of meteors follows a power law between 20 and 60 MHz. The power law is given by $S \propto \nu^\alpha$, where S is the flux density, ν is the frequency, and α is the spectral index. During the peak of the afterglows, $\alpha \sim -4 \pm 1$.

Here we used one of the four meteors given in Obenberger et al. (2016b) for extrapolation. This meteor belongs to a group of faint/common meteors occurring 130 times yr^{-1} π sr^{-1}. It was detected as an unresolved source by the LWA1 at 25.6 MHz, with a flux density of 1800 Jy. Since the MWA has a higher spatial resolution than the LWA1, and the width of a meteor trail is much smaller than the MWA spatial resolution, we assumed that the simulated meteor was extended in 1D in MWA images, along the trail.

Fig. 3 shows the extrapolated peak flux densities of the meteor, assuming different spectral indices. Also shown are comparison plots of the 5σ sensitivity of the MWA (short baselines, 8 s integration and 12 MHz bandwidth). The MWA values were obtained from MWA observational images and data from Sutinjo et al. (2015). As illustrated in Fig. 3, it is estimated that in 72–103 MHz band, the MWA is capable of detecting radio emission from meteors when $\alpha \geq -4$, but it is not able to detect meteors when $\alpha \leq 5$.

We used CASA to put the simulated meteor into the visibility data, and made difference emission images with it (see Fig. 4). The spectral index adopted was −4. To get the best detectability, we made images with baseline upper limits from 30 to 600 m, and top channel limits from 74.9 to 103.2 MHz. The relation between the signal-to-noise ratio (SNR) and the limits is given in Figs 5 and 6. According to these figures, the SNR reaches a peak near channel range 72.3–87.7 MHz and baseline length upper limit 75 m. However, considering other factors such as overlapping with the FM band, sensitivity, and spatial resolution, the channel range was set to 72.3–86.4 MHz, and the baseline length upper limit was set to 120 m (or 32 λ at 80 MHz).
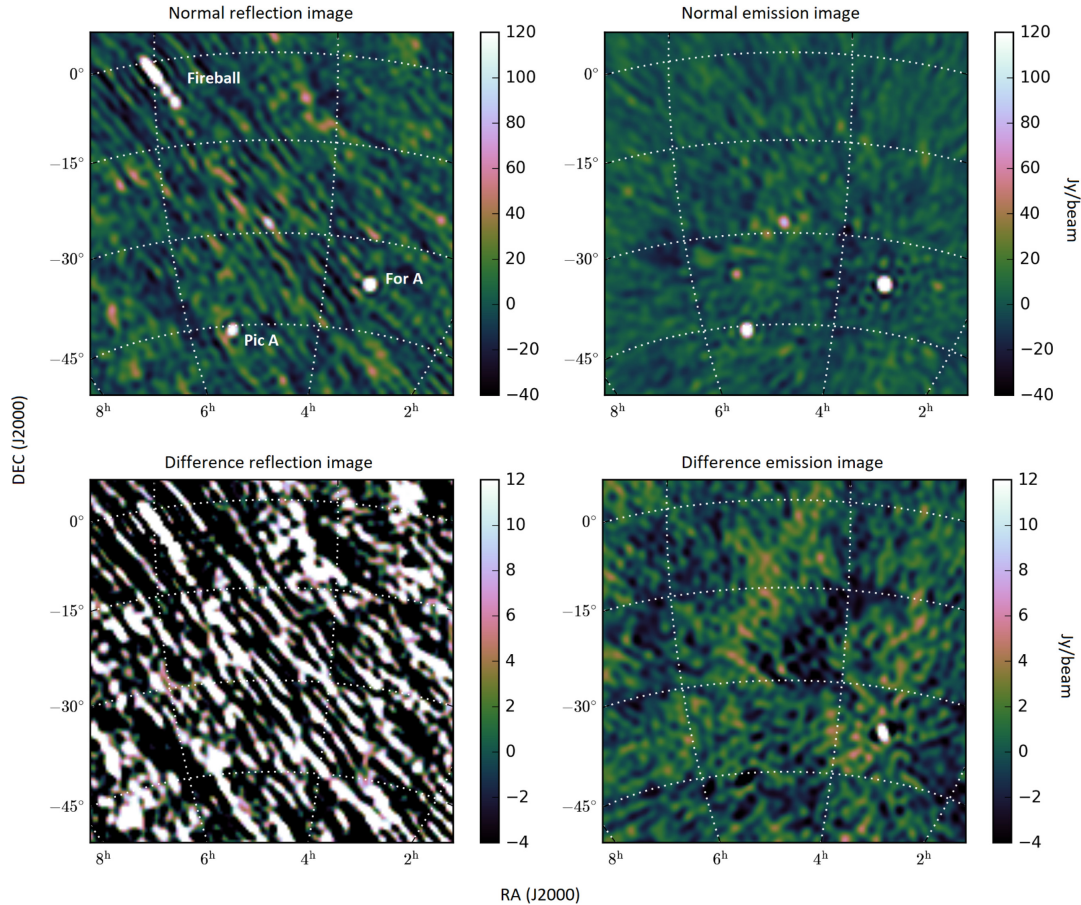
Figure 2. MWA radio images of an 8 s duration, during which a meteor occurred. Top-left: normal reflection image, showing the radio sky with RFI. Background radio sources such as Fornax A and Pictor A can be seen in this image, together with reflected RFI from the ionized meteor trail. Top-right: normal emission image, showing the sky without RFI. This image contains background sources but not reflection from the meteor. Bottom-left: difference reflection image, illustrating a temporal variation in the normal reflection image. Bottom-right: difference emission image, showing a temporal variation in the normal emission image. This image has capability to reveal intrinsic emission from meteors, but no emission is found for the particular meteor event. Pictor A is removed from this image, while Fornax A remains due to scintillation or instrumental effects. Normal images (top) and difference images (bottom) do not share the same colour scale. Compared with *reflection* images (left), *emission* images (right) are based on observational data below FM band, with RFI flagged.

3.4 Source finding

The source finding is done by AEGEAN (Hancock et al. 2012; Hancock et al. 2018), which is designed to detect and characterize sources within radio images; it works by grouping pixels above a given threshold into contiguous groups called islands. AEGEAN also includes a background and noise estimator (BANE) which provides a method for creating background and noise images. In our data processing pipeline, we ran both BANE and AEGEAN on the difference emission images to extract meteors. BANE first formed detailed background maps for the images, then AEGEAN searched for pixels above the 5σ level and grouped them together with nearby pixels above 3σ level into 'islands'. The outputs from AEGEAN included sizes of the islands and their integrated flux densities.

AEGEAN found approximately 2×10^5 islands in 1.2×10^5 images, so we did some selection based on the sizes of meteor events observed by the LWA1 and the projection method. Islands with a

maximum angular size larger than $5°$ and pixel number over 10 were selected to form a list of meteor candidates. The process was able to detect our simulated meteor.

4 RESULTS

Using the data reduction pipeline described above, 5372 events were selected as meteor candidates in our 322 h survey. However, most of them can be attributed to variations in bright radio sources caused by instrumental and/or ionospheric effects. No candidate was confirmed to be a meteor.

We followed a three-step method to check if a candidate was a meteor. First, we compared the candidate with its corresponding normal emission image. If the candidate was coincident with a bright radio source in the normal emission image (like the Fornax A event in Fig. 2), we believe that the candidate was related to the bright
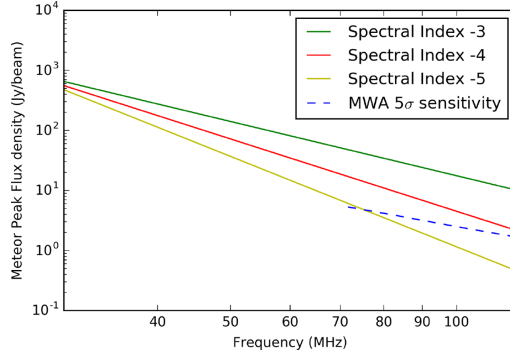
5172   *X. Zhang et al.*

Figure 3. Estimated peak flux densities of the faint/common meteor as observed by the MWA. The solid lines illustrate broad-band spectra of meteors with different spectral indices, while the blue dashed line describes the 5σ sensitivity of the MWA in our observations.
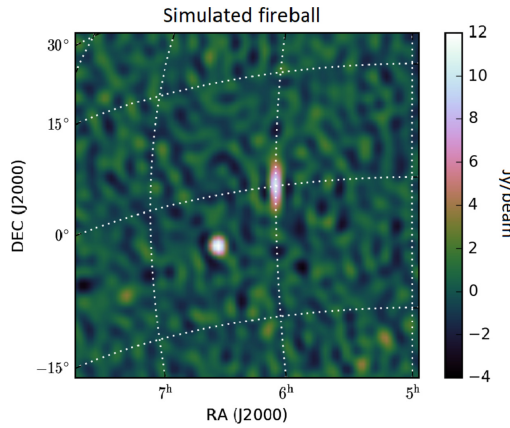

Figure 4. Simulated meteor on a difference image. The spectral index was set to -4, the length set to $4°$ as a point source observed by the LWA1, while the width of meteor set to 2 arcsec. The meteor trail emission was simulated with Gaussian distribution.
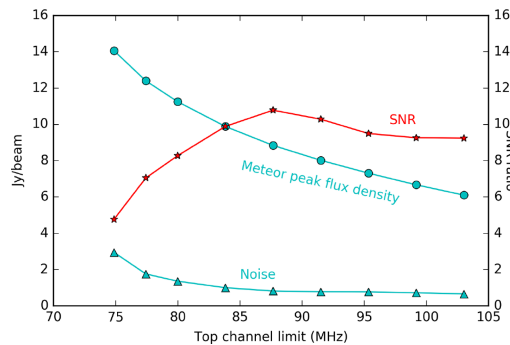

Figure 5. Relation between top channel limit and SNR for the simulated meteor when baseline limit was set to 120 m. The bottom channel is 72.3 MHz in all the tests.
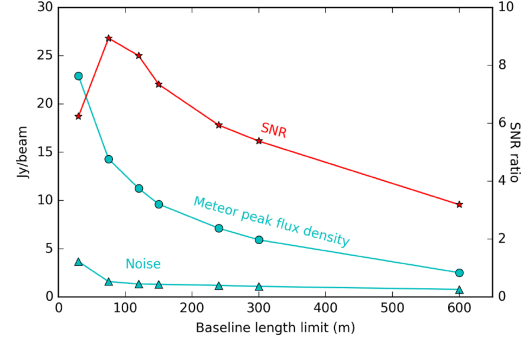

Figure 6. Relation between baseline length limit and SNR for the simulated meteor when top channel was set to 80 MHz.

radio source, i.e. not a meteor. In this way, we excluded the majority of our candidates. Secondly, candidates not related to bright sources in normal images were compared with a subset (above 10 Jy) of the GLEAM catalogue. If a candidate was coincident with a radio source in the catalogue, the candidate would be excluded. Thirdly, for the few candidates that could not be attributed to variabilities in bright radio sources, we checked corresponding optical images from DFN and the reflection images. If a candidate was consistent with an optical meteor or a reflection event, both spatially and temporally, it would be considered a probable event for intrinsic radio emission. However, none of the candidates were consistent with any optical meteors or reflection events.

5 DISCUSSION

When an experiment returns a null result, there are two possibilities: (1) no events were observed because no events occurred and (2) events occurred, but noise or timing prevented detection. In other words, the null result can be attributed to event rate density, flux density, or duration.

Here we provide an analysis of the sensitivity limits of our observational data and interpret the null result in terms of the physical parameters of intrinsic emission from meteors. The analysis is based on a framework by Trott et al. (2013), which was designed to determine constraints on the detection rate of fast transient events. This framework takes into account the primary beam shape, frequency effects, and detection efficiency, resulting in the 2D probability distributions in the sensitivity-rate parameter space.

5.1 Minimum detectable flux density

When meteor emission events do occur, detection is limited by the MWA beam pattern (Sokolowski 2017) and sampling time-scale. We take an unresolved meteor event for example. If this event is detected, its signal P_S must exceed a threshold, given by the noise P_N and some SNR value, C.

$$P_S > C P_N. \tag{1}$$

When an array is used to detect radio signals, P_S can be given as

$$P_S = \frac{1}{\Delta\nu} \int_{\Delta\nu} B(\theta) P(\nu) d\nu, \tag{2}$$

where $\Delta\nu$ is the bandwidth, $B(\theta)$ is the beam model (see Fig. 7), P_ν is the frequency-dependent flux density of the radio source. We
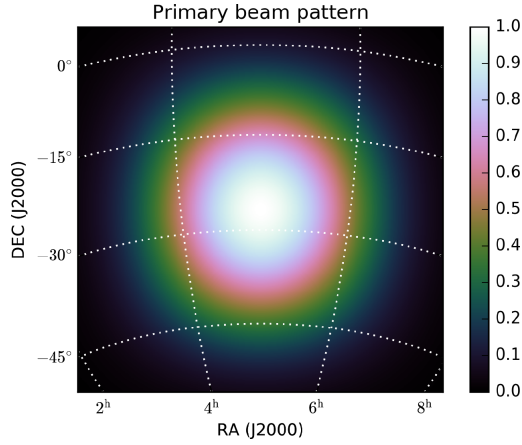
Figure 7. Beam model of the MWA at 80 MHz. Antennas pointed to zenith.
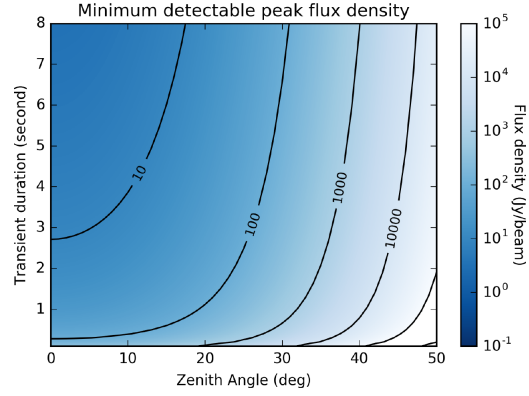

Figure 8. Minimum peak flux density required for meteor event detection within our observations. Detection is limited by the MWA beam model and the meteor event duration. The sampling time-scale is 8 s. Events with durations longer than 8 s have the same minimum detectable peak flux density as 8 s events.

assume that the dependence of beam model on frequency can be neglected in our channel range. The noise P_N can always be given from the system equivalent flux density:

$$P_N = \frac{\text{SEFD}}{\sqrt{n_p N_{ant}(N_{ant} - 1)\Delta\nu\Delta t_s}}, \quad (3)$$

where n_p is the number of polarizations, N_{ant} is the number of antennas within the MWA, and Δt_s is the sampling time-scale.

It is assumed that the flux density of a meteor can be represented by a power law in frequency, so we have $P(\nu) = S_0(\nu/\nu_0)^\alpha$, where S_0 is the flux density at the reference frequency, ν_0.

For some short-duration meteor events, the temporal sampling time may exceed the duration of meteor emission, thus the radio signal received suffers a loss in flux density due to the averaging of the signal over time. Here we introduce the Duration Threshold factor η, which is defined as

$$\eta = \min(\Delta t_{act}/\Delta t_s, 1), \quad (4)$$

where Δt_{act} is the duration of meteor emission and Δt_s is the sampling time. Then we have

$$S_{measure} \approx \eta S_{act} = \begin{cases} S_{act}, & \text{for} \quad \Delta t_{act} \geqslant \Delta t_s \\ \frac{\Delta t_{act}}{\Delta t_s} S_{act}, & \text{for} \quad \Delta t_{act} < \Delta t_s, \end{cases} \quad (5)$$

where $S_{measure}$ is the measured signal flux density and S_{act} is the original signal flux density.

Thus the minimum detectable original flux density at angle θ from beam centre, $S_{min}(\theta)$, can be given by

$$S_{min}(\theta) = \frac{C}{\eta} P_N \left(\frac{1}{\Delta\nu} \int_{\Delta\nu} B(\theta)(\nu/\nu_0)^\alpha d\nu \right)^{-1}. \quad (6)$$

Emission from meteors can be resolved as observed by the MWA, so detection is limited by the peak flux density. We estimated the minimum detectable peak flux density in our observations, which is illustrated in Fig. 8.

5.2 Probability of detection

However, the detected flux density of a radio source is composed of its true flux density S and noise. The noise follows a Gaussian distribution, with mean value $\mu = 0$ and variance σ^2. Thus the

probability for a radio source with true flux density S to be detected above the threshold, $C\sigma$, is given by the cumulative distribution function:

$$P(S > C\sigma) = \int_{C\sigma}^{\infty} \mathcal{N}(S, \sigma^2)dS = \frac{1}{2} + \frac{1}{2}\text{erf}\left(\frac{S - C\sigma}{\sqrt{2}\sigma}\right), \quad (7)$$

where $\mathcal{N}(S, \sigma^2)$ denotes the Gaussian distribution and erf is the error function. The probability that an event is not detected because of noise is the complementary function, $1 - P(S > C\sigma)$.

We assume that meteor afterglows are randomly distributed (both temporally and spatially) with a mean frequency of occurrence. Then the probability that k events occur with an expectation of λ follows the Poisson distribution:

$$P(k; \lambda) = e^{-\lambda}\frac{\lambda^k}{k!}. \quad (8)$$

The probability that at least one event should be detected is

$$P = 1 - P(0; \lambda) = 1 - e^{-\lambda}, \quad (9)$$

Fig. 9 shows the probability of detecting at least one meteor in our observations, given expected event density and event strength. The 'event strength' is defined as

$$S_{act}\eta\Delta t_s = \begin{cases} S_{act}\Delta t_s, & \text{for} \quad \Delta t_{act} \geqslant \Delta t_s \\ S_{act}\Delta t_{act}, & \text{for} \quad \Delta t_{act} < \Delta t_s, \end{cases} \quad (10)$$

to cover events both shorter and longer than the sampling time. The total effective observational time is 308 h, and the frequency range is 72–86 MHz. The rise of meteor event numbers in our observations caused by meteor showers is included.

In Fig. 9, we indicate three LWA1 events with event densities 15, 40, and 130 times $\text{yr}^{-1} \pi \text{ sr}^{-1}$, as described in Obenberger et al. (2016b). A spectral index of -4 is used to extrapolate flux densities of these events to the MWA frequency range. As illustrated in Fig. 9, the probabilities for the MWA to detect these three events in our observations are less than 50 per cent.

5.3 An upper limit on meteor spectral index

According to Obenberger et al. (2016b), the luminosity function of meteor emission resembles a power law, with higher event rates for
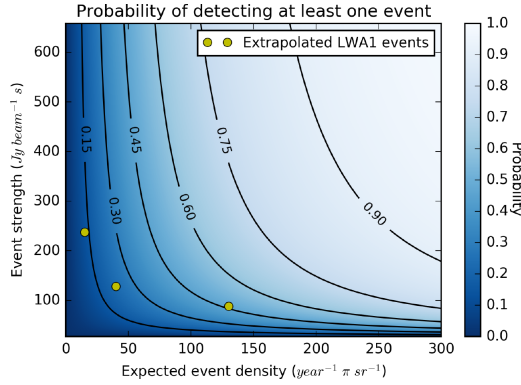
5174   *X. Zhang et al.*

Figure 9. Probability of detecting at least one meteor in our observation. Yellow circles indicate the extrapolated event strength (equation 10) of three *LWA1* events (Obenberger et al. 2016b) at MWA frequencies, assuming a spectral index of −4. Durations of the three LWA1 events are about 40 s at LWA1 band.

fainter meteors. Under the assumption of a spectral index of −4, the three LWA1 events would be above 10σ at MWA frequencies. Under this assumption, fainter meteors with higher event rates above the 5σ detection threshold of the MWA should be abundant. Given we make no such 5σ detections, we give an estimated relation between meteor flux density and event rates, based on which we can derive an upper limit on the spectral index of meteor emission, relevant for our frequency range.

We start with the radio magnitude of meteors, which is defined by the ionization produced per unit length of the meteor path (without any reference to visual luminosity). An approximate radio magnitude relation is deduced by McKinley (1961):

$$M_r = 40 - 2.5 \log_{10} q, \tag{11}$$

where M_r is the radio magnitude of a meteor and q is the electron line density.

According to previous radio observations by radar, there is an empirical relation between meteor radio magnitude and meteor numbers (McKinley 1961):

$$\log_{10} N(< M_r) \simeq 16 - 1.34 \log_{10} q, \tag{12}$$

where $N(< M_r)$ is the total number of meteors of radio magnitude M_r and brighter encountered by the Earth's atmosphere in a 24 h period.

The mechanism for intrinsic radio emission from meteors is still under discussion, with one possible explanation being radiation of Langmuir waves (Obenberger et al. 2015). Thus we assume that the peak flux density of meteor emission is proportional to the peak electron line density, i.e. $S \propto q$ (the width of ionized meteor trails can be neglected due to the low spatial resolution of the MWA images made in this project). By differentiating the cumulative number of meteors we have

$$dN_S \propto S^{-2.34}, \tag{13}$$

where dN_S is the number of meteors between peak flux density S and $S + dS$. Since all the meteor events observed by the LWA1 have durations longer than our sampling time, and significant drops in meteor spectral indices occur after the first 20 s for the three typical events, we estimate that the durations for most meteors detectable
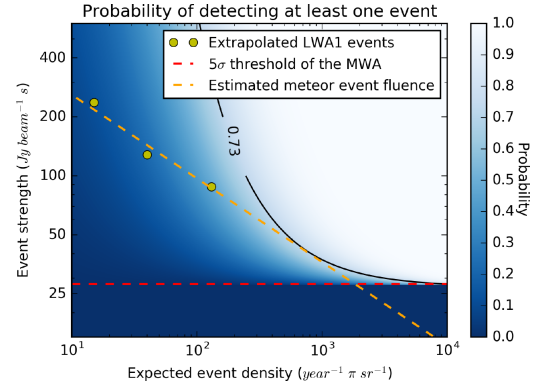

Figure 10. Estimated luminosity function of intrinsic radio emission from meteors. Yellow circles are the extrapolated LWA1 events (Obenberger et al. 2016b) at MWA frequencies, under an assumed spectral index of −4; dashed orange line represents the estimated relation between meteor event strength and event density, as given in equation (13); dashed red line represents the 5σ threshold of the MWA.

Table 4. Parameters of the two satellites observed by the MWA. RCS is short for Radar cross-section.

Parameters	*Duchifat-1*	*Alouette-2*
Period (min)	96.65	117.52
Inclination (deg)	97.91	79.80
Apogee (km)	608	2637
Perigee (km)	588	502
RCS size range (m^2)	<0.1	$0.1 < RCS < 1.0$

to the MWA also exceed the sampling time, i.e. $\eta = 1$. Thus meteor event strength is proportional to peak flux density in our project.

Based on the three meteor events and equation (13), we give an estimated relation between event strength and expected event density, as illustrated in Fig. 10. It is shown that in our survey, the probability of detecting a fainter event is higher than that of the three LWA1 events, but not exceeding 73 per cent.

However, the extrapolated LWA1 events and the estimated meteor strength–rate relation given in Fig. 10 are derived using spectral index −4. If we use spectral index −3, then the probability for the MWA to detect faint meteors in our survey exceeds 95 per cent (see Fig. 11). At spectral index −3.7, the probability of detecting at least one event in our observations is 95 per cent. In other words, we give an estimated meteor spectral index upper limit of −3.7 with 95 per cent confidence.

5.4 Other transient events

Besides meteor reflections and scintillations, some other transient events were also captured in the FM band. Previously, McKinley et al. (2012) and Tingay et al. (2013b) have detected reflected FM signals from the Moon and the International Space Station, respectively with the MWA.

Two of the detected transient events found in our data lasted for minutes and moved tens of degrees across the sky. We overplotted radio images with the positions of satellites and confirmed that these two events were caused by two satellites, *Duchifat-1* and *Alouette-2*. The orbital parameters of the satellites, based on the

Table 5. Parameters of contemporary radio transient detection arrays. The parameters are estimated at 80 MHz for the MWA, 60 MHz for AARTFAAC, and 74 MHz for the LWA1 (Wijnholds & van Cappellen 2011; Tingay et al. 2013a; Ellingson et al. 2013b; Prasad et al. 2014). Only parameters of the low band antennas of AARTFAAC are listed here.

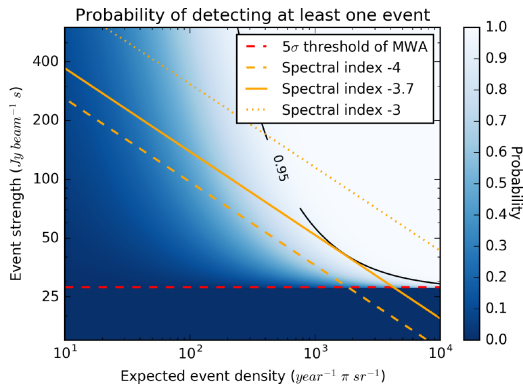| Parameter	MWA	LOFAR (AARTFAAC)	LWA1 (PASI)	LWA1 (phased array mode)
Frequency range (MHz)	80–300	30–80	10–88	10–88
Field of view (sr)	0.06π	π	π	0.005π
Total effective area (m^2)	3016	2617	1393	1393
$T_{sys}(\nu^{-2.55}$ K)	1730	3600	2100	2100
Angular resolution (arcmin)	3	60	120	120
Spectral resolution (kHz)	10	16	75	19.14
Bandwidth (MHz)	30.72	13	0.075	36
Temporal resolution (s)	0.5	1	5	0.04

Figure 11. Luminosity function of intrinsic radio emission from meteors, derived with different spectral indices. The dotted, solid, and dashed orange lines give estimated meteor event strength with spectral indices -3, -3.7, and -4.

Two Line Elements (TLE) set[1] (Hoots 1988), are listed in Table 4. Since neither of the two satellites transmit in the observed FM band, we believe that the transient events caused by the satellites were due to radio reflection of terrestrial FM broadcasting signals. A detailed discussion of the satellite reflection events will be published in the future (Hancock et al. in preparation).

5.5 Potential for other facilities

Considering the spectral index and event rate of meteor emission, the main factors that limit a radio telescope's ability to detect radio emission from meteors are frequency range, field-of-view (FoV), and sensitivity.

Here we give the parameters of some LOFARs in Table 5. The MWA has a high sensitivity, but its meteor detection is restricted by the relatively small FoV and the high-frequency range. The LWA1 has two modes: PASI provides all-sky images, but the bandwidth is narrow, while the phased array mode has a wide bandwidth with a very small FoV. With these two modes, the LWA1 has detected more than 100 meteor emission events, but only obtained a few spectra. AARTFAAC, with its all-sky FoV, the suitable frequency range, and a wide bandwidth, has the best opportunity to collect radio spectra from meteor emission. Since the frequency range of AARTFAAC

overlaps with both the LWA1 and the MWA (lower), it would be possible to directly determine the higher frequency behaviour of events detected by the LWA1.

6 CONCLUSIONS

We have reported a survey for intrinsic radio emission from meteors with the MWA, which spans observing frequencies from 72.3 to 103.0 MHz. Optical observations were also carried out to verify possible candidates. Although radio reflection from ionized meteor trails and optical meteors were detected in the survey, no intrinsic emission was observed. Assuming the radio emission from meteors follows a power law with frequency, we derived an upper limit -3.7 on meteor emission spectral index with a confidence of 95 per cent. This upper limit is consistent with the previous estimation from Obenberger et al. (2016b).

We have also reported the detections of some other transient events, including the reflected FM broadcast signals from satellites in low Earth orbits, which are consistent with previous simulations by Tingay et al. (2013b). These detections show the potential of the MWA for Space Situational Awareness.

REFERENCES

Beech M., Brown P., Jones J., 1995, Earth Moon Planets, 68, 181
Bland P. et al., 2012, Aust. J. Earth Sci., 59, 177

[1] https://www.space-track.org/

5176 *X. Zhang et al.*

Ceplecha Z., Borovička J., Elford W. G., ReVelle D. O., Hawkes R. L., Porubčan V., Šimek M., 1998, Space Sci. Rev., 84, 327
Close S.,, Kelley M., Vertatschitsch L., Colestock P., Oppenheim M., Yee J., 2011, J. Geophys. Res.: Space Phys., 116, A01319
De Pater I., Lissauer J. J., 2015, Planetary Sciences. Cambridge University Press, Cambridge
Dokuchaev V., 1960, Sov. Astron., 4, 106
Ellingson S., Craig J., Dowell J., Taylor G., Helmboldt J., 2013a, in 2013 IEEE International Symposium on Phased Array Systems & Technology. p. 776, IEEE, Waltham, MA
Ellingson S. et al., 2013b, IEEE Trans. Antennas Propag., 61, 2540
Guha A., De B. K., Choudhury A., Roy R., 2012, Ap&SS, 341, 287
Hancock P. J., Murphy T., Gaensler B. M., Hopkins A., Curran J. R., 2012, MNRAS, 422, 1812
Hancock P. J., Trott C. M., Hurley-Walker N., 2018, PASA, 35, e011
Hawkins G. S., 1958, ApJ, 128, 724
Helmboldt J., Ellingson S., Hartman J., Lazio T., Taylor G., Wilson T., Wolfe C., 2014, Radio Sci., 49, 157
Hoots F. R., Roehrich R. L., 1988, Aerospace Defense Command Spacetrack Report, 3, 90
Howie R. M., Paxman J., Bland P. A., Towner M. C., Cupak M., Sansom E. K., Devillepoix H. A., 2017, Exp. Astron., 43, 237
Hurley-Walker N. et al., 2014, Publ. Astron. Soc. Aust., 31, e045
Hurley-Walker N. et al., 2017, MNRAS, 464, 1146
Keay C., Ceplecha Z., 1994, J. Geophys. Res.: Planets, 99, 13163
Keay C. S., 1980, Science, 210, 11
Keay C. S., 1992, Meteoritics, 27, 144
McKinley B. et al., 2012, AJ, 145, 23
McKinley D. W. R., 1961, Meteor Science and Engineering, McGraw-Hill, New York
McMullin J., Waters B., Schiebel D., Young W., Golap K., 2007, in Richard A. Shaw, Frank Hill, David J. Bell., eds, ASP Conf. Ser. Vol. 376,

Astronomical Data Analysis Software and Systems XVI. Astron. Soc. Pac., San Francisco, p. 127
Obenberger K., Dowell J., Hancock P., Holmes J., Pedersen T., Schinzel F., Taylor G., 2016b, J. Geophys. Res.: Space Phys., 121, 6808
Obenberger K., Holmes J., Dowell J., Schinzel F., Stovall K., Sutton E., Taylor G., 2016a, Geophys. Res. Lett., 43, 8885
Obenberger K., Taylor G., Lin C., Dowell J., Schinzel F., Stovall K., 2015, J. Geophys. Res.: Space Phys., 120, 9916
Obenberger K. et al., 2014b, ApJ, 788, L26
Obenberger K. S. et al., 2014a, ApJ, 785, 27
Offringa A., De Bruyn A., Biehl M., Zaroubi S., Bernardi G., Pandey V., 2010, MNRAS, 405, 155
Offringa A., Van de Gronde J., Roerdink J., 2012, A&A, 539, A95
Offringa A. et al., 2014, MNRAS, 444, 606
Offringa A. et al., 2015, Publ. Astron. Soc. Aust., 32, e008
Prasad P., Wijnholds S., Huizinga F., Wijers R., 2014, A&A, 568, A48
Rendtel J., Ogawa H., Sugimoto H., 2017, WGN, J. Int. Meteor Organization, 45, 49
Sokolowski M. et al., 2017, Publ. Astron. Soc. Aust., 34, e062
Sutinjo A., O'Sullivan J., Lenc E., Wayth R. B., Padhi S., Hall P., Tingay S. J., 2015, Radio Sci., 50, 52
Taylor G. et al., 2012, J. Astron. Instrum., 1, 1250004
Tingay S. et al., 2013a, Publ. Astron. Soc. Aust., 30, e007
Tingay S. et al., 2013b, AJ, 146, 103
Trott C. M. et al., 2013, ApJ, 767, 4
Van Haarlem M. et al., 2013, A&A, 556, A2
Wayth R. et al., 2015, Publ. Astron. Soc. Aust., 32, e025
Wijnholds S. J., van Cappellen W. A., 2011, IEEE Trans. Antennas Propag., 59, 1981

This paper has been typeset from a TEX/LATEX file prepared by the author.

CO-AUTHORED PAPER 7 — 3D METEOROID TRAJECTORIES

*E. K. Sansom, T. Jansen-Sturgeon, M. G. Rutten, **H. A. R. Devillepoix**, P. A. Bland, R. M. Howie, M. A. Cox, M. C. Towner, M. Cupák, B. A. D. Hartig*

3D meteoroid trajectories

Eleanor K. Sansom[*,a], Trent Jansen-Sturgeon[a], Mark G. Rutten[b], Hadrien A.R. Devillepoix[a],
Phil A. Bland[a], Robert M. Howie[c], Morgan A. Cox[a], Martin C. Towner[a], Martin Cupák[a],
Benjamin A.D. Hartig[c]

[a] *School of Earth and Planetary Sciences, Curtin University, GPO Box U1987, Perth, WA 6845, Australia*
[b] *Defence Science and Technology Group, Edinburgh, SA 5111, Australia*
[c] *Department of Mechanical Engineering, Curtin University, GPO Box U1987, Bentley, Perth, WA 6845, Australia*

A B S T R A C T

Meteoroid modelling of fireball data typically uses a one dimensional model along a straight line triangulated trajectory. The assumption of a straight line trajectory has been considered an acceptable simplification for fireballs, but it has not been rigorously tested. The unique capability of the Desert Fireball Network (DFN) to triangulate discrete observation times gives the opportunity to investigate the deviation of a meteoroid's position to different model fits. Here we assess the viability of a straight line assumption for fireball data in two meteorite-dropping test cases observed by the Desert Fireball Network (DFN) in Australia – one over 21 s (*DN151212_03*), one under 5 seconds (*DN160410_03*). We show that a straight line is not valid for these two meteorite dropping events and propose a three dimensional particle filter to model meteoroid positions without any straight line constraints. The single body equations in three dimensions, along with the luminosity equation, are applied to the particle filter methodology described by Sansom et al. (2017). Modelling fireball camera network data in three dimensions has not previously been attempted. This allows the raw astrometric, line-of-sight observations to be incorporated directly. In analysing these two DFN events, the triangulated positions based on a straight line assumption result in the modelled meteoroid positions diverging up to 3.09 km from the calculated observed point (for *DN151212_03*). Even for the more typical fireball event, *DN160410_03*, we see a divergence of up to 360 m. As DFN observations are typically precise to < 100 m, it is apparent that the assumption of a straight line is an oversimplification that will affect orbit calculations and meteorite search regions for a significant fraction of events.

1. Introduction

When meteoroids pass through the Earth's atmosphere the luminous phenomena produced can be characterised by its brightness, increasing from meteor to fireball to bolide (Ceplecha et al., 1998). Meteors are typically associated with cometary dust and burn up high in the atmosphere. Fireballs tend to be slower than meteors and more likely of asteroidal origin. These lower entry velocities allow meteoroids to penetrate deeper into the atmosphere, with longer trajectories likely to be influenced by its increasing density. Fireballs are particularly significant as they are frequent enough for dedicated camera networks to capture regularly, whilst still having the potential for objects to survive entry and drop meteorites to Earth. Modelling of fireball trajectories for orbit analysis and meteorite recovery is typically based on a straight line assumption (McCrosky and Boeschenstein, 1965; Spurný et al., 2012; Brown et al., 1994; Hildebrand et al., 2006). The synchronised astrometric observations acquired by the Desert Fireball Network (DFN; Howie et al. 2017) provide a unique opportunity to test this assumption. This work analyses two fireball test cases and introduces a 3D particle filter modelling technique that uses raw observational data to

estimate a trajectory without the need for pre-triangulated data. Although DFN data are used, they are simply to illustrate the issues surrounding the straight line assumption and the functionality of the 3D particle filter technique presented.

1.1. Modelling and observing fireball trajectories

Determining the potential of a fireball to produce a meteorite involves a trajectory analysis of each individual event. The meteoroid can be modelled based on the single body theory of meteoroid dynamics – a set of continuous differential equations representing the evolution of a meteoroid's behaviour as it passes through the atmosphere (Hoppe, 1937; Baldwin and Sheaffer, 1971; Sansom et al., 2017). This is, however, a simplified theory and does not explicitly include any disruptions to the body. Furthermore, many of the trajectory parameters are unknown and assumptions must be made, or models used, to determine their values.

Models such as those used by Ceplecha and Revelle (2005) and Kikwaya et al. (2011) apply a least squares methodology to determine the characteristics of a meteoroid during its flight based on positional

---

observations and light curves. A least squares approach however does not rigorously examine the uncertainties in observations, or the limitations posed by the single body model applied, when evaluating errors. Typically the observational residuals to a straight line fit are quoted as positional uncertainties for the trajectory. This is not valid as the errors induced by using any model must be incorporated.

Even though meteor ablation models (Campbell-Brown and Koschny, 2004; Kikwaya et al., 2011) expand on the single body equations for ablation by including thermal fragmentation mechanisms, their application is limited to small meteor-producing bodies (10^{-12} to 4×10^{-5} kg / 10 μ m to 2 mm ; Campbell-Brown and Koschny 2004).

Hydrodynamic numerical models (such as SOVA (Shuvalov, 1999) and the model of Shuvalov and Artemieva 2002) focus on external processes for modelling the interaction and propagation of shock waves through the atmosphere caused by hypersonic flight of bolides (Artemieva and Shuvalov, 2016). These models do not use raw observational data and are computationally expensive procedures (Artemieva and Pierazzo, 2009). For this reason a pragmatic approach, such as the particle filter technique used by Sansom et al. (2017) (after Ristic et al. 2004), is favoured to characterise meteoroid atmospheric entry of large fireball network data sets.

The Monte Carlo technique of Sansom et al. (2017) iteratively estimates the state of the trajectory system at each observation time. It does not aim to fit the entire trajectory at once. This removes the assumptions and limitations of normal fitting techniques that may force the simplified single body equations to model this more complex system. Despite the particle filter using these equations as a base model, the adaptive approach uses the observations and appropriate covariances to incorporate, to some extent, unmodelled processes (such as fragmentation). The nature of this technique allows a broad range of trajectory parameters (including densities, shapes and ablation parameters) to be explored, and favourable values to be identified, in a more robust way than a brute force least squares approach.

Beside modelling a meteoroid's dynamic trajectory, it is possible to relate the mass loss of the body along the trajectory to the observed brightness of the event, as a portion of the kinetic energy loss is transformed into visible light (Ceplecha et al., 1998). This can be modelled following the differential equation

$$I = -\tau \left(1 + \frac{2}{\sigma v^2}\right) \frac{v^2}{2} \frac{dm}{dt} \times 10^7. \tag{1}$$

The luminosity, I, is typically referred to in *erg s*$^{-1}$ but is given here in SI units of Watts (and thus introducing the conversion factor of $10^7 W s erg^{-1}$). The percentage of energy that is converted to radiation is quantified by the luminous efficiency, τ. v and m are the velocity and mass of the meteoroid with t being the observation time and σ the ablation parameter.

As fireball observations by the DFN are only in the visible wavelengths, as is typical for such networks, the luminosity values need to be adjusted depending on the meteoroid temperature. A value of 1.5×10^{10} is used to relate a typical source temperature of 4500 K to the luminosity in the visual pass-band, I_v (Ceplecha et al., 1998). If the observed brightness values can be expressed in absolute visual stellar magnitudes, M_v, then a comparison may be made to models using Eq. (1) by:

$$\frac{I}{1.5 \times 10^{10}} = I_v = 10^{-0.4M_v}. \tag{2}$$

Incorporating the fireball's calculated luminosity into the particle filter methodology is able to provide an additional observation to the filter, helping to further constrain mass loss estimates. The luminosity of a fireball can be calculated based on the long exposure images or by calibrating the measurements of an external device such as a radiometer.

When a fireball is captured by multiple Desert Fireball Network remote observatories, each camera image is calibrated using the background star field to determine an astrometric azimuth and elevation for positions along the fireball trail. This method of calibration (detailed by Devillepoix et al. (2018)) accounts well for any effects of atmospheric refraction, and the uncertainty introduced by the calibration is typically less than 1 arcminute. The DFN camera systems encode absolute timing in fireball trajectories using a modulated liquid crystal shutter within the lens of each camera (Howie et al., 2017). The De-Brujn encoding embedded within the fireball trail itself is synchronised across the network via GNSS. This gives us the unique capability of individually triangulating meteoroid positions for every discrete time-step with multi-station observations. This has not hereto been possible. Despite the uncertainties, with correct error analysis this triangulation of discrete observation times can give us 'ground truth' positions of the meteoroid with which we can compare different approaches to meteoroid trajectory analyses.

Here we assess the viability of a straight line assumption for fireball data by comparing straight line positions to those calculated using this unique triangulation capability of the DFN. We also propose a three dimensional particle filter to model meteoroid positions without any straight line constraints. The single body equations in three dimensions, along with the luminosity equation, are applied to the particle filter methodology described by Sansom et al. (2017). In doing this, the observations used by the filter to update the state vector are permitted to be in the form of the raw line-of-sight observations in azimuth and elevation as well as luminosities (where available). This drops the simplifying assumption of a straight line trajectory entirely, as particles are free to move in three dimensional space. Error propagation is thorough as the filter considers the observational uncertainties in each azimuth and elevation individually as well as considers trajectory model limitations.

The better the understanding we have of the final state of a meteoroid, and the uncertainties throughout the modelling phase, the more confidence we have in predicted fall regions. This may significantly influence decisions regarding the feasibility of ground-based searches for meteorites.

2. Assessing the limitations of the straight line assumption

Historically, there have been two predominant meteoroid triangulation methods; the method of planes (Ceplecha, 1987) and the straight line least squares (SLLS) method (Borovička, 1990). The method of planes involves finding the best fit, 2D plane for each observatory that contains both the observatory location and the line-of-sight meteoroid observations. The intersection of multiple planes defines the trajectory; in the case of more than two observatories, this will result in multiple trajectory results which are then averaged in practice. The straight line least squares method on the other hand determines a best fit, straight line radiant for the trajectory considering all the raw observations at once. This is done by minimising the angular difference between the observed lines of sight and the line joining the observatory to the closest corresponding point along the best fit radiant line. By assuming a straight line trajectory, this effectively destroys any subtleties in the data by forcing it to fit what may potentially be an oversimplified model. The straight line assumption may be an acceptable simplification for some events, especially short, fast meteors, but may not always be valid for longer fireballs with significant deceleration and should be tested.

A least squares approach however does not rigorously examine the uncertainties in observations, or the limitations posed by the single body model used, when evaluating errors. Typically the observational residuals to a straight line fit are quoted as positional uncertainties for the trajectory. This is not valid as the errors induced by using any model must be incorporated. Despite the decrease in residuals when considering the upper sections of the trajectory only (observations of the fireball above 50 km), it must be noted that this is not a good measure

of the true trajectory uncertainties as the model errors are not taken into account.

The reference frame in which the straight line is fitted also needs be considered for such long, decelerating events and is rarely discussed. It is expected that a fireball trajectory is approximately straight in an inertial reference frame only, and that Earth rotation effects will cause an apparently curved path for an observer on the ground. This requires accurate timing throughout the meteoroid flight. Although Ceplecha (1987) adjust entry vectors for both Earth rotation and gravity, this is intended to correct the heliocentric orbit beyond the sphere of influence of the Earth. The SLLS method of Borovička (1990) allows the incorporation of time differences between measurements to account for Earth rotation effects, though it is not a requirement of the method; the authors even state that the local sidereal time of the observer is usually assumed to be constant throughout a meteor's flight. For short events that do not show any significant deceleration, it is unlikely that these effects would be noticeable within the error of the observations. For fireballs that are longer and show significant deceleration however, this may no longer hold true. Most trajectory analyses of recent fireball events (Brown et al., 2011; Borovička et al., 2013; 2015; Spurný et al., 2017) cite the SLLS of Borovička (1990) as the method of trajectory determination, though it is not made apparent in every case which considerations have been made. Uncertainties in triangulated positions are also often quoted as the residuals to the straight line (Spurný et al., 2010; Borovička et al., 2013; 2015; Spurný et al., 2017) fit without taking into consideration the error of the straight line model and are therefore not a true representation of the trajectory uncertainty.

2.1. Point-wise triangulation

The unique method used by the DFN camera systems to encode absolute timing in fireball trajectories is synchronised across the network via GNSS. The instantaneous meteoroid position for a given time step can therefore be evaluated using what we here refer to as a *point-wise triangulation* (schematically illustrated in Fig. 1). Point-wise triangulation estimates the meteoroid position, ℓ, by minimising the angular separation, θ, between the *calculated* line-of-sight unit vector to ℓ and the *observed* line-of-sight unit vector, $\mathbf{z}^n$ for each observatory, $\mathbf{O}^n$ (where $\mathbf{z}^n$, ℓ and $\mathbf{O}^n$ are in an ECEF rectangular geocentric coordinate system).

$$\theta = \sqrt{\sum_n \left[\arccos\left(\frac{\ell - \mathbf{O}^n}{\|\ell - \mathbf{O}^n\|} \cdot \mathbf{z}^n\right)\right]^2} \tag{3}$$

The resulting individually triangulated positions (ITPs) are used as a reference for comparison of trajectory models.

2.2. Introducing two fireball test cases

Here we detail two fireballs observed by the Desert Fireball Network and assess the appropriateness of a straight line trajectory fit for these cases.

2.2.1. Case 1: DN151212_03 – long, shallow

On the 12th of December 2015, at 11:36:23.826 UTC, a > 21 s long fireball over South Australia was captured by five DFN observatories east of Kati Thanda (hereafter referred to as event *DN151212_03*). DFN systems at this time were designed to capture one 25 s, long exposure image every 30 s, and the fireball was split over two consecutive images. The fireball appeared in the last ∼ 2 s of the first exposure, was unobserved during the gap between exposures, and further captured for another ∼ 14 s in the second exposure, with a final observation time at 11:36:45.526 UTC. Fig. 2 shows the second exposure captured by the observatory closest to the terminal point (DFNO_39). The modulation of the liquid crystal shutter used to encode absolute and relative timing can be seen as long and short dashes along the trajectory. Initially the entire 21.7 s trajectory was fitted using the straight line least squares (SLLS) method following Borovička (1990).
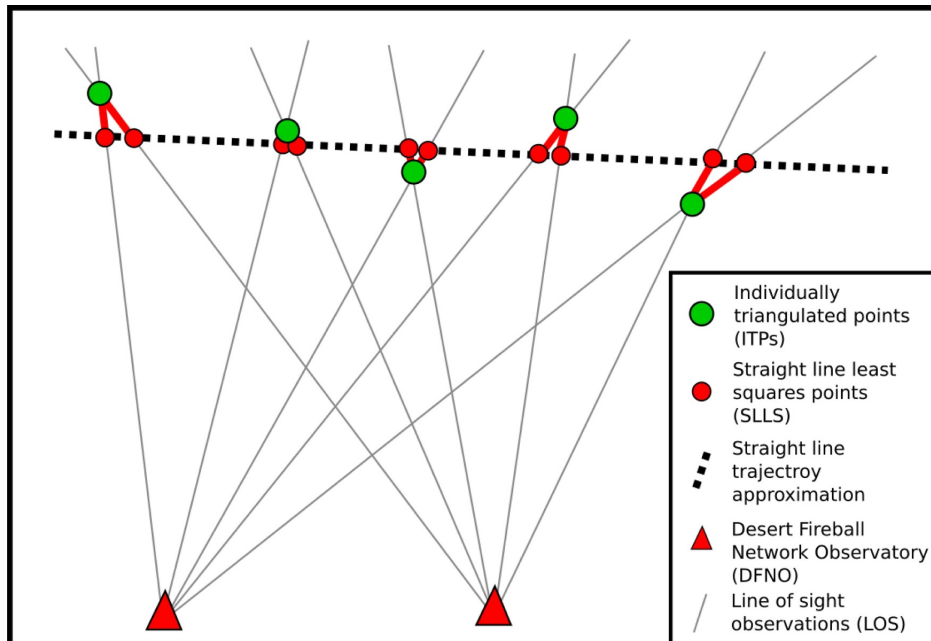
Fig. 1. Schematic representation (not to scale) of five unique time steps observed by two DFNOs. Difference between the straight line least squares trajectory points (red) and the individually triangulated positions (green) are highlighted in red. (For interpretation of the references to colour in this figure legend, the reader is referred to the web version of this article.)

Legend:
- Individually triangulated points (ITPs)
- Straight line least squares points (SLLS)
- Straight line trajectroy approximation
- Desert Fireball Network Observatory (DFNO)
- Line of sight observations (LOS)

Fig. 2. *DN151212_03* fireball as seen from Etadunna Station, South Australia, travelling from North (top) to South (bottom) with a final recorded point at 11:36:45.526 UTC. Calibration with background stars determines azimuth and elevation of trajectory points.

Table 1

Straight line least squares (SLLS) trajectory triangulated in either an inertial (ECI) or non-inertial (ECEF) reference frame for all observations of event *DN151212_03*. Trajectory characteristics (height, velocity, mass) are estimated using an extended Kalman smoother in one dimension on these straight line data. Entry slope is given as an angle from horizontal. Despite the reference frame used to calculate the straight line, radiants are given in J2000 equatorial coordinates for comparison; the angular separation between the two radiants is 13.56′ (0.23°).

DN151212_03 (full)	ECI	ECEF
Entry radiant – RA ($^\circ$)	23.77 ± 0.37	23.99 ± 0.22
Entry radiant – DEC ($^\circ$)	46.17 ± 0.13	46.00 ± 0.15
Initial height (km)	87.7 ± 0.1	88.5 ± 0.1
Initial velocity (km s^{-1})	13.21 ± 0.13	13.15 ± 0.13
Initial mass (kg)	35 ± 2	33 ± 2
Entry slope, γ_e ($^\circ$)	16.4	16.5
Final height (km)	26.5 ± 0.1	26.4 ± 0.2
Final velocity (km s^{-1})	3.03 ± 0.21	2.93 ± 0.11
Final mass (kg)	2.0 ± 0.2	1.9 ± 0.3

As absolute timing is known to a high accuracy, this is preferably performed in an Earth centred, inertial (ECI) reference frame, though a non-inertial (Earth centred, Earth fixed; ECEF) solution is also calculated to assess the variation in fits (and subsequent radiant values are converted to J2000 for comparison). A 1D extended Kalman smoother trajectory analysis (Sansom et al., 2015) on these straight line data estimates the trajectory parameters. The results for both reference frames are given in Table 1.

The cross-track residuals of individual camera observations to the straight line fit (in ECI) can be seen in Fig. 3. These cross-track residuals show the minimum distance between the observed lines of sight and the straight line triangulated trajectory and do not include along-track errors in triangulated positions. The 13.56 arcmin difference in entry radiant between inertial and non-inertial reference frames (Table 1) shows the importance of including Earth rotation effects (this exceeds the typical < 1 arcmin astrometric uncertainties of DFN observations). The > 1 km residuals show this is an inappropriate fit to the trajectory.
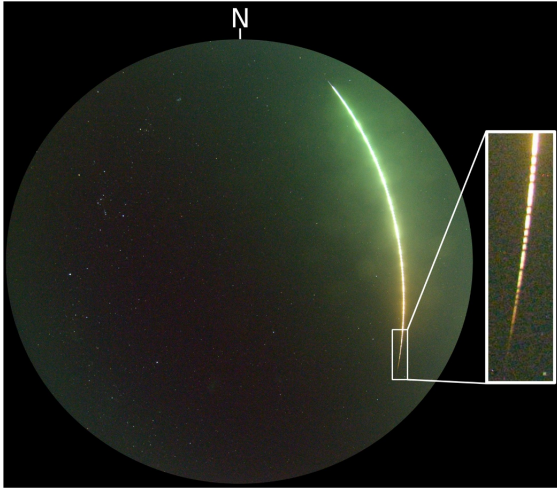
By considering only the observations above 50 km we hope to

improve the fit and calculate a more realistic entry radiant. The cross-track residuals to the straight line fit (in ECI) for its subset are seen in Fig. 4. The decreases in observation residuals to the straight line model shows a significantly improved fit, providing a more reliable entry radiant (43.10′ difference between Tables 1 and 2 ECI values). Despite the decrease in residuals, it must be noted that this is not a good measure of the true trajectory uncertainties as the model errors are not taken into account. Updated entry parameters given in Table 2 are again calculated using an EKS (Sansom et al., 2015), which incorporates both observational and model errors in the quoted uncertainties. Non-inertial SLLS (ECEF) results are also quoted to highlight that despite improved fits in both reference frames, the radiant angles are still separated by nearly 2′ which is double observational uncertainties. A similar exercise can be performed with the lower half of the trajectory (observations < 50 km). Fig. 5 shows that a SLLS fit to these data still does not well represent the data and is little improved from Fig. 3. Rather than continuing to chop the trajectory into increasingly small segments, we can observe the path of the ITPs relative to the entry radiant calculated in Table 2. Fig. 6 is a view looking down the ECI entry radiant (white point). This "down-line" view projects all points onto the plane normal to the straight line trajectory, resulting in the ECI trajectory stacking to a single point. The *x*-axis is truly horizontal, and as the meteoroid travelled from North to South, negative deviations are to the East, while positive deviations are to the West. The y-axis is the deviation above and below the straight line trajectory and values can be translated to true vertical using the cosine of the trajectory slope. From this down-line view, we can gain an understanding of the true non-linearity of the *DN151212_03* meteoroid trajectory; the lower half is not randomly scattered around a straight line as points above 50 km are, rather they show a distinct lateral deviation to the East. This also shows that, despite the 21.7 s trajectory theoretically accumulating a 2.1 km vertical drop due to gravity, this is not the cause of the deviation from a straight line.

This fireball represents an interesting case, showing that effects other than Earth rotation and gravity are involved in significantly influencing trajectories. This long, shallow trajectory however is certainly not a regular event. Next we perform a similar analysis on a more typical fireball case.

2.2.2. Case 2: DN160410_03 – typical event

On the 10th of April 2016, at 13:09:02.526 UTC, a 'typical' fireball was observed by three DFN observatories over central South Australia, near lake Cadibarrawirracanna (event *DN160410_03*, Fig. 7). It is an ideal case to analyse as it was nearly equidistant to all cameras, with the angle of observing planes at 46°/52°/80° (Fig. 8), and 88 of the 91 total observations made (from identifying the starts and ends of the trajectory dashes) were visible in all three still images (Fig. 7). There is little observable fragmentation in the still images and no major peaks noticeable in the light curve which is regular and symmetric. The method used by the DFN to calculate the luminosity of an event is only applicable when an event does not saturate the sensor, which was unfortunately the case for the other two viewpoints, DFNO_27 and DFNO_32.

As with event *DN151212_03*, a straight line least squares (SLLS) triangulation of this event was calculated. Initially for the entire trajectory (Fig. 9), with resulting parameters determined using the EKS given in Table 3. Although this event is steeper and significantly shorter, gravity still contributes a 105 m downward component over the 58 km long trajectory and Earth rotation an apparent 1.9 km lateral deflection to an observer on the ground. The ECI and ECEF entry radiants show a 12.93′ separation (Table 3).

Despite the apparently reasonable fit of the straight line to the entire trajectory in this case, we once again isolate the observations above 50 km and re-triangulate this upper dataset (Fig. 10). The ECI entry radiant changed by a not insignificant 17′ (Table 4).

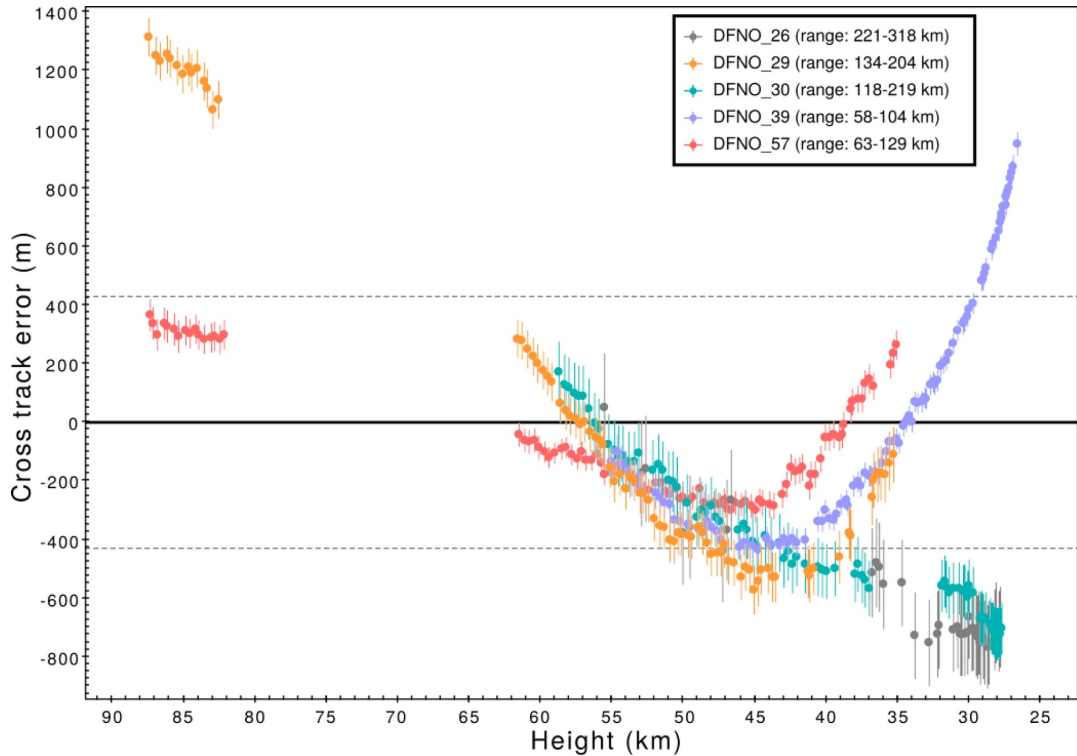With this new entry radiant, we can once again project the ITPs onto

Fig. 3. Cross track residuals for individual station observations of *DN151212_03* to a straight line trajectory fit in an inertial (ECI) reference frame. Range values in legend are the minimum and maximum distances of a station to the fireball trajectory. Error bars on observations are 1σ astrometric errors projected at the corresponding range. The gap between 82 and 62 km corresponds to the ~ 5 s gap between exposures.

the plane normal to it, allowing us to observe how the meteoroid positions track in the lower section of the trajectory (Fig. 11). Despite this event being a more typical example, with acceptable observational residuals, there is still a not insignificant lateral trend to the end meteoroid positions as shown by the ITPs in this figure.

2.2.3. Summary of straight line comparisons

Event *DN151212_03* may be considered unique in its duration, and its non-linear flight path with up to 2.1 km of lateral deviation an anomaly, but in performing a similar analysis to the more typical event *DN160410_03* we are still able to notice a distinct pattern/wander to the end of the trajectory. These deviations from a straight line cannot be accounted for by gravity, and Earth rotation effects are removed when an inertial reference frame is used. It is clear that there are real limitations to the straight line assumption and it is best to consider modelling fireball trajectories without any pre-defined assumptions; allow the raw observations to be the sole influences on the data. To achieve this we can apply the single body equations in three dimensions to the particle filter methodology described by Sansom et al. (2017). This will utilise raw astrometric observations to resolve meteoroid position estimates.

3. Particle filter modelling using three dimensional meteoroid flight and luminosity

The iterative Monte Carlo technique of the particle filter allows a broad range of trajectory parameters (including densities, shapes and ablation parameters) to be explored, and favourable values to be identified, in a more robust way than a brute force least squares

approach. A set of tracer particles are propagated through the motion and luminous equations, and their weightings evaluated at each time step according to their closeness to available observational data. A detailed description of applying particle filters to meteoroid trajectories is presented in Sansom et al. (2017). Although Sansom et al. (2017) apply the single body equations as a model, the adaptive approach uses appropriate covariances to incorporate, to some extent, unmodelled processes such as fragmentation.

Particle filters fall within the class of Bayesian state-space methods which use a vector, **x**, to represent the *state* of a system. In meteoroid trajectory analysis this includes the motion parameters (position and velocity) as well as other trajectory variables.

To use a three dimensional model for flight, we divide positions and velocities into their *x, y, z* components in geocentric coordinates. Incorporating the luminous efficiency into the state vector allows luminosity values to be calculated. Eq. (4) represents the meteoroid state and encapsulates the knowledge of the meteoroid system at a given time t_k.

$$
\mathbf{x}_k = \begin{bmatrix} \ell_{x;k} \\ \ell_{y;k} \\ \ell_{z;k} \\ v_{x;k} \\ v_{y;k} \\ v_{z;k} \\ m_k \\ \kappa_k \\ \sigma_k \\ \tau_k \end{bmatrix} \begin{array}{l} \text{position in X} \\ \text{position in Y} \\ \text{position in Z} \\ \text{velocity in X} \\ \text{velocity in Y} \\ \text{velocity in Z} \\ \text{mass} \\ \text{shape-density parameter} \\ \text{ablation parameter} \\ \text{luminous efficiency parameter.} \end{array} \tag{4}
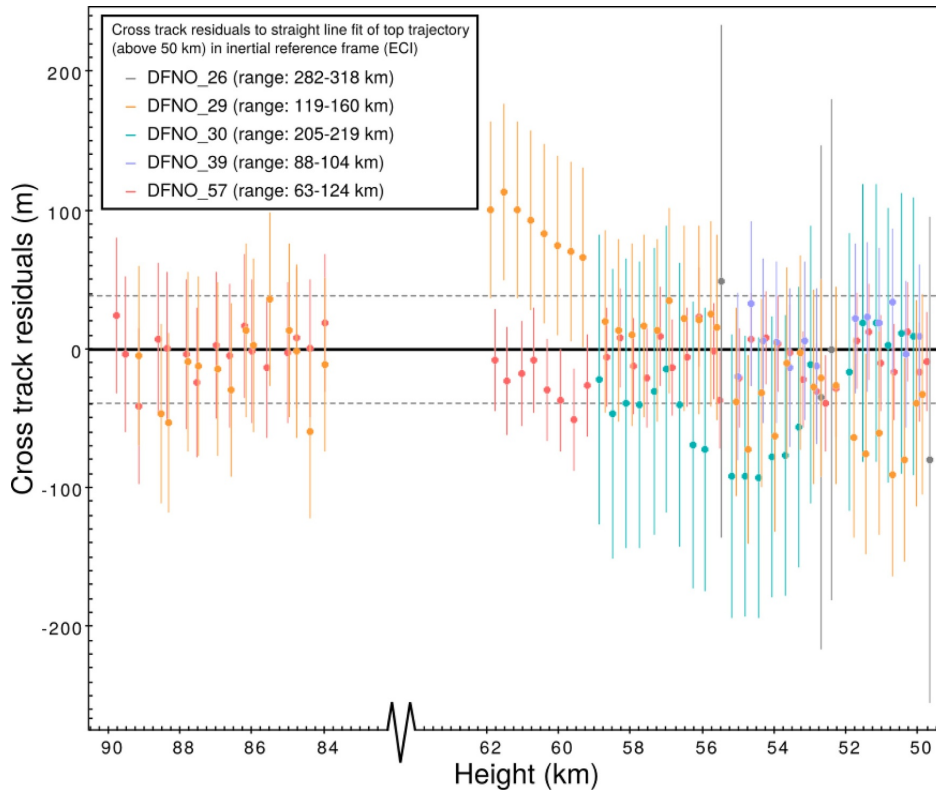$$

Fig. 4. Cross track residuals for the upper half of the *DN151212_03* trajectory to a straight line fit in an inertial (ECI) reference frame. Only observations of the fireball above 50 km were used. Error bars on observations are 1σ astrometric errors projected at the corresponding range.

Table 2
Straight line least squares (SLLS) trajectory triangulated in either an inertial (ECI) or non-inertial (ECEF) reference frame for observations of event *DN151212_03* above 50 km only. Trajectory characteristics (height, velocity, mass) are estimated using an extended Kalman smoother in one dimension on these straight line data. Despite the reference frame used to calculate the straight line, radiants are given in J2000 equatorial coordinates for comparison; the angular separation between the two radiants is 1.77′ (0.03°).

DN151212_03 (> 50 km)	ECI	ECEF
Entry radiant – RA (°)	24.18 ± 0.01	24.14 ± 0.01
Entry radiant – DEC (°)	45.51 ± 0.01	45.51 ± 0.01
Initial height (km)	89.99 ± 0.02	89.97 ± 0.02
Initial velocity (km s^{-1})	13.52 ± 0.06	13.47 ± 0.05
Entry slope, γ_e (°)	17.1	17.1

The shape-density and ablation trajectory parameters are given by

$$\kappa = \frac{1}{2}\frac{c_d A}{\rho_m^{2/3}} \qquad \text{and} \qquad \sigma = \frac{c_h}{c_d H^*},$$

where c_d and c_h the drag and heat transfer coefficients respectively, A is the shape parameter as described by Bronshten (1983), ρ_m the bulk density of the meteoroid, and H^* the enthalpy of sublimation.

This state is determined by assessing the conditional probability density function $p(\mathbf{x}_k|\mathbf{z}_{0:k})$ given an observation $\mathbf{z}_k$ of the system at time t_k ($\mathbf{z}_{0:k}$ therefore being the history of all observations from time t_0 through to time t_k).

This is achieved through the three state-space equations:

(i) The state prior,

$$p(\mathbf{x}_0), \tag{5}$$

which is the probability density function that encapsulates prior knowledge of the state of the system and initialises the recursion.

(ii) The process equation,

$$\mathbf{x}_{k+1} = f(\mathbf{x}_k) + \mathbf{u}_k, \tag{6}$$

defines the evolution of the state in discrete time, with process noise $\mathbf{u}_k$.

(iii) The measurement equation,

$$\mathbf{z}_k = h(\mathbf{x}_k) + \mathbf{w}_k, \tag{7}$$

uses the measurement function $h(\mathbf{x}_k)$ to correlate the state of the meteoroid to the given azimuth and elevation measurements from camera observatories. Observation noise, $\mathbf{w}_k$, is assumed to be Gaussian with a mean of zero and covariance $\mathbf{R}_k$ in degrees ($\mathbf{R}_k$ represents observational error). Further explanation of the measurement function are detailed in Section 3.1.

Although fireball observations are made in discrete time, modelling the meteoroid dynamics is more appropriate using continuous model equations. Continuous-time differential state equations ($f_c(\mathbf{x})$) may be integrated in order to attain the form needed for the process Eq. (6):

$$\mathbf{x}_{k+1} = \int_{t_k}^{t_{k+1}} f_c(\mathbf{x})dt + \mathbf{u}_k. \tag{8}$$

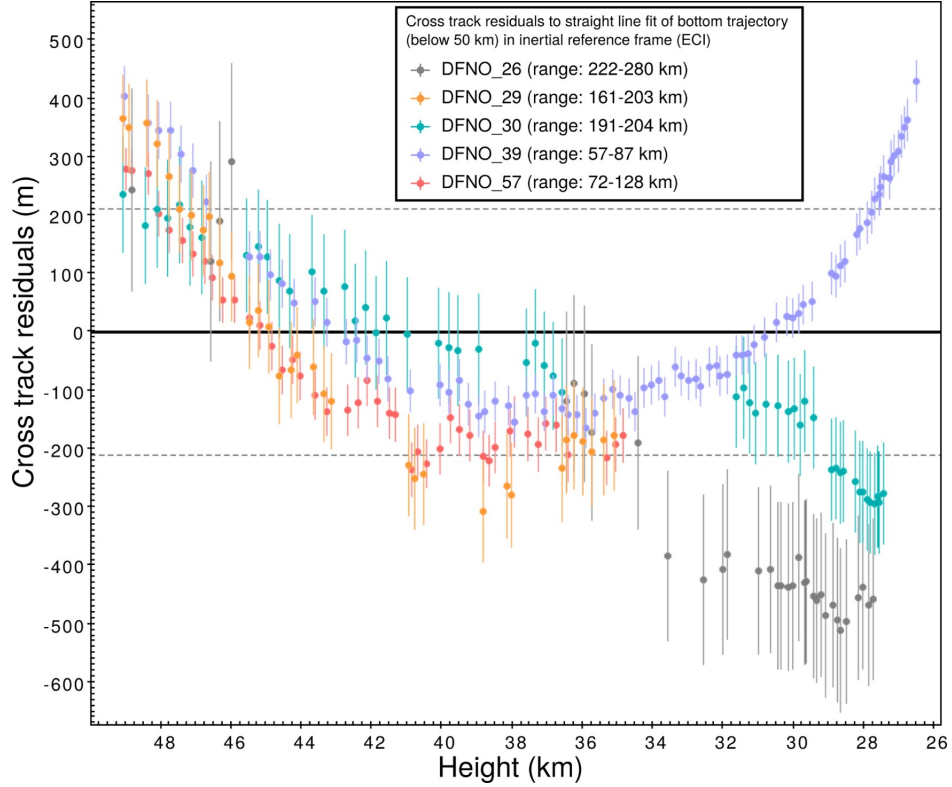Although $f_c(\mathbf{x})$, using the single body equations, is non-linear, the

Fig. 5. Cross track residuals for the lower half of the *DN151212_03* trajectory to a straight line fit in an inertial (ECI) reference frame. Only observations of the fireball below 50 km were used. Error bars on observations are 1σ astrometric errors projected at the corresponding range.

discrete-time process noise, $\mathbf{u}_k$, can be closely approximated by Gaussian noise with zero mean and covariance $\mathbf{Q}_k$ ($\mathbf{Q}_k$ corresponds to how well the process equation represents the true system).

A particle filter is very flexible and requires no constraints on the linearity of state equations, nor the noise distributions (Ristic et al., 2004). This is due to there being no single representation of the state prior, rather a set of N_s weighted particles are used to represent the distribution.

Each ith particle can be represented at any time t_k by its state, $\mathbf{x}_k^i$, and weight, w_k^i as:

$$\{\mathbf{x}_k^i, w_k^i\} \quad i = 1, \dots, N_s, \tag{9}$$

with weights normalised as:

$$\sum_i^{N_s} w_k^i = 1. \tag{10}$$

Particle weights are evaluated according to how well a particle's state represents the available observational data. The weighted mean of the distribution, $\hat{\mathbf{x}}_k$, can be approximated at any time t_k as:

$$\hat{\mathbf{x}}_k = \sum_i^{N_s} w_k^i \mathbf{x}_k^i, \tag{11}$$

with covariance

$$Cov(\mathbf{x}_k) = \sum_i^{N_s} w_k^i (\mathbf{x}_k^i - \hat{\mathbf{x}}_k)(\mathbf{x}_k^i - \hat{\mathbf{x}}_k)^T. \tag{12}$$

There are three steps in running a particle filter, similar to other Bayesian filtering methods: *initialisation, prediction, update.* Sansom et al. (2017) provides a detailed methodology for a one dimensional trajectory model. Here we will outline the variations required to allow a particle filter to be performed in three dimensions and incorporate absolute visual magnitude observations.

3.1. Initialisation using point-wise triangulation

An initial set of particles is required that best represents the state prior (5) of the meteoroid system; initialisation in 3D requires an approximate start location. As the full data set is available at the time of executing the particle filter, the initial position and velocity components may be more accurately estimated from the observational data. The instantaneous meteoroid position for a given time step can be evaluated using *point-wise triangulation* (see Section 2.1). Performing a point-wise triangulation on the first handful of multi-station observations produces a set of individually triangulated positions (ITPs) from which the instantaneous velocity of the meteoroid can be determined – simply taking the difference in positions with time: $\mathbf{v}_k = \frac{d\ell_{k:k+1}}{dt_{k:k+1}}$. Due to the inherent scatter in the ITPs and therefore velocities, v_0 may be reasonably well approximated by assuming constant deceleration between the first few multi-station observations and t_0:

$$\mathbf{v}_0 = \mathbf{v}_m - \frac{d\mathbf{v}}{dt} \times t_m, \tag{13}$$

where t_m is the relative time of the first available *multi-station* observations and the value of $\mathbf{v}_m$ and $\frac{d\mathbf{v}}{dt}$ are determined by a linear least squares fit to the scattered velocities.
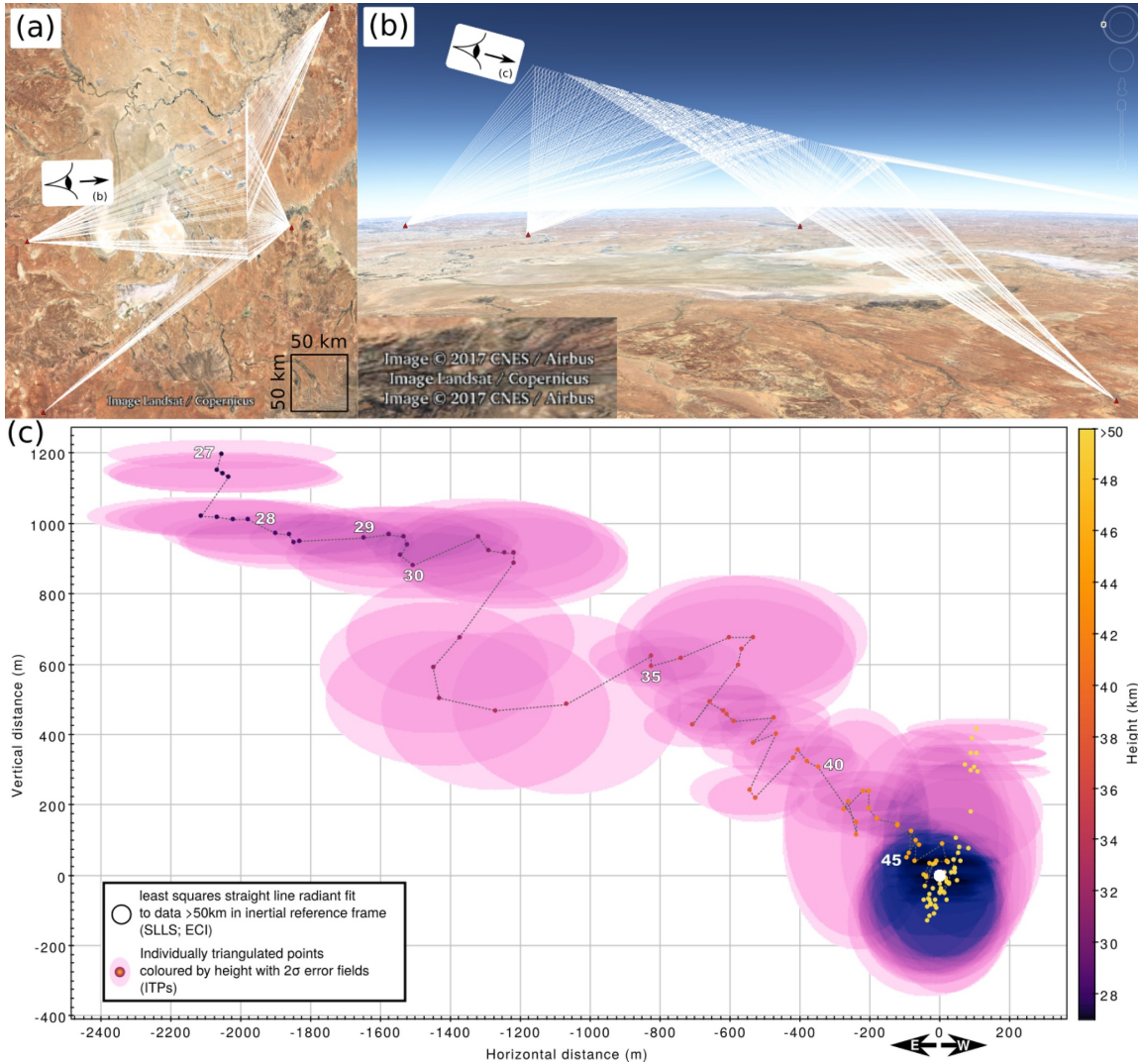
Fig. 6. "Down-line" view (c) as seen by an observer looking down the ECI straight line radiant (illustrated by (a)–(b)) calculated using the top half of the trajectory (points > 50 km; see Fig. 4). This results in the ECI trajectory stacking to a single point (white) whereas the individually triangulated positions (ITPs; coloured points) are projected onto the viewing plane. This plane is normal to the straight line trajectory with the x-axis aligned with the Earth horizontal, and inclined from true vertical by the cosine of the trajectory slope. From this down-line view the ITPs help to illustrate the true non-linearity of the path taken by the meteoroid. (Google Earth image credit: Landsat/Copernicus/CNES/Airbus).

If the first ITP is at t_0, its position can be used to initialise the first three components of the state vector (4). If $t_m \neq t_0$ (multi-station data is not available at t_0), an initial position may then be roughly approximated by rearranging and integrating (13) with respect to time:

$$\ell_0 = \ell_m - \mathbf{v}_0 t_m - \frac{1}{2}\frac{d\mathbf{v}}{dt} \times t_m^2. \tag{14}$$

The initialisation of particle state parameters for position and velocity at t_0 is then drawn from a Gaussian distribution shown by

$$\ell_0^i = \mathcal{N}(\ell_0; \mathbf{P}_{\ell;0}) \qquad \mathbf{v}_0^i = \mathcal{N}(\mathbf{v}_0; \mathbf{P}_{v;0}) \qquad i = 1, ..., N_s \tag{15}$$

where mean values of the ℓ_0 and $\mathbf{v}_0$ vectors are calculated as described above, and covariance values, $\mathbf{P}_0$, are determined by the uncertainty in

this least squares fit and may vary for each directional component.

Possible original values for mass, κ and σ can be randomised within theoretical bounds (see Table 1 of Sansom et al. 2017). A similar concept can be applied to the luminous efficiency; here we randomise within the range 0.01% < τ < 10% after Ceplecha and Revelle (2005) and Ceplecha et al. (1998). All particles are initially weighted equally as $w_0^i = \frac{1}{N_s}$.

3.2. Filter prediction using three dimensional state equations

Recursion commences after initialisation, beginning with a forward prediction of particles from t_k to t_{k+1} by the process Eq. (6).

The change in trajectory parameters κ, σ and τ with time is not well
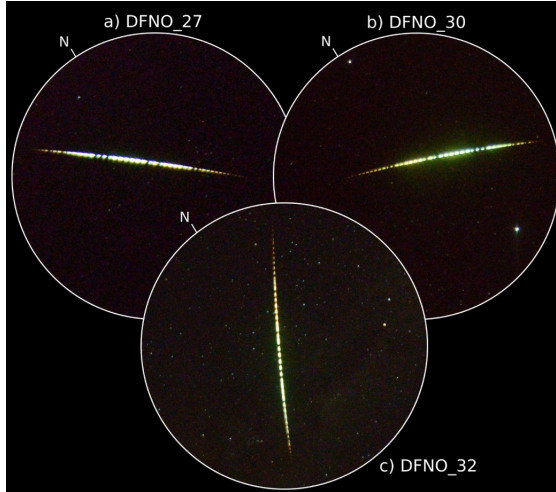
Fig. 7. *DN160410_03* fireball as seen from three DFN stations in South Australia, starting at 13:09:02.526 UTC. Calibration with background stars determines azimuth and elevation of trajectory points.

known and at this stage is assumed to be nil (see discussion related to Eq. (20)):

$$\frac{d\kappa}{dt} = \frac{d\sigma}{dt} = \frac{d\tau}{dt} = 0. \tag{16}$$

In order to analyse the full trajectory in 3D, the differential equations of motion must be split into their vector components:

$$\frac{d\ell}{dt} = \mathbf{v} \tag{17a}$$

$$\frac{d\mathbf{v}}{dt} = -\kappa\rho_a m^{(\mu-1)}\|\mathbf{v}\|\mathbf{v} + \mathbf{g} \tag{17b}$$

$$\frac{dm}{dt} = -\kappa\sigma\rho_a m^{\mu}\|\mathbf{v}\|^3, \tag{17c}$$

where ℓ and $\mathbf{v}$ are the position and velocity vectors, $\mathbf{g}$ is the local gravitational acceleration vector, and $\|\mathbf{v}\|$ is the magnitude of the velocity. μ is the shape change parameter, representing the rotation of the body, here assumed to be 2/3, representing spin rapid enough for ablation to be uniform across the entire surface (Bronshten, 1983). Atmospheric densities, ρ_a, can be calculated using the NRLMSISE-00 atmospheric model (Picone et al., 2002).

This gives the continuous-time state equation for a meteoroid travelling through the atmosphere in 3D as:

$$f_c(\mathbf{x}) = \left[\frac{dl_x}{dt}, \frac{dl_y}{dt}, \frac{dl_z}{dt}, \frac{dv_x}{dt}, \frac{dv_y}{dt}, \frac{dv_z}{dt}, \frac{dm}{dt}, \frac{d\kappa}{dt}, \frac{d\sigma}{dt}, \frac{d\tau}{dt} \right]. \tag{18}$$

with the continuous-time Gaussian process noise $\mathbf{u}_c$ of zero mean and covariance $\mathbf{Q}_c$. The discrete-time process noise covariance, $\mathbf{Q}_k$ can be approximated as

$$\mathbf{Q}_k = \int_{t_k}^{t_{k+1}} e^{Ft} \mathbf{Q}_c e^{F^T t} dt \tag{19}$$

using the linearised form of the process equation, $F = \frac{\partial f_c(\mathbf{x})}{\partial \mathbf{x}}$ (Grewal and Andrews, 1993). In the 3D filter, we use

$$\begin{aligned}
\mathbf{Q}_c = diag \ \ [& (0\,m\,s^{-1}), (0\,m\,s^{-1}), (0\,m\,s^{-1}), \\
& (75\,m\,s^{-2}), (75\,m\,s^{-2}), (75\,m\,s^{-2}), \\
& (0.8 \times m_k\,kg\,s^{-1}), (10^{-3}\,m^2\,kg^{-2/3}\,s^{-1}), \\
& (10^{-4}\,s\,km^{-2}), (0.001\,\%) \,]^2,
\end{aligned} \tag{20}$$

where each element along this square matrix diagonal represents the uncertainty of each differential model equation in (18). That is, the uncertainty in position and velocity components are introduced through noise in the acceleration model (17b), therefore allowing the

Fig. 8. Configuration of *DN160410_03* observations. White observation rays correspond to the start and end points of the trajectory dashes in Fig. 7. (Google Earth image credit: Landsat/Copernicus).

Fig. 9. Cross track residuals for individual station observations of *DN160410_03* to a straight line trajectory fit in an inertial (ECI) reference frame. Range values in legend are the minimum and maximum distances of a station to the fireball trajectory. Error bars on observations are 1σ astrometric errors projected at the corresponding range.
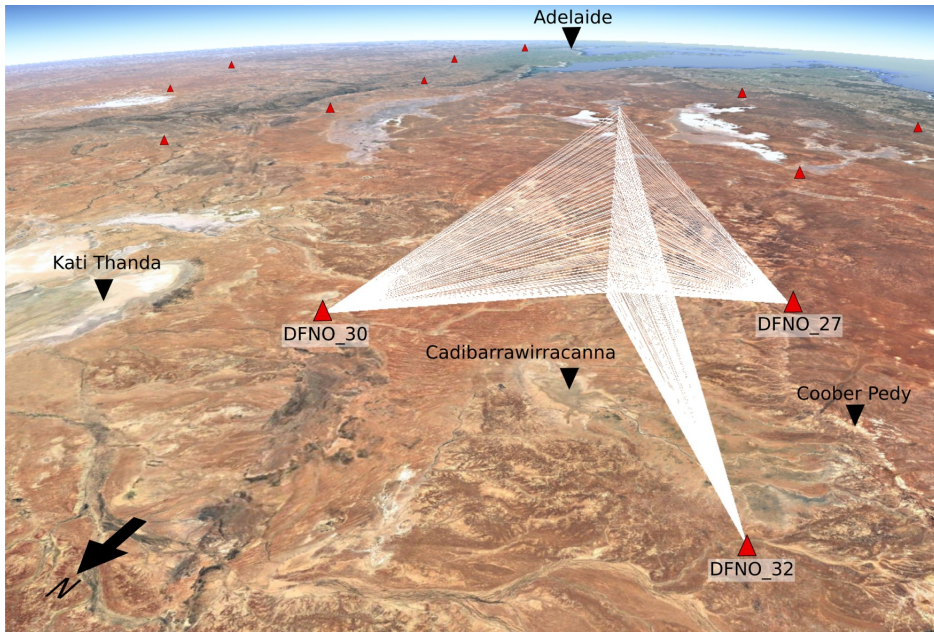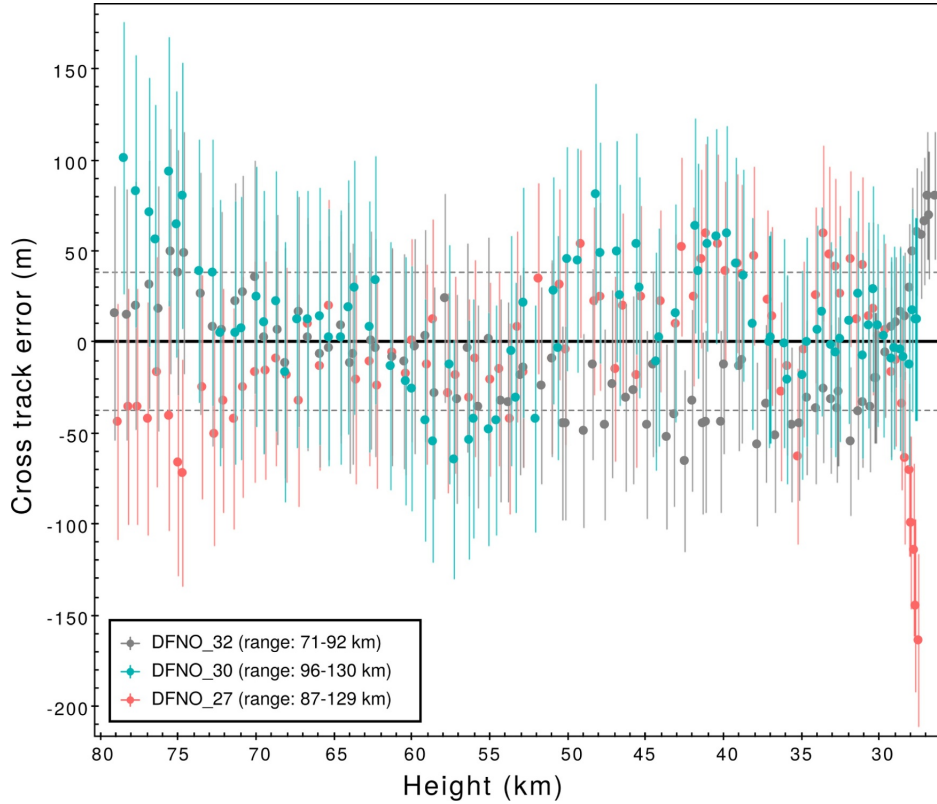
Table 3

Straight line least squares (SLLS) trajectory triangulated in either an inertial (ECI) or non-inertial (ECEF) reference frame for all observations of event *DN160410_03*. Trajectory characteristics (height, velocity, mass) are estimated using an extended Kalman smoother in one dimension on these straight line data. Despite the reference frame used to calculate the straight line, radiants are given in J2000 equatorial coordinates for comparison; the angular separation between the two radiants is 12.93′ (0.22°).

DN160410_03 (full)	ECI	ECEF
Entry radiant – RA (°)	161.76 ± 0.02	161.98 ± 0.02
Entry radiant – DEC (°)	-4.65 ± 0.02	-4.61 ± 0.02
Initial height (km)	79.1 ± 0.05	79.1 ± 0.02
Initial velocity (km s^{-1})	15.2 ± 0.1	15.2 ± 0.1
Initial mass (kg)	1.6 ± 0.7	1.5 ± 0.6
Entry slope, γ_e (°)	64.3	64.8
Final height (km)	26.7 ± 0.07	26.6 ± 0.05
Final velocity (km s^{-1})	4.0 ± 0.4	4.0 ± 0.7
Final mass (kg)	0.05 ± 0.01	0.06 ± 0.01

variance of $d\ell/dt = 0 \, \text{m s}^{-1}$. The process model for dm/dt is not able to fully represent the change of mass due to fragmentation; the process noise is therefore set as a relatively high percentage of the existing mass. Although the trajectory parameters κ, σ and τ are currently assumed to be constant (16), this is not entirely true; process noise is therefore attributed to allow small variations to these parameters throughout the trajectory (20).

The discrete process noise, $\mathbf{Q}_k$, is then calculated from Eq. (19) at

every time step along the trajectory.

3.3. Line-Of-Sight measurement update

Images taken by each observatory show a discontinuous streak across a star background. The Desert Fireball Network uses the modulation of a liquid crystal shutter within the lens of each camera to encode a unique time sequence into the fireball's path (Howie et al., 2017). By comparing the position of the start and end of each fireball segment with the background stars, the azimuth and elevation of each time encoded data point can be determined (Devillepoix et al., 2018).

The astrometric observations of the fireball, $\mathbf{z}_k$, are a series of angular measurements. The measurement function in Eq. (7) extracts the position vector (ℓ) from the state which will be compared to these observations and performs the transformation required. Within this function, ℓ_k^i is converted from geocentric cartesian coordinates to a calculated line-of-sight azimuth and elevation with respect to each observatory. At each t_k, this conversion is required for each station that made an observation. The cartesian vector between each n observatory and the particle position, is rotated into local observatory-centred coordinates (East, North, Up; $[\hat{\mathbf{a}}_k^{i;n}]_{ENU}$) before subdividing it into its altitude and elevation components:

$$az_k^{i;n} = \arctan 2([\hat{\mathbf{a}}_k^{i;n}]_E, \ [\hat{\mathbf{a}}_k^{i;n}]_N) \quad (mod \ 2\pi) \tag{21}$$

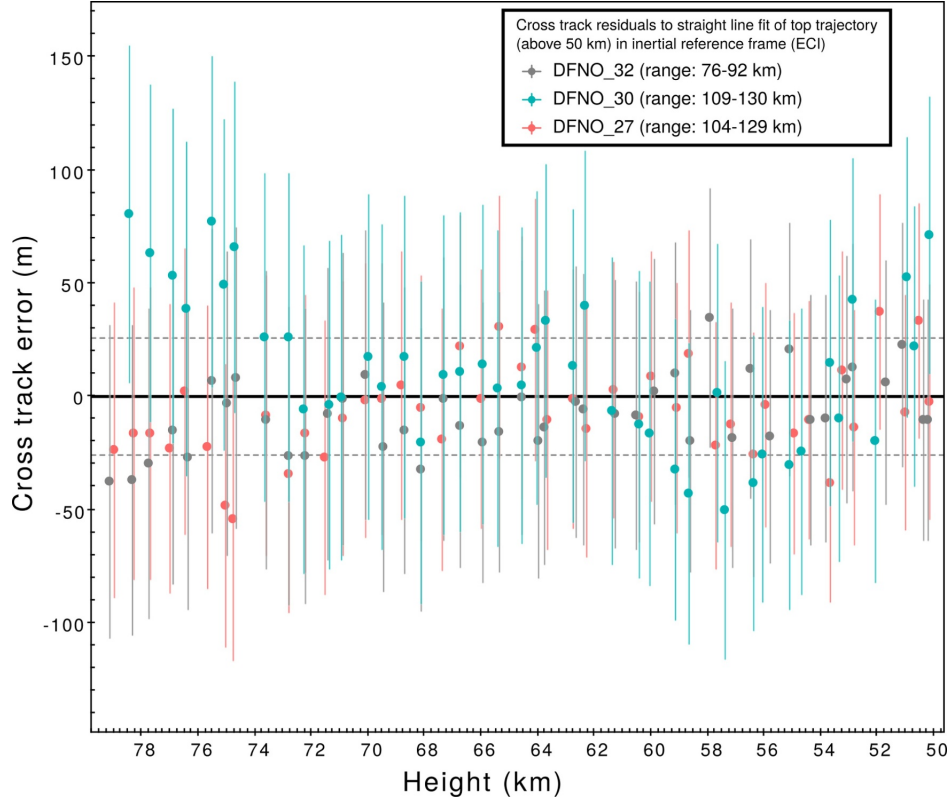$$el_k^{i;n} = \arcsin([\hat{\mathbf{a}}_k^{i;n}]_U). \tag{22}$$

Fig. 10. Cross track residuals for the upper section the *DN160410_03* trajectory to a straight line fit in an inertial (red; ECI) and non-inertial (blue; ECEF) reference frame. Only observations of the fireball above 50 km were used. Error bars on observations are 1σ astrometric errors projected at the corresponding range. (For interpretation of the references to colour in this figure legend, the reader is referred to the web version of this article.)

Table 4

Straight line least squares (SLLS) trajectory triangulated in either an inertial (ECI) or non-inertial (ECEF) reference frame for observations of event *DN160410_03* above 50 km only. Trajectory characteristics (height, velocity, mass) are estimated using an extended Kalman smoother in one dimension on these straight line data. Despite the reference frame used to calculate the straight line, radiants are given in J2000 equatorial coordinates for comparison; the angular separation between the two radiants is 0.21′ (0.004°).

DN160410_03 (> 50 km)	ECI	ECEF
Entry radiant – RA (°)	161.981 ± 0.016	161.984 ± 0.015
Entry radiant – DEC (°)	− 4.469 ± 0.017	− 4.469 ± 0.016
Initial height (km)	79.13 ± 0.01	79.12 ± 0.01
Initial velocity (km s⁻¹)	15.22 ± 0.06	15.18 ± 0.02
Entry slope, γ_e (°)	64.2	64.7

For consistency in calculated and true angular measurements, the azimuth value is expressed within the 0–2π radian range. As an azimuth value of 0 radians is congruent with that of 2π radians, a modulo operation is included in (21).

The result of the measurement function, $\hat{\mathbf{z}}_k^i$ is the predicted line-of-sight unit vectors for a given particle i in azimuth and elevation from all observatories and can be summarised by:

$$\hat{\mathbf{z}}_k^i = [az_k^{i:1}, el_k^{i:1}, az_k^{i:2}, el_k^{i:2}, ...].\tag{23}$$

A multivariate Gaussian probability is then used to calculate the *position* weighting of a particle:

$$[\tilde{w}_k^i]_{pos} = \left(2\pi^{\frac{N_s}{2}}|\mathbf{R}_k|^{\frac{1}{2}}\right)^{-1} e^{-\frac{1}{2}[\hat{\mathbf{z}}_k^i - \mathbf{z}_k]^T \mathbf{R}_k^{-1}[\hat{\mathbf{z}}_k^i - \mathbf{z}_k]},\tag{24}$$

where $|\mathbf{R}_k|$ is the determinant of the observation noise covariance matrix containing azimuth and elevation errors pertaining to each observatory:

$$\mathbf{R}_k = diag\left[Var(az^1),\ Var(el^1),\ Var(az^2),\ Var(el^2),\ ...\right].\tag{25}$$

The observational uncertainties in both azimuth and elevation are linked to the accuracy of picking the start and end points of modulated segments in the fireball image, their calibration and the shutter response time. For all-sky images captured using fish eye lenses, the accuracy in azimuth is much greater than in elevation. Although the DFN observations are syncronised in time, this is not required by the 3D particle filter; only muti-station observations which include absolute timing data are needed.

3.4. Luminosity measurement update

As well as considering the line-of-sight observations, the calculated absolute visual magnitude observations, M_v^{obs}, may also be used to constrain mass loss estimates. Observed luminosities can be obtained from the long exposure images by doing aperture photometry on each shutter break. These measurements are then converted to apparent magnitudes using the stars, accounting for the different exposure times. Apparent magnitudes are finally turned into absolute magnitudes (M_v^{obs}) by doing a distance correction using the basic trajectory solution
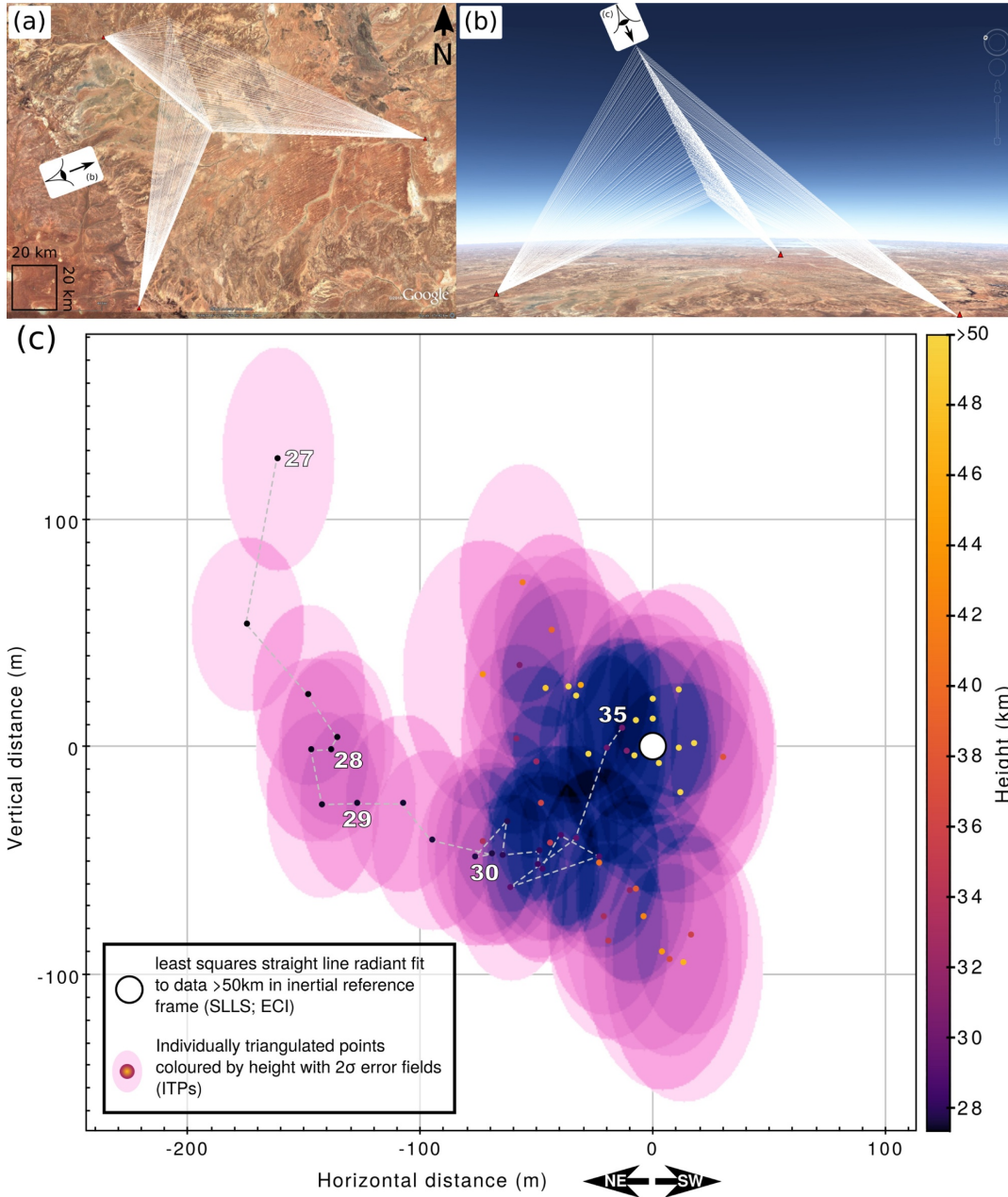
Fig. 11. *DN160410_03* – "Down-line" view (c) as seen by an observer looking down the ECI straight line radiant (illustrated by (a)–(b)) calculated using the top section of the trajectory (points > 50 km; see Fig. 10). This results in the ECI trajectory stacking to a single point (white) whereas the individually triangulated positions (ITPs; coloured points) are projected onto the viewing plane. This plane is normal to the straight line trajectory with the *x*-axis aligned with the Earth horizontal, and inclined from true vertical by the cosine of the trajectory slope. From this down-line view the ITPs help to illustrate the true non-linearity of the path taken by the meteoroid. (Google Earth image credit: Landsat/Copernicus/CNES/Airbus).

given by the SLLS. A combination of Eqs. (1) and (2) are used to calculate the predicted visual magnitude for each particle, M_v^i between t_k and t_{k+1}. The *luminous* weighting for each particle, $[\bar{w}_k^i]_{lum}$ can then be obtained by evaluating the 1D Gaussian probability distribution function

$$[\bar{w}_k^i]_{lum} = \frac{1}{\sqrt{2R_k\,\pi}} e^{-\frac{(M_v^{obs}-M_v^i)^2}{2R_k}}$$

$$(26)$$

where R_k here is the uncertainty in the observed M_v values. This can include errors introduced in the calibration process that is usually

Fig. 12. The absolute distance between individually triangulated positions (ITPs; $y = 0$ with variances in green) and the estimated position of the *DN151212_03* meteoroid using different methods of modelling a meteoroid trajectory: a straight line least squares approximation (SLLS) fitted to the entire suite of observations in an ECI reference frame (grey), a SLLS fitted to the upper (above 50 km) and lower (below 50 km) segments of the trajectory separately (blue; see Section 2) and the results of a 3D particle filter (weighted mean positions in black). The gap between $62 - 84\,km$ corresponds to the time between exposures. The final $1.22\,s$ ($\sim 800\,m$ height) was only observed by a single observatory and no individually triangulated position could be calculated as a reference. (For interpretation of the references to colour in this figure legend, the reader is referred to the web version of this article.)

required to convert arbitrary brightness units to distance-normalised, absolute visual magnitudes.

The overall weighting of each particle including both line-of-sight and absolute magnitude observations can then be calculated as the product of normalised position and luminous weightings:

$$\bar{w}_k^i = [\bar{w}_k^i]_{pos}\,[\bar{w}_k^i]_{lum}, \tag{27}$$

which can then be normalised

$$w_k^i = \frac{\bar{w}_k^i}{\sum_j^{N_s} \bar{w}_k^j}. \tag{28}$$

3.5. Results of the 3D particle filter

As this is a filtering technique, the 3D particle filter iteratively converges upon a final state estimate that combines all observational data, and uncertainties. The estimate at any discrete time is the best guess of the filter up until that point; there is no full trajectory solution. A smoother is able to combine forward and reverse filters to give a full

solution (such as the extended Kalman smoother in Sansom et al. (2015) and multiple model smoother in Sansom et al. (2016)). Particle filter smoothing is still being developed and is not described in this work. To this end, the results desired dictate the order in which observations are presented. As we focus on determining likelihood of final mass estimates for meteorite recovery, we perform a 3D particle filter forward in time on these two test cases using $N_s = 100,000$. If entry masses were to be desired, the filter can be initialised at t_f and run in reverse time order (from terminal point to entry point).

The distance between the ITPs and all predicted particle positions for event *DN151212_03* are shown[1] in Fig. 12 and for event *DN160410_03* in Fig. 13. The weighted mean residuals, as calculated by Eq. (11), are marked in black. ITPs may give us a reasonable indication of meteoroid position, but are sensitive to observational geometry and error. Despite using the ITPs as reference positions for these figures, the

---

[1] In order to graphically represent such a large output file (number of particles plotted = $N_s \times k$) we made use of TOPCAT table processing software which is an open source library for manipulating large tabular data (Taylor, 2005)
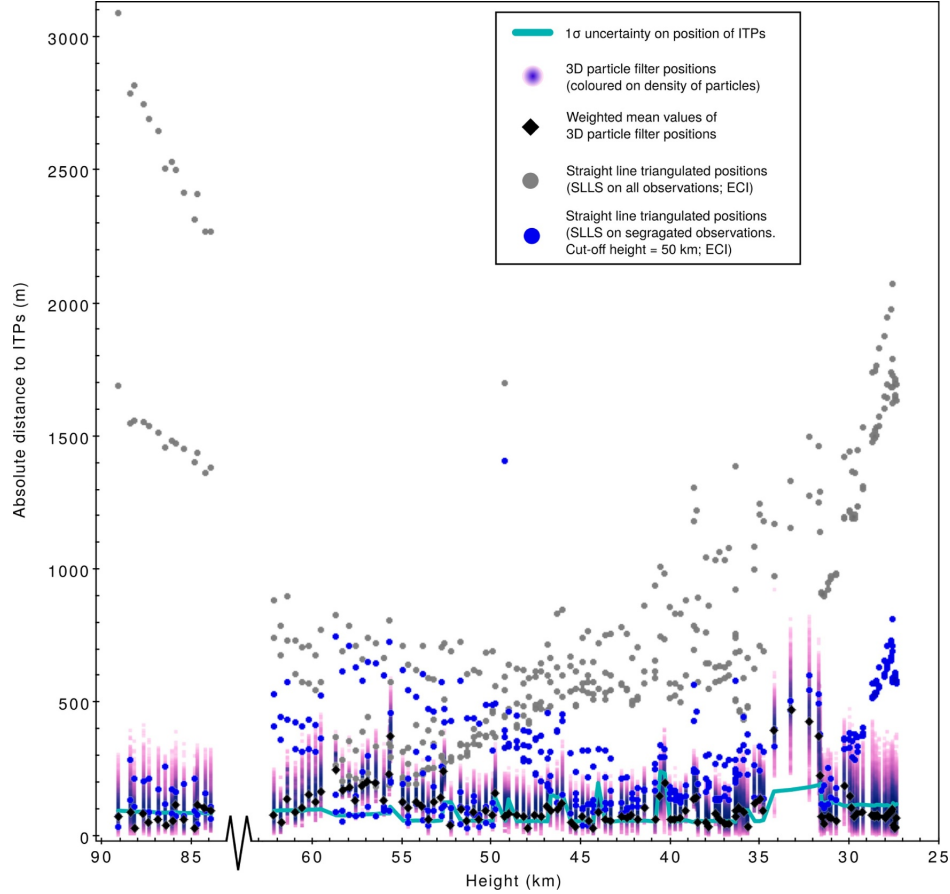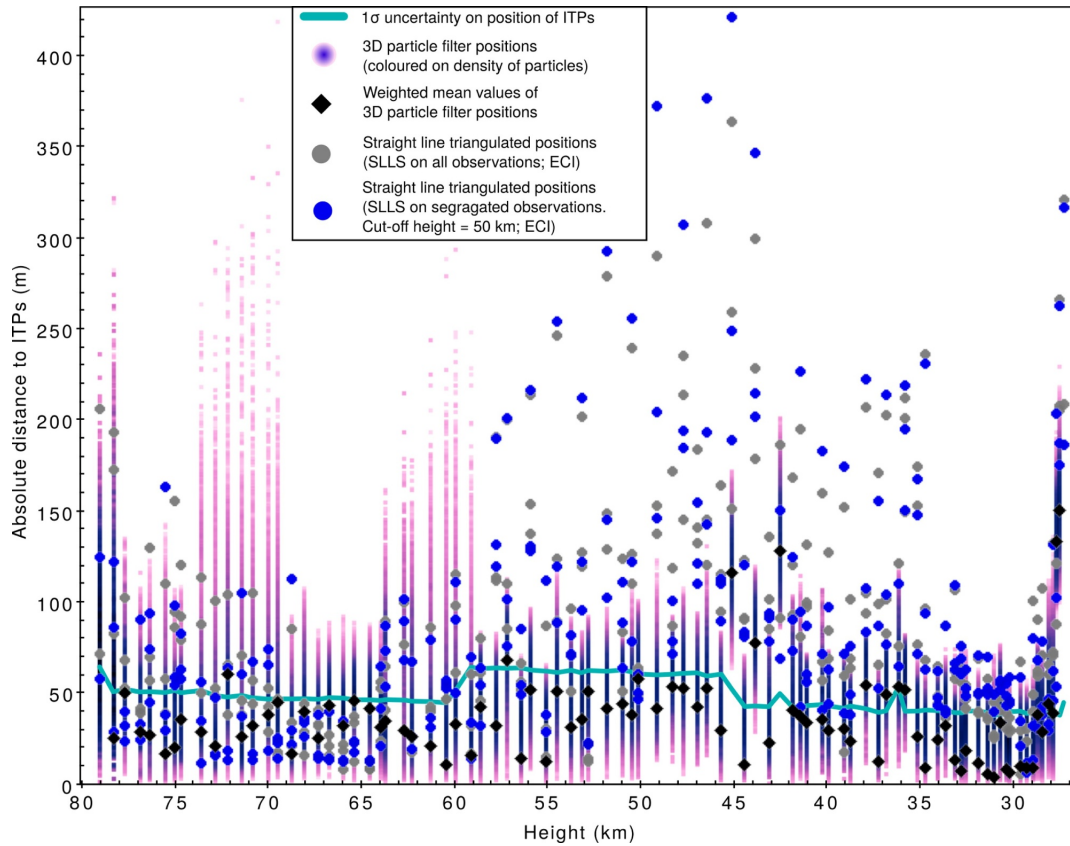
Fig. 13. The absolute distance between individually triangulated positions (ITPs; $y = 0$ with normalised variances in green) and the estimated position of the *DN160410_03* meteoroid using different methods of modelling a meteoroid trajectory: a straight line least squares approximation (SLLS) fitted to the entire suite of observations in an ECI reference frame (grey), a SLLS fitted to the upper (above 50 km) and lower (below 50 km) segments of the trajectory separately (blue; see Section 2) and the results of a 3D particle filter (weighted mean positions in black). (For interpretation of the references to colour in this figure legend, the reader is referred to the web version of this article.)

3D particle filter is weighting estimates based on the raw observations. The history information inherent in the particle 'cloud' provides a certain inertia that prevents unrealistic changes to the overall mean when unfavourable observations are made. Though there is still a flexibility to the estimates that allows to an extent for unmodelled factors (fragmentation etc. not included in the single body equations) to be incorporated, as model uncertainty is considered in the process noise covariance (Eq. (20)).

3.5.1. Case 1: DN151212_03

No absolute brightness data were acquired for this event as the fireball saturated the sensors. The particle filter was still able to calculate theoretical values for M_v, though only normalised values of $[\bar{w}_k^i]_{pos}$ Eq. (24) were used to determine particle weightings for this case.

The maximum deviation of any weighted mean to its corresponding calculated observed position for *DN151212_03* is 470 m, with over half within 80 m. The higher mean values between 34 and 32 km could be related to increased uncertainty in the ITPs for these observations (Fig. 12), or could be indicative of an unmodelled cause. The large gap in Fig. 12 between 62 and 84 km corresponds to the time between exposures. For this event, the final 1.22 s (seven observation times) were only visible from one camera (Fig. 2). The 3D particle filter still estimates positions with single station observations, but the mean final

state estimate at $t_f = 21.14$ s has slightly higher uncertainties because of this. Particles are not shown in Fig. 12 for this final 760 m as no individually triangulated position could be calculated as a reference. The exploration of velocity state-space by the particles can be seen in Fig. 14. Final state estimates are given in Table 5.

3.5.2. Case 2: DN160410_03

The mean particle positions for event *DN160410_03* show a maximum deviation of 150 m, with nearly 80% within 50 m of the ITPs (Fig. 13; black). Not only do the position estimates match the observations well, the calculated values of M_v (evaluated using Eqs. (1) and (2)) also correspond well to the calibrated light curve for DFNO_30 (Fig. 15). The inferior weightings attributed toward the end are most likely due to the calculation using the relatively constant value of τ (around $\sim 0.2\%$). The good correlation between position and luminosity estimates to observational data validates the results of the particle filter, giving confidence to the estimates determined for other state variables through the link in the state equations. The velocities for example can also be compared to those calculated between ITPs and the SLLS positions (Fig. 16). The exploration of this state space is interesting to observe. For example, we can see that a lower velocity option was tested at ~ 55 km but discontinues; a high velocity option around 35 km experiences a similar fate. These discontinued streams can be
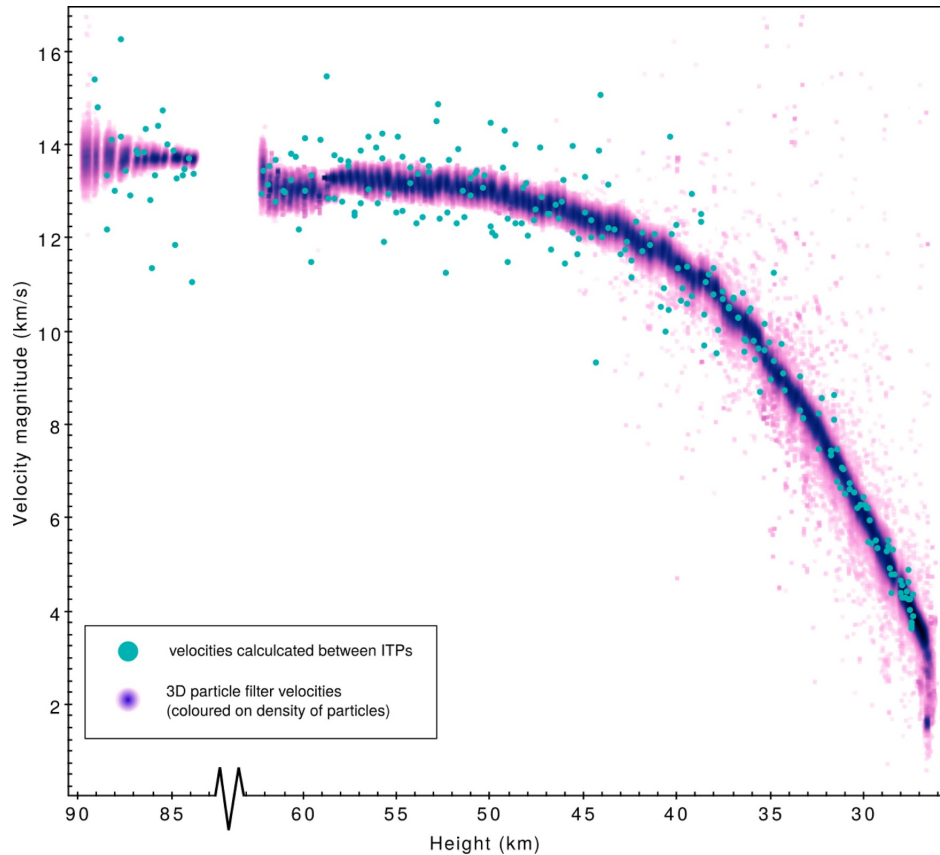
Fig. 14. Magnitude of the velocity vector as calculated by the change in ITP positions with time (green) and as estimated by the 3D particle filter. The gap between 62 and 84 km corresponds to the time between exposures. (For interpretation of the references to colour in this figure legend, the reader is referred to the web version of this article.)

Table 5
Trajectory characteristics, including state values, estimated using the 3D particle filter for the final observation time of both events *DN151212_03* and *DN160410_03*.

Final state values for:	*DN151212_03*	*DN160410_03*
t_f (seconds since start)	21.14	4.66
Height (km)	26.3 ± 0.8	26.3 ± 0.06
Velocity (km s^{-1})	3.5 ± 0.3	3.8 ± 0.1
Mass (kg)	2.7 ± 0.3	0.13 ± 0.02
Shape density coefficient (κ ; m^{3}kg^{-1})	0.0032 ± 0.0001	0.0039 ± 0.0001
↪ Density (kg m^{-3}); if ($A \times c_d$) = 1.5	3610	2650
Ablation coefficient (σ ; s^{2}km^{-2})	0.0141 ± 0.00003	0.0192 ± 0.0003

linked to different mass options (Fig. 17). The final meteoroid states for this exent at $t_f = 4.6$ are also given in Table 5.

4. Discussion

Fireball trajectories are typically approximated as straight line paths over a spherical Earth (Ceplecha and Revelle, 2005). This may be a reasonable assumption for short meteors, but for fireballs, effects that cause deviations to a straight line trajectory are not always negligible. The astrometric uncertainty on DFN observations is typically < 1

arcmin. This high precision, when projected at the observational range to the fireball, gives uncertainties ~ 100 m. Any disturbances to the body greater than this will be resolvable. Gravity and Earth rotation have known effects on trajectories and their observations respectively, and can be quantified. The 231 km long trajectory of the shallow event *DN151212_03* ($\gamma_e = 17°$) was observed for 21.14 s. This means a > 2.1 km downward displacement was experienced due to gravity alone. Over this length of time, at the latitude of the event, an observer on the ground would have moved nearly 8.5 km eastward with Earth's rotation. This must be accounted for if reduction is done in a non-inertial reference frame. Event *DN160410_03* was steeper ($\gamma_e = 65°$) and significantly shorter in both duration (observed for 4.66 s) and length (58 km). Gravity therefore contributes a 105 m vertical displacement. The ground stations will also have moved 1.9 km eastward, affecting apparent velocity vectors in a non-inertial frame.

Fitting a linear trajectory to observations of a meteoroid will reduce the overall effects of gravity (and Earth rotation if using a non-inertial frame) by essentially averaging them out. This may provide usable position data, but will translate into a strong misrepresentation of velocity vectors. The difference in entry radiants calculated in both an inertial (ECI) and non-inertial (ECEF) frame for these trajectories demonstrates the effect of Earth rotation on these entry vectors. For event *DN151212_03* they vary by 13.56′ and for event *DN160410_03* by 12.93′. Entry radiants are used in the calculation of fireball orbits.
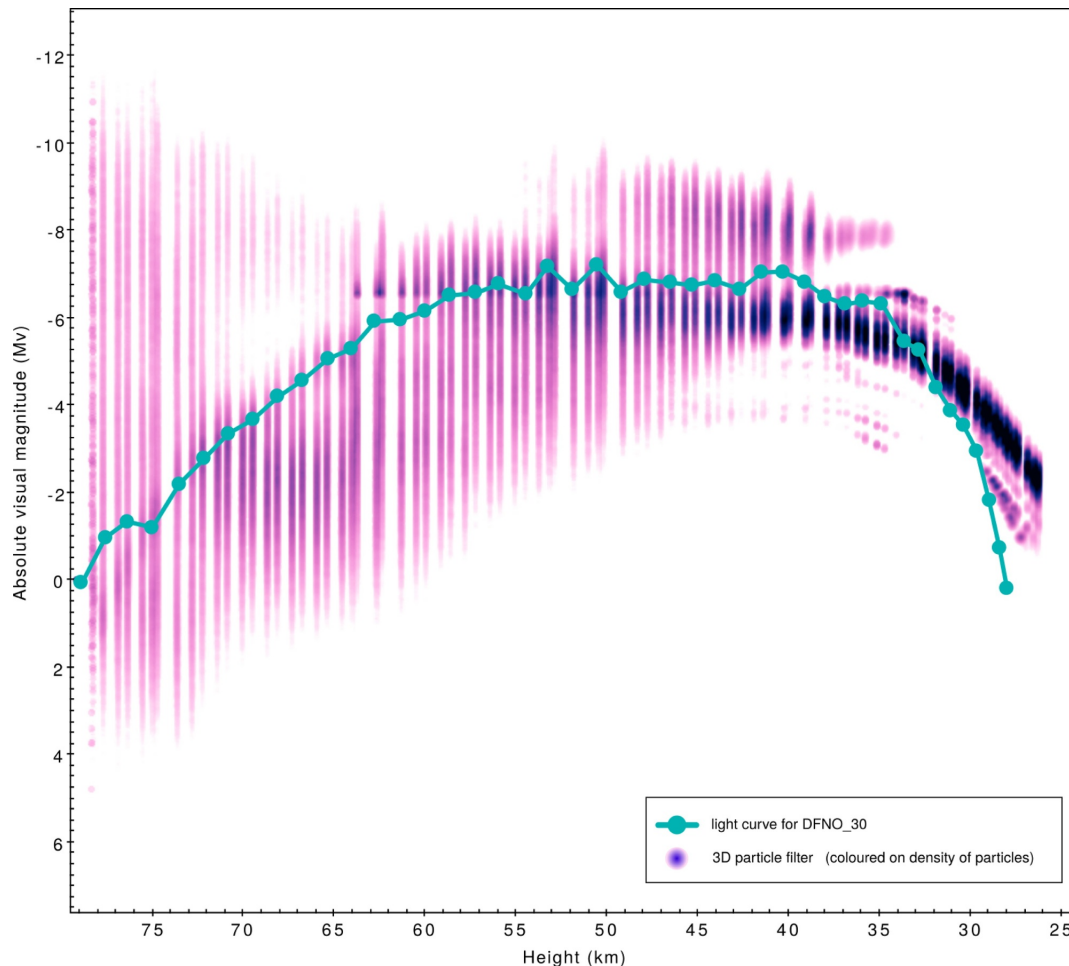
Fig. 15. Comparison of light curve obtained from the DFNO_30 still imagery (green) and predicted absolute visual magnitudes from 3D particle filter (coloured based on density of particles). The inferior match of higher weighted particles to the light curve toward the end can be attributed to the relatively constant value of τ (around $\sim 0.2\%$) used for the calculation of predicted M_v values (Eqs. (1) and (2)). (For interpretation of the references to colour in this figure legend, the reader is referred to the web version of this article.)

Integrating the fireball's motion back in time, performed to determine the heliocentric orbit beyond Earth's sphere of influence, is highly sensitive to both radiant direction and entry velocity. Using an inappropriate model to fit the observations introduces systematic errors to radiant angles, and as shown in Tables 2 and 4, can be far greater than the quoted uncertainties based on the residual fit for longer trajectories. These systematic errors will affect orbit calculations, resulting in the incorrect evaluation of a meteoroid's orbit. The final velocity vector is used in dark flight modelling to estimate meteorite fall positions and will have similar issues, perhaps even more pronounced due to the lower velocities toward the end of the luminous trajectory. Without a means of further testing meteoroid positions, there could be other forces involved that cause unmodelled deviations to a meteoroid trajectory.

Here we use individually triangulated positions (ITPs) as a base for comparison between meteoroid positions calculated using a straight line least squares approximation and a 3D particle filter. The calculation of the ITPs is a unique capability of the DFN as a result of absolute synchronisation of the time encoding between observatories. We have shown for both cases presented that there is a significant deviation of the meteoroid body when comparing ITPs to a straight line trajectory. To some degree the non-linear variability of these fireball trajectories can be visualised in Figs. 6 and 11. The absolute difference between the ITPs and the SLLS results are quantified for event *DN151212_03* in Fig. 12 and for event *DN160410_03* in Fig. 13. For both the long, shallow case (*DN151212_03*), and the steeper, shorter case (*DN160410_03*), the straight line trajectory does not represent the data well. For the triangulated positions using a straight line fitted to the entire data set, positions diverge up to 3.09 km for the former and up to 360 m for the latter. The straight line trajectories fitted to data segmented at 50 km give improved results for *DN151212_03* positions, diverging up to 750 m for the upper trajectory, and 810 m for the lower trajectory (discarding the 1.40 km outlier at 49.2 km). The segmented triangulations for *DN160410_03* show an improvement only in the upper trajectory (290 m), with an increased distance to the ITPs in the lower segment (420 m). These deviations show that factors other than deceleration and ablation are able to significantly influence meteoroid trajectories. These could include aerodynamic effects on non-spherical

Fig. 16. Magnitude of the velocity vector as calculated by the change in ITP positions with time (green), change in straight line least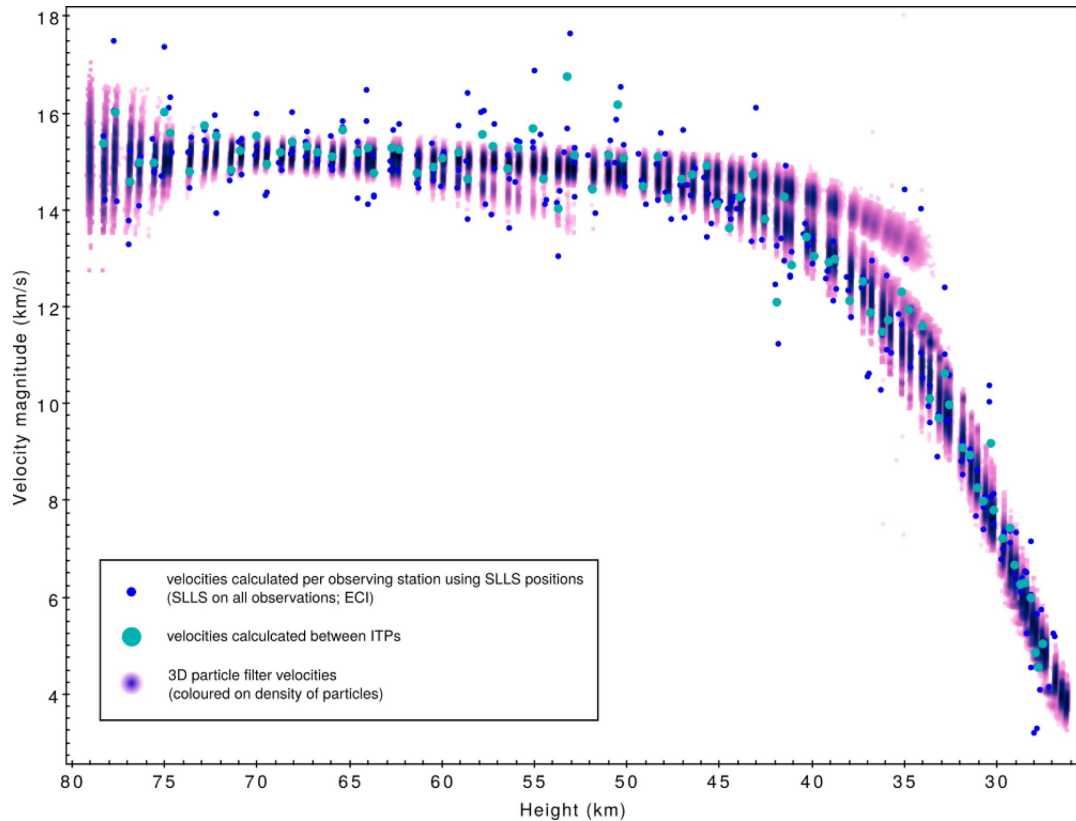 squares (SLLS) triangulated positions for each observatory with time (blue), and estimated by the 3D particle filter. (For interpretation of the references to colour in this figure legend, the reader is referred to the web version of this article.)

bodies and, where fragmentation occurs, the dynamics involved in body disruption.

We can approximate the magnitude of the forces required to cause the deviations seen in Figs. 6 and 11. Over the final 10 s of the *DN151212_03* trajectory (below 50 km), there is a lateral displacement of ∼ 2.1 km. This results in an Eastward acceleration of ∼ 42 m s^{-2}. For a 10 kg body (minimum estimated mass at 50 km altitude), this requires a lateral force of 420 N. The vertical displacement of ∼ 1.2 km seen in Fig. 6 does not include any downward gravity component. As a vertical force would also have to overcome gravity to cause this change, an additional 460 m displacement should be included (gravitational displacement normal to the trajectory over final 10 s = 480 m × cos γ). This gives a ∼ 330 N upward force. Although *DN160410_03* wanders less drastically, a ∼ 230 m lateral displacement from an altitude of 35 km (the final 1.3 s) requires a greater than 500 N lateral force for a 2 kg body (minimum estimated mass at 35 km). From 30.2–27.3 km (the final 0.7 s), a vertical displacement normal to the trajectory of ∼ 170 m would require over a 1000 N force.

Work has been presented in the past on unique Earth-grazing events where a significant effort has been made to determine the path of the meteoroid without the unique use of a SLLS approximation (Borovicka and Ceplecha, 1992; Madiedo et al., 2016). It is interesting to note however that in Borovicka and Ceplecha (1992) there is an observatory almost directly under the event from which the authors were able to determine that there was no curvature to the trajectory outside the observational plane from this viewpoint. For event *DN151212_03*

analysed here, there was a deviation from the SLLS trajectory not only in altitude, but with a significant lateral component. Because of its large size and extreme ablation duration, *DN151212_03* may not be a typical event, however *DN160410_03* is an ideal example of a meteorite dropping fireball. The deviation of the *DN160410_03* fireball from a straight line shows that an SLLS may not be an appropriate approximation for the majority of deep-penetrating (< 50 km altitude) fireballs. The cross-track forces as approximated above, are certainly significant, complicating the ideal straight line scenario and bringing into question the reliability of using this assumption even for small events. Their origins, be they aerodynamic, related to fragmentation or as yet unconsidered, should be investigated.

The complexity of meteoroid trajectories makes it difficult to simulate them with simplified model equations such as given by Eq. (17). Using this single dimension model in a particle filter (e.g. Sansom et al. (2017)) forces the measurement update step to use straight line position values for distance travelled along the trajectory. This misrepresentation of the data in the filter can not only affect position estimates, but may additionally influence other state parameters through the relationship in the state Eq. (17), such as velocity and mass values. As the particle filter is an adaptive approach that uses observations to update state estimates, using the most unprocessed measurements permits subtleties in the data to influence the predicted state. Using the three dimensional model (17), it is able to use the raw line-of-sight observations as described in Section 3.3. Using a 3D particle filter also provides a more robust error analysis as uncertainties are propagated
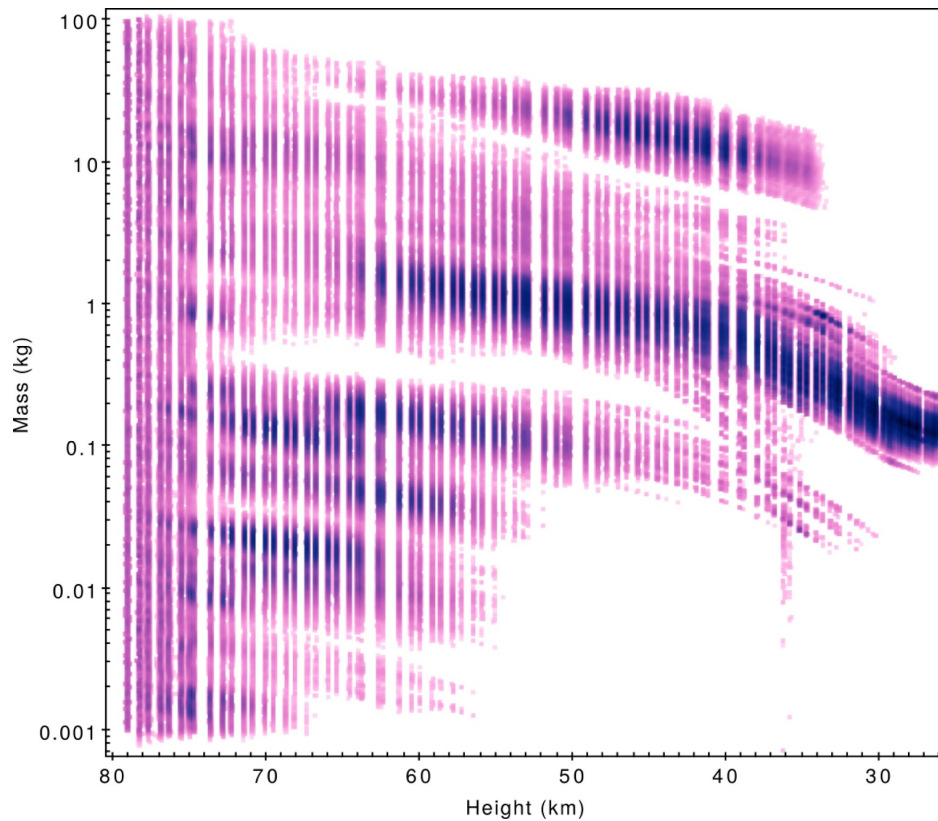
Fig. 17. Masses estimated by the 3D particle filter, coloured by density of particles.

comprehensively from well constrained astrometric errors through to the end of the luminous trajectory. At t_{end}, the remaining particles can be used as a direct input to Monte Carlo dark flight simulations, as presented by Devillepoix et al. (2018). The minimisation of time spent in the field searching for meteorites is of great importance. It is therefore essential to define a search region on the ground that is representative of the statistical results obtained from physical modelling of bright flight observations. The final mass given using an extended Kalman smoother on pre-triangulated straight line data for event *DN151212_03* is 2.0 ± 0.2 kg (Table 1) and 0.05 ± 0.01 (Table 3) for event *DN160410_03*, compared to the 2.7 ± 0.3 kg and 0.13 ± 0.02 kg final masses predicted for these events using the particle filter. Identifying events with greater chances of a successful find will significantly influence decisions about the feasibility of a remote search for a given event. Shallow events in particular, such as *DN151212_03* ($\gamma_e = 15.\,8°$) tend to produce extended fall lines, tens of kilometres long, from small fragments to main body masses. Well constrained final states in these cases are essential.

5. Conclusion

As fireball producing events are typically associated with larger asteroidal debris they have the ability to penetrate deep into the Earth's atmosphere. These events can last tens of seconds, with ground based observations influenced by Earth's rotation and gravity effects resolvable with modern camera resolution. The unique ability of the Desert Fireball Network to triangulate a meteoroid's position at discrete times allows us to investigate the true variability of trajectories. These

individually triangulated positions (ITPs) are used as a reference for comparison to other methods of evaluating meteoroid positions. The flights of two fireballs observed by the Desert Fireball Network were investigated as example events. Triangulating data using a straight line assumption eliminates subtleties in the data that may be indicative of unmodelled processes, such as fragmentation and aerodynamic effects. Deviations from a straight line path of up to 3.09 km for event *DN151212_03* and 360 m for event *DN160410_03* were observed, and a downline view in an inertial reference frame (ECI) shows this is mostly lateral. The investigation in an ECI reference frame eliminates Earth rotation effects, and, as these deviations cannot be accounted for by gravity, must have a different cause. Even the more typical event *DN160410_03* is affected, showing all influences on fireball trajectories should be considered in all deep penetrating cases. The misrepresentation of the start and end of meteoroid trajectories by a straight line fit will affect dark flight models for meteorite search regions as well as orbit determination.

Modelling fireball camera network data in three dimensions has not previously been attempted. The self-contained particle filter approach of Sansom et al. (2017) has been adapted to use a three dimensional dynamic model, and incorporate absolute visual magnitude observations. This allows the raw astrometric observations as seen by each observatory to be incorporated directly into the estimation of a meteoroid state, removing the need for pre-triangulated measurement data. By incorporating the raw observations, errors in each azimuth and elevation can be accounted for and propagated individually. This results in a final state estimate with fully comprehensive errors, leading to more realistic meteorite search areas and will allow an automated,

systematic evaluation of trajectories observed by multiple station camera networks.

Supplementary material

Supplementary material associated with this article can be found, in the online version, at doi:10.1016/j.icarus.2018.09.026.

References

Artemieva, N., Pierazzo, E., 2009. The canyon diablo impact event: projectile motion through the atmosphere. Meteorit.Planet. Sci. 44 (1), 25–42. https://doi.org/10.1111/j.1945-5100.2009.tb00715.x. ISSN 1945-5100.

Artemieva, N.A., Shuvalov, V.V., 2016. From Tunguska to Chelyabinsk via Jupiter. Annu. Rev. Earth Planet. Sci. 44, 37–56. https://doi.org/10.1146/annurev-earth-060115-012218.

Baldwin, B., Sheaffer, Y., 1971. Ablation and breakup of large meteoroids during atmospheric entry. J. Geophys. Res. 76 (19), 4653–4668.

Borovička, J., 1990. The comparison of two methods of determining meteor trajectories from photographs. Bull. Astron. Inst.Czechoslov. 41, 391–396.

Borovicka, J., Ceplecha, Z., 1992. Earth-Grazing fireball of october 13, 1990. Astron. Astrophys. 257, 323–328.

Borovička, J., Spurný, P., Šegon, D., Andreić, Ž., Kac, J., Korlević, K., Atanackov, J., Kladnik, G., Mucke, H., Vida, D., Novoselnik, F., 2015. The instrumentally recorded fall of the Kri{ž}evci meteorite, croatia, february 4, 2011. Meteorit. Planet. Sci. 16 (7). https://doi.org/10.1111/maps.12469.

Borovička, J., Tóth, J., Igaz, A., Spurný, P., Kalenda, P., Haloda, J., Svoreň, J., Kornoš, L., Silber, E., Brown, P., et al., 2013. The Košice meteorite fall: atmospheric trajectory, fragmentation, and orbit. Meteorit. Planet. Sci. 48 (10), 1757–1779.

Bronshten, V.A., 1983. Physics of meteoric phenomena. Geophysics and Astrophysics Monographs. Reidel, Dordrecht, Netherlands.

Brown, P., McCausland, P.J.A., Fries, M., Silber, E., Edwards, W.N., Wong, D.K., Weryk, R.J., Fries, J., Krzeminski, Z., 2011. The fall of the grimsby meteoritei: fireball dynamics and orbit from radar, video, and infrasound records. Meteorit. Planet. Sci. 46 (3), 339–363. https://doi.org/10.1111/j.1945-5100.2010.01167.x.

Brown, P.G., Ceplecha, Z., Hawkes, R.L., Wetherill, G., Beech, M., Mossman, K., 1994. The orbit and atmospheric trajectory of the peekskill meteorite from video records. Nature 367 (6464), 624–626. https://doi.org/10.1038/367624a0.

Campbell-Brown, M.D., Koschny, D., 2004. Model of the ablation of faint meteors. Astron. Astrophys. 418 (2), 751–758. https://doi.org/10.1051/0004-6361:20041001-1.

Ceplecha, Z., 1987. Geometric, dynamic, orbital and photometric data on meteoroids from photographic fireball networks. Bull. Astron. Inst.Czechoslov. 38, 222–234.

Ceplecha, Z., Borovička, J., Elford, W.G., ReVelle, D.O., Hawkes, R.L., Porubčan, V., Šimek, M., 1998. Meteor phenomena and bodies. Space Sci. Rev. 84 (3), 327–471. https://doi.org/10.1023/A:1005069928850.

Ceplecha, Z., Revelle, D.O., 2005. Fragmentation model of meteoroid motion, mass loss, and radiation in the atmosphere. Meteorit. Planet. Sci. 40 (1), 35–54. https://doi.org/10.1111/j.1945-5100.2005.tb00363.x.

Devillepoix, H. A. R., Sansom, E. K., Bland, P. A., Towner, M. C., Cupák, M., Howie, R. M., Jansen-Sturgeon, T., Cox, M. A., Hartig, B. A. D., Benedix, G. K., Paxman, J. P., 2018. The Dingle Dell meteorite: a Halloween treat from the Main Belt. arXiv:1803.02557.

Grewal, M.S., Andrews, A.P., 1993. Kalman Filtering: Theory and Practice. Prentice-Hall Inc., New Jersey.

Hildebrand, A.R., McCausland, P.J.A., Brown, P.G., Longstaffe, F.J., Russell, S.D.J., Tagliaferri, E., Wacker, J.F., Mazur, M.J., 2006. The fall and recovery of the tagish lake meteorite. Meteorit. Planet. Sci. 41 (3), 407–431. https://doi.org/10.1111/j.1945-5100.2006.tb00471.x.

Hoppe, J., 1937. Die physikalischen vorgänge beim eindringen meteoritischer körper in die erdatmosphäre. Astron. Nachr. 262 (10), 169–198.

Howie, R.M., Paxman, J., Bland, P.A., Towner, M.C., Sansom, E.K., Devillepoix, H.A., 2017. Submillisecond fireball timing using de bruijn timecodes. Meteor. Planet. Sci.

Kikwaya, J.-B., Campbell-Brown, M.D., Brown, P.G., 2011. Bulk density of small meteoroids. Astron. Astrophys. 530, A113. https://doi.org/10.1051/0004-6361/201116431.

Madiedo, J.M., Espartero, F., Castro-Tirado, A.J., Pastor, S., de los Reyes, J.A., 2016. An earth-grazing fireball from the daytime erseid shower observed over spain on 2012 june 10. Mon. Not. R. Astron. Soc. 460 (1), 917–922. https://doi.org/10.1093/mnras/stw1020.

McCrosky, R.E., Boeschenstein, H., 1965. The prairie meteorite network. Opt. Eng. 3 (4). 304127–304127

Picone, J.M., Hedin, A.E., Drob, D.P., Aikin, A.C., 2002. NRLMSISE-00 Empirical model of the atmosphere: statistical comparisons and scientific issues. J. Geophys. Res. 107 (A12), 1468.

Ristic, B., Arulampalam, S., Gordon, N., 2004. Beyond the Kalman Filter: Particle Filters for Ttracking Applications. 685 Artech house Boston.

Robitaille, T.P., Tollerud, E.J., Greenfield, P., Droettboom, M., Bray, E., Aldcroft, T., Davis, M., Ginsburg, A., Price-Whelan, A.M., Kerzendorf, W.E., et al., 2013. Astropy: a community python package for astronomy. Astron. Astrophys. 558, A33.

Sansom, E., Rutten, M., Bland, P., 2017. Analyzing meteoroid flights using particle filters. Astron. J. 153 (2), 87.

Sansom, E.K., Bland, P.A., Paxman, J., Towner, M.C., 2015. A novel approach to fireball modeling: the observable and the calculated. Meteorit. Planet. Sci. 50 (8), 1423–1435. https://doi.org/10.1111/maps.12478.

Sansom, E.K., Bland, P.A., Rutten, M.G., Paxman, J., Towner, M.C., 2016. Filtering meteoroid flights using multiple unscented Kalman filters. Astron. J. 152 (5), 148. https://doi.org/10.3847/0004-6256/152/5/148.

Shuvalov, V., 1999. Multi-dimensional hydrodynamic code sova for interfacial flows: application to the thermal layer effect. Shock Waves 9 (6), 381–390. https://doi.org/10.1007/s001930050168.

Shuvalov, V.V., Artemieva, N.A., 2002. Numerical modeling of Tunguska-like impacts. Planet. Space Sci. 50 (2), 181–192. https://doi.org/10.1016/S0032-0633(01)00079-4.

Spurný, P., Bland, P., Shrbený, L., Borovička, J., Ceplecha, Z., Singelton, A., Bevan, A.W.R., Vaughan, D., Towner, M.C., Mcclafferty, T.P., Toumi, R., Deacon, G., 2012. The bunburra rockhole meteorite fall in SW australia: fireball trajectory, luminosity, dynamics, orbit, and impact position from photographic and photoelectric records. Meteorit. Planet. Sci. 47 (2), 163–185. https://doi.org/10.1111/j.1945-5100.2011.01321.x.

Spurný, P., Borovička, J., Baumgarten, G., Haack, H., Heinlein, D., Sørensen, A.N., 2017. Atmospheric trajectory and heliocentric orbit of the Ejby meteorite fall in Denmark on February 6, 2016. Planet. Space Sci. https://doi.org/10.1016/j.pss.2016.11.010.

Spurný, P., Borovička, J., Kac, J., Kalenda, P., Atanackov, J., Kladnik, G., Heinlein, D., Grau, T., 2010. Analysis of instrumental observations of the jesenice meteorite fall on april 9, 2009. Meteorit. Planet. Sci. 45 (8), 1392–1407. https://doi.org/10.1111/j.1945-5100.2010.01121.x.

Taylor, M.B., 2005. TOPCAT & STILTS: starlink table/VOTable processing software. Astronomical Data Analysis Software and Systems XIV. 347. pp. 29.

Co-authored paper 8 — The Creston, California, meteorite fall and the origin of L chondrites

Meteoritics & Planetary Science, in press (2019).
P. Jenniskens, J. Utas, Q-Z. Yin, R. D. Matson, M. Fries, J. A. Howell, D. Free, J. Albers, Jim and **H. A. R. Devillepoix**, *P. A. Bland, A. Miller, R. Verish, L. A. J Garvie, M. E. Zolensky, K. Ziegler, M. E. Sanborn, K. L. Verosub, D. J. Rowland, D. R. Ostrowski, K. Bryson, M. Laubenstein, Q. Zhou, Q-L. Li, X-H. Li, Y. Liu, G-Q Tang, K. Welten, M. W. Caffee, M. M. M. Meier, A. A. Plant, C. Maden, H. Busemann, M. Granvik, and The Creston Meteorite Consortium.*

The Creston, California, meteorite fall and the origin of L chondrites

Peter JENNISKENS [1,2]*, Jason UTAS [3], Qing-Zhu YIN [4], Robert D. MATSON[5],
Marc FRIES [6], J. Andreas HOWELL [7], Dwayne FREE [7], Jim ALBERS[1],
Hadrien DEVILLEPOIX [8], Phil BLAND [8], Aaron MILLER[9], Robert VERISH[10],
Laurence A. J. GARVIE [11], Michael E. ZOLENSKY [6], Karen ZIEGLER [12],
Matthew E. SANBORN[4], Kenneth L. VEROSUB[4], Douglas J. ROWLAND [13],
Daniel R. OSTROWSKI [2,14], Kathryn BRYSON [2,14], Matthias LAUBENSTEIN [15],
Qin ZHOU [16], Qiu-Li LI [17], Xian-Hua LI [17], Yu LIU [17], Guo-Qiang TANG [17],
Kees WELTEN [18], Marc W. CAFFEE[19], Matthias M. M. MEIER [20], Amy A. PLANT [20],
Colin MADEN [20], Henner BUSEMANN [20], Mikael GRANVIK [21,22]
(The Creston Meteorite Consortium)

[1]SETI Institute, Carl Sagan Center, Mountain View, California 94043, USA
[2]NASA Ames Research Center, Moffett Field, California 94035, USA
[3]Institute of Geophysics and Planetary Physics, UCLA, Los Angeles, California 90095, USA
[4]Department of Earth and Planetary Sciences, University of California at Davis, Davis, California 95616, USA
[5]Leidos, Seal Beach, San Diego, California 90704, USA
[6]Astromaterials Research and Exploration Science, NASA Johnson Space Center, Houston, Texas 77058, USA
[7]Spalding Allsky Camera Network, SkySentinel, LLC (SSL), Melbourne, Florida 32940, USA
[8]Faculty of Science & Engineering, Curtin University, Bentley, Perth, Western Australia 6102, Australia
[9]Ancient Earth Trading Co., Atascadero, California 93423, USA
[10]Meteorite Recovery Lab, Escondido, California 92046, USA
[11]Center for Meteorite Studies, School of Earth & Space Exploration, Arizona State University, Tempe, Arizona 85287, USA
[12]Institute of Meteoritics, University of New Mexico, Albuquerque, New Mexico 87131, USA
[13]Center for Molecular and Genomic Imaging, Department of Biomedical Engineering, UC Davis, Davis, California 95616, USA
[14]Bay Area Environmental Research Institute, 625 2nd St., Suite 209, Petaluma, California 94952,USA
[15]Ist. Naz. di Fiscia Nucleare, Lab. Naz. del Gran Sasso, I-67100 Assergi (AQ), Italy
[16]National Astronomical Observatories, Chinese Academy of Sciences, Beijing 100012, China
[17]State Key Laboratory of Lithospheric Evolution, Inst. Geol. and Geophys., Chinese Acad. Sci., Beijing 100029, China
[18]Space Sciences Laboratory, University of California, Berkeley, California 94720, USA
[19]PRIME Laboratory, Purdue University, West Lafayette, Indiana 47907, USA
[20]Institute of Geochemistry and Petrology, ETH Zürich, CH-8092, Zürich, Switzerland
[21]University of Helsinki, Department of Physics, FI-00014, Helsinki, Finland
[22]Luleå University of Technology, Division of Space Technology, S-98128 Kiruna, Sweden
*Corresponding author. E-mail: petrus.m.jenniskens@nasa.gov

Abstract–It has been proposed that all L chondrites resulted from an ongoing collisional cascade of fragments that originated from the formation of the ~500 Ma old asteroid family Gefion, located near the 5:2 mean-motion resonance with Jupiter in the middle Main Belt. If so, L chondrite pre-atmospheric orbits should be distributed as expected for that source region. Here, we present contradictory results from the orbit and collisional history of the October 24, 2015, L6 ordinary chondrite fall at Creston, CA (here reclassified to L5/6). Creston's short 1.30 ± 0.02 AU semimajor axis orbit would imply a long dynamical evolution if it originated from the middle Main Belt. Indeed, Creston has a high cosmic ray exposure age of 40–50 Ma. However, Creston's small meteoroid size and low $4.23 \pm 0.07°$ inclination indicate a short dynamical lifetime against collisions. This suggests, instead, that Creston originated most likely in the inner asteroid belt and was delivered via the ν_6 resonance. The U-Pb systematics of Creston apatite reveals a Pb-Pb age of

4,497.1 ± 3.7 Ma, and an upper intercept U-Pb age of 4,496.7 ± 5.8 Ma (2σ), circa 70 Ma after formation of CAI, as found for other L chondrites. The K-Ar (age ~4.3 Ga) and U,Th-He (age ~1 Ga) chronometers were not reset at ~500 Ma, while the lower intercept U-Pb age is poorly defined as 770 ± 320 Ma. So far, the three known L chondrites that impacted on orbits with semimajor axes a <2.0 AU all have high (>3 Ga) K-Ar ages. This argues for a source of some of our L chondrites in the inner Main Belt. Not all L chondrites originate in a continuous population of Gefion family debris stretching across the 3:1 mean-motion resonance.

INTRODUCTION

There is an ongoing effort to identify the source of L chondrites in the asteroid belt. The delivery resonance and inclination of the source region can be identified in a statistical sense from meteorite falls for which an atmospheric impact trajectory and pre-atmospheric orbit are calculated (Jenniskens 2014). So far, five L5 and L6 chondrites have yielded pre-impact orbits: Innisfree, Jesenice, Park Forest, Villalbeto de la Peña, and Novato.

About two-thirds of L chondrites have a common 470 ± 6 Ma Ar-Ar and U-Pb resetting age, especially those that show shock blackening (Anders 1964; Haack et al. 1996; Alexeev 1998; Scott 2002; Korochantseva et al. 2007; Weirich et al. 2012; Yin et al. 2014; Li and Hsu 2016; Wu and Hsu 2017). In addition, L chondrite falls were much more common 470 Ma ago, where they are found in the fossil record of terrestrial strata dated to 467.3 ± 1.6 Ma (Schmitz et al. 2001, 2016).

It has been proposed that the Gefion asteroid family, located near the 5:2 mean-motion resonance, was formed at that time and this is the source of these shocked L chondrites (Nesvorný et al. 2009). While delivery was rapid, initially, via the 5:2 mean-motion resonance, the meteorites would now be delivered to Earth more efficiently via the 3:1 mean-motion resonance. Gefion is the only known family with large members of L (as opposed to H and LL) chondrite composition (Vernazza et al. 2014) and some asteroids found in the 3:1 mean-motion resonance, e.g., (355) Gabriella, (14470) Utra, and (1722) Goffin, have L chondrite-like spectra (Fieber-Beyer and Gaffey 2015). In more recent years, however, the reflection spectra of some Gefion family members were found to resemble that of H chondrites and basaltic achondrites (McGraw et al. 2017) and the age of the Gefion family may be older than required, 1103 ± 386 Ma according to Spoto et al. (2015), who did not include the initial velocity at ejection, however.

There could be more than one source region of L chondrites in the main asteroid belt. It has been argued that large groups of compositionally similar asteroids are a natural outcome of planetesimal formation (Youdin 2011; Vernazza et al. 2014). Also, the current asteroid population is mostly composed of reassembled matter from large-scale disruptions of an earlier generation of planetesimals (Bottke et al. 2005). If so, the L chondrite parent body may have broken into several daughter asteroids during an initial disruption of the L chondrite parent body long ago, each of which could later have created an asteroid family in a different part of the Main Belt.

More than one recent collision created the meteoroids that now impact Earth. L5 and L6 chondrites have a broad distribution of cosmic ray exposure ages (CRE). The CRE age identifies the moment in time when a collision caused the meteoroid to no longer be shielded from cosmic rays by a few meters of overlaying burden. The broad distribution implies that multiple disruptive collision or cratering events produced this meteorite type (Marti and Graf 1992; Eugster et al. 2006; Wasson 2012). Note that L3 and L4 chondrites appear to have different CRE age distributions than L5 or L6 chondrites, and are not considered here. At this moment, there are no observed L3 or L4 falls with measured pre-atmospheric orbits.

Here, we report on the October 24, 2015 fall of the ordinary chondrite Creston near Paso Robles, California. Two hundred and eighteen eyewitnesses reported the fireball (American Meteor Society event number 2635-2015). Fourteen witnesses close to the path heard sonic booms shortly after the fireball. Seismic stations timed tremors when the shock wave coupled to the ground. Based on the visual and seismic sightings, six Doppler radar returns from the United States National Oceanic and Atmospheric Administration (NOAA) next generation weather radar network (NEXRAD) were identified that were likely from falling meteorites (Fries et al. 2016). Based on the radar-defined search area, the first stone was located on October 27, now named CR01 and classified as an L6 ordinary chondrite (Bouvier et al. 2017). The stone had shattered when it hit a metal fence post. Five other meteorites were found in the following month, with a total weight of 852.3 g (Table 1).

Two of the meteorites (CR05 and CR06) were made available for nondestructive analysis (Fig. 1), while

The Creston, California, meteorite fall   3

Table 1. Creston meteorite masses and find locations.

CR#	Date of find	Mass (g)	Latitude (N)	Longitude (W)	Altitude (m)	Finder
01[b]	October 27, 2015	~396[a]	35.57508	120.49847	397	Robert & Ann Marie Ward
02[b]	October 28, 2015	69.2	~35.568	~120.481	~499	Terry Scott
03	October 31, 2015	102.2	~35.568	~120.481	~499	Terry Scott
04	November 16, 2015	108	~35.568	~120.481	~499	Michael Farmer
05[b]	November 19, 2015	72.681	~35.565	~120.467	~477	(local finder/via Sonny Clary)
06[b]	November 21, 2015	95.549	35.56547	120.46747	477	Aaron Miller

[a]Broken on impact.
[b]Meteorites studied here.
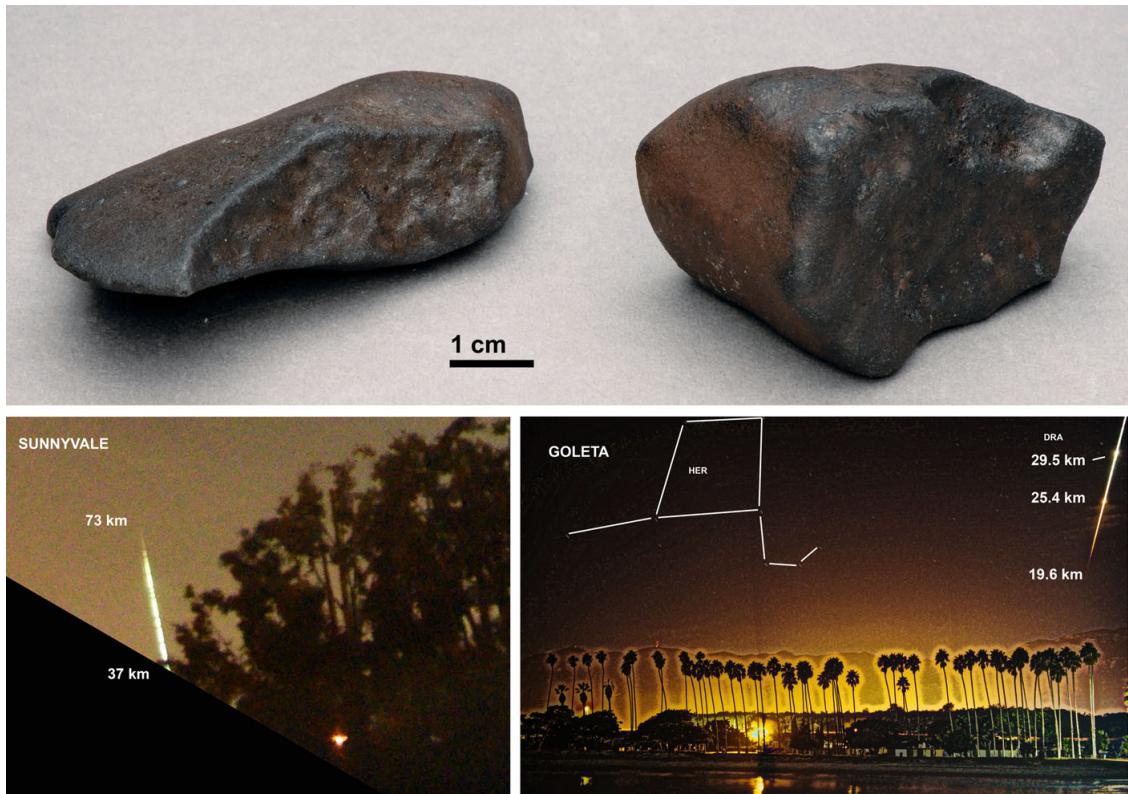
Fig. 1. Top) Optical photographs of Creston meteorites #5 (left) and #6. Notice how each meteorite has one side that is more reddish colored, the irregular surface in the case of C05 and the fresher flatter surface in the case of C06, respectively. Bottom) Creston bolide from Sunnyvale (cropped image) and Goleta.

fragments of meteorites CR01 and CR02 were used for destructive analysis. We determined the pre-atmospheric orbit and the collision history of the meteorites in order to investigate whether Creston originated from the same source as other L chondrites with known pre-atmospheric orbits. We also comprehensively characterized the meteorite mineralogically, petrographically, geochemically, isotopically, and magnetically.

EXPERIMENTAL METHODS

Meteoroid Trajectory and Orbit

The fireball was recorded by an automated digital camera developed for the Desert Fireball Network (DFN) during testing at the Cameras for Allsky Meteor Surveillance project (CAMS; Jenniskens et al. 2011)

station in Sunnyvale, California (Fig. 2). The camera consists of a Nikon D810 digital still camera equipped with a liquid crystal shutter that interupts the image 10 times per second, with some breaks kept dark to encode the time during the exposure (Fig. 1, lower left). At the time of the fall, the skies in Sunnyvale were hazy and illuminated by a full Moon. Few stars are visible in the image. Images from the previous night were used to calibrate the background star field with a mean observed-calculated astrometric precision of O-C = 1.0' (Table 2).

A second digital still image, a single exposure, was obtained from the pier at Goleta by Christian M. Rodriguez of Santa Barbara and posted on a social media website. The meteor is captured near the right edge of the image, entering from a corner (Fig. 1, lower right). Upon

request, the original image was made available for analysis to reveal a rich star field, including a star on the right side of the meteor trail. Rodriguez saw the fireball and stopped the exposure about 5 s after it faded. The field of view is relatively small, resulting in an O-C = 0.24'.

The fireball was also captured in two SkySentinel allsky cameras, one at Riverside, operated by Richard Garcia, and one in El Segundo, operated by Dave Goodyear (Fig. 3). Station locations relative to Sunnyvale and Goleta are shown in Fig. 2. Both cameras are small image format (640 × 480 pixels), low-light video cameras equipped with an allsky lens. In Riverside, there is more obstruction near the horizon than in El Segundo, the latter capturing the same two flares as seen in Goleta. In Riverside, only the first flash
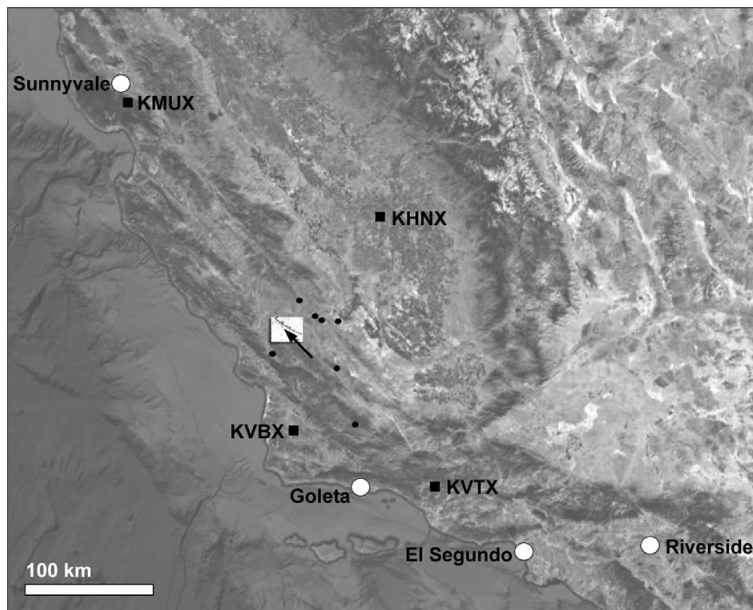
Fig. 2. California map with location of camera stations (open circles), radar stations (black squares), and seismic stations (black dots). (White area is enlarged in Fig. 5.)

Table 2. Camera station locations, sampling rate, and astrometric precision.

#	Station	Latitude (N)	Longitude (W)	Altitude (m)	Type	Frame rate (Hz)	O-C (')	Range (km)
1	Sunnyvale	37.34781	122.03896	60	Digital Still w. Shutter	10.00	1.0 ± 0.7	264
2	Goleta	34.41508	119.82893	11	Digital Still	–	0.24 ± 0.14	146
3	Riverside	33.91367	117.34020	471	Allsky Video	29.97	4.4 ± 3.1	331
4	El Segundo	33.92745	118.41215	46	Allsky Video	29.97	4.4 ± 3.3	250
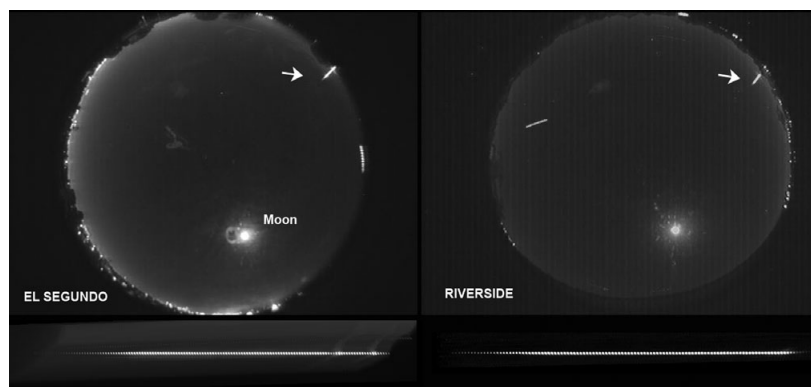
Fig. 3. Creston bolide from (left) El Segundo and (right) Riverside in SkySentinel video. Below each allsky image summary is a sequence of video frames showing the meteor in detail (moving from left to right toward the horizon).

is recorded. The Iris software was used to track the meteor's position and brightness in the video frames. No stars are visible in the individual image frames, but after averaging a number of frames, sufficient stars can be found for calibration above 15° elevation. The zenith angles (z) of the meteor as a function of time were computed from pixel coordinates by fitting the exponential model as a function of zenith distance described in Borovicka et al. (1995). Observed-calculated root-mean-square precision for 82 stars (above 15° elevation) was O-C = 4.4'. This is sufficient to align the observed light curve to the trajectory solution, but not enough to help improve the trajectory solution from combining the Sunnyvale and Goleta observations.

Meteorite Petrography, Bulk Chemistry, and Isotopes

Petrographic analysis of CR01 was done initially at the Arizona State University and reported in Bouvier et al. (2017). At NASA Johnson Space Center (JSC), electron microprobe analysis (EPMA) of a subsample of CR02 was performed to evaluate metamorphic conditions of the rock and verify the initial classification. These analyses were made using a Cameca SX100 microprobe at the E-beam laboratory of the Astromaterials and Exploration Science (ARES) Division of JSC. Natural mineral standards were used, and analytical errors are at the 0.1 wt% level for most elements. We used a 1 μm focused beam in all analyses, at 15 kV and 20 nA. The moderately and highly shocked lithologies were analyzed separately, for comparison.

Oxygen isotope studies were performed at the University of New Mexico. Three subsamples of 1.20, 1.30, and 0.80 mg, respectively, were acid-treated in order to remove any possible terrestrial contamination.

Molecular oxygen was released from the samples by laser-assisted fluorination (20 or 50 W far-infrared CO_2 laser) in a BrF_5-atmosphere, producing molecular O_2 and solid fluorides, from which excess BrF_5 was removed by reaction with hot NaCl. The oxygen was purified by freezing at −196 °C, followed by elution at ~300 °C into a He-stream. NF_3 is then separated in a gas chromatography column and frozen again at −196 °C to remove He. The O_2 is then released directly into a dual inlet mass spectrometer (Thermo Finnigan MAT 253). The San Carlos olivine standards (~1–2 mg) were analyzed daily. Each mass spectroscopic analysis consists of 20 cycles of standard-sample comparisons (e.g., Popova et al. 2013).

Chromium isotope and bulk chemical composition measurements were completed at the University of California, Davis (UC Davis). A fusion crust-free fragment (50.8 mg) was crushed into a powder and placed into a polytetrafluoroethylene (PTFE) Parr capsule along with a 3:1 mixture of concentrated HF: HNO_3 acid. The PTFE capsule was placed into a stainless steel jacket and heated in a 190 °C oven for 96 h. After complete dissolution, an aliquot of the solution was used for Cr isotopes and the remaining solution was used for major, minor, and trace element concentration determination. Chromium was separated from the bulk sample using a three-column chemical separation procedure described previously by Yamakawa et al. (2009). After separating Cr from the sample matrix, the isotopic composition of the purified Cr fraction was analyzed using a Thermo Triton Plus thermal ionization mass spectrometer at UC Davis. A total Cr load of 12 μg was loaded onto four outgassed W filaments (3 μg of Cr per filament). The Cr separated from Creston was bracketed by four filaments loaded with NIST SRM 979 Cr standard solution at the same

total Cr load as the Creston fractions. Chromium isotopic compositions are reported as parts per 10,000 deviation from the measured SRM 979 standard (ε-notation).

An aliquot set aside from the same dissolved sample above before Cr separation was used to determine the concentrations for a suite of elements (major, minor, and trace) using Thermo Element XR high-resolution inductively coupled plasma mass spectrometer at UC Davis. The analytical methods for this procedure have been described previously (Jenniskens et al. 2012, 2014; Popova et al. 2013).

Meteorite Cosmic Ray Exposure, K-Ar and U,Th-He Ages

To determine the cosmic ray exposure age and meteoroid size, cosmogenic radionuclide concentrations were analyzed by means of nondestructive high purity germanium (HPGe) gamma spectroscopy. Two specimens of Creston (CR05 and CR06) were measured in the underground laboratories at the Laboratori Nazionali del Gran Sasso (LNGS) (Arpesella 1996) for 14.74 days (CR06, 263 days after the fall) and 15.90 days (CR05, 278 days after the fall), respectively. The counting efficiencies have been calculated using thoroughly tested Monte Carlo codes.

Additional measurements of cosmogenic radionuclides ^{10}Be and ^{36}Cl were obtained from a sample of CR02 weighting ~52 mg. At UC Berkeley, the sample was gently crushed in an agate mortar and the powder dissolved in concentrated HF/HNO_3 along with a carrier solution containing approximately 2.8 mg of Be and 3.5 mg of Cl. After complete dissolution of the sample, an aliquot was taken for chemical analysis by ICP-OES and radionuclides were separated and purified for measurement by accelerator mass spectroscopy (AMS) at Purdue University.

At ETH Zürich, the CRE age and K-Ar age were determined from noble gas concentrations. Two samples of CR02 were prepared by breaking apart a ~70 mg piece of Creston. The samples were weighed, wrapped in Al foil, and loaded into an in-house built noble gas mass spectrometer. Noble gases were extracted by a furnace heated by electron bombardment to 1700–1800 °C in a single heating step, and separated into a He and Ne, and an Ar fraction by temporarily freezing the Ar to a charcoal cooled by liquid nitrogen. Analysis was done according to a protocol most recently described in Meier et al. (2017). Helium-4 and all Ne and Ar isotopes were measured, together with the ion species H_2O^+, $^{35}Cl^+$, $^{37}Cl^+$, $^{40}Ar^+$, and CO_2^+, which were monitored to potentially correct for interferences on the masses of the noble gas isotopes, but all

interferences proved to be negligible. The two samples were analyzed back-to-back, and bracketed with two Al blanks. Blank contributions to total signals were <0.04% on ^{4}He, <0.8%, and <4% on all Ne and Ar isotopes, respectively.

Meteorite U-Pb and Pb-Pb Ages

U-Pb ages for Creston were determined at the National Astronomical Observatories (NAO), Chinese Academy of Sciences (CAS) in Beijing. The detailed analytical procedure for U-Pb dating of phosphate grains in terrestrial rocks can be found in Li et al. (2010), which was further refined and applied successfully to meteorites (Popova et al. 2013; Zhou et al. 2013; Yin et al. 2014). Backscattered electron images of phosphate grains in a polished mount of CR01 were imaged with a Carl Zeiss SUPRA-55 field-emission scanning electron microscope (FESEM) equipped with energy dispersive spectrometer (EDS). The probe current was 300 pA at an accelerating voltage of 15 kV. This step was essential in selecting suitable analytical spots in the subsequent ion probe session for U-Pb dating to avoid microfractures, inclusions, and other observed physical defects in the individual phosphate grains. The analytical spots are identified in Fig. 4.

In situ isotopic analysis of U-Pb for phosphate grains was performed on the large radius magnetic sector multicollector, secondary ion mass spectrometer (SIMS), a Cameca IMS-1280HR at the Institute of
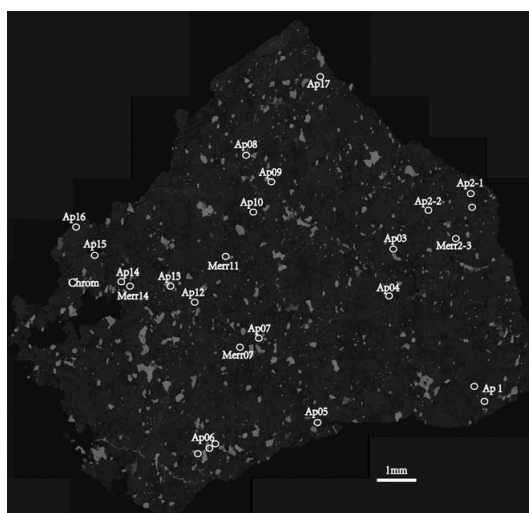

Fig. 4. Apatite grains in Creston CR01. Ap = apatite; Chrom = chromite; Merr = merrillite.

The Creston, California, meteorite fall 7

Geology and Geophysics (IGG), Chinese Academy of Sciences (CAS) in Beijing. The O^{2-} primary ion beam was accelerated at -13 kV, with an intensity ranging between 8 and 9 nA. The Köhler illumination mode was used with a 200 mm diameter aperture, resulting in an elliptical spot size of 20×30 mm^2 on the target. Positive secondary ions were extracted with a 10 kV potential. A monocollector electron multiplier (EM) was used as the detection device to measure secondary ion beam intensities of $^{204}Pb^+$, $^{206}Pb^+$, $^{207}Pb^+$, $^{208}Pb^+$, $^{232}Th^+$, $^{238}U^+$, $^{232}Th^{16}O^+$, $^{238}U^{16}O^+$, $^{238}U^{16}O_2^+$, and a matrix reference peak of $^{40}Ca_2^{31}P^{16}O_3^+$ at a mass resolution of approximately 9000 (defined at 50% height). The $^{40}Ca_2^{31}P^{16}O_3^+$ signal was used as reference peak for tuning the secondary ions, energy, and mass adjustments. Pb/U ratios were calibrated with power law relationship between $^{206}Pb^{*+}/^{238}U^+$ and $^{238}U^{16}O_2^+/^{238}U^+$ relative to an apatite standard of NW-1 (1160 Ma) that comes from the same complex at Prairie Lake as that of the Sano et al. (1999) apatite standard (PRAP). Uranium concentration is calibrated relative to the Durango apatite, which contains approximately 9 ppm of U (Trotter and Eggins 2006). The detection limit is approximately 4 ppb of U in apatite. The $^{206}Pb/^{238}U$ standard deviation measured in the standard was propagated to the unknowns. Each measurement consisted of 10 cycles, with the total analytical time of about 23 min. Due to the low uranium concentration, all of the merrillites failed to yield useful Pb-Pb age information. The uncertainties for individual apatite analyses are reported as 1σ. The weighted average of $^{206}Pb^*/^{238}U$ and Pb-Pb ages, quoted at the 95% confidence level, was calculated using ISOPLOT 3.0.

The ^{204}Pb counts are very low in all apatite grains. Most points have zero counts, which indicate the common lead levels are very low. We assumed that the common lead level is mostly surface contamination, and correction

using modern terrestrial common lead composition was applied. Given the very low level of ^{204}Pb and common Pb fraction f_{206} (%), using the primordial lead composition (Tatsumoto et al. 1973) instead of terrestrial common lead would make no difference in the calculated radiogenic lead composition. To illustrate the point, we plotted the common lead corrected data in both the normal Wetherill-type concordia diagram, inverse Tera-Wasserburg diagram, as well as the 3-D linear regression of the total lead as measured (without correction for initial or common lead) in $^{207}Pb/^{206}Pb$ versus $^{238}U/^{206}Pb$ plane (Wendt and Carl 1984; Wendt 1989; Ludwig 1998). The similar results (not shown here) among the three panels within errors indicate that the unknown common Pb isotope composition and its correction are insignificant for age calculations.

RESULTS

Trajectory and Orbit

The exact time of the onset of the fireball was derived from the CAMS low-light video cameras (Jenniskens et al. 2011). GPS synchronization of the DFN camera was unreliable at the time of the event. The fireball was just below the camera field of view at the CAMS station at Fremont Peak Observatory. A single-frame flash (<0.05 s long) was detected in cameras 62, 71, and 73 at 05:47:48.8 ± 0.2 UTC, and a weaker flash at 05:47:49.1 ± 0.2 UTC, which are interpreted to be the two flares seen in Fig. 1.

Results for the trajectory and orbit derived from triangulation of Sunnyvale with Goleta are given in Table 3 and Fig. 5. The convergence angle between the intersecting planes through meteor and station is only 7.2°. The solution based on DFN/Sunnyvale and Goleta is most sensitive to systematic errors in the DFN

Table 3. Trajectory and orbit, October 24, 2015.

Trajectory (apparent):		Orbit (geocentric):	
Time begin (UT)	05:47:44.3 ± 0.1	Solar longitude (°)	210.2828 ± 0.0001
Right ascension (°, apparent)	25.90 ± 0.07	Right ascension (°, geocentric)	28.50 ± 0.10
Declination (°, apparent)	+4.83 ± 0.10	Declination (°, geocentric)	−0.70 ± 0.18
Entry speed (km/s, apparent)	16.00 ± 0.26	Entry speed (km/s, geocentric)	11.26 ± 0.34
Latitude begin (°, N)	35.347 ± 0.028	Perihelion distance (AU)	0.7670 ± 0.0053
Longitude begin (°, W)	120.226 ± 0.022	Semimajor axis (AU)	1.300 ± 0.019
Altitude begin (km)	~70 km	Eccentricity	0.410 ± 0.013
Latitude end (°, N)	35.557 ± 0.014	Inclination (°, J2000)	4.228 ± 0.070
Longitude end (°, W)	120.487 ± 0.080	Argument of perihelion (°)	79.20 ± 0.13
Altitude end (km)	21.0 ± 0.5	Node (°)	30.458 ± 0.006
Altitude maximum (km)	29.5 ± 0.5	True anomaly (°)	280.49 ± 0.11
Azimuth radiant (S, °)	314.5 ± 0.8	Epoch (UT)	2015-10-24.24148
Entry angle (°)	50.6 ± 0.8	Mass (kg)	10–100
Convergence angle (°)	7.2 ± 0.2	Diameter (m)	0.20–0.40
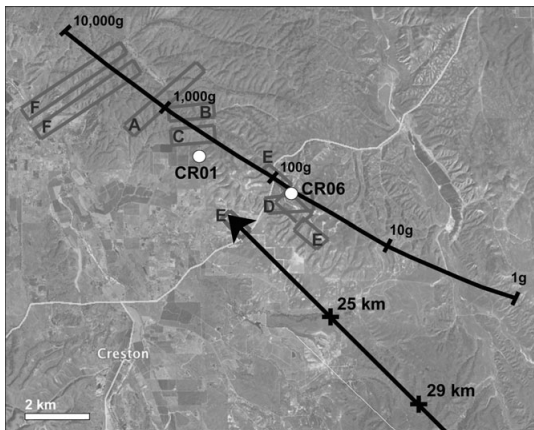
Fig. 5. Creston meteorite strewn field map (inset to Fig. 2). The ground-projected meteor trajectory (arrow) has 25 and 29 km altitude points marked. The calculated fall locations for meteorites of different masses (1 g–10 kg) are shown by a tick line. Radar reflections from falling meteorites are labeled (A–F). White dots show the actual find location of meteorites.

Fig. 6. Error range in the derived semimajor axis and inclination for local and global astrometry of the DFN allsky image.

camera observations. The (1-sigma) uncertainty in the triangulation was evaluated by a Monte Carlo simulation around the three velocity components. Two calibration methods were taken to derive the astrometry from the DFN camera, which resulted in slightly different positions of the trajectory. The first used star positions localized in the region around the meteor trajectory to fit the lens distortion parameters. The second used a global calibration. The localized method resulted in less systematic errors, but higher random errors as fewer stars were involved. The global effort may seem more accurate, but appeared to introduce systematic errors at the position of the meteor. This is clearly shown in Fig. 6, which gives two orbital elements of the fitted pre-atmospheric orbit for a range of solutions that cover the astrometric uncertainty. The calculated trajectory shifted by 2.3 km SE in the global method compared to the local method. The resulting direction of the radiant was different by 0.8°, which translates into a 0.3° systematic error in inclination. On the other hand, because of the large distance to the meteor, the velocities are not much affected. By comparing the measured trajectory positions to that of the recovered meteorites (Fig. 5), we were able to determine that the local calibration method gave the most reliable results. Those are tabulated in Table 3.

Using the wind sonde data from Oakland at 0 h and 12 h UT (http://weather.uwyo.edu/upperair/sounding.html), the wind drift of meteorites of different masses were calculated assuming a spherical shape and density of 3.2 g cm^{-3}. Figure 5 shows the calculated

positions relative to the first-method trajectory for 1 g, 10 g, 100 g, and 1 kg masses falling from an altitude of 29 and 25 km, at the time of the flares. Notice how the recovered meteorite masses were found close to the predicted positions for the trajectory calculated using the local calibration method.

Six Doppler radar returns from three separate radars of the NOAA NEXRAD weather radar network were identified that could be from falling meteorites or dust (Bouvier et al. 2017). The earliest radar signature ("A," Fig. 5) appears in imagery from the radar with call letters "KVTX" (Los Angeles, California, with location shown in Fig. 2) at an altitude of 16.5 km above sea level (ASL) at 05:49:10.4 UTC—just 80 s after the meteor passed the 29.5 km altitude point (05:47:50.3 UTC), where the first breakup was recorded as a flare in the meteor imaging (Fig. 1). The radar-reported timing (05:47:57.6 UTC) is corrected for the time it takes the radar to adjust to the next-higher elevation level with each sweep. The new time implies that this signature "A" is due to fine material, approximately ~0.06 g in mass. However, it is found above the 1.2 kg point in the predicted strewn field.

Radar "KVBX" (Vandenberg Air Force Base) recorded signatures of what may be falling meteorites from 5.8 km ASL at 05:50:06.5 UTC ("B" and "C," Fig. 5), and from 6.9 km ASL at 05:51:36.3 UTC ("D"). The time lag of 136 s and 225 s to those altitudes, respectively, would correspond approximately to the fall time of 68 g and 3.5 g meteorites. Instead, these signatures are found above the 700 g and 70 g

The Creston, California, meteorite fall   9

points, respectively (Fig. 5). Radar "KHNX" (San Joaquin) recorded several returns at 05:51:34.1 at an altitude of 4.0 km, from 14 g meteorites ("E," Fig. 5). These reflections are above the 90 g point.

Finally, "KMUX" (San Francisco) recorded a pair of returns at 16.6 km altitude at 06:00:02.7 UTC ("F," Fig. 5), many minutes after the meteor. They are perhaps due to slow falling fine debris.

All recovered ~100 g meteorites are fully fusion crusted (Fig. 1), which confirms that they originated in a breakup before the end of the luminous trajectory. In contrast, the radar returns are only consistent with the measured trajectory if there was aggressive ongoing fragmentation after the main breakups at 29 and 25 km altitude. In particular, the final detection suggests ongoing fragmentation following the 29 km breakup and small debris settling to lower altitudes. Such ongoing fragmentation was also observed during breakup of the Novato meteoroid (Jenniskens et al. 2014). It is not impossible that these small 3–10 g meteorites would consist of broken fragments that are not fully crusted.

The light curve of this event is remarkably flat (Fig. 7). Each break in the DFN camera trace (marked "SV") provided a brightness measurement. The SkySentinel cameras ("RV" and "ES") brightness in each video frame was calibrated using the image of the Moon (Fig. 3), as well as the images of stars in the integrated image. Finally, the photographic trace is shown as a line marked "GO." Based on the CAMS video, the peak intensity of the very brief first (29 km) flare may be half a magnitude brighter, during a 1/60th second video field, than measured from the integrated intensity of the photometric trace (arrow).

The fall area is not far from the San Andreas Fault and densely populated by seismic stations. Seismic signatures were detected by nine stations (Table 4). Several traces show two bursts, possibly from the 29 and 25 km breakup events (Fig. 8). If so, the
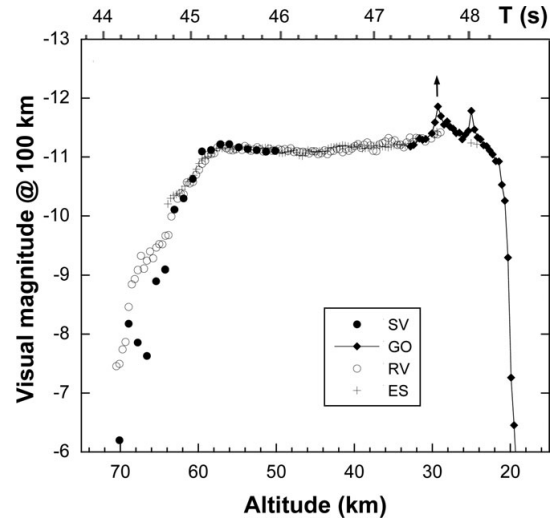
Fig. 7. The meteor visual light curve as seen from each camera station, normalized to a common distance of 100 km, as a function of time after 05:47:00 UTC and altitude.

corresponding distances imply a relatively high 334 m s^{-1} average sound speed. The strongest signal was measured at station SMM (Simmler) close to the track in the uprange direction, and that one is single-peaked, just like the signal at station MPP (Macpherson Peak) in about that same azimuthal direction. In this direction, the shock waves appear to have overlapped.

Mineralogical and Geochemical Properties of the Meteorite

The meteorite's interior was light gray and sprinkled with small (<1 mm) metal and troilte grains, as described by Bouvier et al. (2017). The stones exhibit shock melt veins, some to 2 mm thick, which are

Table 4. Seismic detections of the sonic boom.

Station ID	Station Name	Latitude (N)	Longitude (W)	Altitude (m)	Arrival Time (UT)	Relative Time (s)[a]	Range (km)[b]	Az (S, °)
CI.PHL	Park Hill	35.40773	120.54556	355	05:49:30.0	101.2	33	46
PB.B072	Parkfield	35.83100	120.34500	398	05:50:12.5	143.7	47	190
PB.B078	Parkfield	35.83770	120.34520	387	05:50:12.5	143.7	48	190
PB.B079	Parkfield	35.71570	120.20570	437	05:49:58.0	129.2	42	220
PB.B901	Parkfield	35.68970	120.14200	275	05:50:05.5	136.7	44	231
PB.B900	Parkfield	35.68600	120.00300	220	05:50:33.5	164.7	52	242
CI.VES	Vestal	35.84089	119.08469	154	05:54:25.0	396.2	130	256
CI.SMM	Simmler	35.31420	119.99581	599	05:50:41.5	172.7	53	299
CI.MPP	McPherson Peak	34.88848	119.81362	1739	05:52:19.0	270.2	93	321

[a]Time relative to 05:47:48.8 UT.
[b]From 29.5 km altitude fragmentation event.
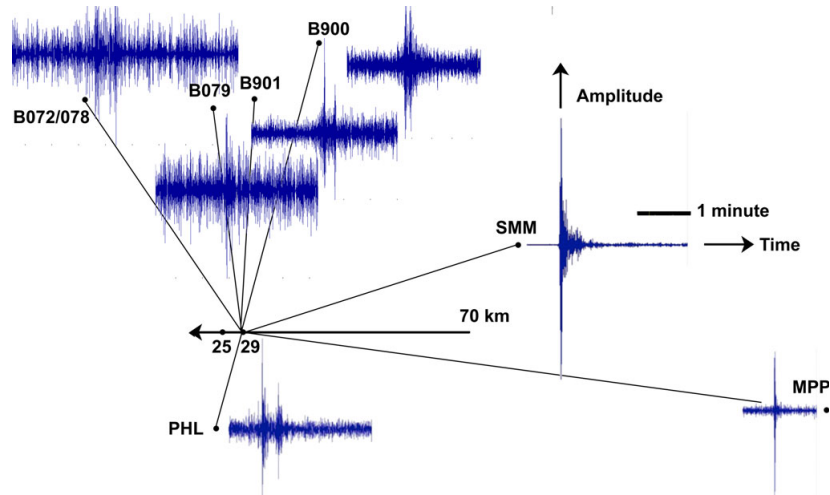
Fig. 8. Airburst generated seismic signatures as seen in different azimuth directions relative to the meteor trajectory (arrow).

sometimes broken at places along well-developed shiny black slickenside surfaces. We analyzed the moderately and highly shocked lithologies separately, for comparison. We found that olivine in both lithologies had identical compositions (and so are combined here), being an average olivine composition $Fa_{23.3\pm1.4}$ and a maximum CaO content of 0.053 (PMD=2.1%, $n = 10$), and low-Ca pyroxene with an average composition of $Fs_{23.5\pm3.5}Wo_{1.2\pm0.5}$ (PMD = 1.4%, $n = 8$), with Fe/Mn = 28.0 $\pm$ 2.2. These results differ slightly from those reported by Bouvier et al. (2017). These earlier results were: $Fa_{24.8\pm0.4}$ ($n = 11$), $Fs_{21.1\pm0.2}Wo_{1.3\pm0.2}$ ($n = 14$), with pyroxene Fe/Mn = 28.1 $\pm$ 1.3. Differences may be on account of varying equilibration of olivine and pyroxene grains or chondrules across the sampled stones.

Only two barred olivine chondrules were apparent in the investigated section. Plagioclase grains up to 200 μm are abundant, with compositions generally in the range $An_{26}Ab_{61}Or_{13}$ to $An_{27}Ab_{62}Or_{11}$, with one aberrant grain found with the composition $An_{18}Ab_{70}Or_{11}$. Chromite and troilite grains measuring up to 300 μm, and Fe-Ni metal grains up to 400 μm are abundant. As reported by Bouvier et al. (2017), a well-developed 1 mm thick shock vein had the typical blebs and spheres of Fe-Ni metal and sulfides. Fine-grained melt pockets were present but rare. Shock melt veins and pockets are heterogeneously distributed throughout the section, indicating a shock level of S4 (Stöffler et al. 1991).

The thin section may not be typical of all meteorites. X-ray CT scans of CR05 (Fig. 9, left) and CR06 (Fig. 9, right) were obtained by methods described in Jenniskens et al. (2014), and show only sparse and thin shock veins, without clear interconnected irregular melt veins, which is more typical of shock stage S3 (Stöffler et al. 1991). Brecciation is evident from a nonhomogeneous distribution of metals and chondrules, the bright white spots and dark roundish features in Figs. 9C and 9D, respectively.

The new results appear to be slightly less equilibrated than L6, but are within the compositional field of L5/6, and therefore suggest rather more variable metamorphic heating than had been previously proposed. We classify the meteorite as L5/6 and shock stage S3/4, with weathering stage W0.

The classification of L is confirmed by the magnetic susceptibility $^{10}log(\chi)$, measured at U.C. Davis. The value ranged from 4.79 to 4.93, with a mean of 4.86, which is in the middle of the range for unweathered L-type chondrites (Rochette et al. 2012). The measurement depended on the orientation of the meteorite in the magnetic susceptibility bridge. Trace element abundances compared to those of standard Orgueil (Table 5) also align better with the average of L chondrites than that of, say, LL chondrites (Fig. 10).

Further confirmation comes from oxygen and chromium isotope analysis of two independent aliquots of Creston. Stable isotope data results for CR01 in ‰ VSMOW are: $\delta^{17}O' = 3.537$, 3.781, and 3.618; $\delta^{18}O' = 4.582$, 5.210, and 4.828; and $\Delta^{17}O' = 1.118$, 1.030, and 1.069, respectively. The prime symbol refers to values of the ratio $^{17}O/^{16}O$ and $^{18}O/^{16}O$ being plotted on a natural log scale, so that dependencies are linear: $\delta^{17}O' = 1000 * \ln$

The Creston, California, meteorite fall 11
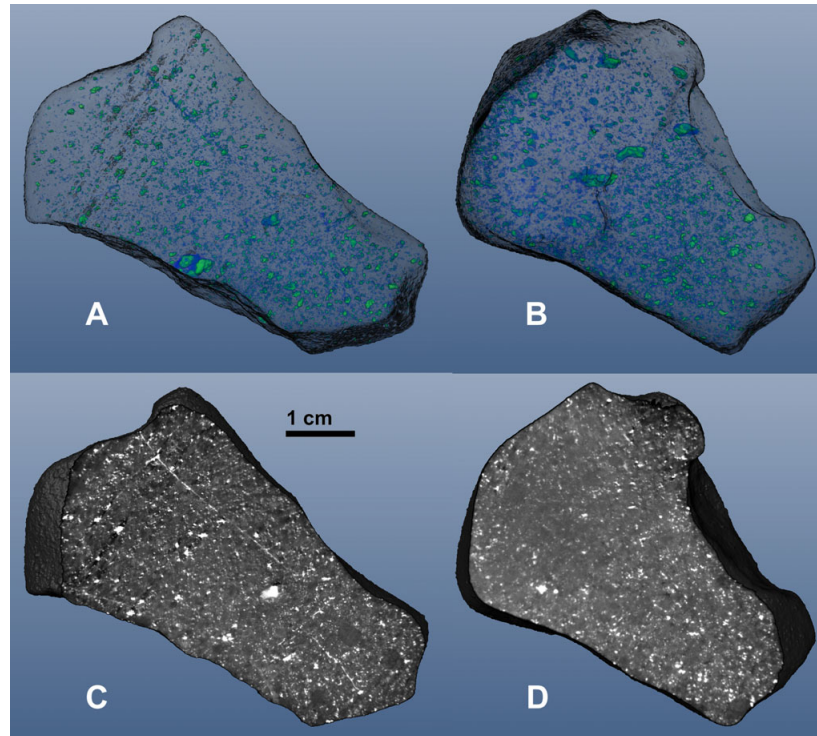
Fig. 9. X-ray CT scans of Creston meteorite CR05 (A and C) and CR06 (B and D). Top diagrams (A and B) visualize the 3-D internal metal grain distribution. Metal grains have highest density for X-rays. Bottom panels (C and D) show CT slices through the meteorites. The diffuse gray corresponds to the fine grain matrix, while the bright white spots correspond to the metal grains and metal-filled shock veins.

($[^{17}O/^{16}O]_{sample}/[^{17}O/^{16}O]_{standard(VSMOW)}$), and similar for $\delta^{18}O$' (Jenniskens et al. 2012). These values fall within the range of other known L chondrites: $\delta^{17}O$' = 3.0–3.8 and $\delta^{18}O$' = 4.2–5.6, in the overlap area between L and LL and at the upper end of the $\delta^{17}O$' range (Clayton et al. 1991). Combined with the olivine composition, the oxygen isotope values place Creston squarely in the L chondrite domain (Fig. 11). The $\varepsilon^{54}Cr$ isotopic composition of Creston is -0.38 ± 0.11. This isotopic composition is indistinguishable from previously analyzed L chondrites including Knyahinya, Novato, Villalbeto de la Peña, and Lundsgård (Trinquier et al. 2007; Jenniskens et al. 2014; Schmitz et al. 2016). When combining $\varepsilon^{54}Cr$ and $\Delta^{17}O$ isotopic compositions, Creston plots directly within the ordinary chondrite field (Fig. 11).

The crack distribution in X-ray CT scans implies a density of 0.5 fractures/cm^2 larger than 1 cm in length and a Weibull coefficient of $\alpha = 0.22 \pm 0.10$, which compares to the $\alpha = 0.185$ measured for L5, S3, Bluff (a) (Bryson and Ostrowski 2017). The bulk density of the meteorite determined with a helium pycnometer is 3.2933 ± 0.0005 g cm^{-3} (CR05) and 3.2486 ± 0.0006 g cm^{-3} (CR06), compared to 3.42 ± 0.05 g cm^{-3} for Villalbeto de la Peña (Llorca et al. 2005). The grain density is 3.597 ± 0.010 and 3.583 ± 0.004 g cm^{-3}, respectively (Villalbeto de la Peña: 3.59 ± 0.05 g cm^{-3}) for a porosity of 8.44 ± 0.02 and $9.33 \pm 0.01\%$ (Villalbeto: 4.7%), using methods described in Ostrowski and Bryson (2016).

Meteorite Collision History

Negligible activity of ^{60}Co (<1.7 dpm kg^{-1}) suggests that the pre-atmospheric size of the Creston meteoroid was rather small and no significant production of secondary thermal neutrons took place within the meteoroid during its recent cosmic ray exposure in space (Table 6). Normalized to the composition of an ordinary L chondrite, the measured ^{26}Al activity is consistent with that expected for a small-size L chondrite (Bhandari et al. 1989; Bonino et al. 2001; Leya and Masarik 2009).

Table 5. Major, minor, and trace element composition in Creston.

		Orgueil (this)	Orgueil[a]	Creston			Orgueil (this)	Orgueil[a]	Creston
Li	ppm	1.52	1.47	1.02	Cd	ppm	0.691	0.674	0.028
Be	ppm	0.022	0.03	0.028	Sb	ppm	0.14	0.13	0.057
Na	Wt%	0.49	0.5	0.63	Cs	ppb	0.187	0.189	0.008
Mg	Wt%	9.53	9.58	12.28	Ba	ppm	2.3	2.46	2.311
Al	Wt%	0.81	0.85	0.94	La	ppm	0.242	0.246	0.401
P	Wt%	0.11	0.1	0.15	Ce	ppm	0.63	0.6	0.898
K	Wt%	0.057	0.054	0.065	Pr	ppm	0.088	0.091	0.133
Ca	Wt%	0.88	0.92	1.19	Nd	ppm	0.478	0.464	0.628
Sc	ppm	5.85	5.9	7.43	Sm	ppm	0.149	0.152	0.199
Ti	Wt%	0.055	0.05	0.071	Eu	ppm	0.061	0.058	0.081
V	ppm	60.2	54.3	71.9	Gd	ppm	0.203	0.205	0.311
Cr	ppm	2705	2650	1903	Tb	ppm	0.042	0.038	0.055
Mn	Wt%	0.2	0.19	0.24	Dy	ppm	0.248	0.255	0.419
Co	ppm	510	506	320.9	Ho	ppm	0.59	0.057	0.083
Fe	Wt%	19.33	18.5	19.01	Er	ppm	0.159	0.163	0.25
Ni	Wt%	1.01	1.08	0.101	Tm	ppm	0.027	0.026	0.038
Cu	ppm	127	131	74.8	Yb	ppm	0.161	0.169	0.263
Zn	ppm	318	312	36.6	Lu	ppm	0.028	0.025	0.039
Ga	ppm	8.98	9.8	2.72	Hf	ppm	0.101	0.106	0.175
Rb	ppm	2.27	2.31	2.07	Ta	ppm	0.018	0.015	0.021
Sr	ppm	7.8	7.81	7.81	Tl	ppm	0.127	0.142	0.003
Y	ppm	1.6	1.53	1.89	Pb	ppm	2.61	2.63	0.051
Zr	ppm	3.9	3.62	5.11	Th	ppm	0.033	0.031	0.049
Nb	ppm	0.288	0.279	0.351	U	ppm	0.007	0.008	0.016

[a]Reference values for Orgueil taken from Lodders (2003) and Lodders et al. (2009).
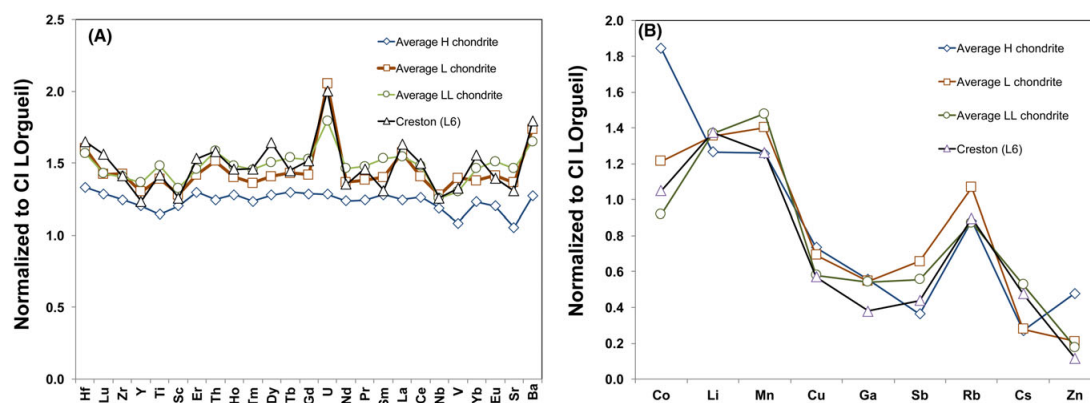
Fig. 10. Trace element abundances relative to Orgueil in order of decreasing condensation temperature for (A) refractory siderophile and lithophile elements and (B) for chalcophile elements and halogens.

When we compare the radionuclide concentrations with cosmic ray production estimations for ^{26}Al (Leya and Masarik 2009), ^{60}Co (Eberhardt et al. 1963; Spergel et al. 1986), ^{54}Mn (Kohman and Bender 1967), and ^{22}Na (Bhandari et al. 1993), the best agreement in the sequence of the given isotopes is obtained for radii of $r = 10–20$ cm, <20 cm, 8–12 cm, and 5–10 cm, respectively. These are upper limits to the size at the time of fall. Combining all results, we infer a roughly spherical meteoroid with 10–20 cm radius. The ^{22}Na/^{26}Al ratios of the two specimens are 1.42 ± 0.15 and 1.55 ± 0.17, respectively. That makes Creston similar to Jesenice with respect to the radionuclide content (Bischoff et al. 2011).
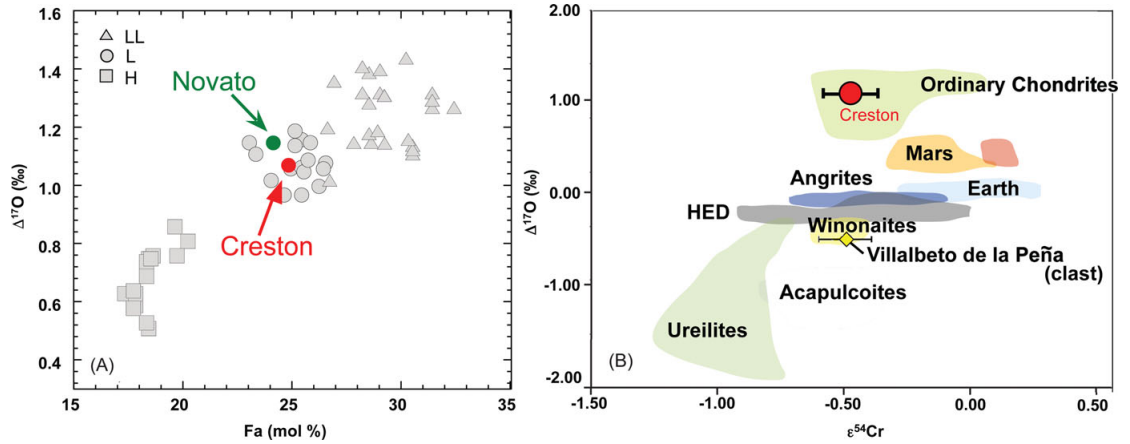
Fig. 11. Meteorite classification. A) $\Delta^{17}O$ versus Fa mol% in olivine in Creston compared with other ordinary chondrites, based on data from Troiano et al. (2011) and references therein, Popova et al. (2013), and Jenniskens et al. (2014). B) Comparison of the $\Delta^{17}O$-$\varepsilon^{54}Cr$ isotopic composition of Creston with achondrite and noncarbonaceous chondrite groups. Adapted after Schmitz et al. (2016), also plotting the Winonaite clast of Villalbeto de la Peña (Bischoff et al. 2013).

Table 6. Massic activities of cosmogenic radionuclides (in dpm kg^{-1}) corrected to the time of fall of the meteorite October 24, 2015. Errors in gamma-ray activities include a 1σ uncertainty of 10% in the detector efficiency calibration; those in AMS activities are dominated by counting statistics.

Nuclide Method	Half-life –	CR02 (dpm kg^{-1}) AMS	CR05 (dpm kg^{-1}) γ-ray	CR06 (dpm kg^{-1}) γ-ray
^{58}Co	70.83 d	–	9 ± 4	<14
^{56}Co	77.236 d	–	<18	8 ± 3
^{46}Sc	83.787 d	–	14 ± 3	<12
^{57}Co	271.8 d	–	6 ± 1	8 ± 1
^{54}Mn	312.3 d	–	58.0 ± 5.9	52.7 ± 5.4
^{22}Na	2.60 y	–	68.4 ± 5.0	72.6 ± 5.4
^{60}Co	5.27 y	–	<1.7	<1.7
^{44}Ti	60 y	–	<2.8	<2.7
^{36}Cl	3.01 × 10^5 y	8.6 ± 0.1	–	–
^{26}Al	7.17 × 10^5 y	–	48.2 ± 3.6	46.7 ± 3.7
^{10}Be	1.39 × 10^6 y	20.3 ± 0.2	–	–

The activity of the short-lived radioisotopes with half-life less than the orbital period represents the production integrated over the last segment of the orbit. The fall of Creston occurred during the solar cycle 24 maximum. The cosmic ray flux was low in the 6 months prior to the fall, so that the activities for the very short-lived radionuclides are expected to be low (see Table 6). The naturally occurring radionuclides (Table 7) are low also, but in the range of other concentrations measured in ordinary L chondrites (Wasson and Kallemeyn 1988).

Table 7. Concentration of primordial radionuclides (ng g^{-1} for U and Th chains and mg g^{-1} for ^{40}K) in the specimens of the Creston stone measured by nondestructive gamma-ray spectroscopy. Errors include a 1σ uncertainty of 10% in the detector efficiency calibration.

Nuclide	Half-life	CR05	CR06
^{232}Th	1.405 × 10^{10} y	35.5 ± 2.5	34.2 ± 2.4
^{238}U	4.468 × 10^9 y	9.8 ± 0.8	9.2 ± 0.8
^{40}K	1.251 × 10^9 y	810 ± 80	720 ± 70

The ^{10}Be concentration of 20.3 dpm kg^{-1} is consistent with irradiation near the center of an object with a radius of about 20 cm (Leya and Masarik 2009) or a near-surface irradiation (5–10 cm depth) in a larger object (up to ~75 cm radius). The ^{36}Cl concentration of 8.6 dpm kg^{-1} shows no neutron-capture contribution and therefore favors a relatively small meteoroid. Combining ^{10}Be with ^{21}Ne concentration (see below) gives a ^{21}Ne/^{10}Be cosmic ray exposure age of 50–54 Ma.

Creston does not contain solar wind or other trapped noble gases. Hence, it is not a regolith breccia. Indeed, only a few % of all L chondrites are. Based on ^{22}Ne/^{22}Ne = 1.10 ± 0.01 (Table 8) and the model calculations by Leya and Masarik (2009), it derives from a meteoroid with at least 20 cm radius, consistent with the one derived from radionuclides. Creston has a CRE age of about 40–50 Ma based on the empirically calibrated ^{22}Ne/^{21}Ne-^{21}Ne and ^{22}Ne/^{21}Ne-^{38}Ar methods (Dalcher et al. 2013).

Table 8. Noble gas concentrations of He, Ne, and Ar in Creston.

	CR01-NG-1[a]	CR01-NG-2[a]	Total[a]
^{3}He	n.m.	n.m.	n.m.
^{4}He	742(3)	711(2)	725(2)
^{20}Ne/^{22}Ne	0.838(7)	0.839(6)	0.838(5)
^{21}Ne/^{22}Ne	0.913(1)	0.902(2)	0.907(1)
^{20}Ne	12.7(1)	12.9(1)	12.8(1)
^{36}Ar/^{38}Ar	0.736(23)	0.755(19)	0.746(15)
^{40}Ar/^{36}Ar	3230(100)	3200(80)	3210(60)
^{36}Ar	1.76(6)	1.78(4)	1.77(4)
^{22}Ne$_{cos}$/^{21}Ne$_{cos}$	1.09(1)	1.11(1)	1.10(1)
^{21}Ne$_{cos}$	15.17(4)	15.40(4)	15.30(3)
^{38}Ar$_{cos}$	2.35(2)	2.30(2)	2.32(1)
^{4}He$_{rad\,(=non\text{-}cos)}$	336(31)	295(32)	314(31)
CRE-^{21}Ne (Ma)	39(5)	42(6)	41(6)
CRE-^{38}Ar (Ma)	50(2)	51(2)	50(2)
U,Th-He (Ga)	1.11	0.99	1.05
K-Ar (Ga)	4.32	4.31	4.31
Mass (mg)	32.6	37.0	69.6

[a]All concentrations are given in 10^{-8} cm³ STP/g (1 cm³ STP = 2.687×10^{19} atoms). Values in parentheses indicate uncertainties on the last digit. Uncertainties of concentrations (and thus, CRE ages) do not include the uncertainty of the standard amounts, which is about 3%. T = CRE ages, R = radiogenic gas retention ages.

The U,Th-He age (corrected for cosmogenic ^{4}He via ^{21}Ne$_{cos}$) of Creston is ~1 Ga and the K-Ar age is ~4.3 Ga (Table 8). Both are significantly higher than their counterparts in L chondrite Villalbeto de la Peña, which has a similar CRE age as Creston. Both ages assume L-chondritic abundances of K, U, and Th listed in Tables 4 and 7 (Wasson and Kallemeyn 1988).

The U-Pb systematics of Creston apatite reveals an upper intercept age of 4497.9 ± 5.8 Ma (Wetherial diagram) and 4496.7 ± 5.8 Ma (2σ) (Tera-Wasserburg diagram), respectively. Results for individual apatite grains are given in Table 9. A total of 37 apatite grains give a weighted average ^{207}Pb/^{206}Pb age at 4497.1 ± 3.7 Ma (2σ) (Fig. 12). Compared to the earliest solar system solids having formed 4,568.2 Ma ago (Bouvier and Wadhwa 2010), the measured age is 71.1 ± 3.7 Ma after the formation of the solar system. The measurements also show a lower intercept age at 755 ± 320 Ma (Tera-Wasserburg reserve Concordia) and 771 ± 320 Ma (Wetherial Concordia), respectively.

DISCUSSION

The L Chondrite Source Region

Table 10 provides a summary of the various age estimates and compares results to those obtained from other L5 and L6 chondrite falls for which atmospheric

trajectories and pre-atmospheric orbits were derived. Columns are in order of increasing semimajor axis of the orbit.

Note that each past orbit sampled a different range of CRE age (Table 10), suggesting all L chondrites studied so far originated in different collision events (Jenniskens et al. 2014). Creston's CRE age and oxygen isotope compositions are similar to those of Villalbeto de la Peña (Llorca et al. 2005), but Villalbeto de la Peña has a significantly different olivine Fa and pyroxene Fs mineral composition. This meteorite is otherwise exceptional also because it has a Winonaite-related fragment in a hydrothermally metamorphosed polymict L-chondritic breccia (Bischoff and Schultz 2004; Bischoff et al. 2013), suggesting Villalbeto de la Peña came from a different source altogether (Fig. 11). We still may be looking at all different collision events.

Oxygen isotope values for Creston differ significantly from those of Park Forest (Simon et al. 2004). While Creston plots closer to a group of both high δ17O' and δ18O' values for L chondrites in Clayton et al. (1991), Park Forrest plots closer to a group of both low values. This may point to different source regions. Novato has similar oxygen isotopes, mineral composition, and shock stage. The known ranges of oxygen isotope and olivine and pyroxene composition values (e.g., Rubin 1990; Clayton et al. 1991) are reflected in those measured for the six L chondrites with known orbits.

The U-Pb age of Creston is within error identical to, but with better precision than, the 4472 ± 31 Ma measured for L6 chondrite Novato (Yin et al. 2014). This is due to the fact the U-Pb data points for the measured phosphates in Creston are concentrated near the upper intercept (Fig. 12), whereas the data points for Novato (greater Pb loss) are spread along the discordia (cf. fig. 5 in Yin et al. 2014). Thus, the upper intercept age of Creston is better defined than Novato, while the opposite is true for the lower intercept ages. The age of upper intercept is thought to signify the time of blocking temperature for Pb diffusion in phosphate minerals associated with extensive collisional impacts. This shows significant impacts occurred on the L chondrite parent body until about 70 Ma after formation of the first solids (4568 Ma ago). This epoch was earlier linked to the Earth–Moon-forming giant impact, suggesting that fragments from that event impacted the parent body in the asteroid belt at relatively high speed (Yin et al. 2014; Bottke et al. 2015). Most recently, Barboni et al. (2017) suggested Moon impact event occurred earlier than >4.51 ± 0.01 Ga ago, i.e., before 57 Ma after formation of the first solids in the solar system, more in line with the earlier suggestion based on Hf-W ages of the Moon-

Table 9. SIMS U-Pb isotopic data of apatite from Creston. Spot positions are identified in Fig. 4.

Spot	U (ppm)	Th (ppm)	Th/U	^{204}Pb (cps)	^{204}Pb/^{206}Pb	f_{206} (%)	^{207}Pb^a/^{206}Pb^a	±1σ (%)	^{207}Pb^a/^{235}U	±1σ (%)	^{206}Pb^a/^{238}U	±1σ (%)	$t_{207/206}$ (Ma)	±1σ	$t_{207/235}$ (Ma)	±1σ	$t_{206/238}$ (Ma)	±1σ
1-1@1	5.0	7.4	1.48	n.d.	—	—	0.5989	0.63	81.9	2.9	0.992	2.83	4505	9	4485	30	4441	92
1-1@2	5.6	8.3	1.48	n.d.	—	—	0.5900	0.69	84.7	3.9	1.042	3.81	4484	10	4520	40	4601	126
1-2@1	5.2	7.4	1.43	0.051	0.0003	0.57	0.5890	0.76	82.5	2.7	1.015	2.54	4481	11	4493	27	4518	83
1-2@2	5.9	9.1	1.54	n.d.	—	—	0.5917	0.92	80.9	3.2	0.992	3.04	4488	13	4473	32	4441	98
1-3@1	5.1	7.3	1.43	0.019	0.0001	0.21	0.5897	0.82	87.1	3.3	1.071	3.24	4483	12	4547	34	4693	109
2-1@2	5.3	8.8	1.67	n.d.	—	—	0.6074	0.48	81.3	3.6	0.971	3.54	4526	7	4479	36	4375	113
2-1@3	6.2	9.6	1.54	0.034	0.0003	0.55	0.5957	1.18	75.8	4.0	0.923	3.87	4497	17	4408	41	4215	121
2-1@4	5.2	8.0	1.52	0.034	0.0002	0.37	0.5957	1.14	84.0	3.2	1.023	2.94	4498	17	4511	32	4542	97
2-2@1	6.3	10.6	1.68	0.034	0.0002	0.35	0.5937	0.63	80.0	2.8	0.977	2.71	4493	9	4462	28	4393	87
2-2@2	5.9	10.3	1.73	n.d.	—	—	0.5963	0.33	83.0	4.1	1.009	4.07	4499	5	4499	42	4498	133
2-2@3	5.7	9.3	1.64	n.d.	—	—	0.5965	0.95	80.3	3.5	0.977	3.42	4500	14	4466	36	4392	110
2-2@4	7.5	13.0	1.74	0.085	0.0007	1.40	0.5904	0.82	81.9	3.3	1.007	3.15	4484	12	4486	33	4490	103
2-3@1	6.3	9.8	1.55	n.d.	—	—	0.5907	0.52	71.1	3.5	0.873	3.47	4485	8	4344	36	4046	105
2-3@2	7.0	10.9	1.57	0.102	0.0009	1.63	0.5791	0.65	69.2	3.0	0.867	2.93	4456	10	4317	31	4023	88
3-1@1	5.8	8.4	1.47	0.038	0.0003	0.50	0.5884	1.21	77.7	3.2	0.958	2.98	4480	18	4433	33	4333	95
3-1@2	7.2	10.5	1.47	n.d.	—	—	0.5944	0.76	78.6	2.7	0.959	2.58	4494	11	4444	27	4335	82
3-1@3	7.6	11.2	1.47	0.019	0.0002	0.29	0.5922	0.50	77.1	3.0	0.945	3.00	4489	7	4426	31	4288	95
4-1@1	5.6	8.0	1.43	n.d.	—	—	0.5980	0.29	82.5	3.3	1.000	3.34	4503	4	4493	34	4469	108
4-1@2	6.0	9.3	1.55	n.d.	—	—	0.5970	0.58	84.4	2.7	1.026	2.65	4501	8	4516	28	4551	87
4-1@3	7.5	10.9	1.45	n.d.	—	—	0.5986	1.10	78.0	4.6	0.945	4.47	4505	16	4437	47	4289	142
4-1@4	6.5	10.0	1.53	0.034	0.0003	0.55	0.5838	0.88	77.1	3.5	0.958	3.34	4468	13	4425	35	4332	106
4-1@5	6.1	10.3	1.69	n.d.	—	—	0.5926	0.59	78.1	3.8	0.956	3.72	4490	9	4439	39	4326	118
4-1@6	5.8	8.8	1.53	n.d.	—	—	0.5848	1.04	80.0	4.2	0.992	4.02	4471	15	4462	43	4443	130
4-1@7	5.5	8.2	1.49	n.d.	—	—	0.5978	0.69	84.5	2.9	1.025	2.84	4503	10	4517	30	4549	93
5-1@1	5.4	8.7	1.60	0.034	0.0002	0.42	0.5974	0.62	83.0	2.9	1.007	2.83	4502	9	4499	29	4492	92
5-1@2	5.6	10.0	1.77	0.057	0.0004	0.77	0.5961	0.74	89.1	3.4	1.084	3.32	4499	11	4570	35	4734	112
6-1@1	5.4	8.6	1.60	n.d.	—	—	0.6074	0.59	86.2	2.8	1.029	2.75	4526	9	4536	29	4561	91
6-1@2	5.1	8.0	1.58	n.d.	—	—	0.5903	0.93	90.7	3.6	1.114	3.49	4484	14	4588	37	4826	120
6-1@3	5.0	7.6	1.53	n.d.	—	—	0.6004	0.67	85.1	4.3	1.028	4.28	4509	10	4524	44	4559	141
7-1@1	4.4	5.9	1.34	n.d.	—	—	0.5994	0.47	91.2	2.8	1.103	2.80	4507	7	4593	29	4793	95
7-1@2	4.8	6.9	1.44	0.051	0.0003	0.63	0.5788	0.91	84.2	3.1	1.056	2.97	4456	13	4514	32	4646	99
14-1@1	4.6	7.3	1.59	n.d.	—	—	0.5950	0.80	89.4	2.8	1.090	2.72	4496	12	4574	29	4753	92
14-1@2	4.8	7.8	1.63	n.d.	—	—	0.5933	0.91	87.9	3.2	1.075	3.07	4492	13	4557	33	4706	103
16-1@1	5.1	7.8	1.55	n.d.	—	—	0.6091	0.95	96.3	3.3	1.146	3.13	4530	14	4648	33	4924	109
16-1@2	5.6	8.6	1.54	n.d.	—	—	0.6026	0.88	88.7	3.3	1.067	3.20	4514	13	4565	34	4681	107
16-1@3	5.8	9.2	1.58	n.d.	—	—	0.6011	0.82	95.2	2.8	1.149	2.71	4511	12	4637	29	4931	94
17-3@1	7.4	11.5	1.54	0.034	0.0001	0.22	0.5969	0.97	97.5	8.7	1.185	8.69	4500	14	4661	92	5038	311

[a] Radiogenic, using the modern terrestrial Pb as common lead compositions ^{206}Pb/^{204}Pb = 18.703 and ^{207}Pb/^{206}Pb = 0.836 (Stacey and Kramers 1975); n.d. = not detected.
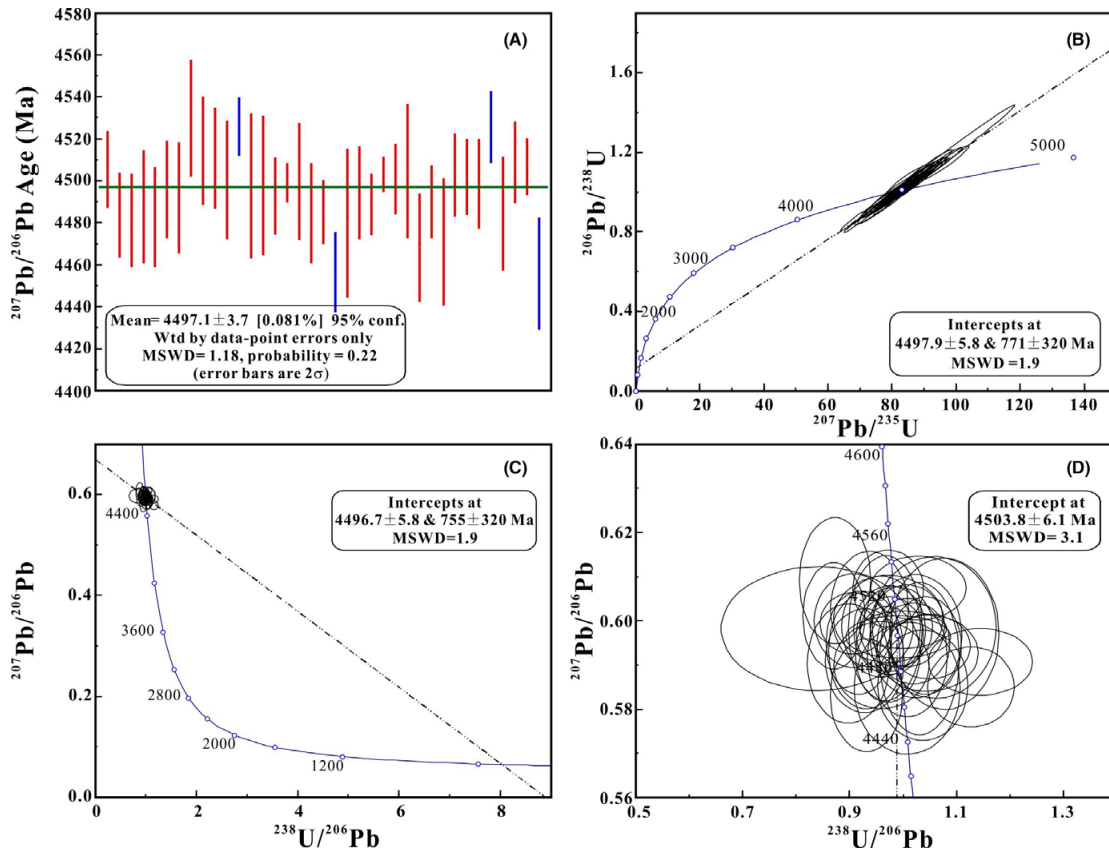
Fig. 12. Summary of Pb-Pb measurements on Creston. A) A mean Pb-Pb age is 4,497.1 ± 3.7 (0.081%), with 95% confidence. B) Intercepts for Pb-U age are at 771 ± 320 Ma and 4497.9 ± 5.8 [±11] Ma. MSWD = 1.9. C) Intercepts for Pb-Pb age are at 755 ± 320 Ma and 4496.7 ± 5.8 [±11] Ma. MSWD = 1.9. D) Detail of (C).

forming impact (e.g., Yin et al. 2014). The two interpretations of the Moon-forming giant impact timing are in apparent conflict, and require resolutions with future work.

Creston experienced additional heating events later in its history. The high K-Ar age and U,Th-He ages (Table 10) suggest that Creston's radiogenic clock was either not fully reset during the 467 Ma collision event that is thought to have formed the Gefion family, or that Creston originated from a source other than the Gefion family. The measured K-Ar age is identical to that of Innisfree (Goswami et al. 1978), an L5 (S3) type ordinary chondrite with a similar short semimajor axis orbit (Table 10). However, the lower intercept ages have such high uncertainty that they overlap with both the 1050 Ma U,Th-He age and the 467 Ma resetting signature detected in Novato (Jenniskens et al. 2014; Yin et al. 2014) and Park Forest (Meier et al. 2017).

The downward trend for U,Th-He ages relative to K-Ar ages is thought to be due to gas loss, with ^{4}He having a higher diffusivity than ^{40}Ar (and shorter half-life of ^{40}K relative to ^{238}U and ^{232}Th [Wasson 2012]). In the overall diagram of U,Th-He ages versus K-Ar ages (Fig. 13), Creston, Novato, and Park Forest are among the most displaced.

Solid gray symbols in Fig. 13 show meteorites for which U,Th-He, K-Ar and CRE ages are available. It is possible that Creston was liberated in the same collision as L5 Tane and L6 Nogata (Takaoka et al. 1989), L6 Mihonoseki (Shima et al. 1993), and L6 Kaptal-Aryk (Welten et al. 2001).

The orbit of Creston is considerably more evolved than that of previously observed meteorite falls. The semimajor axis is only 1.30 ± 0.02 AU, as opposed to 1.7–2.5 AU for other L chondrite falls observed so far. As with Villalbeto de la Peña, the cosmic ray exposure

The Creston, California, meteorite fall 17

Table 10. L chondrites with known orbits: classification criteria, collision history, and mean dynamical lifetimes for ejection from different source regions. The dynamical lifetimes in bold (1-sigma) and italic bold (2-sigma) are in agreement with the measured CRE age.

	Creston (this study)	Jesenice (1)	Innisfree (2)	Novato (3)	Villalbeto (4)	Park Forest (5)
Classification:	L5/6, S3/4	L6, S3	L5, S3 breccia	L6, S4 breccia	L6, S4 breccia	L5, S5 breccia
Fa	23.3 ± 1.4	25.1 ± 0.4	25.3 ± 0.2	24.1 ± 0.4	24.2 ± 0.2	24.7
Fs	23.3 ± 3.5	21.1 ± 0.4	–	20.7 ± 0.5	20.3 ± 0.2	20.7
Wo	1.2 ± 0.5	1.5	–	1.5 ± 0.2	1.6 ± 0.2	1.6
$\delta 17O'$	3.65 ± 0.12	–	–	3.70 ± 0.10	3.60 ± 0.26	3.44 ± 0.02
$\delta 18O'$	4.87 ± 0.32	–	–	4.83 ± 0.19	5.61 ± 0.50	4.68 ± 0.07
$\Delta 17O'$	1.072 ± 0.044	–	–	1.149 ± 0.022	1.1	–
K-Ar age (Ma)	4310 ± 100	3275 ± 205	4100 ± 300	550, 1520 ± 250	700	490 ± 70
^{40}Ar-^{39}Ar age (Ma)	–	~4300	–	–	–	–
U-Pb lower intercept age (Ma)	(755 ± 320)	–	–	473 ± 38	–	–
U,Th-He age (Ma)	1050 ± 60	2300 ± 500	–	460 ± 220	–	430 ± 90
U-Pb upper intercept age (Ma)	4496.7 ± 5.8	–	–	4472 ± 31	–	–
CRE age (Ma)	45 ± 5	~15	28 ± 3	9 ± 1[a]	48 ± 5	14 ± 2
Collisional lifetime in Main Belt (Ma)[b]	8.9	6.3	4.3	5.9	8.9	12.9
Semimajor axis (AU)	1.30 ± 0.02	1.75 ± 0.07	1.872	2.09 ± 0.08	2.3 ± 0.2	2.53 ± 0.19
Inclination (°)	4.23 ± 0.07	9.6 ± 0.5	12.28	5.51 ± 0.04	0.0 ± 0.2	3.2 ± 0.3
Dynamical age for ejection from inner belt:						
Hungaria (i ~ 23°)	–[c]	52.4 ± 1.8	58.1 ± 2.2	19.8 ± 3.2	31.6 ± 3.9	29.9 ± 2.4
ν_6 inner (a < 2.5; i < 4°)	22.2 ± 5.1	*12.2 ± 1.0*	*20.2 ± 2.3*	9.4 ± 1.5	11.9 ± 2.5	**13.7 ± 1.3**
ν_6 inner (a < 2.5; i > 4°)	**33.4 ± 11.0**	*11.3 ± 0.8*	11.2 ± 1.0	6.1 ± 0.4	13.8 ± 1.6	**12.2 ± 0.7**
4:1	9.2 ± 2.6	5.1 ± 0.6	12.9 ± 2.2	0.9 ± 0.7	2.5 ± 0.3	3.8 ± 0.4
7:2 (a < 2.5 AU)	21.3 ± 5.9	21.5 ± 2.3	18.9 ± 2.1	*28.1 ± 8.9*	15.3 ± 1.2	**16.3 ± 0.6**
3:1 (a < 2.5 AU)	12.9 ± 3.4	7.0 ± 1.1	11.1 ± 2.6	3.5 ± 1.8	1.2 ± 0.1	0.9 ± 0.2
From central belt:						
ν_6 inner (a > 2.5 AU)	–	**27.8 ± 22.8**	–	**15.8 ± 14.8**	~1.8	4.5 ± 2.0
7:2 (a > 2.5 AU)	–	**19.5 ± 5.8**	5.0 ± 2.4	9.4 ± 5.1	7.1 ± 3.9	**14.9 ± 4.6**
n6 outer (i ≤ 18°)	–	*7.1 ± 3.0*	8.7 ± 1.1	–	4.4 ± 1.4	6.8 ± 1.2
3:1 (a > 2.5, i > 6°, incl. Gefion family)	–	*48.1 ± 39.2*	*21.1 ± 16.8*	2.0 ± 0.6	6.8 ± 3.5	1.8 ± 0.4
3:1 (a > 2.5 AU, i < 6°)	10.4 ± 8.3	**11.1 ± 5.9**	*13.9 ± 7.3*	2.7 ± 0.9	0.8 ± 0.2	0.7 ± 0.1
ν_6 outer (i > 18°)	–	~24.4	13.7 ± 4.2	–	–	4.2 ± 1.5
Phocaea (i ~ 22°)	–	83.2 ± 14.6	78.6 ± 12.7	36.9 ± 15.8	**82.8 ± 38.2**	37.2 ± 8.2
Teutonia	4.9 ± 1.0	7.5 ± 1.3	12.0 ± 2.4	3.7 ± 0.4	1.3 ± 0.1	0.7 ± 0.1
8:3	–	*17.7 ± 7.3*	*12.5 ± 6.4*	0.9 ± 0.5	1.0 ± 0.3	2.4 ± 0.7
5:2 (incl. Gefion)	–	*7.3 ± 3.4*	*9.3 ± 7.7*	**6.3 ± 3.7**	0.5 ± 0.1	0.4 ± 0.1
From outer belt:						
2:1	–	*~10.7*	~10.6	–	–	0.7 ± 0.5

[a]With one collision in last 3–5 Ma.

[b]Collisional lifetime is based on size and is about 1.4 $\sqrt{r}$, with r the radius in cm. In Main Belt, based only on size: possibly underestimated by factor of 3–5 (see text).

[c]No model orbits evolved into a Creston-like orbit. Data from: (1) Bischoff et al. (2011), Welten et al. (2016); (2) Halliday (1977), Goswami et al. (1978), Rubin (1990); (3) Jenniskens et al. (2014); Yin et al. (2014); (4) Bischoff et al. (2013), Llorca et al. (2005); (5) Simon et al. (2004), and Meier et al. (2017).

age is considerably longer than the expected dynamical lifetime of ~9 Ma against collisions in the asteroid belt. The CRE age is inconsistent with the short dynamical lifetime of asteroids originating in the Gefion family (Jenniskens et al. 2014). Only highly inclined source regions or sources at the inner edge of the inner asteroid belt produce such long dynamical lifetimes.

Based on the measured orbit of Creston, the dynamical lifetimes were calculated for a range of possible source regions (Table 10). A model describing the evolution of small asteroids was
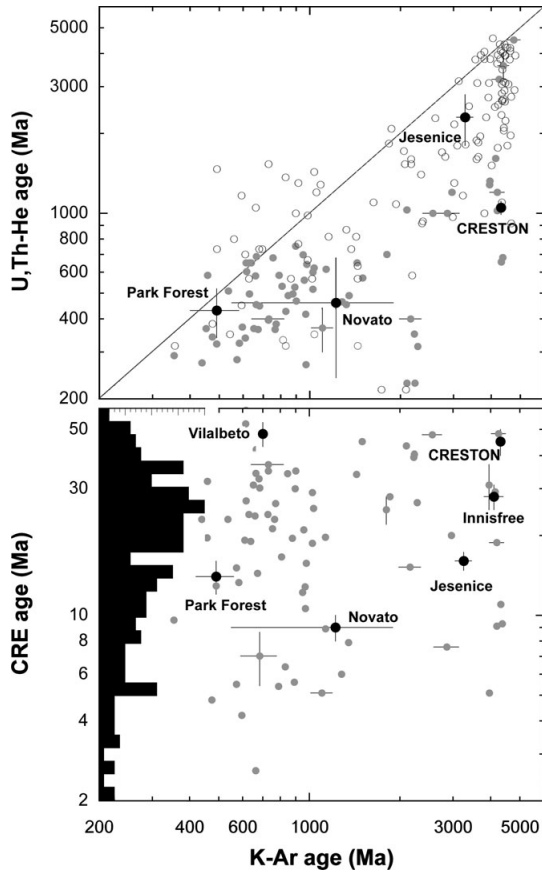
Fig. 13. U,Th-He and CRE age versus K-Ar age for L chondrites. Solid circles are data from Crabb and Schultz (1981), Takaoka et al. (1989), Marti and Graf (1992), Welten et al. (2001, 2004), Eugster et al. (2007), Kita et al. (2013), Trigo-Rodriquez et al. (2014), Leya (2015), Mahajan et al. (2016), and Li et al. (2016). Open circles are U,Th-He and K-Ar age data from Wasson (2012), for which no CRE age information is available. Inset shows CRE histogram (range $N = 0$–20) from Marti and Graf (1992) and more recent data, including data with no K-Ar ages available.

developed that started with 92,449 test asteroids, distributed across the Main Belt (Granvik et al. 2016, 2017). Of these, 70,708 evolved into NEO orbits. Typically thousands of test asteroids originated from each of several source regions. The median lifetime was calculated and is listed in Table 10. The most consistent source for Creston would be in the inner asteroid belt at inclinations above 4°, arriving to Earth via the ν_6 resonance. All other source regions probed tend to produce shorter CRE ages or no model orbits evolved into a Creston-like orbit.
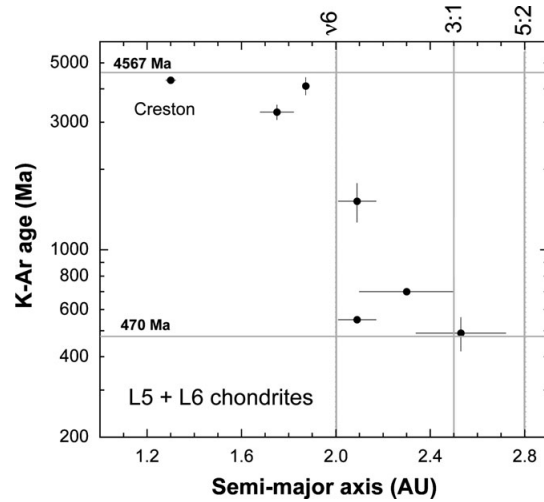

Fig. 14. The meteorite's K-Ar age compared to the semimajor axis (a) of the impact orbit, showing that all meteorites with high K-Ar ages impacted Earth on a short a <2 AU orbit.

The three meteorites with high K-Ar ages, Jesenice, Innisfree, and Creston, are also the meteorites that approached on short semimajor axis (a <2 AU) orbits (Fig. 14). This would be consistent in a scenario where these meteorites come to Earth via the ν_6 resonance from a newly identified source region in the inner Main Belt, but from three different collision events. The CRE age of Jesenice is uncertain. The nominal 3.8 ± 0.3 Ma CRE age may be underestimated, with signs of prior exposure for ~15 Ma in a larger object prior to breaking gently (i.e., perhaps not a collision) 1.6 Ma ago (Welten et al. 2016). The ~15 Ma age would correspond better to the 12 Ma dynamical lifetime expected for a source deep in the inner asteroid belt, arriving via the ν_6 resonance (Table 10).

The three meteorites have inclinations of 9.6°, 12.3°, and 4.2°, suggesting that source has a ~4–13° inclination. Candidate S-class asteroid families include the small families associated with 254 Augusta ($a_{proper} = 2.19$ AU, $i_{proper} = 5°$) and 12 km 1646 Rosseland ($a_{proper} = 2.36$ AU, $i_{proper} = 8°$), and the large family associated with 2076 Levin ($a_{proper} = 2.27$ AU, $i_{proper} = 5°$), which has a formation age 366 ± 125 Ma (Spoto et al. 2015). The Flora family was earlier proposed as an L chondrite parent (Nesvorný et al. 2002), but is now thought to be the source of LL chondrites (Popova et al. 2013; Jenniskens 2014).

The L chondrites with the 470 Ma signature have low 0–6° inclinations, lower than the 8.6–9.6° proper inclination of the Gefion family. It is possible that another

source than Gefion is responsible for the shock-blackened L chondrites with the 470 Ma signature.

CONCLUSIONS

Creston and Novato originated from sites on the same L chondrite parent body that experienced one or more of the first hits after the Moon-forming event. Compositionally they are identical. However, CRE age and approach orbit on impact are different. While Novato arrived from a collision 9 Ma ago on an orbit that might be consistent with a collision cascade from the Gefion family and arriving at Earth via the 3:1 resonance, Creston's short impact orbit and high 45 ± 5 Ma CRE age imply it originated from the inner asteroid belt and came to Earth via the v_6 resonance.

We postulate that the parent body of L chondrites was disrupted during the impact event recorded in U-Pb and Pb-Pb ages 4497 ± 6 Ma ago, after which two or more reassembled rubble pile daughter asteroids dispersed over the asteroid belt. The daughter asteroid of Novato may have settled in the middle asteroid belt and disrupted ~470 Ma ago. The daughter asteroid from which Creston originated ended up in the inner asteroid belt, not far from the v_6 resonance.

The L chondrites with small semimajor axis orbits (a <2 AU), namely Creston, Innisfree, and Jesenice, sample three different collision events, perhaps from this same inner belt source. All three have a K-Ar age >3 Ga and are not shock-blackened.

Editorial Handling—Dr. Josep M. Trigo-Rodríguez

REFERENCES

Alexeev V. A. 1998. Parent bodies of L and H chondrites: Times of catastrophic events. *Meteoritics & Planetary Science* 33:145–152.

Anders E. 1964. Origin, age, and composition of meteorites. *Space Science Reviews* 3:583–714.

Arpesella C. 1996. A low background counting facility at Laboratori Nazionali del Gran Sasso. *Applied Radiation and Isotopes* 47:991–996.

Barboni M., Boehnke P., Keller B., Kohl I. E., Schoene B., Young E. D., and McKeegan K. D. 2017. Early formation of the Moon 4.51 billion years ago. *Science Advances* 3: e1602365.

Bhandari N., Bonino G., Callegari E., Cini Castagnoli G., Mathew K. J., Padia J. T., and Queirazza G. 1989. The Torino H6 meteorite shower. *Meteoritics* 24:29–34.

Bhandari N., Mathew K. J., Rao M. N., Herpers U., Bremer K., Vogt S., Wölfli W., Hofmann H. J., Michel R., Bodemann R., and Lange H.-J. 1993. Depth and size dependence of cosmogenic nuclide production rates in stony meteoroids. *Geochimica et Cosmochimica Acta* 57:2361–2375.

Bischoff A. and Schultz L. 2004. Abundance and meaning of regolith breccias among meteorites (abstract #5118). 67th Annual Meeting of the Meteoritical Society.

Bischoff A., Jersek M., Grau T., Mirtic B., Ott U., Kucera J., Horstmann M., Laubenstein M., Herrmann S., Randa Z., Weber M., and Heusser G. 2011. Jesenice—A new meteorite fall from Slovenia. *Meteoritics & Planetary Science* 46:793–804.

Bischoff A., Dyl K., Horstmann M., Ziegler K., and Young E. 2013. Reclassification of Villalbeto de la Peña—Occurrence of a Winonaite-related fragment in a hydrothermally metamorphosed polymict L-chondritic breccia. *Meteoritics & Planetary Science* 48:628–640.

Bonino G., Bhandari N., Murty S. V. S., Mahajan R. R., Suthar K. M., Shukla A. D., Shukla P. N., Cini Castagnoli G., and Taricco C. 2001. Solar and galactic cosmic ray records of the Fermo (H) chondrite regolith breccia. *Meteoritics & Planetary Science* 36:831–839.

Borovicka J., Spurny P., and Keclikova J. 1995. A new positional astrometric method for all-sky cameras. *Astronomy & Astrophysics Supplement* 112:173–178.

Bottke W. F., Durda D. D., Nesvorny D., Jedicke R., Morbidelli A., Vokrouhlicky D., and Levison H. F. 2005. Linking the collisional history of the main asteroid belt to its dynamical excitation and depletion. *Icarus* 179:63–94.

Bottke W. F., Vokrouhlicky D., Marchi S., Swindle T., Scott E. R. D., Weirich J. R., and Levison H. 2015. Dating the Moon-forming impact event with asteroidal meteorites. *Science* 348:321–323.

Bouvier A. and Wadhwa M. 2010. The age of the solar system redefined by the oldest Pb-Pb age of a meteoritic inclusion. *Nature Geoscience* 3:637–641.

Bouvier A., Gattacceca J., Agee C., Grossman J., and Metzler K. 2017. The Meteoritical Bulletin, No. 104. *Meteoritics & Planetary Science* 52. https://doi.org/10.1111/maps.12930.

Bryson K. L. and Ostrowski D. R. 2017. Meteorite fractures and scaling for asteroid atmospheric entry (abstract #2501). 48th Lunar and Planetary Science Conference. CD-ROM.

Clayton R. N., Mayeda T. K., Olsen E. J., and Goswami J. N. 1991. Oxygen isotope studies of ordinary chondrites. *Geochimica et Cosmochimica Acta* 55:2317–2337.

Crabb J. and Schultz L. 1981. Cosmic-ray exposure ages of the ordinary chondrites and their significance for parent body stratigraphy. *Geochimica et Cosmochimica Acta* 45:2151–2160.

Dalcher N., Caffee M. W., Nishiizumi K., Welten K. C., Vogel N., Wieler R., and Leya I. 2013. Calibration of cosmogenic noble gas production in ordinary chondrites based on ^{36}Cl- ^{36}Ar Ages. Part 1: Refined produced rates for cosmogenic ^{21}Ne and ^{38}Ar. *Meteoritics & Planetary Science* 48:1841–1862.

Eberhardt P., Geiss J., and Lutz H. 1963. Neutrons in meteorites. In *Earth science and meteoritics*, edited by Geiss J. and Goldberg E. D. Amsterdam, the Netherlands: North Holland. pp. 143–168.

Eugster O., Herzog G. F., Marti K., and Caffee M. W. 2006. Irradiation records, cosmic-ray exposure ages, and transfer times of meteorites. In *Meteorites and the early solar system II*, edited by Lauretta D. S. and McSween H. Y. Jr. Tucson, Arizona: The University of Arizona Press. pp. 829–851.

Eugster O., Lorenzetti S., Krähenbühl U., and Marti K. 2007. Comparison of cosmic-ray exposure age and trapped noble gases in chondrule and matrix samples of ordinary, enstatite, and carbonaceous chondrites. *Meteoritics & Planetary Science* 42:1351–1371.

Fieber-Beyer S. K. and Gaffey M. J. 2015. Near-infrared spectroscopy of 3:1 Kirkwood Gap asteroids III. *Icarus* 257:113–125.

Fries M., Fries J., Hankey M., and Matson R. 2016. Meteorite falls observed in U.S. Weather radar data in 2015 and 2016 (to date). 79th Meteoritical Society meeting, Berlin, Germany. Abstract. 1 p.

Goswami J. N., Lal D., Rao M. N., Sinha N., and Venkatesan T. R. 1978. Particle track and rare gas studies of Innisfree meteorite. *Meteoritics* 13:481–484.

Granvik M., Morbidelli A., Jedicke R., Bolin B., Bottke W. F., Beshore E., Vokrouhlicky D., Delbo M., and Michel P. 2016. Super-catastrophic disruption of asteroids at small perihelion distances. *Nature* 530:303–305.

Granvik M., Morbidelli A., Vokrouhlicky D., Bottke W. F., Nesvorny D., and Jedicke R. 2017. Escape of asteroids from the main belt. *Astronomy & Astrophysics* 598:A52.

Haack H., Farinella P., Scott E. R. D., and Keil K. 1996. Meteoritic, asteroidal, and theoretical constraints on the 500 Ma disruption of the L chondrite parent body. *Icarus* 119:182–191.

Halliday I. 1977. Photographic observations and orbit of the Innisfree meteorite. *Meteoritics & Planetary Science* 12:248–249.

Jenniskens P. 2014. Recent documented meteorite falls, a review of meteorite—Asteroid links. In *Meteoroids 2013*, edited by Jopek T., Rietmeijer F. J. M., Watanabe J., and Williams I. P. Proceedings of the astronomical conference held at A.M. University, Poznan, Poland, Aug 26–30, 2013. Poznan: A. M. University Press. pp. 57–68.

Jenniskens P., Gural P. S., Dynneson L., Grigsby B. J., Newman K. E., Borden M., Koop M., and Holman D. 2011. CAMS: Cameras for Allsky Meteor Surveillance to establish minor meteor showers. *Icarus* 216:40–61.

Jenniskens P., Fries M. C., Yin Q.-Z., Zolensky M., Krot A. N., Sandford S. A., Sears D., Beauford R., Ebel D. S., Friedrich J. M., Nagashima K., Wimpenny J., Yamakawa A., Nishiizumi K., Hamajima Y., Caffee M. W., Welten K. C., Laubenstein M., Davis A. M., Simon S. B., Heck P. R., Young E. D., Kohl I. E., Thiemens M. H., Nunn M. H., Mikouchi T., Hagiya K., Ohsumi K., Cahill T. A., Lawton J. A., Barnes D., Steele A., Burton A. S., Dworkin J. P., Elsila J. E., Pizzarello S., Ogliore R.,

Smitt-Kopplin P., Harir M., Hertkorn N., Verchovsky A., Grady M., Nagao K., Okazaki R., Takechi H., Hiroi T., Smith K., Silber E. A., Brown P. G., Albers J., Klotz D., Hankey M., Matson R., Fries J. A., Walker R. J., Puchtel I., Lee C. A., Erdman M. E., Eppich G. R., Roeske S., Gabelica Z., Lerche M., Nuevo M., Girten B., and Worden S. P. (the Sutter's Mill Meteorite Consortium). 2012. Radar-enabled recovery of the Sutter's Mill Meteorite, a carbonaceous chondrite regolith breccia. *Science* 338:1583–1587.

Jenniskens P., Rubin A. E., Yin Q.–Z., Sears D. W. G., Sandford S. A., Zolensky M. E., Krot A. N., Blair L., Kane D., Utas J., Verish R., Friedrich J. M., Wimpenny J., Eppich G. R., Ziegler K., Verosub K. L., Rowland D. J., Albers J., Gural P. S., Grigsby B., Fries M. D., Matson R., Johnston M., Silber E., Brown P., Yamakawa A., Sanborn M. E., Laubenstein M., Welten K. C., Nishiizumi K., Meier M. M. M., Busemann H., Clay P., Caffee M. W., Schmitt–Kopplin P., Hertkorn N., Glavin D. P., Callahan M. P., Dworkin J. P., Wu Q., Zare R. N., Grady M., Verchovsky S., Emel'yanenko V., Naroenkov S., Clark D. L., Girten B., and Worden P. S. 2014. Fall, recovery and characterization of the Novato L6 Chondrite Breccia. *Meteoritics & Planetary Science* 49:1388–1425.

Kita N. T., Welten K. C., Valley J. W., Spicuzza M. J., Nakashima D., Tenner T. J., Ushikubo T., MacPherson G. J., Welzenbach L., Heck P. R., Davis A., Caffee M. W., Laubenstein M., and Nishiizumi K. 2013. Fall, classification, and exposure history of the Mifflin L5 chondrite. *Meteoritics & Planetary Science* 48: 641–655.

Kohman T. P. and Bender M. L. 1967. Nuclide production by cosmic rays in meteorites and on the Moon. In *High-energy nuclear reactions in astrophysics—A collection of articles*, edited by Shen B. S. P. New York: W. A. Benjamin Inc. pp. 169–245.

Korochantseva E. V., Trieloff M., Lorenz C. A., Buykin A. I., Ivanova M. A., Schwarz W. H., Hopp J., and Jessberger E. K. 2007. L-chondrite asteroid breakup tied to Ordovician meteorite shower by multiple isochron ^{40}Ar-^{39}Ar dating. *Meteoritics & Planetary Science* 42:113–130.

Leya I. 2015. Data from the Noble Gas Cosmochemistry group at the University of Bern, Switzerland. Website: http://archive.space.unibe.ch/noblegas/data.html. Last accessed November 30, 2017.

Leya I. and Masarik J. 2009. Cosmogenic nuclides in stony meteorites revisited. *Meteoritics & Planetary Science* 44:1061–1086.

Li S. and Hsu W. 2016. U-Pb dating of the shock melt veins in two L6 chondrites. 79th Annual Meeting of the Meteoritical Society, 7–12 Aug, 2016, Berlin, Germany, A6057.

Li S. J., Leya I., Wang S. J., and Smith T. 2016. Cosmic-ray exposure ages of chondrites collected in Grove Mountains, Antarctica. 79th Annual Meeting of the Meteoritical Society, 7–12 Aug, 2016, Berlin, Germany, A6356.

Li Q.-L., Li X.-H., Liu Y., Tang G.-Q., Yang J.-H., and Zhu W.-G. 2010. Precise U-Pb and Pb-Pb dating of phanerozoic baddeleyite by SIMS with oxygen flooding technique. *Journal of Analytical Atomic Spectrometry* 25:1107–1113.

Llorca J., Trigo-Rodríguez J. M., Ortiz J. L., Docobo J. A., García-Guinea J., Castro-Tirado A. J., Rubin A. E., Eugster O., Edwards W., Laubesntein M., and Casanova

The Creston, California, meteorite fall   21

I. 2005. The Villalbeto de La Peña meteorite fall: I. Fireball energy, meteorite recovery, strewn field, and petrography. *Meteoritics & Planetary Science* 40:795–804.

Lodders K. 2003. Solar system abundances and condensation temperatures of the elements. *The Astrophysical Journal* 591:1220–1247.

Lodders K., Palme H., and Gail H. P. 2009. Abundances of the elements in the solar system. In *Solar system*, edited by Truemper J. E. Berlin, Germany: Springer. pp. 560–630.

Ludwig K. R. 1998. On the treatment of concordant uranium-lead ages. *Geochimica et Cosmochimica Acta* 62:665–676.

Mahajan R. R., Varela M. E., and Joron J. L. 2016. Santa Lucia (2008) (L6) chondrite, a recent fall: Composition, noble gases, nitrogen and cosmic ray exposure age. *Earth, Moon, and Planets* 117:65–76.

Marti K. and Graf T. 1992. Cosmic-ray exposure history of ordinary chondrites. *Annual Review of Earth and Planetary Sciences* 20:221–243.

McGraw A. M., Reddy V., and Sanchez J. A. 2017. Do L-chondrites come from the Gefion asteroid family? (abstract #1778). 48th Lunar and Planetary Science Conference. CD-ROM.

Meier M. M. M., Welten K. C., Riebe M. E., Riebe I., Caffee M. W., Gritsevich M., Maden C., and Busemann H. 2017. Park Forest (L5) and the asteroidal source of shocked L chondrites. *Meteoritics & Planetary Science* 52:1561–1576.

Nesvorný D., Morbidelli A., Vokrouhlický D., Bottke W. F., and Broz M. 2002. The Flora family: A case of the dynamically dispersed collisional swarm? *Icarus* 157:155–172.

Nesvorný D., Vokrouhlický D., Morbidelli A., and Bottke W. F. 2009. Asteroidal source of L chondrite meteorites. *Icarus* 200:698–701.

Ostrowski D. R. and Bryson K. L. 2016. Physical properties comparison of ordinary chondrite classes. 79th Annual Meeting of the Meteoritical Society, 7–12 Aug, 2016, Berlin. LPI Contribution No. 1921, id. 6510.

Popova O. P., Jenniskens P., Emel'yanenko V., Kartashova A., Biryukov E., Khaibrakhmanov S., Shuvalov V., Rybnov Y., Dudorov A., Grokhovsky V. I., Badyukov D. D., Yin Q.-Z., Gural P. S., Albers J., Granvik M., Evers L. G., Kuiper J., Kharlamov V., Solovyov A., Rusakov Y. S., Korotkiy S., Serdyuk I., Korochantsev A. V., Larionov M. Y., Glazachev D., Mayer A. E., Gisler G., Gladkovsky S. V., Wimpenny J., Sanborn M. E., Yamakawa A., Verosub K., Rowland D. J., Roeske S., Botto N. W., Friedrich J. M., Zolensky M., Le L., Ross D., Ziegler K., Nakamura T., Ahn I., Lee J. I., Zhou Q., Li X.-H., Li Q.-L., Liu Y., Tang G.-Q., Hiroi T., Sears D., Weinstein I. A., Vokhmintsev A. S., Ishchenko A. V., Schmitt-Kopplin P., Hertkorn N., Nagao K., Haba M. K., Komatsu M., and Mikouchi T. 2013. Chelyabinsk airburst, damage assessment, meteorite recovery, and characterization. *Science* 342:1069–1073.

Rochette P., Gattacceca J., and Lewandrowski M. 2012. Magnetic classification of meteorites and application to the Soltmany fall. *Meteorites* 2:67–71.

Rubin A. E. 1990. Kamacite and olivine in ordinary chondrites: Intergroup and intragroup relationships. *Geochimica et Cosmochimica Acta* 54:1217–1232.

Sano Y., Oyama T., Terada K., and Hidaka H. 1999. Ion microprobe U-Pb dating of apatite. *Chemical Geology* 153:249–258.

Schmitz B., Tassinari M., and Peucker-Ehrenbrink B. 2001. A rain of ordinary chondritic meteorites in the early Ordovician. *Earth and Planetary Science Letters* 194:1–15.

Schmitz B., Yin Q.-Z., Sanborn M. E., Tassinari M., Caplan C. E., and Huss G. R. 2016. A new type of solar system material recovered from Ordovician marine limestone. *Nature Communications* 7:11,851–11,858.

Scott E. R. D. 2002. Meteorite evidence for the accretion and collisional evolution of asteroids. In *Asteroids III*, edited by Bottke W., Cellino A., Paolicchoi P., and Binzel R. Tucson, Arizona: The University of Arizona Press. pp. 697–709.

Shima M., Okada A., and Nagao K. 1993. The chondrite Mihonoseki: New observed fall. Proceedings, 24th Lunar and Planetary Science Conference. pp. 1297–1298.

Simon S. B., Grossman L., Clayton R. N., Mayeda T. K., Schwade J. R., Sipiera P. P., Wacker J. F., and Wadhwa M. 2004. The fall, recovery, and classification of the Park Forest meteorite. *Meteoritics & Planetary Science* 39:625–634.

Spergel M. S., Reedy R. C., Lazareth O. W., Levy P. W., and Slatest L. A. 1986. Cosmogenic neutron-capture-produced nuclides in stony meteorites. Proceedings, 16th Lunar and Planetary Science Conference. *Journal of Geophysical Research Supplement* 91:D483–D494.

Spoto F., Milani A., and Knezevic Z. 2015. Asteroid family ages. *Icarus* 257:275–289.

Stacey J. S. and Kramers J. D. 1975. Approximation of terrestrial lead isotope evolution by a two-stage model. *Earth and Planetary Science Letters* 26:207–221.

Stöffler D., Keil K., and Scott E. R. D. 1991. Shock metamorphism of ordinary chondrites. *Geochimica et Cosmochimica Acta* 55:3845–3867.

Takaoka N., Wakabayashi F., Shima M., and Wakabayashi F. 1989. Noble gas record of Japanese chondrites. *Z. Naturforshung* 44a:935–944.

Tatsumoto M., Knight R. J., and Allegre C. J. 1973. Time differences in the formation of meteorites as determined from the ratio of Lead-207 to Lead-206. *Science* 180:1279–1283.

Trigo-Rodriquez J. M., Llorca J., Weyrauch M., Bischoff A., Moyano-Cambero C. E., Keil K., Laubenstein M., Pack A., Madiedo J. M., Alonso-Azcárate J., Riebe M., Wieler R., Ott U., Tapia M., and Mestres N. 2014. Ardón: A long hidden L6 chondrite fall. 77th Annual Meeting of the Meteoritical Society, id. 5068.

Trinquier A., Birck J.-L., and Allègre C. J. 2007. Widespread [54]Cr heterogeneity in the inner solar system. *The Astrophysical Journal* 655:1179–1185.

Troiano J., Rumble D. III, Rivers M. L., and Friedrich J. M. 2011. Compositions of three low-FeO ordinary chondrites: Indications of a common origin with the H chondrites. *Geochimica et Cosmochimica Acta* 75:6511–6519.

Trotter J. A. and Eggins S. M. 2006. Chemical systematics of conodont apatite determined by laserablation ICPMS. *Chemical Geology* 223:196–216.

Vernazza P., Zanda B., Binzel R. P., Hiroi T., DeMeo F. E., Birlan M., Hewins R., Ricci L., Barge P., and Lockhart M. 2014. Multiple and fast: The accretion of ordinary chondrite parent bodies. *The Astrophysical Journal* 791:120–142.

Wasson J. T. 2012. *Meteorites: Classification and properties*, 2nd ed. London, UK: Springer. 205 p.

Wasson J. T. and Kallemeyn G. W. 1988. Compositions of chondrites. *Philosophical Transactions of the Royal Society of London Series A, Mathematical and Physical Sciences* 325:535–544.

22   P. Jenniskens et al.

Weirich J. R., Swindle T. D., Isachsen C. E., Sharp T. G., Li C., and Downs R. T. 2012. Source of potassium in shocked ordinary chondrites. *Geochmicia et Cosmochimica Acta* 98:125–139.

Welten K. C., Nishiizumi K., and Caffee M. W. 2001. The search for meteorites with complex exposure histories among ordinary chondrites with low 3He/21Ne ratios (abstract #2148). 32nd Lunar and Planetary Science Conference. CD-ROM.

Welten K. C., Nishiizumi K., Finkel R. C., Hillegonds D. J., Jull A. J. T., Franke L., and Schultz L. 2004. Exposure history and terrestrial ages of ordinary chondrites from the Dar al Gani region, Libya. *Meteoritics & Planetary Science* 39:481–498.

Welten K. C., Caffee M. W., and Nishiizumi K. 2016. The complex cosmic ray exposure history of Jesenice (L6): Possible evidence for ejection from parent body by tidal disruption or YORP related effects (abstract #2924). 47th Lunar and Planetary Science Conference. CD-ROM.

Wendt I. 1989. Geometric considerations of the three dimensional U/Pb data presentation. *Earth and Planetary Science Letters* 94:231–235.

Wendt I. and Carl C. 1984. U/Pb dating of discordant 0.1 Ma old secondary U minerals. *Earth and Planetary Science Letters* 73:278–284.

Wu Y. and Hsu W. 2017. Petrology, mineralogy and in situ U-Pb dating of Northwest Africa 11042. 80th Annual Meeting of the Meteoritical Society (LPI Contribution Number 1987) A6190.

Yamakawa A., Yamashita K., Makishima A., and Nakamura E. 2009. Chemical separation and mass spectrometry of Cr, Fe, Ni, Zn, and Cu in terrestrial and extraterrestrial materials using thermal ionization mass spectrometry. *Analytical Chemistry* 81:9787–9794.

Yin Q.-Z., Zhou Q., Li Q.-L., Li X.-H., Liu Y., Tan G.-Q., Krot A. N., and Jenniskens P. 2014. Records of the Moon-forming impact and the 470 Ma disruption of the L chondrite parent body in the asteroid belt from U-Pb apatite ages of Novato (L6). *Meteoritics & Planetary Science* 49:1426–1439.

Youdin A. N. 2011. On the formation of planetesimals via secular gravitational instabilities with turbulent stirring. *The Astrophysical Journal* 731:99–117.

Zhou Q., Ying Q.-Z., Edward D. Y., Li X.-H., Wu F.-Y., Li Q.-L., Liu Y., and Tang G.-Q. 2013. SIMS Pb-Pb and U-Pb age determination of eucrite zircons at <5 micron scale and the first 50 Ma of the thermal history of Vesta. *Geochimica et Cosmochimica Acta* 110:152–175.

Bibliography

The meteoritical bulletin, no. 106. *Meteoritics & Planetary Science*, 2017.

I. Andreoni, K. Ackley, J. Cooke, A. Acharyya, J. R. Allison, G. E. Anderson, M. C. B. Ashley, D. Baade, M. Bailes, K. Bannister, A. Beardsley, M. S. Bessell, F. Bian, P. A. Bland, M. Boer, T. Booler, A. Brandeker, I. S. Brown, D. A. H. Buckley, S. W. Chang, D. M. Coward, S. Crawford, H. Crisp, B. Crosse, A. Cucchiara, M. Cupák, J. S. de Gois, A. Deller, H. A. R. Devillepoix, D. Dobie, E. Elmer, D. Emrich, W. Farah, T. J. Farrell, T. Franzen, B. M. Gaensler, D. K. Galloway, B. Gendre, T. Giblin, A. Goobar, J. Green, P. J. Hancock, B. A. D. Hartig, E. J. Howell, L. Horsley, A. Hotan, R. M. Howie, L. Hu, Y. Hu, C. W. James, S. Johnston, M. Johnston-Hollitt, D. L. Kaplan, M. Kasliwal, E. F. Keane, D. Kenney, A. Klotz, R. Lau, R. Laugier, E. Lenc, X. Li, E. Liang, C. Lidman, L. C. Luvaul, C. Lynch, B. Ma, D. Macpherson, J. Mao, D. E. McClelland, C. McCully, A. Möller, M. F. Morales, D. Morris, T. Murphy, K. Noysena, C. A. Onken, N. B. Orange, S. Osłowski, D. Pallot, J. Paxman, S. B. Potter, T. Pritchard, W. Raja, R. Ridden- Harper, E. Romero-Colmenero, E. M. Sadler, E. K. Sansom, R. A. Scalzo, B. P. Schmidt, S. M. Scott, N. Seghouani, Z. Shang, R. M. Shannon, L. Shao, M. M. Shara, R. Sharp, M. Sokolowski, J. Sollerman, J. Staff, K. Steele, T. Sun, N. B. Suntzeff, C. Tao, S. Tingay, M. C. Towner, P. Thierry, C. Trott, B. E. Tucker, P. Väisänen, V. V. Krishnan, M. Walker, L. Wang, X. Wang, R. Wayth, M. Whiting, A. Williams, T. Williams, C. Wolf, C. Wu, X. Wu, J. Yang, X. Yuan, H. Zhang, J. Zhou, and H. Zovaro. Follow Up of GW170817 and Its Electromagnetic Counterpart by Australian- Led Observing Programmes. *Publications of the Astronomical Society of Australia*, 34:e069, Dec. 2017. doi: 10.1017/pasa.2017.65.

D. J. Asher and K. Izumi. Meteor observations in Japan: new implications for a Taurid meteoroid swarm. MNRAS, 297:23–27, June 1998. doi: 10.1046/j.1365-8711.1998.01395.x.

D. J. Asher, S. V. M. Clube, and D. I. Steel. Asteroids in the Taurid Complex. MNRAS, 264:93, Sept. 1993. doi: 10.1093/mnras/264.1.93.

Astropy Collaboration, T. P. Robitaille, E. J. Tollerud, P. Greenfield, M. Droettboom, E. Bray, T. Aldcroft, M. Davis, A. Ginsburg, A. M. Price-Whelan, W. E. Kerzendorf, A. Conley, N. Crighton, K. Barbary, D. Muna, H. Ferguson, F. Grollier, M. M. Parikh, P. H. Nair, H. M. Unther, C. Deil, J. Woillez, S. Conseil, R. Kramer, J. E. H. Turner, L. Singer, R. Fox, B. A. Weaver, V. Zabalza, Z. I. Edwards, K. Azalee Bostroem, D. J. Burke, A. R. Casey, S. M. Crawford, N. Dencheva, J. Ely, T. Jenness, K. Labrie, P. L. Lim, F. Pierfederici, A. Pontzen, A. Ptak, B. Refsdal, M. Servillat, and O. Streicher. Astropy: A community Python package for astronomy. A&A, 558:A33, Oct. 2013. doi: 10.1051/0004-6361/201322068.

Y. Audureau, C. Marmo, S. Bouley, M.-K. Kwon, F. Colas, J. Vaubaillon, M. Birlan, B. Zanda, P. Vernazza, S. Caminade, and J. Gatteccecca. FreeTure: A Free software to capTure meteors for FRIPON. In J.-L. Rault and P. Roggemans, editors, *Proceedings of the International Meteor Conference, Giron, France, 18-21 September 2014*, pages 39–41, Feb. 2014.

P. B. Babadzhanov and G. I. Kokhirova. Densities and porosities of meteoroids. A&A, 495:353–358, Feb. 2009. doi: 10.1051/0004-6361:200810460.

M. Beech, M. Hargrove, and P. Brown. The running of the bulls: a review of Taurid fireball activity since 1962. *The Observatory*, 124:277–284, Aug. 2004.

G. K. Benedix, L. V. Forman, L. Daly, B. Godel, L. Esteban, M. M. M. Meier, C. Maden, H. Busemann, Q. Z. Yin, M. Sanborn, K. Ziegler, J. W. Strasser, K. C. Welten, M. W. Caffee, D. P. Glavin, J. P. Dworkin, P. A. Bland, J. P. Paxman, M. C. Towner, M. Cupák, E. K. Sansom, R. M. Howie, H. A. R. Devillepoix, M. A. Cox, T. Jansen-Sturgeon, B. A. D. Hartig, and A. W. R. Bevan. Mineralogy, Petrology and Chronology of the Dingle Dell Meteorite. In *80th Annual Meeting of the Meteoritical Society 2017*, page 6229, 2017.

E. Bertin. Automatic Astrometric and Photometric Calibration with SCAMP. In C. Gabriel, C. Arviset, D. Ponz, and S. Enrique, editors, *Astronomical Data Analysis Software and Systems XV*, volume 351 of *Astronomical Society of the Pacific Conference Series*, page 112, July 2006.

R. P. Binzel, A. S. Rivkin, J. S. Stuart, A. W. Harris, S. J. Bus, and T. H. Burbine. Observed spectral properties of near-Earth objects: results for population distribution, source regions, and space weathering processes. Icarus, 170: 259–294, Aug. 2004. doi: 10.1016/j.icarus.2004.04.004.

A. Bischoff, J.-A. Barrat, K. Bauer, C. Burkhardt, H. Busemann, S. Ebert, M. Gonsior, J. Hakenmüller, J. Haloda, D. Harries, D. Heinlein, H. Hiesinger, R. Hochleitner, V. Hoffmann, M. Kaliwoda, M. Laubenstein, C. Maden, M. M. M. Meier, A. Morlok, A. Pack, A. Ruf, P. Schmitt-Kopplin, M. SchöNbäChler, R. C. J. Steele, P. Spurný, and K. Wimmer. The Stubenberg meteorite – An LL6 chondrite fragmental breccia recovered soon after precise prediction of the strewn field. *Meteoritics and Planetary Science*, 52:1683–1703, Aug. 2017. doi: 10.1111/maps.12883.

R. C. Blaauw, M. Campbell-Brown, and A. Kingery. Optical meteor fluxes and application to the 2015 Perseids. MNRAS, 463:441–448, Nov. 2016. doi: 10.1093/mnras/stw1979.

P. A. Bland. Fireball cameras: The Desert Fireball Network. *Astronomy and Geophysics*, 45:5.20–5.23, Oct. 2004. doi: 10.1046/j.1468-4004.2003.45520.x.

P. A. Bland and N. A. Artemieva. The rate of small impacts on Earth. *Meteoritics and Planetary Science*, 41:607–631, Apr. 2006. doi: 10.1111/j.1945-5100.2006. tb00485.x.

P. A. Bland, P. Spurný, M. C. Towner, A. W. R. Bevan, A. T. Singleton, W. F. Bottke, R. C. Greenwood, S. R. Chesley, L. Shrbený, J. Borovička, Z. Ceplecha, T. P. McClafferty, D. Vaughan, G. K. Benedix, G. Deacon, K. T. Howard, I. A. Franchi, and R. M. Hough. An Anomalous Basaltic Meteorite from the

Innermost Main Belt. *Science*, 325:1525, Sept. 2009. doi: 10.1126/science. 1174787.

P. A. Bland, P. Spurný, A. W. R. Bevan, K. T. Howard, M. C. Towner, G. K. Benedix, R. C. Greenwood, L. Shrbený, I. A. Franchi, G. Deacon, J. Borovička, Z. Ceplecha, D. Vaughan, and R. M. Hough. The Australian Desert Fireball Network: a new era for planetary science. *Australian Journal of Earth Sciences*, 59:177–187, Mar. 2012. doi: 10.1080/08120099.2011.595428.

B. T. Bolin, M. Delbo, A. Morbidelli, and K. J. Walsh. Yarkovsky V-shape identification of asteroid families. Icarus, 282:290–312, Jan. 2017. doi: 10.1016/j.icarus.2016.09.029.

J. Borovička. The comparison of two methods of determining meteor trajectories from photographs. *Bulletin of the Astronomical Institutes of Czechoslovakia*, 41: 391–396, Dec. 1990.

J. Borovička and Z. Charvát. Meteosat observation of the atmospheric entry of 2008 TC_3 over Sudan and the associated dust cloud. A&A, 507:1015–1022, Nov. 2009. doi: 10.1051/0004-6361/200912639.

J. Borovička, P. Spurný, and J. Keclikova. A new positional astrometric method for all-sky cameras. *Astronomy and Astrophysics Supplement*, 112:173, July 1995.

J. Borovička, P. Spurný, P. Kalenda, and E. Tagliaferri. The Morávka meteorite fall: 1 Description of the events and determination of the fireball trajectory and orbit from video records. *Meteoritics and Planetary Science*, 38:975–987, July 2003. doi: 10.1111/j.1945-5100.2003.tb00293.x.

J. Borovička, P. Spurný, P. Brown, P. Wiegert, P. Kalenda, D. Clark, and L. Shrbený. The trajectory, structure and origin of the Chelyabinsk asteroidal impactor. Nature, 503:235–237, Nov. 2013a. doi: 10.1038/nature12671.

J. Borovička, J. Tóth, A. Igaz, P. Spurný, P. Kalenda, J. Haloda, J. Svoreå, L. Kornoš, E. Silber, P. Brown, and M. HusáRik. The Košice meteorite fall: Atmo-

spheric trajectory, fragmentation, and orbit. *Meteoritics and Planetary Science*, 48:1757–1779, Oct. 2013b. doi: 10.1111/maps.12078.

J. Borovička, P. Spurný, and P. Brown. *Small Near-Earth Asteroids as a Source of Meteorites*, pages 257–280. University of Arizona Press, 2015. doi: 10.2458/ azu_uapress_9780816532131-ch014.

J. Borovička, P. Spurný, V. I. Grigore, and J. Svoreň. The January 7, 2015, superbolide over Romania and structural diversity of meter-sized asteroids. Planet. Space Sci., 143:147–158, Sept. 2017. doi: 10.1016/j.pss.2017.02.006.

J. Borovička. Astrometry with all-sky cameras. *Publications of the Astronomical Institute of the Czechoslovak Academy of Sciences*, 79, Jan. 1992.

W. F. Bottke, A. Morbidelli, R. Jedicke, J.-M. Petit, H. F. Levison, P. Michel, and T. S. Metcalfe. Debiased Orbital and Absolute Magnitude Distribution of the Near-Earth Objects. Icarus, 156:399–433, Apr. 2002. doi: 10.1006/icar.2001. 6788.

E. Bowell, J. Virtanen, K. Muinonen, and A. Boattini. *Asteroid Orbit Computation*, pages 27–43. University of Arizona Press, 2002.

L. Bradley, B. Sipocz, T. Robitaille, E. Tollerud, Z. Vinícius, C. Deil, K. Barbary, H. M. Günther, M. Cara, M. Droettboom, A. Bostroem, E. Bray, L. A. Bratholm, T. E. Pickering, M. Craig, G. Barentsen, S. Pascual, adonath, J. Greco, W. Kerzendorf, StuartLittlefair, L. Ferreira, F. D'Eugenio, and B. A. Weaver. astropy/photutils: v0.3, Nov. 2016.

V. A. Bronshten. The physics of meteoritic phenomena. *Moscow Izdatel Nauka*, 1981.

V. A. Bronshten. *Physics of Meteoric Phenomena*. Geophysics and Astrophysics Monographs. Reidel, Dordrecht, Netherlands, 1983. ISBN 9789027716545.

P. Brown, R. E. Spalding, D. O. ReVelle, E. Tagliaferri, and S. P. Worden. The flux of small near-Earth objects colliding with the Earth. Nature, 420:294–296, Nov. 2002. doi: 10.1038/nature01238.

P. Brown, D. Pack, W. N. Edwards, D. O. Revelle, B. B. Yoo, R. E. Spalding, and E. Tagliaferri. The orbit, atmospheric dynamics, and initial mass of the Park Forest meteorite. *Meteoritics and Planetary Science*, 39:1781–1796, Nov. 2004. doi: 10.1111/j.1945-5100.2004.tb00075.x.

P. Brown, P. J. A. McCausland, M. Fries, E. Silber, W. N. Edwards, D. K. Wong, R. J. Weryk, J. Fries, and Z. Krzeminski. The fall of the Grimsby meteorite I: Fireball dynamics and orbit from radar, video, and infrasound records. *Meteoritics and Planetary Science*, 46:339–363, Mar. 2011. doi: 10.1111/j.1945-5100.2010.01167.x.

P. Brown, V. Marchenko, D. E. Moser, R. Weryk, and W. Cooke. Meteorites from meteor showers: A case study of the Taurids. *Meteoritics and Planetary Science*, 48:270–288, Feb. 2013a. doi: 10.1111/maps.12055.

P. Brown, P. Wiegert, D. Clark, and E. Tagliaferri. Orbital and physical characteristics of meter-scale impactors from airburst observations. Icarus, 266: 96–111, Mar. 2016. doi: 10.1016/j.icarus.2015.11.022.

P. G. Brown, A. R. Hildebrand, M. E. Zolensky, M. Grady, R. N. Clayton, T. K. Mayeda, E. Tagliaferri, R. Spalding, N. D. MacRae, E. L. Hoffman, D. W. Mittlefehldt, J. F. Wacker, J. A. Bird, M. D. Campbell, R. Carpenter, H. Gingerich, M. Glatiotis, E. Greiner, M. J. Mazur, P. J. McCausland, H. Plotkin, and T. Rubak Mazur. The Fall, Recovery, Orbit, and Composition of the Tagish Lake Meteorite: A New Type of Carbonaceous Chondrite. *Science*, 290: 320–325, Oct. 2000. doi: 10.1126/science.290.5490.320.

P. G. Brown, J. D. Assink, L. Astiz, R. Blaauw, M. B. Boslough, J. Borovička, N. Brachet, D. Brown, M. Campbell-Brown, L. Ceranna, W. Cooke, C. de Groot-Hedlin, D. P. Drob, W. Edwards, L. G. Evers, M. Garces, J. Gill, M. Hedlin, A. Kingery, G. Laske, A. Le Pichon, P. Mialle, D. E. Moser, A. Saffer, E. Silber, P. Smets, R. E. Spalding, P. Spurný, E. Tagliaferri, D. Uren, R. J. Weryk, R. Whitaker, and Z. Krzeminski. A 500-kiloton airburst over Chelyabinsk and an enhanced hazard from small impactors. Nature, 503: 238–241, Nov. 2013b. doi: 10.1038/nature12741.

D. Brownlee, P. Tsou, J. Aléon, C. M. O. D. Alexander, T. Araki, S. Bajt, G. A. Baratta, R. Bastien, P. Bland, P. Bleuet, J. Borg, J. P. Bradley, A. Brearley, F. Brenker, S. Brennan, J. C. Bridges, N. D. Browning, J. R. Brucato, E. Bullock, M. J. Burchell, H. Busemann, A. Butterworth, M. Chaussidon, A. Cheuvront, M. Chi, M. J. Cintala, B. C. Clark, S. J. Clemett, G. Cody, L. Colangeli, G. Cooper, P. Cordier, C. Daghlian, Z. Dai, L. D'Hendecourt, Z. Djouadi, G. Dominguez, T. Duxbury, J. P. Dworkin, D. S. Ebel, T. E. Economou, S. Fakra, S. A. J. Fairey, S. Fallon, G. Ferrini, T. Ferroir, H. Fleckenstein, C. Floss, G. Flynn, I. A. Franchi, M. Fries, Z. Gainsforth, J. P. Gallien, M. Genge, M. K. Gilles, P. Gillet, J. Gilmour, D. P. Glavin, M. Gounelle, M. M. Grady, G. A. Graham, P. G. Grant, S. F. Green, F. Grossemy, L. Grossman, J. N. Grossman, Y. Guan, K. Hagiya, R. Harvey, P. Heck, G. F. Herzog, P. Hoppe, F. Hörz, J. Huth, I. D. Hutcheon, K. Ignatyev, H. Ishii, M. Ito, D. Jacob, C. Jacobsen, S. Jacobsen, S. Jones, D. Joswiak, A. Jurewicz, A. T. Kearsley, L. P. Keller, H. Khodja, A. L. D. Kilcoyne, J. Kissel, A. Krot, F. Langenhorst, A. Lanzirotti, L. Le, L. A. Leshin, J. Leitner, L. Lemelle, H. Leroux, M.-C. Liu, K. Luening, I. Lyon, G. MacPherson, M. A. Marcus, K. Marhas, B. Marty, G. Matrajt, K. McKeegan, A. Meibom, V. Mennella, K. Messenger, S. Messenger, T. Mikouchi, S. Mostefaoui, T. Nakamura, T. Nakano, M. Newville, L. R. Nittler, I. Ohnishi, K. Ohsumi, K. Okudaira, D. A. Papanastassiou, R. Palma, M. E. Palumbo, R. O. Pepin, D. Perkins, M. Perronnet, P. Pianetta, W. Rao, F. J. M. Rietmeijer, F. Robert, D. Rost, A. Rotundi, R. Ryan, S. A. Sandford, C. S. Schwandt, T. H. See, D. Schlutter, J. Sheffield-Parker, A. Simionovici, S. Simon, I. Sitnitsky, C. J. Snead, M. K. Spencer, F. J. Stadermann, A. Steele, T. Stephan, R. Stroud, J. Susini, S. R. Sutton, Y. Suzuki, M. Taheri, S. Taylor, N. Teslich, K. Tomeoka, N. Tomioka, A. Toppani, J. M. Trigo-Rodríguez, D. Troadec, A. Tsuchiyama, A. J. Tuzzolino, T. Tyliszczak, K. Uesugi, M. Velbel, J. Vellenga, E. Vicenzi, L. Vincze, J. Warren, I. Weber, M. Weisberg, A. J. Westphal, S. Wirick, D. Wooden, B. Wopenka, P. Wozniakiewicz, I. Wright, H. Yabuta, H. Yano, E. D. Young, R. N. Zare, T. Zega, K. Ziegler, L. Zimmerman, E. Zinner, and M. Zolensky. Comet 81P/Wild 2 Under a Microscope. *Science*, 314: 1711, Dec. 2006. doi: 10.1126/science.1135840.

M. R. Calabretta and E. W. Greisen. Representations of celestial coordinates in FITS. A&A, 395:1077–1122, Dec. 2002. doi: 10.1051/0004-6361:20021327.

Z. Ceplecha. Multiple fall of Příbram meteorites photographed. 1. Double-station photographs of the fireball and their relations to the found meteorites. *Bulletin of the Astronomical Institutes of Czechoslovakia*, 12:21, 1961.

Z. Ceplecha. Geometric, dynamic, orbital and photometric data on meteoroids from photographic fireball networks. *Bulletin of the Astronomical Institutes of Czechoslovakia*, 38:222–234, July 1987.

Z. Ceplecha and R. E. McCrosky. Fireball end heights - A diagnostic for the structure of meteoric material. J. Geophys. Res., 81:6257–6275, Dec. 1976. doi: 10.1029/JB081i035p06257.

C. F. Chyba, P. J. Thomas, and K. J. Zahnle. The 1908 Tunguska explosion - Atmospheric disruption of a stony asteroid. Nature, 361:40–44, Jan. 1993. doi: 10.1038/361040a0.

R. I. Citron, A. Shah, S. Sinha, C. Watkins, and P. Jenniskens. Meteorite Recovery Using an Autonomous Drone and Machine Learning. In *Lunar and Planetary Science Conference*, page 2528, Mar. 2017.

S. V. M. Clube and W. M. Napier. The microstructure of terrestrial catastrophism. MNRAS, 211:953–968, Dec. 1984. doi: 10.1093/mnras/211.4.953.

F. Colas, B. Zanda, J. Vaubaillon, S. Bouley, C. Marmo, Y. Audureau, M. K. Kwon, J.-L. Rault, S. Caminade, P. Vernazza, J. Gattacceca, M. Birlan, L. Maquet, A. Egal, M. Rotaru, C. Birnbaum, F. Cochard, and O. Thizy. French fireball network FRIPON. In J.-L. Rault and P. Roggemans, editors, *International Meteor Conference Mistelbach, Austria*, pages 37–40, Jan. 2015.

G. S. Collins, H. J. Melosh, and R. A. Marcus. Earth Impact Effects Program: A Web-based computer program for calculating the regional environmental consequences of a meteoroid impact on Earth. *Meteoritics and Planetary Science*, 40:817, June 2005. doi: 10.1111/j.1945-5100.2005.tb00157.x.

N. L. de Lacaille, T. Henderson, F. Baily, and S. Herschel, John Frederick William. *A Catalogue of 9766 Stars in the Southern Hemisphere, for the beginning of the year 1750, from the observations of the Abbé de Lacaille, made at the Cape of Good Hope in the years 1751 and 1752.* 1847.

H. A. R. Devillepoix, P. A. Bland, M. C. Towner, M. Cupák, E. K. Sansom, T. Jansen-Sturgeon, R. M. Howie, J. Paxman, and B. A. D. Hartig. Status of the Desert Fireball Network. In A. Roggemans and P. Roggemans, editors, *International Meteor Conference Egmond, the Netherlands, 2-5 June 2016*, pages 60–62, Jan. 2016.

H. A. R. Devillepoix, E. K. Sansom, P. A. Bland, M. C. Towner, M. CupáK, R. M. Howie, T. Jansen-Sturgeon, M. A. Cox, B. A. D. Hartig, G. K. Benedix, and J. P. Paxman. The Dingle Dell meteorite: A Halloween treat from the Main Belt. *Meteoritics and Planetary Science*, 53:2212–2227, Oct. 2018. doi: 10.1111/maps.13142.

H. A. R. Devillepoix, P. A. Bland, E. K. Sansom, M. C. Towner, M. Cupák, R. M. Howie, B. A. D. Hartig, T. Jansen-Sturgeon, and M. A. Cox. Observation of metre-scale impactors by the Desert Fireball Network. MNRAS, 483:5166–5178, Mar 2019. doi: 10.1093/mnras/sty3442.

J. D. Drummond. A test of comet and meteor shower associations. Icarus, 45:545–553, Mar. 1981. doi: 10.1016/0019-1035(81)90020-8.

A. Dubietis and R. Arlt. Taurid resonant-swarm encounters from two decades of visual observations. MNRAS, 376:890–894, Apr. 2007. doi: 10.1111/j.1365-2966.2007.11488.x.

A. Egal, M.-K. Kwon, F. Colas, J. Vaubaillon, and C. Marmo. The challenge of meteor daylight observations. In A. Roggemans and P. Roggemans, editors, *International Meteor Conference Egmond, the Netherlands, 2-5 June 2016*, pages 73–75, Jan. 2016.

A. Egal, P. S. Gural, J. Vaubaillon, F. Colas, and W. Thuillot. The challenge associated with the robust computation of meteor velocities from video and

photographic records. Icarus, 294:43–57, Sept. 2017. doi: 10.1016/j.icarus.2017.04.024.

P. Farinella, D. Vokrouhlický, and W. K. Hartmann. Meteorite Delivery via Yarkovsky Orbital Drift. Icarus, 132:378–387, Apr. 1998. doi: 10.1006/icar.1997.5872.

D. Farnocchia, S. R. Chesley, P. G. Brown, and P. W. Chodas. The trajectory and atmospheric impact of asteroid 2014 AA. Icarus, 274:327–333, Aug. 2016. doi: 10.1016/j.icarus.2016.02.056.

D. Farnocchia, P. Jenniskens, D. K. Robertson, S. R. Chesley, L. Dimare, and P. W. Chodas. The impact trajectory of asteroid 2008 TC$_3$. Icarus, 294:218–226, Sept. 2017. doi: 10.1016/j.icarus.2017.03.007.

M. P. Fay. Two-sided Exact Tests and Matching Confidence Intervals for Discrete Data. *The R Journal*, 2(1):53–58, 2010.

M. Fries and J. Fries. Doppler weather radar as a meteorite recovery tool. *Meteoritics and Planetary Science*, 45:1476–1487, Sept. 2010. doi: 10.1111/j.1945-5100.2010.01115.x.

M. Fries, L. Le Corre, M. Hankey, J. Fries, R. Matson, J. Schaefer, and V. Reddy. Detection and rapid recovery of the Sutter's Mill meteorite fall as a model for future recoveries worldwide. *Meteoritics and Planetary Science*, 49:1989–1996, Nov. 2014. doi: 10.1111/maps.12249.

C. Froeschle and H. Scholl. Gravitational splitting of Quadrantid-like meteor streams in resonance with Jupiter. A&A, 158:259–265, Apr. 1986.

K.-H. Glassmeier, H. Boehnhardt, D. Koschny, E. Kührt, and I. Richter. The Rosetta Mission: Flying Towards the Origin of the Solar System. Space Sci. Rev., 128:1–21, Feb. 2007. doi: 10.1007/s11214-006-9140-8.

M. Granvik and P. Brown. Identification of meteorite source regions in the Solar System. Icarus, 311:271–287, Sept. 2018. doi: 10.1016/j.icarus.2018.04.012.

M. Granvik, A. Morbidelli, R. Jedicke, B. Bolin, W. F. Bottke, E. Beshore, D. Vokrouhlický, M. Delbò, and P. Michel. Super-catastrophic disruption of asteroids at small perihelion distances. Nature, 530:303–306, Feb. 2016. doi: 10.1038/nature16934.

M. Granvik, A. Morbidelli, R. Jedicke, B. Bolin, W. F. Bottke, E. Beshore, D. Vokrouhlický, D. Nesvorný, and P. Michel. Debiased orbit and absolute-magnitude distributions for near-Earth objects. Icarus, 312:181–207, Sept. 2018. doi: 10.1016/j.icarus.2018.04.018.

S. Greenstreet, H. Ngo, and B. Gladman. The orbital distribution of Near-Earth Objects inside Earth's orbit. Icarus, 217:355–366, Jan. 2012. doi: 10.1016/j.icarus.2011.11.010.

E. W. Greisen and M. R. Calabretta. Representations of world coordinates in FITS. A&A, 395:1061–1075, Dec. 2002. doi: 10.1051/0004-6361:20021326.

M. Gritsevich, V. Dmitriev, V. Vinnikov, D. Kuznetsova, V. Lupovka, J. Peltoniemi, S. Mönkölä, J. Brower, and Y. Pupyrev. Constraining the Pre-atmospheric Parameters of Large Meteoroids: Košice, a Case Study. In *Assessment and Mitigation of Asteroid Impact Hazards, Astrophysics and Space Science Proceedings, Volume 46. ISBN 978-3-319-46178-6. Springer International Publishing Switzerland, 2017, p. 153*, volume 46, page 153, Jan. 2017. doi: 10.1007/978-3-319-46179-3_8.

M. I. Gritsevich. Determination of parameters of meteor bodies based on flight observational data. *Advances in Space Research*, 44:323–334, Aug. 2009. doi: 10.1016/j.asr.2009.03.030.

I. Halliday. Photographic Fireball Networks. *NASA Special Publication*, 319:1, 1973.

I. Halliday, A. A. Griffin, and A. T. Blackwell. The Innisfree meteorite fall - A photographic analysis of fragmentation, dynamics and luminosity. *Meteoritics*, 16:153–170, June 1981.

I. Halliday, A. A. Griffin, and A. T. Blackwell. Detailed data for 259 fireballs from the Canadian camera network and inferences concerning the influx of large meteoroids. *Meteoritics and Planetary Science*, 31:185–217, Mar. 1996. doi: 10.1111/j.1945-5100.1996.tb02014.x.

M. Hankey and V. Perlerin. IMO's new online fireball form. *WGN, Journal of the International Meteor Organization*, 43:2–7, Feb. 2015.

I. Hasegawa. Predictions of the meteor radiant point associated with a comet. PASJ, 42:175–186, Feb. 1990.

D. M. Hawkins. The problem of overfitting. *Journal of Chemical Information and Computer Sciences*, 44(1):1–12, 2004. doi: 10.1021/ci0342472. PMID: 14741005.

P. R. Heck, B. Schmitz, H. Baur, A. N. Halliday, and R. Wieler. Fast delivery of meteorites to Earth after a major asteroid collision. Nature, 430:323–325, July 2004. doi: 10.1038/nature02736.

P. R. Heck, B. Schmitz, H. Baur, and R. Wieler. Noble gases in fossil micrometeorites and meteorites from 470 Myr old sediments from southern Sweden, and new evidence for the L-chondrite parent body breakup event. *Meteoritics and Planetary Science*, 43:517–528, Mar. 2008. doi: 10.1111/j.1945-5100.2008.tb00669.x.

P. R. Heck, B. Schmitz, W. F. Bottke, S. S. Rout, N. T. Kita, A. Cronholm, C. Defouilloy, A. Dronov, and F. Terfelt. Rare meteorites common in the Ordovician period. *Nature Astronomy*, 1:0035, Jan. 2017. doi: 10.1038/s41550-016-0035.

A. H. Hildebrand, L. T. J. Hanton, F. Ciceri, R. Nowell, E. Lyytinen, E. A. Silber, P. G. Brown, N. Gi, P. Jenniskens, J. Albers, and D. Hladiuk. Characteristics of a Well Recorded, Bright, Meteorite-Dropping Fireball, British Columbia. In *Lunar and Planetary Science Conference*, volume 49 of *Lunar and Planetary Inst. Technical Report*, page 3006, Mar. 2018.

J. Hoppe. Die physikalischen Vorgänge beim Eindringen meteoritischer Körper in die Erdatmosphäre. *Astronomische Nachrichten*, 262(10):169–198, 1937.

R. M. Howie, J. Paxman, P. A. Bland, M. C. Towner, M. Cupák, E. K. Sansom, and H. A. R. Devillepoix. How to build a continental scale fireball camera network. *Experimental Astronomy*, May 2017a. doi: 10.1007/s10686-017-9532-7.

R. M. Howie, J. Paxman, P. A. Bland, M. C. Towner, E. K. Sansom, and H. A. R. Devillepoix. Submillisecond fireball timing using de Bruijn time-codes. *Meteoritics and Planetary Science*, 52:1669–1682, Aug. 2017b. doi: 10.1111/maps.12878.

Z. Ivezic, T. Axelrod, W. N. Brandt, D. L. Burke, C. F. Claver, A. Connolly, K. H. Cook, P. Gee, D. K. Gilmore, S. H. Jacoby, R. L. Jones, S. M. Kahn, J. P. Kantor, V. V. Krabbendam, R. H. Lupton, D. G. Monet, P. A. Pinto, A. Saha, T. L. Schalk, D. P. Schneider, M. A. Strauss, C. W. Stubbs, D. Sweeney, A. Szalay, J. J. Thaler, J. A. Tyson, and LSST Collaboration. Large Synoptic Survey Telescope: From Science Drivers To Reference Design. *Serbian Astronomical Journal*, 176:1–13, June 2008. doi: 10.2298/SAJ0876001I.

T. Jansen-Sturgeon, E. K. Sansom, and P. A. Bland. Comparing Analytical and Numerical Approaches to Meteoroid Orbit Determination using Hayabusa Telemetry. *ArXiv e-prints*, art. arXiv:1808.05768, Aug. 2018.

P. Jenniskens. *Meteor Showers and Their Parent Comets*. Cambridge University Press, 2006. ISBN 9780521853491.

P. Jenniskens. Recent documented meteorite falls, a review of meteorite - asteroid links. *Meteoroids 2013*, July 2014.

P. Jenniskens, M. H. Shaddad, D. Numan, S. Elsir, A. M. Kudoda, M. E. Zolensky, L. Le, G. A. Robinson, J. M. Friedrich, D. Rumble, A. Steele, S. R. Chesley, A. Fitzsimmons, S. Duddy, H. H. Hsieh, G. Ramsay, P. G. Brown, W. N. Edwards, E. Tagliaferri, M. B. Boslough, R. E. Spalding, R. Dantowitz, M. Kozubal, P. Pravec, J. Borovička, Z. Charvat, J. Vaubaillon, J. Kuiper, J. Albers, J. L. Bishop, R. L. Mancinelli, S. A. Sandford, S. N. Milam, M. Nuevo, and S. P. Worden. The impact and recovery of asteroid 2008 TC$_3$. Nature, 458: 485–488, Mar. 2009. doi: 10.1038/nature07920.

P. Jenniskens, P. S. Gural, L. Dynneson, B. J. Grigsby, K. E. Newman, M. Borden, M. Koop, and D. Holman. CAMS: Cameras for Allsky Meteor Surveillance to establish minor meteor showers. Icarus, 216:40–61, Nov. 2011. doi: 10.1016/j.icarus.2011.08.012.

P. Jenniskens, M. D. Fries, Q.-Z. Yin, M. Zolensky, A. N. Krot, S. A. Sandford, D. Sears, R. Beauford, D. S. Ebel, J. M. Friedrich, K. Nagashima, J. Wimpenny, A. Yamakawa, K. Nishiizumi, Y. Hamajima, M. W. Caffee, K. C. Welten, M. Laubenstein, A. M. Davis, S. B. Simon, P. R. Heck, E. D. Young, I. E. Kohl, M. H. Thiemens, M. H. Nunn, T. Mikouchi, K. Hagiya, K. Ohsumi, T. A. Cahill, J. A. Lawton, D. Barnes, A. Steele, P. Rochette, K. L. Verosub, J. Gattacceca, G. Cooper, D. P. Glavin, A. S. Burton, J. P. Dworkin, J. E. Elsila, S. Pizzarello, R. Ogliore, P. Schmitt-Kopplin, M. Harir, N. Hertkorn, A. Verchovsky, M. Grady, K. Nagao, R. Okazaki, H. Takechi, T. Hiroi, K. Smith, E. A. Silber, P. G. Brown, J. Albers, D. Klotz, M. Hankey, R. Matson, J. A. Fries, R. J. Walker, I. Puchtel, C.-T. A. Lee, M. E. Erdman, G. R. Eppich, S. Roeske, Z. Gabelica, M. Lerche, M. Nuevo, B. Girten, and S. P. Worden. Radar-Enabled Recovery of the Sutter's Mill Meteorite, a Carbonaceous Chondrite Regolith Breccia. *Science*, 338:1583, Dec. 2012. doi: 10.1126/science.1227163.

P. Jenniskens, A. E. Rubin, Q.-Z. Yin, D. W. G. Sears, S. A. Sandford, M. E. Zolensky, A. N. Krot, L. Blair, D. Kane, J. Utas, R. Verish, J. M. Friedrich, J. Wimpenny, G. R. Eppich, K. Ziegler, K. L. Verosub, D. J. Rowland, J. Albers, P. S. Gural, B. Grigsby, M. D. Fries, R. Matson, M. Johnston, E. Silber, P. Brown, A. Yamakawa, M. E. Sanborn, M. Laubenstein, K. C. Welten, K. Nishiizumi, M. M. M. Meier, H. Busemann, P. Clay, M. W. Caffee, P. Schmitt-Kopplin, N. Hertkorn, D. P. Glavin, M. P. Callahan, J. P. Dworkin, Q. Wu, R. N. Zare, M. Grady, S. Verchovsky, V. Emel'Yanenko, S. Naroenkov, D. L. Clark, B. Girten, and P. S. Worden. Fall, recovery, and characterization of the Novato L6 chondrite breccia. *Meteoritics and Planetary Science*, 49:1388–1425, Aug. 2014. doi: 10.1111/maps.12323.

P. Jenniskens, Q. Nénon, J. Albers, P. S. Gural, B. Haberman, D. Holman,

R. Morales, B. J. Grigsby, D. Samuels, and C. Johannink. The established meteor showers as observed by CAMS. Icarus, 266:331–354, Mar. 2016a. doi: 10.1016/j.icarus.2015.09.013.

P. Jenniskens, Q. Nénon, P. S. Gural, J. Albers, B. Haberman, B. Johnson, D. Holman, R. Morales, B. J. Grigsby, D. Samuels, and C. Johannink. CAMS confirmation of previously reported meteor showers. Icarus, 266:355–370, Mar. 2016b. doi: 10.1016/j.icarus.2015.08.014.

P. Jenniskens, Q. Nénon, P. S. Gural, J. Albers, B. Haberman, B. Johnson, R. Morales, B. J. Grigsby, D. Samuels, and C. Johannink. CAMS newly detected meteor showers and the sporadic background. Icarus, 266:384–409, Mar. 2016c. doi: 10.1016/j.icarus.2015.11.009.

P. Jenniskens, J. Utas, Q.-Z. Yin, R. D. Matson, M. Fries, J. A. Howell, D. Free, J. Albers, H. Devillepoix, P. Bland, A. Miller, R. Verish, L. A. J. Garvie, M. E. Zolensky, K. Ziegler, M. E. Sanborn, K. L. Verosub, D. J. Rowland, D. R. Ostrowski, K. Bryson, M. Laubenstein, Q. Zhou, Q.-L. Li, X.-H. Li, Y. Liu, G.-Q. Tang, K. Welten, M. W. Caffee, M. M. M. Meier, A. A. Plant, C. Maden, H. Busemann, M. Granvik, and T. C. M. Consortium). The creston, california, meteorite fall and the origin of l chondrites. *Meteoritics & Planetary Science*, in press, 2019. doi: 10.1111/maps.13235. URL https://onlinelibrary.wiley.com/doi/abs/10.1111/maps.13235.

E. Jones, T. Oliphant, P. Peterson, et al. SciPy: Open source scientific tools for Python, 2001–. URL http://www.scipy.org/. [Online; accessed ¡today¿].

C. S. Keay. Electrophonic sounds from large meteor fireballs. *Meteoritics & Planetary Science*, 27(2):144–148, 1992.

K. Keil, D. Stoeffler, S. G. Love, and E. R. D. Scott. Constraints on the role of impact heating and melting in asteroids. *Meteoritics and Planetary Science*, 32, May 1997. doi: 10.1111/j.1945-5100.1997.tb01278.x.

T. Kluyver, B. Ragan-Kelley, F. Pérez, B. Granger, M. Bussonnier, J. Frederic, K. Kelley, J. Hamrick, J. Grout, S. Corlay, P. Ivanov, D. Avila, S. Abdalla,

and C. Willing. Jupyter notebooks – a publishing format for reproducible computational workflows. In F. Loizides and B. Schmidt, editors, *Positioning and Power in Academic Publishing: Players, Agents and Agendas*, pages 87 – 90. IOS Press, 2016.

D. Lang, D. W. Hogg, K. Mierle, M. Blanton, and S. Roweis. Astrometry.net: Blind Astrometric Calibration of Arbitrary Astronomical Images. *The astronomical journal*, 139:1782–1800, May 2010. doi: 10.1088/0004-6256/139/5/1782.

J. Laskar and M. Gastineau. Existence of collisional trajectories of Mercury, Mars and Venus with the Earth. Nature, 459:817–819, June 2009. doi: 10.1038/nature08096.

LIGO Scientific Collaboration, Virgo Collaboration, Fermi GBM, INTEGRAL, IceCube Collaboration, AstroSat Cadmium Zinc Telluride Imager Team, IPN Collaboration, The Insight-HXMT Collaboration, ANTARES Collaboration, The Swift Collaboration, AGILE Team, The 1M2H Team, The Dark Energy Camera GW-EM Collabor ation, the DES Collaboration, The DLT40 Collaboration, GRAWITA: GRAvitational Wave Inaf TeAm, The Fermi Large Area Telescope Collaboration, ATCA: Australia Telescope Compact Array, ASKAP: Australian SKA Pathfinder, Las Cumbres Observatory Group, OzGrav, DWF(Deeper, Wider, Faster Program), AST3, and CAASTRO Collaborations, The VINROUGE Collaboration, MASTER Collaboration, J-GEM, GROWTH, JAGWAR, Caltech-NRAO, TTU-NRAO, and NuSTAR Collaborations, Pan-STARRS, TheMAXITeam, TZACConsortium, KU Collaboration, NordicOptical Telescope, ePESSTO, GROND, Texas Tech University, SALT Group, TOROS: Transient Robotic Observatory of the SouthCollaboration, The BOOTES Collaboration, MWA: Murchison Widefield Array, The CALET Collaboration, IKI-GW Follow-up Collaboration, H.E.S.S. Collaboration, LOFAR Collaboration, LWA: Long Wavelength Array, HAWC Collaboration, The Pierre Auger Collaboration, ALMA Collaboration, Euro VLBI Team, Pi of the Sky Collaboration, The Chandra Team at McGill University, **DFN:**

Desert Fireball Network, ATLAS, High Time Resolution Universe Survey, RIMAS, RATIR, and SKA South Africa/MeerKAT, and **3677 authors**. Multimessenger Observations of a Binary Neutron Star Merger. ApJ, 848:L12, Oct. 2017. doi: 10.3847/2041-8213/aa91c9.

T. Lister, S. Greenstreet, E. Gomez, E. J. Christensen, and S. M. Larson. The LCOGT NEO Follow-up Network. In *AAS/Division for Planetary Sciences Meeting Abstracts*, volume 48 of *AAS/Division for Planetary Sciences Meeting Abstracts*, page 405.06, Oct. 2016.

J. M. Madiedo, J. L. Ortiz, J. M. Trigo-Rodríguez, J. Dergham, A. J. Castro-Tirado, J. Cabrera-Caño, and P. Pujols. Analysis of bright Taurid fireballs and their ability to produce meteorites. Icarus, 231:356–364, Mar. 2014. doi: 10.1016/j.icarus.2013.12.025.

R. E. McCrosky and H. Boeschenstein. The Prairie Meteorite Network. *Optical Engineering*, 3(4):304127–304127, 1965.

W. McKinney. Data structures for statistical computing in python. In S. van der Walt and J. Millman, editors, *Proceedings of the 9th Python in Science Conference*, pages 51 – 56, 2010.

E. P. Milley. Physical properties of fireball-producing earth-impacting meteoroids and orbit determination through shadow calibration of the buzzard coulee meteorite fall. Master's thesis, University of Calgary, 7 2010.

M. Mommert, D. Farnocchia, J. L. Hora, S. R. Chesley, D. E. Trilling, P. W. Chodas, M. Mueller, A. W. Harris, H. A. Smith, and G. G. Fazio. Physical Properties of Near-Earth Asteroid 2011 MD. ApJ, 789:L22, July 2014a. doi: 10.1088/2041-8205/789/1/L22.

M. Mommert, J. L. Hora, D. Farnocchia, S. R. Chesley, D. Vokrouhlický, D. E. Trilling, M. Mueller, A. W. Harris, H. A. Smith, and G. G. Fazio. Constraining the Physical Properties of Near-Earth Object 2009 BD. ApJ, 786:148, May 2014b. doi: 10.1088/0004-637X/786/2/148.

A. Morbidelli, R. Gonczi, C. Froeschle, and P. Farinella. Delivery of meteorites through the nu$_6$ secular resonance. A&A, 282:955–979, Feb. 1994.

T. Nakamura, T. Noguchi, M. Tanaka, M. E. Zolensky, M. Kimura, A. Tsuchiyama, A. Nakato, T. Ogami, H. Ishida, M. Uesugi, T. Yada, K. Shirai, A. Fujimura, R. Okazaki, S. A. Sandford, Y. Ishibashi, M. Abe, T. Okada, M. Ueno, T. Mukai, M. Yoshikawa, and J. Kawaguchi. Itokawa Dust Particles: A Direct Link Between S-Type Asteroids and Ordinary Chondrites. *Science*, 333:1113, Aug. 2011. doi: 10.1126/science.1207758.

L. Neslusan, J. Svoren, and V. Porubcan. A computer program for calculation of a theoretical meteor-stream radiant. A&A, 331:411–413, Mar. 1998.

D. Nesvorný, D. Vokrouhlický, A. Morbidelli, and W. F. Bottke. Asteroidal source of L chondrite meteorites. Icarus, 200:698–701, Apr. 2009. doi: 10.1016/ j.icarus.2008.12.016.

J. Oberst, S. Molau, D. Heinlein, C. Gritzner, M. Schindler, P. Spurny, Z. Ceplecha, J. Rendtel, and H. Betlem. The "European Fireball Network": Current status and future prospects. *Meteoritics and Planetary Science*, 33, Jan. 1998. doi: 10.1111/j.1945-5100.1998.tb01606.x.

A. Olech, P. Żołądek, M. Wiśniewski, R. Rudawska, M. Bęben, T. Krzyżanowski, M. Myszkiewicz, M. Stolarz, M. Gawroński, M. Gozdalski, T. Suchodolski, W. Węgrzyk, and Z. Tymiński. 2015 Southern Taurid fireballs and asteroids 2005 UR and 2005 TF50. MNRAS, 461:674–683, Sept. 2016. doi: 10.1093/ mnras/stw1261.

A. Olech, P. Żołądek, M. Wiśniewski, Z. Tymiński, M. Stolarz, M. Bęben, D. Dorosz, T. Fajfer, K. Fietkiewicz, M. Gawroński, M. Gozdalski, M. Kałużny, M. Krasnowski, H. Krygiel, T. Krzyżanowski, M. Kwinta, T. Łojek, M. Maciejewski, S. Miernicki, M. Myszkiewicz, P. Nowak, K. Polak, K. Polakowski, J. Laskowski, M. Szlagor, G. Tissler, T. Suchodolski, W. Węgrzyk, P. Woźniak, and P. Zaręba. Enhanced activity of the Southern Taurids in 2005 and 2015. MNRAS, 469:2077–2088, Aug. 2017. doi: 10.1093/mnras/stx716.

T. E. Oliphant. *Guide to NumPy*. CreateSpace Independent Publishing Platform, USA, 2nd edition, 2015. ISBN 151730007X, 9781517300074.

C. Palotai, R. Sankar, D. L. Free, J. A. Howell, E. Botella, and D. Batcheldor. Analysis of June 2, 2016 bolide event. *ArXiv e-prints*, Jan. 2018.

J. Paxman and P. Bland. Fireballs in the sky: Improving the accuracy of crowd sourced fireball observation through the application of smartphone technology. In *Lunar and Planetary Science Conference*, volume 45, page 1731, 2014.

F. Pérez and B. E. Granger. IPython: a system for interactive scientific computing. *Computing in Science and Engineering*, 9(3):21–29, May 2007. ISSN 1521-9615. doi: 10.1109/MCSE.2007.53. URL https://ipython.org.

J. M. Picone, A. E. Hedin, D. P. Drob, and A. C. Aikin. NRLMSISE-00 empirical model of the atmosphere: Statistical comparisons and scientific issues. *Journal of Geophysical Research (Space Physics)*, 107:1468, Dec. 2002. doi: 10.1029/2002JA009430.

M. Popescu, M. Birlan, D. A. Nedelcu, J. Vaubaillon, and C. P. Cristescu. Spectral properties of the largest asteroids associated with Taurid Complex. A&A, 572:A106, Dec. 2014. doi: 10.1051/0004-6361/201424064.

O. Popova, J. Borovička, W. K. Hartmann, P. Spurný, E. Gnos, I. Nemtchinov, and J. M. Trigo-Rodríguez. Very low strengths of interplanetary meteoroids and small asteroids. *Meteoritics and Planetary Science*, 46:1525–1550, Oct. 2011. doi: 10.1111/j.1945-5100.2011.01247.x.

V. Reddy, J. A. Sanchez, W. F. Bottke, E. A. Cloutis, M. R. M. Izawa, D. P. O'Brien, P. Mann, M. Cuddy, L. Le Corre, M. J. Gaffey, and G. Fujihara. Chelyabinsk meteorite explains unusual spectral properties of Baptistina Asteroid Family. Icarus, 237:116–130, July 2014. doi: 10.1016/j.icarus.2014.04.027.

H. Rein and D. Tamayo. WHFAST: a fast and unbiased implementation of a symplectic Wisdom-Holman integrator for long-term gravitational simulations. MNRAS, 452:376–388, Sept. 2015. doi: 10.1093/mnras/stv1257.

D. O. Revelle and Z. Ceplecha. Analysis of identified iron meteoroids: Possible relation with M-type Earth-crossing asteroids? A&A, 292:330–336, Dec. 1994.

D. P. Rubincam. Possible lack of low-mass meteoroids in the Earth's meteoroid flux due to space erosion? Icarus, 299:161–165, Jan. 2018. doi: 10.1016/j. icarus.2017.07.020.

E. Sansom and et al. Fall and recovery of the Murrili meteorite. *submitted to MAPS*, 2018.

E. Sansom, J. Ridgewell, P. Bland, and J. Paxman. Meteor reporting made easy-The Fireballs in the Sky smartphone app. In A. Roggemans and P. Roggemans, editors, *International Meteor Conference Egmond, the Netherlands, 2-5 June 2016*, pages 267–269, Jan. 2016a.

E. K. Sansom. *Tracking Meteoroids in the Atmosphere: Fireball Trajectory Analysis*. PhD thesis, Curtin University, 2016. URL +http://hdl.handle.net/20. 500.11937/55061.

E. K. Sansom, P. Bland, J. Paxman, and M. Towner. A novel approach to fireball modeling: The observable and the calculated. *Meteoritics and Planetary Science*, 50:1423–1435, Aug. 2015. doi: 10.1111/maps.12478.

E. K. Sansom, P. A. Bland, M. G. Rutten, J. Paxman, and M. C. Towner. Filtering Meteoroid Flights Using Multiple Unscented Kalman Filters. AJ, 152:148, Nov. 2016b. doi: 10.3847/0004-6256/152/5/148.

E. K. Sansom, M. G. Rutten, and P. A. Bland. Analyzing Meteoroid Flights Using Particle Filters. AJ, 153:87, Feb. 2017. doi: 10.3847/1538-3881/153/2/87.

E. K. Sansom, T. Jansen-Sturgeon, M. G. Rutten, H. A. R. Devillepoix, P. A. Bland, R. M. Howie, M. A. Cox, M. C. Towner, M. Cupák, and B. A. D. Hartig. 3D meteoroid trajectories. Icarus, 321:388–406, Mar 2019. doi: 10.1016/j. icarus.2018.09.026.

B. Schmitz, M. Tassinari, and B. Peucker-Ehrenbrink. A rain of ordinary chondritic meteorites in the early Ordovician. *Earth and Planetary Science Letters*, 194:1–15, Dec. 2001. doi: 10.1016/S0012-821X(01)00559-3.

L. Shrbený and P. Spurný. Precise Data on Photographic Fireballs Belonging to the Taurid Complex Observed within Czech Fireball Network. In *Asteroids, Comets, Meteors 2012*, volume 1667 of *LPI Contributions*, page 6436, May 2012.

B. Sicardy, J. Talbot, E. Meza, J. I. B. Camargo, J. Desmars, D. Gault, D. Herald, S. Kerr, H. Pavlov, F. Braga-Ribas, M. Assafin, G. Benedetti-Rossi, A. Dias-Oliveira, A. R. Gomes-Júnior, R. Vieira-Martins, D. Bérard, P. Kervella, J. Lecacheux, E. Lellouch, W. Beisker, D. Dunham, M. Jelínek, R. Duffard, J. L. Ortiz, A. J. Castro-Tirado, R. Cunniffe, R. Querel, P. C. Yock, A. A. Cole, A. B. Giles, K. M. Hill, J. P. Beaulieu, M. Harnisch, R. Jansen, A. Pennell, S. Todd, W. H. Allen, P. B. Graham, B. Loader, G. McKay, J. Milner, S. Parker, M. A. Barry, J. Bradshaw, J. Broughton, L. Davis, H. Devillepoix, J. Drummond, L. Field, M. Forbes, D. Giles, R. Glassey, R. Groom, D. Hooper, R. Horvat, G. Hudson, R. Idaczyk, D. Jenke, B. Lade, J. Newman, P. Nosworthy, P. Purcell, P. F. Skilton, M. Streamer, M. Unwin, H. Watanabe, G. L. White, and D. Watson. Pluto's Atmosphere from the 2015 June 29 Ground-based Stellar Occultation at the Time of the New Horizons Flyby. ApJ, 819:L38, Mar. 2016. doi: 10.3847/2041-8205/819/2/L38.

W. C. Skamarock, J. B. Klemp, J. Dudhia, D. O. Gill, D. M. Barker, M. G. Duda, X. Y. Huang, W. Wang, and J. G. Powers. A description of the advanced research wrf version 3. Technical report, NCAR Technical Note NCAR/TN-475+STR, 2008.

R. H. Soja, W. J. Baggaley, P. Brown, and D. P. Hamilton. Dynamical resonant structures in meteoroid stream orbits. MNRAS, 414:1059–1076, June 2011. doi: 10.1111/j.1365-2966.2011.18442.x.

M. Sokolowski. *Investigation of astrophysical phenomena in short time scales with "Pi of the Sky" apparatus.* PhD thesis, -, Oct. 2008.

SonotaCo. A meteor shower catalog based on video observations in 2007-2008. *WGN, Journal of the International Meteor Organization*, 37:55–62, Apr. 2009.

R. B. Southworth and G. S. Hawkins. Statistics of meteor streams. *Smithsonian Contributions to Astrophysics*, 7:261, 1963.

P. Spurný. Exceptional fireballs photographed in central Europe during the period 1993-1996. Planet. Space Sci., 45:541–555, May 1997. doi: 10.1016/ S0032-0633(97)00006-8.

P. Spurný, J. Oberst, and D. Heinlein. Photographic observations of Neuschwanstein, a second meteorite from the orbit of the Příbram chondrite. Nature, 423:151–153, May 2003. doi: 10.1038/nature01592.

P. Spurný, J. Borovička, and L. Shrbený. Automation of the Czech part of the European fireball network: equipment, methods and first results. In *Near Earth Objects, our Celestial Neighbors: Opportunity and Risk*, volume 236, pages 121–130, May 2007. doi: 10.1017/S1743921307003146.

P. Spurný, J. Borovička, J. Kac, P. Kalenda, J. Atanackov, G. Kladnik, D. Heinlein, and T. Grau. Analysis of instrumental observations of the Jesenice meteorite fall on April 9, 2009. *Meteoritics and Planetary Science*, 45:1392–1407, Aug. 2010. doi: 10.1111/j.1945-5100.2010.01121.x.

P. Spurný, P. A. Bland, L. Shrbený, M. C. Towner, J. Borovička, A. W. R. Bevan, and D. Vaughan. The Mason Gully Meteorite Fall in SW Australia: Fireball Trajectory and Orbit from Photographic Records. *Meteoritics and Planetary Science Supplement*, 74:5101, Sept. 2011.

P. Spurný, P. A. Bland, J. Borovička, M. C. Towner, L. Shrbený, A. W. R. Bevan, and D. Vaughan. The Mason Gully Meteorite Fall in SW Australia: Fireball Trajectory, Luminosity, Dynamics, Orbit and Impact Position from Photographic Records. In *Asteroids, Comets, Meteors 2012*, volume 1667 of *LPI Contributions*, page 6369, May 2012a.

P. Spurný, P. A. Bland, L. Shrbený, J. Borovička, Z. Ceplecha, A. Singelton, A. W. R. Bevan, D. Vaughan, M. C. Towner, T. P. McClafferty, R. Toumi, and G. Deacon. The Bunburra Rockhole meteorite fall in SW Australia: fireball trajectory, luminosity, dynamics, orbit, and impact position from photographic and photoelectric records. *Meteoritics and Planetary Science*, 47: 163–185, Feb. 2012b. doi: 10.1111/j.1945-5100.2011.01321.x.

P. Spurný, J. Borovička, H. Haack, W. Singer, K. Jobse, and D. Keuer. Trajectory and orbit of the Maribo CM2 meteorite from optical, photoelectric and radar records. In *Meteoroids 2013*, 2013.

P. Spurný, J. Haloda, J. Borovička, L. Shrbený, and P. Halodová. Reanalysis of the Benešov bolide and recovery of polymict breccia meteorites - old mystery solved after 20 years. A&A, 570:A39, Oct. 2014. doi: 10.1051/0004-6361/201424308.

P. Spurný, J. Borovička, J. Haloda, L. Shrbený, and D. Heinlein. Two Very Precisely Instrumentally Documented Meteorite Falls: Žďár nad Sázavou and Stubenberg - Prediction and Reality. In *79th Annual Meeting of the Meteoritical Society*, volume 1921 of *LPI Contributions*, page 6221, Aug. 2016.

P. Spurný, J. Borovička, H. Mucke, and J. Svoreň. Discovery of a new branch of the Taurid meteoroid stream as a real source of potentially hazardous bodies. A&A, 605:A68, Sept. 2017. doi: 10.1051/0004-6361/201730787.

M. B. Taylor. TOPCAT & STIL: Starlink Table/VOTable Processing Software. In P. Shopbell, M. Britton, and R. Ebert, editors, *Astronomical Data Analysis Software and Systems XIV*, volume 347 of *Astronomical Society of the Pacific Conference Series*, page 29, Dec. 2005.

M. Towner and et al. Fireball streak detection with minimal CPU processing requirements for the Desert Fireball Network data processing pipeline. *PASA*, submitted.

J. M. Trigo-Rodríguez, J. Borovička, P. Spurný, J. L. Ortiz, J. A. Docobo, A. J. Castro-Tirado, and J. Llorca. The Villalbeto de la Peña meteorite fall: II.

Determination of atmospheric trajectory and orbit. *Meteoritics and Planetary Science*, 41:505–517, Apr. 2006. doi: 10.1111/j.1945-5100.2006.tb00478.x.

J. M. Trigo-Rodríguez, E. Lyytinen, M. Gritsevich, M. Moreno-Ibáñez, W. F. Bottke, I. Williams, V. Lupovka, V. Dmitriev, T. Kohout, and V. Grokhovsky. Orbit and dynamic origin of the recently recovered Annama's H5 chondrite. MNRAS, 449:2119–2127, May 2015. doi: 10.1093/mnras/stv378.

C. Tubiana, C. Snodgrass, R. Michelsen, H. Haack, H. Böhnhardt, A. Fitzsimmons, and I. P. Williams. 2P/Encke, the Taurid complex NEOs and the Maribo and Sutter's Mill meteorites. A&A, 584:A97, Dec. 2015. doi: 10.1051/0004-6361/201425512.

A. Unewisse and A. Cool. A Guide to the DST Airglow Database. Technical Report DST-Group-GD-0978, Defence Science and Technology (DST) Group, Oct. 2017.

S. E. Urban, T. E. Corbin, and G. L. Wycoff. The ACT Reference Catalog. AJ, 115:2161–2166, May 1998. doi: 10.1086/300344.

S. van der Walt, J. L. Schönberger, J. Nunez-Iglesias, F. Boulogne, J. D. Warner, N. Yager, E. Gouillart, and T. a. Yu. scikit-image: image processing in python. *PeerJ*, 2:e453, June 2014. ISSN 2167-8359. doi: 10.7717/peerj.453.

P. Vernazza, R. P. Binzel, C. A. Thomas, F. E. DeMeo, S. J. Bus, A. S. Rivkin, and A. T. Tokunaga. Compositional differences between meteorites and near-Earth asteroids. Nature, 454:858–860, Aug. 2008. doi: 10.1038/nature07154.

D. Vida, P. G. Brown, and M. Campbell-Brown. Modelling the measurement accuracy of pre-atmosphere velocities of meteoroids. MNRAS, 479:4307–4319, Oct. 2018. doi: 10.1093/mnras/sty1841.

D. Vokrouhlicky and P. Farinella. Orbital evolution of asteroidal fragments into the nu_6 resonance via Yarkovsky effects. A&A, 335:351–362, July 1998.

F. Whipple. *Photographic Meteor Studies, III. The Taurid Shower*. Harvard reprint. Astronomical Observatory of Harvard College, 1940.

F. L. Whipple. Photographic meteor studies I. In *Publications of the American Astronomical Society*, volume 9 of *Publications of the American Astronomical Society*, page 136, 1939.

F. L. Whipple and S. El-Din Hamid. On the Origin of the Taurid Meteor Streams. *Helwan Institute of Astronomy and Geophysics Bulletins*, 41:3–30, 1952.

J. Wisdom. Meteorites may follow a chaotic route to Earth. Nature, 315:731–733, June 1985. doi: 10.1038/315731a0.

X. Zhang, P. Hancock, H. A. R. Devillepoix, R. B. Wayth, A. Beardsley, B. Crosse, D. Emrich, T. M. O. Franzen, B. M. Gaensler, L. Horsley, M. Johnston-Hollitt, D. L. Kaplan, D. Kenney, M. F. Morales, D. Pallot, K. Steele, S. J. Tingay, C. M. Trott, M. Walker, A. Williams, C. Wu, J. Ji, and Y. Ma. Limits on radio emission from meteors using the MWA. MNRAS, 477:5167–5176, July 2018. doi: 10.1093/mnras/sty930.